

**Structurally controlled fluid flow in
geothermal reservoirs: Insights from
the field and laboratory**



UNIVERSITY OF
LIVERPOOL

*Thesis submitted in accordance with the requirements of the
University of Liverpool for the degree of Doctor in Philosophy by*

Steven John Beynon

March 2022

For Kim,

who supported me throughout this journey,

and for Éowyn,

who joined us along the way

Declaration of Authorship and Funding Information

I, Steven John Beynon, declare that this thesis, “Structurally controlled fluid flow in geothermal reservoirs: Insights from the field and laboratory” and the work presented in it are my own.

I confirm that:

- This thesis was completed as a part of a research degree at the University of Liverpool.
- The material contained in the thesis has not been presented, nor is currently being presented, either wholly or in parts, for any other degree or qualifications.
- Where I have consulted published studies, this has been clearly referenced.
- Where the work was part of a collaborative effort, I have made clear what others have done and what I have contributed myself.

Parts of the thesis have been published or are in preparation for publication as:

Chapter 2: Beynon, S.J., Faulkner, D.R., McNamara, D.D., Gomila, R. and Jensen E. (*In Preparation*) **Structural Controls on Fluid Circulation in a Transtensional Duplex: Lessons from an Exhumed Geothermal System.**

- *Author contributions and affiliations:* Steven J. Beynon (School of Environmental Science, University of Liverpool, UK): Conceptualisation, Methodology, Investigation and Data Collection, Formal Analysis, Validation, Visualisation, Writing (Original Draft);
Daniel R. Faulkner (School of Environmental Science, University of Liverpool, UK): Conceptualisation, Supervision, Funding Acquisition, Visualisation, Writing (Review & Editing);
David D. McNamara (School of Environmental Science, University of Liverpool, UK): Conceptualisation, Supervision, Visualisation, Writing (Review & Editing);
Rodrigo Gomila (Department of Geosciences, University of Padova, Italy): Investigation (Data collection);
Erik Jensen (Department of Geological Sciences, Universidad Católica del Norte, Antofagasta, Chile): Investigation (Data collection).

Chapter 3: Beynon, S.J., McNamara, D.D., Faulkner, D.R., Jensen, E. and Gomila, R. (*In Preparation*) **The Creation and Maintenance of Structural Permeability: Unravelling the Temporal Evolution of Fluid Flow in an Exhumed Duplex-Hosted Geothermal System.**

- *Author contributions and affiliations:* Steven J. Beynon (School of Environmental Science, University of Liverpool, UK): Conceptualisation, Methodology, Investigation and Data Collection, Formal Analysis, Validation, Visualisation, Writing (Original Draft);

David D. McNamara (School of Environmental Science, University of Liverpool, UK): Conceptualisation, Supervision, Visualisation, Writing (Review & Editing);

Daniel R. Faulkner (School of Environmental Science, University of Liverpool, UK): Supervision, Funding Acquisition, Visualisation;

Rodrigo Gomila (Department of Geosciences, University of Padova, Italy): Investigation (Data collection);

Erik Jensen (Department of Geological Sciences, Universidad Católica del Norte, Antofagasta, Chile): Investigation (Data collection).

Chapter 4: Beynon, S.J. and Faulkner, D.R. (2020) Dry, damp, or drenched? The Effect of Water Saturation on the Frictional Properties of Clay Fault Gouges, *Journal of Structural Geology* 140, 104094.

- Submitted 6 December 2019; Revised 10 May 2020; Accepted 18 May 2020.
- (Note some minor modifications to the published version of this chapter have been made to provide more context within the wider framework of the thesis).
- Author contributions and affiliations: Steven J. Beynon: Methodology, Investigation, Formal Analysis, Validation, Visualisation, Writing (Original Draft);
Daniel R. Faulkner: Conceptualisation, Supervision, Funding Acquisition, Visualisation, Writing (Review & Editing).

Parts of the thesis also form the basis of extended conference abstracts (and associated presentations), with author affiliations and contributions as stated above:

- **Elements of Chapters 2 and 3:** Beynon, S.J., McNamara, D.D., Faulkner, D.R., Gomila, R., Jensen E. and Lavallee, Y. (2021) Structural controls on fluid circulation in a transtensional duplex: Lessons from an exhumed geothermal system (Atacama Fault Zone, Chile), *Proceedings of the World Geothermal Congress, Reykjavik, Iceland, 21-26 May 2021*.
- **Elements of Chapter 5:** Beynon, S.J., Faulkner, D.R., McNamara, D.D. and Lavallee, Y. (2021) An Experimental Approach to Assist in Quantifying Fracture Sealing Mechanisms in Geothermal Systems, *Proceedings of the World Geothermal Congress, Reykjavik, Iceland, 21-26 May 2021*.

Parts of the thesis have formed the basis of short conference abstracts (and associated posters or presentations) as detailed below, with author affiliations and contributions as stated above:

- **Elements of Chapter 2:** Beynon, S.J., Faulkner, D.R., McNamara, D.D., Gomila, R. and Jensen E. (2021) Fluid Flow in an Exhumed Geothermal System: Exploring the distribution of structural permeability in a transtensional duplex (Atacama Fault Zone, Chile). 12th *European Geothermal PhD Days (Online), 15-16 February 2021*.

- **Elements of Chapter 3:** Beynon, S.J., McNamara, D.D., Faulkner, D.R. and Lavalley, Y. (2020) Fluid Flow in an Exhumed Geothermal System: Hydrothermal Vein Morphology and Composition within the Atacama Fault Zone, Chile. *Proceedings: Tectonic Studies Group Annual Meeting, Hull, UK, 7-9 January 2020.*
- **Elements of Chapter 4:** Beynon, S.J., Faulkner, D.R., Lavalley, Y. and McNamara, D.D. (2018) Investigating clay-bearing fractures in geothermal reservoirs using triaxial shear deformation. *9th European Geothermal PhD Days, Zurich, 14-16 March 2018.*

Beynon, S.J. and Faulkner, D.R. (2019) Dry, damp or drenched? The effect of water on the frictional properties of clay fault gouges. *Proceedings: Tectonic Studies Group Annual Meeting, Bergen, Norway, 14-16 January 2019.*

Beynon, S.J. and Faulkner, D.R. (2019) Dry, damp or drenched? Experimentally measuring the effect of pore fluid on the frictional properties of clay fault gouges. *Proceedings: Gordon Research Conference on Rock Deformation, Boston, Massachusetts, 18-24 August 2019.*

Beynon, S.J. and Faulkner, D.R. (2019) The effect of 'dryness' on the frictional properties of clay fault gouges. *Proceedings: American Geophysical Union Annual Conference, San Francisco, California, 9-13 December 2019.*
- **Elements of Chapter 5:** Beynon, S.J., Faulkner D.R., McNamara, D.D. and Lavalley, Y. (2019) The effect of fluid pressure and composition on hydrothermal vein precipitation rate, permeability and microstructure. *Proceedings: Tectonic Studies Group Annual Meeting, Bergen, Norway, 14-16 January 2019.*

Finally, a report produced during an internship undertaken as part of a three-month break from this PhD, submitted to the British Geological Survey on 31st March 2020, contains some information similar to aspects of the methodology in Chapters 3 and 4:

- Beynon, S.J. (2020) Geomechanical Properties of the Carboniferous Middle Coal Measures: Influence on fracture fluid flow and frictional stability during geothermal utilisation. *Unpublished Report.*

Funding: Work presented within this thesis was conducted during a PhD study supported by the Natural Environment Research Council (NERC) EAO Doctoral Training Partnership, fully funded by NERC (Grant ref. no. NE/L002469/1).

Signed:



Steven Beynon

March 2022.

Abstract

The understanding of fluid flow within the Earth's crust is of great importance to our knowledge of geohazards (such as earthquakes) and use of georesources (such as geothermal energy). Fluid flow in crystalline rocks is largely controlled by the permeability of faults and their associated fracture networks, the physical properties and temporal history of which can control to what degree they act as flow conduits or barriers. Better constraints are required as to how these fracture networks form, how fluids are transported within them, how they respond to deformation and how permeability may evolve with time. In an applied context, this insight into the physiochemical processes ongoing in deep, high temperature, fractured hydrothermal systems has the potential to increase the long-term productivity and sustainability of geothermal energy production.

Since fault properties and behaviours are difficult to observe at depth, an approach using field analogues and laboratory experiments is key to understanding such complex systems. In the field, an exhumed duplex-hosted hydrothermal system was studied (using statistical analyses of mechanical damage and mineralogical data from fractures sealed by epithermal precipitation) to investigate the fault properties that control the spatial and temporal heterogeneity of structurally controlled fluid flow within fault damage zones. In the laboratory, a range of thin section analyses and experimental rock deformation techniques are employed to investigate how hydrothermal fluid flow affects the composition, texture and mechanical behaviour of altered host rock and epithermal veins within it. The frictional strength and stability of argillic alteration (i.e. clay 'gouges' more typical of fault cores) is also investigated experimentally, with a focus on the effect of fluids on deformation processes.

Field data show that the density and connectivity of structural damage across the studied fault duplex is predictably heterogeneous at a range of scales, conforming to previous observations suggesting that such variation may be caused by the amount of fault displacement coupled with regional fault density. Analysis of epithermal precipitation within fractures reveals that in general fluid flow is greatest in areas of high structural density, with most sealing by precipitation having occurred in thin fractures favourably oriented perpendicular to the minimum principal stress (σ_3). Laboratory data indicate that the nature of precipitation (i.e. vein composition and texture) evolves both spatially and temporally. Furthermore, the degree of propylitic alteration in the fractured host rock appears to control where subsequent creation of structural permeability takes place, rather than the presence of a vein itself as a planar discontinuity. With regards to argillic alteration, the frictional strength of clay fault gouges increases as water is progressively removed, whilst their frictional stability decreases, suggesting that the saturation state of clays may play a part in controlling permeability and fluid flow through seismicity. The presence of water appears to be key in promoting time- and slip-

dependent frictional changes, constraining operative grain-scale deformation mechanisms to those that are fluid assisted.

The data presented here have important implications for geothermal exploration, as well as elements of production and stimulation by fluid injection within Enhanced Geothermal Systems. It is understood that further insight could be gained through a more quantitative understanding of fracture sealing processes that commonly cause issues with flow rates in geothermal wells, namely the influence of changing fluid pressures, temperatures and chemistries on the nature, rate and volume of precipitation. With this goal in mind, a new high-pressure, high temperature triaxial deformation apparatus has been designed and built to simulate a range of upper crustal geothermal gradients whilst under confining pressure. Here, the new apparatus is described in detail, and a suite of experiments is proposed based on a comprehensive literature review, whereby fluid containing minerals in solution can be flowed through a fractured rock core at a range of carefully controlled physical conditions. It is hoped that this experimental setup may soon provide crucial data to help improve models of fluid flow and permeability evolution in structurally controlled geothermal reservoirs, and ultimately the long-term productivity and sustainability of geothermal energy production.

Table of Contents

<u>Declaration of Authorship and Funding Information</u>	I
<u>Abstract</u>	IV
<u>Table of Contents</u>	VI
<u>List of Figures</u>	IX
<u>List of Tables</u>	XII
<u>Acknowledgements</u>	XIII
<u>1 Introduction</u>	1
1.1 Context: The Significance of Structurally Controlled Fluid Flow	1
1.2 Background: The Distribution, Formation and Destruction of Structural Permeability and its Implications for Geothermal Energy	3
1.2.1 Fault Zone Architecture and Rheology in the Upper Crust	3
1.2.2 Fracture formation and Permeability Creation	6
1.2.3 Permeability Destruction (Fracture Sealing)	11
1.2.4 Application to fractured geothermal reservoirs	15
1.3 Methodological Overview: Approaches to understanding fracture-hosted fluid flow and strength	19
1.4 Summary and Thesis Structure	23
<u>2 Structural Controls on Fluid Circulation in a Transtensional Duplex: Lessons from an Exhumed Geothermal System</u>	26
Abstract	26
2.1 Introduction	26
2.2 Geological Setting	30
2.3 Methodology	33
2.4 Results	36
2.4.1 Large-Scale 2D Fault Distribution Within the Fault Duplex	36
2.4.2 Fracture Damage Surrounding Duplex Faults (1D)	37
2.4.3 Vein Thickness Within Fault Damage Zones (1D)	41
2.4.4 2D Damage Distribution Within Fault Damage Zones	47
2.5 Discussion	49
2.5.1 Fault and Fracture Density Within and Outside of the Duplex	49
2.5.2 Damage Distributions on Individual Faults (1D)	50
2.5.3 Heterogenous 2D Damage Distribution	52
2.5.4 Implications for Hydrothermal Fluid Flow in Dilatational Fault Duplexes	53
2.6 Conclusions	56

3	<u>The Creation and Maintenance of Structural Permeability: Unravelling the Temporal Evolution of Fluid Flow in an Exhumed Duplex-Hosted Geothermal System</u>	58
	Abstract	58
	3.1 Introduction	59
	3.2 Geological Setting and Site Overview	63
	3.3 Methodology	64
	3.4 Results	66
	3.4.1 Vein Mineralogy and Microstructures	66
	3.4.2 Regional Distribution of Precipitate	71
	3.4.3 Structural Orientations of Vein Phases	73
	3.4.4 Laboratory Insights into Vein Reactivation	79
	3.5 Discussion	82
	3.5.1 Spatial and temporal variation of fluid flow in a duplex hosted geothermal system as recorded by hydrothermal veining	82
	3.5.2 The influence of hydrothermal veining and alteration on mechanical strength and maintenance of structural permeability	87
	3.6 Conclusions	90
4	<u>The Effect of Water Saturation on the Frictional Properties of Clay Fault Gouges</u>	92
	Abstract	92
	4.1 Introduction	92
	4.2 Methodology	96
	4.2.1 Phyllosilicate Gouge Sample Properties	97
	4.2.2 Sample Preparation	98
	4.2.3 Experimental Procedure	100
	4.2.4 Data Analysis	103
	4.3 Results	104
	4.3.1 Analysis of Absolute Water Content	104
	4.3.2 Friction Coefficient	105
	4.3.3 Rate and State Parameters	108
	4.3.4 Kaolinite Microstructure	110
	4.4 Discussion	111
	4.4.1 Evolution of Friction Coefficient with Saturation State	111
	4.4.2 Evolution of Rate and State Parameters	114
	4.4.3 Evolution of strength, stability, and microstructure	116
	4.4.4 Implications of Study for Fault Slip in Nature and Experiments	117
	4.5 Conclusions	119
5	<u>The Design of a Novel Experimental Approach to Investigate the Nature, Rate and Volume of Fracture Sealing in Geothermal Systems</u>	121
	Abstract	121
	5.1 Introduction	121
	5.2 Potential Controls on the Nature and Volume of Precipitation	124
	5.2.1 Controls on Deviation from Chemical Equilibrium	124

5.2.2	Controls on Mineral and Vein Textures	129
5.2.3	Controls on the Rate and Volume of Precipitation	132
5.2.4	Experimental Approaches – A Brief Review	137
5.3	Design Specifications and Calibration of a High-Temperature, High-Pressure Triaxial Deformation Apparatus	139
5.3.1	Introduction	139
5.3.2	Overview of Design	141
5.3.3	Design Specifics	142
5.3.4	Testing and Calibration	162
5.4	Experiments to Investigate the Nature, Rate and Volume of Precipitate	167
5.4.1	Overview	167
5.4.2	Creating a Range of Experimental Variables	168
5.4.3	Subsequent Analysis of Experimental Cores	176
5.5	Discussion	176
5.5.1	Relating Chemical Disequilibrium in Simple Systems to More Complex Natural Geothermal Systems	176
5.5.2	Expected Experimental Vein Textures and Their Applicability to Natural Veins	179
5.6	Summary	183
6	Summary, Implications and Future Work	186
6.1	Recap of Context and Research Approach	186
6.2	Results and Implications	189
6.2.1	How is Fault Damage - and Hence Structural Permeability - Spatially Distributed Across a Fault Zone?	189
6.2.2	How do Early Phases of Fracture Sealing Influence Subsequent Fluid Flow Events, and Therefore the Temporal Evolution of Structural Permeability?	190
6.2.3	How do Hydrothermal Fluids and Resultant Alteration Mineralogy Affect the Mechanical and Frictional Strength of a Fractured Geothermal Reservoir?	191
6.2.4	What are the Key Controls on the Nature, Rate and Volume of Precipitation in Structurally Hosted Hydrothermal Systems?	192
6.3	Suggestions for Future Work	193
References		196
Appendices		223
A	: Fieldwork Methodology and Data	223
B	: Laboratory Methodology and Data	23634
C	: Supplementary Information for the New High-Pressure, High-Temperature Deformation Apparatus	2475
Digital Appendices		27674

List of Figures

Figure 1.1: An illustration of the types of geothermal resource available for exploitation	1
Figure 1.2: The relationship between fault architecture, fracture density and permeability	3
Figure 1.3: a) Schematic frictional response to steps in sliding velocity b) Variations in friction coefficient and constitute parameters a-b for rocks with different clay contents	6
Figure 1.4: Schematic illustration of a fracture and parameters that define fluid flow, in the context of a) a fracture at outcrop and b) an experimental core sample	7
Figure 1.5: a) Griffith-Mohr-Coulomb failure criteria for Mode I, II and III fractures depicted in Mohr space b) Effects of different types of fault interaction on the angles at which extension veins may form in a damage zone	9
Figure 1.6: Conceptual models for vein formation: a) Pump model b) Valve model c) Fluid pressure excursion model	10
Figure 1.7: An illustration of the transient nature of permeability in a hydrothermal fracture network	12
Figure 1.8: Schematic classification of vein textures	13
Figure 1.9: Examples of the types of regional structures most favourable to allowing sustained, high temperature geothermal fluid upwelling	16
Figure 1.10: Stability ranges of alteration minerals commonly found within hydrothermal systems	17
Figure 1.11: a) Example of a hydrothermally sealed fracture formed at depth b) Example of geothermal pipework infrastructure with significant calcite scaling	18
Figure 1.12: a) Schematic diagram of a linear scanline b) A grid of terms used to describe fracture/vein spatial distribution c) An illustration of how intersecting fractures can be categorized	20
Figure 1.13: a) Schematic drawing of the Faulkner triaxial apparatus b) Front control panel of the triaxial apparatus c) Uniaxial loading apparatus with a Brazilian jig in place	21
Figure 1.14: Summary of the rationale behind key questions to be addressed within this thesis, and a brief overview of how each of the core chapters presented here aims to address them	25
Figure 2.1: The relationship between fault architecture, fracture density and permeability	28
Figure 2.2: a) & b) Simplified structural maps of the Atacama Fault System c) Simplified geological map of the field area d) Simplified schematic diagrams of a transtensional duplex	31
Figure 2.3: a) Outcrop of the Bolfin Fault showing the progression from fault gouge, through foliated and unfoliated cataclasite to the damage zone b) Photograph illustrating the methodology of 1D transects c) Photograph illustrating part of a 2D outcrop map, where veins were digitally traced. Photographs d) to i) are examples of veins at damage zone outcrops	32
Figure 2.4: a) Schematic diagram of a linear scanline b) An illustration of terms used to describe fracture/vein spatial distribution	34
Figure 2.5: Regional variation in fault intensity and frequency across the Caleta-Coloso Duplex	37
Figure 2.6: a) Mean normalised vein intensity and mean vein spacing for all veins intersected with 1D transects b) Bias-corrected average normalised vein intensity at each site	38
Figure 2.7: a) Range of normalised total vein thickness for each site b) Relationship between normalised total vein thickness & bias-corrected normalised vein intensity for each transect	43
Figure 2.8: Maps of vein traces with 2D vein frequency and intensity	48
Figure 2.9: a) Maps of all vein traces with 2D vein connectivity b) A ternary plot showing the proportion of connecting node types between vein traces at each site	49
Figure 2.10: Log-linear plot of normalised vein intensity with distance from second-order fault	51
Figure 3.1: a) & b) Simplified structural maps of the Atacama Fault System c) Simplified geological map of the field area d) Simplified schematic diagrams of a transtensional duplex	63
Figure 3.2: Photomicrograph images, backscatter scanning electron microscopy images, and cathodoluminescence images highlighting the range of mineral compositions, textures, and relationships across the duplex a) temporally and b) spatially, with c) also highlighting examples crack-seal and stretching vein textures	69
Figure 3.3: a) Regional variation in the amount and type of precipitate across the duplex b) Relative amounts of total measured vein material across the duplex for each vein phase	72
Figure 3.4: Kamb contour stereonet and rose plots of total vein precipitate by orientation	74

Figure 3.5: Vein thickness distributions and rose plots of total vein precipitate and bias-corrected orientation frequency	75
Figure 3.6: Bar chart displaying the number of crack-seal/stretching veins at each site across the duplex. Rose plots illustrate the variation in orientations of crack-seal/stretching veins	78
Figure 3.7: a) Laboratory setup of the Brazilian Jig b) Laboratory data showing the tensile strength of chlorite and epidote veins in Mode I (0°) and Mode II/III (30°, 60°) orientations as well as at 90° to the compressional axis c) Typical experimental fracture traces from Brazilian tests on samples represented in plot b)	80
Figure 3.8: a) Thin section images of relatively unaltered host rock and relatively altered host rock b) XRD-determined mineralogical compositions of unaltered and altered host rock. c) Photograph showing the experimental setup for unconfined compressional strength (UCS) tests. d) Laboratory data showing the UCS of unaltered and altered host rock as well as chlorite and epidote veins in Mode I orientations (0° to compressional axis)	81
Figure 3.9: a) Summary radar plot showing the percentage of all measured vein precipitate and all measured veins across the duplex b) Radar plots for each successive vein phase	86
Figure 3.10: Summary of modelled data showing the effect of vein orientation on successive tensile fracturing in low, medium and high strength ratios of host rock to veins	88
Figure 4.1: Schematic frictional response to steps in sliding velocity for a) velocity- strengthening friction and b) velocity-weakening friction	95
Figure 4.2: Crystal structures of a) 1:1 Kaolinite and b) 2:1 Mg-Montmorillonite c) Interlayer water films affect the frictional properties of sheet materials	98
Figure 4.3: a) Sample assembly setup prior to being placed into the pressure vessel b) Schematic representation of a vacuum connection to the sample assembly	99
Figure 4.4: Modelled simulation of the time taken to equilibrate a vacuum across a ~1 mm thick kaolinite-rich gouge sample	102
Figure 4.5: Method used to determine yield friction coefficient (μ_y) in a) a typical example of a saturated sample, and b) a typical example of a dry sample	103
Figure 4.6: a) Results of Thermogravimetric Analysis (TGA) performed on initially room humidity kaolinite and montmorillonite b) Results of mass loss during heating to 130 °C in a vacuum oven	105
Figure 4.7: Friction coefficient evolution with displacement for a) kaolinite-rich china clay and b) Mg-montmorillonite at different saturation states	106
Figure 4.8: Summary of yield and steady state friction coefficients for kaolinite-rich china clay and Mg-montmorillonite	107
Figure 4.9: a) a-b values; b) a values, c) b values and d) dc values for i) kaolinite-rich china clay and ii) Mg-montmorillonite for each saturation state scenario	110
Figure 4.10: SEM image of typical microstructures exhibited in kaolinite-rich gouge when a), b) and c) saturated, d), e) and f) at room humidity, g), h) and i) vacuum dry and j), k) and l) heated in a pressure vessel to 130 °C and allowed to cool before shearing	111
Figure 5.1: A summary of key questions to be addressed within this chapter and through planned experimental work	123
Figure 5.2: Phase diagram for water highlighting the temperature and pressure conditions explored in this study	125
Figure 5.3: Concentration (ppm) v water temperature (°C) plots for a) SiO ₂ crystallinity b) calcite, at various confining pressures c) calcite, w with various partial pressures of CO ₂ and d) calcite, with various water salinities	126
Figure 5.4: Confining Pressure v Dissolved Mineral Concentration (Solubility) with changes in temperature for a) Amorphous Silica and b) Calcite	127
Figure 5.5: Conceptual models for vein formation a) Pump model b) Valve model c) Fluid pressure excursion model	130
Figure 5.6: Schematic classification of vein textures	131
Figure 5.7: a) Quartz precipitation rate constants with temperature estimated b) Relationships between calcite saturation, flow velocities, vein apertures, vein lengths and precipitation rate	135

Figure 5.8: a) Schematic drawing of the Faulkner triaxial apparatus b) An illustration of how confining and pore pressures are introduced, controlled and measured	139
Figure 5.9: Experimental setup used to investigate the impact of fluid chemistry (supersaturated fluids) on rock permeability.	140
Figure 5.10: Graphical representation of the constructed assembly	141
Figure 5.11: Technical drawing of the sample assembly within the 'HY2' pressure vessel	142
Figure 5.12: Photographs showing furnace preparation at several stages	143
Figure 5.13: A plot illustrating kanthal wire resistivity	144
Figure 5.14: Schematic illustration of the furnace and windings	145
Figure 5.15: Technical drawing of the sample assembly	146
Figure 5.16: a) The completed furnace b) Detailed view of banana jacks within the two upper MACOR® plates c) View from the bottom of the assembly of the furnace within the stainless-steel can, surrounded by tightly packed alumina wool insulation d) Side view of the assembly	151
Figure 5.17: Schematic illustration of the new design of a collar to fit the recessed area of the upper piston in Sample Assembly B in order to limit gas convection around the piston	152
Figure 5.18: Schematic illustration of the sample configuration for calibration	153
Figure 5.19: a) Top-view photograph showing the constructed assembly b) Photograph showing how Sample Assembly B, with jacketed sample and Sample Assembly C attached as in Figure 5.18, is inserted into the central bore	154
Figure 5.20: Photograph of the pressure vessel and surrounding high-pressure pipework showing the electrical feeds connected up	155
Figure 5.21: Photographs of the temperature control box	156
Figure 5.22: Schematic diagram showing a top view of Sample Assembly A, illustrating how connections are made between the temperature control box and the sample assembly	157
Figure 5.23: A sketch illustrating the connecting end of the furnace power cables that thread into the brass Top Bus Clamps within Sample Assembly A	157
Figure 5.24: Electrical circuit diagram of the temperature control unit	158
Figure 5.25: The P6100 WEST Controller	158
Figure 5.26: Diagram depicting the design of a new front panel for the temperature control unit	159
Figure 5.27: Schematic illustration of the cooling jackets and baseplate	160
Figure 5.28: Photograph showing the cooling jackets around the pressure vessel and connected to the water mains	160
Figure 5.29: Schematic diagram highlighting the key areas to measure temperature with a variable thermocouple, as well as the position of a control thermocouple	163
Figure 5.30: A webcam image and schematic representation of the scale used to measure the relative position of the variable and control thermocouples within the sample assembly	164
Figure 5.31: A temperature profile recorded by the variable calibration thermocouple	166
Figure 5.32: Schematic summary diagram of a) the experimental sample setup and b) the range of experimental conditions (varying temperature, fluid pressure and rate of change)	167
Figure 5.33: Aerial maps and author's photograph showing the sampling location of quartzite used for experimental cores.	168
Figure 5.34: A visual overview of the types of experiment to be conducted and expected degrees of disequilibrium of the fluid with respect to amorphous silica for each	174
Figure 5.35: Natural vein textures in the literature inferred to have precipitated quickly from supersaturated solutions upon a dramatic change in hydrothermal conditions	180
Figure 5.36: Syntaxial alum vein microstructures (after Hilgers et al., 2004)	181
Figure 5.37: Photomicrographs showing the composition and microstructures of SiO ₂ precipitate from the experiments of Okamoto et al. (2010)	182

List of Tables

<i>Table 2.1: A description of field sites across the study area</i>	36
<i>Table 2.2: a) Intensity and b) spacing data from analyses of 1D transects at Sites 1-5</i>	39
<i>Table 2.3: Intensity data from analyses of 1D transects at Sites 1-5 for the chlorite-epidote-quartz vein phase and the calcite-dominated vein phase</i>	41
<i>Table 2.4: a) Epidote-bearing vein thickness data from analyses of 1D transects b) Cumulative thickness statistics: mean, median, skewness, kurtosis, and coefficient of variation</i>	44
<i>Table 2.5: Total amount of vein precipitate, normalised for transect length, from analyses of 1D transects for the chlorite-epidote-quartz vein phase and the calcite-dominated vein phase</i>	46
<i>Table 2.6: Intensity (P_{21}) and frequency (P_{20}) data from vein trace analyses at 2D outcrops for Sites 1a, 3 and 4</i>	47
<i>Table 3.1: A description of field sites across the study area</i>	65
<i>Table 3.2: Total measured amount of precipitate by vein phase (mm) and proportions of vein phases by site (%)</i>	71
<i>Table 3.3: Proportions of vein phases across the duplex (%)</i>	71
<i>Table 3.4: Calculations of the Mineralogy Value for relatively altered and unaltered host rocks used in laboratory experiments</i>	90
<i>Table 4.1: Yield and steady state friction coefficient (μ) data for experiments on kaolinite-rich china clay and Mg-montmorillonite</i>	108
<i>Table 5.1: Descriptions of fundamental parts of the sample assembly</i>	148
<i>Table 5.2: Suggested calibrations to perform prior to any experimental work</i>	165
<i>Table 5.3: Outline of the order of preparation and measurements for proposed experimental work</i>	169
<i>Table 5.4: Range of planned experiments using amorphous silica as a mineral aggregate</i>	173
<i>Table 5.5: Expected results of the above experiments based on theoretical data</i>	174
<i>Table 5.6: Summary of fluid pressure gradients required to induce flow rates comparable to natural fractured reservoirs</i>	176

Acknowledgements

Behind the text, data and figures of this thesis lies the story of an undulating personal journey. It's been a journey that in many ways exceeded expectations, teaching me some invaluable lessons, giving me some incredible experiences, and developing me both as a scientist and as a person. It's also been a journey impacted by many life-changing events that were largely unforeseen at the beginning: getting married, raising a daughter and being caught in the midst of a global pandemic. Ultimately, it's been an unforgettable journey.

First and foremost, I would like to thank my supervisors, Dan, Dave and Yan, for giving me the opportunity to embark on this PhD in the first place, and for their support and encouragement throughout the process. Most of all, I am indebted to their combined vast amount of knowledge and experience that was always on hand, from which I have benefitted greatly. Each have had their part in steering my research path, linking me with new people, providing good advice and company along the way whilst keeping me optimistic through their own passion for the subject. Dan apparently has endless knowledge and curiosity when it comes to experimental techniques (as well endless anecdotes about travel-related mishaps!). Dave – and Yan – always helped to relate everything back to geothermal applications, and always had time to chat even when swamped with other work. I'd also like to acknowledge the varied contributions of other staff members, in particular Betty, John and Janine, each of whom added to my overall experience in many ways. I came into this PhD thinking I knew a fair amount about structural geology, volcanology and geothermal energy, excited to learn more about all of them alongside rock deformation, seismology and mineralogy. After a few years with those named above, I finish knowing so much more, yet knowing also that the knowledge I do have is just a drop in the ocean – this has been a very humbling experience.

I am grateful to NERC and the EAO-DTP for providing funding and plentiful training opportunities throughout the PhD – without them, this project would not have even begun. I would also like to thank many others at the University of Liverpool, mainly within the Rock Deformation Laboratory and Experimental Volcanology Laboratory but also in the CTL, for enriching my experience in many ways. Gary, Mike and John were the go-to guys for any practical advice on anything to do with the lab and workshop, as well as the main providers of entertainment throughout each lab day. They gave up much of their time to help me, particularly in the early days of my experimental work but also throughout the build of the new assembly. From their teaching I feel much more capable to do anything that involves just a bit of thought and DIY – both in the lab and outside. I'd also like to thank fellow PhD students from the two labs – namely Josh, Jenny, Amy, Izzy, Louisa, Elliot, the two Joes and Laura – as well as a few visiting post-docs (particularly Sabine and Marieke) for good companionship and discussions throughout the course of the PhD. I'm also grateful for the good times spent with students on the wider DTP programme (Josh had the pleasure of being my designated

roommate on all these events - cheers for putting up with me!), and the experience I gained whilst demonstrating – most notably driving a minibus full of students across Tenerife...

I was fortunate to have the chance to meet and work with many others through the course of my PhD. My field trips to Chile (and visit to Padova) would not have been possible or enjoyable without the help and companionship of Rodrigo, Erik, Simone, Guilio, Michele, Guilia and Elena – thanks to all for an unforgettable two months in the desert! We are all indebted to Rodrigo's family for putting us up in Antofagasta, too. I take with me some fantastic memories from Chile and hope to return to the rocks, stars, camanchaca, empanadas and pisco one day. Through various lab visits and conferences I have also had the pleasure to spend time with a number of people – too many to list individually here, in Manchester, Durham, Plymouth, Zurich, Boston and Bergen – that have each provided a memorable highlight of my PhD and invariably also taught me something new. I am also grateful to Alison and the team of people involved in the UKGEOS Glasgow internships, too, for giving me the opportunity to be involved in the project and gaining valuable experience in writing proposals and applying my research.

Finally, a note to my friends and family: I'm incredibly grateful to all of you who have all played important parts in getting me to where I am today and helped me through a challenging few years – whether you know it or not, I couldn't have done any of this without you. (I'd name you all, but you probably won't read this anyway...). Kim – you encouraged me to do this in the first place and kept me going, for which I both thank you and question why you wanted to put me through all of that! It's been a rollercoaster few years for both of us, and all the words written here (which I doubt even you will read!) all contain memories of every one of those ups and downs. Whilst I was writing Chapter 2, we were spending all our free time building the campervan. We got married as I was concluding Chapter 4 and preparing it for publication. I wrote large parts of Chapter 3 in the sunny garden as you were getting ready to pop and the world went into lockdown (we never did make it to Iceland...). Éowyn was born the day after I produced Figure 3.3, and she certainly made finishing Chapter 5 a challenge (alongside lockdown measures), but also more of a reason to see it all through to the end.

I had big plans for this thesis. My 'to-do' list could have at least doubled its length, and I will always wonder what could have been if I'd explored different avenues – or more importantly, if my work hadn't been rudely interrupted by a pandemic whilst experiencing depression and then raising a child. Nevertheless, I'm proud of everything presented in this thesis and will look back on it fondly from wherever my journey leads next.

As geothermal fluids interact with the host rock during flow, however, changing physiochemical conditions often cause minerals held within solution to precipitate, with the potential to drastically reduce fluid flow rates or even 'switch off' the geothermal system entirely (e.g. Davatzes and Hickman, 2012; Griffiths et al., 2016). Enhanced Geothermal Systems (EGS), which often require a degree of stimulation to create or maintain a permeable fracture network at depth, are receiving more attention in recent years, however require significant geomechanical de-risking to become economically viable (Ghassemi, 2012; Boretti, 2022). For both conventional geothermal and EGS reservoirs, better constraints of how fracture networks form, how they evolve with time and how fluids are transported in these systems will help define more accurate models and potentially increase the long-term productivity and sustainability of fluid flow within fractured reservoirs (e.g. Zimmermann et al., 2009; Ghassemi, 2012).

The study of fault distribution and development in the upper crust provides insights into the mechanical, hydraulic and seismic properties of the fault and its associated fracture network, and ultimately aids the understanding of structurally controlled fluid flow (Caine et al., 1996; Chester et al., 1993; Hickman et al., 1995; Gudmundsson et al., 2001; Faulkner et al., 2003, 2008; Wibberley and Shimamoto, 2003). The physical properties and temporal history of faults can control to what degree they act as high-permeability flow conduits or impermeable barriers (e.g. Sibson, 1996). Permeability is largely governed by a balance of fracture formation processes (e.g. brittle failure) and fracture destruction processes (e.g. mechanical wear or hydrothermal mineral precipitation) (Sibson, 1994; Wibberley et al., 2008). Whilst many aspects of permeability distribution within faults and the wear/precipitation mechanisms that can affect it are well understood, many questions remain, such as how permeability varies between interacting faults, and how hydrothermal precipitation affects long-term permeability evolution and mechanical strength (e.g. Ghassemi, 2012). Such fault properties and behaviours are difficult to observe at depth, hence an approach using field analogues and laboratory experiments is key to understanding such complex systems.

This chapter provides a brief overview of several aspects of upper crustal rock deformation and fluid flow that will be built upon in greater depth in subsequent chapters, with *Section 1.2* focussing on the structure of fault zones, their transient permeability, and the nature of hydrothermal mineralisation, as well as the application of such knowledge to fractured geothermal reservoirs. Methodological approaches to understanding fracture-hosted fluid flow and strength based on theory and practise in field and experimental geomechanics are discussed in *Section 0*. Finally, the research questions identified on this basis of this brief review are introduced in *Section 1.4* and explored in *Chapters 2 to 5*. Since the core chapters of this thesis have been written as stand-alone manuscripts for publication, some repetition of material occurs as key concepts are re-introduced.

1.2 Background: The Distribution, Formation and Destruction of Structural Permeability and its Implications for Geothermal Energy

1.2.1 Fault Zone Architecture and Rheology in the Upper Crust

In the upper crust, brittle deformation occurs via cataclasis along discrete displacement zones over a wide range of scales to form faults and fractures (e.g. Blenkinsop, 2000). The heterogeneity of fault zones plays a fundamental role in controlling the mechanics of faulting and earthquakes as well as the distribution of fluid flow. While the fault core generally forms a low-permeability barrier to fluid flow, in brittle crust the damage zone is considered to display high hydraulic connectivity, preventing the development of overpressure (Townend and Zoback, 2000). Fractured rock can have markedly different mechanical and hydraulic properties to intact rock. The seismogenic zone is typically demarcated by crustal depths of $\sim < 20$ km (Marone, 1998), however in areas of elevated heat flow such as those targeted for geothermal exploration may be as shallow as $< \sim 3$ km (Boden, 2017; Sibson, 2001). Within this zone, structurally controlled fluid flow is generally focused in the permeable damage zone of a fault. This damage zone may range from several microns to more than hundreds of metres wide and comprises fractures and faults over several length scales generated via seismic events. The damage zone forms adjacent to a narrower, less permeable fault core that typically comprises fault gouge and cataclasite (*Figure 1.2*) (Chester and Logan, 1986; Barton et al., 1995; Caine et al., 1996; Wibberley et al., 2008, Savage and Brodsky, 2011; Faulkner et al., 2003, 2008, 2010).

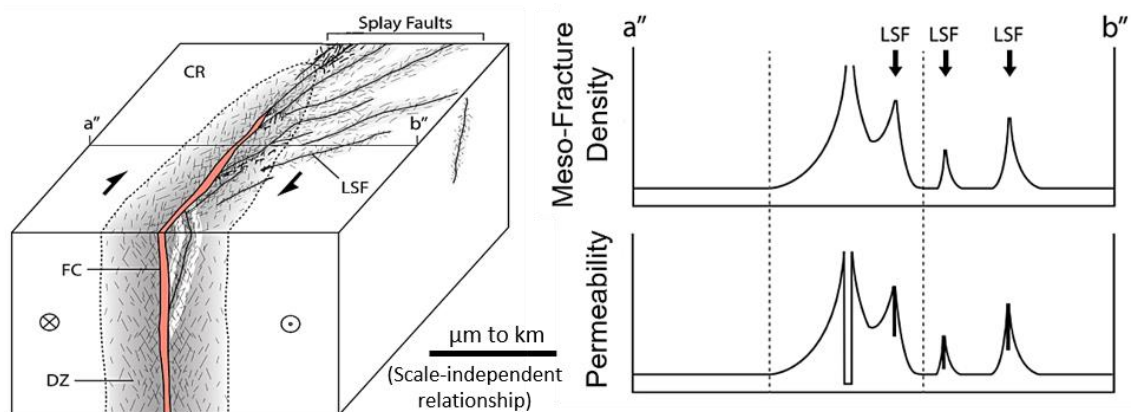


Figure 1.2: The scale-independent relationship between fault architecture, fracture density and permeability (after Ostermeijer et al., 2020, based on Chester and Logan, 1986; Caine et al., 1996 and Faulkner et al., 2010). CR = Country rock; FC = Fault core; DZ = Damage zone; LSF = Large splay fault.

Damaged fault rocks are generally more permeable than intact rocks, and hence play a key role in the migration of fluids and precipitation of minerals in and around fault zones over the seismic cycle (e.g. Sibson, 1994; Evans et al., 1997; Lockner et al., 2000; Lawther et al., 2016). Fault damage can be accrued via processes such as coalescence/linking of structures (Childs et al., 2009), cumulative wear with displacement (Chester and Chester, 2000), coseismic damage (Rice et al., 2005; Rempe et al., 2013; Aben et al., 2016) or fault linkage involving a process zone

(Cowie and Scholz, 1992). The types of structures present within damage zones (e.g. minor faults, low-displacement fractures and extension veins) are largely dependent on the physical conditions at failure and properties of the host rock (Chester and Logan, 1986; Faulkner et al., 2003; Wibberley et al., 2008; Faulkner et al., 2010), and can vary in scale from macro-damage (i.e. $\sim 10^1$ - 10^3 m: 1-3 orders of magnitude smaller than the main km-scale fault), to meso-damage ($\sim 10^{-2}$ - 10^1 m: 3-5 orders of magnitude smaller) and micro-damage ($< \sim 10^{-2}$ m: > 5 orders of magnitude smaller) (Shipton and Cowie, 2001). To fully understand damage zone variability within such fault zones, it is necessary to quantitatively characterise fracture patterns at a range of scales.

With increased fault maturity and displacement, the density of damage adjacent to a fault core has been shown to be predictably higher (*Figure 1.2*), with damage zone width also scaling with the amount of fault displacement (Anders and Wiltschko, 1994; Schulz and Evans, 2000; Wilson et al., 2003; Mitchell and Faulkner, 2009; Savage and Brodsky, 2011; O'Hara et al., 2017). Damage zone complexity and heterogeneity can also increase as a result of interactions between faults, which may be greatest in the presence of pre-existing structures and lithological variation (Myers and Aydin, 2004; Faulkner et al., 2008; Gudmundsson et al., 2002, 2010; O'Hara et al., 2017; Ostemeijer et al., 2020). The nature of permeability may be variable along strike as well as between faults, and the architecture of damage zones generally evolves with fault growth, with successive failure episodes overprinting each other (Blenkinsop, 2008; Mitchell and Faulkner, 2009). Damage zone characteristics can therefore be highly variable between different fault systems (e.g. Cox, 1995; Cunningham and Mann, 2007; Faulkner et al., 2010), with the mechanics of regional structures not well constrained - in particular how damage is distributed and how fluids and fractures interact within them (Cembrano et al., 2005; Nixon et al., 2019). Comparisons between different datasets can be problematic due to a lack of consistency in data sampling scales, techniques and terminology, as well as lithological and tectonic differences (Choi et al., 2016). In *Chapter 2*, a quantitative approach to assessing the spatial distribution of damage across a fault zone, as well as surrounding individual faults, aims to improve the understanding of how damage zones control the distribution of permeability and fluid flow.

Whilst the fault damage zone hosts most fluid flow, the fault core accommodates the most strain (Scholz, 1987; Wilson et al., 2005). Fault cores are considered to develop via repeated localisation of shear failure during fault displacement, with fault tip propagation followed by fault linkage at all scales (Peacock and Sanderson, 1991; Walsh et al., 2002, 2003). As a result, fine-grained fault gouge is able to develop via a combination of mechanical attrition of the fault wall and authigenic crystallisation (Caine et al., 1986; Chester and Logan, 1986; Rutter and Maddock, 1987; Chester and Chester, 1998). Enhanced pressures and temperatures in hydrothermal fault zones alters minerals present within the fault gouge in terms of dehydration, consolidation and mineralogy, thereby changing the fault's mechanical and seismic properties

(Saffer and Marone, 2003; Sánchez-Roa et al., 2016; 2018). As well as forming a permeability barrier, the typical prevalence of phyllosilicates within fault gouges has been inferred as a major reason for overall mechanical weakness of faults on scales over several orders of magnitude (Shimamoto and Logan, 1981; Saffer and Marone, 2003; Underwood, 2007; Faulkner et al., 2008; Collettini et al., 2009; Tembe et al., 2009; Lockner et al., 2011). In the laboratory, phyllosilicate-rich fault gouges have consistently been shown to be frictionally weak (e.g. Ikari et al., 2007, 2009, Moore and Lockner, 2004, 2007; Morrow et al., 1992, 2000, 2017), not adhering to Byerlee's law, which states that friction coefficients (μ) in the upper crust are invariably $0.6 \leq \mu \leq 0.85$ (Byerlee, 1978). μ can be defined as in Equation 1.1:

$$\mu = \tau / \sigma'_n, \quad (\text{Eq. 1.1})$$

where τ is shear stress and σ'_n is the effective normal stress.

The frictional weakness of phyllosilicate-rich fault gouges have been attributed in part to their mineral structure and water content, where μ has been shown to decrease with increased content of particular clays as well as structurally- and surface-bound water (e.g. Morrow et al., 1992; Moore and Lockner, 2004, 2007; Tembe et al., 2010; Behnsen and Faulkner, 2012) (*Figure 1.3*). The variation in such fault gouge physiochemical properties within fault zones has been invoked as a primary reason for aseismic creep behaviour within major faults, such as the San Andreas Fault (Lockner et al., 2011; Chang et al., 2013) and within the Soultz-sous-Forêts geothermal field (Bourois and Bernard, 2007). *Chapter 4* aims to explore how the presence of different phyllosilicates within fault gouge or clay-filled fractures impacts their frictional strength, in particular considering the impact of water content within the gouge.

The presence of water in clay gouges has also been cited as a possible cause of variation in frictional stability (e.g. Moore and Lockner, 2004; Ikari et al., 2011; Meller and Kohl, 2014). Whether a fault displays stable behaviour during frictional sliding is determined by the constitutive rate- and state-dependent parameters a , b and d_c (*Figure 1.3a*). a represents an initial direct effect on μ scaled according to a change in displacement rate, and b describes how μ exponentially evolves over a characteristic distance d_c at a new slip velocity. Whilst a is considered to relate to gouge thickness, normal stress, surface roughness and particle size (Linker and Dieterich, 1992; Marone, 1998), b is considered to relate to the quality of asperities in contact across the sliding interface and hence the strength and orientation of the stress field (Li et al., 2011; Scholz, 2010). Rate dependence can be important in determining whether deformation is stable or unstable (Lockner et al., 2011): Positive values of $a-b$ describe velocity strengthening behaviour, whilst negative $a-b$ values describe velocity-weakening behaviour (Dieterich, 1972, 1978, 1979; Ruina, 1983; Blanpied et al., 1998; Marone, 1998). As well as through differences in water content and fluid pressures, such variations may also be induced by differences in clay content and/or crystallographic properties of the minerals present within the gouge (e.g. Meller and Kohl, 2014; *Figure 1.3b*).

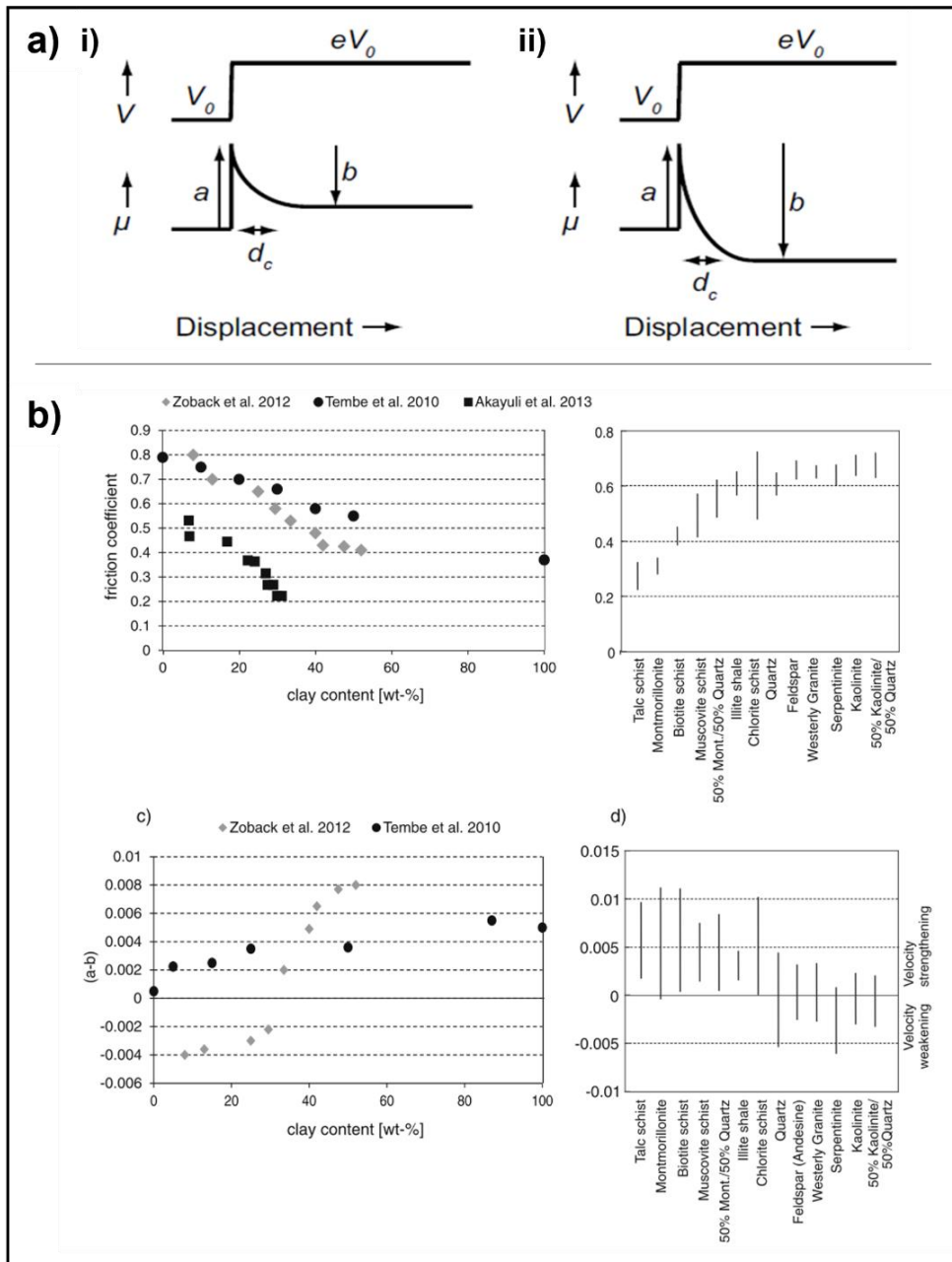


Figure 1.3: a) Schematic frictional response to steps in sliding velocity for i) velocity-strengthening friction and ii) velocity-weakening friction (after Den Hartog, 2013). b) Variations in friction coefficient and constitute parameters $a-b$ for rocks with different clay contents and phyllosilicate mineral types (after Meller and Kohl, 2014, with data from Tembe et al., 2010 (quartz-illite); Ikari et al., 2011 (various phyllosilicates); Zoback et al., 2012 (shale) and Akayuli et al., 2013 (soil)). In all samples, as clay content increases, μ decreases and $a-b$ increases.

1.2.2 Fracture Formation and Permeability Creation

Macroscopic faults and fractures in low porosity, crystalline rocks can either form by stress-driven processes (i.e. nucleation, interaction and coalescence of tensile microfractures in the absence of significant fluid pressure) or fluid-driven processes (i.e. fractures formed by high fluid pressure gradients and propagating away from the high pressure zone), or most likely a combination of both (Sibson, 1996; Cox, 2005). The development of fractures and fault zones

(i.e. their architecture and interconnectivity) creates a network of fluid pathways in hydrothermal environments. Fluid flux through fractures occurs as a result of an interplay between fracture permeability and fluid pressure gradient. For porous material (e.g. intact rock or fault gouge), where fluid pressure gradients often have a strong vertical component, this flux can be described using Darcy's law of steady state flow (Equation 1.2):

$$Q = -\frac{kA\Delta P}{\mu}, \quad (\text{Eq. 1.2})$$

where Q is the volumetric flow rate in ms^{-3} , k is the permeability of the rock or gouge in m^2 , A is the cross-sectional area in m^2 , μ is the dynamic viscosity of the fluid in Pas and ΔP is the change in pressure over this length in Pa (Jaeger et al., 2007; Gudmundsson, 2011).

For fractured material with a low primary porosity and permeability, high structural anisotropy renders the permeability tensor more relevant to estimates of fluid flow, which is more dependent on tectonic environment (e.g. Faulkner and Armitage, 2013; Farquharson et al., 2015). Flow rates in fractured rocks are better described by the cubic law (Equation 1.3), such that:

$$Q = \frac{W}{\mu L} \frac{a_h^3}{12} \Delta p, \quad (\text{Eq. 1.3})$$

W is the fracture width in m , μ is the dynamic viscosity of the fluid in Pas , L is the fracture length in m , a_h is the fracture hydraulic aperture in m , and ΔP is the change in fluid pressure in Pa (Brown et al., 1995; Zimmerman and Bodvarsson, 1996; Taylor, 1999; Zimmerman and Yeo, 2000; Jaeger et al., 2007; Gudmundsson, 2011; He et al., 2021). Each of these parameters is illustrated schematically for theoretical and laboratory fractures in *Figure 1.4*.

Considering Equations 1.2 and 1.3 together, the permeability of a fracture can be expressed as in Equation 1.4, which indicates that fracture aperture exerts a strong control over permeability, (although its effect is not as significant as for flow rate):

$$k_f = a_h^2 / 12. \quad (\text{Eq. 1.4})$$

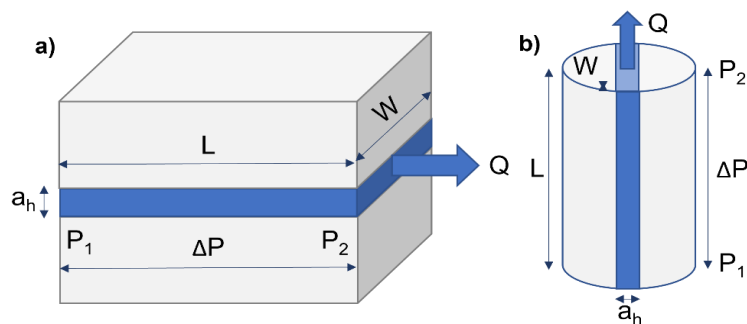


Figure 1.4: Schematic illustration of a fracture and its parameters that define fluid flow, in the context of a) a fracture at outcrop and b) an experimental core sample.

Whilst empirical equations may give a good approximation of permeability and flow properties, they incorporate many simplifications and assumptions of fractures observed in the field or laboratory. Fluid flow properties may be influenced by parameters that are often impractical to measure in detail in natural fractures, for example, variation in fracture wall permeability due to the presence of microfractures, or variation in fracture aperture along its length. When estimating permeabilities of fractures in the field, many assumptions must be made about the processes that have formed and subsequently deformed them, such as changes in the stress field and vein formation by mineral precipitation. Upscaling fracture lengths from the laboratory to the field often dramatically alters the physiochemical processes that will occur during fluid flow, for example resulting in increased chemical reaction along the fracture wall (partly due to increased contact times, and partly due to greater complexity in natural fluids compared to those typical used in laboratory experiments) and promoting advective rather than laminar flow (e.g. Elkhoury et al., 2013). In nature, fracture walls are rarely planar, meaning that apertures may vary significantly around an estimated mean value. Fluid flow properties are therefore affected by factors such as fracture roughness that increase flow tortuosity. For the cubic flow law to apply (Equation 1.3), fractures should have a length to aperture ratio >3 and a Reynolds number (which describes flow turbulence) <25 (Leckenby et al., 2005). It is also important to note intrinsic variability, which can only be assessed by measuring a wider range of samples. Whilst permeability of intact rock samples may underestimate bulk reservoir permeability, macro-fractured samples may give an overestimate (Heap and Kennedy, 2016). All of these factors and more must be considered when scaling fracture permeability from the laboratory to the field and relating it to empirical estimates.

In its simplest terms, brittle failure can occur in rocks on account of stress orientations that produce either tensile (Mode I), hybrid (Mode II) or shear (Mode III) fractures (e.g. Anderson, 1951; Jaeger et al., 2007; Gudmundsson, 2011) (*Figure 1.5a*). There are two end-member processes for achieving brittle failure: fluid-driven and stress-driven (Cox, 2010). Stress-driven tensile fractures generally propagate away from small-scale stress concentrations and coalesce towards shear failure (e.g. Engelder, 1987; Blenkinsop, 2008; Barnhoorn et al., 2010), whereas fluid-driven tensile fractures (hydrofractures) develop as a result of overpressure (e.g. Cox, 2005; Barnhoorn et al., 2010). Hydrofractures typically form where pore fluid pressure (P_f) exceeds the sum of the rock's tensile strength (T) and its least principal stress (σ_3) and where $\sigma_1 - \sigma_3 < 4T$ (*Figure 1.5*). Tensile fractures generally form approximately normal to the σ_3 orientation and parallel to the $\sigma_1 - \sigma_2$ principal plane, whilst shear fractures generally form a plane at $\sim 30^\circ$ to σ_1 (Ashby and Sammis, 1990; Healy et al., 2006; Healy, 2008). Most fractures conducive to fluid flow are related to critically stressed, potentially active faults in frictional equilibrium with the in-situ stress field, and orientation is therefore critical to whether the fracture will be hydraulically conducive (Brown et al., 1987). Indeed, significant proportions of fluid flow in geothermal reservoirs can be attributed to few, well-oriented fractures, inducing strong permeability anisotropy (Barton et al., 1995; Aydin, 2000).

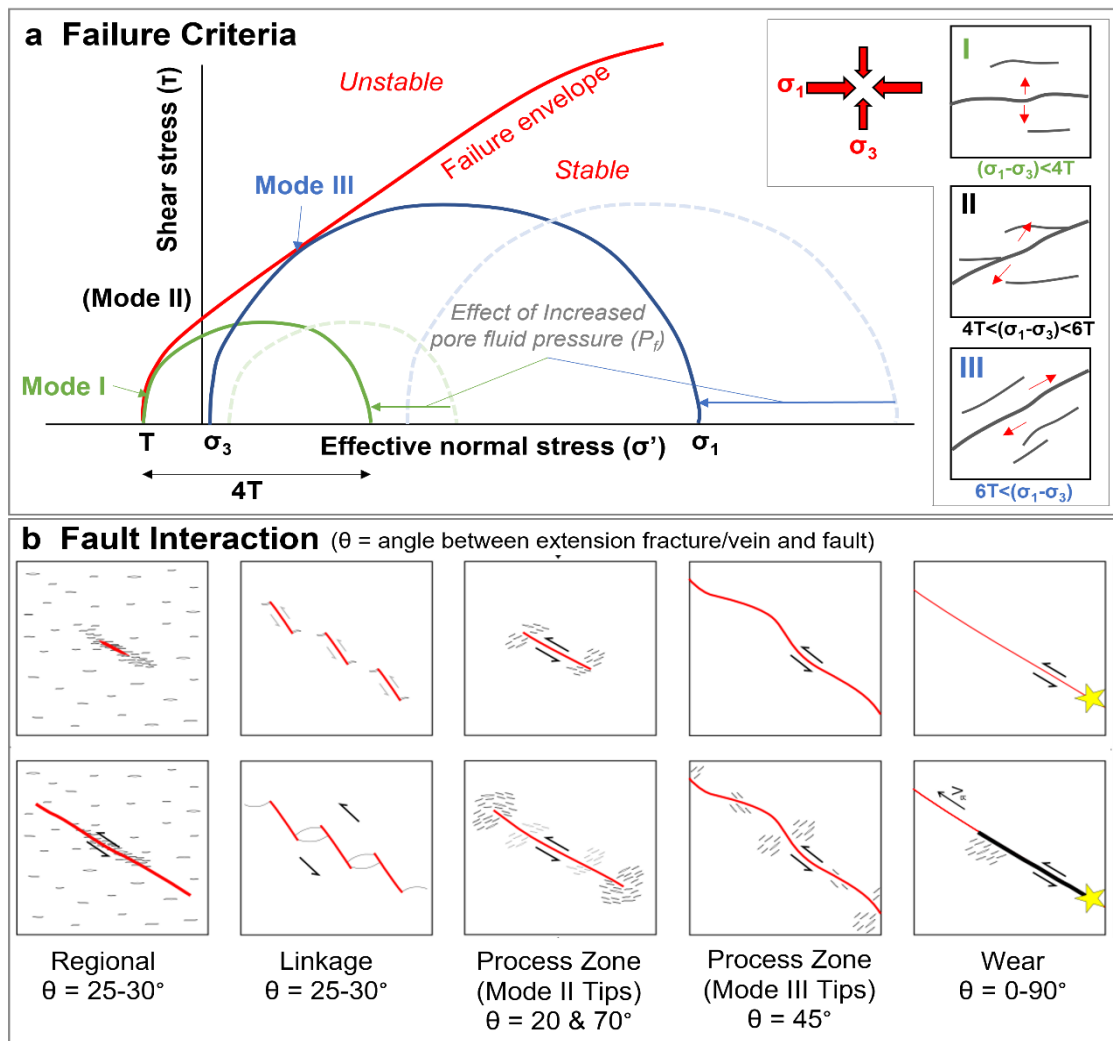


Figure 1.5: a) Griffith-Mohr-Coulomb failure criteria for Mode I, II and III fractures depicted in Mohr space, where σ = principal stress and T = tensile strength. Also illustrated is the effect of increased fluid pressure on likelihood of failure (P_f). Schematic illustrations of Mode I, II and III fractures are also described in terms of regional stress. b) Effects of different types of fault interaction on the angles at which extension veins may form in a damage zone (after Mitchell and Faulkner, 2009; based on Wilson et al., 2003 and Blenkinsop, 2008).

Interaction between faults and fractures within a wider structural network is also an important consideration when assessing the permeability of a fault zone, and can affect the overall intensity and connectivity of the fracture network and the orientation at which fractures form (Wilson et al., 2003; Berger, 2007; Blenkinsop, 2008; Mitchell and Faulkner, 2009; Sanderson and Nixon, 2015; Healy et al., 2017) (Figure 1.5b). Whilst little flow occurs in isolated fractures, as strain increases beyond the percolation threshold fractures will grow and nucleate such that connectivity is greater and fluid flux is more evenly distributed with shorter, less tortuous paths (Cox, 2005). Structurally-hosted fluid flow is generally focused in 'backbone' structures – fractures with long lengths and a high density of fractures of differing orientations abutting or crossing it (e.g. Cox, 2005; Sanderson and Nixon, 2015). Large stress rotations have previously been attributed to an increase in fracture density and structural permeability through the

damage zone towards the fault core (Faulkner et al., 2006), for which the effect is generally larger in isotropic rocks (Healy, 2008). Pre-existing planes of weakness can influence (and be influenced by) local stress conditions (e.g. Barton et al., 1995; Caine et al., 1996; Townend and Zoback, 2000; Healy, 2008), for example by reducing the tensional strength and the required differential stress and fluid pressure for a fracture to form (Bons, 2000). Stress concentrations as a result of such heterogeneities have been cited as the cause for increased fracture connectivity and significant fluid flow in non-optimally oriented structures (Brown et al., 1987; Barton et al., 1995; Caputo and Hancock, 1999; Wilson et al., 2003; Wallis et al., 2012; Virgo et al., 2013). In *Chapter 3*, the effect of heterogeneities in the form of sealed fractures (i.e. mineral veins) on successive fracturing events and permeability creation is considered.

Several models exist for structurally controlled advective fluid flow processes (e.g. Sibson, 1996, 2001; Blanpied et al., 1992; Rice, 1992, Cox, 2005). In the seismic pumping model (Sibson et al., 1975) (*Figure 1.6a*) fluid migrates down a potential gradient into a dilation site opened by accumulating differential stress or increasing fluid pressure, before dilation site collapse expels the fluids. In the fault valve model (Sibson, 1981; 1990) (*Figure 1.6b*), dilation rate is greater than fluid flux, developing a temporary underpressure in the void and driving fluid into the dilation site. In the fluid pressure excursion (matrix-to-fracture pumping) model (Etheridge et al. 1984) (*Figure 1.6c*), fracture opening takes place in regions of local fluid overpressure. Cyclic hydraulic fracturing may also occur, due to sealing during rapid fluid flow along a pressure gradient followed by extensional failure once the minimum effective stress exceeds the tensile strength (Hilgers and Urai 2002a).

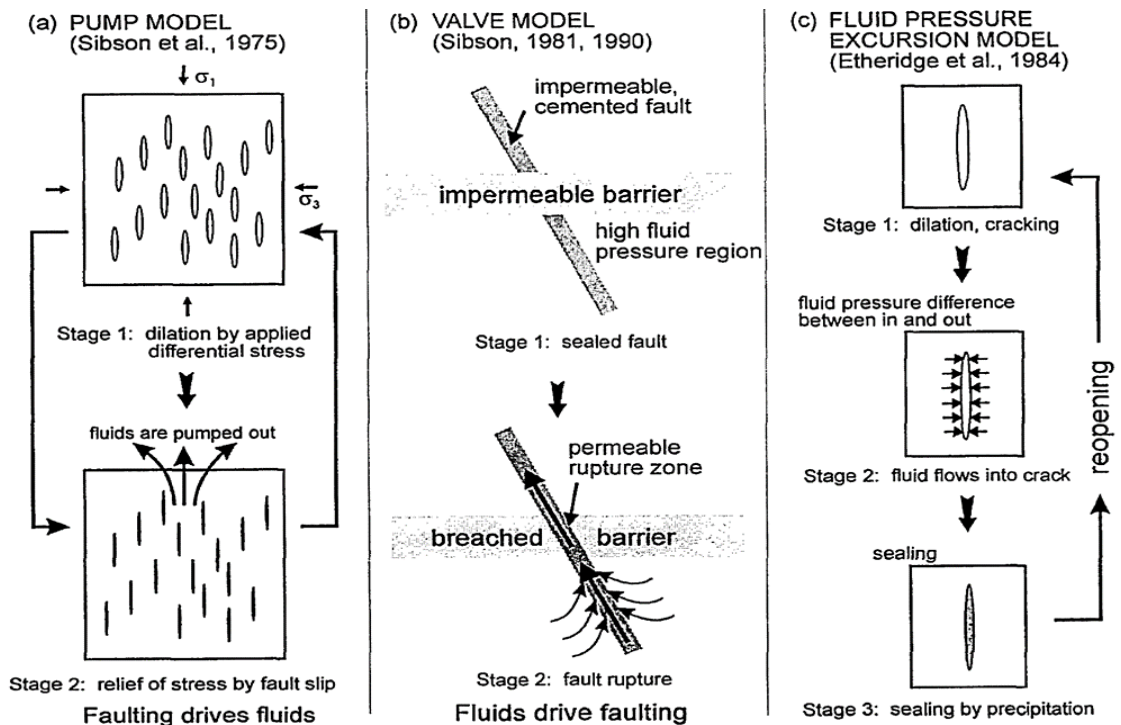


Figure 1.6: Conceptual models for vein formation (after Lee et al., 1996). a) Pump model (Sibson et al., 1975). b) Valve model (Sibson, 1981; 1990). c) Fluid pressure excursion model (Etheridge et al., 1984).

The source of crustal fluids depends on the geological setting, and may be of meteoric, sedimentary, metamorphic or magmatic origin, affecting their chemical properties (e.g. abundance of dissolved solids and volatiles) (Ármansson, 2012). As well as influencing structurally controlled permeability directly, fluid flow can influence deformation behaviour through both mechanical and fluid-rock interaction processes and can significantly affect rock strength (e.g. Brace et al., 1966; Lockner et al., 1992; Healy et al., 2006; Wyering et al., 2014). As a result, of complex thermal, hydraulic, mechanical and chemical interactions between the fluid and host rock, the fractured rock mass may become hydrothermally altered (e.g. Laubach et al., 2004; Cox, 2010; Bons et al., 2012). Hydrothermal alteration has been shown to change a rock's mechanical strength (e.g. Sousa et al., 2005; Nara et al., 2011; Pola et al., 2012, 2014; Heap et al., 2014; Wyering et al., 2014, 2015), in places aiding localisation of strain in the crust, and hence may influence the formation of later fractures with the potential to host fluid flow.

1.2.3 Permeability Destruction (Fracture Sealing)

In each of the structurally controlled fluid flow scenarios depicted in *Figure 1.6*, loss of permeability may be experienced relatively rapidly as a result of either mechanical or chemical processes. Mechanically, structural permeability may be reduced by continued slip along a fracture (reducing asperities and producing fault gouge) (e.g. Rutter and Maddock, 1987), or through reduction in fluid pressure causing the fracture to narrow or close (e.g. Cox, 1995, 1999; Sibson, 1995, 1996, 1997; Faulkner et al., 2010; Rempe et al., 2018). Chemically, permeability can be lost via fracture healing, where minerals are transported locally through diffusion and solution transfer creep (e.g. Smith and Evans, 1984; Brantley et al., 1990; Fisher and Brantley, 1992; Hickman et al., 1995). Wherever dissolved minerals are transported some distance via supersaturated fluids and precipitated upon a change in physiochemical conditions, this is termed fracture sealing (e.g. Rimstidt and Barnes, 1980; Sibson, 1990; Lee et al., 1996; Lee and Morse, 1999; Martin and Lowell, 2000; Hilgers et al., 2004; Okamoto et al., 2010; Doubra et al., 2017). The creation of fluid pressure and/or temperature gradients (e.g. as a result of seismic processes or fluid extraction via geothermal wells) can change the solubility state of a hydrothermal fluid (e.g. Oliver and Bons, 2001; Wiltschko and Morse, 2001), which may contain a diverse mix of minerals in solution (e.g. Giggenbach, 1981, 1995). As well as causing sealing through mineral precipitation and loss of permeability as a result, pressure and temperature fluctuations may also reverse such vein-forming reactions, causing mineral breakdown resulting in porosity and permeability generation (e.g., Heap et al., 2012, 2013, 2017).

The nature of fracture-controlled permeability in brittle faults is dynamic and episodic over the course of the seismic cycle (*Figure 1.7*) and is ultimately controlled by evolving connectivity between propagating faults within a larger structure (Cox, 1995). Any permeability reduction in the fault core would likely increase fluid pressures in the fault damage zone, resulting in brittle failure that typically induces short periods of high-flux flow, usually followed by long periods of low or no flow as fractures are sealed once more (e.g. Cox, 1999; Sibson, 2001). Earthquake

recurrence intervals are typically >1000 years (Nicol et al., 2005), however mineral precipitation within fractures in the fault damage zone may destroy permeability much more quickly.

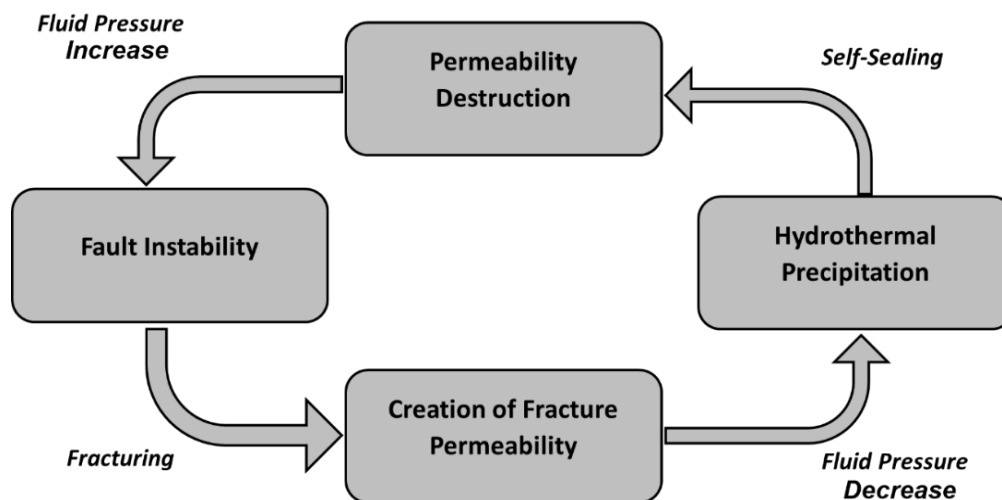


Figure 1.7: An illustration of the transient nature of permeability in a hydrothermal fracture network.

Whilst *Chapters 2 and 3* of this thesis consider the creation of fracture permeability, *Chapters 3, 4 and 5* address aspects of fracture sealing and permeability destruction by hydrothermal precipitation as a result of changing fluid conditions. The composition and texture of sealed fractures (i.e. mineral veins) present within fault damage zones provides a useful record of pressure, temperature and strain history, fluid compositions, and interactions between fluids and fractured host rock (Bons et al., 2012). Since many geothermal areas have no surface manifestations, the field study of this ‘palaeo-permeability’ in exhumed systems (i.e. frozen hydrothermal activity) (*Chapter 3*) offers an analogue of structural networks and fracture-forming processes that can be used to establish the evolution and sustainability of contemporary fractured geothermal systems (Dobson et al., 2003; Sibson, 1996; Faulkner et al., 2010; Faulds et al., 2011; Gomila et al., 2016; Griffiths et al., 2016; Sanderson, 2016). Laboratory studies of the mechanical and frictional strength of sealed fractures formed at a range of conditions within the geothermal system can also help to understand the precise mechanisms by which syntectonic veins form and deform, which are not well understood (Barker et al., 2006; Bons et al., 2012; Gomila et al., 2016; Hilgers and Urai, 2002a).

Veins are formed by crystal growth from supersaturated fluids in areas of dilation, and can be useful in the analysis of deformation processes as well as those relating to fluid flow (e.g. Ramsay and Huber, 1983; Cox, 1999). Veins can be classified according to their macroscopic, microscopic or growth morphology (Bons, 2000; Bons et al., 2012) (*Figure 1.8*).

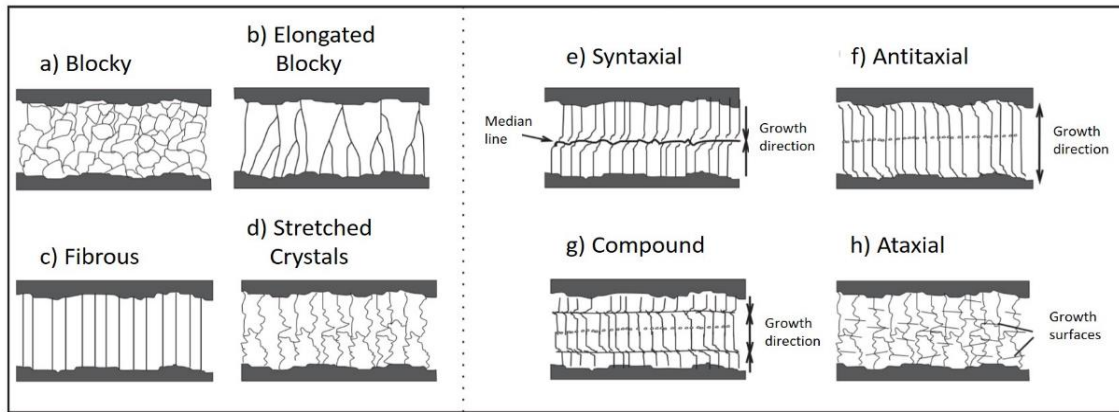


Figure 1.8: Schematic classification of vein textures, modified from Olivares et al. (2010).

Microscopic morphology relates to the texture and arrangement of crystals within a vein (which may be described as blocky, elongate blocky, fibrous or stretched), and growth morphology describes where nucleation has occurred and the direction of crystal growth. Vein formation (fracture sealing) can occur as a single precipitation event (e.g. via a rapid decrease in the pressure of circulating fluids), or as multiple crack-seal or crack-jump events caused by fluid pressure or strain oscillations (e.g. Ramsay, 1980). When the vein is formed of a mineral that is not a major constituent of the host rock, antitaxial veins typically form (i.e. those with two growth surfaces – one on each fracture wall). Otherwise, syntaxial growth (with a single growth surface) usually occurs. In ataxial veins, the position of the growth surface changes through time; vein crystals then grow epitaxially off grains in the wall rock. Stretching veins may seal from both fracture walls (bitaxial) or from one (unitaxial) (Bons, 2000; Hilgers et al., 2000; Bons et al., 2012; McNamara et al., 2016).

Analysis of the composition, texture and thickness of veins – as well as the compositional and thickness distributions and connectivity within wider vein networks - is important in order to describe and predict the evolving permeability of fracture networks and the fluid flow mechanisms by which they may have formed (Roberts et al., 1998; Sanderson et al., 2008) – these aspects are explored in *Chapter 3*. Estimating the evolution of permeability of exhumed fractured geothermal systems is difficult, however, and only theoretical permeability may be determined from the presence of mineral veins using Equation 1.5:

$$k = ((2\pi c^2 a_h^3 / (2l^3)) f, \quad (\text{Eq. 1.5})$$

where k = permeability, c = fracture radius, a_h = fracture hydraulic aperture, l = spacing between fractures and f = connectivity between fractures (Guegen and Palciauskas, 1994). Aperture has a greater control over permeability than fracture spacing.

Laboratory-based experiments in *Chapter 3* explore the influence of epithermal veining and propylitic alteration – which is usually a product of high temperature fluid circulation (i.e. >260 °C – Robb, 2004; Boden, 2017) - on the mechanical strength of fractured rock. Experiments in *Chapter 4*, however, address the strength and stability of fractures sealed with lower

temperature argillic precipitation (e.g. Boden, 2017; Lázaro, 2015), namely phyllosilicates. Fine-grained, platy phyllosilicates are commonly abundant within fault gouge, having formed via mechanical attrition of the fault wall and authigenic crystallisation (Chester and Logan, 1986; Chester and Chester, 1998), significantly reducing permeability with progressive core development (Sánchez-Roa et al., 2016). Under hydrothermal conditions, the nucleation of faults in filled fractures (and hence the recurrence intervals of seismic events) are controlled in part by rate competition between permeability reduction and strength recovery. Due to their low permeability, the effect of increasing pore-fluid pressure may be magnified in clay-rich fault gouges, reducing effective stress and fault strength and promoting failure (e.g. Morrow et al., 1992; Faulkner and Rutter, 2001; Frye and Marone, 2002; Faulkner et al., 2018), hence playing a key role in driving the seismic / structural fluid flow cycle (cf. *Figure 1.7*).

Heat transport and precipitation are generally diffusion-dominated in low permeability reservoirs and advection-dominated in high permeability reservoirs (Ghassemi, 2012). The physiochemical mechanisms by which fractures seal by precipitation – and consequently the timescales over which this can happen - are not well understood. The nature, rate, and volume of fracture sealing in hydrothermal systems ultimately depends on whether the system is in chemical equilibrium. Precipitation is likely to be driven by complex interplay of different processes that disturb this equilibrium and change the saturation state of a fluid with respect to a particular mineral, such temperature of the fluid or rock mass, the confining or fluid pressure and/or the fluid chemistry (e.g. Fournier, 1989; Rimstidt, 1997; Wiltschko and Morse, 2001; Doubra et al., 2017). Vein textures may be controlled by the relative dominance of crystal nucleation versus growth/kinetics (e.g. Rimstidt and Barnes, 1980; Lasaga, 1981; Martin and Lowell, 2000; Bons, 2000; Hilgers et al., 2001, 2004; Bons et al., 2012), the understanding of which can assist in identifying precipitation rates in natural, exhumed hydrothermal systems. Whilst there is some consensus on the aforementioned issues, there is disagreement regarding the fluid flux required to seal a fracture; the combination of fluid flux, fracture physical properties and degree of disequilibrium between the fluid and mineral may all affect the expected volume of precipitation (Lee and Morse, 1999). Published estimates of fracture sealing rates in hydrothermal areas are extremely varied. For example, whilst some authors suggest that a fracture could close via precipitation on timescales of hours to months (Brantley et al., 1990; Laubach, 1997; Tranter et al., 2020), others indicate that timescales are more likely to be in the order of tens to millions of years (Lee and Morse, 1999; Tenthorey et al., 2003). This variability however is largely a result of differences in modelling and laboratory conditions that render these studies incomparable – for example, the cited investigations use fractures of different apertures, compositions and roughness; fluid systems with different mineral species in solution at different levels of saturation; and different ranges of temperatures and pressures. To improve the understanding of how each of these variables in turn affect sealing rates, a systematic set of experiments must be performed at a range of conditions defined by existing models. This is what *Chapter 5* of this thesis sets out to achieve.

1.2.4 Application to Fractured Geothermal Reservoirs

As introduced in *Section 1.1*, a production well drilled into a conventional, structurally controlled hydrothermal system targets zones of high flux, high temperature fluids in naturally fractured rocks. Successful, long-term geothermal power production is strongly dependent on maintaining high permeabilities (generally >5 mD, or $5 \times 10^{-14} \text{m}^2$) and fluid flux (e.g. $>10 \text{Ls}^{-1}$) to transfer heat from depth to surface (e.g. Mock et al., 1997; Zimmerman et al., 2009; Ghassemi, 2012). Fracture stimulation of EGS reservoirs also has ever increasing importance, with the aim of maintaining a hydrologically active structural network through creating or reopening blocked/closed fractures (e.g. Barton et al., 1995; Zimmermann et al., 2009; Ghassemi, 2012). Fracture stimulation is most commonly performed hydraulically (where pore pressure in a zone within the well is raised to be greater than σ_3 (e.g. Axelsson et al., 2006; Legarth et al., 2005; Miller, 2015)); thermally (through cycled injection of cold water into a zone within the well (e.g. Axelsson et al., 2006; Grant et al., 2013; Siratovich et al., 2015); or through acid treatment (where acidic fluids are injected into fractures with the aim of removing calcite scaling (e.g. Axelsson et al., 2006; Zimmermann et al., 2011)).

The brief introduction to a range of geological concepts introduced in this chapter shows that structural permeability can be variable in time and space, and there are numerous ways in which it can be reduced by mechanical or chemical processes. Structural geological perspectives are therefore invaluable to EGS as well as conventional systems, as understanding local stress conditions, fracture patterns and the nature of successive fracturing events prior to stimulation is crucial to ensuring that permeability is created in the desired orientation, preventing wellbore instability and induced seismicity, and ultimately improving the longevity of a geothermal resource (Moeck et al., 2009; Zoback et al., 2010; Ghassemi, 2012; Ellsworth, 2013).

Geothermal systems tend to perform better with increasing structural complexity, where long-term, critically stressed areas keep fluid pathways open for longer (Faulds et al., 2011). In accordance with *Section 1.2.1*, few geothermal production areas (comprising zones of long-term enhanced structural permeability with high temperature fluid recharge), occur on the mid-segments of major normal faults. Areas usually more suitable for hydrothermal fluid flow are those where major faults interact, such as hard-linkage zones in fault duplexes (also termed step-overs / relay ramps), fault terminations (e.g. horse-tailing structures), accommodation zones and dilatational fault intersections, on account of more frequent fault movements and less clay-rich mineral fills (Berger, 2007; De Paola et al., 2007; Faulds et al., 2011, 2013) (*Figure 1.9*). Such structural complexity may act to inhibit the development of new through-going faults and therefore increase an area's suitability as a geothermal production area by providing long-term, enhanced structural permeability (Cunningham and Mann, 2007; De Paola et al., 2007).

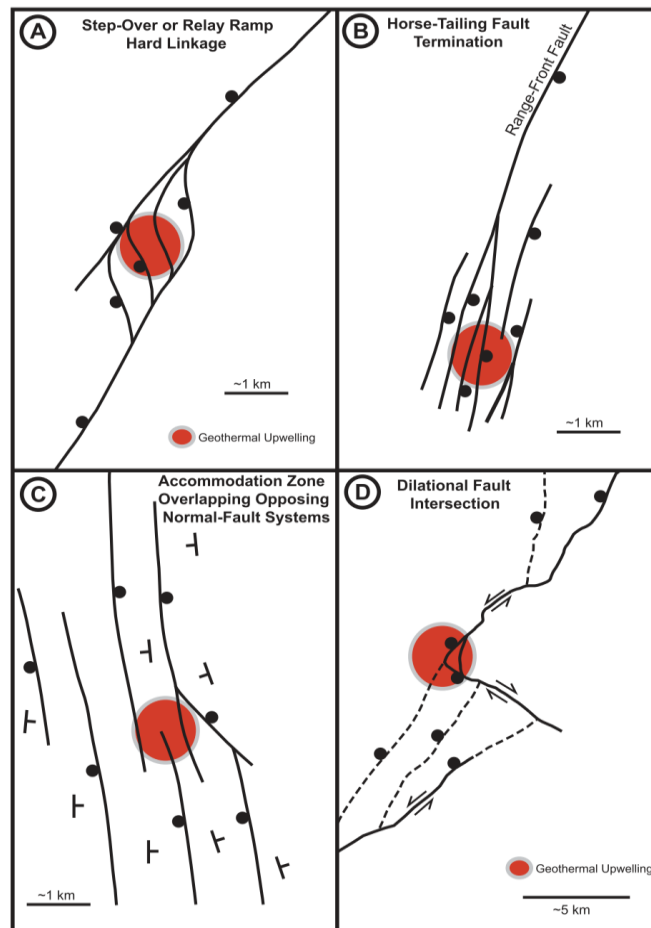


Figure 1.9: Examples of the types of regional structures most favourable to allowing sustained, high temperature geothermal fluid upwelling (after Faulds et al., 2011).

Given that geothermal areas can be prone to dynamic stress changes (Grant and Bixley, 2011), it must be ensured that fluid injection amounts and rates are adjusted to the in-situ stress field, as well as rock strength conditions, to ensure that changes in fluid pressure do not induce failure (e.g. Moeck et al., 2009; Ghassemi, 2012; *Figure 1.5a*). Understanding the stress field response to fluid extraction/injection in both conventional and EGS reservoirs ensures that wellbores remain stable, desired flow pathways are kept open and flow rates remain high (e.g. Ellsworth, 2013; Zoback 2010; Siratovich et al., 2016). Sites typically considered favourable for stimulation within EGS reservoirs are those that include pre-existing, critically stressed and optimally oriented fractures (Ghassemi, 2012), with examples including Soultz-sous-Forêts (Baria et al., 1999) and the Coso field (Sheridan et al., 2003; Megel et al., 2005).

Fractured host rocks in producing geothermal areas experience a wide range of physiochemical conditions that are usually in disequilibrium with those of geothermal fluids, often promoting mineral precipitation from solution and alteration of minerals to more stable phases (e.g. Pola et al., 2012, 2014; Thien et al., 2015). Most reservoir rocks in which structurally controlled fluid flow occurs have been hydrothermally altered to form minerals that can be used to understand the fluid flow and temperature history of the system (e.g. 'geothermometer' indicator minerals

shown in *Figure 1.10*). As a result of these mineralogical changes, the mechanical strength of the host rock also changes. The strength of the host rock is of particular interest to the geothermal industry as it directly affects how and where fractures form to create structural permeability (*Section 1.2.2*). Improved knowledge of how alteration influences rock strength can also help improve drilling efficiency and guide drill bit selection (Wyering et al., 2012, 2014).

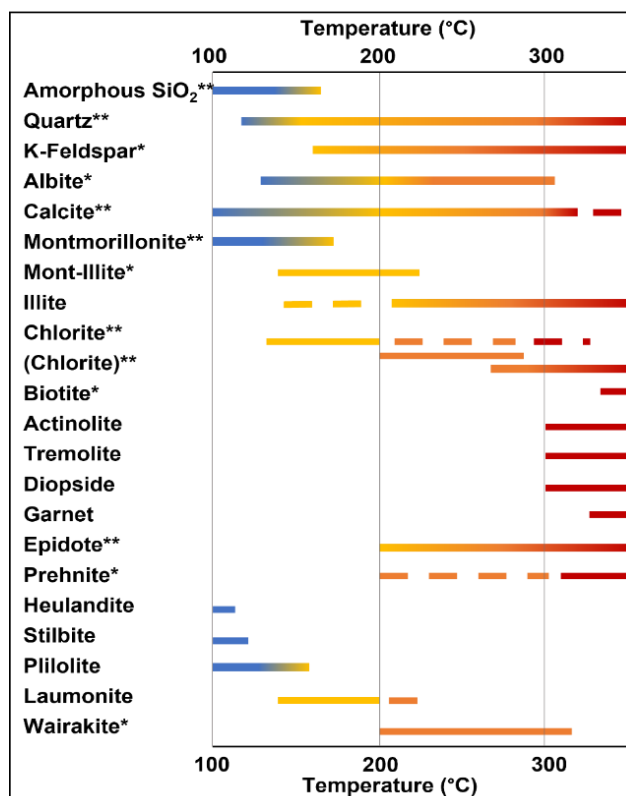


Figure 1.10: Stability ranges of alteration minerals commonly found within hydrothermal systems (modified from Henley and Ellis (1983) and Boden (2017)). Asterisks indicate the relative importance of the mineral considered within the framework of this study.

On the margins of upflow zones, clays often form due to hydrolytic alteration (Boden, 2017). Clays are increasingly recognised as ‘problem minerals’ in geothermal reservoirs due to their prevalence in fractures, with low permeability creating barriers to fluid flow (Vidal et al., 2018). With increasing depth and temperature, mineral transformations may occur (e.g. the transition of smectites – such as montmorillonite - to illite), which are known to cause frictional instabilities (Brown et al., 2003; Ikari et al., 2009b). In EGS reservoirs, injection of fluids to nominally dry clay-bearing fractures may also change their physical properties and frictional strength/stability (*Section 1.2.1*). Such changes in frictional behaviour can make a fracture more susceptible to unstable, brittle failure and hence can strongly affect permeability creation and fluid flow in geothermal reservoirs. Operation-related seismicity as a result of fluid injection or extraction is common in conventional geothermal and EGS projects (e.g. Majer et al., 2007), and is usually associated with shear slip on pre-existing fracture planes as a result of reduced normal stress and increased fluid pressure, particularly wherever fluids are injected into hot, dry rocks that contain naturally poorly connected fracture networks and high proportions of clay minerals

(e.g. Pine and Batchelor, 1984; Ghassemi, 2012). Whilst micro-seismicity useful in interpreting fracture growth, geometry and permeability - and may indeed increase permeability through shear dilation - it also has the potential to cause unstable failure in fractures of undesirable orientations and induce seismicity (Ghassemi, 2012, Meller and Kohl, 2014). Fully understanding the strength and stability of fractures sealed by clays and other minerals can therefore also mitigate against well failures and negative societal responses to induced seismicity, both of which have the potential to halt the development of geothermal projects.

The temporal evolution of fracture permeability (and in particular the conditions at which fractures are most likely to be sealed by precipitation) requires further investigation to improve the efficiency and overall success of geothermal projects (e.g. Dobson et al., 2003; Genter et al., 2010; Ghassemi, 2012; Griffiths et al., 2016). Fluid pressure reduction during fluid extraction is common in producing geothermal systems where natural recharge rates are lower than extraction rates, particularly in low permeability reservoirs (e.g. Majer and Peterson, 2007; Bromley et al., 2013). Conversely, higher permeability areas may be prone to influx of cooler fluids due to high recharge rates that do not allow sufficient time for fluids to extract heat from the surrounding rock mass. Reports of decreased flow rates and well head pressures during geothermal production are common (e.g. Árnason, 2020), and are often attributed to scaling within the well blocking fluid pathways and reducing permeability.

Changes in the pressure and temperature of the fluid during production, as well as mixing of geothermal fluids, could drive fluid solubility with respect to particular minerals, and hence permeability and flow rates, in either direction (e.g. Bodvarsson, 1988; Bromley et al., 2013; Árnason, 2020). Common examples of mineral precipitates are quartz and calcite, which can occur within fractures at depth and near the surface, as well as in wellbores and pipework (Figure 1.11), with the area at most risk of permeability destruction largely dependent on the change in fluid conditions experienced and the chemistry of the host rock (Ármannsson, 2012).



Figure 1.11: a) Example of a hydrothermally sealed fracture formed at depth (a quartz-epidote-calcite vein from the field site studied in Chapters 2 and 3). b) Example of geothermal pipework infrastructure with significant calcite scaling.

Silica solubility increases with pressure and temperature, hence such deposits are usually most problematic within surface equipment and reinjection wells rather than at depth in production wells, with quartz the main phase at high reservoir temperatures and other silica polymorphs at lower temperatures. Calcite, in contrast, has a retrograde solubility, and hence precipitates at the surface with cooler reservoir conditions but at depth in hotter reservoir conditions, however is also strongly dependent on the amount of CO₂ in the geothermal fluid. The process of fracture sealing may in turn lead to changes in physical characteristics including permeability and rock strength, hence also the productivity, longevity and stability of the geothermal system (e.g. Thien et al., 2015). These factors further highlight the need to understand controls on physiochemical conditions at depth and the evolution of fractured reservoirs over time.

1.3 Methodological Overview: Approaches to Understanding Fracture-Hosted Fluid Flow and Strength

The outstanding issues highlighted above relating to the study of hydrothermal fluid flow, sealing mechanisms and mechanical strength of hydrothermally altered rocks can be investigated in a number of ways. Since subsurface data gained via drilled wells can be sporadic and expensive, with physical properties at depth often estimated based on indirect drilling parameters, geological analogues and models are important tools in building a clearer picture of a potential geothermal system (e.g. Árnason, 2020; Wyering et al., 2014). Hence an approach combining the study of exhumed analogues and data from experimental analyses, as presented in this thesis, can be hugely beneficial to our understanding of geothermal systems prior to drilling. A brief introduction to some of the principles and methods used within the thesis is presented here, however these are repeated in greater detail wherever relevant within the core chapters.

Field-based methods are particularly useful in exploring the regional variation of structural permeability both within individual fault damage zones and across fault zones (*Chapter 2*), as well as the temporal evolution of fracture sealing by precipitation from fluids within a fault zone (*Chapter 3*). Several key attributes must be characterized in the field in order to predict the palaeo-permeability of a rock mass, namely fracture orientation, frequency/spacing (S') and aperture (e.g. Ortega et al., 2006; Sanderson et al., 2008). The most common technique used to sample vein or fracture networks in the field, and the method used in this study, is via a linear scanline (1D transect) (Priest, 1993; Sanderson and Nixon, 2015), which encounters N fractures over a length L (*Figure 1.12a*). After subtracting from L the length of unmeasured sections, the normalized average 1D intensity (I , or P_{10}) is defined as the number of fractures per unit length, N/L (Sanderson and Nixon, 2015). Whilst most previously published studies have concentrated on 1D analyses of fracture distribution, few (e.g. Ostermeijer et al., 2020) have considered 2D distribution. 2D fracture intensity (P_{21}) is defined as the total length of fractures intersected by a sampling window within the wider mapped area (Sanderson and Nixon, 2015; Healy et al., 2017). Where a structure's length is not considered, the number of fractures intersected by the

scan window is termed fracture frequency (P_{20}) (Figure 1.12b). Considered together, these analyses provide a representation of regional fault or fracture distributions, and also provide insight into how structures interact. Fracture connectivity, another important aspect of structural permeability, can be assessed by categorising the types of interactions between fractures, with fracture ‘nodes’ typically defined as being either isolated, abutting, or crossing, with each suggesting greater connectivity (Figure 1.12c). Few datasets have analysed the distribution of successive vein sets across a fault network to investigate how permeability may have evolved throughout the evolution of a hydrothermal system, therefore this study takes these 1D and 2D analyses further by also taking into account the composition and thickness of mineral precipitation within fractures.

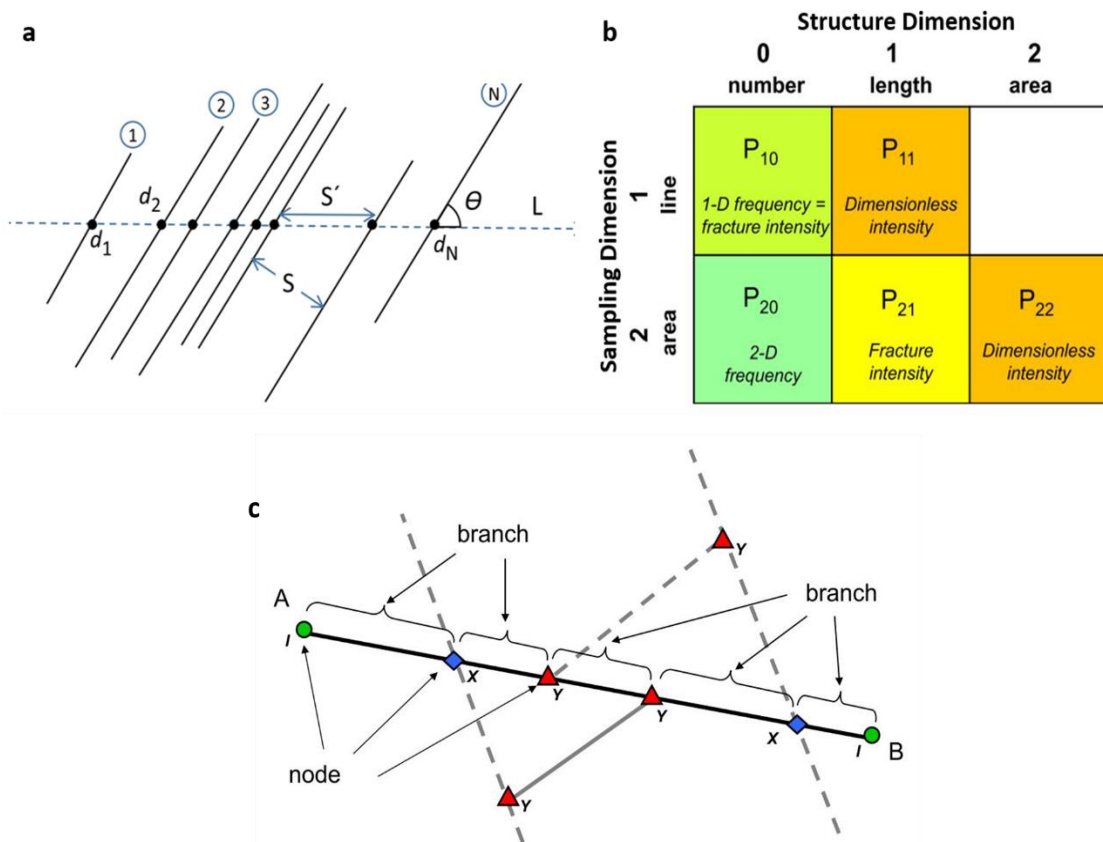


Figure 1.12: a) Schematic diagram of a linear scanline encountering N fractures over a length L . Each fracture is a distance d from a known reference point and oriented at an angle ϑ to the scanline. The spacing S' between each fracture is measured perpendicular to the fracture (S). b) A grid of terms used to describe fracture/vein spatial distribution, in terms of the dimension of sampling and the dimension of the structures measured. c) An illustration of how intersecting fractures can be categorized, with I nodes (isolated fracture tips, green circles), Y nodes (fractures abutting against another, red triangles) and X nodes (fractures crossing another, blue diamonds) defining the ends of fracture segments (branches) (Modified from Sanderson and Nixon, 2015).

The use of such field data must also take into account its inherent limitations. The methods described above ultimately create an orientation and length bias – this bias is greatest when multiple vein or fracture sets at different orientations are sampled with a single scanline, and

must be corrected for (Terzaghi, 1965; Watkins et al., 2015; *Appendix A- Section A4*). Structural datasets are sensitive to censoring and truncation, where long and thin veins/fractures respectively may be under-represented due to the limits of the measurement resolution or size of the sampled outcrop (both an issue related to the chosen study scale, which must be consistent throughout) (e.g. Bonnet et al., 2001; Zeeb et al., 2013; Healy et al., 2017). All estimates of density, intensity and connectivity presented should therefore be considered as minimum values.

Laboratory-based experiments allow the testing of isolated parameters on a carefully selected set of samples, and here aim to provide further insights into what aspects of hydrothermal alteration and fracture sealing influence the mechanical strength of fractured rock (*Chapter 3*), how physiochemical properties of mineral fill within sealed fractures influences the frictional strength and stability of fractured rock (*Chapter 4*), and how the variation and rate of change of physical conditions within a hydrothermal system influence the nature, rate and volume of precipitation from fluids occurring within fractures (*Chapter 5*). The experimental apparatus most used within this study is the Faulkner triaxial deformation pressure vessel within the University of Liverpool's Rock Deformation Laboratory (*Figure 1.13a,b*; and described in greater detail in *Appendix B – Section B3*).

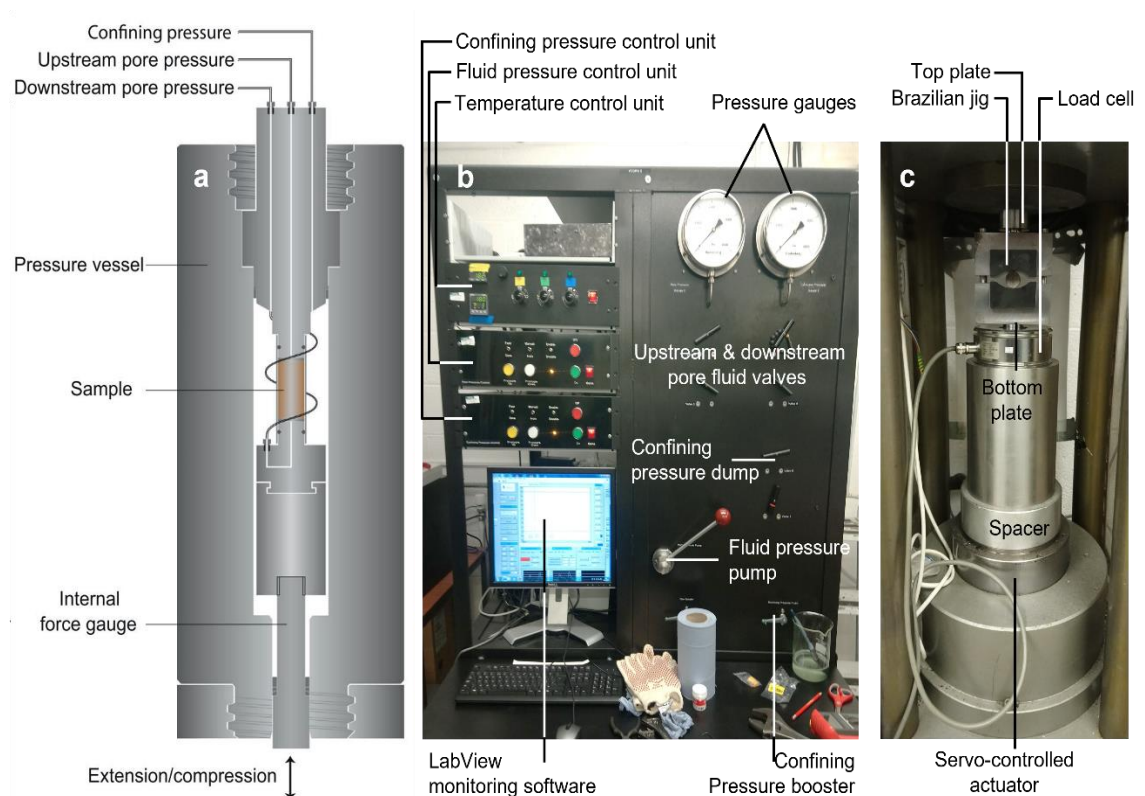


Figure 1.13: a) Schematic drawing of the Faulkner triaxial apparatus used in Chapter 4 and forming the basis of Chapter 5 (after Faulkner and Armitage, 2003). b) Photograph of the front control panel of the triaxial apparatus. c) Photograph of the uniaxial loading apparatus with a Brazilian jig in place.

The triaxial apparatus can perform experiments under confining pressures of up to 250 MPa and pore pressures of up to 200 MPa (both servo-controlled with a resolution better than 0.1 MPa and a measurement resolution better than 0.02 MPa). Core samples and direct shear jigs within the sample assembly can also be subjected to a 300 kN axial load, which is generated by a servo-controlled electromechanical actuator, monitored using an internal force gauge (with a resolution better than 0.05 kN) and controlled using displacement or force feedback (Faulkner and Armitage, 2013). The triaxial deformation apparatus (and similar setups elsewhere) has been used to investigate many physical characteristics of rocks or fault gouge at a wide range of controllable pressures, with or without the effect of water as a pore fluid. The most notable, relevant examples to this thesis are those that explore controls on mechanical strength and structural permeability (e.g. Moore et al., 1994; Morrow et al., 2001; Mitchell and Faulkner, 2008; Faulkner and Armitage, 2013; Siratovich et al., 2016) and frictional properties of fault gouge (e.g. Morrow et al., 2000; Moore and Lockner, 2004, 2007; Behnsen and Faulkner, 2012, 2013; Morrow et al., 2017; Sanchez-Roa et al., 2017).

Parameters that have not been extensively studied due to current design limitations, however, are the effect of room humidity on deformational processes without the presence of a pore fluid, and the effect of increased temperatures on deformational processes and fracture sealing at high pressures. With increased depth in the Earth's crust, increased dehydration, mechanical consolidation and mineral transformation may occur (Marone and Scholz, 1988; Saffer and Marone, 2003; Ikari et al., 2009b). Samples that are unintentionally partially saturated as a result of room humidity at laboratory conditions may therefore not be applicable to regions of high geothermal gradients and poor fracture connectivity. Effects are of particular importance in phyllosilicate minerals, the frictional behaviours of which change significantly with changing saturation states (Byerlee, 1978; Moore and Lockner, 2004). In caprocks forming part of carbon capture and storage projects, for example, drying clays potentially leading to increased permeability and fault strength is of some concern (Armitage et al., 2010; De Jong et al., 2014; Vilarrasa and Carrera, 2015). *Chapter 4* provides an experimental investigation of these variables.

Experimental studies of the behaviour of fractured and hydrothermally altered rocks at high temperatures as well as pressures are of great importance to the geothermal industry, as they will help to realistically recreate conditions at depth whilst being able to isolate and experiment with different aspects of the physical system. Whilst the current setup at the University of Liverpool makes use of a series of knuckle band heaters around the outside of the pressure vessel, temperatures above ~ 250 °C cannot be reached, and the variability and dispersion of heat energy is not sufficient to maintain reliable, stable temperatures across a sample. A redesign of the existing apparatus is therefore required. Based on cumulative knowledge acquired from past and present staff and students within the University of Liverpool's Rock Deformation Laboratory (who have been formulating designs for a new sample assembly for

several years), alongside unpublished information from laboratories at the University of Manchester, the United States Geological Survey (USGS), and University of Montpellier amongst others, a new design (together with the scientific principles behind each component and details on its calibration) is outlined in *Chapter 5*. A new triaxial sample assembly, allowing for higher achievable temperatures as well as more reliably controlled, focused temperatures, would allow the production of datasets that could be highly beneficial to studies of fluid flow in geothermal systems.

Other laboratory methods employed within this thesis (most notably in *Chapter 3*) are Uniaxial Compressive Strength (UCS) tests (*Figure 1.13c*), which aim to give an indication of strength without the sample being subjected to high confining pressures (cf. Baud et al., 2006); Brazilian Tensile Strength (BTS) tests (*Figure 1.13c*), which measures the stress required to split a rock disc through tensile forces (cf. McNamara et al., 2014); X-Ray Diffraction (XRD), which quantifies the mineralogical composition of samples (cf. Pola et al., 2012); and thin section analysis via optical petrography, scanning electron microscopy and cathodoluminescence, aiming to provide detail on the mineralogical composition, texture and microstructure of natural and experimental veins and hydrothermally altered host rock samples (cf. McNamara et al., 2016).

1.4 Summary and Thesis Structure

Via a combination of field- and laboratory-based analyses, this thesis aims to improve the understanding of some of the physiochemical processes ongoing in deep, high-temperature, fractured geothermal systems. More specifically, it aims to reduce exploration and production uncertainty by drawing on aspects of geomechanics, structural geology and geochemistry to produce field and laboratory datasets that can be used to improve models of processes ongoing in the subsurface. It is also intended that further academic understanding can be added to the fields of rock mechanics, structural geology and seismology. To this aim, based on the rationale presented in this introductory chapter, a series of questions and research methods have been formulated (*Figure 1.14*) that will investigate how structurally controlled hydrothermal fluid flow varies spatially within a fault zone and evolves over time. Particular focus is given to fluid-rock interaction, exploring how hydrothermal alteration and veining affects the mechanical behaviour of a fractured reservoir and subsequent permeability creation, as well as the rates of permeability destruction as a result of fracture sealing by precipitation at the physical conditions typically experienced in geothermal reservoirs.

In *Chapter 2*, an exhumed analogue geothermal system is used to investigate how structurally controlled fluid flow may be heterogeneously distributed both across individual faults and across kilometre-scale fault systems, through an analysis of sealed fracture distributions. In *Chapter 3*, the same exhumed system is used to study the temporal nature of structural permeability in hydrothermal systems through analysis of an assemblage of mineral veins. Sampled veins have been further analysed in the laboratory to produce an experimental dataset

aiming to further understand the impact of anisotropy and hydrothermal alteration on the mechanical strength of a geothermal reservoir and successive fracturing events. In *Chapter 4*, the focus of investigation is moved from high temperature, epithermal fracture precipitation within the damage zone, to lower temperature, argillic precipitation more typical of a fault core. Here, a range of direct shear experiments under high pressure conditions in the laboratory aim to better understand the impact of clay mineral type and saturation state on the frictional strength and stability of faults and fractures. *Chapter 5* aims to investigate the physiochemical processes involved in permeability destruction by precipitation in fractures through the creation of a new high-pressure, high-temperature laboratory apparatus. As well as outlining the specifics of the design, equipment calibration and experimental techniques, the chapter summarises the rationale behind choosing particular experimental conditions that target conditions of maximum precipitation from mineral-doped solutions. Finally, *Chapter 6* summarises the work presented here and considers its wider implications and potential for further research.

Rationale: Whilst fluid flow properties of individual faults have been described extensively, variability within larger scale fault structures is less well understood.

Question: How is fault damage - and hence structural permeability - spatially distributed across a fault zone?

- **Chapter 2** investigates the degree of damage heterogeneity across a km-scale fault zone (i.e. permeability creation).
- *Analytical methods include field mapping of structures known to have hosted fluid flow (i.e. mineral veins) via 1D and 2D approaches, and subsequent statistical and spatial data analyses of fracture trace maps, spacing and aperture.*
- **Chapter 3** considers the spatial and temporal heterogeneity of fluid flow and fracture sealing within the same km-scale fault zone.
- *Analytical methods include statistical and spatial analyses of mineral vein composition, orientation and thickness data collected via 1D transects in the field.*

Rationale: Fault-hosted hydrothermal systems are often long-lived and contain evidence of multiple generations of fluid flow in the form of mineral veins.

Question: How do early phases of fracture sealing influence subsequent fluid flow events, and therefore the temporal evolution of structural permeability?

- **Chapter 3** investigates how individual mineral veins record evidence of multiple phases of fracture sealing by precipitation, and explores how the amount of precipitation varies in relation to the regional state of stress.
- *Analytical methods include stereographic analysis of mineral vein compositions, thicknesses and orientations collected via 1D transects in the field, as well as optical petrography, scanning electron microscopy and cathodoluminescence analyses of thin-sectioned vein samples.*

Rationale: Precipitation of minerals within micro- and macro-fractures changes the mechanical properties of rocks and creates discontinuities that vary in mechanical behaviour according to a range of mineral properties.

Question: How do hydrothermal fluids and resultant alteration mineralogy affect the mechanical and frictional strength of a fractured geothermal reservoir?

- **Chapter 3** investigates the influence of propylitic alteration and epithermal veining on the mechanical strength of isotropic host rock, and also considers the effect of vein orientation on rock strength.
- *Analytical methods include X-Ray Diffraction analyses of altered and unaltered host rock, and compressional and tensile strength experiments on cored samples.*
- **Chapter 4** considers the impact of argillic fracture-hosted alteration containing high proportions of phyllosilicates on the frictional strength and stability of fractures.
- *Analytical methods include direct shear experiments at high confining pressures on two phyllosilicate gouge samples with varying degrees of water saturation.*

Rationale: The nature and rate of fracture sealing by precipitation varies according to a range of physiochemical parameters that can take a hydrothermal system out of equilibrium - these are well understood via theoretical means but little has been done experimentally at high pressures and temperatures to help understand what factors are most important in destroying permeability in geothermal systems.

Question: What are the key controls on the nature, rate and volume of precipitation in structurally-hosted hydrothermal systems?

- **Chapter 5** reviews the theoretical understanding of how the degree of change in pressure, temperature and other fluid properties influences the amount of minerals that can be held in solution by hydrothermal fluids, and introduces the rationale behind a new experimental apparatus built to investigate the effect of these parameters on the nature and rate of precipitation within synthetic fractures.
- *Analytical methods include the design of a new high-pressure, high-temperature sample assembly to perform experiments within existing rock deformation apparatus, and modelling of physiochemical conditions to predict zones of maximum precipitation in hydrothermal systems.*

Figure 1.14: Summary of the rationale behind key questions to be addressed within this thesis, and a brief overview of how each of the core chapters presented here aims to address them.

2 Structural Controls on Fluid Circulation in a Transtensional Duplex: Lessons from an Exhumed Geothermal System

Abstract

Geothermal reservoirs require high permeability to sustain fluid flow, which is often controlled by fracture networks. To understand the evolution of geothermal systems and develop them successfully, the physical properties and spatial distribution of permeable fracture networks within different fault systems must be characterised. It is also important to understand the dynamic nature of permeability in terms of the relationship between tectonics and fluid flow, which can be achieved via the study of mineral veins precipitated in the fracture network in analogous structural settings. The Caleta-Coloso transtensional duplex, part of the Atacama Fault System in Chile, is considered an analogue for a fault-hosted geothermal system. The duplex, formed almost entirely in granodioritic host rock, is bounded by two sinistral strike-slip faults, and contains later transtensional to extensional faults. Fractures in the fault damage zones are sealed by a mineral assemblage of chlorite-epidote-quartz-calcite. Through statistical analysis of mechanical damage and mineralogical data collected via 1D linear transects and 2D outcrop surface mapping, the structural controls on episodic flow are characterized to help identify spatial variations in permeability and fluid flux in this particular geothermal system. Measurements of both 1D and 2D vein intensity suggest that damage is heterogenous at multiple scales. Areas within the duplex have undergone more brittle deformation than areas outside, with greater connectivity also suggesting higher paleo-permeability. Intensity decreases along strike away from the duplex centre as well as with distance from major faults, conforming to previous observations that suggest the amount of fault displacement coupled with regional fault density may be the primary causes of intensity variation. Connectivity, as assessed via fracture trace maps, appears to be controlled by the presence of abutting linkage structures, suggesting that fluid flow phases are strongly influenced by pre-existing structures. Analysis of two distinct vein phases (chlorite-epidote-quartz and calcite) suggests that fluid flow in general uses the whole of the open fracture network, however flow within the duplex may have been more clustered compared to a more uniform distribution outside of the duplex. These data have implications for understanding the areas which may be considered suitable targets for geothermal drilling sites in similar structural settings, suggesting that areas within a fault overlap zone provide higher permeability than those outside, in particular those adjacent to dense networks of high-displacement faults in areas with multiple pre-existing structural fabrics.

2.1 Introduction

The development of faults and fractures in the upper crust play a crucial role in controlling fluid flow. The study of these prevalent structural features provides important insights into their mechanical, hydraulic and seismic properties (Chester et al., 1993; Hickman et al., 1995; Caine

et al., 1996; Gudmundsson et al., 2001; Faulkner et al., 2003, 2008; Wibberley and Shimamoto, 2003). Whilst the application of such studies to mineral exploration (e.g. Cox, 1995, 1999) and production from hydrocarbon reservoirs (e.g. Gartrell et al., 2004) has been known for some time, it is of ever-increasing importance in its application to geothermal exploration of fractured reservoirs (e.g. Evans, 2005; Evans et al., 2005; Dezayes et al., 2010; Davatzes and Hickman, 2010; Wallis et al., 2012; Sanchez et al., 2013; Kissling et al., 2015). In order to understand the evolution of geothermal systems and develop them successfully, it is important to characterize the properties and spatial distribution of permeable fracture networks within different fault systems and constrain the complex relationship between tectonics and fluid flow in terms of the dynamic nature of permeability. The field study of 'palaeo-permeability' in exhumed systems, which usually contain frozen hydrothermal activity in the form of mineral veins, provides a useful analogue that can be used to improve the understanding of contemporary fractured geothermal systems in similar tectonic settings (e.g. Faulkner et al., 2010; Faulds et al., 2011; Gomila et al., 2016; Sanderson, 2016).

Structurally controlled fluid flow is typically focused in the permeable damage zone of a fault. This damage zone may be up to hundreds of metres wide, and forms adjacent to a narrower, less permeable core typically comprising fault gouge and cataclasite (*Figure 2.1*) (Chester and Logan, 1986; Barton et al., 1995; Caine et al., 1996; Wibberley et al., 2008, Savage and Brodsky, 2011; Faulkner et al., 2003, 2008, 2010). Small-scale structures in fault damage zones are often underrepresented in sub-surface studies with respect to larger structures (Nixon et al., 2019), yet they induce markedly different mechanical and hydraulic properties compared to intact rock (e.g. Sibson, 1994, 1996, 2000; Evans et al., 1997). Many deformation mechanisms at a range of scales play an important role in controlling damage zone permeability. Damage can be accrued via processes such as coalescence/linking of structures (Childs et al., 2009), cumulative wear with displacement (Chester and Chester, 2000), coseismic damage (Rice et al., 2005) or fault linkage involving a process zone (Cowie and Scholz, 1992). Enhanced hydraulic connectivity as a result of damage is considered to prevent development of fluid overpressures, hence maintaining stable crustal stress levels (Townend and Zoback, 2000). With increased fault maturity and displacement, damage zones may increase in width and - as a result of interactions between faults - complexity and heterogeneity, which may increase in the presence of pre-existing structures and lithological variation (Gudmundsson et al., 2002, 2010; Myers and Aydin, 2004; Faulkner et al., 2008; O'Hara et al., 2017; Ostemeijer et al., 2020). Importantly, damage zone characteristics can vary between different fault systems (e.g. Cox, 1995; Mitchell and Faulkner, 2009); the presence of subsidiary/splay faults, for example, may overprint on damage levels relating to the main fault, or indeed relating to other subsidiary faults (*Figure 2.1*).

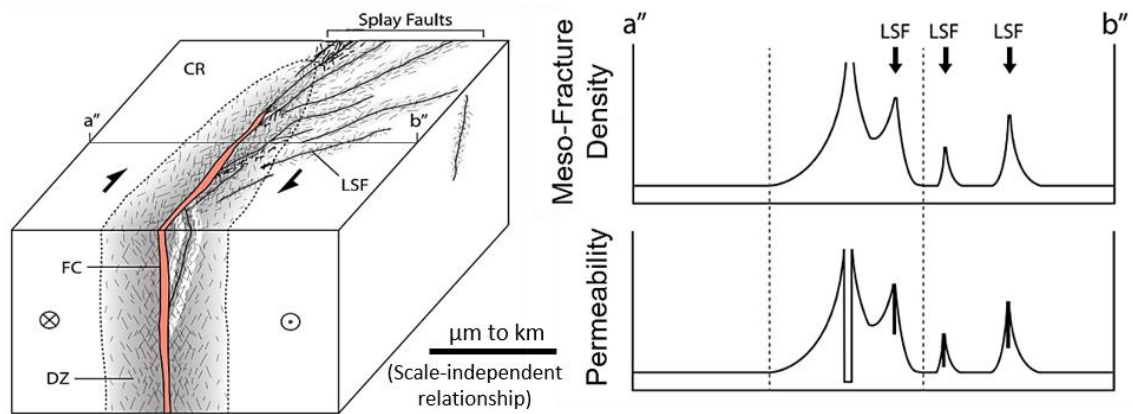


Figure 2.1: The relationship between fault architecture, fracture density and permeability (after Ostermeijer et al., 2020; based on Chester and Logan 1986; Caine et al. 1996 and Faulkner et al. 2010).

Fault duplexes (variably termed stepovers, bends, relay ramps or jogs) (illustrated schematically in Figure 2.2d) represent sites of fault interaction and linkage between overstepping faults (e.g. Peacock and Sanderson, 1991; Berger, 2007; Cunningham and Mann, 2007; De Paola et al., 2007). Such structures develop as a fault periodically propagates on one side of the structure and ‘shuts off’ the fault on the other side (Cembrano et al., 2005; Wakabayashi et al., 2004). Transtensional duplexes comprise a complex interaction of extensional-shear (i.e. Mode II) and purely extensional (i.e. Mode I) fractures. Overstepping fault segments are able to link and accommodate stretching and can cause local rotation of the regional stress field (Sibson, 1985, 1996; Woodcock and Fisher, 1986; Peacock and Sanderson, 1991; De Paola et al., 2007). Enhanced fault and fracture development and their distribution and geometry within the fault overlap zone are considered to be important sites for increased permeability and fluid transport within the Earth’s crust (Wilcox et al. 1973; Crowell 1974; Aydin and Nur 1982, 1985; Sibson, 1987; Walsh et al., 2003; Leckenby et al., 2005; Berger, 2007; Choi et al., 2016; Nixon et al., 2019). Such structures host around one third of geothermal systems in the Great Basin, USA (Faulds et al., 2013), and elsewhere have been shown to contain significant hydrothermal mineral deposits (Lindsay et al., 1995). The mechanics of such features, however, are not well constrained, particularly regarding how fluids and fractures (both strike-slip and dip-slip) interact to form veins within fracture networks (Cembrano et al., 2005). Whilst the importance of extensional duplexes as fault-related structures that control the flow of fluid (either by acting as flow conduits or barriers) is well-documented, there is still a need to consider their dynamic evolution (e.g. De Paola et al., 2007) and quantify the damage distribution and intensity within them (e.g. Nixon et al., 2019).

To fully understand damage zone variability within such fault zones, it is necessary to quantitatively characterise fracture patterns at a range of scales. At macro- and meso-scale (i.e. where fault/fracture lengths are in the order of 1-5 orders of magnitude smaller than the main fault ($\sim 10^2$ to $\sim 10^3$ m: Shipton and Cowie, 2001)), understanding how structural mechanisms interplay to control fracture length, aperture and density is important (e.g. Sanderson, 2016).

For example, fracture density has been shown to decay with distance from the fault core, either exponentially (Anders and Wiltschko, 1994; Wilson et al., 2003; Mitchell and Faulkner, 2009) or following a power law (Savage and Brodsky, 2011; O'Hara et al., 2017), ultimately controlling damage zone widths. This decay has been shown to scale with fault length and displacement (Scholz et al., 1993; Vermilye and Scholz, 1998; Mitchell and Faulkner, 2009; Savage and Brodsky, 2011; Faulkner et al., 2011), and in turn may be linked to predictions of fracture mechanics models that show a decaying stress field with distance from the fault (e.g. Scholz et al., 1993). At a microstructural level (fracture lengths $<10^{-2}$ m), fracture density appears to show similar characteristics: for example, Faulkner et al. (2011) have shown that microfracture density in alteration haloes surrounding shear veins scales with displacement. Dominant mechanisms of permeability creation and destruction at this scale include fluid migration and percolation, reseal hardening or weakening, rock mechanical properties, physio-chemical growth of minerals and crack-seal mechanisms (Sibson, 1996; Faulkner and Rutter, 2000; Woodcock et al., 2007; Faulkner et al., 2010, 2011; Bons et al., 2012).

As pressure and temperature increases (either with depth or during the fault's temporal evolution as a host of hydrothermal fluid flow), the mechanical and hydraulic characteristics of individual fluid pathways become more dynamic as fractures continuously open and close as part of the seismic cycle further complicating damage heterogeneity. Coseismic permeability destruction may occur by closure of fractures or by sealing by mineral precipitation (e.g. Cox, 1995, 1999, 2010; Sibson, 1996; Faulkner et al., 2010; Bons et al., 2012; Rempe et al., 2018). Veins are mineral aggregates that precipitated from a fluid in dilatational sites and can occur as a single precipitation event or as multiple crack-sealing events (Ramsay, 1980). The composition of minerals precipitated in vein networks provides a record of pressure and temperature, fluid compositions, and interactions between fluids and fractured host rock. In geothermal areas, mineral precipitation can rapidly seal fractures (Dobson et al., 2003; Griffiths et al., 2016; McNamara et al., 2016), resulting in sudden changes in permeability and fluid pressure (Wiltschko and Morse, 2001). The precise mechanisms by which syntectonic veins form, however, is not well understood (Hilgers and Urai, 2002a; Barker et al., 2006; Bons et al., 2012; Gomila et al., 2016). Analysis of the thickness - and thickness distributions - of vein networks is important in order to describe and predict the connectivity of fracture networks and the mechanisms by which they may have formed (Roberts et al., 1998; Sanderson et al., 2008).

This study characterises the damage surrounding low displacement duplex imbricate faults that cut through a single low porosity crystalline protolith. Whilst the fluid flow properties of individual faults have been described extensively, larger scale fault structures such as duplexes are rarely described (e.g. Faulkner et al., 2010 and references therein). In this study, we provide a new structural network characterisation of a transtensional duplex developed in low-porosity crystalline rocks. Data were collected from the damage zones of subsidiary faults (with slip displacements ranging from $\sim 10^{-1}$ to $\sim 10^2$ m) forming part of the Atacama Fault System (AFS) in

northern Chile (*Figure 2.2*). The distribution of mineral veins were used as a proxy for fluid flow to understand more fully the spatial heterogeneity occurring in duplex-hosted geothermal systems. The AFS provides a rare opportunity to study an exhumed transtensional duplex that has hosted hydrothermal circulation and address how fractures and permeability are distributed, as well as whether these types of structure represent an enhanced prospect for geothermal exploration.

2.2 Geological Setting

The AFS is a c.1000 km long sinistral strike-slip structure between Iquique (21°S) and La Serena (30°S). It initially developed as a sinistral transpressional arc-related ductile fault between 190-110Ma, owing to oblique South-Eastward subduction of the Aluk plate - at a retreating subduction boundary - beneath South America (Scheuber and Andriessen, 1990; Royden, 1993; Taylor et al., 1998; Scheuber and González, 1999; Cembrano et al., 2005). The fault zone, which in the study area cuts a broadly similar range of protoliths, has since been exhumed from seismogenic depths and contains structures ranging over 7 orders of magnitude (10^{-4} to 10^4 m) (Jensen et al., 2011). Host rock in the field area comprises Early Jurassic ortho-amphibolite and ortho-granulite (*Figure 2.2c*) (Cembrano et al., 2005) intruded by late Jurassic diorite and granodiorite. NW-striking microdioritic dykes cut the igneous complex and represent the last igneous activity in the area (Cembrano et al., 2005), inducing sinistral and dextral mylonitic foliations up to ~145 Ma (Scheuber and González, 1999). Later brittle, sinistral strike-slip events (~132 Ma) reactivated these mylonitic fabrics as the subduction boundary began to advance obliquely (Scheuber and Andriessen, 1990; Scheuber et al., 1995; Taylor et al., 1998; Scheuber and González, 1999). Duplex formation likely occurred c. 106 Ma during transpressional strike-slip deformation (Dallmeyer et al., 1996). Miocene-Pliocene normal dip-slip reactivation has also been documented (e.g. Dewey and Lamb, 1992) and attributed to subduction-related earthquakes due to ENE-subduction of the Nazca plate (González et al., 2003, 2006).

The Caleta Coloso Duplex (CCD) is bounded by the Bolfin and Jorgillo Faults: overstepping NNW-trending and steeply E-dipping strike-slip faults splaying off the sinistral Coloso Fault (*Figure 2.2c, d*). Amount of displacement on the duplex-bounding faults is at least 10-200m and records predominantly shear structures (Cembrano et al., 2005). The >45 km long Bolfin Fault forming the western boundary of the CCD dips steeply to the East and comprises a 50-100 m thick core dominated by cataclasite (Jensen et al., 2011). The footwall of the fault appears more deformed than outside of the duplex, however the latter is less well exposed due to the presence of Cenozoic cover. Duplex imbricate faults (i.e. second- and third-order faults) developed progressively by splaying off both bounding faults (Cembrano et al., 2005) and accommodate along-strike stretching and vertical displacement within the duplex via a combination of low-displacement NW-SE transtensional and N-S dip-slip movements. Fault blocks created by this fault interaction pattern have been subject to up to ~30-35° clockwise rotation (Taylor et al., 1998). Fault and fracture networks concentrated between the two bounding faults host a large

proportion of total CCD mineralisation, as expected due to the suction pump (precipitation by depressurization) mechanism for strike-slip / extensional duplexes (Sibson, 1987).

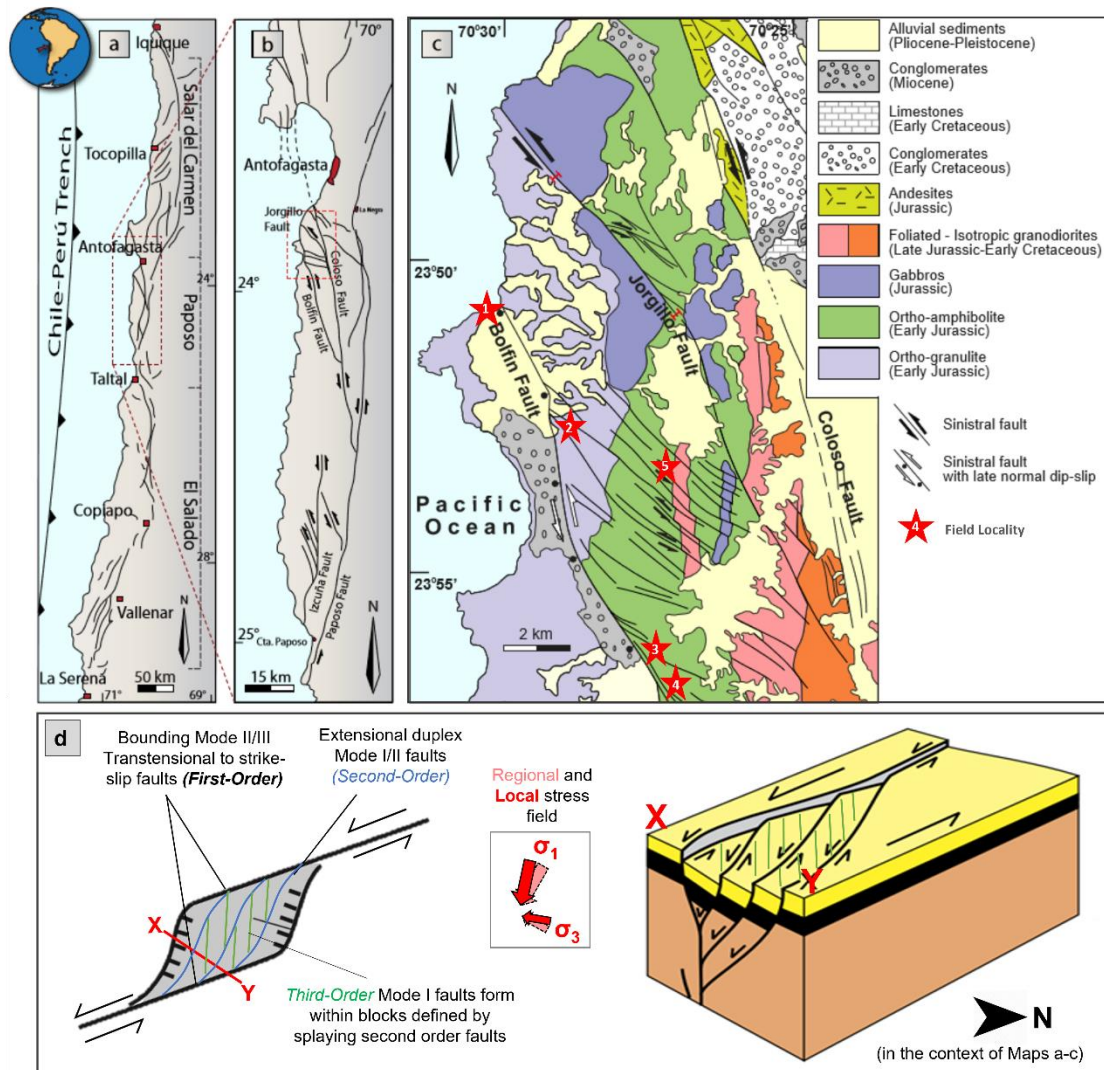


Figure 2.2: a) and b) Simplified structural map of the Atacama Fault System and c) Simplified geological map of the field area (modified from Cembrano et al., 2005). Field localities are marked as red stars. d) Simplified schematic diagrams of a transtensional duplex (in plan view, as well as cross sectional view across the transect X-Y) in the context of local and regional stress fields) (adapted from Wakabayashi et al., 2004; Cembrano et al., 2005 and De Paola et al., 2007).

Second- and third-order faults often form ‘self-similar’ strike-slip duplexes at various scales (Cembrano et al., 2005; Scheuber and González, 1999; Faulkner et al., 2011; Jensen et al., 2011; Stanton-Yonge et al., 2020). Second-order duplex structures are defined by a set of ~NW-SE-trending faults (Figure 2.2c, d), with core widths of <2 m (Jensen et al., 2011), dipping steeply to the NE (Taylor et al., 1998; Cembrano et al., 2005). Kinematics of the brittle structures are predominantly sinistral strike-slip with a minor extensional component, and minimum displacements of 10-100 m have been suggested, with only the higher displacement faults showing evidence of a significant fault core (Jensen et al., 2011). ~E-W-trending third-order faults generally formed later within blocks defined by second-order faults (Figure 2.2d). Growth

mineral fibres and Riedel shears within third-order faults indicate normal displacement of up to ~10 cm (Cembrano et al., 2005). These faults have predominantly normal kinematics and dip at a wide range of angles to both North and South. Fault core thicknesses are at most a few centimetres, and normal displacements range between 0.01 – 0.1 m (Herrera et al., 2005; Olivares, 2004).

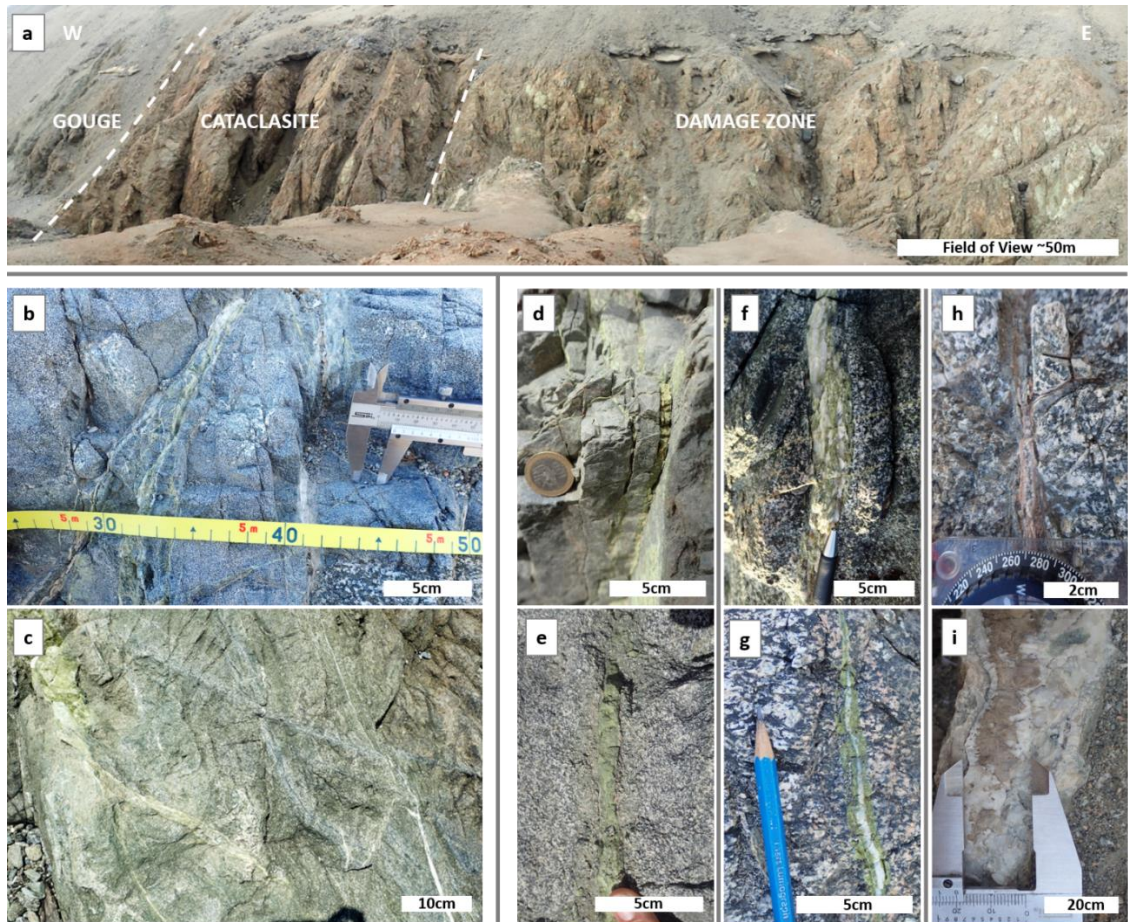


Figure 2.3: a) Outcrop of the Bolfin Fault at Site 2 showing the progression from fault gouge, through foliated and unfoliated cataclasite to the damage zone. Field of view is ~50 m. In subsidiary faults, the scale of this progression is reduced. b) Photograph illustrating the methodology of 1D transects, where vein properties were recorded at each intersection with the tape measure. c) Photograph illustrating part of a 2D outcrop map, where veins on an approximately horizontal surface were digitally traced. Photographs d) to i) are examples of veins at damage zone outcrops: d) and e) = epidote with minor chlorite; f) and g) = epidote + quartz; h) and i) = calcite-dominated (blocky and microcrystalline), with varying amounts of quartz and other minerals).

Preserved Mode I and II veins within the damage zones of faults within the CCD (Figure 2.3a) - as well as gouge and cataclasite in the fault core - contain mineral assemblages of chlorite, epidote and quartz (Figure 2.3d-g) indicative of contemporaneous faulting and fluid transport under retrograde low-greenschist facies conditions (~280-350 °C) and depths of ~3 to 6 km (Olivares, 2004; Cembrano et al., 2005; Herrera et al., 2005; Arancibia et al., 2014). These occur as both fault-veins with microstructures such as banding and fractured grains suggesting

synkinematic precipitation, and as extension veins where microstructures such as euhedral crystal growth from fracture walls are interpreted to indicate longer-duration growth into open, fluid-filled fractures (e.g. Herrera et al., 2005). Propylitic alteration of biotite and feldspars to chlorite around these veins is evident from alteration haloes, reflecting an interconnected network of microfractures surrounding macrofractures (Faulkner et al., 2011). These vein phases are variably cut or exploited by later calcite-dominated veins (*Figure 2.3h-i*), which in some areas has been shown to have precipitated in open fractures at subhydrostatic pressures (Herrera et al., 2005). A second phase of calcite occurring with smectite (palygorskite), gypsum, halite and haematite is easily distinguishable from earlier phases and linked to Miocene-Pliocene fault reactivation due to coseismic elastic rebound of the forearc (González and Carrizo, 2003; Cembrano et al., 2005). Whilst vein compositional evidence suggests that there is clearly a temporal evolution of hydrothermal activity, the most common vein sets are those containing chlorite, epidote and quartz formed in the early history of the geothermal system. These veins provide a snapshot of the fault system at a single crustal depth; any depth dependency of damage zone and vein formation is therefore minimized. The results of this study focus primarily on this phase.

2.3 Methodology

Several key vein attributes must be characterized in the field in order to predict the palaeo-permeability of a rock mass, namely their orientation, frequency, spacing and thickness (aperture) (e.g. Ortega et al., 2006; Sanderson et al., 2008). The most common technique used to sample vein or fracture networks in the field, and the method used in this study, is via a linear scanline (1D transect) (Priest, 1993; Sanderson and Nixon, 2015) (*Figure 2.3b, Figure 2.4a*). A linear scanline encounters N fractures over a length L . After subtracting from L the length of unmeasured sections, the average intensity (I) (the number of fractures per unit length) can be calculated as N/L . When calculated from a linear transect, this parameter is termed the average normalised vein intensity, P_{10} (Sanderson and Nixon, 2015; *Figure 2.4b*). The relationship between individual fractures may also be calculated from 1D transects as the spacing (S') (*Figure 2.4a*). From these data, the coefficient of variation (CoV) - a dimensionless measure of the spacing variation indicating the fracture distribution (Gillespie et al., 1993) where values >1 indicate clustered, not regular, veins - can be calculated as $\sigma S'/S'$. From a Kuiper's Test of uniformity, the parameter V^* (a function of Kuiper's V and N) can be used to test the null hypothesis of uniformity, where if $V^* > 1.75, 2.0$ and 2.3 the null hypothesis of uniformity can be rejected at the 95%, 99% and 99.9% levels: Stephens, 1970); rejection suggests a heterogeneous vein distribution (Sanderson et al., 2019).

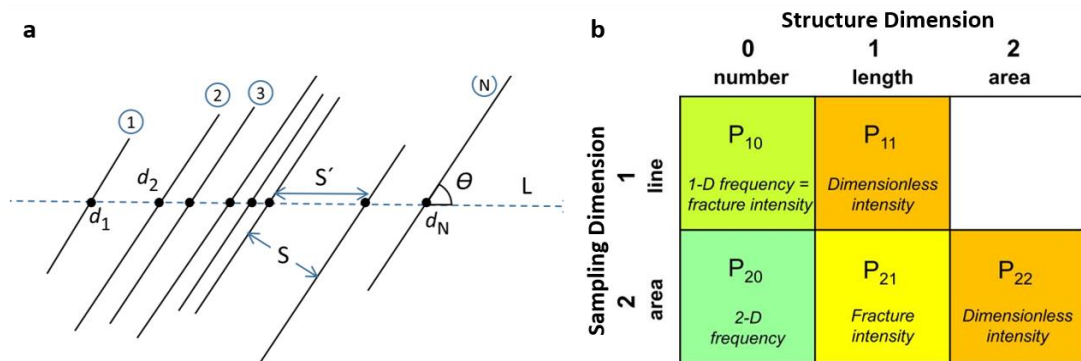


Figure 2.4: a) Schematic diagram of a linear scanline encountering N fractures over a length L . Each fracture is a distance d from a known reference point and oriented at an angle ϑ to the scanline. The spacing S' between each fracture is measured perpendicular to the scanline however can also be measured perpendicular to the fracture (S). b) An illustration of terms used to describe fracture/vein spatial distribution in terms of the dimension of sampling and the dimension of the structures measured (Modified from Sanderson and Nixon, 2015).

In this study, data were analysed for 836 veins from 15 1D transects covering 5 sites (Figure 2.5). At transect level, data were analysed for actual and cumulative vein frequency and vein spacing (S') with distance (d) from the fault. To be comparable at site level, data from individual transects were normalised for transect length, with data gaps as result of poor exposure removed, and only sites a similar distance from a second-order fault (where known) were directly compared. At site level, data were analysed for mean, median and standard deviation of normalised average intensity (calculated in bins of 1 m length except where data gaps were present); and mean gradient, standard deviation, skewness, kurtosis and CoV for cumulative frequency and spacing.

Several limitations must be considered when considering the implications of 1D datasets. Employing this method ultimately creates an orientation and length bias that is greatest when multiple vein or fracture sets at different orientations are sampled with a single scanline (Watkins et al., 2015). Scanlines were therefore chosen to best represent the fracture sets present and be consistent when comparing more than one. Veins or fractures striking at a low angle to the scanline are under-represented until corrected for using the method of Terzaghi (1965) (Appendix A, Section A4), and (relative to those at high angles) will result in intensity underestimates as well as spacing overestimates. 1D datasets are sensitive to censoring, where long veins or fractures may be under-represented due to the limits of the outcrop or transect length. Data truncation may also occur whereby thin veins are under-represented; this results in only minimum or maximum sizes being recorded respectively.

Whilst most previously published studies have concentrated on 1D analyses of fracture distribution, few (e.g. Ostermeijer et al., 2020) have considered 2D distribution. 2D analyses of the duplex at a regional scale were made by digitally tracing fractures from a published geological map (Gobierno de Chile, 2003) and importing a .svg file into FracPaQ (A MATLAB™

toolbox for the quantification of fracture patterns (Healy et al., 2017)). The 2D fracture network parameters intensity and frequency (which in the literature is also variably termed 'density') (*Figure 2.4b*) were calculated using the circular scan window method (Mauldon et al., 2001) for 500 x 500 m areas to form a grid across the duplex. Fault or fracture intensity (P_{21} ; Sanderson and Nixon, 2015; Healy et al., 2017) was calculated as the total length of the faults intersected by the scan window within the area covered by the window. Where a structure's length is not considered, the number of fractures intersected by the scan window is termed fracture frequency (P_{20}) (*Figure 2.4b*). Considered together, these analyses provide a representation of fault or fracture distributions in a 2D space. Intensity and frequency are important attributes in assessing the fluid flow properties of a rock mass, particularly in two dimensions as they provide insight into how structures interact.

2D datasets are also sensitive to truncation and censoring (Zeeb et al., 2013), largely due to the resolution limits of the sampling method (Bonnet et al., 2001). This was carefully controlled between sites (e.g. by fracture tracing at a set zoom level, cf. Healy et al., 2017) to ensure no further biases occurred. All 2D analyses are subject to edge effects such that veins at the edges of the mapped area have not been drawn due to limited exposure. Vein density and intensity are underestimated here and all values presented should be considered as minimum values.

Well-exposed field areas (*Figure 2.2, Figure 2.3*) were identified based on satellite mapping and previous field campaigns. During reconnaissance mapping, major faults were generally recognised by the presence of ramblas/arroyos (dry creeks), which provided access to outcrops as well as exposing vertical sections through faults. Six areas from five different structural settings across the duplex ('sites') are discussed in this study, as described in *Table 2.1* and *Appendix A* and referred to in subsequent figures. These sites were chosen to represent a wide range of localized structural settings typical of duplex structures, whilst also capturing the regional variation that occurs in all directions – from outside of the duplex, from the edge of the overlap structure to the centre of the overlap adjacent to a boundary fault, and finally into the very centre of the duplex equidistant from both boundary faults. Whilst results presented here will ultimately only illustrate the differences between these specific sites, it is hoped that this also provides a reasonable representation of overall variation.

Linear transects (e.g. *Figure 2.3b*) were taken sub-perpendicular to the orientation of second-order faults (i.e. approximately SW-NE), where faults are defined as structures containing at least a partially-developed core and, if determinable, some evidence of displacement. At some sites the relationship to a major fault was less clear, however this is noted wherever this was the case. At selected sites orthomosaics of horizontal outcrops were created using a drone-mounted camera (e.g. *Figure 2.3c*) in order to create vein trace maps for 2D analyses. The coordinate system used was WGS84 transverse Mercator. FracPaQ assumes that fracture traces lie on a statistically flat 2D surface; although relatively flat outcrops were selected in the field, this is likely to result in minor error.

Table 2.1: A description of field sites (data measurement and sampling locations) across the study area. Further details are provided in Appendix A.

Site	Description
1	'Outside of the Duplex': Site 1a: ~280 m West of the 1 st order Bolfin Fault core, covered by one 7 m transect adjacent and perpendicular to a potential 2 nd order fault with sinistral displacement in the order of ~30 cm. Site 1b: ~11 km SSW of Site 1a, ~280 m West of the Bolfin Fault, covered by one 9.5 m transect adjacent and perpendicular to a potential 2 nd order fault. A ~10x5 m vein map was also made here using a high-resolution drone image.
2	'Northern Margin': ~180 m East of the Bolfin fault, on the northern margin of the mapped extensional duplex footwall, and adjacent and perpendicular to a 2 nd order fault. Covered by 3 transects totalling ~30 m. At this site, a ~2.5 m transect was also taken in the damage zone of the main Bolfin Fault, immediately adjacent to the core.
3	'Dilatational Jog': ~200-370 m East of the Bolfin Fault and ~8 km SSE of Site 2, a complex structure adjacent to a bend in the Bolfin Fault. Covered by 3 transects totalling 17 m, all adjacent and perpendicular to 2 nd order faults, with 2 also parallel to 3 rd order faults. A ~5x5 m vein map was also created here using a high-resolution drone image.
4	'Distributed Fault': ~200 m East of the main fault and ~2 km SSE of Site 3. The site is described in Jensen et al. (2011) as having a total distributed (2 nd order) fault thickness of ~17 m. Horizontal displacement is estimated at a few metres. Covered by 2 structural transects totalling 17 m, and another 9 m transect ~800 m further East, perpendicular to a less distributed 2 nd order fault. A ~7x7 m vein map was also made at one area using an ortho-rectified photomosaic, as published in Jensen et al. (2011).
5	'Central Duplex': ~3000 m East of the Bolfin Fault and ~1950 m West of the Jorgillo Fault, and also described in Arancibia et al. (2014). Covered by 3 structural transects totalling 17.5 m, adjacent and perpendicular to 2 nd order faults, with one also parallel to a 3 rd order fault.

2.4 Results

In *Section 2.4.1*, large-scale fault distribution in the Caleta-Coloso Duplex is analysed to provide context for the outcrop-scale study. Selected vein data from 1D transects adjacent to selected second- and third-order faults at outcrop are presented in *Section 2.4.2* – these data provide an indication of damage variability around the duplex. This dataset is then expanded upon in *Section 2.4.3* using vein thickness data as a proxy for the amount of fluid that has flowed through these damage zones. In *Section 2.4.4* 2D data are presented and used to explore damage zone heterogeneity at outcrop scale.

2.4.1 Large-Scale 2D Fault Distribution Within the Fault Duplex

Figure 2.5 shows the regional heterogeneity of fault intensity (P_{21}) and frequency (P_{20}) across the CCD. In general both 2D intensity and frequency are much greater within the duplex structure than outside of it, whilst within the overlap structure itself both appear to increase

towards its apparent 'centre', approximately in the centre of the map. Highest values ($P_{21} \approx 12 \text{ km}^{-1}$; $P_{20} \approx 0.4 \text{ km}^{-2}$) occur adjacent to duplex-bounding faults, yet high values are also found around other second-order faults extending into the centre of the duplex structure. Averaged P_{20} and P_{21} were also calculated for 1 km^2 areas around each studied site outcrop (Figure 2.5) and generally conform to the same picture. At Site 1, outside of the duplex, P_{21} is close to zero since only one second-order fault has been mapped. Within the duplex, greatest P_{21} and P_{20} values are recorded around Site 3, in the fault jog near a major bounding fault (9.3 km^{-1} and 0.082 km^{-2} respectively). Lower P_{21} and P_{20} values are seen around Site 4, in the distributed fault zone near a major bounding fault (6.17 km^{-1} and 0.40 km^{-2} respectively). Density and intensity are lower still around Site 2 on the edge of the duplex (5.56 km^{-1} ; 0.63 km^{-2}) and Site 5 at the greatest distance from any bounding fault (5.25 km^{-1} ; 0.36 km^{-2}).

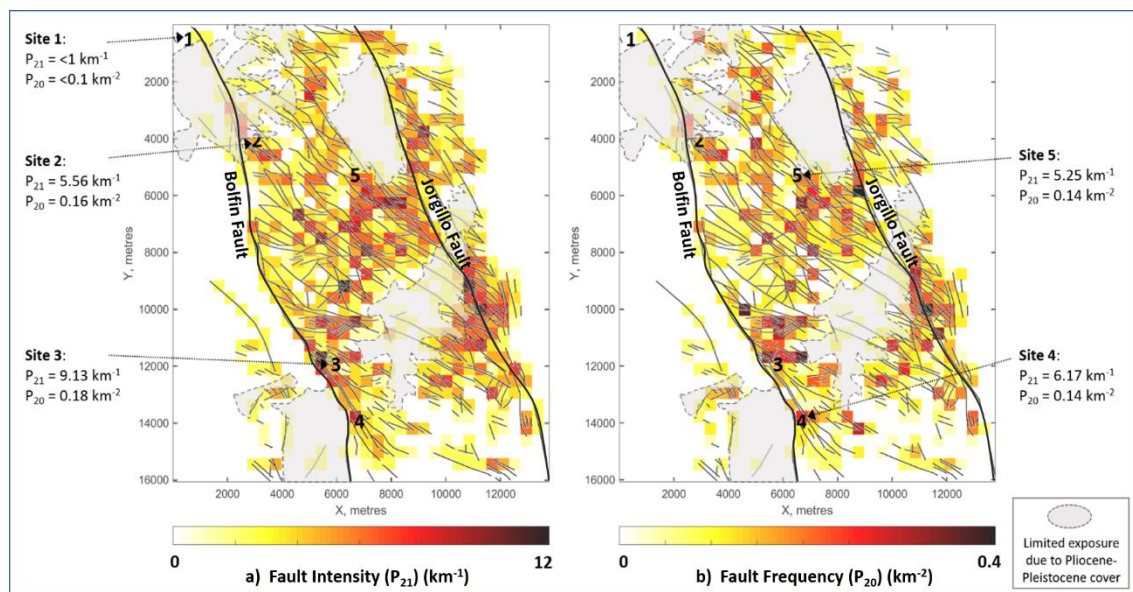


Figure 2.5: Regional variation in a) fault intensity (P_{21}) and b) frequency (P_{20}) across the Caleta-Coloso Duplex, which is defined as comprising structures between the Bolfin and Jorgillo Faults. Sites refer to areas studied in detail at outcrop (see Section 3 and Figure 2.6). See Appendix A (Section A2) for original structural data, traced from a regional geological map (Gobierno de Chile, 2003).

2.4.2 Fracture Damage Surrounding Duplex Faults (1D)

Average normalised vein intensity (P_{10}) (Figure 2.6a, Table 2.2) provides an indirect measure of the amount of fluid flow each site has experienced adjacent to second-order faults. To ensure data are comparable between all sites and transect, average P_{10} values were calculated using only measurements made within 4 m of the main fault. Both measured and corrected data for all veins suggest that veining is more intense at Site 3 (in the dilatational jog near a major bounding fault) and Site 4 (a distributed fault zone near a major bounding fault) than elsewhere in the fault zone. P_{10} values and average cumulative intensity gradients are greater here, in particular compared to Site 1 outside of the duplex. Sites 2 and 5 (on the northern edge and in the centre of the duplex respectively) have similar average gradients, lower than sites nearer the duplex-bounding faults but higher than outside of the duplex. Standard deviations are low

both within and between transects at Site 1 (Table 2.2). At all sites within the duplex, larger standard deviations indicate significant P_{10} variability within transects, particularly at Site 4 where high variability also occurs between transects (likely due to the added uncertainty of measuring within a more distributed fault zone). For comparison, immediately adjacent to the main Bolfin Fault, P_{10} and gradient of cumulative vein frequency are much higher.

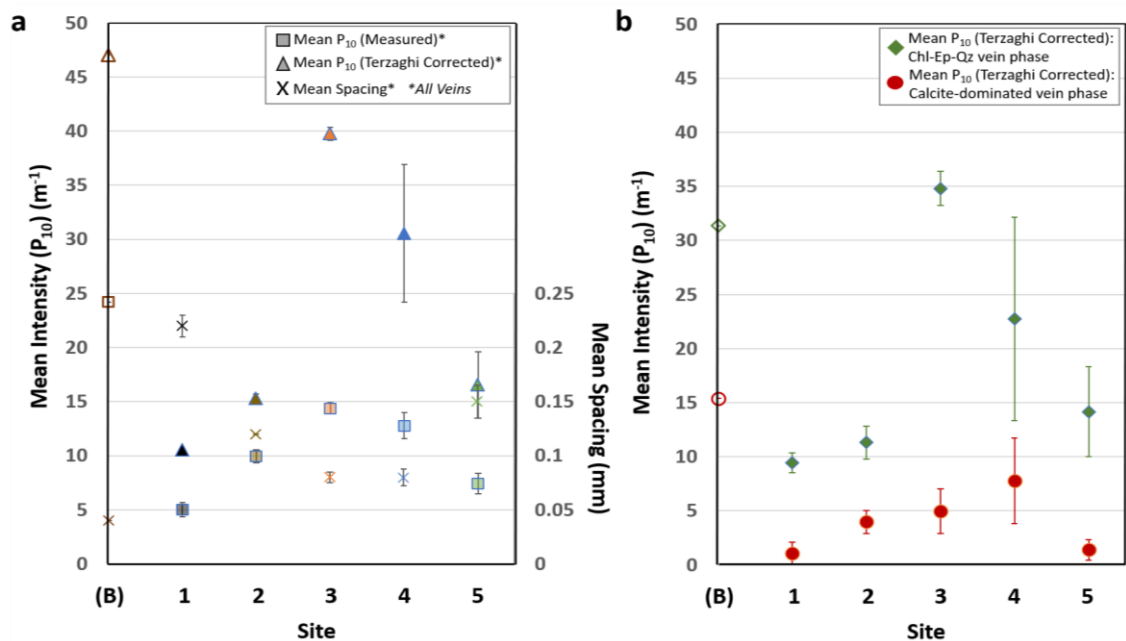


Figure 2.6: a) Mean normalised vein intensity (P_{10} , m^{-1}) (measured (squares) and Bias-corrected (triangles)) and mean vein spacing (mm) (crosses) for all veins intersected with 1D transects, grouped by site. b) Bias-corrected average normalised vein intensity (P_{10} , m^{-1}) for the chlorite-epidote-quartz vein phase (diamonds) and the calcite-dominated vein phase (circles) at each site. All data are normalized for transect length to allow comparison. Error bars in each case represent standard deviations between individual transects.

Average 1m-binned vein spacing is greatest outside of the duplex (Site 1), with spacing here significantly greater than on the edge or in the centre of the duplex (Sites 2 and 5) and more than double that of sites adjacent to duplex-bounding faults (Sites 3 and 4) (Figure 2.6a; Table 2.2). For comparison, adjacent to the first-order Bolfin Fault, average vein spacing is much lower than adjacent to all second-order faults. Cumulative distributions of spacing indicate that outside of the duplex veins have a relatively uniform distribution, reflected by low values of skewness, kurtosis and coefficient of variation (CoV) for Site 1 (Table 2.2). The Kuiper test however gives a V^* high enough to reject the null hypothesis of a random sample from a uniform distribution at the 99% level. A non-uniform negative exponential distribution is also evident at Site 5. Elsewhere within the duplex, veins are generally spaced much more closely, supporting vein intensity data. Skewness and kurtosis values are highest at Site 3, whilst higher CoV and V^* represent more of a scale invariant fractal distribution where veins are concentrated into clusters with gaps of varying size. Similar patterns of irregularity are observed at Sites 2 and 4, as well as in the damage zone of the Bolfin Fault.

Table 2.2: a) Intensity and b) spacing data from analyses of 1D transects at Sites 1-5. Length=distance along scanline in metres; N=number of veins measured; Intensity=number of veins/m for entire traverse, with standard deviations (SD) within transects and (in brackets) between transects; Spacing: mean, median (in metres), skewness, kurtosis and coefficient of variation; Kuiper Test: V, V* confidence level for rejection of null hypothesis of uniformity, where values ≈ 1 (i.e. standard deviation of spacing \approx mean) are indicative of a negative exponential distribution. (* transect data gaps have been omitted); Underlined transect names indicate distributed rather than planar second-order faults.

a)

Site	Transect	Length (m)	Intensity			N (corr.)	P ₁₀ (corr.) (m ⁻¹)*	SD ₂	Cumulative Intensity Gradient
			N	(P ₁₀ , m ⁻¹)*	SD ₁				
1a	PE-W-1	8.25	33	6.17	1.34	75	10.64		
1b	FB-S-1	9.40	45	3.57	2.11	81	10.38		
1				4.87	1.73	156	10.51	0.13	4.07
								(1.30)	
(2)	<u>SQ-B-1</u>	2.20	48	23.50	7.50	96	47.06	0.00	29.9
2	SQS-1	6.48	41	9.75	5.29	144	14.86		
2	SQS-3	7.84	47	8.20	3.87	87	15.70		
2				9.65	4.58	231	15.28	0.42	7.3
								(1.15)	
3	FB-T-1	3.53	85	15.00	2.16	135	40.54		
3	FB-M-1	7.33	85	12.67	3.77	135	39.13		
3	FB-C-1	4.00	57	14.25	2.77	211	39.59		
3				13.97	2.90	481	39.75	0.59	14.8
								(0.97)	
4	PAR-C-1	9.53	82	9.25	3.31	346	39.45		
4	<u>PAR-D-1</u>	10.50	113	14.71	3.06	209	27.14		
4	<u>PAR-T-1</u>	6.40	65	13.25	7.36	127	25.05		
4				12.40	4.58	682	30.55	6.35	12.6
								(2.31)	
5a	CCD-N-1	9.18	36	5.40	4.82	77	12.98		
5a	CCD-T-1	6.68	36	9.00	3.54	79	16.19		
5b	CCD-S-1	2.50	63	11.50	3.50	48	20.43		
5				7.20	4.18	204	16.53	3.05	8.6
								(1.80)	

b)

Site	Transect	Length (m)	Mean		Median		Skewness	Kurtosis	CoV	V'	V*
			(mm)	SD ₁	(mm)						
1a	PE-W-1	8.25	0.20	0.17	0.15	1.26	1.36	0.86	0.007	1.73	
1b	FB-S-1	9.40	0.24	0.29	0.11	1.58	1.76	1.24	0.013	2.50	
1			0.22	0.23	0.13	1.71	2.95	1.07	0.010	2.11	
(2)	SQ-B-1	2.20	0.04	0.05	0.02	2.88	9.98	1.44	0.011	3.45	
2	SQS-1	6.48	0.12	0.16	0.07	2.18	5.66	1.27	0.009	2.33	
2	SQS-3	7.84	0.12	0.14	0.07	1.80	3.27	1.21	0.009	2.63	
2			0.12	0.15	0.07	1.99	4.47	1.24	0.009	2.48	
3	FB-T-1	3.53	0.09	0.09	0.05	1.10	0.35	1.03	0.004	3.25	
3	FB-M-1	7.33	0.08	0.08	0.05	2.17	8.41	0.97	0.006	4.05	
3	FB-C-1	4.00	0.07	0.08	0.04	2.39	7.62	1.11	0.006	2.47	
3			0.08	0.10	0.05	5.08	41.04	1.34	0.005	3.25	
4	PAR-C-1	9.53	0.11	0.10	0.08	1.45	1.95	0.97	0.005	3.40	
4	<u>PAR-D-1</u>	10.50	0.07	0.07	0.04	1.29	0.83	1.06	0.004	4.15	
4	<u>PAR-T-1</u>	6.40	0.07	0.17	0.04	2.10	5.16	1.17	0.006	3.08	
4			0.08	0.12	0.04	3.74	25.33	1.26	0.005	3.55	
5a	CCD-N-1	9.18	0.18	0.20	0.14	1.75	2.97	1.11	0.010	2.01	
5a	CCD-T-1	6.68	0.12	0.12	0.06	1.18	1.12	1.01	0.005	2.17	
5b	CCD-S-1	2.50	0.09	0.07	0.08	1.73	3.95	0.85	0.009	2.26	
5			0.15	0.16	0.10	1.91	4.48	1.11	0.007	2.09	

When considered in terms of different vein phases (i.e. the chlorite-epidote-quartz phase and the calcite-dominated phase) (*Figure 2.6b; Table 2.3*), it becomes apparent that the epidote-bearing phase is dominant, with damage relating to this fluid-flow event focused predominantly adjacent to the duplex-bounding fault at Site 3, and to a variable extent at Site 4. The intensity of damage filled by the calcite-precipitating flow event is also largely concentrated in these areas, but to a larger degree at Site 5. For both events, the amount of damage in the damage zone of the Bolfin Fault is considerably greater than that in the damage zones of most other second-order faults across the duplex.

Table 2.3: Intensity data from analyses of 1D transects at Sites 1-5 for the chlorite-epidote-quartz vein phase and the calcite-dominated vein phase (see Appendix A for further details).

			Intensity (Chl-Ep-Qz Vein Phase)			Intensity (Cc-Dominated Vein Phase)		
Site	Transect	Length (m)	Intensity (corr.)			Intensity (corr.)		
			N (corr.)	(P ₁₀ , m ⁻¹)*	SD ₂	N (corr.)	(P ₁₀ , m ⁻¹)*	SD ₂
1a	PE-W-1	8.25	60	8.51		15	2.13	
1b	FB-S-1	9.40	81	10.38		0	0.00	
1			141	9.45	0.94	15	1.06	1.06
(2)	SQ-B-1	2.20	64	31.37	0	32	4.30	0
2	SQS-1	6.48	95	9.80		49	5.06	
2	SQS-3	7.84	71	12.82		16	2.89	
2			166	11.31	1.51	65	3.97	1.08
3	FB-T-1	3.53	109	32.73		26	7.81	
3	FB-M-1	7.33	121	35.07		14	4.06	
3	FB-C-1	4.00	195	36.59		16	3.00	
3			425	34.80	1.58	56	4.96	2.06
4	PAR-C-1	9.53	304	34.66		42	4.79	
4	<u>PAR-D-1</u>	10.50	169	21.95		40	5.19	
4	<u>PAR-T-1</u>	6.40	59	11.64		68	13.36	
4			532	22.75	9.42	150	7.78	3.95
5a	CCD-N-1	9.18	63	10.62		14	2.36	
5a	CCD-T-1	6.68	58	11.89		21		
5b	CCD-S-1	2.50	47	20.00		1	0.43	
5			168	14.17	4.15	36	1.39	0.97

2.4.3 Vein Thickness Within Fault Damage Zones (1D)

Vein thicknesses may be used as an indication of past fluid flow events, i.e. the volume of minerals precipitated from hydrothermal fluids sealing fractures within a rock mass. Most precipitation across the studied parts of the duplex is concentrated at Site 3, with more than three times the amount of vein material per metre than outside of the duplex (Site 1) (*Figure 2.7a; Table 2.4*). Elsewhere within the duplex, the amount of precipitate is intermediate and generally more variable. This is particularly true in the duplex centre (Site 5), where variability is largely on account of sporadic thick calcite veins. Variability on the edge of the duplex (Site 2) is likely due to two transects being taken either side of the same fault; it appears that epidote-bearing veins were more dominant on its Western side, highlighting a strong fault asymmetry.

A good positive linear correlation exists between average bias-corrected P_{10} values and vein thickness within each individual transect for both the chlorite-epidote-quartz vein phase and the calcite-dominated vein phase (Figure 2.7b; Table 2.5), suggesting that fluid flow was relatively evenly distributed through the duplex-hosted fracture network. The aforementioned variability at Site 2 is however evident in Figure 2.7b in the form of an outlier. An anomalous value for the calcite-dominated vein phase at Site 5 highlights that in the later phase of fluid flow precipitation did not occur homogeneously here, and rather was focussed within a few main conduits. This analysis is limited by orientation data not being included in the scope of this study, however this is considered in Chapter 3.

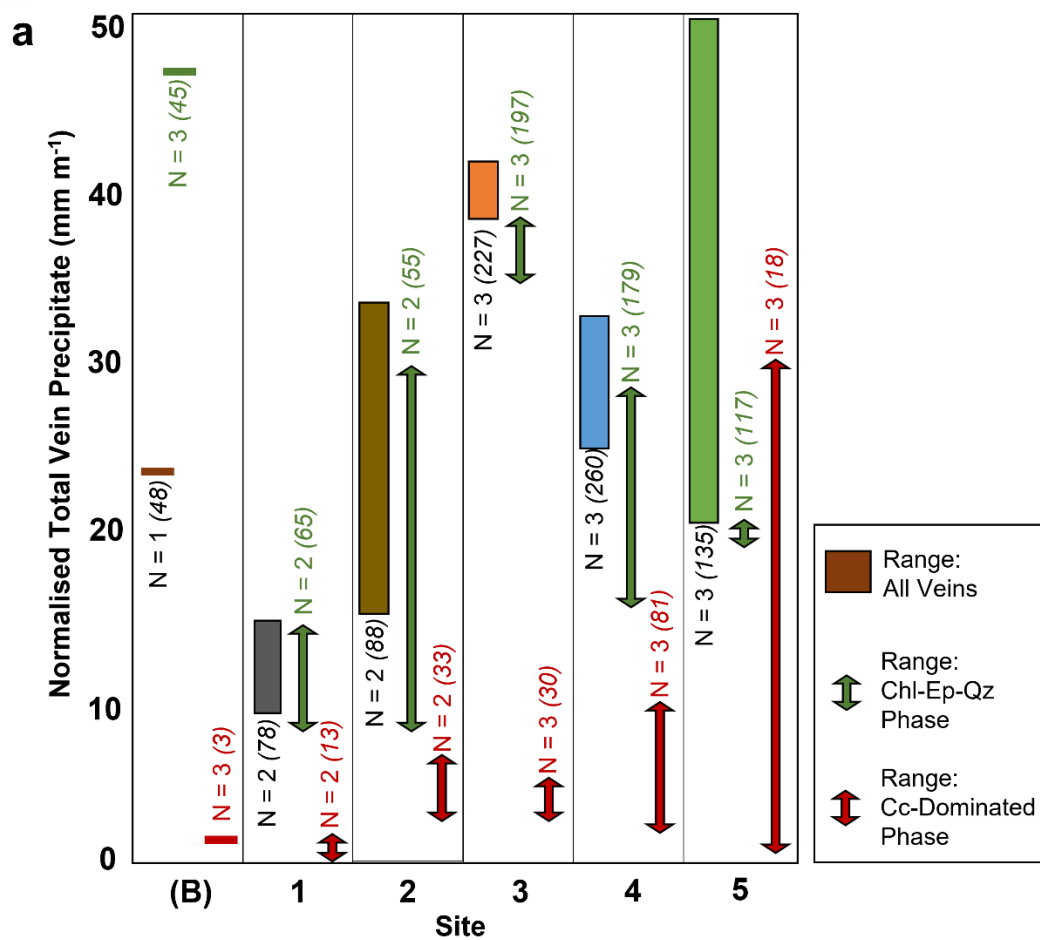


Figure 2.7 (Part a – see following page for full caption).

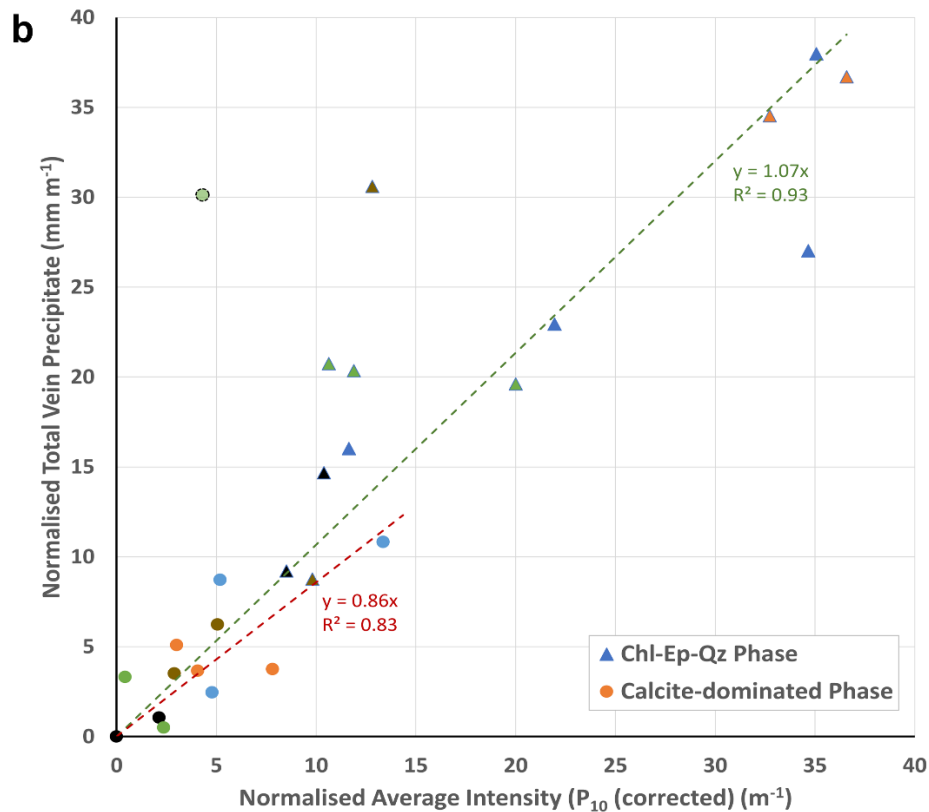


Figure 2.7: a) Ranges of normalised total vein thickness (mm per m) for each site. Values are derived by dividing the total thickness of veins intersected in a transect by the transect length (with data gaps omitted) (Table 2.4). N = number of transects used to formulate the range and (in brackets) number of individual veins used to formulate total thickness (Table 2.2). b) The relationship between normalised total vein thickness and bias-corrected normalised vein intensity (P_{10}) for each individual transect for the chlorite-epidote-quartz vein phase (triangles) and the calcite-dominated vein phase (circles).

All sites show similar normalised average vein thicknesses (2.11 to 3.17 (± 0.65 to 0.96) mm, with thicknesses and variability between transects slightly greater outside of the duplex than within. Cumulative thickness distribution statistics (Table 2.4) indicate that data skewed towards thinner veins at all sites. Relatively high V' values and V^* values >2 throughout the dataset allow the rejection of the null hypothesis of random sample uniformity at all levels in all sites and transects. This is particularly true at sites adjacent to duplex-bounding faults (Sites 3 and 4), where higher skewness and kurtosis values and lower CoV values represent an overall scale invariant fractal distribution. Low skewness and kurtosis values outside of the duplex (Site 1), as well as in the duplex centre (Site 5), show the most uniform distributions. For comparison, skewness, kurtosis, CoV, V' and V^* adjacent to the Bolfin Fault are all very high, indicating the dominance of thin fractures and clustering. The gradient of cumulative vein thicknesses with distance from a second-order fault also represent the uniformity of precipitation and extensional strain accommodated in the damage zone (Gillespie et al., 1996). Gradients are lowest outside of the duplex at Site 1 and are 2-3 times greater within the duplex (Table 2.4), with highest gradients adjacent to duplex-bounding faults (Sites 3 and 4). R^2 values indicate that greatest variability occurs outside of the duplex but also in the duplex centre (Site 5).

Table 2.4: a) Epidote-bearing vein thickness data from analyses of 1D transects at Sites 1-5. Length = distance along scanline in metres; Normalised thickness comparisons are represented by the total vein thickness divided by the transect length and also presented as a percentage of total measured precipitate across the duplex; cumulative thickness gradient with variance (R^2). b) Cumulative thickness statistics: mean (with standard deviations within transects (and between transects in brackets)), median (in metres), skewness, kurtosis, and coefficient of variation; Kuiper Test: V , V^* confidence level for rejection of null hypothesis of uniformity, where values ≈ 1 (i.e. standard deviation of spacing \approx mean) are indicative of a negative exponential distribution. (* transect data gaps have been omitted). Underlined transect names indicate distributed rather than planar second-order faults.

a)

Site	Transect	Length (m)	Thickness / Length* (mm m ⁻¹)	% Total Duplex Precipitate	Cumulative Thickness Gradient	R^2
1a	PE-W-1	8.25	10.28	0.03	6.8	0.95
1b	FB-S-1	9.40	14.68	0.05	9.1	0.91
1			12.48	0.08	8.0	0.93
(2)	<u>SQ-B-1</u>	2.20	23.24	0.05	29.9	
2	SQS-1	6.48	15.02	0.03	20.5	0.89
2	SQS-3	7.84	34.12	0.10	24.9	0.98
2			24.57	0.13	22.7	0.94
3	FB-T-1	3.53	40.46	0.11	35.2	0.97
3	FB-M-1	7.33	41.65	0.12	26.6	0.98
3	FB-C-1	4.00	39.64	0.12	31.4	0.97
3			40.58	0.35	31.1	0.97
4	PAR-C-1	9.53	29.48	0.09	31.9	0.95
4	<u>PAR-D-1</u>	10.50	31.65	0.07	27.6	0.96
4	<u>PAR-T-1</u>	6.40	26.84	0.05	23.5	0.97
4			29.32	0.21	27.7	0.96
5a	CCD-N-1	9.18	21.25	0.07	31.8	0.92
5a	CCD-T-1	6.68	50.47	0.06	26.6	0.95
5b	CCD-S-1	2.50	22.94	0.06	9.4	0.97
5			31.55	0.19	22.6	0.95

b)

Site	Transect	Length (m)	Mean		Median		Skewness	Kurtosis	CoV	V'	V*
			(mm)	SD ₁	(mm)						
1a	PE-W-1	8.25	2.05	3.02	1.00	2.96	9.44	1.42	0.013	3.63	
1b	FB-S-1	9.40	4.06	3.31	2.00	1.87	3.04	1.01	0.012	2.42	
1			3.17	3.17	1.50	2.29	5.11	1.20	0.012	3.03	
				(0.96)							
(2)	SQ-B-1	2.20	0.99	2.57	0.50	4.60	22.02	2.60	0.018	5.89	
2	SQS-1	6.48	1.92	4.15	2.00	3.37	14.86	1.18	0.009	2.45	
2	SQS-3	7.84	3.08	3.30	2.00	2.55	6.94	1.33	0.011	3.55	
2			2.50	3.93	1.00	2.37	13.79	1.16	0.010	3.00	
				(0.64)							
3	FB-T-1	3.53	2.37	3.58	1.50	3.60	18.00	1.30	0.008	5.98	
3	FB-M-1	7.33	3.38	2.82	1.75	1.34	1.17	1.03	0.007	5.23	
3	FB-C-1	4.00	2.25	2.83	1.00	1.86	2.88	1.15	0.008	3.46	
3			2.66	3.28	1.50	2.90	12.17	1.24	0.007	4.89	
				(0.94)							
4	PAR-C-1	9.53	2.68	3.59	2.00	2.24	5.84	1.09	0.006	4.14	
4	<u>PAR-D-1</u>	10.50	1.67	2.35	1.50	3.45	18.30	1.12	0.004	4.29	
4	<u>PAR-T-1</u>	6.40	1.97	2.31	1.50	2.51	7.51	1.11	0.005	2.80	
4			2.11	2.83	1.25	2.72	9.56	1.15	0.005	3.75	
				(0.65)							
5a	CCD-N-1	9.18	3.11	3.94	2.00	2.32	6.48	1.12	0.011	2.39	
5a	CCD-T-1	6.68	3.29	4.15	1.50	1.74	2.37	1.26	0.012	3.02	
5b	CCD-S-1	2.50	1.04	0.87	0.50	2.30	5.37	1.03	0.015	3.19	
5			2.36	2.99	1.50	2.12	4.74	1.15	0.013	3.26	
				(0.85)							

Table 2.5: Total amount of vein precipitate, normalised for transect length, from analyses of 1D transects at Sites 1-5 for the chlorite-epidote-quartz vein phase and the calcite-dominated vein phase (see Table 2.4 caption for further details).

Site	Transect	Length (m)	Amount of Precipitate (Chlorite-Epidote-Quartz Vein Phase)		Amount of Precipitate (Calcite-Dominated Vein Phase)	
			Total Thickness / Transect Length* (mm m ⁻¹)	% of Measured Duplex Precipitate	Total Thickness / Transect Length* (mm m ⁻¹)	% of Measured Duplex Precipitate
1a	PE-W-1	8.25	9.22	0.03	1.06	0.01
1b	FB-S-1	9.40	14.68	0.04	0.00	0.00
1			11.95	0.06	0.53	0.01
(2)	SQ-B-1	2.20	14.41	0.06	8.8	0.10
2	SQS-1	6.48	8.77	0.04	6.24	0.07
2	SQS-3	7.84	30.60	0.08	3.52	0.04
2			19.68	0.12	4.88	0.11
3	FB-T-1	3.53	34.53	0.10	3.77	0.04
3	FB-M-1	7.33	37.97	0.10	3.68	0.04
3	FB-C-1	4.00	36.70	0.10	5.11	0.06
3			36.40	0.30	4.18	0.14
4	PAR-C-1	9.53	27.02	0.07	2.45	0.03
4	<u>PAR-D-1</u>	10.50	22.94	0.08	8.71	0.10
4	<u>PAR-T-1</u>	6.40	16.02	0.07	10.83	0.12
4			21.99	0.22	7.33	0.25
5a	CCD-N-1	9.18	20.74	0.05	0.51	0.01
5a	CCD-T-1	6.68	20.35	0.13	30.12	0.34
5b	CCD-S-1	2.50	19.62	0.06	3.32	0.04
5			20.24	0.24	1.91	0.39

2.4.4 2D Damage Distribution Within Fault Damage Zones

Similar to the methods outlined in Section 4.1, 2D analyses at outcrop-scale were made by using FracPaQ to analyse the spatial characteristics of fracture traces from orthomosaics captured via a drone-mounted camera at selected outcrops. *Figure 2.8 and Table 2.6* show the 2D variability in vein intensity (P_{21}) and frequency (P_{20}) (Sanderson and Nixon, 2015) within and between sites. Average P_{21} and P_{20} are greatest at Site 3, with mean and maximum values significantly higher than at Sites 1a and 4. There is considerable variation at all sites that appears to relate spatially to the position of major faults. When compared to intensity data from 1D transects from the same outcrops (*Figure 2.8*), 2D data from Site 1 falls within the standard deviation, however 1D transects at Sites 3 and 4 appear overestimate 1D intensity with respect to 2D intensity by a factor of 3.

Table 2.6: Intensity (P_{21}) and frequency (P_{20}) data from vein trace analyses at 2D outcrops for Sites 1a, 3 and 4. Also shown are % of I (Isolated), Y (Abutting) and X (Crossing) nodes indicating the connectivity of the vein networks.

Site	Mean Intensity (P_{21} , m^{-1})	Max Intensity (P_{21} , m^{-1})	Mean Frequency (P_{20} , m^{-2})	Max			
				Frequency (P_{20} , m^{-2})	I Nodes (%)	Y Nodes (%)	X Nodes (%)
1a	2.5	10.1	15	97	71	25	4
3	9.3	37.7	151	798	51	48	1
4	3.2	14.4	23	159	62	36	1

The topology of vein or fracture networks can be analysed in terms of the relative proportions of connecting nodes (i.e. vein/fracture terminations), which may be isolated (I), or connecting (more specifically abutting (Y) or crossing (X)) (Manzocchi, 2002; Sanderson and Nixon, 2015). These proportions reflect the connectivity of the network, with a greater number of Y+X nodes typically resulting in higher permeability and more I nodes reflecting less connected network (Manzocchi, 2002; Healy et al., 2017). The connectivity depends on the number, orientation, intensity and length of veins/fractures, and is usually scale-independent (Sanderson and Nixon, 2018). Although connectivity has a direct effect on properties such as permeability, this is also controlled by relationships between individual fractures (such as spacing) as well as their geometry (Sanderson and Nixon, 2015); these factors may be scale dependent (Sahu and Roy, 2020). *Figure 2.9a* shows the distribution of connecting node density across three sites, whilst *Figure 2.9b* and *Table 2.5* show relative proportions of node types. Connectivity is greatest at Site 3, with a greater ratio of I nodes to Y nodes decreasing relative connectivity at Site 4 and further at Site 1a. At Site 3, connecting nodes are well-distributed throughout the outcrop, whereas at Sites 4 and 1a connecting nodes form clusters that partially coincide with clusters of vein density (*Figure 2.8, Figure 2.9*).

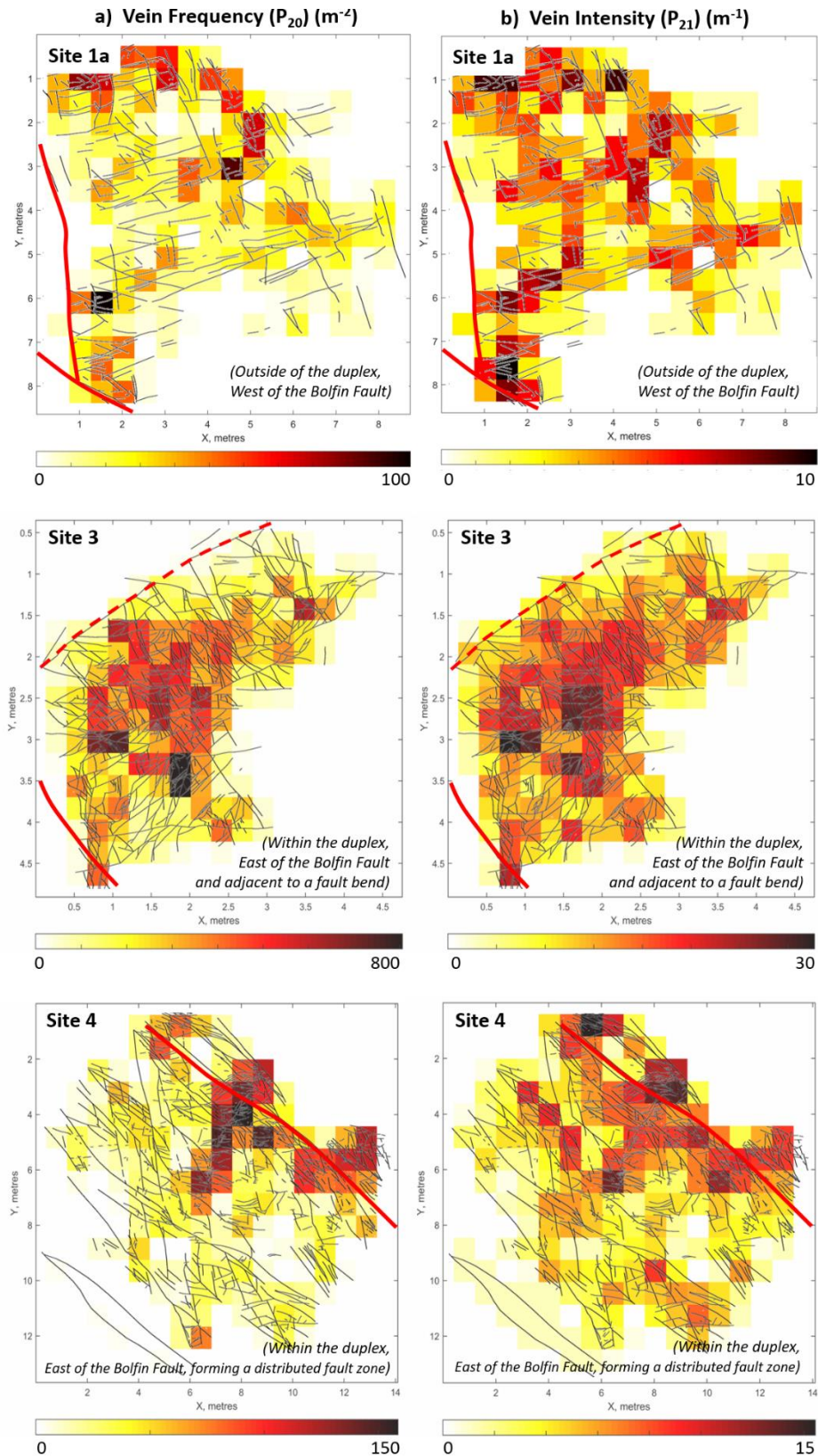


Figure 2.8: Maps of vein traces with a) 2D vein frequency (P_{20}) and b) intensity (P_{21}) from i) Site 1a, outside of the duplex, ii) Site 3, within a dilatational jog inside the duplex, and iii) Site 4, within a distributed fault zone inside the duplex. Red lines indicate inferred position of second- and third-order faults (solid and dashed lines respectively), defined by either evidence of >30 cm displacement, a fault core, or both. Maps were generated using FracPaQ from vein trace maps of images taken using a drone-mounted camera, as depicted in Appendix A (Section A2).

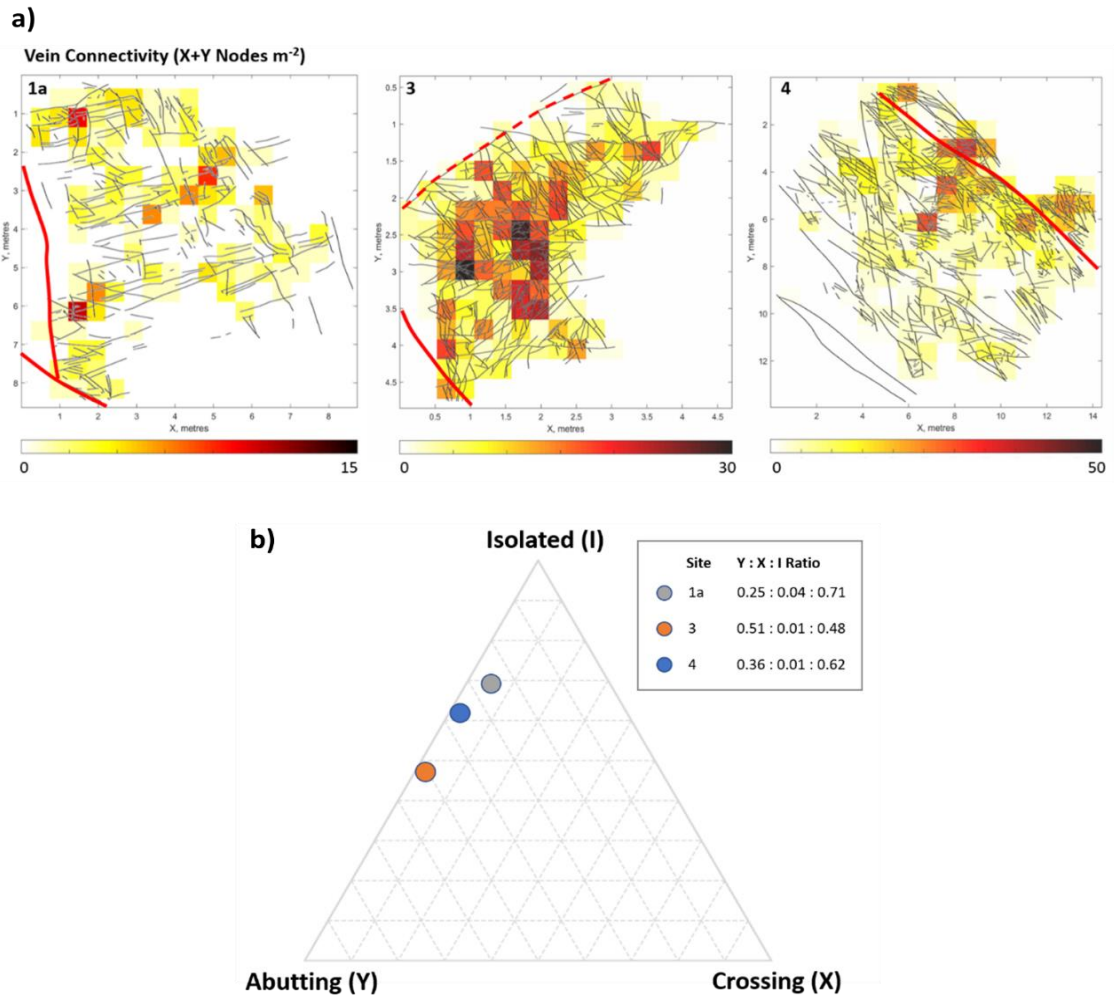


Figure 2.9: a) Maps of all vein traces with 2D vein connectivity (i.e. number of X and Y nodes per m²) from i) Site 1a, outside of the duplex and ii) Site 3, within a dilatational jog inside the duplex, and iii) Site 4, within a distributed fault zone inside the duplex. Red lines indicate inferred position of second- and third-order faults (solid and dashed lines respectively), defined by evidence of >30 cm displacement and/or a fault core. Maps were generated using FracPaQ from vein trace maps of images taken using a drone-mounted camera, as depicted in Appendix A (Section A2). b) A ternary plot showing the proportion of connecting node types between vein traces at each site.

2.5 Discussion

2.5.1 Fault and Fracture Density Within and Outside of the Duplex

Our data show that the transtensional duplex contains a greater density of faults and (filled) fractures in comparison to regions surrounding the duplex, reflecting the nature of fluid flow at regional- to outcrop-scale in the active fracture network at the time of vein formation. Structural networks also vary within the duplex itself: sites adjacent to bounding faults appear to record the most intense and clustered vein networks. In agreement with Nixon et al. (2019), damage varies along the strike of the duplex bounding fault, such that intensity generally increases towards the centre of the overlap structure. It should be noted however that comparisons of these types of data to other datasets are often problematic due to a lack of consistency between sampling techniques, measurement scales, nomenclature and differences

in lithology/tectonics (Faulkner et al., 2010; Choi et al., 2016). When considered in terms of the regional distribution of faults across the duplex (*Figure 2.5*), the variability in average vein intensities (*Figure 2.6*) may be explained by the density of kilometre-scale faulting.

Damage within the duplex appears to be more homogeneously distributed than outside (i.e. to the West of the Bolfin Fault and at the margins of the overlap structure), where a more heterogeneous distribution implies that kilometre-scale deformation is localised to a few large faults. Nixon et al. (2019) suggest that this pattern is due to increased stresses associated with a greater number of (smaller) faults formed as a result of bounding fault interactions. Where a higher density of these faults occurs, it is expected that the damage zones of these individual faults may interact with each other, which over time may result in damage accumulation and significantly increase metre-scale fracture intensity. This effect is schematically illustrated within the dashed lines of the plot in *Figure 2.1* and has also been observed on subsidiary faults of the nearby Caleta-Coloso Fault (Mitchell and Faulkner, 2009). Larger faults are considered to have propagated via the coalescence, nucleation and interaction of smaller tensile fractures (Jensen et al., 2011). Furthermore, previous work has suggested that this and other fault systems display self-similar characteristics as a result of scale-invariant processes (Jensen et al., 2011). Hence it is reasonable to assume that a higher density of kilometre-scale faulting occurs as a result of a higher density of outcrop and sub-outcrop-scale fracturing.

2.5.2 *Damage Distributions on Individual Faults (1D)*

It is well established that fracture density decays with distance from the fault core (e.g. Schulz and Evans, 2000; Wilson et al., 2003; Mitchell and Faulkner, 2009; McLean and McNamara, 2011; Savage and Brodsky, 2011; O'Hara et al., 2017). As well as showing variation at kilometre scale (*Figure 2.5*), the normalised average vein intensity (P_{10}) (i.e. *Figure 2.6*), when plotted as a function of distance from known second-order faults in 1 m bins, also appears to decrease with distance from the fault at metre scale (*Figure 2.10*). The rate of drop-off of fracture intensity has been shown to exponentially decrease with distance from the fault at variable rates according to the amount of displacement (Mitchell and Faulkner, 2009), hence damage zone widths are ultimately likely to vary accordingly. Variations in the intensity of veining has also however been shown to relate to the distribution of fault intersections and tips rather than displacement (Nixon et al., 2019). No direct measurements of fault displacement were made as part of this study, however Jensen et al. (2011) suggest that minimum net displacements on second-order faults within the CCD vary between 10-100 m, whilst Mitchell and Faulkner (2009) measured displacements ranging between 1.2 m and 220 m. Using published relationships between fault displacement and damage zone width (Mitchell and Faulkner, 2009; Faulkner et al., 2011; Savage and Brodsky, 2011; Choi et al., 2016) we estimate that the width of the damage zones on these faults should be in the range of ~0.1-115 m. Published relationships between displacement and fault length (Grasemann et al., 2011; Stanton-Yonge et al., 2020) suggest that lengths of second-order faults may be in the range of 250 – 2500 m, which broadly agrees with the regional geological map (Gobierno de Chile, 2003).

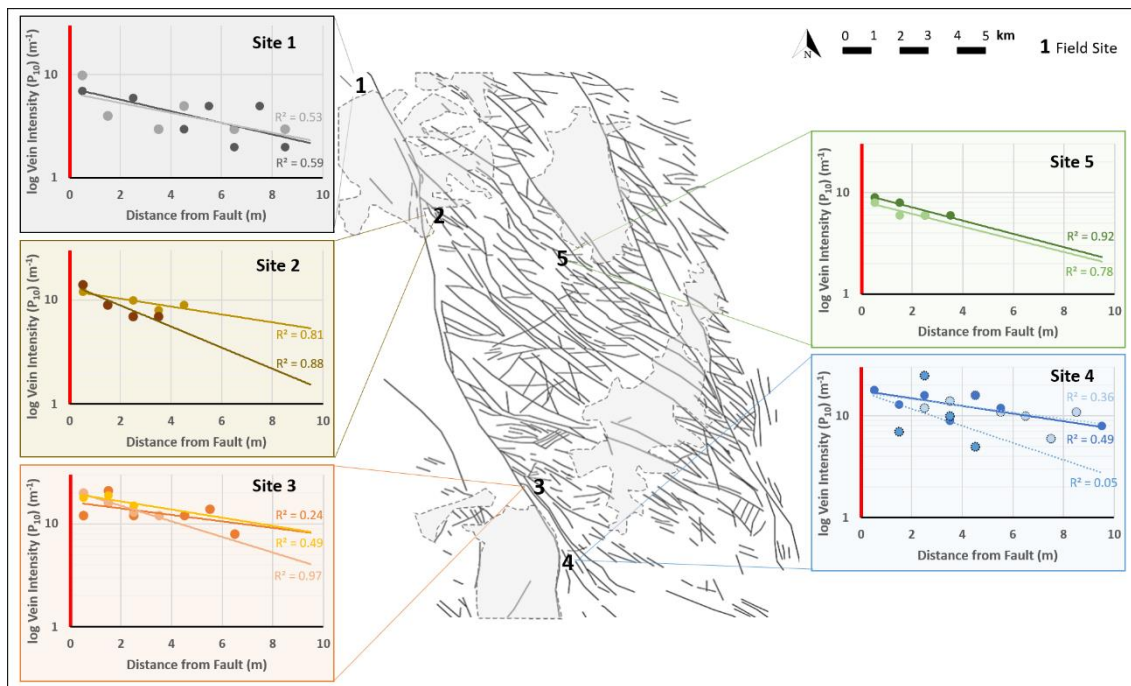


Figure 2.10: Log-linear plot of normalised vein intensity (measured P_{10} , m^{-1}) with distance from second-order fault (0 m, red), in 1 m bins. Trendlines for each transect are depicted by solid lines; dashed lines are transects within distributed faults (Site 4) where the exact position of the fault at 0m is uncertain.

Mitchell and Faulkner (2009) showed that critical macrofracture density adjacent to second-order faults (also within the CCD) appears to be consistent at around 100 fractures per metre. Maximum vein density immediately adjacent to second-order faults to the Bolfin Fault also appears to be fairly consistent (Figure 2.10), although only at around 8-12% (mean = 10%) of the critical fracture density. Sampling frequencies for this dataset however should arguably have been greater nearer the fault core (cf. Mitchell and Faulkner, 2009; Ostermeijer et al., 2020). Orthogonal transect directions have not been considered cf. Mitchell and Faulkner (2009). Rather, data was bias-corrected. Critical vein densities are lowest in the duplex centre and highest adjacent to bounding faults. This overall lower critical density is attributed to a larger proportion of fractures forming either later in the geothermal system (i.e. calcite veins) or during subsequent exhumation (e.g. Cembrano et al., 2005; Herrera et al., 2005; Arancibia et al., 2014). Without considering background density, it is estimated from extrapolating exponential trendlines in Figure 2.10 that damage zone widths vary between ~12-38 m. Damage zone widths in sites outside of the duplex and at the greatest distance from duplex-bounding faults are all <17 m (with one exception at Site 2 on the northern edge of the duplex), whilst those at sites closer to the duplex bounding faults are all >17 m (with one exception in the distributed fault at Site 4). Assuming a background density level 10% of that measured by Mitchell and Faulkner (2009) (i.e. $\sim 0.3 m^{-1}$), damage zone widths are estimated at ~4-6 m and ~10-20 m. Whereas most fit an exponential decay model reasonably well, some data (those with the smallest damage zone widths and inferred displacements) appear to conform slightly better to a power law decay model (cf. Savage and Brodsky, 2011; O'Hara et al., 2017), although

relatively short transects and some gaps in data do not allow us to draw any meaningful conclusions here. Using the relationship presented by Mitchell and Faulkner (2009), these data suggest that fault displacements at sites outside of the duplex and away from duplex-bounding faults may be in the order of ~10-15 m, whereas displacements on second-order faults nearer the duplex-bounding faults are higher, in the order of ~15-25 m.

The damage zones accrued by sufficiently large second-order faults (cf. Mitchell and Faulkner, 2009) may be subject to complexities, for example in how they interact with each other wherever regional fault density is high, potentially causing some variability in fracture intensity with distance from the fault. This is most likely to be the case at Site 3 where regional fault intensity is highest. With increased displacement, fault zones can become more complex as low-displacement and pure extensional structures in the same regional stress field progressively coalesce and link (e.g. Cox and Scholz, 1988; Martel, 1990; Cembrano et al., 2005; Laubach et al., 2014). This fault growth model has previously been proposed for the wider study area (Jensen et al., 2011). Whereas the earliest vein-forming phases were less influenced by pre-existing structures (besides ductile fabrics and dykes), later phases were likely strongly influenced by planar brittle structures recording the earlier event. Shear fractures can grow either from the reactivation of pre-existing structures under a rotating stress field or from the coalescence of tension cracks (e.g., Scholz et al., 1993; Crider and Peacock, 2004; Healy et al., 2006). Extension fracturing is likely to become more localised and isolated over time; whether permeability related to these structures plays an important role in fluid flow is dependent on the linkage with other vein arrays during repeated seismic cycles.

2.5.3 *Heterogenous 2D Damage Distribution*

Whilst normalised average vein intensities calculated from one-dimensional transects highlight a regional variation that can at least partly be explained by kilometre-scale fault density and displacement, two-dimensional damage is also heterogeneously distributed at outcrop scale (*Figure 2.8*). This heterogeneous 2D damage distribution appears to relate to the distributions and intersections of 2nd and 3rd order faults, however is unclear due to outcrop erosion in these areas as well as edge effects of fracture trace mapping. Strain is differently partitioned between structures of different types (e.g. bounding faults, splay faults and sealed fractures), which helps to maintain an overall stress compatibility across the structural duplex (Nixon et al., 2019). Each 2nd and 3rd order fault that transfers stress from the 1st order bounding fault may be considered to perturbate the stress field around it, and as a result the propagation of splay faults that link them may be controlled by these interacting local stress fields (Jensen et al., 2011). Where faults of differing orientation meet, therefore, a wider range of fracture orientations can be expected, resulting in greater densities and connectivity as seen *here* (*Figure 2.8, Figure 2.9*). Local stress concentrations within the duplex may be greater as a result of more interactions between a denser regional fault network (*Figure 2.5*), promoting more frequent and widespread fluid flow that may be highly variable through individual structures.

2D analyses presented here also suggest that areas within the duplex have a better-connected fracture network than outside (*Figure 2.9*). The general dominance of abutting (Y) over crossing (X) connecting nodes throughout implies that later vein formation may be strongly influenced by pre-existing structures (this hypothesis is explored in *Chapter 3*). In turn, this also suggests that as the structural network evolved, fluid flow became more dispersed and tortuous, causing individual structures to have lower fluid fluxes and hence less precipitation (Walsh et al., 1998; Cox, 1999). The similarity in metre-scale distributions of intensity, density and connectivity suggests that higher densities are produced when veins of different orientations interact to produce linkage structures. This is however less apparent outside of the duplex, where regional fault density is much lower (*Figure 2.5*). Since the heterogeneity of density intensity and connectivity appears to relate to the proximity to major faults (e.g. Cox, 1995; Barnhoorn et al., 2010; *Figure 2.10*) we infer that in areas of high fault density major faults form part of the fluid flow 'backbone'. Sealed fractures forming apparently isolated veins, of which there are a greater proportion outside of the duplex, represent sites of localised fluid discharge that have drawn fluid from this backbone in the downstream part of the hydrothermal system (e.g. Cox, 1995).

Connectivity in the dilatational jog (Site 3) is notably high and well-distributed across the whole outcrop, whereas within the more distributed fault (Site 4), a lower and more heterogenous intensity, density and connectivity are apparent, in line with variability evident in *Figure 2.10*. Vein spacing analyses (*Table 2.2*) also indicate that sites within the duplex tend to form more heterogenous clustered damage zones, compared to more uniform distributions outside. From this it is interpreted that palaeo-permeability would have shown similar distributions; this however cannot be reliably estimated as vein phases representing distinct periods of fluid flow could not be separated from 2D maps owing to complex vein relationships at a scale beyond the resolution of images. Interactions between linking structures more representative of the regional stress creates connectivity that may produce a ~100-fold permeability increase (Wallis et al., 2002; Kissling et al., 2015). Fluid-driven extensional fractures develop where there is overpressure, hence clustering suggests that sealed fracture networks within the duplex were closer to the percolation threshold (Cox, 1999, 2005). Structural control has therefore apparently focussed hydrothermal fluids into localised channels that relate to interactions of local stress fields around major faults (cf. Rowland and Sibson, 1998).

2.5.4 Implications for Hydrothermal Fluid Flow in Dilatational Fault Duplexes

A better understanding of fluid flow within duplex structures may have commercial significance for many types of subsurface resource exploration projects, for example hydrocarbon migration in similarly sited petroleum reservoirs (e.g. Aydin, 2000; Sibson, 2000; Gartell et al., 2004). Long-lasting duplex-hosted hydrothermal systems are also known to be important sites of high-grade ores, which are typically deposited along abandoned normal fault systems developed after the duplex has migrated (Berger, 2007). Extensional duplexes often also form zones of high heat

flow and crustal dilation that can be exploited as sources of geothermal energy. Examples of contemporary duplex-hosted geothermal systems include the Coso field, California (Lees, 2002) and the Cerro Prieto field, Mexico (Glowacka et al., 1999), and similar zones of strike-slip fault interaction are also currently a target for increased permeability and geothermal energy production in the United Kingdom (the United Downs Deep Geothermal Energy Project – Ledingham et al., 2019). The studied site was chosen as a suitable analogue for contemporary geothermal systems in part due to its apparent high density and complexity of faulting, but also due to the presence of pervasive mineral veins. The distribution of these veins indicates that significant fluid flow has occurred primarily within the duplex structure either during or post-faulting, whilst their composition suggests that this fluid flow occurred during a period of elevated heat flow (i.e. whilst the area formed part of an active magmatic arc). These topics are explored further in the next chapter.

The dynamic nature of permeability within duplex structures influences coseismic and post-seismic fluid redistribution within them, and hence the nucleation and propagation of seismic ruptures in such tectonic settings (e.g. Sibson, 1985, 1996, 2000). Geothermal systems tend to perform better with increasing structural complexity, where long-term, critically stressed areas keep fluid pathways open for longer with networks of closely spaced fractures (Faulds et al., 2011, 2013). Data presented here therefore have important implications for the siting of production wells in similar structures to target zones of enhanced permeability and fluid flow. Whilst a more complex fracture network appears to improve the fracture connectivity and - as a result - permeability within a duplex-hosted geothermal system, increased complexity in contemporary systems ultimately increases exploration uncertainty.

Such spatial variability in fault and permeability properties as documented here could, if sought to be understood during the reconnaissance of a similar geothermal system, significantly increase exploration risks and costs. For example, in an area where it is not possible to gather detailed evidence about the structural properties of the reservoir in the field, understanding will need to be based on a greater number of drilled wells and/or geophysical techniques such as gravity or magnetotelluric surveys. Without a detailed understanding of the fracture network, the risk of negative consequences such as induced seismicity or poor flow rates and energy production is increased, which may lead to the failure of a geothermal project. Hence, it is suggested that more exhumed analogue reservoirs are studied, with the aim of providing an ever-improving model of the structural variability within such systems. Further analysis of vein phase distributions (considered in *Chapter 3*) would also allow for refinement of models that aim to understand how fluids of different temperatures are distributed across such structures, allowing targeting of high temperature upwelling zones and avoidance of cooler fluid influxes.

Together with an assessment of fault damage, analyses of vein thicknesses across the studied duplex (*Figure 2.7*) can be used to inform on the history of fluid flow (e.g. Berger, 2007). Since

permeability and fluid flow are known to increase in proportion to the square and cube of the fracture aperture respectively (as described in *Chapter 1* – Equations 1.3 and 1.4), larger vein thicknesses are assumed to represent a greater palaeo-permeability and fluid flux. Estimates of total precipitates (and hence fluid flow) are considered to be a minimum as felsic haloes of alteration minerals, created by fluid flow through microcracks, are also present around most veins (Faulkner et al., 2011; Jensen et al., 2011); further limitations regarding these assumptions are addressed in *Chapter 5*). Fluid flow as a result of enhanced permeability usually only occurs when faults are actively deforming, hence the distribution of veins at a local scale is apparently controlled by the structural configuration of the active fault zone at crustal scale (Sibson, 1981, 1990; Cox, 1995, 1999). From the data presented here, we can infer that fluid flow in this transtensional duplex was apparently not controlled by individual faults or fractures, but rather was distributed across the whole duplex structure in correlation with fracture intensity. Hence, flow is inferred to have increased in relation to interactions between a denser set of heterogeneous regional faults. Cumulative thickness gradients presented in *Table 2.4* indicate that volumes of precipitate – and hence assumed amounts of fluid – were 2-3 times greater within the duplex than outside of it. Figure 2.7 and *Table 2.4* also highlight that precipitation within the duplex is more clustered compared to more uniform distributions outside of the duplex, further emphasising the heterogeneity of fluid flow at this scale and seemingly indicating the importance of fracture interaction and fault evolution in controlling structural permeability (e.g. Walsh et al., 1998; Sanderson et al., 2008).

Fluid distribution patterns are ultimately transient and governed by the evolving connectivity between propagating minor faults (Cox, 1995). Complex structures are considered to inhibit the development of new faults, promoting long-term enhanced structural permeability and fluid flow as the proportion gaping Mode I/II fractures increases (e.g. Sibson, 1985, 2000; De Paola et al., 2007). For example, Cox (1995) showed that vein formation in a fault zone was focussed within a dilatational jog with a greater density of dilatant structures and higher permeability, with vein geometry indicative of repeated fluid pressure and shear stress fluctuations associated with fault valve behaviour (cf. Sibson, 1996, 2000). Indeed, as discussed in *Sections 2.5.1 and 2.5.3*, structural complexities in the study area within the duplex and adjacent to the bounding fault have been shown to increase both fracture intensity and connectivity, suggesting that a more complex range of local stress concentrations within the duplex may promote more frequent and widespread fluid flow that can be highly variable through individual structures. It is therefore important to consider the reservoir's structural history (e.g. in terms of the distribution of fracture-hosted precipitation and host rock alteration from past fluid flow events that may inhibit flow and modify local stresses), in order to establish their influence on structural permeability.

With knowledge of the order of precipitation of the mineral assemblage coupled with a general understanding of evolving stress in active extensional duplexes (Cunningham and Mann 2007;

Berger et al., 2007; De Paola et al., 2007; Sibson, 1996, 2000) (factors that are considered in greater depth in *Chapter 3*), we can infer that some, but not all, principal flow conduits and linkage structures would have been open to fluid flow at similar times. Within the duplex, it is likely that earlier phases of fluid flow (i.e. events precipitating chlorite, epidote and quartz) would have reduced permeability through fracture sealing processes, thereby changing local stress conditions and perhaps allowing a new set of fractures to open. This is exemplified by *Figure 2.7* showing how sites of dominant precipitation have apparently relocated within the duplex between distinct fluid flow phases. In the context of geothermal energy exploitation, it is worth noting that the migration of fluids within the duplex may have important implications for exploration risk and project success. For example, during the extraction of geothermal fluids from high permeability, high temperature upwelling zones, the impact of changing fluid pressures on principal stress orientations (discussed in the following chapter) must be carefully considered. Where multiple fracture orientations are present, the potential for fault reactivation and induced seismicity may be significantly increased. Within fluid recharge zones, into which cooled fluids may be reinjected, the effect of temperature differentials must also be considered to avoid thermally shocking the reservoir and potentially also inducing seismicity. Finally, the impact of reopening new fractures within permeable zones adjacent to duplex bounding faults must be considered in terms of frictional stability: since the development of major throughgoing faults in extensional duplexes is typically restricted, and fluid flow therefore concentrated in adjacent areas, major faults within such systems may have partially dried in areas of high heat flow. In well-developed faults such as the Bolfin Fault, which comprises a high proportion of clay minerals that are susceptible to frictional instabilities upon changing hydration states (e.g. Faulkner et al., 2008; Tembe et al., 2009; Lockner et al., 2011), there may be a significant risk of major fault reactivation and seismicity. This topic is explored within *Chapter 4*.

2.6 Conclusions

In this chapter, statistical analyses of structural outcrop data have been presented, which aim to convey the heterogenous distribution of fluid-hosting fractures across an exhumed transtensional duplex. Analyses also aimed to explore how this affects our understanding of fracture permeability in structurally similar geothermal systems. The following observations suggest that extensional duplex structures represent a focus for enhanced fluid flow that will be controlled by fault networks, however there are many important variables to consider when considering where in particular fluid flux may be greatest.

- Indicators of mechanical damage around second-order faults to duplex-bounding faults show that the Caleta-Coloso Duplex contains a greater density of faults and fractures in comparison to surrounding regions, inferred to represent higher palaeo-permeability. Fracture damage within the duplex is systemically related to faults on all scales, and damage intensity increases along strike into the duplex.

- Data appear to conform to previous observations of fracture density drop-off with distance from a fault, suggesting that the amount of displacement on a fault coupled with the regional fault density may be the primary causes of intensity variation.
- Two-dimensional damage within fault damage zones is heterogeneously distributed. Sites with higher average fracture intensity generally show less outcrop-scale variability and greater fracture connectivity. Connectivity, which ultimately controls permeability, appears to be controlled by the presence of abutting linkage structures, suggesting that later fluid flow phases are strongly influenced by pre-existing structures and are perhaps more tortuous as a result.
- Veins (and hence principal fluid flow zones) within the duplex tend to form in clusters compared to a more uniform distribution outside of the duplex. Analysis of two distinct vein phases (chlorite-epidote-quartz and calcite) suggests that fluid flow in general uses the whole of the open fracture network, however phases precipitating calcite are limited to certain areas. Some complexities and implications of this will be explored in more detail in *Chapter 3*.

These data have implications for understanding which areas may be considered suitable targets for geothermal drilling sites in similar structural settings, suggesting that stimulating areas adjacent to a high density of high-displacement faults in areas with multiple pre-existing structural fabrics may create greater permeability than other areas within a duplex structure, although all areas within the overlap zone provide a better target than those outside of it.

Further study would be required to determine whether the selected sites accurately represent the position within the duplex rather than simply highlighting intrinsic variability. Further analysis of vein geometry and textures within each identified mineral phase (*Chapter 3*) also aim to develop an understanding of high- and low-temperature flow events and the influence of alteration and pre-existing fabric orientations on later fluid flow events, which have implications on the longevity of a geothermal system. Finally, considerations of proportions of each mineral phase within veins (*cf. Chapter 3*), as well as sealing mechanisms at micro-scale (*cf. Chapter 5*), may potentially yield information that helps to reduce inherent uncertainties arising from using vein thickness as an indication of fluid flow, since different amounts of vein material may precipitate at different rates given different conditions or mineralogical phases.

Acknowledgements

Work presented here was fully funded by Natural Environment Research Council (NERC grant ref. no. NE/L002469/1) as part of a PhD conducted via the EAO DTP, whose support is gratefully acknowledged. Thanks are also extended to Giulio Di Toro and the field team from University of Padova and Universidad Catolica Del Norte (particularly Erik Jensen, Rodrigo Gomila, Michele Fondriest and Simone Masoch) for invaluable guidance, support, logistical assistance and aspects of data collection in the field. Finally, for help with new scripts in FracPaQ we thank Dave Healy and Roberto Rizzo.

3 The Creation and Maintenance of Structural Permeability: Unravelling the Temporal Evolution of Fluid Flow in an Exhumed Duplex-Hosted Geothermal System

Abstract

Permeability in isotropic geothermal reservoirs is largely controlled by fracture networks forming damage zones of major faults. An understanding of the temporal history of how these fracture networks are created and destroyed (e.g. via sealing by mineral precipitation), as well as the physical properties of the fractured host rock, are thus of fundamental importance when considering the development and evolution of a geothermal system. A transtensional duplex structure within an exhumed propylitic system, part of the Atacama Fault System in northern Chile, provides an analogue for contemporary geothermal systems hosted in similar structures. Using a combination of fieldwork and laboratory work, fault damage zones within the duplex have been studied to bring together relevant aspects of regional fracture-hosted fluid flow, fracture formation, sealing mechanisms, and effects of alteration on rock strength to help understand the temporal evolution of the system. The composition and texture of sampled Mode I/II epithermal veins varies according to where within the duplex they have precipitated, and during what stage of the system's evolution they formed. Measured vein orientations, combined with a timeline of precipitation, inform on the evolution of the state of stress during fluid flow in this geothermal system. Within the duplex, most vein material has precipitated in extensional structures favourably oriented perpendicular to the minimum principal stress (σ_3) (~WNW-ESE), with thin (<~2 mm) fractures appearing to have most control on fluid flow within this system. Crack-seal/stretching veins - implying fracture reactivation - almost always form sub-parallel to the dominant precipitation orientation and are most common in structurally complex areas adjacent to the duplex-bounding fault. In the laboratory, Uniaxial Compressive Strength tests show that mechanical strength of a hydrothermally altered host rock is greater than that of unaltered host rock. The presence of a vein within the host rock however, regardless of orientation, does not appear to significantly affect strength or influence fracture patterns, as evidenced by Brazilian Tensile Strength tests. It is suggested therefore that degree of alteration controls where subsequent creation of structural permeability takes place, rather than the presence of a vein itself as a planar discontinuity. In the studied duplex, preferential structural grain formed by veining does not appear to create new permeability in a different direction to that expected through an assessment of regional stress, however other mineral assemblages are likely to affect this. This study highlights the importance of assessing the extent of pre-existing fracture-related precipitation and alteration in a prospective geothermal area prior to drilling, or prior to changing effective pressures via reservoir operation. Anisotropy reactivation will have variable influence on permeability within a duplex structure with fracture reactivation the most common process facilitating fluid flow.

3.1 Introduction

As introduced in *Chapter 2*, fault and fracture development in the upper crust is important in controlling fluid flow and provides insights into the mechanical, hydraulic and seismic properties of faults (Caine et al., 1996; Chester et al., 1993; Hickman et al., 1995; Gudmundsson et al., 2001; Faulkner et al., 2003, 2008; Wibberley and Shimamoto, 2003). In recent years the development of both natural and enhanced geothermal systems in a variety of isotropic host rocks (e.g. igneous and metamorphic basement lithologies) has increased, with fluid flow in these systems largely controlled by fracture networks within a fault's permeable damage zone (Chester and Logan, 1986; Caine et al., 1996; Wibberley et al., 2008, Davatzes and Hickman, 2010; Faulkner et al., 2003, 2008, 2010; Dezayes et al., 2010; Bertani, 2016). High permeabilities and near-hydrostatically pressured fluids (i.e. high flow rates) are required to efficiently transport hot fluids (Limberger et al., 2018; Sibson, 2000), hence an understanding of fracture generation, precipitation history, and physical properties are of fundamental importance when considering the development and evolution of a geothermal system. Whilst the previous chapter explored spatial and scaling variations of permeable fracture networks to help understand fluid flow within a transtensional duplex, this chapter will focus on how the same network has evolved over time and how successive phases of fracture sealing and hydrothermal alteration of the host rock may influence later structurally controlled fluid flow. Data presented here are discussed in terms of implications for the temporal evolution of a geothermal system.

Fault duplex structures (as described in greater detail in *Chapter 2*) develop as a fault periodically propagates on one side of the structure and 'shuts off' the fault on the other side (Cembrano et al., 2005; Wakabayashi et al., 2004). Overstepping fault segments can link and accommodate stretching and rotation of the regional stress field (Sibson, 1985; Woodcock and Fisher, 1986; Peacock and Sanderson, 1991; De Paola et al., 2007). Transtensional duplexes comprise a complex interaction of extensional-shear (i.e. Mode II) and purely extensional (i.e. Mode I) fractures, and their formation and evolution is largely dependent on the tensile strength of the host rock, differential stress ($\sigma_1 - \sigma_3$) and pore fluid pressures (Sibson 1996, 2000). Enhanced fault and fracture development within the fault overlap zone are considered to be important sites for fluid transport (e.g. Sibson, 1987; Berger, 2007; De Paola et al., 2007; Nixon et al., 2019), and the distribution and orientation of fractures within them can significantly influence permeability and fluid flow properties (e.g. Leckenby et al., 2005; Choi et al., 2016). Whilst dense fracture sets generally increase structural permeability, fracture orientation must also be considered to identify the interaction between fractures and therefore which sets are contributing most to structurally controlled fluid flow (Wallis et al., 2012).

Fluid-transporting fractures are temporally dynamic in that they may both operate as interconnected, open fluid flow pathways but also behave as fluid flow barriers, thereby decreasing the effectiveness of a potential geothermal resource (Dobson et al., 2003; Genter et al., 2010; Ball et al., 2015; Griffiths et al., 2016, McNamara et al., 2016). Structural permeability

may be reduced by the continued slip along a fracture (reducing asperities and producing fault gouge) and reduction in fluid pressure (causing the fracture to narrow or close) (Sibson, 1995, 1996, 1997; Rutter and Maddock, 2007; Faulkner et al., 2010; Rempe et al., 2018). In this chapter, however, we focus on how structural permeability may be reduced through sealing by hydrothermal mineralisation (e.g. Rimstidt and Barnes, 1980; Sibson, 1990; Oliver and Bons, 2001; Wiltschko and Morse, 2001; Cox, 2010; Bons et al., 2012). As well as causing sealing, pressure and temperature fluctuations may also reverse vein-forming precipitation reactions, causing mineral breakdown resulting in porosity and permeability generation (e.g., Heap et al., 2012, 2013, 2017). The amount, composition and texture of vein fill provides a record of pressure, temperature and strain history, fluid compositions, and interactions between fluids and fractured host rock (Bons et al., 2012). The field study of this 'palaeo-permeability' in an exhumed system offers a useful analogue of structural networks and fracture-forming processes that can be used to establish the evolution and sustainability of contemporary fractured geothermal systems, particularly those with no surface manifestations (Sibson, 1996; Faulkner et al., 2010; Faulds et al., 2011; Gomila et al., 2016; Sanderson, 2016).

Mineral vein textures are largely a function of crystal nucleation and growth and the kinetics of these processes (e.g. Bons, 2000; Bons et al., 2012), and can therefore be used to gain insight into the pressure/temperature conditions that the fractured host rock has experienced as well as the local stress conditions – this topic is explored further in *Chapter 5*. Vein formation (fracture sealing) can occur as a single precipitation event (e.g. a rapid decrease in the pressure of circulating fluids), or as multiple crack-seal or crack-jump events caused by fluid pressure or strain oscillations (e.g. Ramsay, 1980). As well as potentially creating permeability barriers, sealing by precipitation as a result of complex thermal-hydraulic-mechanical-chemical interactions (e.g. Fisher and Brantley, 1992; Laubach et al., 2004; Bons et al., 2012) has been shown to change a rock's mechanical strength. In general, it has been established that rocks containing planar discontinuities are usually weaker than those that are intact (Pluymakers et al., 2020), however the mechanical properties of a sealed fracture depend on many factors including the mineralogical composition and texture of the host rock, strength and morphology of vein crystals (hence indirectly also the rate of fluid flow, pressure-temperature conditions, mineral nucleation and growth processes, and fluid chemical composition) and adhesion of the vein to the host rock (e.g. Oliver and Bons, 2001; Hilgers and Tenthorey, 2004).

Whilst fluid flow through fractures often results in vein precipitation, fluid percolation through microfractures in the adjacent host rock causes hydrothermal alteration that can be highly variable both between and within geothermal reservoirs as a result of changes in by pressure, permeability, rock type, temperature, and time (Pola et al., 2012). The dissolution of primary minerals and precipitation of secondary minerals that occurs has been shown to affect the mechanical strength of the rock (e.g. Sousa et al., 2005; Nara et al., 2011; Pola et al., 2012, 2014; Heap et al., 2014; Wyering et al., 2014, 2015) and hence may influence later fracture-hosted fluid flow events. Since compressive failure in strong, low porosity, isotropic rocks occurs

through the coalescence of pre-existing microcracks (e.g. Ashby and Sammis, 1990; Lockner et al., 1992), the intensity of microfracturing has a strong negative correlation with unconfined compressive strength (UCS) and a positive correlation with permeability that will change as fractures and microcracks are sealed with alteration minerals (Siratovich et al., 2014). The strength of the host rock is of particular interest to the geothermal industry because few reservoir rocks are 'fresh': improved knowledge of how alteration influences rock strength can help improve drilling efficiency and guide drill bit selection (Wyering et al., 2012, 2014).

Siratovich et al. (2014) suggested that physical and mechanical properties are largely independent of alteration mineralogy, however many studies have shown that hydrothermal alteration causes a reduction in compressive strength (e.g. Rigopoulos et al, 2010; Meller and Kohl, 2014; Siratovich et al., 2016). Clay-rich alteration zones have also been shown to locally rotate stress fields up to 90°, resulting in high fracture densities in wells (Meller and Kohl, 2014). Tugrul and Zarif (1999) found that textural characteristics influenced rock strength more than mineralogy. Despite the high variability in the degree of alteration in typical geothermal areas, Wyering et al. (2015, 2017) showed that mechanical strength can be predicted using the relative percentage of primary and secondary mineralisation, mineral hardness, connected porosity and fracture abundance (which they developed into an alteration strength index). Hydrothermal alteration does not however cause a significant deviation in the relationships expected between physical and mechanical properties (e.g. increased density and decreased porosity, faster wave propagation and increased compressional strength with depth) (Wyering et al., 2014).

As well as altering the permeability and mechanical strength of a reservoir, sealed fractures can influence (and be influenced by) local stress conditions (e.g. Barton et al., 1995; Caine et al., 1996; Townend and Zoback, 2000; Healy, 2008) and the nature of subsequent fracturing (e.g. Caputo and Hancock, 1999; Virgo et al., 2013) – the latter of which is common but not well understood (Virgo et al., 2014). Both are important in assessing the longevity of a geothermal resource, as well as the effect of production on wellbore stability in conventional geothermal systems (Ellsworth, 2013), and the effect of stimulation by fluid injection on local stresses, fault reactivation, and induced seismicity in EGS reservoirs (Moeck et al., 2009). Most structures conducive to fluid flow are those that are critically stressed and in frictional equilibrium with the in-situ stress field (Healy, 2008). Multiple deformation events on a strike-slip fault generally develop a vertical array of tensile fractures and a dominant horizontal permeability anisotropy normal to σ_1 ; indeed, significant proportions of fluid flow in some geothermal reservoirs are attributed to fractures of a single orientation (Barton et al., 1995). However, fault interactions and heterogeneous structural grain (i.e. pre-existing veins and fractures) may also produce important fault-parallel and oblique fracture sets (Lockner et al., 1992; Wilson et al., 2003; Healy, 2008; Virgo et al., 2014). Heterogeneities in fracture aperture and degree of mineralisation can cause stress concentrations that have been cited as the cause for increased fracture density and connectivity - and significant fluid flow - in non-optimally oriented structures (Brown et al., 1987; Barton et al., 1995; Wilson et al., 2003; Wallis et al., 2012).

Upon sealing, fractures develop cohesion, form a mechanical discontinuity and accommodate tensile stress in a different manner to that of the surrounding host rock. Existing planes of weakness can reduce the tensile strength and the required differential stress and fluid pressure for a fracture to form (Bons, 2000). In the presence of older vein sets, new fractures may cut the pre-existing vein, or be deflected/refracted, terminate or bifurcate against another structure, changing the relationship of the vein and the regional stress orientation (Virgo et al., 2013). The ratio between host rock and vein strength determines where a new fracture will localise, with weak veins likely to cause fracture localisation within the vein to create a crack-seal microstructure, and strong veins likely to create stretching ('crack-jump') microstructures where new fractures form in the adjacent host rock (Caputo and Hancock, 1999; Bons, 2000; Bons et al., 2012). The angle of orientation with respect σ_1 may be the most important factor in determining whether a vein influences later fracturing (Turichshev and Hadjigeorgiou, 2017). The influence of a planar discontinuity's orientation on rock tensile strength has been explored for a range of anisotropic rocks, however data are lacking on the effect of single heterogeneities such as veins (Pluymakers et al., 2020). Lower angles of misorientation between a vein and a tensile fracture normal to σ_1 are likely to result in a greater degree of interaction (Virgo et al. 2013) and a lower tensile strength (He and Afolagboye, 2018). Where misorientation angles between the two are higher, tensile fractures are more likely to propagate across the vein at a higher tensile strength, whilst intermediate angles tend to result in fracture deflection at low tensile strengths (Virgo et al., 2013; Turichshev and Hadjigeorgiou, 2017).

This chapter will detail the temporal evolution of veining within an exhumed duplex-hosted geothermal system in the Atacama Fault Zone, Chile, aiming to bring together aspects of fracture formation, fracture sealing processes, and the effects of alteration on rock strength on regional fracture-hosted fluid flow. *Section 3.2* gives an overview of the regional geological setting, before providing an overview of the methodology employed at selected field sites as well as during subsequent data analysis and laboratory tests in *Section 3.3*. Examples of studied vein compositions and textures are presented in *Section 3.4.1*, and *Section 3.4.2* presents the results of spatial precipitation distribution analyses. *Section 3.4.3* details how the orientations of these veins vary spatially across the duplex and temporally in terms of successive vein phases and highlights a particular interest in crack-seal-type veins. *Section 3.4.4* uses laboratory data on the compressive strength of host rocks with differing degrees of alteration and on the tensile strength of veins with varied orientations to complement the field data and help to understand the effect of hydrothermal alteration and vein orientation on the creation and maintenance of structural permeability. *Section 3.5* discusses the data in terms of the influence of precipitation on the mechanical strength of veins and host rock, the influence of regional stress on precipitation and the reactivation of pre-existing structures, with the chapter's conclusions summarised in *Section 3.6*.

3.2 Geological Setting and Site Overview

The Atacama Fault System (AFS) and the associated Caleta Coloso Duplex (CCD) that contains the study area were described in detail in *Chapter 2* and are summarised briefly again here. The AFS is a c.1000 km long sinistral strike-slip structure between Iquique (21°S) and La Serena (30°S). The fault zone cuts dominantly Early Jurassic ortho-amphibolite and ortho-granulite (Cembrano et al., 2005) (*Figure 3.1*). Structures ranging over 7 orders of magnitude (10^{-4} to 10^4 m) (Jensen et al., 2011) are related to brittle, sinistral strike-slip events (~ 132 Ma and ~ 106 Ma - Scheuber et al., 1995; Taylor et al., 1998; Scheuber and González, 1999; Dallmeyer et al., 1996), and are overprinted on sinistral transpressional arc-related ductile deformation dated at 190-110Ma (Cembrano et al., 2005; Scheuber and Andriessen, 1990; Royden, 1993; Taylor et al., 1998; Scheuber and González, 1999). These structures have subsequently modified by Miocene-Pliocene normal dip-slip reactivation (Dewey and Lamb, 1992; González et al., 2003, 2006).

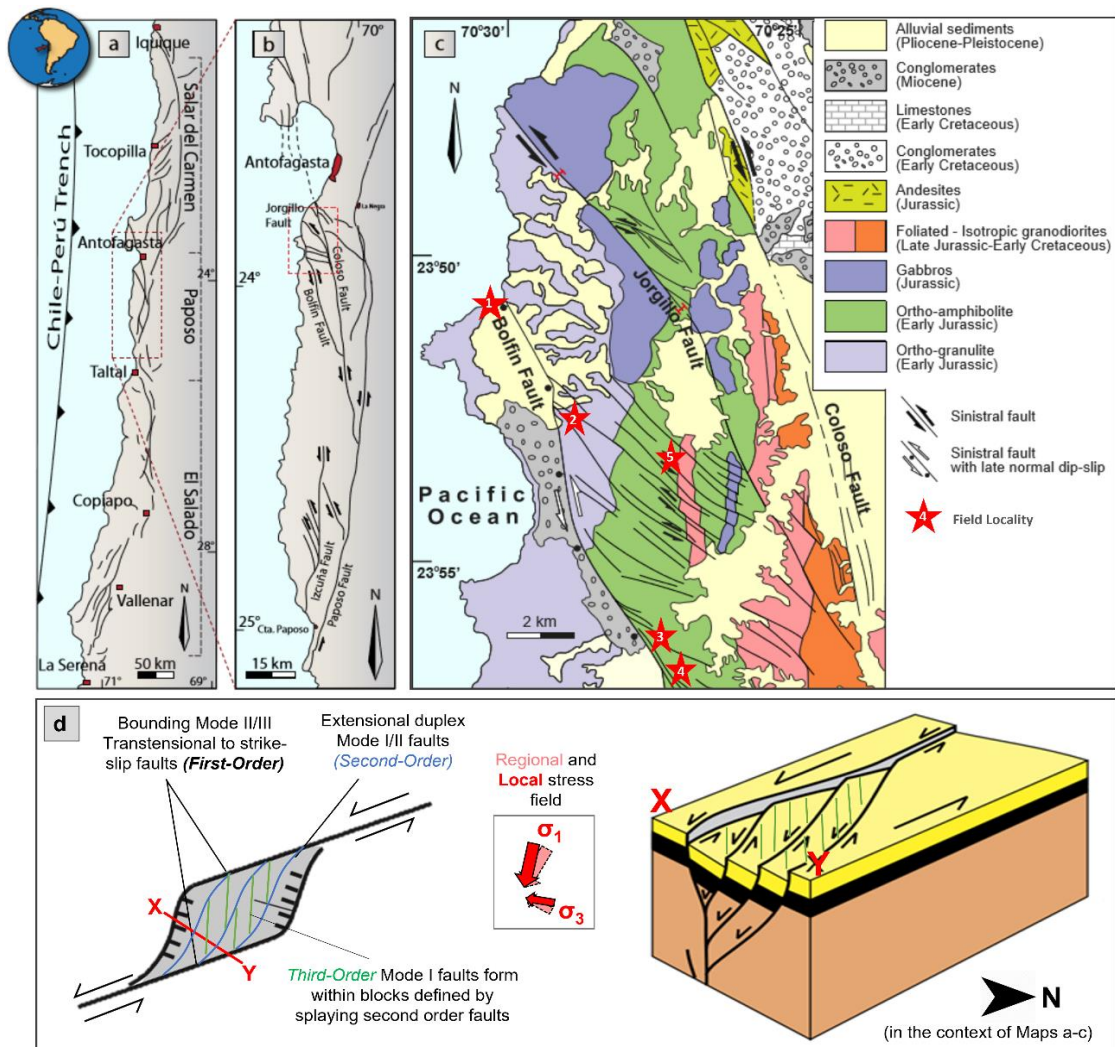


Figure 3.1: a) and b) Simplified structural map of the Atacama Fault System and c) Simplified geological map of the field area (modified from Cembrano et al., 2005). Field localities are marked as red stars. d) Simplified schematic diagrams of a transtensional duplex (in plan view, as well as cross sectional view across the transect X-Y) in the context of local and regional stress fields) (adapted from Wakabayashi et al., 2004; Cembrano et al., 2005 and De Paola et al., 2007).

The CCD is a transtensional duplex system bounded by the NNW-trending and steeply E-dipping Bolfin and Jorgillo strike-slip faults that show displacements of at least 10-200m (Cembrano et al., 2005). Duplex imbricate faults (i.e. second- and third-order faults) developed progressively by splaying off both bounding faults (Cembrano et al., 2005; Scheuber and González, 1999; Faulkner et al., 2011; Jensen et al., 2011; Stanton-Yonge et al., 2020) (*Figure 3.1*) and accommodate along-strike stretching and vertical displacement within the duplex via a combination of low-displacement NW-SE transtensional and N-S dip-slip movements respectively. ~E-W-trending third-order faults generally formed later within blocks defined by second-order faults, and minimum displacements of 10-100 m (second-order faults) and 0.01-0.1 m (third-order faults) have been suggested (Jensen et al., 2011; Herrera et al., 2005; Olivares, 2004). Fault and fracture networks concentrated between the two bounding faults host a large proportion of total CCD mineralisation.

3.3 Methodology

In this study, vein orientation and thickness data were analysed for 836 veins from 15 1D transects. As outlined in greater detail in *Chapter 2* and *Appendix A*, six areas from five different structural settings across the duplex ('sites') are discussed in this study, as described in *Table 3.1* and referred to in subsequent figures. Linear transects were taken sub-perpendicular to the orientation of second-order faults (i.e. approximately NE-SW), where faults are defined as structures containing at least a partially-developed core and, if determinable, some evidence of displacement. At some sites the relationship to a major fault was less clear, however this is noted wherever this was the case.

36 veins of varying compositions were sampled in the field and cut perpendicular to the vein. Cut samples were mechanically polished using diamond pastes and made into 30 µm uncovered thin sections. As well as standard optical petrography, backscatter Scanning Electron Microscopy (SEM) and cold cathode cathodoluminescence (CL) analyses were also performed (*Appendix B, Section B1*). Imaged vein textures have been classified according to their macroscopic, microscopic, and growth morphology as described in Bons (2000) and Bons et al. (2012) (also see *Chapter 1*). Veins are considered to be Mode I (extensional) where there is no evidence of shear motion. Mode II/III (transtensional to shear) veins are defined as those with an initial displacement direction oblique to the sealed fracture surface. The majority of analysed veins have been classified as Mode I or II, with just ~5% classified as Mode III.

Thin sectioning of unaltered and hydrothermally altered host rock, alongside X-Ray Diffraction (XRD) analyses (*Appendix B, Section B1*), was also carried out to provide chemical and textural context for the laboratory analyses described below. 'Unaltered' host rock was sampled >100 m from the nearest fault at Site 2 and showed little visible evidence of alteration mineralogy in the field. 'Altered' host rock sampled at the same site was taken adjacent to a second-order fault in an area of dense veining, however did not contain any veins itself.

Table 3.1: A description of field sites (data measurement and sampling locations) across the study area. More detailed information is provided in Appendix A.

Site	Description
1	'Outside of the Duplex': Site 1a: ~280 m West of the 1 st order Bolfin Fault core, covered by one 7 m transect. Site 1b: ~11 km SSW of Site 1a, ~280 m West of the Bolfin Fault, covered by one 9.5 m transect adjacent and perpendicular to a potential 2 nd order fault. 5 veins were sampled and later thin-sectioned.
2	'Northern Margin': ~180 m East of the Bolfin fault, on the northern margin of the mapped extensional duplex footwall, and adjacent and perpendicular to a 2 nd order fault. Covered by 3 transects totalling ~30 m. 7 veins were sampled and later thin-sectioned.
3	'Dilatational Jog': ~200-370 m East of the Bolfin Fault and ~8 km SSE of Site 2, a complex structure adjacent to a bend in the Bolfin Fault. Covered by 3 transects totalling 17 m, all adjacent and perpendicular to 2 nd order faults, with 2 also parallel to 3 rd order faults. 9 veins were sampled and later thin-sectioned.
4	'Distributed Fault': ~200 m East of the main fault and ~2 km SSE of Site 3. The site is described in Jensen et al. (2011) as having a total distributed (2 nd order) fault thickness of ~17 m. Horizontal displacement is estimated at a few metres. Covered by 2 structural transects totalling 17 m, and another 9 m transect ~800 m further East, perpendicular to a less distributed 2 nd order fault. 7 veins were sampled and later thin-sectioned.
5	'Central Duplex': ~3000 m East of the Bolfin Fault and ~1950 m West of the Jorgillo Fault, and also described in Arancibia et al. (2014). Covered by 3 structural transects totalling 17.5 m, adjacent and perpendicular to 2 nd order faults, with one also parallel to a 3 rd order fault. 5 veins were sampled and later thin-sectioned.

Data collected in the field (vein orientation, thickness, mineral composition(s) and notable textures or kinematic indicators along defined 1D transects as described in *Table 3.1*) were analysed to investigate the total amount of precipitate distributed across the fault duplex. When separated into mineralogies indicative of successive precipitation phases, these data are interpreted to represent phases of palaeo-fluid flow. The total amount of precipitate at each site was calculated as a total of all measured vein thicknesses at each site, normalised for the lengths of transects. Proportions of each mineral phase were calculated across the duplex as a whole and also for each site. Data were also analysed to investigate the spatial distribution and temporal evolution of vein orientations. All measured vein orientations, corrected for orientation bias as described in *Chapter 2* and *Appendix A (Section A4)*, were plotted by site as poles to planes with Kamb contours, alongside planes and poles of observed 1st, 2nd and 3rd order faults at the same site. The distribution of total amount of precipitate across each site was plotted as the amount of measured vein thickness within 10° orientation bins, with standard deviations from the mean also calculated. Average vein thickness per 10° orientation

bin was also plotted, alongside histograms of vein thicknesses at each site to indicate vein thickness distributions. Together, these plots provide an indication of how the amount of vein precipitate may correlate with local fracture distributions and regional stress patterns.

To investigate the effect of vein orientation on sealed fracture reactivation, indirect (Brazilian) tensile strength experiments (*Appendix B, Section B1*) were conducted - in accordance with the D3967-16 laboratory standard (ASTM International, 2016) - on 2 rock discs cored through relatively unaltered host rock, 2 through hydrothermally altered host rock, and 16 through altered host rock containing chlorite (8 samples) and epidote (8 samples) veins at a range of orientations (0° , 30° , 60° and 90° with respect to σ_1). To investigate the influence of hydrothermal alteration and presence of veining on rock strength, Unconfined Compressive Strength (UCS) tests (*Appendix B, Section B1*) were conducted on 2 cored samples of hydrothermally altered host rock and 2 cored samples of relatively unaltered host rock, as well as cores of altered host rock containing chlorite- and epidote-filled Mode I veins (2 samples each). Core samples were cut to 20 mm in diameter and ~ 50 mm long, and deformed in a uniaxial apparatus at a rate of $1 \mu\text{ms}^{-1}$ until failure occurred, in accordance with the D7012-14 laboratory standard (ASTM International, 2014).

3.4 Results

3.4.1 Vein Mineralogy and Microstructures

Both Mode I and II veins are found in our study areas. Whilst the majority are considered to be Mode I, 8% of measured veins across the duplex contain crystal opening fibres that are not perpendicular to their fracture walls, indicating transtension, or show evidence of slickenlines that indicate either normal (Mode I/II) or shear (mode II/III) reactivation (cf. Faulkner et al., 2011). Of this 8%, $\sim 70\%$ are located at Sites 3 and 4 and 84% show evidence of sinistral offset. It is also common to see Mode III veins, usually comprising a chlorite-epidote-quartz gouge, within or adjacent to Mode I/II veins within a few metres of fault cores at all sites. Veins measured within fault damage zones in the study area contain dominant mineral assemblages of chlorite, epidote and quartz, with minor calcite, clays (e.g. palygorskite) and salts (e.g. gypsum). Vein composition and texture varies temporally with respect to evolving geothermal fluid flow within in this structural network (*Figure 3.2a*), as evident from the relationships between minerals in individual polyphase veins and between multiple vein generations. Composition and texture also varies according the spatial location within the duplex (*Figure 3.2b*), and 20% of the total vein population shows evidence of crack-seal or stretching vein textures (*Figure 3.2c*).

(a) Temporal variations in vein texture/composition:

Early Chlorite-Epidote-Quartz

Scale:  = 1mm

With few exceptions, chlorite thinly lines fracture walls. This phase is followed by epidote (where often euhedral crystals define a syntaxial texture), then blocky quartz. Chlorite and epidote are often synchronous, as are epidote and quartz. Epidote-dominated phases within the duplex (adjacent to the bounding fault) are often microcrystalline.



(Site 1: PEW-09)



(Site 4: PAR-03)



(Site 3: FB-20-04)

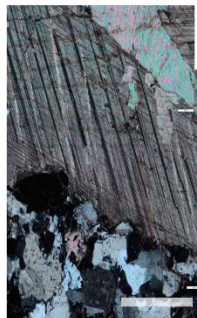


(Site 3: FB-FW-06)



Later Calcite:

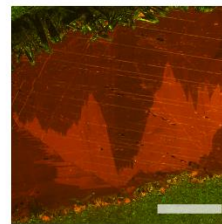
Calcite is rare except in the duplex centre. At Site 5, calcite forms new veins in old structures, with blocky textures and evidence of chemical zoning within crystals. Elsewhere, calcite usually fills voids and forms blocky textures with smaller crystals. CL analysis shows less internal chemical zoning but differences between multiple calcite phases.



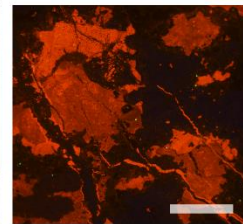
(Site 2: SQ-15)



(Site 5: CCD-CC-02)



(Site 1: PEW-W-02)



(Site 3: FBS-FW-06)



(Site 5: CCD-CC-01) (NB image orientation 90° to other images – vein walls vertical)

Figure 3.2: (Part a: See Page 69 for full caption).

(b) Spatial variations in vein texture/composition:

Outside of the Duplex

Scale:  = 1mm

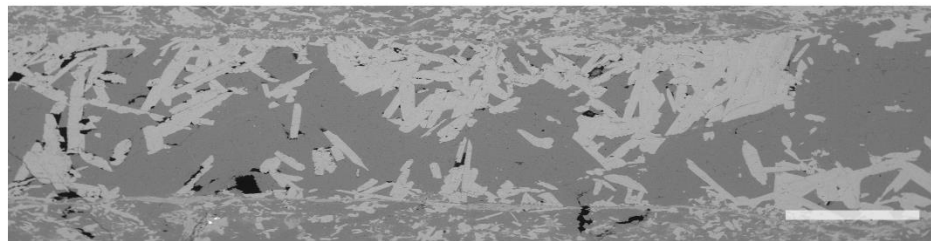
Relatively planar walls; syntaxial growth of epidote; coarse syntaxial growth of quartz; rare voids filled with calcite; Little deformation



(Site 1: PEW-06)



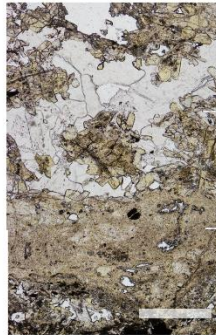
(Site 1: PEW-02)



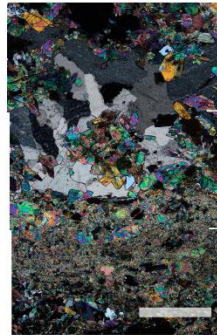
(Site 1: PEW-06)

Within the Duplex

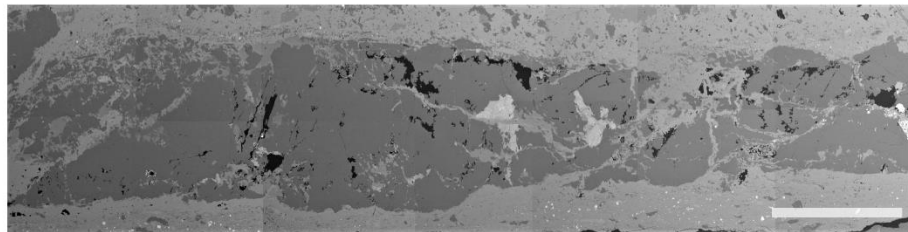
Complex fracture walls; often composite veins; microcrystalline epidote; brecciated quartz-epidote regions common; calcite forms new veins within old structure



(Site 3: FB-FW-06)



(Site 4: PAR-03)



(Site 3: FB-04)

Figure 3.2: (Part b: See Page 69 for full caption).

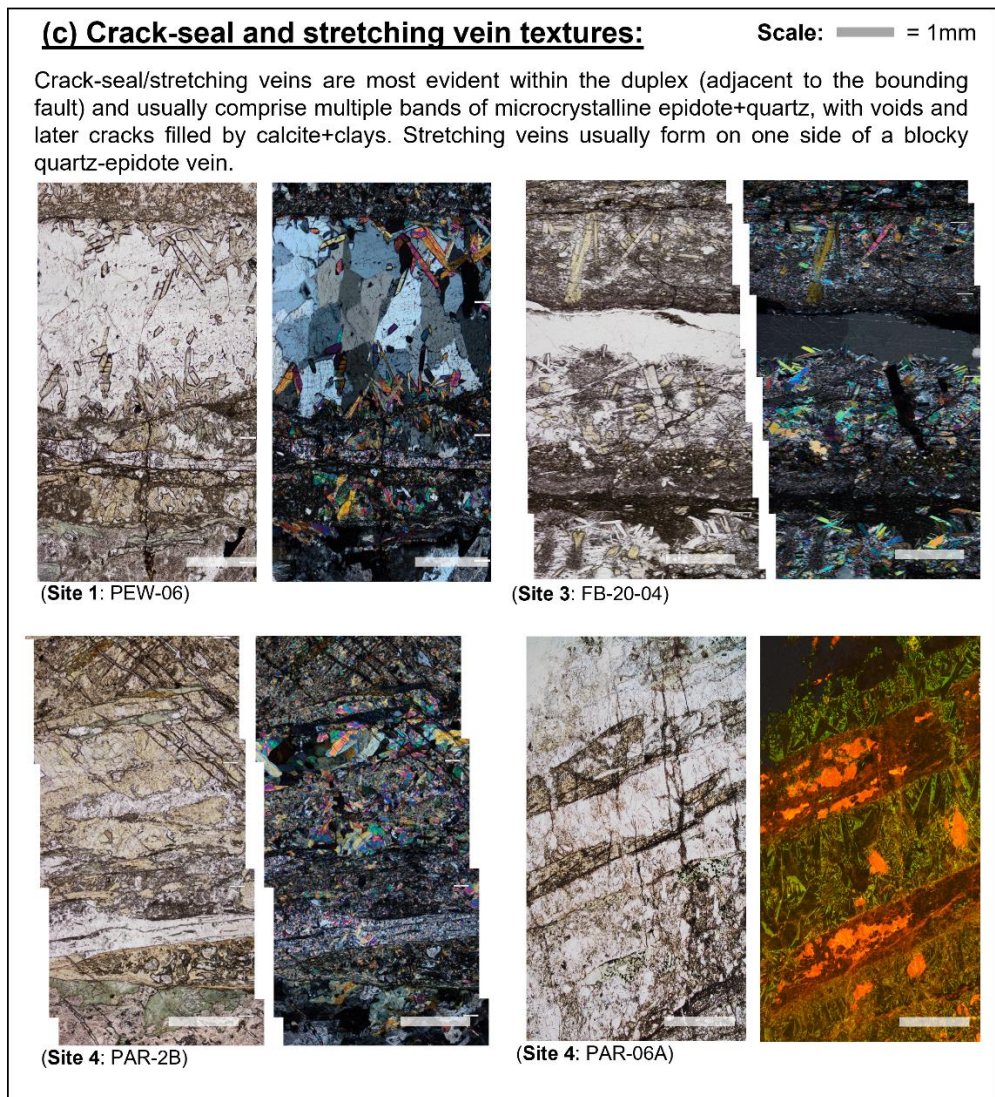


Figure 3.2: Photomicrograph images (plane polarised light and crossed polarised light), backscatter scanning electron microscopy images, and cathodoluminescence images highlighting the range of mineral compositions, textures, and relationships across the duplex, a) temporally and b) spatially, with c) also highlighting examples crack-seal and stretching vein textures. White scale bars on images represent 1 mm.

Temporally (*Figure 3.2a*), chlorite precipitate forms a lining on the vein walls and represents the first phase of fracture sealing. Following this, epidote precipitates either as elongate euhedral crystals, or within a brecciated mass alongside chlorite and/or quartz. Quartz often precipitates coevally with epidote, or as blocky or elongate blocky quartz crystals post epidote scaling. These vein mineralisation phases are often succeeded by a later calcite precipitation phase, which typically fills open voids and microfractures and occasionally forms veins with blocky or asymmetric ataxial crystals. A second phase of calcite, smectite (palygorskite), gypsum, halite, and possibly haematite ('D3') is distinguishable from earlier mineralisation phases using optical petrography and CL. Chemical changes both during the growth of individual calcite crystals as well as between precipitation phases are evident with CL analysis.

Outside of the duplex (*Figure 3.2b(i)*), vein walls are typically planar, and only occasionally lined by a thin (<10 µm) layer of chlorite precipitate. Extensive alteration in the wall rock around these fractures and inclusion of entrained clasts within these fractures are rare relative to observations made within the duplex. Early epidote precipitation within these veins shows a syntaxial texture in 3 out of 5 thin sections, with ~100-800 µm elongate crystals oriented sub-perpendicular to the vein wall. Post-epidote formation, quartz forms predominantly subhedral, elongated, blocky crystals up to ~1 mm across. In 2 veins, however, small (<100 µm) interlocking quartz and epidote crystals suggest periods of coeval precipitation. Calcite is present in 2 samples but have likely been oversampled in the field. Calcite occurs within late microfractures or as open void, crystalline precipitation, with CL analyses indicating more than one phase of precipitation occurred. Crack-seal and/or stretching vein textures are evident in 2 of 5 samples.

Within the duplex (*Figure 3.2b(ii)*), vein walls are usually less clearly defined than they are outside of the duplex. Identifiable vein walls usually show evidence of low-grade alteration - mostly chloritisation of plagioclase - and are coated with a thin layer of chlorite precipitation, though thicker than that observed in fractures outside of the duplex (up to ~100 µm). This chlorite layer is often mixed with microcrystalline epidote. Euhedral, syntaxial epidote precipitation is occasionally observed (in 6 of 31 samples, with crystal lengths up to of ~200 µm), though microcrystalline epidote precipitation is almost ubiquitous. Further away from the edge of the vein this epidote is usually present alongside quartz. Quartz occasionally forms large euhedral crystals (in 8 of 31 thin sections quartz crystals are ~400 µm to ~2 mm and form similar textures to observed vein quartz outside of the duplex), though is more commonly present in veins as smaller crystal sizes (<<100 µm), often within a brecciated mass coeval with epidote precipitation. Calcite veins are most common within the duplex centre (present within 3 out of 4 thin sections at Site 5), where it forms veins as well as filling open voids. In calcite veins within the duplex centre, CL analyses indicate that large (up to 4 mm), euhedral calcite crystals are often chemically zoned parallel to crystal faces. Adjacent to the duplex bounding fault, calcite is present in 6 out of 31 thin sections as open voids and veins, yet lacks any evidence of chemical zoning; though two precipitation phases can be identified using CL signatures in across multiple veins.

Crack-seal and/or stretching vein textures are observed in 9 of 31 thin sectioned veins within the duplex (29 % - comparable to the 20 % observed in the field). *Figure 3.2c* shows a range of crack-seal and/or stretching vein textures that are observed throughout the study area, two thirds of which are found at Sites 3 and 4 within the duplex. Crack-seal veins generally comprise multiple bands of microcrystalline epidote-quartz, with voids and later fractures filled by calcite and the 'D3' mineral phase. Stretching veins usually form on one side of a blocky quartz-epidote vein. All crack-seal/stretching veins commonly contain hydrothermally altered wall rock fragments entrained within the fracture vein minerals. Many crack-seal/stretching vein also play host to Mode III veins – particularly those proximal to major faults within the duplex.

3.4.2 Regional Distribution of Precipitate

Figure 3.3 shows how the total amount of mineral precipitate is distributed across the fault duplex (with data detailed in Table 3.2 and Table 3.3). Approximately 30 % of all mineral precipitation has occurred at Site 3, with a further 22 % at both Sites 4 and 5. At Site 2, the northern margin of the duplex, the proportion of mineral precipitation decreases to 18 %, and outside of the duplex (Site 1) the proportion of mineral precipitation is 9 %. For each site the total amount of precipitate is shown by proportion of the six identified vein mineral phases in temporal order; chlorite, chlorite and epidote (undifferentiated), epidote, epidote and quartz (undifferentiated), quartz, calcite, and 'D3' (clay, salt, and calcite). Figure 3.3 highlights that total precipitation amounts across Sites 1 to 4 are dominated (~66-75 %) by early chlorite- and epidote- mineralisation phases, with later calcite and 'D3' phases contributing <20 %. At Site 5, 8 calcite and 2 quartz veins with thicknesses >>5 mm dominate the total amount of mineral precipitate, with chlorite- and epidote-bearing phases accounting for only ~25 % of all measured vein material.

Table 3.2: Total measured amount of precipitate by vein phase (mm) and proportions of vein phases by site (%).

Site	Chlorite	Chlorite- Epidote	Epidote	Quartz	Epidote- Quartz	Calcite	D3	Total amount of precipitate (mm)
Total measured amount of precipitate (mm)								
1	3	52	24	60.5	40	1	6.5	187
2	16	0	179.5	59	0	0	80	334.5
3	49.7	117	169	74	117	54	13.1	593.8
4	32.8	109	216.1	74.4	62.5	78.9	64.6	638.3
5	7.3	10.5	107.6	126.5	16.5	153.8	4	426.2
Proportion of vein phase by site (%)								Total proportion of duplex precipitate (%)
1	2%	32%	28%	13%	21%	1%	3%	9%
2	5%	18%	0%	54%	0%	0%	24%	18%
3	8%	12%	20%	28%	20%	9%	2%	30%
4	5%	12%	17%	34%	10%	12%	10%	22%
5	3%	44%	16%	72%	11%	54%	1%	22%

Table 3.3: Proportions of vein phases across the duplex (%).

Site	Chlorite	Chlorite/Epidote	Epidote	Epidote/Quartz	Quartz	D3	Calcite
1	7%	35%	6%	35%	27%	9%	1%
2	21%	0%	27%	0%	15%	59%	0%
3	37%	25%	14%	32%	11%	5%	12%
4	23%	21%	17%	16%	10%	25%	16%
5	12%	19%	36%	17%	37%	3%	71%

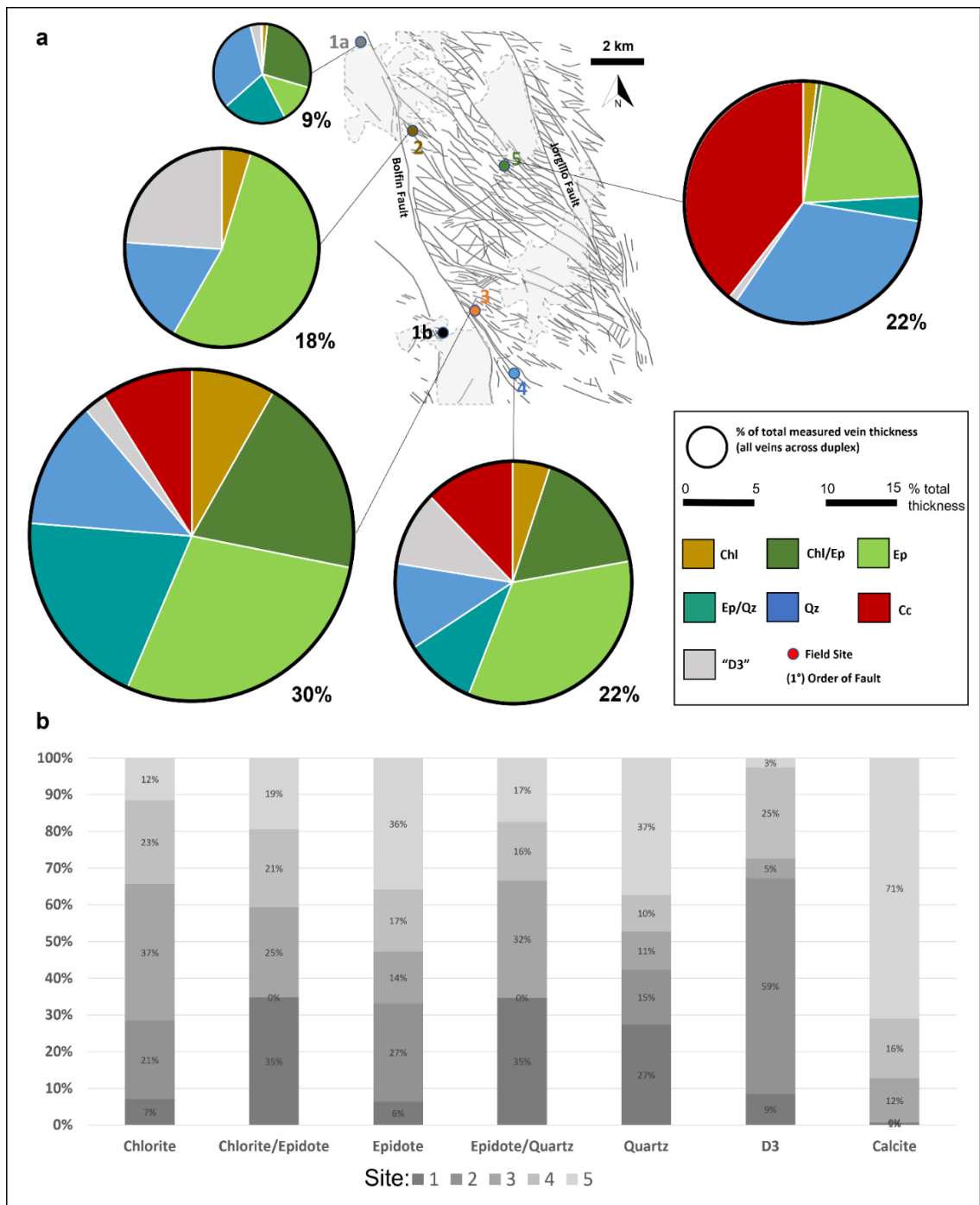


Figure 3.3: a) Regional variation in the amount and type of precipitate across the duplex. Pie charts are scaled according to the relative amount of total measured vein material at each site across the duplex and display the proportions of six vein phases identified (chlorite (brown), chlorite + epidote (dark green), epidote (light green), epidote + quartz (turquoise), quartz (blue), calcite (red) and 'D3' (clay, salts and calcite) (grey). b) Relative amounts of total measured vein material across the duplex (i.e. Sites 1-5) for each vein phase.

With regards to each successive precipitation phase, chlorite is most common at sites adjacent to the duplex-bounding fault (i.e. Sites 2 (21 %), 3 (31 %) and 4 (23 %)). Mixed-phase chlorite/epidote veins, however, are most common outside of the duplex (35 %). Epidote usually occurs without other mineral phases within the duplex, with epidote-only veins comprising 34 to 72 % of all epidote-bearing veins at Sites 2-5. Outside of the duplex, mixed phase epidote-bearing veins (i.e. with chlorite or quartz) are more common, with epidote-only veins accounting for just 13 %. Two thirds (67 %) of all mixed-phase epidote/quartz veins are found at Sites 1 and 3. Later quartz-only veins comprise 10-15 % of all veins at Sites 2 through 4, increasing to 27-37 % at Sites 1 and 5. Whilst the first five phases of precipitation as described here show only subtle spatial trends, late calcite and 'D3' precipitation phases show much clearer preference for different areas of the duplex. 71 % of all calcite precipitate measured occurs at Site 5, with none appearing at Sites 1 and 2. At Site 5, total thickness of calcite veins is anomalously large owing to a few thick veins encountered in one transect. 59 % of all 'D3' veins are recorded at Site 2, with a further ~25 % at Site 4.

3.4.3 Structural Orientations of Vein Phases

3.4.3.1 All Veins (Spatial Variation)

Dominant vein strike trends across the duplex, as shown in Kamb contour plots of all veins (*Figure 3.4; Appendix A, Table A3.1*), vary between ~100°-280° (ESE-WNW) and ~170°-350° (N-S). These orientations likely relate to those of identified 1st, 2nd and 3rd order faults at each site. The distribution of the total amount of mineral precipitate does not however directly correlate with the dominant frequency of vein orientations and varies across the duplex (*Figure 3.4; Appendix A, Tables A3.2, A3.3 and A3.4*). At all sites, the total amount of precipitate is predominantly concentrated in thin veins (50-60 % have a thickness of <2 mm) (*Figure 3.5; Appendix A, Table A3.5*). The highest proportions of very thin veins (<1 mm; 37-40 %) and the highest proportion of thick veins (>5 mm; 19-20 %), are located within Sites 2 and 5. For comparison, narrow-aperture veins (i.e. <1 mm thick) represent 26 - 31 % of the total vein population at Sites 1, 3 and 4, whilst wide-aperture veins (>5 mm) constitute just 10-12 % of the total. At Sites 3 and 4, vein thicknesses are more uniformly distributed, although with a slight skew towards thinner veins.

At Site 1, outside of the duplex, *Figure 3.4* indicates that the majority (55 %) of veins are steeply dipping (75 % >60°) and sub-perpendicular to the 1st order Bolfin Fault striking NNW-SSE (i.e. ~ESE-WSW). A subordinate number of veins (32 %) are sub-parallel to a potential 2nd order fault in the area striking NW-SE. The thickest veins (5 mm on average) (*Figure 3.5*) and majority of total precipitate (46 %), however, in fact occur within veins that are sub-parallel to the 1st order fault. A thick vein set (with an average thickness of 7 mm) striking at 30° to this (NNE-SSE) contributes little (~5 %) to overall precipitate.

At Site 2, two strong vein orientation sets are observed, one sub-parallel to the 1st order ~N-S striking fault (25 % of all veins), and another sub-parallel to a NW-SE striking 2nd order fault (59 % of all veins), again steeply dipping (71 % >60°). Whilst the number of veins is relatively evenly distributed between the two orientation sets, 71 % of mineral precipitate is concentrated in structures parallel to, or at 30° to the NW-SE striking 2nd order faults (*Figure 3.4*). Thickest veins (averaging 5-6 mm) have also formed either parallel or at 30° to dominant vein orientations (i.e. ~NW-SE, N-S, and WNW-ESE) (*Figure 3.5*) with a similarly thick but uncommon vein set sub-perpendicular to the dominant vein orientation (i.e. ~NE-SW, contributing to <10 % of total precipitate). Thickest veins at Site 2 apparently form a conjugate set related to the orientation of 2nd order faults (NW-SE), and between them represent 71 % of all precipitate at this site.

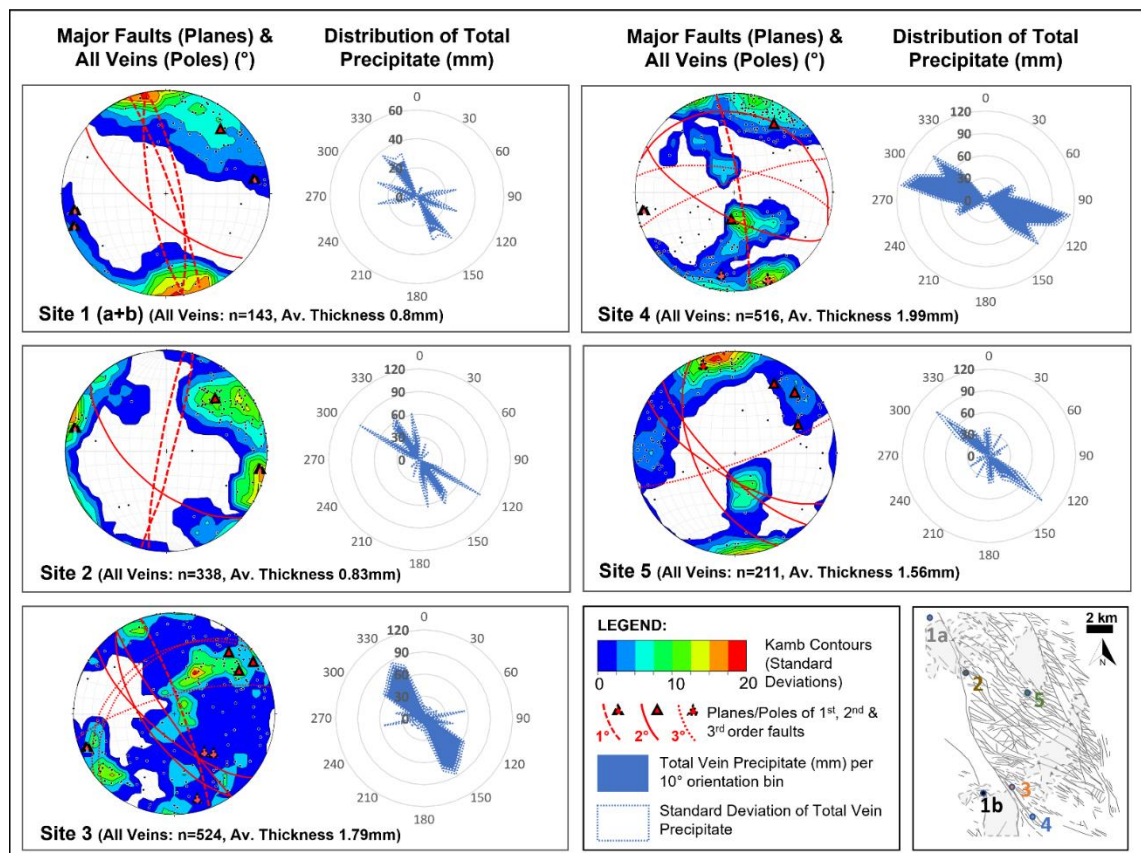


Figure 3.4: Kamb contour stereonet and rose plots of total vein precipitate by orientation (bias-corrected as in Appendix A, Section A4). Kamb contour plots for all veins are overprinted with planes and poles (red) for any identified major fault orientations. Blue filled rose plots display total measured vein thickness (mm) per 10° orientation bin for all vein phases. Dotted white/blue lines show the standard deviation of total vein precipitate.

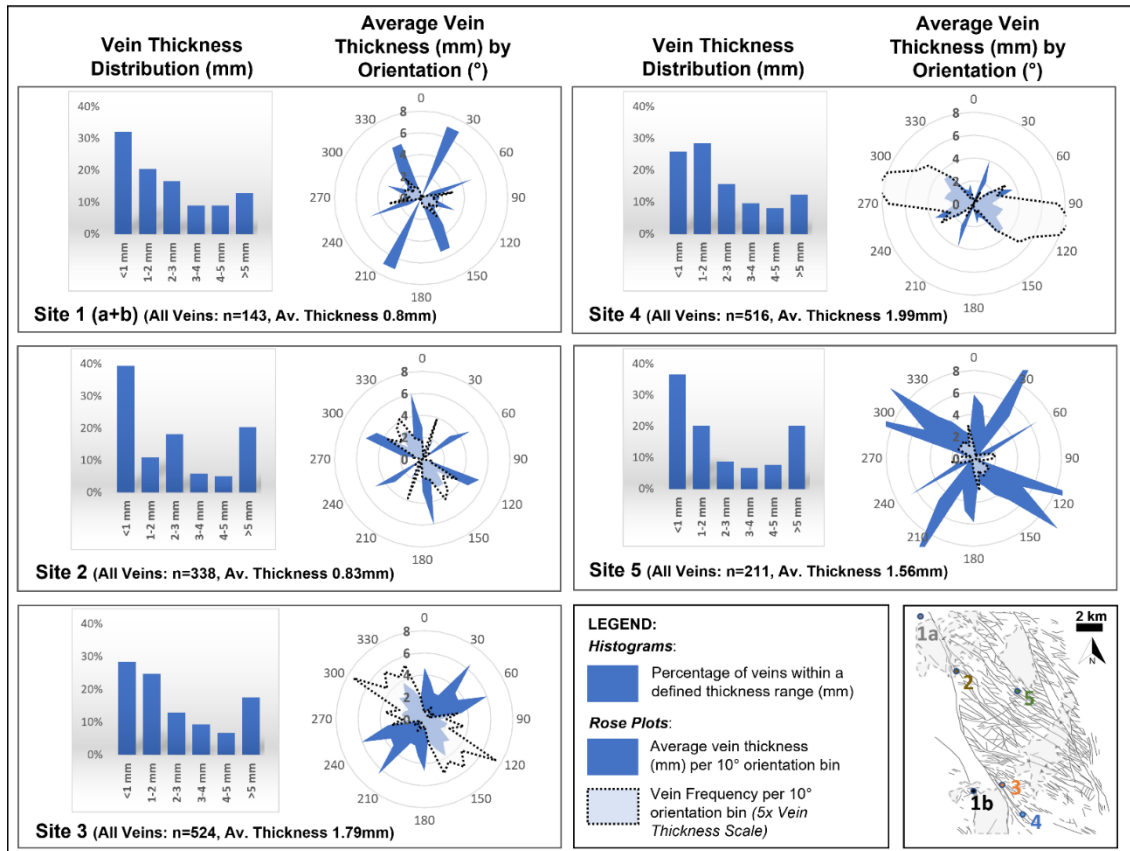


Figure 3.5: Vein thickness distributions and rose plots of total vein precipitate and bias-corrected orientation frequency. Blue filled rose plots display average vein thicknesses per 10° orientation bin for all vein phases. White filled rose plots (dotted black lines) display average vein thicknesses per 10° orientation bin for all vein phases. White / light blue filled rose plots display the total number of veins per 10° orientation bin (frequency = mm scale x5).

Vein orientations at Site 3 are complex due to the presence of multiple interacting fault orientations and the presence of sub-horizontal dipping veins – steeply dipping veins (>60°) account for just 59 % of all veins at this site. The majority (59 %) of veins strike ~30° either side of ~NW-SE striking 2nd order faults, but also sub-parallel to a NNW-SSE striking 1st order fault and sub-perpendicular to ~NE-SW 3rd order extensional faults (Figure 3.4). 50 % of these veins, however, have a dip that is significantly shallower than the 1st and 2nd order faults (which dip at 74-82°). Minor vein sets (representing 19 % of all veins) are also sub-parallel to WSW-ENE striking 3rd order faults and sub-perpendicular to the 1st and 2nd order faults. The picture is much less complicated when considering amount of precipitate alone, however, as most material (58 %) is concentrated within structures sub-parallel to the NW-SE striking 2nd order fault, with only minor amounts (13 %) associated with 1st and 3rd order faults. Thickest veins (5-6 mm on average) form perpendicular to the dominant vein orientation (~NW-SE) (Figure 3.5). Reflecting the complication in the multimodal distribution of vein orientations, average vein thickness distribution is also multimodal, with high average thicknesses (5-6 mm) also at 30° and 60° to the dominant vein orientation (i.e. ~N-S and WSW-ESE).

At Site 4, two strong vein sets have formed sub-parallel to two 3rd order faults striking WSW-ENE and WNW-ESE, with 68 % steeply dipping at >60° (representing 69 % of all veins) (*Figure 3.4*). A further vein set also strikes sub-parallel to two 2nd order faults striking WNW-ESE at 60° dip to each other. The orientation difference between 2nd and 3rd order faults is less clear at this site, hence it is difficult to attribute relative amounts of mineral precipitate to each. The majority (66 %) of precipitated material is observed striking at a similar orientation to the two dominant vein sets. Thickest vein sets (3-4 mm on average), however, are perpendicular or at 30° degrees to this dominant vein orientation (i.e. WSW-ESE, NW-SE and NNE-SSW), with some distribution in average thickness also apparently controlled by the presence of 3rd order faults striking WSW-ENE and WNW-ESE (*Figure 3.5*).

At Site 5 a dominant vein set (accounting for 24 % of all veins) has formed oblique (~30°) to ~NW-SE striking 2nd order faults and sub-parallel to a WSW-ENE striking 3rd order fault, and 75 % of veins have a steep dip (>60°) similar to that of the major faults (68-84°) (*Figure 3.4*). Strong veins sets are also evident sub-parallel to the NW-SE 2nd order fault (32 %, with 85 % dipping >60°) and sub-perpendicular to the WSW-ENE 3rd order fault (i.e. NNW-SSE) (26 %, with 73 % dipping >60°). Veins associated with the 3rd order fault, however, appear to contribute little to the total amount of precipitate, most of which (49 %) is concentrated within NW-SE striking structures parallel to 2nd order faults. Some of the thickest veins measured at this site (6-10 mm on average) are also within 30° of this orientation (*Figure 3.5*). The range in observed fault distributions may mask the fact that some of these thick veins are parallel to the ~NW-SE striking 2nd order fault, whereas some may be oriented at 30° to the fault – together these vein orientations represent 52 % of all veins at this site. Similarly thick vein sets (6-10 mm) are either oriented sub-perpendicular or at 30° to another dominant vein set (representing 29 % of veins) striking parallel to a 3rd order fault oriented WSW-ESE (i.e. ~NE-SW and ~N-S).

3.4.3.2 Individual Vein Phases (Temporal Variation)

When individual vein phases are considered temporally, an evolving picture of the stress state across the duplex begins to emerge. During the chlorite-dominated precipitation phase (*Appendix A: Figure A3.1a*) veins usually form a bimodal distribution (which may be conjugate sets) striking ~NW-SE to ~NNW-SSE. The thickest chlorite veins (1-2 mm and rarely up to 3 mm) correlate with at least one of these dominant orientations. During the mixed chlorite-epidote phase, thickest veins (2-4 mm) usually form oblique (~30°) to the dominant set, which again is ~NW-SE to ~NNW-SSE. At Site 1 the most common vein orientation regardless of vein mineral phase is consistently steeply dipping (68 % at >70° dip), striking dominantly ~E-W. In terms of spatial variations during the chlorite-dominated precipitation phase, at Site 2 early chlorite veins are oriented dominantly NNW-SSE to NNE-SSW. At Site 3, the chlorite-dominated vein set is largely dipping sub-horizontally (46 % at <45°) at a wide range of strikes from ~WNW-ESE to ~N-S as well as ~NE-SW, with a steeper dipping (>60°) NW-SE striking trend also evident. At Site

4, most chlorite-dominated veining (61 %) is steeply dipping ($>60^\circ$) and strikes approximately E-W to NNE-SSW. At Site 5, chlorite-dominated veining only forms a weak \sim E-W strike trend.

The later epidote-dominated phases (*Appendix A: Figure A3.1b*) bear resemblance to the chlorite-epidote phase and indicate that the thickest epidote veins (2-9 mm) usually form either parallel to or at 30° to the most common strike orientation, which ranges from \sim E-W to \sim NNW-SSE. During the mixed quartz-epidote phase, most thick veins (21-100 % of veins 2-12 mm thick) seal structures oblique ($\sim 30^\circ$), rather than parallel to, the modal vein strike (WNW-ESE to NNW-SSE), however otherwise this phase largely mirrors the epidote-only phase. Field observations at Site 2 indicate that chlorite veins are generally cross-cut by NE-SW striking epidote veins. With regards to spatial variations within the duplex, at Site 3, the steeply dipping \sim NE-SW trend observed during the chlorite precipitating phase hosts the thickest veins (average ~ 8 mm) during the later epidote-only vein phase, and accounts for 45 % of all epidote-only veins. A subordinate sub-horizontal ($<45^\circ$) trend is also evident that accounts for 28 % of the epidote-only veins. The dominant trend reverts back to a weak NW-SE strike during the development of the quartz-epidote vein phase. At Site 4, a bimodal strike orientation is evident, with E-W striking structures and an additional orientation at 30° to strike and/or dip sealing with 2-4 mm thick epidote and/or epidote-quartz. At Site 5, epidote-dominated veining forms a broad \sim E-W striking trend, with minor epidote vein subsets also striking \sim N-S and \sim NE-SW. Dominant \sim E-W structures rarely host thick epidote veins, with veins 4-12 mm thick limited instead to the N-S and NE-SW striking structures.

The quartz vein phase (*Appendix A: Figure A3.1c*), is comparable to the earlier quartz-epidote phase, whereby thickest veins (4-8 mm) form either parallel to the modal orientation, which ranges between \sim ENE-WSW and \sim N-S, or form conjugate structures at 30° either side. At sites 1 and 5, however, structures conducive to precipitating thick veins are sub-perpendicular and at 60° to the dominant \sim NNW-SSE orientation, forming thick veins striking \sim NNE-SSW to \sim NE-SW. At Site 3, the quartz-dominated veining phase principally seals NE-SW structures that are steeply-dipping (68 % $>60^\circ$), however thick (4-8 mm) quartz veins are also evident at 60° to this strike (i.e. NNE-SSW). At Site 4, structures commonly observed in earlier vein phases (i.e. those striking \sim WNW-ESE to \sim NW-SE) are also recorded by quartz veins. Thick quartz veins (4-6 mm), however, also seal less common structures oblique to this (i.e. WSW-ENE). At Site 5, quartz forms new steeply dipping ($>60^\circ$) \sim N-S striking structures, and a shallower dipping ($30-60^\circ$) \sim E-W striking set.

Calcite and subsequent 'D3' veins are usually thickest parallel to the strike of maximum vein frequency (*Appendix A: Figure A3.1d*). Where calcite veins are present, they strike \sim E-W to \sim NNW-SSE, with thickest veins 3-4 mm on average (except at Site 5 where calcite veins are anomalously thick, averaging ~ 14 mm). At Site 3, calcite veining is dominantly sub-horizontal with 65 % of veins dipping $<45^\circ$ striking \sim WNW-ESE. Subordinate steeper dipping ($>60^\circ$) calcite veins strike N-S, NE-SW, E-W and NW-SE in almost equal proportions. At Site 4, calcite vein

orientations largely mirror trends observed in earlier vein phases, forming a bimodal strike distribution at E-W to WNW-ESE and ~NW-SE. At Site 5, calcite veins principally precipitate in ~NE-SW-striking structures and are moderately-steeply dipping (40-70°), with some minor variation. During the late 'D3' phase a new NNW-SSE strike orientation, previously unobserved in earlier vein phases, becomes dominant at Site 2. Thick veins (>5 mm on average) seal structures of this orientation but also less common perpendicular structures (4-5mm on average). The few thin (<2 mm) 'D3' veins present at Sites 3 and 5 have a dominant bimodal strike distribution of ~E-W and ~NW-SE. At Site 4, 'D3' veins are typically (55 %) oriented ~E-W, with the thickest veins (~2 mm) striking at 30° either side of this trend.

3.4.3.3 Crack-Seal / Stretching Veins

Across the duplex, a total of 161 crack-seal or stretching veins were identified (20 % of the total recorded vein population). *Figure 3.6* shows the distribution of these veins across the duplex. 91 % are distributed within Sites 2, 3 and 4, and increase in frequency from North to South along the duplex bounding fault. All crack-seal / stretching veins, regardless of whether they are reopened during the epidote, quartz, calcite or 'D3' phase, display an average strike of ~120-300 (~WNW-ESE to NW-SE) and dip steeply at >70°. This is a trend similar to that of most 2nd order faults across the duplex, and the dominant axis of orientation of all veins (*Figure 3.4*).

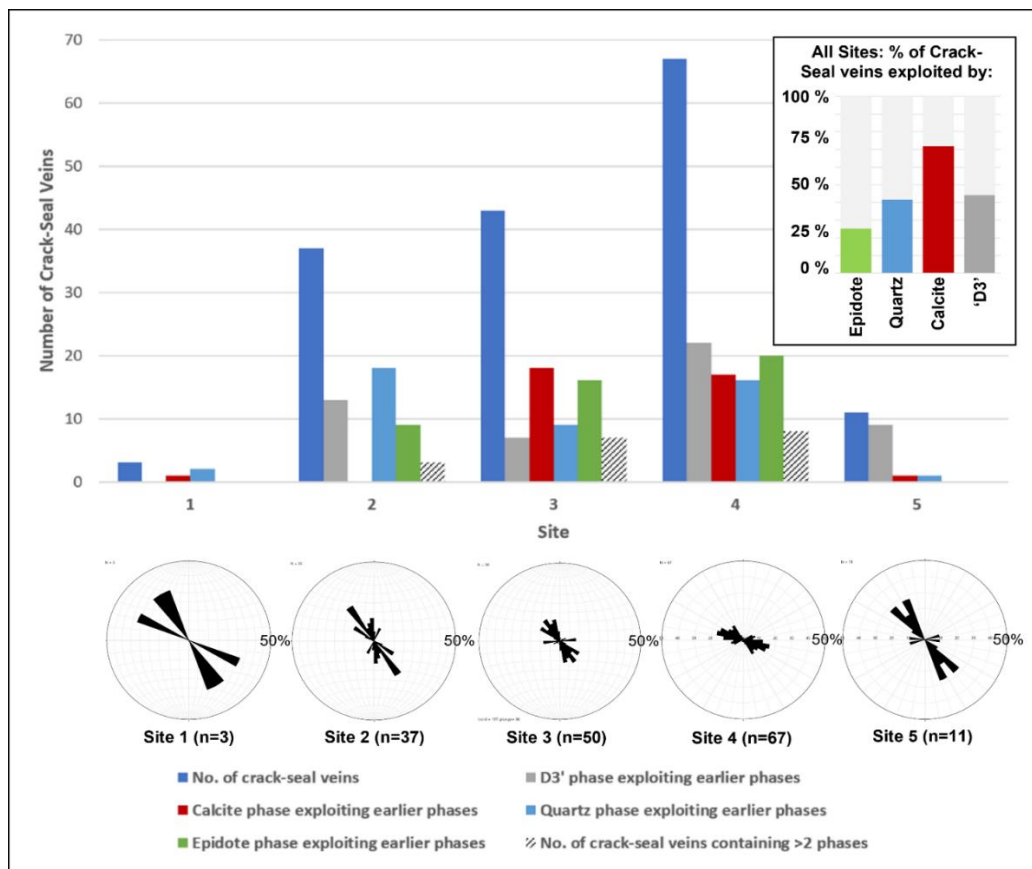


Figure 3.6: Bar chart displaying the number of crack-seal/stretching veins at each site across the duplex, indicating proportions of vein phases that have exploited an earlier phase. Rose plots illustrate the variation in orientations of crack-seal / stretching veins across the duplex.

Considering the precipitation phases present within the crack-seal / stretching veins, 75 % of all chlorite- and epidote-bearing veins form new structures rather than exploiting existing ones, however these veins are commonly exploited by later phases. The quartz-bearing phase, of which 45 % of all recorded veins across the duplex are present as part of crack-seal or stretching textures, is observed in 21-49 % of the 161 veins. 70 % of all calcite veins form a crack-seal phase; calcite is observed in 25-48 % of crack-seal / stretching veins at Sites 3 and 4 but is absent elsewhere. The 'D3' phase forms the final precipitation in 19-33 % of all veins showing this texture, however >50 % of all 'D3' veins form new structures rather than exploit existing ones.

3.4.4 Laboratory Insights into Vein Reactivation

3.4.4.1 Effects of Vein Orientation on Tensile Strength

The tensile strength of intact unaltered host rock (*Figure 3.7a, b; Appendix B, Table B2.1*) varies between 7.66-7.81 MPa, whilst the tensile strength of intact altered host rock varies between 8.14-8.66 MPa. Considering the effects of the presence of veins on the tensile strength, veined samples vary between ~7-9 MPa for chlorite-sealed fractures and ~5-11 MPa for epidote-sealed fractures (*Figure 3.7b*). A very poor correlation between vein thickness and tensile strength (*Figure 3.7b, inset*) suggests that vein thickness has little bearing on results. Varying the orientation of the vein also appears to have little bearing on the tensile strength, except perhaps that results are more varied wherever veins are not oriented either parallel or perpendicular to σ_1 . Traces of failed sample fracture patterns (*Figure 3.7c*) clearly show that fractures invariably form parallel to the σ_1 axis regardless of vein orientation. However, whilst single, clean fractures form parallel to the vein where the vein is parallel to σ_1 , wherever the vein is oriented differently (particularly at 30° or 60° to σ_1) the vein appears to deflect and/or bifurcate the throughgoing fracture, and perhaps accounts for slightly lower tensile strength values in these samples.

3.4.4.2 Effects of Veining and Alteration on Compressive Strength

Thin section analyses of relatively unaltered host rock reveal minor amounts of actinolite and varied ratios of quartz-feldspar along the diorite-granodiorite series, with isotropic textures (*Figure 3.8a(i)*). These observations broadly agree with those made on similar rocks (Scheuber and González, 1999; Mitchell and Faulkner, 2009). Hydrothermally altered host rock comprises more quartz and feldspar (Na-plagioclase end member, occasionally zoned) than the unaltered host rock, and there is a greater proportion of chlorite and fine mixed epidote/muscovite/amphibole matrix in altered samples relative to unaltered samples (*Figure 3.8a(ii)*). In hydrothermally altered samples feldspar is commonly altered to sausserite, and minor zoisite, smectite (palygorskite). Secondary calcite (often displaying twinning) is also observed within the fine matrix of hydrothermally altered samples. Rare foliation and a low degree of cataclasis with S-C and S-S' fabrics are observed, particularly in samples closer to major faults.

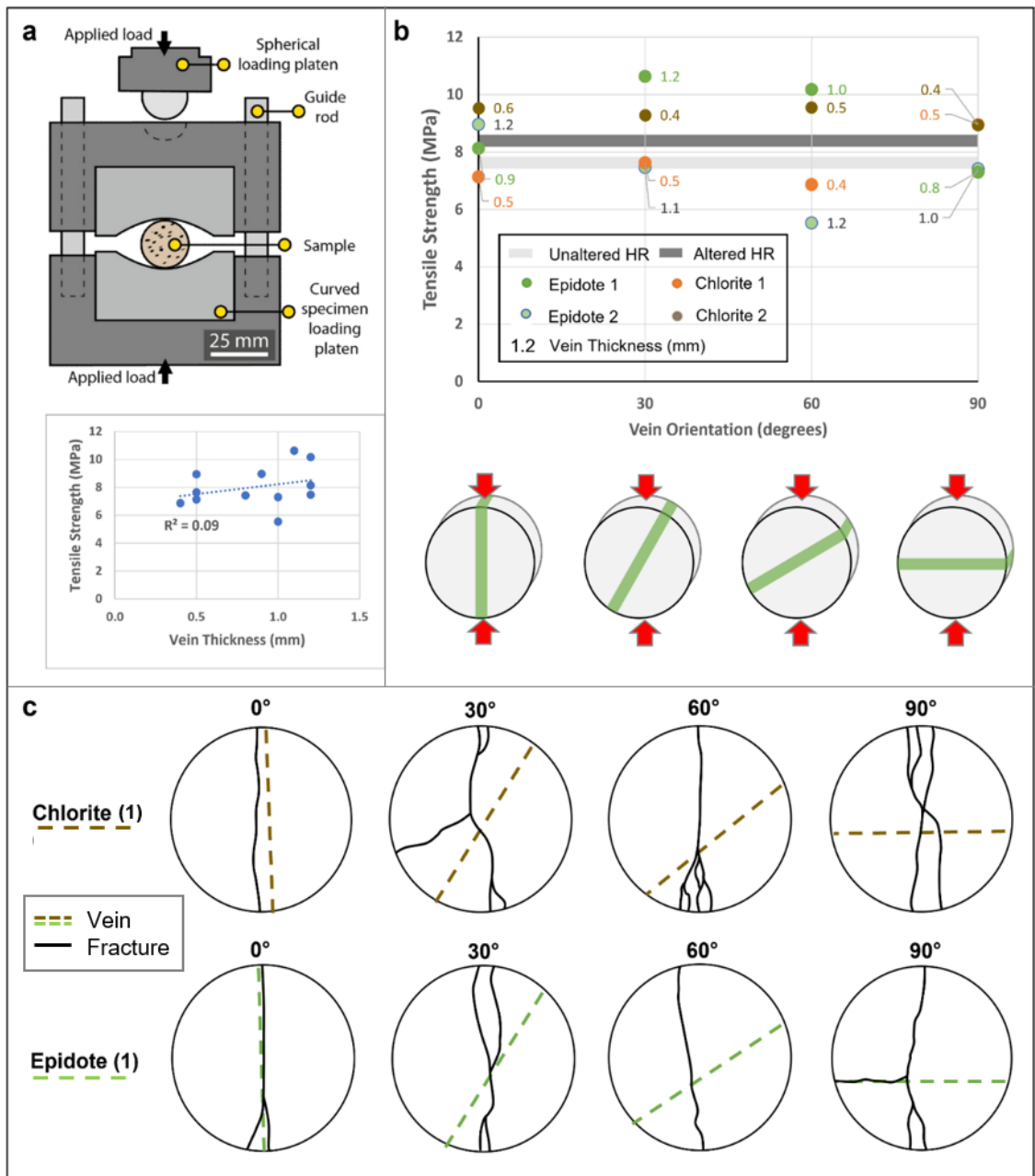


Figure 3.7: a) Laboratory setup of the Brazilian Jig to measure the tensile strength of 20 mm diameter, 10 mm length cored disc samples (after Allen et al., 2020). b) Laboratory data showing the tensile strength of chlorite and epidote veins in Mode I (0°) and Mode II/III (30°, 60°) orientations as well as at 90° to the compressional axis. These data are compared to the range of tensile strengths for non-veined unaltered and altered host rock. The inset plot shows weak correlation between vein thickness and tensile strength, suggesting that this factor has little influence on results. c) Typical experimental fracture traces from Brazilian tests on samples represented in plot b), where dashed brown/green lines indicate the position of the chlorite/epidote veins respectively, and solid black lines mark the surface trace of the fracture.

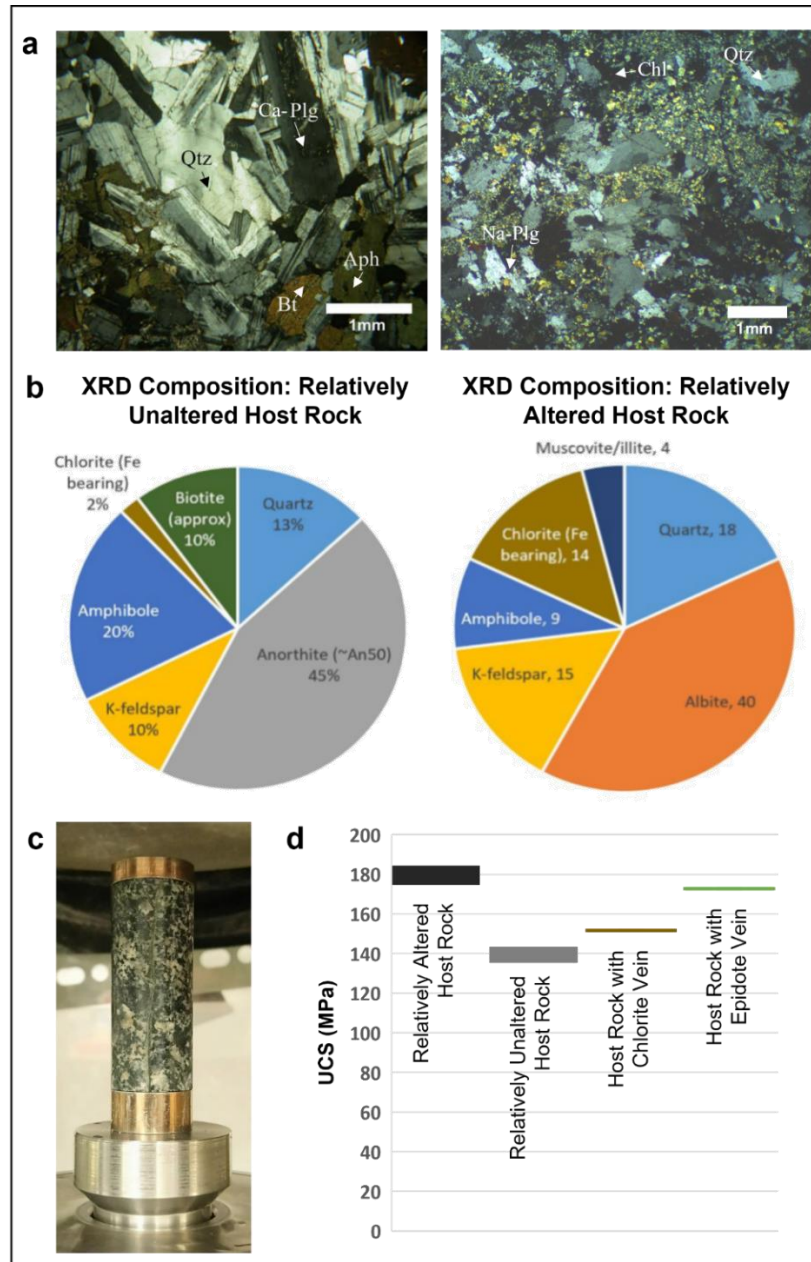


Figure 3.8: a) Thin section images of relatively unaltered host rock (after Mitchell and Faulkner, 2009) and relatively altered host rock (from Site 3). b) XRD-determined mineralogical compositions of unaltered and altered host rock. c) Photograph showing the experimental setup for unconfined compressional strength (UCS) tests. d) Laboratory data showing the UCS of unaltered and altered host rock as well as chlorite and epidote veins in Mode I orientations (0° to compressional axis).

XRD data indicate that Ca- and K-feldspars comprise 55 % of the relatively unaltered host rock, with a further 20 % amphibole, 13 % quartz and 10 % biotite (Figure 3.8b; Appendix B (Table B2.2)). Na- and K feldspars comprise 55% of the altered host rock, with a further 18 % quartz, 14 % chlorite, 9 % amphibole and 4 % muscovite/illite. Experimental data show that relatively unaltered host rock has a lower unconfined compressional strength (UCS) (135-143 MPa) than hydrothermally altered host rock (174-185 MPa) (Figure 3.8c, d; Appendix B (Table B2.3)). Cores containing chlorite Mode I veins have UCS values of 152 MPa, while epidote Mode I veins have UCS values of 173 MPa.

3.5 Discussion

3.5.1 Spatial and temporal variation of fluid flow in a duplex hosted geothermal system as recorded by hydrothermal veining

3.5.1.1 Evolution of fluid properties and distribution

In this exhumed, extensional, duplex-hosted geothermal system, we observe a propylitic mineral assemblage that evolves through a sequence of alteration assemblages; chlorite, mixed chlorite-epidote, epidote, mixed epidote-quartz, quartz, calcite, and finally to palygorskite and salts as the 'D3' phase (*Figure 3.2*). The presence of chlorite and epidote is typically indicative of elevated temperatures (>260 °C) (Robb, 2004), although Cembrano et al. (2005) suggest somewhat lower temperatures of ~101-252 °C based on fluid inclusion analyses on similar vein assemblages from elsewhere in the study area. Other works suggest that the dominant vein assemblage in the study area (i.e. chlorite-epidote-quartz) is indicative of contemporaneous faulting and fluid transport under retrograde low-greenschist facies conditions (~280-350 °C) at depths of ~3 to 6 km (Cembrano et al., 2005; Olivares, 2004; Herrera et al., 2005; Arancibia et al., 2014). In this study, these vein compositions are often observed to be mixed/coeval, suggesting that they precipitated at similar times during the tectonic history of the study area, in agreement with previous studies suggesting their formation during the latter stage of the Late Jurassic–Early Cretaceous magmatic arc (~125-118Ma - Scheuber and Andriessen, 1990; Cembrano et al., 2005). Chlorite-related textures are generally indistinguishable, however epidote textures are usually either syntaxial (potentially reflecting slow, low-energy crystal growth into open, fluid-filled fractures (Bons, 2000; Hilgers et al., 2000; Bons et al., 2012; McNamara et al., 2016)) or microcrystalline, potentially reflecting fast, high-energy precipitation processes (e.g. Caine et al., 2010; Okamoto et al., 2010). Whilst syntaxial epidote veins occur throughout the duplex, microcrystalline epidote has only been observed at sites adjacent to the duplex-bounding fault, suggesting a spatial control on such potential rapid, energetic fluid flow processes. Textures in quartz-bearing veins may be euhedral and blocky, however are usually microcrystalline within the duplex, supporting the same interpretation.

Chlorite, epidote, and quartz veins are often followed by calcite-dominated precipitation (*Figure 3.2*). Whilst it cannot be argued with certainty from data presented here that calcite precipitation occurred during the same phase of tectonic activity as chlorite-epidote-quartz precipitation, Scheuber and Andriessen (1990) and Scheuber and Reutter (1992) have shown using fission track data that such veins likely record the final stages of a geothermal fluid system that cooled below 100°C at ~118Ma. Calcite is a highly reactive mineral typically found in geothermal systems with temperatures of ~140-300 °C (and wherever fluids have high concentrations of dissolved CO₂). Calcite dissolution usually occurs in areas where colder fluids are circulating, whereas precipitation occurs in hotter circulation zones (Andre et al., 2006), and is mostly controlled by boiling, dilution and condensation of fluids (Simmons and Christenson, 1994). Indeed, near Site 5, calcite has been shown to have precipitated in open fractures at sub-

hydrostatic pressures (Herrera et al., 2005). Growth textures within calcite crystals, as evidenced by chemical zoning in CL analysis that is likely related to the relative abundance of Fe and Mn (Long and Agrell, 1965) (*Figure 3.2*), suggest that fluid chemistry has not only evolved to produce polyphase crystallisation with time, but also during growth of a single precipitation phase. Asymmetric antitaxial growth forming elongate blocky textures (e.g. Bons et al., 2012) is typical of calcite veins in the study area, which have previously been interpreted to indicate long-duration crystal growth into open, fluid-filled fractures (Herrera et al., 2005), however caution is reserved regarding this interpretation based on the content of *Chapter 5*. The lack of deformation structures (e.g. fracturing or twinning) within most calcite crystals suggests that this was the most recent tectonic event in most areas (cf. McNamara et al., 2016).

Our observations of sampled veins, coupled with support from other published studies, show that during the formation of this duplex system the temperature and chemistry of the circulating geothermal fluid evolves with time. Spatial distributions of mineral phases around duplex faults shown in *Figure 3.3* also indicate that fractures exploited by later fluids (i.e. those precipitating calcite, clays and salts) are not always the same as those exploited by earlier chlorite-, epidote- and quartz-precipitating fluids. Whilst earlier vein phases are dominant along the duplex-bounding Bolfin Fault, particularly further into the structurally densest area, later phases have predominantly focused on the margins of the overlap structure but also in the duplex centre at the greatest distance from bounding faults. Potential reasons for this could be that early precipitation has decreased permeability and increased rock strength to a point where new fractures must be created elsewhere – this is discussed further in *Section 3.5.2*. Fluid circulation within this geothermal system is interpreted to migrate over time, which has significant implications for geothermal development in terms of the exploration of where the highest temperatures or most recent fluid flow occurs within these systems.

Observations at outcrop and in thin section indicate widespread crack-seal/stretching vein textures (e.g. *Figure 3.2c*) formed mainly during the epidote-quartz deformation phase at sites adjacent to the Bolfin Fault (i.e. Sites 2, 3 and 4) (*Figure 3.6*). Whilst fracture permeability in general decreases with progressive mineral precipitation, this trend is disrupted by crack-seal processes, hence it is important to understand where structures most favorably oriented to reactivate are likely to be (Cox, 1999). Crack-seal processes are generally associated with cyclic increases in fluid pressure and mineral stress concentrations (Wiltschko and Morse, 2001), but may also result from differential stress because of overlapping fault geometry (Cembrano et al., 2005), which together may be indicative of boiling, shear deformation and/or fracture collapse. More frequent crack-seal events are likely to occur within well-oriented structures such as those with an orientation parallel to the axis of maximum compression (σ_1) (see *Section 3.5.2*), and are more likely to open repeatedly and sustain long-term fluid flow (Wallis et al., 2002; Davatzes and Hickman, 2010). Veins outside of the duplex and at greatest distances from the bounding faults generally display structures less indicative such energetic formation processes (i.e. lower temperature and pressure) and less subsequent deformation (*Figure 3.2*, *Figure 3.6*).

3.5.1.2 Tectonic controls on hydrothermal veining

The spatial and temporal evolution in precipitation, in terms of composition and texture as discussed above, is only part of the picture that can be further understood by considering vein orientation. The orientation of structures with respect to the maximum principal stress (σ_1) impacts which structures are critically stressed and thus potential fluid flow pathways (Sibson, 1985, 1996, 2000; Berger et al., 2007; De Paola et al., 2007). Mechanical anisotropy – which within the relatively isotropic host rock studied here may be defined by a set of planar mineral veins – generally has most control on failure when the angle between σ_1 and a plane of weakness is $\sim 30^\circ$ (Donath, 1961), however interactions between faults complicate patterns of local stress (as introduced in *Chapter 1*). Structures perpendicular to σ_1 are also likely to open during relative extension, for example during periods of high fluid pressures under tensional local stress fields (Sibson, 1996; Pérez-Flores et al., 2017), whilst local cooling can promote fracture opening on pre-existing planes via rock contraction (Siratovich et al., 2015; Lamur et al., 2018). Analysis of regional fault patterns in the wider study area (Scheuber and González, 1999) suggests that the axis of maximum compressional stress (σ_1) is likely oriented \sim WNW-ESE (309/01), with the maximum extension direction (σ_3) oriented NNE-SSW (040/14). Hence it would be reasonable to expect, in a purely isotropic host rock, Mode I/II veins to form parallel to the σ_3 orientation (i.e. \sim WNW-ESE) and at 30° to σ_1 (i.e. \sim E-W or \sim NW-SE) respectively.

The 1st order Bolfin Fault, oriented approximately NW-SE to NNW-SSE throughout the study area (*Figure 3.1, Figure 3.4*), has the most observable impact on sealed fracture distributions – and therefore inferred palaeo-fluid flow – outside of and at the edge of the main duplex structure (Sites 1 and 2), to which the most numerous veins, contributing the most precipitate, are approximately parallel. At the site closer to the denser regional structure, a greater proportion of veins are also parallel to 2nd order faults striking \sim NE-SW. Thicker veins (<5 mm but up to 21 mm) have also formed at $\sim 30^\circ$ to the NE-SW-striking faults and likely represent an important pulse of fluid flow at Site 2. Analysis of successive vein phases (*Appendix A: Figure A3.1*) suggests that there is limited change in preferred fluid flow orientation (and therefore stress) throughout the duplex history at these sites. Further within the duplex structure, where the density of 2nd and 3rd order faults is much greater (see *Chapter 2*), the control of these typically \sim E-W to \sim NNW-SSE-striking faults on mineral vein orientation is more pronounced, with more complex vein orientation patterns indicating a more complex history of structurally controlled fluid flow (*Figure 3.4, Figure 3.5*). The dilatational jog (Site 3) exemplifies this; here the dominant vein set (accounting for 63% of all veins, 58% of which are thin veins <2 mm in aperture) is oriented parallel to - or at 30° to - 2nd order faults (i.e. striking WNW-ESE to NNW-SSE, sub-parallel to σ_1). A greater range of vein orientations suggests that local stresses within the duplex may also have been more variable.

Data presented here suggest that thin fractures oriented approximately parallel to σ_1 generally represent the most dominant permeable structures in the geothermal system. This is generally

in agreement with Massiot et al. (2015) and McNamara et al. (2015, 2016), who show that wide-aperture fractures in the Rotokawa geothermal field (New Zealand) are usually situated outside of permeable zones. The importance of individual fracture aperture on permeability anisotropy however is variable depending on the area – for example, fluid flow in the Te Mihi geothermal field (New Zealand) has conversely been shown to be controlled largely by wide aperture fractures (McNamara et al., 2019). Wider aperture fractures are generally considered to dominate the structural permeability of a rock mass once thinner fractures are sealed inwards from the fracture walls (Marrett and Laubach, 1997; Davatzes and Hickman, 2009; Wallis et al., 2012), consistent with observations here that suggest wide-aperture fractures become important fluid conduits later in the history of the geothermal system. In this study, spatial position within the fault duplex also appears to affect which structures are most important as fluid conduits, with wide-aperture structures representing proportionally more fluid flow away from major faults. Palaeo-fluid flow at Site 5 (in the centre of the duplex structure) is in part represented by some very wide (5-48 mm) veins. Thick ~ENE-WSW-striking calcite-bearing veins observed in the field are however not numerous (accounting for just 5% of all veins at Site 5). Whilst the dominant vein orientation in this area strikes ~ENE-WSW (parallel to 3rd order faults and σ_3), most vein material (50%) has precipitated parallel to 2nd order faults striking ~NW-SE, as is the case elsewhere within the structurally densest part of the duplex. Wider aperture veins represent 24% of all veins at Site 3 (<5 mm but rarely >8 mm), and are mostly oriented sub-parallel to ESE-WNW to E-W-striking 3rd order faults. This less-favourably oriented vein set with respect to regional stress probably represents a more major fluid flow control within this region of the geothermal system than elsewhere, perhaps due to its location adjacent to a bend in the Bolfin Fault allowing for a denser set of 3rd order structures (see *Chapter 2*).

A temporal evolution of stress emerges when considering successive vein phases precipitating within the duplex (*Appendix A: Figure A3.1*). Early chlorite veins at Site 3 record fluid flow in a wide range of orientations (primarily striking NW-SE and sub-horizontal but also striking ~NE-SW, ~N-S and ~E-W), which are apparently intermittently exploited by later phases: chlorite+epidote (~NW-SE); epidote+quartz (~NE-SW); quartz (~NW-SE and sub-horizontal) and calcite (sub-horizontal, ~NE-SW and ~NW-SE). Significant ranges in vein orientations are typically a result of local rotations of the stress field, rather than the regional stress, and are complicated by interactions with pre-existing structures (e.g. Faulkner et al., 2006; De Paola et al., 2007; Healy, 2008). It is possible that the changes in mechanical strength that occur upon precipitation (discussed in *Section 3.5.2*) can induce the relocation of structurally controlled fluid flow to a new existing, or possibly even generate a new, fracture orientation set, despite that fracture set not being the most favourable orientation for reactivation within a given in-situ stress state. At less structurally complex sites within the duplex (e.g. Site 5), fewer orientations of early chlorite veins apparently limit the orientation variation in later vein phases. Here, ~NW-SE and ~E-W strikes of chlorite veins, approximately parallel to the dominant 2nd and 3rd order faults respectively, are consistently reflected in later events, until the epidote

phase introduces a strong trend at a 30° shallow dip (also striking NW-SE / E-W?), and the quartz phase introduces a new ~N-S strike trend. Late calcite veins are almost always very wide and seal structures oriented sub-parallel to 2nd order faults (~NW-SE), suggesting that during this phase a few, wide-aperture fractures controlled most of the fluid flow in this area.

Overall, whilst there are important variations spatially, *Figure 3.9a* illustrates that the total amount of precipitate across the duplex is primarily concentrated within favourably oriented structures with respect to the regional state of stress – i.e. those that are purely extensional (perpendicular to σ_3) – throughout the history of the geothermal system. Veins oriented more ~E-W (i.e. ~30° to the σ_1 axis) are more notable in the field on account of their greater thicknesses yet overall constitute a small percentage of veins and total precipitate, from which it can be inferred that these structures were not particularly favourable for fluid flow. When considered in terms of the temporal evolution of vein formation with respect to regional stress across the duplex, *Figure 3.9b* shows that whilst ~WNW-ESE structures are consistently open to fluid flow and precipitation throughout the system’s history, other structures conduct fluid more intermittently. Assuming that there was no significant change in the regional stress orientation during the geothermally active period, this may suggest that early precipitation could be changing the rock’s permeability, mechanical properties and therefore local fluid pressures and stress state. This inference conforms with previous findings that local stress rotations are common and often significant within individual fault damage zones and regional duplex structures (e.g. Faulkner et al., 2006; De Paola et al., 2007), and that high-temperature geothermal areas are prone to dynamic stress changes (Grant and Bixley, 2011).

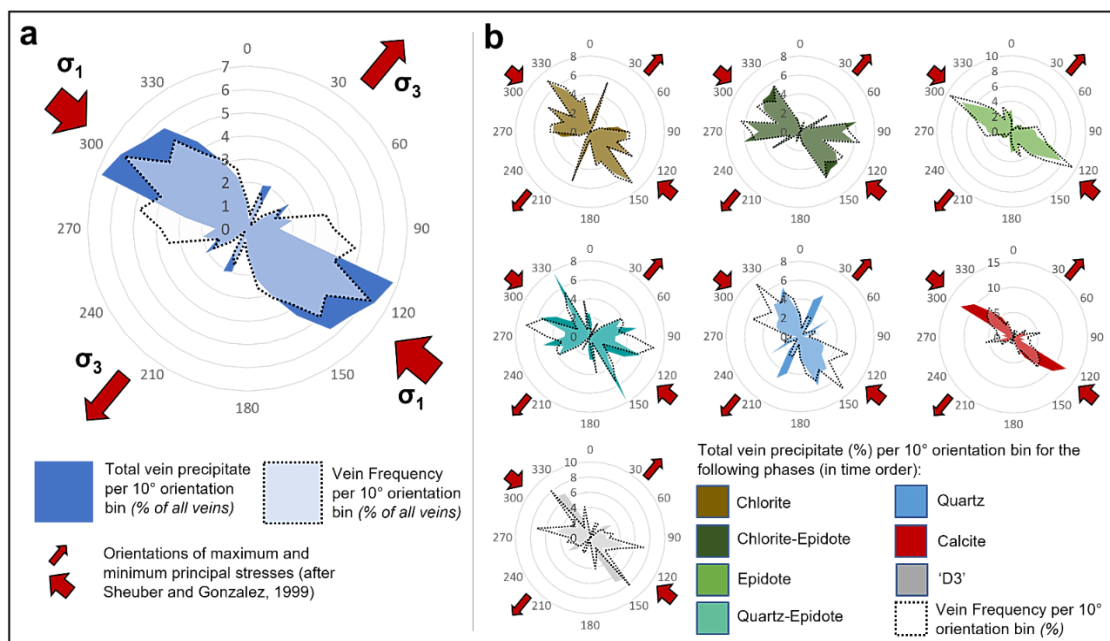


Figure 3.9: *a*) Summary radar plot showing percentages of all measured vein precipitate (blue) and all measured veins (dashed line) across the duplex, in relation to the regional state of stress inferred by Scheuber and González (1999). *b*) Radar plots for each successive vein phase illustrating the temporal evolution of vein formation and amounts of precipitation in relation to the regional state of stress.

3.5.2 *The influence of hydrothermal veining and alteration on mechanical strength and maintenance of structural permeability*

Since fluid flow can be localised within fault duplexes (*Chapter 2*), fracture sealing and hydrothermal alteration are considered to allow rapid strength recovery. Whilst the presence of chlorite and epidote veins forming the early precipitation phases in this geothermal system has been shown to increase the compressional strength of the host rock (*Figure 3.8*), the same veins appear to have little impact on its tensile strength (*Figure 3.7*). Other studies (e.g. Virgo et al., 2013; McNamara et al., 2014; He and Afolagboye, 2018) have previously shown that rocks with fabric (e.g. mineral layering or veins) oriented parallel to σ_1 have lower tensile strength than intact rock containing no fabric. Furthermore, pre-existing fabric apparently has little influence on later tensile fractures when it is oriented at $>60^\circ$ to σ_1 (Pluymakers et al., 2020). Weaker tensile strengths of more favourably oriented structures with respect to σ_1 have been inferred elsewhere to indicate that fluid flow makes use of existing Mode I fracture networks via crack-seal mechanisms rather than through the generation of new fractures, however no such conclusion can be drawn here. *Figure 3.7* clearly indicates that the orientation of the vein with respect to the σ_1 axis has little bearing on either the host rock tensile strength resulting fracture patterns upon failure, suggesting that these veins do not significantly impact where fractures form. This may be in part due to the relatively small thicknesses of veins studied here: thin veins apparently have little influence on stress concentrations at the tip of propagating fractures regardless of their individual inherent strength (Virgo et al., 2013). McNamara et al. (2014) showed a negative correlation exists between tensile strength and vein thickness, however no such correlation was present for veins <2 mm. Some variation in tensile strength evident here is seemingly controlled by a parameter other than vein orientation or thickness.

The similar tensile strengths of intact host rock and host rock containing veins observed in this study can be considered advantageous from a geothermal prospectivity context. As some veining does not facilitate crack-seal activity, it forces the generation of alternate fracture orientations in the system, ultimately creating a more structurally complex fracture fluid flow network and enhancing the circulation of geothermal fluids (e.g. Kissling et al., 2015). Whilst weak veins have elsewhere been shown to localise fractures within vein material and be capable of reactivating even when highly misoriented to the preferred fracturing orientation, stronger veins with respect to the host rock are more likely to arrest or deflect propagating fractures, or not interact with the fracture at all (Caputo and Hancock, 1999; Virgo et al., 2013) (*Figure 3.10*). Experimental data presented here, where vein reactivation is rare and most new fractures either cross-cut veins or bifurcate upon contact (cf. Bertram and Kalthoff, 2003), reflect model data akin to a vein to host rock strength ration of $\geq 1:1$ (Virgo et al., 2013, *Figure 3.10*). Epidote and chlorite veins may only have a local influence on lateral connectivity between main structures through fracture deflection. It is certainly possible however that experimental samples here represent a biased subset of strong veins, and misoriented weak veins may also exist in the study area that are capable of reactivating and creating linking structures.

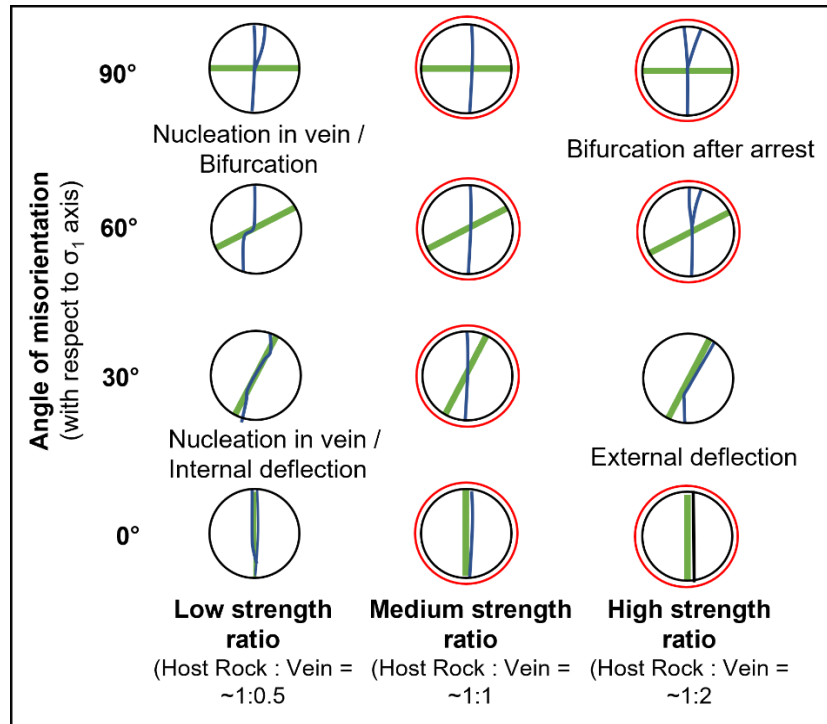


Figure 3.10: A summary of modelled data (modified from Virgo et al., 2013) showing the effect of vein orientation on successive tensile fracturing in low, medium and high strength ratios of host rock to veins. A low strength ratio and high angle of misorientation results in fracture nucleation within the vein and/or bifurcation; a low strength ratio and low angle of misorientation results in fracture nucleation within the vein and/or internal deflection of the fracture; a high strength ratio and high angle of misorientation results in bifurcation after fracture arrest; and a low angle of misorientation results in external deflection of the fracture. Red circles indicate the types of interaction observed in experimental data in this study.

The propylitic alteration of the host rock in the vein walls seen in *Figure 3.2* is generally indicative of the circulation of Fe- and Mg-bearing hydrothermal fluids (Robb, 2004), and suggests that fluids were not only circulating through macrofractures, but also within microfracture damage zones surrounding them. Such structurally-controlled fluid flow within the studied system has caused the breakdown of amphibole, biotite and feldspars to chlorite and muscovite (*Figure 3.8b,a*), which agrees with similar findings from other studies in this area (e.g. Cembrano et al., 2005; Herrera et al., 2005; Faulkner et al., 2011). Preliminary X-Ray Fluorescence data collected in the field (not presented here) indeed appear to suggest that hydrothermally altered host rocks are chemically enriched in Fe_2O_3 , TiO_2 , MgO , MnO and K_2O whilst being depleted in Ca (in agreement with Arancibia et al., 2014), which supports the aforementioned compositional changes and perhaps indicates that vein material (e.g. epidote) has formed via leaching from the host rock. As the degree of host rock alteration within a fault's damage zone relates to both the density and thickness of veins (e.g. Faulkner et al., 2011), the presence of veins may in fact control subsequent fracturing and fluid flow in that the micro-damage zones between veins ultimately allow fluid to permeate the surrounding host rock and form the alteration mineralogy that has a clear bearing on rock strength (*Figure 3.8d*).

The dissolution and alteration of primary minerals, and precipitation of secondary minerals caused by the movement of hot, dissolved-ion rich fluids, affects the rock mechanical properties and distribution of permeable zones (e.g. Heap et al., 2012, 2013). Laboratory data (*Figure 3.8*) suggest that early propylitic alteration may have increased the strength of the rock mass and/or significantly decreased the permeability in some areas, such that calcite- and 'D3'-precipitating fluids have exploited other areas of the duplex structure instead. Veins appear not to be a plane of weakness but rather strengthen the rock: the presence of chlorite and epidote veins increases the compressional strength of the host rock (by ~10 MPa and ~30 MPa respectively in Mode I orientation). A higher degree of host rock alteration without the presence of any veins further increases the compressional strength relative to the unaltered host rock by ~40 MPa). This is contrary to other published studies, which argue that rock mechanical properties are largely independent of alteration mineralogy (Siratovich et al., (2014) or show that altered samples fail at lower compressional stresses than those that are unaltered (Siratovich et al., 2016; Pola et al., 2012; 2014). Experimental data of Siratovich et al., (2014), however, indicate that stronger rocks (i.e. those with a high UCS) contain fewer microcracks, suggesting that fracture sealing may have significantly reduced microcrack surface area in our samples.

Wyering et al. (2015) consider that the relative proportion of primary to secondary minerals, and particularly the hardness of minerals present, are the principle contributing factors to rock strength. Described as a power law relationship, the greater the proportion of hard minerals present, the greater the predicted UCS. Whilst XRD data presented here (*Figure 3.8b*) shows an estimated 6 % increase in typically weak platy minerals (e.g. chlorite and muscovite/illite with a Moh's Hardness of 1.5-3) in the relatively altered host rock, as well as a decreased abundance of relatively strong amphibole (Moh's Hardness = 5.5) of 11 %, the increased strength of the relatively altered host rock may be explained by the increased abundance of strong minerals such as silica (Moh's Hardness = 7) and K-Feldspar (Moh's Hardness = 6.5) (both by 5 %). Assuming that connected porosity and fracture abundance are similar in both samples, mineralogy values are in accordance with our findings that the relatively altered host rock is stronger than the unaltered host rock, and suggests that it is at least partly controlled by its greater proportion of hard minerals (*Table 3.4*). Whilst it is likely that more altered samples contain a greater abundance of fractures and microcracks (on the premise that these are the fluid conduits that instigated alteration processes in the first place), there is little evidence for such structures in analysed thin sections (e.g. *Figure 3.8a*), hence the assumption that this parameter is less important than mineralogy in this case remains valid. This alteration is likely to impact fluid pressures, the distribution of which strongly influences the style of faulting and mineralisation (Sibson, 1996). The degree of alteration and resultant strength of the host rock will also have implications on the rate of penetration during drilling of a geothermal well: for example, using the modified alteration strength index of Wyering et al. (2017) as a guide, drilling through unaltered host rock here would have a rate of penetration of ~2.8-5 mhr⁻¹, whilst drilling through altered host rock would have a slower rate of penetration of ~2.2-4.7 mhr⁻¹.

Table 3.4: Calculations of the Mineralogy Value (a component of the Alteration Strength Index (ASI) – Wyering et al., 2015) for relatively altered and unaltered host rocks used in laboratory experiments. The Mineralogy Value is the sum of the product of each individual mineral's relative proportion within the sample and its hardness index (which itself is related to Moh's Hardness Scale - Wyering et al., 2015).

Mineral	Relatively Unaltered Host Rock (%)	Relatively Altered Host Rock (%)	Moh's Hardness	Hardness Index (Wyering et al., 2015)	ASI Mineralogy Value (Wyering et al., 2015) (Unaltered)	ASI Mineralogy Value (Wyering et al., 2015) (Altered)
Quartz	13	18	7	2.1	27.3	37.8
Albite	0	40	6.5	1.7	0.0	68.0
Anorthite	44	0	6	1.3	57.2	0.0
K-feldspar	10	15	6	1.3	13.0	19.5
Amphibole	20	9	5.5	1.3	26.0	11.7
Fe-Chlorite	2	14	1.5	0.1	0.2	1.4
Muscovite/illite	0	4	3	0.5	0.0	2.0
Biotite	10	0	3	0.5	5.0	0.0
Total	99	100	-	-	128.7	140.4

3.6 Conclusions

In this chapter, data have been presented that characterises regional fracture-hosted fluid flow, fracture formation, sealing mechanisms, and effects of alteration on rock strength within an exhumed duplex-hosted geothermal system in the Atacama Fault Zone, Chile. Analysis of this characterisation and the patterns it reveals has important implications for aspects of structural evolution and thus fluid flux within a duplex hosted geothermal system.

- The distribution of chlorite-epidote-quartz-calcite veins (representing evolving P-T conditions) varies both spatially and temporally across a transtensional duplex structure, such that late veining occurs well within the duplex only, while early veining is ubiquitous across the system.
- This spatial and temporal variation in veining suggests that early vein precipitation events increased rock strength, thus causing a permeability reduction and encouraging fracture generation and fluid flow to relocate elsewhere in the duplex. Laboratory data show that the mechanical strength of intact hydrothermally altered host rock - and fractured host rock sealed with hydrothermal precipitate - is greater than that of unaltered host rock.
- Analysis of vein orientations and thicknesses reveal that, within the duplex, the majority of vein material has precipitated in favourably oriented extensional structures perpendicular to the minimum horizontal stress (σ_3 - ~ENE-WSW). Whilst wide-aperture

veins (>~5 mm) have also formed oblique and perpendicular to these structures, these represent a low percentage of veins and total precipitate; Thin veins (<~2 mm) appear to be most representative of fluid flow within this geothermal system, with some exceptions away from major duplex-bounding faults.

- Crack-seal / stretching veins are most common adjacent to the duplex-bounding fault, and almost always form parallel to the dominant orientation of precipitation. However, pre-existing hydrothermal veins show little influence on the formation or subsequent fractures. The degree of alteration exhibits a stronger control on later fracture formation than does the presence of pre-existing geothermal veins.

Anisotropy reactivation has important implications: In a producing geothermal reservoir, the response of the stress field to fluid extraction and reinjection affects the longevity of the resource. In EGS reservoirs, where fluid injection is not adjusted to the in-situ stress field and rock strength conditions, it is important to understand the potential for fault reactivation prior to stimulation to prevent undesirable seismicity accompanying enhanced permeability (Moeck et al., 2009; Ellsworth, 2013). Pre-existing structures appear to be important in controlling the onset of permeable fracture networks during later deformation and should be carefully considered when analysing a potential fractured geothermal reservoir.

It is suggested that future work, as well as using datasets from a wider range of structural and hydrothermal settings, explores how alteration and veining affects mechanical strength at conditions more applicable to those of a typical geothermal reservoir (i.e. high effective pressures and temperatures), which is partly explored in *Chapter 5*. Fluid inclusion analyses would add a quantitative component to the temporal evolution of fluid conditions in this particular geothermal system. Future work should also employ a wider range of microstructural and geochemical analyses to shed more light on vein textures, for example using Electron Back-Scatter Diffraction (EBSD) and Energy Dispersive Spectroscopy (EDS) to investigate crystallographic orientation and chemical changes between and within vein crystals, which would provide greater detail on how stress evolved and how individual fractures sealed.

Acknowledgements

Work presented here was fully funded by Natural Environment Research Council (NERC grant ref. no. NE/L002469/1) as part of a PhD conducted via the EAO DTP, whose support is gratefully acknowledged. Thanks are also extended to Giulio Di Toro and the field team from University of Padova and Universidad Catolica Del Norte (particularly Erik Jensen, Rodrigo Gomila, Michele Fondriest and Simone Masoch) for invaluable guidance, support, logistical assistance and aspects of data collection in the field. Thin sections were prepared by CGG Robertson and Burnham Petrographics, and relevant laboratory training was provided by colleagues in the Rock Deformation Laboratory (for rock cutting and core preparation) and in the Central Teaching Laboratory (for SEM and CL microscopy) at the University of Liverpool.

4 The Effect of Water Saturation on the Frictional Properties of Clay Fault Gouges

Abstract

Clay minerals often constitute a significant proportion of fault cores, where fault gouge develops via a combination of mechanical attrition of the fault wall and authigenic crystallisation. Increasing pressures and temperatures with depth alter the minerals present within the fault gouge in terms of dehydration, consolidation and mineralogy, changing the fault's mechanical and seismic properties as a result. The physics of clay friction, in particular the effect of free and interstitial bound (interlayer) water, however, is poorly understood. In this chapter, laboratory experiments were conducted on synthetic clay gouges under carefully controlled saturation states. Kaolinite (a 1:1 sheet silicate) and montmorillonite (a 2:1 smectite) were chosen specifically to investigate the effect of dehydration on frictional properties in swelling versus non-swelling clays respectively. Samples were sheared at room temperature under triaxial pressure at the following conditions: water saturated; room humidity; thermally dried and at room humidity; in a vacuum at room humidity; thermally dried and in a vacuum; in a vacuum and thermally dried within the pressure vessel. As water is removed from the clays, friction coefficient (μ) is shown to increase by a factor of 3 in the 2:1 smectite and a factor of 2 in the 1:1 sheet silicate, with largest increases in thermally dried samples. Data are generally consistent with published μ values, however other factors besides water are presumed to contribute to their variation. Analysis of constitutive frictional parameters (a-b) show that the clays show velocity-strengthening behaviour at all conditions, however as water is removed the gouges become less frictionally stable. The amount of displacement or time required to establish a new steady state μ upon a change in sliding velocity (d_c) decreases markedly in drier samples. Experimental data coupled with microstructural analyses suggest that the presence of water is key in promoting time and slip dependent frictional changes, constraining operative grain-scale deformation mechanisms to those that are fluid assisted. They also highlight the optimum laboratory procedures to investigate the frictional properties of clay-bearing materials in a consistent manner. With regards to implications for geothermal exploration, both kaolinite and smectites are common low temperature alteration minerals that are prevalent in many hydrothermal systems, with smectites increasingly recognised as 'problem minerals' due to their low permeability creating barriers to fluid flow and frictional instabilities as they transition to illite at depth. This study contributes a level of understanding that can help prevent induced seismicity during geothermal production, or during stimulation of dry Enhanced Geothermal System (EGS) reservoirs by fluid injection.

4.1 Introduction

The purpose of this chapter is to investigate the contribution of water bound to phyllosilicates on their frictional behaviour. Understanding this behaviour is fundamental to constraining the

larger scale behaviour of fault zones, informing models of fault strength and stability in geothermal reservoirs, as well as carbon storage sites and geological repositories of radioactive waste. Within upper crustal fault cores, fault gouge develops by a combination of mechanical attrition of the fault wall and authigenic crystallisation (Rutter and Maddock, 1987). Phyllosilicates are commonly abundant within this gouge (Sánchez-Roa et al., 2016). With a crystallographic structure capable of retaining large amounts of water (Schleicher et al., 2012), they may significantly influence fluid-assisted healing mechanisms, e.g. by forming planes of weakness with increased mobility and increasing the rate of pressure solution compaction (Bos and Spiers, 2000; Bos et al., 2000; Schleicher et al., 2013). In the laboratory, clay-rich fault gouges are consistently shown to be frictionally weak (Byerlee, 1978; Rutter and Maddock, 1987; Ikari et al., 2009a). In the field, the presence of clays has been inferred as a major reason for overall mechanical weakness of faults on scales over several orders of magnitude, from metre-scale faults (e.g. in the Soultz-sous-Forêts geothermal field – Bourois and Bernard, 2007), to kilometre-scale strike-slip faults (c) and subduction megathrusts (Saffer and Marone, 2003; Underwood, 2007; Den Hartog, 2013).

Clay contents in the fault core as low as 15-20% can significantly reduce fault strength (Shimamoto and Logan, 1981; Colletini et al., 2009). With depth, increasing pressures and temperatures in fault zones alters clay minerals in terms of dehydration, consolidation and mineralogy, thereby changing the fault's mechanical and seismic properties (Saffer and Marone, 2003; Sánchez-Roa et al., 2016; 2018). Dehydration in layered phyllosilicates is expected to occur with increased temperature and crustal depth (Bird, 1984). A decrease in water content may occur as a result of the loss of free and interstitial bound (interlayer) water (Morrow et al., 2000; Sánchez-Roa et al., 2018; Vidal and Dubacq, 2009). Dehydration may also occur by removal of water from hydroxyl (OH) groups within the crystal structure, thereby changing the hydration state, however this is not considered to be an important factor at the temperatures used for thermal dehydration in this study. Where the number of phyllosilicate-bound water layers is fixed, dehydration occurs by slight continuous loss of the interlayer water (associated with most volume decrease) after initial rapid removal of free water (<~0-120 °C). Larger, discontinuous losses of water layers and comparatively minor volume decreases also occur upon progressive collapse of the interlayer space (>~120 °C) (Bala et al., 2000; Vidal and Dubacq, 2009). Smectites (swelling clays) are increasingly recognised as 'problem minerals' in geothermal reservoirs due to their prevalence in fractures, with low permeability creating barriers to fluid flow (Vidal et al., 2018) and mineral transitions to illite at depth creating frictional instabilities (Brown et al., 2003; Ikari et al., 2009b). The presence, and more specifically dehydration, of smectites is considered to be an important factor in controlling the propagation of subduction zone earthquakes and the limits of seismicity (e.g. Faulkner et al., 2011; Morrow et al., 2000; Saffer and Marone, 2003; Takahashi et al., 2009), and has also been shown to contribute to land subsidence and sediment overpressuring (Bethke, 1986).

Many authors have attempted to explain the fact that phyllosilicates seemingly do not adhere to Byerlee's law of static friction coefficients (μ) (Byerlee, 1978), where $0.6 \leq \mu \leq 0.85$ (e.g. Ikari et al., 2007, 2009, Moore and Lockner, 2004, 2007; Morrow et al., 1992; Morrow et al., 2000, 2017; Saffer and Marone, 2003). The upper limit of μ in clays is often found in laboratory experiments to be much lower than expected (e.g. $0.03 < \mu < 0.50$ for montmorillonite, chlorite and illite (Ikari et al., 2009a)). Whilst a positive correlation of μ with effective normal stress, said to be characteristic of sheet-silicate gouges, has been described in montmorillonite (Moore and Lockner, 2007), μ has also been shown to decrease (and shear strength increase), with effective normal stress in smectite and illite (Saffer et al., 2001; Saffer and Marone, 2003; Ikari et al., 2007). Frictional weakening has often been attributed to lubrication of clay grains by thin films of adsorbed water (aqueous pore fluid), which may be expelled by increased effective normal stress (Israelachvili et al., 1988) thereby increasing μ (Moore and Lockner, 2007), or to sub-critical delamination of phyllosilicates (Den Hartog et al., 2020). Due to their low permeability, the effect of increasing pore fluid pressure may be magnified in clay-rich fault gouges, reducing effective stress and fault strength and promoting failure (Faulkner and Rutter, 2001; Frye and Marone, 2002; Noda and Shimamoto, 2005; Faulkner et al., 2018). Dry friction coefficients of clays measured in the laboratory are assumed to be the upper limit of strength at depth on a given fault, since increases in pressure are likely to remove water films from platy surfaces and increase shear strength (Israelachvili et al., 1988; Renard and Ortoleva, 1997).

Published data on individual clay frictional properties is variable; such variability may result from differences in room humidity and/or sample saturation state, which is usually not well-defined or controlled (Reinen et al., 1994; Frye and Marone, 2002; Moore and Lockner, 2004; Ikari et al., 2007, 2009a; Morrow et al., 2017; Tetsuka et al., 2018). No truly dry reference condition for phyllosilicates has yet been established, and many fall into the 'partially saturated' region of Figure 6 in Morrow et al. (2017), despite initially being referred to as 'dry'. Montmorillonite, for example, has yielded μ values between 0.06 and 0.78 in tests conducted under supposedly similar conditions in different laboratories, which has been attributed to different deformation processes occurring under different relative saturation states (Moore and Lockner, 2007; Morrow et al., 2017). The correlation between dry friction coefficient and interlayer (001) bonding energy (ILBE) (Giese, 1978, 1979; Moore and Lockner, 2004) is debated partly because of the disparity in test conditions used to obtain μ values, such as variations in the applied stress and non-comparable controls on the distribution of grain size and shape (Behnsen and Faulkner, 2012; Sakuma and Suehara, 2015).

The relationship between sliding friction, displacement and displacement rate can be described by constitutive relationships of rate- and state-dependent parameters (Dieterich, 1972, 1978, 1979; Ruina, 1983; Blanpied et al., 1998; Marone, 1998). Although modelling of these parameters has been successfully applied to many datasets in order to understand the stability of frictional sliding, the micro-scale physiochemical mechanisms responsible for behaviours

they describe are poorly understood. Upon a change in displacement rate, an initial direct effect occurs where μ is scaled by a constant 'a' (Figure 4.1). μ then exponentially evolves over a characteristic distance, ' d_c ', which is considered to relate to gouge layer thickness, normal stress, surface roughness and particle size (Biegel et al., 1989; Li et al., 2011; Linker and Dieterich, 1992; Marone, 1998; Marone and Kilgore, 1993). Effective contact time evolves during shear, and is derived from the ratio of d_c to the slip velocity (Dieterich, 1979; Mair and Marone, 1999). The magnitude of the change is scaled by a constant 'b'; this 'state' effect is a proxy for the quality and/or area of asperities in contact across the sliding interface. These variables are related by two coupled equations – the friction law, and either the Aging (time-dependent) Law (Dieterich, 1978) or the Slip Law (Ruina, 1983). The friction coefficient is a function of the current sliding velocity (rate), and the state variable can be thought of as a memory of past sliding (Ruina, 1983). State evolution in terms of time or slip remains a matter of debate (Bhattacharya et al., 2017). The Slip Law implies that any frictional change requires slip, whereas Dieterich's law implies that state and friction evolve purely as a function of time if frictional surfaces are in contact, even with zero velocity. Once sliding is initiated, frictional resistance transiently adjusts to a new steady state. Since deformation mechanisms may differ between dry and saturated sheet silicate gouges, the velocity dependence of dry and saturated shear strengths may also differ (Moore and Lockner, 2004).

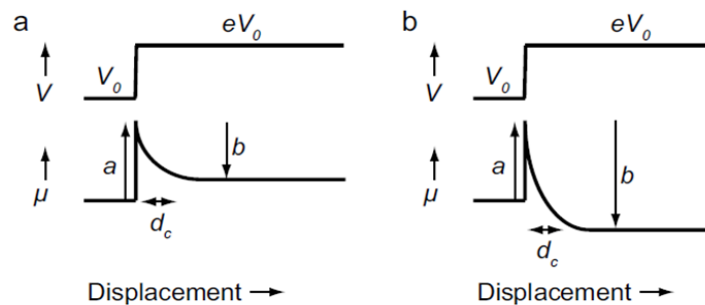


Figure 4.1: Schematic frictional response to steps in sliding velocity for a) velocity- strengthening friction and b) velocity-weakening friction (after Den Hartog, 2013). Samples tested here show velocity-strengthening behaviour and would not result in seismicity.

Rate dependence can be important in determining whether deformation is stable or unstable (Lockner et al., 2011). At low effective pressures (12-60 MPa) and displacement rates between $0.5\text{-}300\ \mu\text{m s}^{-1}$, clay-rich gouges typically display stable fault creep and velocity-strengthening behaviour, such that $(a-b) > 0$ (Figure 4.1) (Logan and Rauenzahn, 1987; Morrow et al., 1992; Scholz, 1998; Ikari et al., 2007, 2009a, 2011). The constants a and b (Figure 4.1) are ≈ 0.01 (Bhattacharya et al., 2017), but may vary by an order of magnitude with changing temperature and humidity (Blanpied et al., 1998). For example, alumina gouge has been shown to transition from velocity-strengthening to velocity-weakening behaviour at $\sim 55\text{-}60\%$ room humidity (Frye and Marone, 2002). Whilst smectites are usually velocity-strengthening (e.g. Ikari et al., 2009a), slight velocity-weakening behaviour has been observed under specific conditions, such as at low normal stresses and higher displacement rates (Saffer and Marone, 2003).

In response to the uncertainty in the role of water in determining frictional properties highlighted by previous studies, this study explores how friction coefficient and the constitutive parameters of frictional stability, a , b and d_c (*Figure 4.1*) behave in relation to the amount of free and hydrogen-bound water in kaolinite and Mg-montmorillonite samples in carefully controlled laboratory experiments. It is hoped that this work will help to understand the effect of different saturation states on micromechanical processes that are responsible for phyllosilicate friction, as well as how laboratory studies can effectively investigate this.

4.2 Methodology

A total of 18 triaxial direct shear experiments were performed to determine the frictional strength and constitutive parameters on 2 clays under different saturation states. 6 experiments were carried out on kaolinite-rich china clay, each with a repeat run, and 6 on Mg-montmorillonite. Repeat runs were not performed on montmorillonite due to a limited amount of material. Each experiment included three velocity steps. Tests were run under the following experimental conditions for each gouge sample, at a confining pressure (P_c) of 60 MPa unless otherwise indicated. Where heat was applied, 130 °C was chosen as a temperature that was high enough to remove free and interstitial bound water from the clays, but lower than that required to promote structural changes (e.g. OH structural water layers strongly coordinated to the interlayer cations; dehydroxylation) (Takahashi et al., 2009; Bala et al., 2000).

1. “Saturated”: Samples were prepared at room humidity (50-60 %), and sheared with 80 MPa P_c and 20 MPa deionised water fluid pressure (P_f) applied;
2. “Room Dry”: Samples were prepared at room humidity (50-60 %), transferred to the pressure vessel, and sheared at room humidity after ensuring the sample assembly and pore fluid pipework was thoroughly dry;
3. “Room Dry + Vacuum”: Samples were prepared at room humidity (50-60 %), transferred to the pressure vessel, and sheared with a vacuum applied to the pore-fluid inputs of the thoroughly dry sample assembly to prevent humidity changes during the experiment;
4. “Oven Dry”: Samples were prepared at room humidity (50-60 %) before being dried in a vacuum oven at 130 °C for 20 hours and cooled to room temperature under vacuum. Samples were transferred to the pressure vessel and sheared at room humidity after ensuring the sample assembly and pore fluid pipework was thoroughly dry;
5. “Oven Dry + Vacuum”: Samples were prepared at room humidity (50-60 %) before being dried in a vacuum oven at 130 °C for 20 hours and cooled to room temperature under vacuum. Samples were transferred to the pressure vessel and sheared with a vacuum applied to the pore-fluid inputs of the thoroughly dry sample assembly to prevent humidity changes during the experiment;

6. "Heat + Vacuum in Vessel": Samples were prepared at room humidity (50-60 %) and transferred to the pressure vessel, where they were heated under vacuum in the thoroughly dry sample assembly to 130 °C for ~20 hours and allowed to cool to room temperature whilst still under vacuum. Samples were then sheared under vacuum.

4.2.1 *Phyllosilicate Gouge Sample Properties*

Gouges explored in this study are kaolinite-rich gouge and Mg-montmorillonite gouge. These clays were chosen specifically to investigate the effect of dehydration on frictional properties in swelling versus non-swelling clays. The kaolinite-rich china clay sample had a grain-size fraction of <2µm and comprised 75% kaolinite, 14% illite/muscovite, 8% K-feldspar and 3% quartz (analysed by X-ray diffraction - XRD). The Mg-montmorillonite sample used was the same as described in Behnsen and Faulkner (2013), derived from Wyoming bentonite (obtained from RS Minerals). This sample, shown by XRD to contain >98% montmorillonite, was separated by centrifugation and also contained only the <2 µm grain-size fraction. The principal cation was exchanged for Mg using the methodology described in Behnsen and Faulkner (2013). The amount of water adsorbed onto clay surfaces strongly correlates with the mineral's specific surface area (SSA) (Diamond and Kinter, 1958; Moore and Lockner, 2007). Montmorillonite has a SSA of ~600-800 m²/g for the grain size fraction used in this study (<2 µm), mostly located within its interlayer surfaces, which enables it to hold more water than kaolinite and illite, with SSAs of ~7-30 m²/g and 67-100 m²/g respectively (Diamond and Kinter, 1958).

Phyllosilicates are characterised by stacked platy crystals of one or more silicate tetrahedral (T) layers and a hydroxyl (OH) and Al-/Mg-based octahedral (O) layer (Behnsen and Faulkner, 2012; Lázaro, 2015) (*Figure 4.2*). Both kaolinite and montmorillonite are common low temperature alteration minerals, usually formed by low temperature hydrothermal breakdown of feldspar and volcanic glass respectively (Lázaro, 2015; Inoue and Utada, 1988). Kaolinite (Al₂Si₂O₅(OH)₄) is a dioctahedral 1:1 sheet silicate, where T-O sheets are bonded to the adjacent sheet via long hydrogen-oxygen bonds. Sheets have a basal spacing of 0.7 nm, are charge-balanced, and the bonds that hold successive layers together are relatively weak (Lázaro, 2015). Free water molecules may be bonded to the external layers of kaolinite T-O sheets. Montmorillonite (Ca_{0.16}(Mg_{2.67}Al_{0.33})(Si_{3.34}Al_{0.66})O₁₀(OH)₂·nH₂O) (Moore and Reynolds, 1997) is a dioctahedral smectite variety of a 2:1 sheet silicate, where each layer comprises an octahedral sheet between two tetrahedral sheets (T-O-T). Chemical substitutions in the sheets, which have a basal spacing of ~1 to ~1.5 nm, result in a residual layer charge, and sheets are separated by cations (in this case Mg) for charge balance (Karnland et al., 2016; Lázaro, 2015). In naturally occurring montmorillonite, cations may be a mix of Na⁺, Ca²⁺, K⁺ and Mg²⁺. Unlike kaolinite, montmorillonite is a swelling clay in which dipolar water may be bonded to both external crystal surfaces *and* the interlayer cations. Depending on the cation type, which have different bonding energies, significant quantities of water (with a thickness of up to 4 nm) may be bound by the interlayer cation (Behnsen and Faulkner, 2013; Karnland et al., 2016; Moore and Lockner, 2007;

Morrow et al., 2017; Vidal and Dubacq, 2009). Cation substitution and associated water uptake/removal occurs relatively easily with changes in temperature, pressure and fluid chemistry (Schleicher et al., 2013). Mg-Montmorillonite is chemically and structurally similar to the Mg-rich trioctahedral smectite saponite (Inoue and Utada, 1988; Karnland et al., 2016), which has been inferred to be the principal cause of frictionally weak sections of the San Andreas Fault Zone from the SAFOD core (Carpenter et al., 2012; Holdsworth et al., 2011; Lockner et al., 2011).

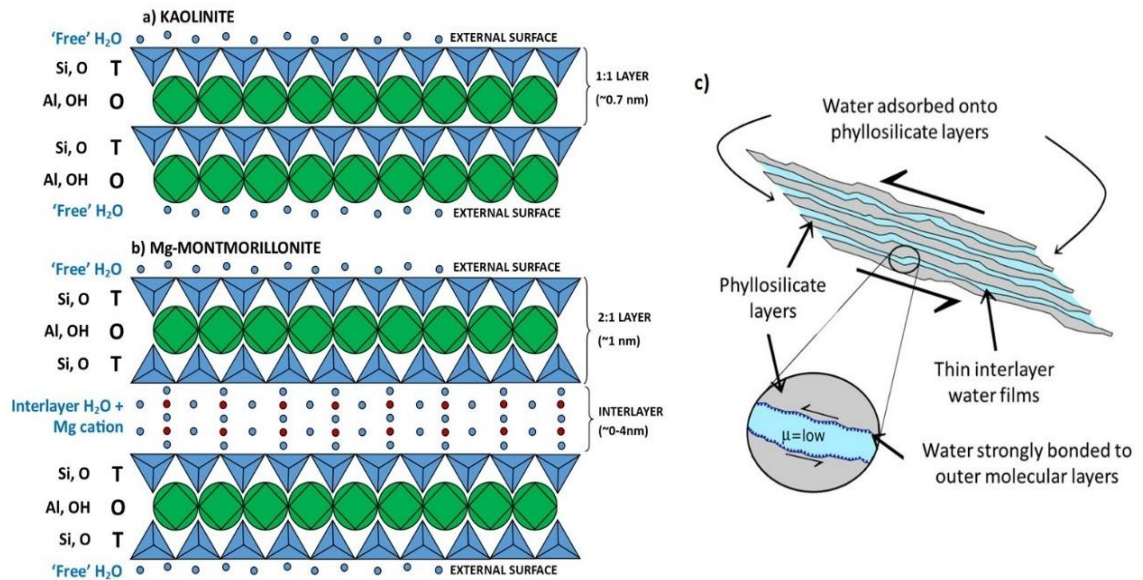


Figure 4.2: Crystal structures of a) 1:1 Kaolinite and b) 2:1 Mg-Montmorillonite. The latter can absorb more water due to the presence of interlayer surfaces, where water molecules are bonded to the interlayer cation (Mg). c) Interlayer water films affect the frictional properties of sheet materials by forming a low μ shear interstitial surface bound to T-O-T layers (T = tetrahedral, O = octahedral), or as free water to external surfaces.

4.2.2 Sample Preparation

For both clay types, 1.2 g of powdered clay gouge (size fraction $<2 \mu\text{m}$) was placed into a stainless-steel direct shear assembly (Figure 4.3a), with a contact surface area of 720 mm^2 . To prevent sample loss during preparation, this was pre-compacted with a hand lever press into a uniformly $\sim 1 \text{ mm}$ thick wafer with a 5 MPa normal stress. Saturated, room humidity and room humidity vacuum experiments were prepared in a laboratory relative humidity of $\sim 55\text{-}60 \%$.

For experiments run with oven dry samples, compacted gouge was placed together with the slider assembly (without the PVC jacket) into a vacuum oven at $\sim 130 \text{ }^\circ\text{C}$ for ~ 20 hours. The combination of time and temperature was considered to be sufficient to remove any adsorbed water from the clays based on data published in Mackenzie, (1957), Carpenter et al. (2016), Ikari et al. (2007) and Morrow et al. (2017), and was also supported in this study with thermogravimetric analysis (Section 4.2.3.1). Prior to testing, samples were allowed to cool to room temperature whilst still under vacuum.

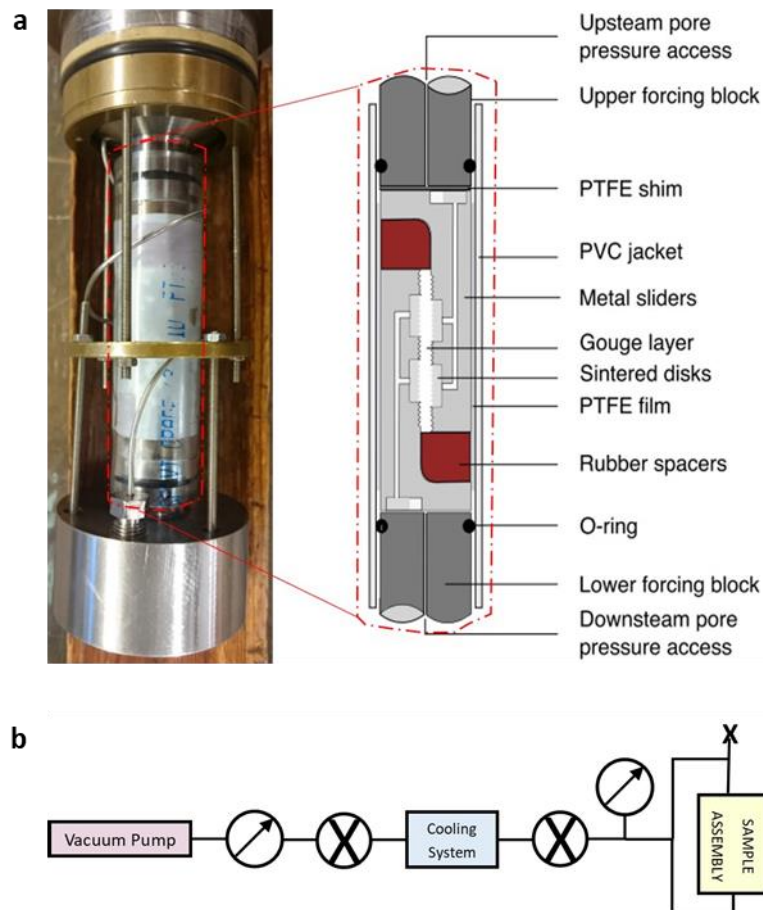


Figure 4.3: a) Sample assembly setup prior to being placed into the pressure vessel, with schematic illustration of the configuration used (total length of schematic view ~ 75 mm). The configuration is jacketed, and silicon oil is used as the confining medium. In non-saturated experiments, a vacuum is applied to the sample through pore pressure access points (after Faulkner et al., 2018). b) Schematic representation of a vacuum connection to the sample assembly. Gauges are indicated by diagonal arrows; valves are indicated by crosses.

After heating (if applicable), metal sliders were wrapped in PTFE film (in order to reduce friction between sliders and jacket). The slider assembly was inserted into a PVC jacket in all experiments besides those heated within the vessel (see later), in which case a more heat-resistant viton (fluoroelastomer) tubing was used. PVC jackets have been shown to be sufficiently weak so as not to contribute significant error to clay friction measurements (Behnsen and Faulkner, 2012); differences between PVC and viton tubing was not tested in this study but are assumed to be comparable. The setup above was then immediately inserted into a sample assembly as shown in *Figure 4.3a* (and described in Faulkner et al., 2018), and placed into a triaxial deformation apparatus. Total preparation time, which could be crucial in oven dried samples as they may be rapidly contaminated with room humidity, was never longer than ~ 10 -15 minutes.

4.2.3 Experimental Procedure

4.2.3.1 Analysis of absolute water content

In order to measure relative water loss between room dry samples (experiment type 2) and those that were heated (experiment types 4-6), two methods were employed: 1. Direct mass difference before and after heating to 130 °C; 2: Thermogravimetric Analysis (TGA). Relative room humidity was on average ~50-60 %.

In direct mass difference measurements, the 1.2 g gouge sample and the 65.0 g metal sliders were weighed separately immediately before and after heating in a vacuum oven at 130 °C. Relative mass loss was recorded as a percentage of total mass difference, separately and combined for the sample and metal sliders. The difference between the two sample measurements is regarded as the water loss from the sample in wt% between conditions in experiment type 2 (“room dry”) and experiment type 4 (“oven dry”). The gouge sample and metal sliders were also weighed after being removed from the vacuum oven. This was done immediately, and at intervals of 5, 10, 15 and 30 minutes in order to observe the effect of time spent at room humidity on water reabsorption in the sample. The difference between values obtained ‘immediately’ and after 15 minutes was interpreted to reflect water loss between experiment type 2 (“room dry”) and experiment type 5 (“oven dry + vacuum”), representing the typical time taken to transfer the sample from the oven to the assembly and pressure vessel before applying a vacuum.

TGA analyses were carried out using a Netzsch Simultaneous Thermogravimetric Analysis (STA) 449 F1 Jupiter analyser using a sapphire (Al_2O_3) disk as a reference standard. TGA measures the change in sample mass during heating under vacuum, which is interpreted to indicate volatile release. The difference between the initial mass and final mass is regarded as the water loss from the sample in wt% between conditions in experiment type 2 (“room dry”) and experiment type 6 (“heat + vacuum in vessel”), since in the latter experiment the sample was not exposed to room humidity conditions at any point during preparation or testing.

4.2.3.2 Friction Tests

Experimental conditions were chosen to represent various methods for removing water films from clay grain surfaces. All tests were performed in a triaxial deformation apparatus in the University of Liverpool’s Rock Deformation Laboratory (as in Faulkner and Armitage (2013) and *Appendix B: Section B3*). All mechanical loading was carried out at room temperature (~22 °C) and at 60 MPa effective pressure (P_{eff}) (where $P_{\text{eff}} = P_c - P_f$). For saturated experiments, confining pressure was carefully applied at a rate of ~0.1 MPas⁻¹. ensuring that the sample was thoroughly saturated before compacting, yet without inducing overpressure and fluidising the gouge.

The pore fluid used was deionised water, which was introduced to the upstream and downstream ends of the metal sliders (*Figure 4.3a*). Pore pressure was introduced at a rate of ~0.05 MPas⁻¹ and a fluid diffusion model (based on Faulkner et al. (2017)) was used to calculate

pore fluid pressure equilibration times. For kaolinite, at minimal confining pressures, assuming a sample thickness of 1mm, an initial permeability of $\sim 10^{-19} \text{m}^2$ (as measured in this study using the pulse-transient method (*Appendix B: Table B4.2 and Figure B4.1a*), porosity of 20% (an approximate porosity of 100% clay that has experienced a small amount of confining pressure or shear strain estimated from Crawford et al. (2008) and Faulkner and Rutter (2000)), deionised water viscosity of $2.5 \times 10^{-5} \text{Pa}\cdot\text{s}$ (Likhachev, 2003) and compressibility of $4.5 \times 10^{-4} \text{MPa}^{-1}$ (Kell, 1975), an equilibration time of ~ 0.5 to 1 hours was deemed sufficient. For Mg-montmorillonite, this was increased to >20 hours due to lower permeabilities ($\sim 10^{-20} \text{m}^2$ (to 10^{-22}m^2) (Behnsen and Faulkner, 2013; C. A. Morrow et al., 2017; this study (*Appendix B: Table B4.2, Figure B4.2b*)), particularly once water promotes clay swelling (Aksu et al., 2015). This step was deemed important, since if pore-fluid pressure is not given sufficient time to equilibrate (drain), gouge can appear falsely stronger, particularly in the early stages of an experiment, and velocity-strengthening behaviour can appear velocity-weakening (Moore and Lockner, 2011; Faulkner et al., 2018). Fluid was allowed to infiltrate the sample via three porous sintered disks normal to the sample on each side, resulting in an even distribution of fluid pressure across the gouge wafer. A steady fluid pressure and pore fluid volume before and during experiments was taken as an indicator that the sample was fully saturated and adequately drained.

The surfaces of the stainless-steel sliders are grooved in order to prevent shear localisation at the slider-sample interface. Initial contact area between the slider surface and the sample was 720mm^2 . Samples were sheared to 6.25mm displacement by applying a constant axial piston driving rate, resulting in a final contact area of $\sim 845 \text{mm}^2$. An area correction was not applied to the data throughout the experiment (which would result in final μ being ~ 8 -10 % lower than reported here), since areas overlapping non-grooved areas of the metal sliders, filled by very low strength silicon rubber spacers (Sanchez-Roa et al., 2017), do not significantly contribute to frictional strength. Displacement rates were varied so as to investigate rate and state friction properties, with a run-in at $0.3 \mu\text{ms}^{-1}$ for 2.5 mm to allow the development of a steady state shear strength (Faulkner et al., 2018), followed by three velocity steps to $3 \mu\text{ms}^{-1}$ and back down again every 0.5 mm.

4.2.3.3 Vacuum Setup and Use

Care was taken to ensure that the vacuum applied to the sample assembly was present and quantified at all times during experiments. In order to do this, the pore fluid system was configured as in *Figure 4.3b*. The vacuum level was initially tested with minimal capillary tubing and connections, and without connecting it to the sample assembly, in order to test the best achievable vacuum level. Further tests were then carried out with the sample assembly connected using a blank sample. A comparable vacuum level was achieved in each of these tests, indicating the system is capable of being sufficiently sealed. 0.04 ± 0.1 mbar was the best vacuum level achieved, varying to 0.13 ± 0.1 mbar in some tests.

A suitable level of vacuum was achieved within a few minutes with a blank sample in place. With clay gouge samples, however, the time taken to achieve a vacuum is affected by the porosity and permeability of the sample and metal sliders, the thickness of the gouge sample, mean free path of air molecules, air viscosity at room temperature, and air compressibility. The time required for equilibration of a vacuum in clay samples was estimated using the same model as described in *Section 4.2.3.2*. Parameters used were the same as those used to estimate water saturation time, except substituting air viscosity for water viscosity ($1.98 \times 10^{-5} \text{ Pa}\cdot\text{s}$) and air compressibility for water compressibility (10 MPa^{-1}). Fluid diffusion modelling outputs indicate that for kaolinite, an equilibration time of ~ 40 minutes is sufficient to achieve a vacuum throughout the sample (*Figure 4.4*). For montmorillonite, which has a lower starting porosity and permeability (Behnsen and Faulkner, 2013), an equilibration time of ~ 4 hours is more applicable. Samples were left under vacuum overnight prior to each vacuum test (~ 15 hours).

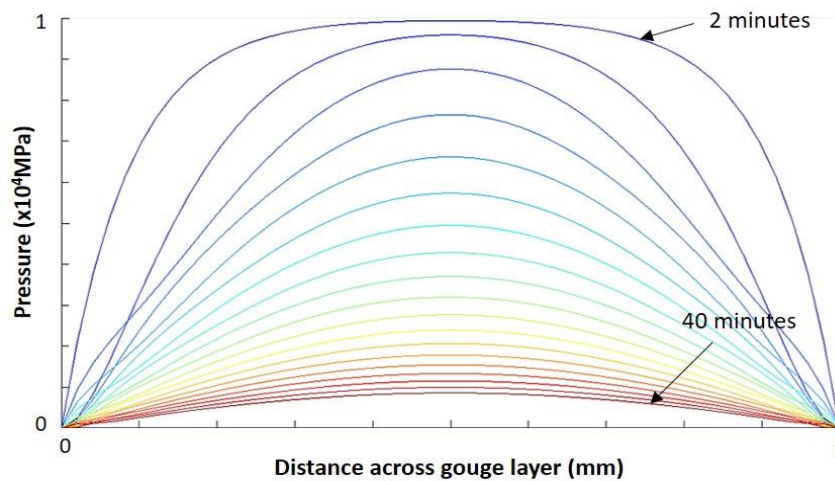


Figure 4.4: Modelled simulation of the time taken to equilibrate a vacuum across a ~ 1 mm thick kaolinite-rich gouge sample. Each time step represents ~ 2 minutes. See text for parameters used.

4.2.3.4 Scanning Electron Microscopy

A range of sheared samples were selected for microstructural analysis under the scanning electron microscope (SEM), aimed at representing a transition from the wettest to driest sheared gouge. Microstructures are assumed to represent deformation processes occurring in the final velocity step. Gouge wafers were carefully removed from the slider setup, air-dried at ~ 25 °C, and impregnated with epoxy resin under a vacuum. It was noted that, in particular in dry montmorillonite samples, the wafers quickly began to fall apart once exposed to room humidity, which rendered some unsuitable for SEM analysis. Difficulties in preparing montmorillonite in epoxy also arose from the extremely low permeability of the samples. Due to a combination of these factors, only kaolinite microstructures are considered in this study.

Once dry, blocks were cut perpendicular to the sliding surface and parallel to the shear direction, turned 90 degrees and re-impregnated with the same epoxy resin. Sample blocks were then polished using aluminium oxide powder (to $0.03 \mu\text{m}$ grain size) and carbon coated. The internal microstructure of each gouge wafer was analysed on a Philips SEM.

4.2.4 Data Analysis

4.2.4.1 Friction Coefficient

The coefficient of sliding friction (μ) was calculated for each datapoint (recorded at 2 Hz) from the measured shear stress and normal stress by applying Equation 4.1:

$$\mu = \tau / \sigma'_n \quad (\text{Eq. 4.1})$$

(Byerlee, 1978), where τ is shear stress and σ'_n is the effective normal stress (in this case confining pressure minus pore pressure).

There is no convention for defining when during an experiment friction coefficient should be defined, partly due to the fact that different samples reach a steady-state microstructure before others (which is difficult to determine). This has resulted in some confusion within the literature as to how comparable studies between different authors and laboratories may be. In this study, steady state μ is taken as the value reached after ~ 2.5 mm of displacement, immediately prior to the first displacement velocity jump. In all experiments, μ at this point has minimal variation and approximately represents the mean value after the yield point. μ at yield point (μ_y) is defined as the intersection between two lines of best fit drawn 1. through the loading stage, and 2. through the steady state sliding stage following yield (Figure 4.5).

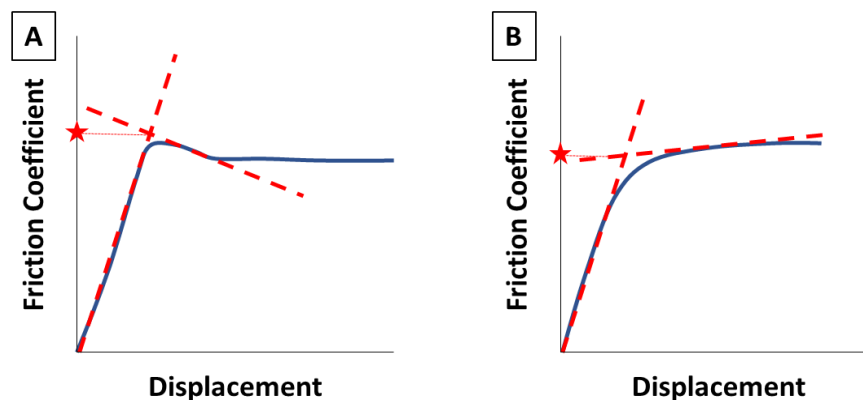


Figure 4.5: Method used to determine yield friction coefficient (μ_y) in a) a typical example of a saturated sample, and b) a typical example of a dry sample. μ_y is indicated by a red star, equal to the intersection of two best fit lines (red) drawn through the friction coefficient – displacement curve (blue) immediately either side of the 'shoulder' (deviation from linearity).

4.2.4.2 Rate and State Friction Modelling

The frictional stability was calculated using the friction state parameter $a-b$, as derived by Dieterich (1978, 1981) from the constitutive law describing rate- and state-dependent friction. This relationship is schematically illustrated in Figure 4.1 for a) velocity-strengthening and b) velocity-weakening behaviour, where $a-b$ values are positive and negative respectively.

Rate and state parameters were determined from velocity up-steps using a non-linear least-squares fitting routine with the machine stiffness treated as a fitting parameter (Noda and

Shimamoto, 2009). d_c may either be a product of time or slip distance (Dieterich, 1979; Ruina, 1983). The constitutive law used for modelling was the Aging Law (Dieterich, 1978; Marone, 1998; Bhattacharya et al., 2017), for which standard deviations are up to 8 times smaller than the Slip Law. Data were fit by a single set of state variables (a , b , d_c) with a linear detrend.

4.3 Results

4.3.1 Analysis of Absolute Water Content

Mass loss during thermal sample preparation was measured using an electronic balance immediately before and after being vacuum oven dried at 130 °C for 20 hours. This is interpreted to represent water loss between conditions in experiment type 2 (“room humidity”) and experiment type 4 (“oven dry”). From three samples, this method yielded average mass losses during heating of 0.53 wt% (absolute loss 0.006 g) in kaolinite and 7.95 wt% (absolute loss 0.060 g) in Mg-montmorillonite (*Figure 4.4*), implying negligible and considerable water loss respectively. Metal sliders dried from room humidity also showed evidence of considerable water loss, decreasing in mass during heating by 0.26 ± 0.09 g (0.40 ± 0.14 wt%). After 5 minutes, regained mass due to water reabsorption reduced the relative mass loss in kaolinite to, on average, 0.16 wt% and 5.15 wt% in Mg-montmorillonite (*Figure 4.6*). After 10, 15 and 30 minutes, relative mass loss values in kaolinite remained fairly consistent at 0.26, 0.26 and 0.10 wt% respectively; in Mg-montmorillonite, relative mass loss values decreased to 4.96, 4.49 and 2.23 wt% respectively. Mass loss after ~15 minutes is interpreted to represent water loss between conditions in experiment type 2 (“room humidity”) and experiment type 5 (“oven dry + vacuum”).

Relative water loss in kaolinite from room humidity samples heated to and held at 130 °C, as measured via STA, was ~0.3 % for kaolinite and ~4.5 % for Mg-montmorillonite (*Figure 4.6*). This is interpreted to represent water loss between conditions in experiment type 2 (“room humidity”) and experiment type 6 (“heat + vacuum in vessel”). In both sample types, most mass loss occurred during the first hour of heating (50-130 °C). Mg-montmorillonite continued to lose some mass during the 6-hour 130 °C hold period, whereas kaolinite did not. An increase in temperature to 200 °C at the end of the test produced a further ~0.4 % mass loss in Mg-montmorillonite but had no effect in kaolinite.

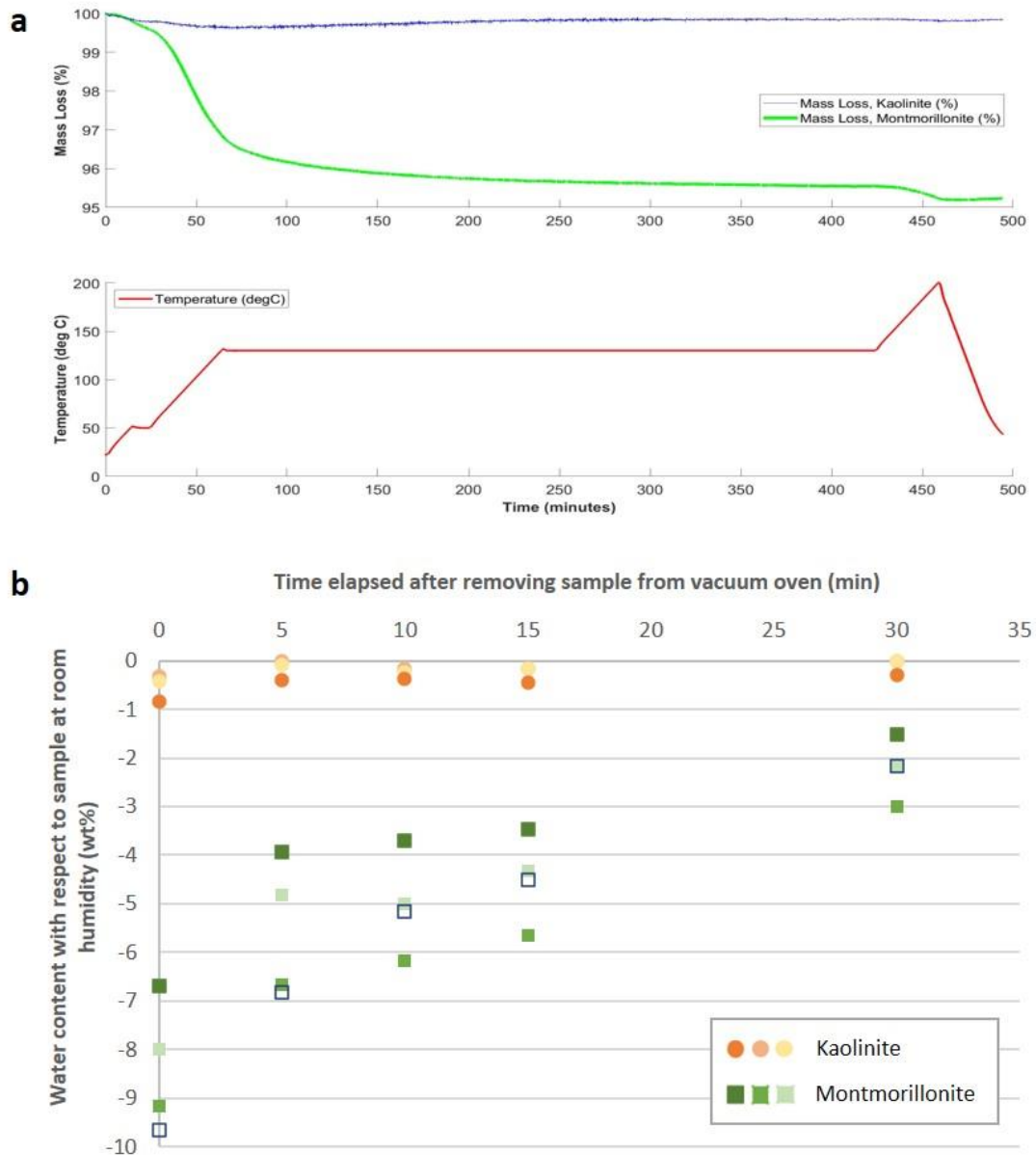


Figure 4.6: a) Results of Thermogravimetric Analysis (TGA) performed on initially room humidity kaolinite and montmorillonite. Samples were heated to 130 °C at 2 °Cmin⁻¹ and held for 6 hours, before being heated further to 200 °C to investigate mass loss beyond temperatures used in sample preparation. b) Results of mass loss during heating to 130 °C in a vacuum oven with respect to the mass of initially room humidity kaolinite and montmorillonite.

4.3.2 Friction Coefficient

Friction coefficient data is summarised in Table 4.1 and Figure 4.7 and Figure 4.8. When fully saturated, kaolinite gouge (Figure 4.7a) has an initial yield strength peak of 0.27 and reaches a slightly lower steady state at 0.25. Values for ‘dry’ kaolinite vary considerably, with yield strengths ranging from 0.28 to 0.4, and steady state values ranging from 0.29 to 0.49, resulting in an overall rounder yield curve than that of saturated samples.

Fully saturated Mg-montmorillonite gouge (*Figure 4.5b*) is weaker, with a peak yield strength of 0.16 and a lower steady state of 0.12. ‘Dry’ values vary to a much greater extent than those of kaolinite, with yield strengths ranging from 0.17 to 0.58, and steady state values ranging from 0.19 to 0.57. Samples that have been subject to thermal drying during preparation, however, consistently display μ values of ~ 0.57 . Plot shapes for ‘dry’ Mg-montmorillonite are also rounder at yield point, but not to the same extent as those for kaolinite.

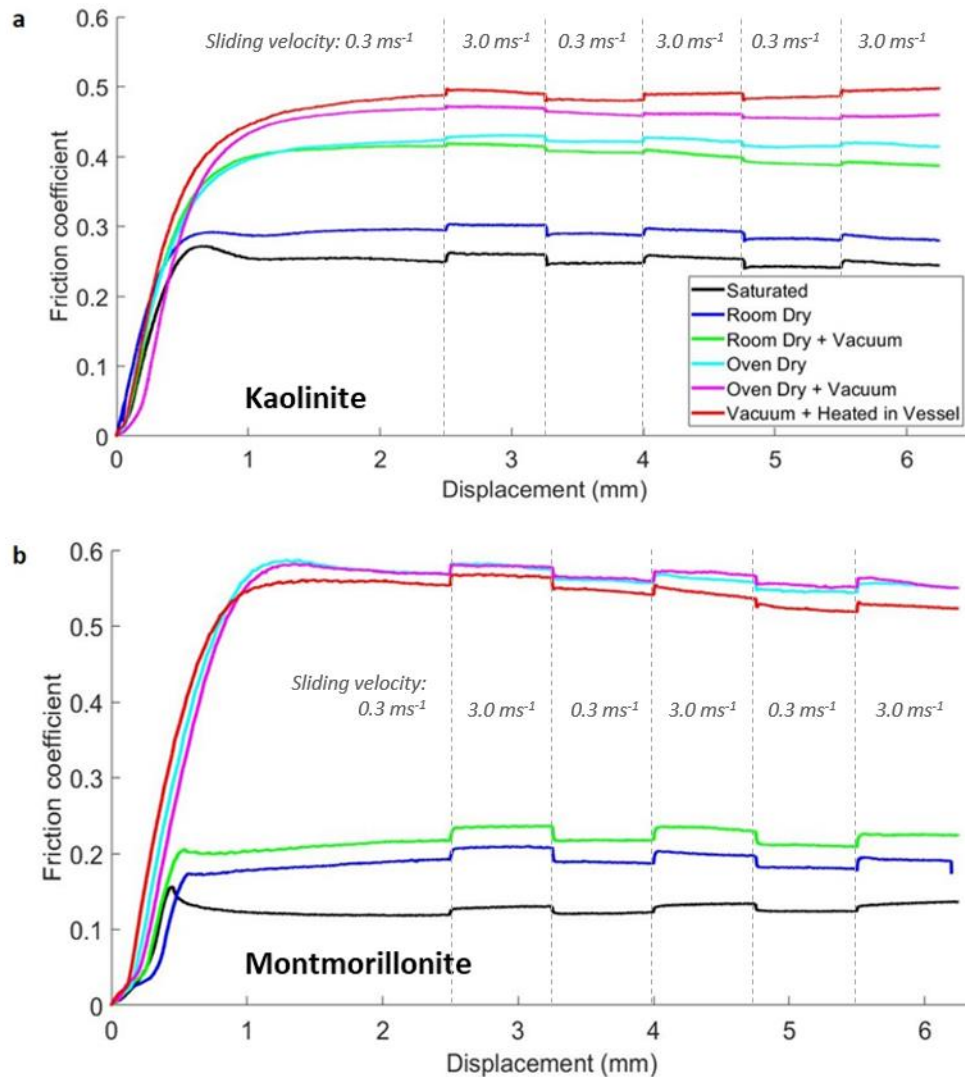


Figure 4.7: Friction coefficient evolution with displacement for a) kaolinite-rich china clay and b) Mg-montmorillonite at different saturation states. Initial displacement rate was 0.3 microns per second. Velocity steps at 2.5 mm, 4 mm and 4.75 mm displacement represent an increase in displacement rate (sliding velocity) to 3 microns per second for 0.75 mm, before resuming to 0.3 microns per second. Effective pressure in each scenario was 60 MPa.

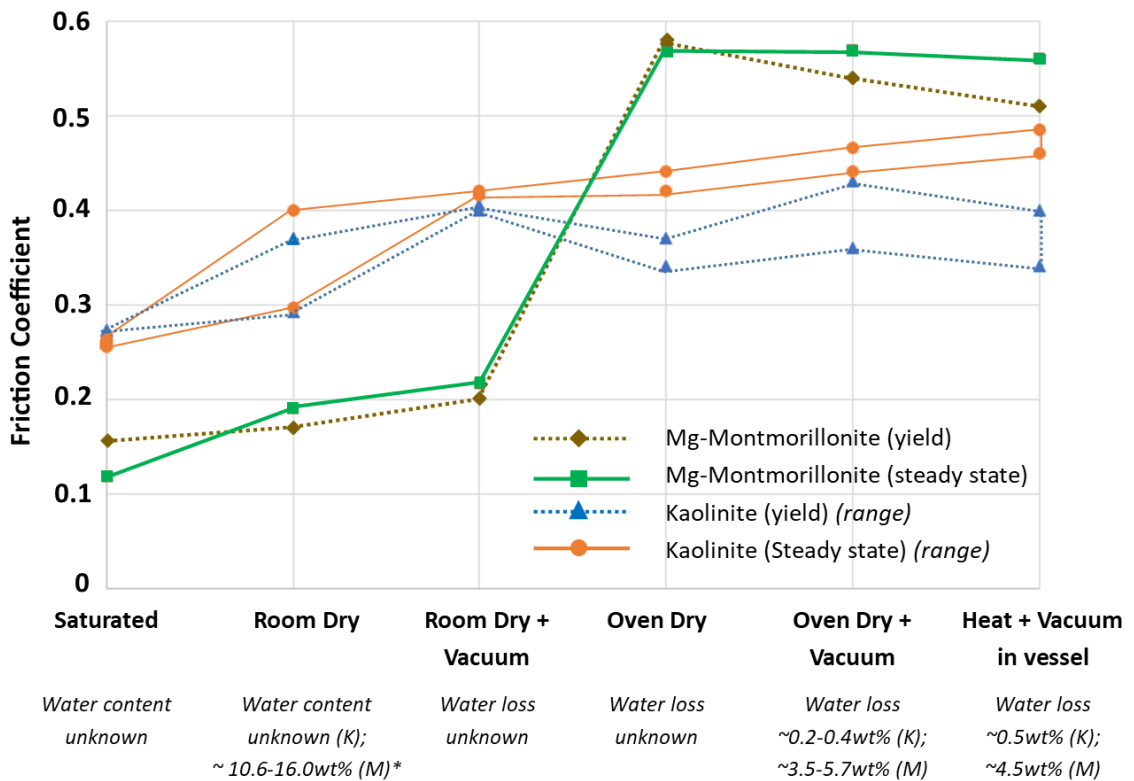


Figure 4.8: Summary of yield (dotted lines) and steady state (solid lines) friction coefficients for kaolinite-rich china clay (blue triangles and orange circles respectively) and Mg-montmorillonite (brown diamonds and green squares respectively), for each saturation state scenario. Ranges of minimum and maximum recorded data are shown for kaolinite.

Repeatability of the experimental dataset is illustrated by the range of kaolinite data in Table 4.1 and Figure 4.8. For all experiments except those at room humidity, repeatability for kaolinite was excellent for both yield and steady state μ , with a maximum variation of ~ 0.025 during an identical experiment. For experiments at room humidity, data were much more variable, with μ for kaolinite ranging between ~ 0.3 and ~ 0.4 . This variation is likely due to differences in absolute water content within the sample caused by minor fluctuations in room humidity. μ for saturated Mg-montmorillonite in this study (0.12) is comparable to that measured on the same sample in Behnsen and Faulkner (2013) (0.11), hence despite tests not being repeated, results for montmorillonite are not expected to vary greatly.

The difference between yield strength and steady state friction coefficient is also highlighted in Figure 4.8. With increasing confidence of 'dryness', yield strength becomes progressively lower than steady state strength. For example, in room humidity kaolinite, yield strength is 0.01 to 0.03 lower than steady state friction coefficient, whereas in the sample tested under vacuum after being heated in the vessel, yield strength is 0.09 to 0.13 lower than steady state. In fully saturated samples, yield strength is consistently slightly higher than steady state friction coefficient. Steady state conditions are reached in most samples after ~ 1.5 -2 mm of displacement, prior to the 2.5 mm point used to obtain this reading.

Table 4.1: Yield and steady state friction coefficient (μ) data for experiments on kaolinite-rich china clay and Mg-montmorillonite.

Sample ID	Sample Type	Experiment Type	μ (yield)	μ (SS)	Shear Stress (yield) (MPa)	Shear Stress (SS) (MPa)
KLSAT01	Kaolinite-rich china clay	Saturated	0.273	0.262	16.38	15.72
KLSAT02	Kaolinite-rich china clay	Saturated	0.272	0.255	16.32	15.3
KLSAT03	Kaolinite-rich china clay	Saturated	0.265	0.26	15.9	15.6
KLRH01	Kaolinite-rich china clay	Room Humidity	0.292	0.296	17.52	17.76
KLRH02	Kaolinite-rich china clay	Room Humidity	0.37	0.4	22.2	24
KLVD01	Kaolinite-rich china clay	Vacuum Dry	0.405	0.42	24.3	25.2
KLVD02	Kaolinite-rich china clay	Vacuum Dry	0.4	0.415	24	24.9
KLODX01	Kaolinite-rich china clay	Oven Dry, no vacuum	0.34	0.42	20.4	25.2
KLODX02	Kaolinite-rich china clay	Oven Dry, no vacuum	0.37	0.44	22.2	26.4
KLODV01	Kaolinite-rich china clay	Oven Dry + Vacuum	0.43	0.465	25.8	27.9
KLODV02	Kaolinite-rich china clay	Oven Dry + Vacuum	0.36	0.44	21.6	26.4
KLVH01	Kaolinite-rich china clay	Vacuum + Heated in Vessel	0.4	0.485	24	29.1
KLVH02	Kaolinite-rich china clay	Vacuum + Heated in Vessel	0.34	0.46	20.4	27.6
MMSAT01	Mg-Montmorillonite	Saturated	0.156	0.118	9.36	7.08
MMRH01	Mg-Montmorillonite	Room Humidity	0.17	0.19	10.2	11.4
MMVD01	Mg-Montmorillonite	Vacuum Dry	0.2	0.217	12	13.02
MMODX01	Mg-Montmorillonite	Oven Dry, No Vacuum	0.58	0.57	34.8	34.2
MMODV01	Mg-Montmorillonite	Oven Dry + Vacuum	0.54	0.57	32.4	34.2
MMVH01	Mg-Montmorillonite	Vacuum + Heated in Vessel	0.51	0.56	30.6	33.6

4.3.3 Rate and State Parameters

Rate and state friction data are summarised in *Appendix B (Table B4.1)* and *Figure 4.9*. Data from some experiments are not included in this analysis due to significant error in the modelling process, where standard deviation was greater than the total range of values across the dataset and hence deemed unreliable. Both kaolinite and Mg-montmorillonite display velocity-strengthening behaviour ($a-b$ is positive) for all experiments (*Figure 4.7a*). For kaolinite, $a-b$ values range from ~ 0.001 to ~ 0.006 . The smallest $a-b$ values for kaolinite are exhibited in all ‘dry’ samples, with considerable variation between different modelled velocity steps. For Mg-montmorillonite, $a-b$ values range from ~ 0.003 to ~ 0.008 . Again, the smallest $a-b$ values for Mg-montmorillonite were exhibited in ‘dry’ samples, particularly in those that were thermally treated.

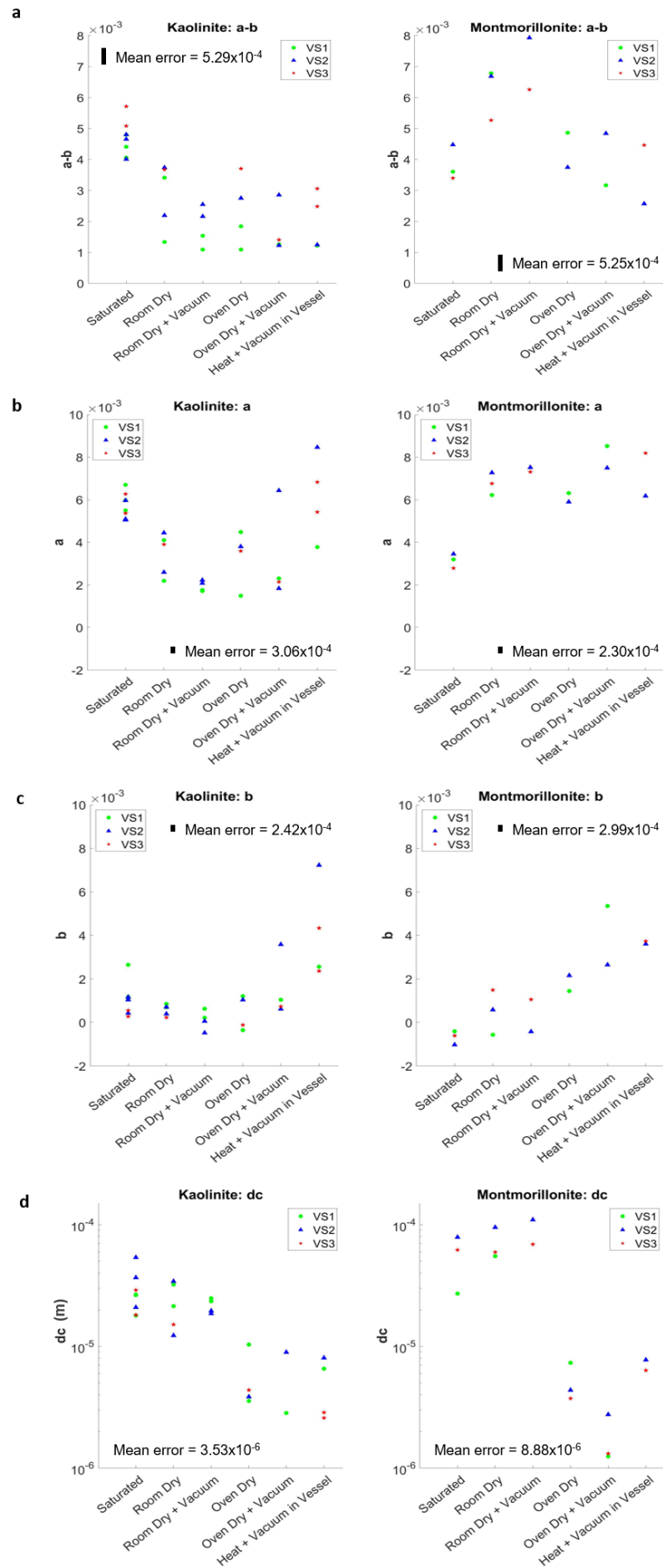


Figure 4.9: a) a-b values; b) a values, c) b values and d) d_c values (in metres) for i) kaolinite-rich china clay and ii) Mg-montmorillonite for each saturation state scenario. Velocity steps (VS) 1 to 3 (2.5 mm, 4 mm and 5.5 mm displacement respectively) are displayed as green circles, blue triangles and red stars respectively. Mean error (standard deviation) is displayed as a scaled bar. Note that d_c values are plotted on a log scale for clarity.

Values of a (Figure 4.9b) for kaolinite vary between ~ 0.001 to ~ 0.08 , initially with a general trend towards lower values between saturated and drier samples, yet increasing in scatter between modelled velocity steps for the driest samples. For Mg-montmorillonite, a values vary between ~ 0.002 and ~ 0.09 , with higher values in drier samples than in saturated. Values of b (Figure 4.9c) for kaolinite vary between ~ 0.001 and ~ 0.08 , with highest values in the driest samples and little difference between saturated and 'room dry' experiments. Driest experiments display considerable variation between different modelled velocity steps. For Mg-montmorillonite, b values vary between ~ 0.001 and ~ 0.005 , and also display an increase towards drier samples, particularly in those that have been heated.

Values of d_c (Figure 4.9d) for kaolinite vary between ~ 3 and ~ 50 microns, with a clear trend towards lower values in drier samples, with some variation between modelled velocity steps. For Mg-montmorillonite, d_c values vary between ~ 1 and ~ 100 microns. Lowest values are also in drier samples, yet here there is a marked decrease between similar values in non-thermally treated and thermally treated samples. There is no obvious correlation between each successive velocity step and value of a, b or d_c in either material.

4.3.4 Kaolinite Microstructure

SEM images of sheared kaolinite fault gouges, representing the microstructures developed during the final velocity step, display an evolution between saturated and vacuum + oven dry samples (Figure 4.10). Using the terminology of Rutter et al. (1986), saturated samples display two prominent Y boundary shears towards each edge of the sample (Figure 4.10a-c), with a lack of observable microstructures in between them. Where Riedel (R_1) and P shears are observed, they are generally poorly developed and rarely linked. Samples sheared at room humidity (Figure 4.10d-f) again have prominent Y shears, however these are more irregular than in saturated samples and often filled with small, angular 'clasts' of material. P shears are well developed through the sample where present, and are linked to R_1 shear crenulations, but again are rare. In samples prepared at room humidity and run under vacuum (Figure 4.10 g-i), and those heated to 130 °C and cooled in the pressure vessel under vacuum (Figure 4.10 j-l), the internal microstructure is markedly different to samples sheared at room humidity. Rather than shear localisation occurring on two Y shears, multiple Y and P foliations appear to accommodate deformation throughout the sample, with abundant R_1 and R' shears oblique to these.

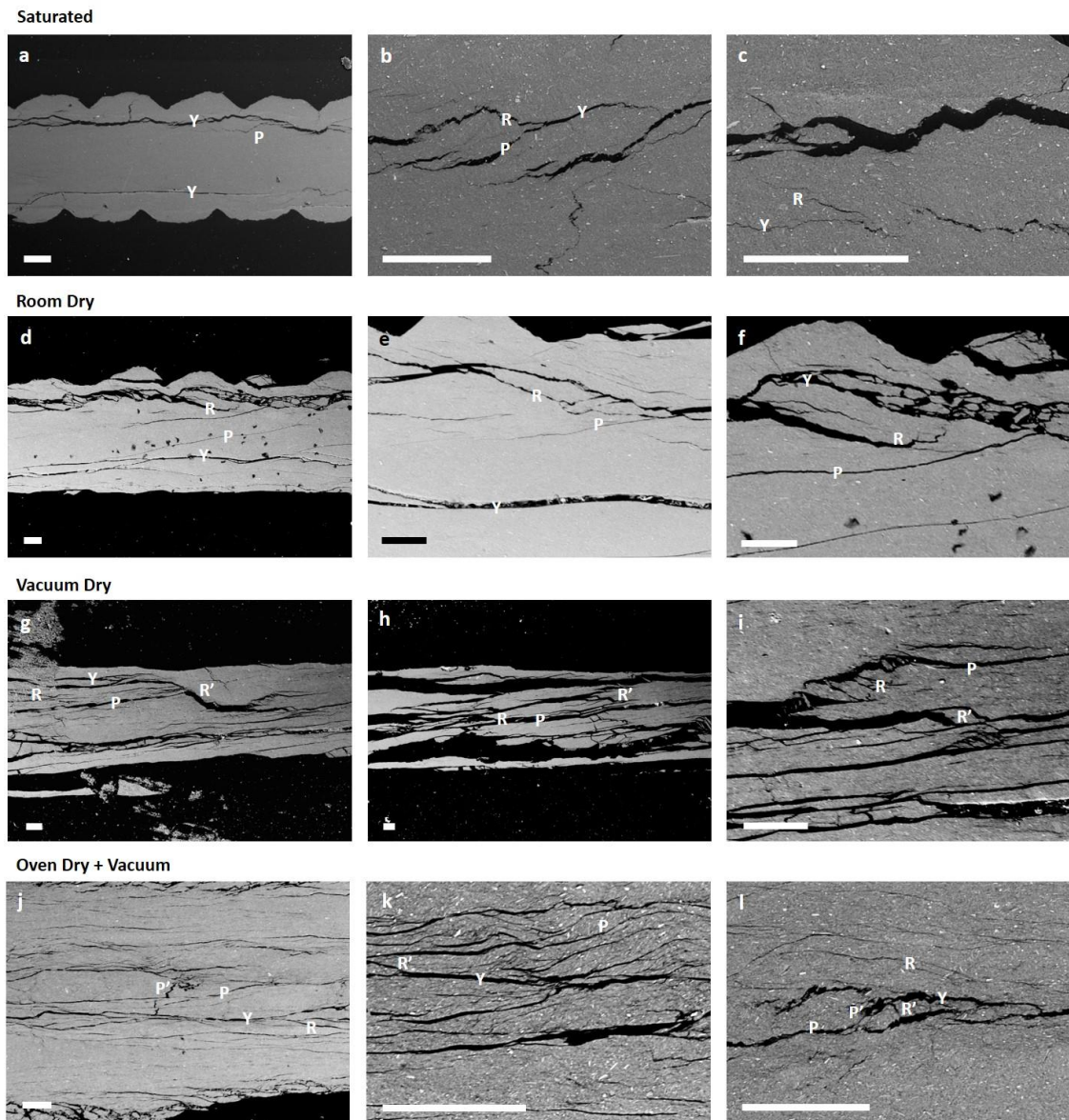


Figure 4.10: SEM image of typical microstructures exhibited in kaolinite-rich gouge, sheared to 6.25 mm displacement at 60 MPa effective pressure, when a), b) and c) saturated, d), e) and f) at room humidity, g), h) and i) vacuum dry and j), k) and l) heated in a pressure vessel to 130 °C and allowed to cool before shearing. Shear direction in all images is dextral. Scale bars in the bottom left of each image represent 100 μm . The majority of the sample (light grey) is interpreted using EDS to be largely kaolinite with minor illite/muscovite. Non-platy white areas are interpreted to be K-feldspar. Quartz is also present in minor quantities.

4.4 Discussion

4.4.1 Evolution of Friction Coefficient with Saturation State

Experimental results presented here show increasing friction coefficient with removal of free and interlayer water in both kaolinite-rich china clay and Mg-montmorillonite. Factors such as water pH, pressure-temperature conditions, and grain size, shape, composition and distribution may all influence to some degree the amount of water that may be adsorbed by phyllosilicates and hence the friction coefficient (e.g. Behnsen and Faulkner, 2012; Morrow et al., 2000;

Sakuma and Suehara, 2015), however all of these have been kept consistent for each material in all experiments. Published μ data for these minerals show considerable differences between different studies and laboratories, and the question we aim to address here is whether the level of 'dryness' of the experiments conducted (which is not always specified) can explain the differences reported in the literature.

Sheet minerals with thin films of interlayer water between them, such as montmorillonite, have a shear strength that increases as the number of layers decreases (Israelachvili et al., 1988) (*Figure 4.2*). The amount of free and interstitial bound water inferred to have been lost during vacuum drying of room dry samples at elevated temperatures in this study (*Figure 4.6*) is consistent with Morrow et al. (2017), (7.2-7.9 wt% water loss in montmorillonite), whilst Bird (1984), Ikari et al. (2007) and Carpenter et al. (2016) all reported a higher water loss of 11-16 wt%. The majority of free and interstitial bound water in Mg-montmorillonite removed upon heating to 130 °C (~4.5-9.5 %) occurs within the first hour, and >90 % of this is removed within 3 hours, which agrees with published time-dependent drying curves for Ca-montmorillonite (Ikari et al., 2007). An increase in temperature to ~200 °C from 130 °C resulted in a further ~0.4 wt% decrease in water in both STA and direct mass experiments (*Figure 4.6*), suggesting that some interstitial water was still present in the Mg-montmorillonite sample in experiment types 4, 5 and 6. Mg-smectites with three water layers have been shown to contain >~8 wt% water, whilst two water layer arrangements contain ~7–8 wt%, one water layer arrangements contain ~4–6 wt% and dry layers contain <~3 wt% water (Schleicher et al., 2013), although some higher values have been reported (e.g. Bird, 1984; Ikari et al., 2007). Colten-Bradley (1987) showed that whilst one water layer may be expelled from a two-layer montmorillonite at 67-80 °C, the remaining layer may still be present up to 192 °C. Indeed, dehydration does not necessarily have a clear end point and may continue beyond 200 °C (e.g. Bala et al., 2000). It is therefore important to state that whilst we can infer that a substantial amount of free and interstitial water has been removed from our samples, minor amounts of interstitial water may remain in the montmorillonite. Since the removal of a single water interlayer causes the largest frictional strength increase (Bird, 1984), the possibility that a small amount may remain in the sample at the temperatures used during preparation in this study will likely have negligible impact.

Assuming ambient temperature and room humidity are consistent between studies, and therefore that montmorillonite at room humidity contains interstitial bound water in a two-layer configuration (Bird, 1984), absolute differences in water contents at room humidity are likely strongly controlled by crystal structure, layer charge and cation type (Behnsen and Faulkner, 2012; Bird, 1984; Ikari et al., 2007; Karnland et al., 2016; Morrow et al., 2000; Sakuma and Suehara, 2015; Vidal and Dubacq, 2009). In 'dry' phyllosilicates, μ is often much larger than expected in relation to a suggested positive correlation with interlayer (001) bonding energy (ILBE) (Moore and Lockner, 2007; Morrow et al., 2000; Kosoglu et al., 2010; Sakuma and Suehara, 2015; Sanchez-Roa et al., 2017), whereby polar water molecules are bonded to layer

surfaces in proportion to surface energy and increasing hydrophilicity. Whilst the structural charge in kaolinite crystals is low, in montmorillonite the charge is large due to the low crystallinity of the mineral and isomorphic substitutions on the silica tetrahedra (García-Romero and Suarez, 2018; Karnland et al., 2016; Vidal and Dubacq, 2009). This charge is balanced by the interlayer cation, which as discussed above also has a control on the water content. High friction coefficients in phyllosilicates with high ILBE may in fact be an effect of how removal of interlayer water alters the d-spacing, and therefore ILBE, of the crystals.

The measured wet friction coefficients for Mg-montmorillonite and kaolinite in this work compare favourably to those summarised and measured by Morrow et al. (2017) and Behnsen and Faulkner (2012) respectively. All clays exhibit low permeability, especially in the presence of water (Behnsen and Faulkner, 2011). Faulkner et al. (2018) showed how these low permeability materials may additionally be affected by initial compaction or dilation in fully saturated tests, even when displacement rates are relatively slow. This issue is exacerbated the lower permeability the clay is. For water saturated tests, Morrow et al. (2017) have shown that differences in reported friction coefficients in montmorillonite ($\mu = 0.06-0.48$) (in experiments carried out by Summers and Byerlee, 1977; Shimamoto and Logan, 1981; Logan and Rauenzahn, 1987; Morrow et al., 1992, 2000; Brown et al., 2003; Saffer and Marone, 2003; Ikari et al., 2007; Moore and Lockner, 2007; Behnsen and Faulkner, 2012, 2013) can largely be explained by the partial saturation of samples wherever insufficient time is allowed for pore-fluid pressures to equilibrate. Another second order variation for wet friction coefficients in the 2:1 swelling smectite can be produced by the cation type, which Behnsen and Faulkner (2013) have demonstrated can produce a two-fold difference in μ . Friction coefficient of Mg-montmorillonite in this study is almost identical to that of Behnsen and Faulkner (2013) (~ 0.11), however variations in the interlayer cation were shown to increase μ by up to ~ 0.15 . In kaolinite, water saturated friction coefficients have been reported as ~ 0.2 to ~ 0.53 (Behnsen and Faulkner 2012), comparable to ~ 0.27 reported here. In this study, increase in steady state μ in the 1:1 sheet silicate with each measured decrease in absolute water content is gradual but shows a total increase of 0.22 (~ 0.27 to ~ 0.49 ; *Figure 4.8*). This is considered to represent the effect of removing free water from the external surfaces of 1:1 phyllosilicate crystals (*Figure 4.2*). A similar trend of increasing friction coefficient with decreasing humidity has been observed in alumina gouge (Frye and Marone, 2002) albeit with a smaller increase in μ of ~ 0.04 due to its lower capacity for water retention. In the 2:1 swelling smectite, a more marked increase in μ between Mg-montmorillonite samples not heated and those heated during preparation (from 0.22 to 0.57) may be explained by the additional mass of interlayer water being removed from montmorillonite during the heating stage (*Figure 4.2, Figure 4.6, Figure 4.8*).

For dry tests, as mentioned previously, the degree to which the samples are dry is often not constrained or quantified. Published laboratory μ values for 'dry' kaolinite gouge have been shown to vary between ~ 0.4 and ~ 0.85 (Behnsen and Faulkner, 2012). These μ values are

consistent with thermally dried samples in this study (~ 0.42 to ~ 0.49), however it is unlikely that the level of 'dryness' can fully explain the spread of 'dry' values reported elsewhere, suggesting other factors are contributing. One such factor may be at what stage during an experiment μ is reported. Moore and Lockner (2004), for example, have reported μ after a greater amount of shear, often displaying some strain hardening, which is seen particularly in the sawcut slider geometry. Another contributing factor potentially accounting for slightly lower friction coefficients in this study (and smaller absolute differences between wet and dry experiments) is the influence of 14 % illite/muscovite in the kaolinite-rich gouge - minerals with a lower electrostatic component of surface energy and separation energy. Published 'dry' μ values for montmorillonite gouge are extremely variable (0.22-0.78) (Summers and Byerlee, 1977; Shimamoto and Logan, 1981; Logan and Rauenzahn, 1987; Morrow et al., 1992, 2000; Brown et al., 2003; Saffer and Marone, 2003; Ikari et al., 2007; Moore and Lockner, 2007; Behnsen and Faulkner, 2012, 2013), yet again the range is comparable to those detailed in this study (0.19-0.57). Whilst the large range in published values could potentially also be partially explained by cation type, elevated pore pressure and variable water contents (Kosoglu et al., 2010; Behnsen and Faulkner, 2013; Morrow et al., 2017), this study shows clearly the marked effect of dehydration on the friction coefficient. This data is in agreement with Ikari et al. (2007), where μ values for Ca-montmorillonite under 100 MPa normal stress increase from ~ 0.03 to ~ 0.41 as water contents decrease from ~ 19 wt% to ~ 2 wt%.

Other notable observations can be made from these experiments on how water affects the evolution of phyllosilicate strength which is not necessarily due to the *level* of 'dryness'. More saturated clay gouges attain an observable peak yield stress before weakening to a lower steady state, whereas drier clay gouges undergo a more gradual increase in stress towards steady state (*Figure 4.7*). Similar trends have also been observed in alumina (Frye and Marone, 2002), and may be attributed to the development of Riedel- (R) and P-shears during early compaction, which may localise into Boundary- (Y) shears at peak stress (Logan et al., 1992; Haines et al., 2013) (*Figure 4.9*). As previously mentioned, stress peaks may also arise in low permeability samples during initial loading as water is expelled from pore space and crystal surfaces of clays; this occurs wherever pore-fluid pressures have not had sufficient time to equilibrate (Haines et al., 2013; Morrow et al., 2017; Faulkner et al., 2018). Where water films have been fully removed by heating, extra consolidation may be required to compact the clay grains, but μ is not reduced.

4.4.2 Evolution of Rate and State Parameters

The parameters within the rate and state formulation are not physical parameters, although many authors have attempted to relate them to physical processes in order to allow extrapolation beyond the conditions at which they were measured. By conducting experiments at various saturation states and noting how a , b and d_c respond, some insight can be gained into the deformation processes.

a-b values, which represent the frictional stability of a material (*Figure 4.1*), are typically positive (velocity-strengthening) in clays. In general, at an effective pressure of 60 MPa, a-b values for clays interpreted to have higher water contents are greater than those of drier clays (*Figure 4.9*). This suggests that some type of fluid-assisted strengthening is taking place, which is perhaps related to the dissolution, transport and precipitation of other soluble phases within the gouge (e.g. Pluymakers and Spiers, 2015). Relevant chemical conditions and timescales allowing these processes have not however been considered in detail. Reducing the absolute water content of kaolinite gouge appears to change the effectiveness of the dominant deformation mechanisms, resulting in greater rate and state effects in samples that have been dried. The specific drying method applied to kaolinite gouge, however, does not seem to significantly affect results. In Mg-montmorillonite, samples that have been thermally dried appear to have markedly greater rate and state effects than those that have been dried at room humidity: our data show that in its driest state, a-b values for Mg-montmorillonite decrease to ~ 0.0025 - 0.0045 from ~ 0.0055 - 0.008 under room humidity conditions. Whilst Morrow et al. (2017) showed that comparable a-b values for Mg-montmorillonite increase in drier states, with respect to saturated conditions, to 0.006 - 0.01 , Ikari et al. (2007) showed that a-b values decrease to $< \sim 0.01$ and may even become negative when water contents are reduced to < 4.5 wt%. Saturated a-b values for Mg-montmorillonite reported here (~ 0.0034 - 0.0045) are generally higher than those reported by Logan et al. (1992) (0.0005), Ikari et al. (2007) (~ 0.0025), Tembe et al. (2010) (0.0005) and Morrow et al. (2017) (0.0002 - 0.0069) at comparable stresses and sliding velocities.

With regards to the specific parameters, the rate variable, a , is a material-dependent velocity scaling factor (*Figure 4.1*), suggested to be a thermally-controlled Arrhenius mechanism (Dieterich and Kilgore, 1994; Rice et al., 2001; Bhattacharya et al., 2017; Aharonov and Scholz, 2018). a values for saturated Mg-montmorillonite in this study (~ 0.0028 to ~ 0.0038) (*Figure 4.9b*) are comparable to the lowest values presented by Logan and Rauenzahn (1987) (0.001 to 0.095). Whilst the rate parameter is lower in saturated Mg-montmorillonite samples, no clear trend is evident to speculate on the influence of *degree* of saturation, other than the fact that the rate effect is larger in drier Mg-montmorillonite. a values for kaolinite initially display a decreasing trend with as water content is reduced, reaching a minimum in vacuum dried, room humidity samples (*Figure 4.9b*), however values within the same range are exhibited in the driest samples, suggesting that this trend may be insignificant. The b value is the scaling factor for the state response to a step in sliding velocity (*Figure 4.1*), interpreted to relate to the strength of asperities in contact (i.e. quality of the contact surface) (Rice et al., 2001; Li et al., 2011) or healing of the contact surface area (Dieterich and Kilgore, 1996). Strength recovery during frictional sliding has been shown to be limited for phyllosilicate-rich materials (Carpenter et al., 2016), and healing is particularly negligible where humidity is low (Dieterich and Conrad, 1984; Frye and Marone, 2002). In this study, the b value appears to be dependent on degree of saturation in both clay types (*Figure 4.9c*). The state effect is magnified as samples become

drier, apparently with a marked increase once heat is applied during the drying stage. This trend broadly corresponds to that seen in similar humidity-dependent experiments on alumina (Frye and Marone, 2002). Slight negative b values (*Figure 4.9c*) imply an increase in contact area with velocity in samples with a higher water content.

The characteristic distance, d_c , required for μ to exponentially decay to a new steady state, b (*Figure 4.1*) is thought relate to surface roughness and particle size; more specifically the slip necessary to renew surface contacts (Marone, 1998). Time-dependent healing (strength recovery, expressed as the parameter b) and velocity-dependent sliding are considered to be material constants acting in parallel (Dieterich, 1981; Dieterich and Conrad, 1984; Beeler et al., 1994; Beeler and Tullis, 1995; Marone, 1998). Observations here (*Figure 4.9c,d*) support the conclusion that fluid-assisted, time-dependent healing mechanisms are operative in gouge containing water but are effectively switched off in the driest phyllosilicates. Both b and d_c values are strongly controlled by the presence of water in both kaolinite and Mg-montmorillonite samples, and removal of water dramatically reduces d_c by up to one order of magnitude in kaolinite, and up to two orders of magnitude in thermally dried Mg-montmorillonite (*Figure 4.9d*). It seems clear that whatever deformation mechanisms are operating during frictional sliding are strongly influenced by the presence of water. Candidate deformation mechanisms that have been suggested in the literature include sub-critical crack growth, dissolution-precipitation creep (pressure solution), dislocation creep (hydrolytic weakening), or hydrogen bonding between adsorbed water molecules (c.f. Bos et al., 2000; Bos and Spiers, 2001; Chester, 1995; den Hartog et al., 2020; Dieterich and Kilgore, 1994; Hickman and Evans, 1995; Kronenberg and Tullis, 1984; Rutter, 1983; Rutter and Mainprice, 1978), all of which would have an Arrhenius component. Further experiments conducted at a range of temperatures might help to further characterise the response of rate and state parameters to changing physical conditions and identify the principal deformation mechanisms.

4.4.3 Evolution of strength, stability, and microstructure

This study suggests that the level of ‘dryness’ also has a direct influence on the microstructure formed during shear, even when all other factors are kept constant. A decrease in frictional stability in drier clay gouges may be an inherent material property related to the evolution of microstructures and changes in the quality of surface contact, asperity contact area and angle.

Shear strain in gouge tends to concentrate along well-developed weak zones that control the overall strength of the material (Collettini et al., 2009; Lockner et al., 2011), which is most evident here in saturated gouges (*Figure 4.10*). The width of localised shear zones (between Y boundary shears) appears to decrease as water is removed from the sample (e.g. from $\sim 500 \mu\text{m}$ in saturated kaolinite to $< 200 \mu\text{m}$ in vacuum dry + heated kaolinite) (*Figure 4.10a-c and j-l*), however these observations must be treated with caution due to the fragility and potential distortion of microstructure during drying and SEM preparation. More abundant P , R_1 and R' fractures in drier samples (*Figure 4.10d-l*) together with more distributed deformation requires

less displacement on individual microfractures; deformation mechanisms acting on a smaller scale in drier samples may explain lower d_c values. Although more tests would be required to increase statistical significance, d_c values in the final velocity step (VS3) are generally lower than those from VS1 and VS2 (Figure 4.9d), which may be interpreted as the smoothing of principal boundary shears with increased time and displacement. Similar interpretations may be made regarding lower VS3 a and b values than in earlier velocity steps for the driest kaolinite samples (Figure 4.9b, c), suggesting that more displacement may be required to reduce frictional resistance and promote healing. Brittle structures may be locked in place until R_1 Riedel shears become interlinked with P shears, or a Y shear plane develops to reduce frictional strength (Figure 4.10). As the sample is sheared, healing may occur due to the reactivation of Riedel shears, enhancing fluid-assisted healing processes, or existing Riedel shears may heal and new shears form. Moore and Lockner (2007b) showed that saturated montmorillonite deforms along concentrated planes, whereas dry montmorillonite gouge (heated to 130°C and prepared at room humidity) is subject to abrasion, wear and fracture during shear. Without microstructural analysis of Mg-montmorillonite samples and with little supporting evidence in the way of rate and state parameter data we are unable to draw similar conclusions here.

It must be noted that some or all microstructures may be significantly influenced by drying methodology either before or after shear deformation. During air- or oven-drying, shrinkage may occur whereby remnant water between grains produces an inter-particle adhesion force, which may distort grain geometry (Aiyama et al., 2019). It may thus be inferred that our drying methodologies could have generated a weak grain fabric in the sample that could later be exploited during deformation. Additionally, post-experimental air-drying of gouge wafers may have further distorted microstructures generated during shear deformation. Drying and deformation microstructures have not been differentiated in this study, however upon the recommendation of Aiyama et al. (2019), freeze-drying of gouge samples will be considered for future studies involving more detailed microstructural analyses.

4.4.4 Implications of Study for Fault Slip in Nature and Experiments

Understanding the individual factors controlling frictional strength and stability in clay fault gouges, and the dehydration properties of individual phyllosilicates within them, is crucial to understanding fault mechanics, in particular the operative grain-scale deformation mechanisms. Crustal strength may be significantly overestimated by strength envelopes if the effects of fluid-assisted deformation mechanisms in fault zones are not accounted for (Bos and Spiers, 2000). The variation of physiochemical properties within fault gouges has been invoked as a primary reason for aseismic creep behaviour of major faults, such as the San Andreas Fault (Lockner et al., 2011; Chang et al., 2013) and within the Soultz-sous-Forêts geothermal field (Bourois and Bernard, 2007). Maximum (i.e. truly dry) friction coefficient in phyllosilicates is only achieved under careful laboratory conditions and saturated data is most likely to be observed in nature. That being said, increased dehydration, mechanical consolidation, mineral

transformation and hence frictional instabilities may occur with depth (e.g. within the smectite-illite transition zone) (Marone and Scholz, 1988; Brown et al., 2003; Saffer and Marone, 2003; Ikari et al., 2009b), meaning that partially saturated to 'dry' data may be more applicable to regions of high geothermal gradients and poor fracture connectivity. Partially saturated data may also be applicable to caprocks forming part of a carbon capture and storage project, where drying clays potentially leading to increased permeability and fault strength is of some concern (Armitage et al., 2010; De Jong et al., 2014; Vilarrasa and Carrera, 2015). With increasing depth, both water content and the interlayer space decrease in 2:1 swelling smectites (*Figure 4.2*). Although it is possible for two or more mineral hydration states to coexist (Schleicher et al., 2013), many fault zones have been described where release of mineral-bound water from phyllosilicates appears to occur in stages at particular metamorphic pressure-temperature conditions, such as the sepiolite-bearing Galera Fault Zone (Sanchez-Roa et al., 2018) and the saponite-bearing San Andreas Fault, as observed via the SAFOD core (Lockner et al., 2011; Carpenter et al., 2012). At average geothermal gradients, montmorillonite with two interstitial water layers can occur naturally at ~4-6km and dehydrates fully between ~6 and ~11km (Bird et al., 1984). Rates of dehydration with depth have been shown, in this study and elsewhere, to vary not only with pressure and temperature but also with phyllosilicate crystal structure and the interlayer cation type (Sanchez-Roa et al., 2018; Vidal and Dubacq; 2009).

The methodology used when preparing samples for 'dry' friction tests in the laboratory should be carefully considered. Firstly, friction coefficients of rock that has been ground and mixed during sample preparation may be greater than that of a natural fault where fabric has developed and weak materials have localised, thus gouge may be even weaker in its undisturbed state than in laboratory measurements (Collettini et al., 2009; Lockner et al., 2011). The combination of elevated pore pressures and development of strongly foliated layers with low frictional strength has been used to explain exceptionally weak faults (Faulkner and Rutter, 2001; Lockner et al., 2011; Behnsen and Faulkner, 2012). Secondly, heating samples to remove water films from clay grain surfaces is essential, especially in 2:1 sheet silicates. Failure to do this results in huge variability in friction coefficients and markedly different constitutive parameters. Performing experiments under vacuum appears to aid water removal in some clays (e.g. kaolinite) but has a minor effect overall relative to the effect of heating. In order to maintain good data compatibility in clay friction experiments between laboratories, fully equilibrated saturated samples should also be used. The low permeability of clays, particularly montmorillonite, slows the attainment of fluid pressure equilibrium (Morrow et al., 2017) leading to erroneous predictions of μ (Morrow et al., 2017; Faulkner et al., 2018). Care must be taken when considering published data on frictional parameters for sheet silicates. This study has followed the guidelines of Faulkner et al. (2018) and Morrow et al. (2017) in finding a balance between test geometry, strain rate, compaction rate, and fluid expulsion that leads to an acceptably equilibrated fluid pressure. If data are to be presented for unsaturated clays, the

drying methodology should be outlined in full, and samples should be heated thoroughly under vacuum immediately prior to testing.

4.5 Conclusions

These initial tests provide constraints on the impact of clays on fault behaviour as well as the optimal experimental techniques used to study them, most notably:

- Saturation state has a large effect on strength and stability of clay-filled faults, which is much more pronounced in 2:1 swelling smectites than 1:1 sheet silicates. Friction coefficient increases by up to a factor of 3 in Mg-montmorillonite and by a factor of 2 in a kaolinite-rich gouge with increased 'dryness'.
- Published μ values are generally consistent with those presented in this study, however it is unlikely that the level of 'dryness' can fully explain the spread of values, particularly those for dry friction coefficients. This suggests that other factors are contributing, such as crystal structure, layer charge and cation type, grain properties, and at what stage in the experiment μ is reported.
- Rate and state parameters evolve with saturation state, such that as water is removed clay gouges become less stable (a-b values decrease), and the amount of displacement or time required to establish a new steady state friction coefficient upon a change in sliding velocity (d_c) decreases.
- Fluid-assisted deformation mechanisms operating during frictional sliding are strongly influenced by the presence of water, which also has a direct influence on the microstructure formed during shear, even when all other factors are kept constant.
- So long as the sample has been heated, a vacuum appears to have little effect on friction coefficient, although it may promote a lower yield. If data are to be presented for unsaturated clays, drying methodology should be outlined in full, and samples should be heated thoroughly under vacuum prior to testing as soon as possible thereafter.

Acknowledgements

Work presented here was fully funded by Natural Environment Research Council (NERC grant ref. no. NE/L002469/1) as part of a PhD conducted via the EAO DTP, whose support is gratefully acknowledged. Funding was also gained via a standard grant (NERC grant ref. no. NE/P002943/1). Thanks are also extended to the two reviewers for their constructive feedback that helped to improve the article during publication; Steve Crowley for his assistance in the design of the vacuum setup; Gary Coughlan for technical assistance in University of Liverpool's Rock Deformation Laboratory; Sabine den Hartog and Marieke Rempe for their invaluable discussions; and to University of Liverpool's SEM and Thermal Laboratories.

This chapter is based on the following publication, for which details on author contributions are given in the *Declaration of Authorship and Funding Information*:

Beynon, S.J. and Faulkner, D.R. (2020) Dry, damp, or drenched? The effect of water saturation on the frictional properties of clay fault gouges, *Journal of Structural Geology* 140, 104094.

5 The Design of a Novel Experimental Approach to Investigate the Nature, Rate and Volume of Fracture Sealing in Geothermal Systems

Abstract

Fluid flow in crystalline geothermal reservoirs is largely controlled by faults and fracture networks, within which high permeabilities and flow rates are required to efficiently transport heat energy. During geothermal production or stimulation by fluid injection, physiochemical properties of fluids are often taken out of equilibrium with the surrounding fractured host rock as a result of changing temperatures, pressures or fluid chemistry. As a consequence, mineral precipitation from solution may occur within fracture networks (i.e. fracture sealing to form mineral veins), causing irreversible loss of permeability, efficiency and ultimately production. Fracture sealing has been shown theoretically to be a function of time, temperature and fracture dimensions, and is also dependent on changes in fluid pressure and composition, however there is little consistency in experimental work. Relatively little experimental research has been done to investigate the hydrodynamic effects on fracture sealing, particularly regarding the crystal textures that can help identify precipitation rates and the conditions that control sealing rates and volumes. In this chapter, published data regarding the controls on chemical disequilibrium, the nature and rate/volume of precipitation are reviewed, summarising the experimental approaches to understanding this issue performed to date. In order to constrain these variable existing data, a new high-pressure, high-temperature triaxial deformation apparatus has been built, the design and calibration of which is described in detail. The purpose of this new apparatus is to precisely simulate a range of upper crustal geothermal gradients whilst under confining pressure, simultaneously allowing the flux of a fluid containing minerals in solution (e.g. quartz or calcite) to be controlled within an experimentally fractured rock core. Two proposed types of experiment to investigate the nature, rate and volume of fracture sealing are described - 'static' and 'dynamic' - that aim to simulate precipitation via diffusional and advective fluid flow processes respectively, within a synthetically created fractured core sample with well-defined physical properties. Data emerging from this new experimental setup, when considered alongside existing published data and natural microstructures, may be used to better constrain the range of physiochemical conditions under which precipitation is most likely to reduce structural permeability in geothermal reservoirs, thereby improving subsurface models and efficient operation in geothermal production and/or stimulation.

5.1 Introduction

Natural and enhanced geothermal resources are increasingly found to be hosted in low primary permeability crystalline reservoirs, within which fluid flow is largely controlled by faults and

fracture networks (Bertani, 2016; Brace, 1980; Dezayes et al., 2010). Within these fracture networks, high permeability and near-hydrostatically pressured fluids (i.e. high flow rates) are required in order to efficiently transport hot fluids to the surface (Limberger et al., 2018; Sibson, 2000). As a consequence of geothermal fluid extraction, however, geochemical systems are potentially taken out of equilibrium, potentially resulting in mineral precipitation in fracture networks at depth or in surface pipework and causing irreversible loss of permeability, efficiency and ultimately production (Lowell et al., 1993; Dobson et al., 2003; Tranter et al., 2020). The formation of mineral scaling (commonly silica, calcite or barite) in pipelines and reinjection wells is common wherever geothermal fluids are supersaturated with the mineral in question, with precipitation of dissolved solids most likely in cases of steam extraction or fluid cooling (Brown and Dunstall, 2000). As discussed in *Chapter 3* and *Chapter 4*, sealing by precipitation may also result in significant strength changes (e.g. Sibson et al., 1988) that could affect the mechanical strength and stability of the rock mass and hence drilling processes. In order to better understand the evolution of geothermal systems and develop them successfully, it is important to study the physiochemical processes through which fracture networks may seal by mineral precipitation from hydrothermal fluids (Dobson et al., 2003; Gomila et al., 2016).

Fluid flow, and hence vein formation, is typically focused in the permeable damage zone of a fault, where processes such as fluid migration and percolation, reseal hardening or weakening, rock mechanical and transport properties, chemical and physical growth of minerals, palaeostress orientations, and crack-seal mechanisms all play an important role (Bons et al., 2012; Faulkner et al., 2010, 2011; Faulkner and Rutter, 2000; Sibson, 1996; Woodcock et al., 2007). Syntectonic veins (i.e. mineral aggregates precipitated from a fluid in dilatational sites) are pervasive within the upper crust and can reflect either diffusive or advective fluid transport processes occurring in conjunction with cataclasis during relatively low-grade deformation (Oliver and Bons, 2001; Blenkinsop, 2002; Elburg et al., 2002). Experimental studies have shown that the flow of hydrothermal fluids through fractured rock causes significant permeability reduction over time that is due largely to healing and sealing of macro- and microfractures, with rates of permeability loss apparently dependent on temperature (e.g. Moore et al., 1994; Morrow et al., 2001). Further quantifying the coupled processes of dissolution/precipitation and deformation alongside their influence on fracture permeability is therefore critical to understanding fluid transport evolution in geothermal systems (Espinoza et al., 2011).

The mineralogy, chemistry and microstructure of veins provides a record of pressures, temperatures, strain histories, fluid compositions, transport processes and interactions between fluids and the fractured host rock. Fracture sealing processes are sensitive to a wide range of interacting factors linking chemistry to microstructure (for example, the degree of fluid supersaturation, mineral growth mechanisms (kinetics) and fluid flux (e.g. Hilgers et al., 2004)), yet each of these processes require further investigation in order to fully understand the evolution and sustainability of fractured geothermal systems. Sealing is often achieved

transiently via pulsed fluid transport as fluid/reservoir conditions are taken out of equilibrium, hence vein textures are considered to reflect the various crystallisation mechanisms at play in fluid-filled fractures (Bons, 2000; Oliver and Bons, 2001; Hilgers and Urai, 2002b; Okamoto et al., 2008; Bons et al., 2012). It has been suggested that in a geothermal field where mineral-rich fluids are at conditions that favour precipitation, structural permeability will likely be short-lived (e.g. Laubach and Diaz-Tushman, 2009). However, relatively little research has been done to investigate hydrodynamic effects on fracture or well scaling, particularly regarding the conditions that can reduce the rate of scaling and the crystal textures that can help identify precipitation rates – ultimately a better understanding of this will allow larger temperature drops during geothermal production, or the extraction of greater amounts of steam, with fewer scaling problems, resulting in a more efficient resource (Brown and Dunstall, 2000).

Ultimately, whether precipitation occurs in a fracture depends on whether the system is in chemical equilibrium; changes in conditions such as the temperature of the fluid or rock mass, the confining or fluid pressure and/or the fluid chemistry may take the system out of equilibrium, hence driving precipitation. This is discussed in *Section 5.2.1*. The nature of precipitation may be controlled by the relative dominance of crystal nucleation versus growth/kinetics, the understanding of which assists in the use of vein microstructures to identify the speed of precipitation from natural, exhumed hydrothermal systems (*Section 5.2.2*). Whilst there is some consensus on the aforementioned issues, a number of recent studies are in disagreement regarding the fluid flux required to seal a fracture. Fluid flux, the physical properties of a fracture and the degree of disequilibrium between the fluid and mineral (or a combination of all of these) may affect the expected *volume* of precipitation – this is discussed in *Section 5.2.3*). The three key themes that are addressed within this chapter are outlined in *Figure 5.1*.

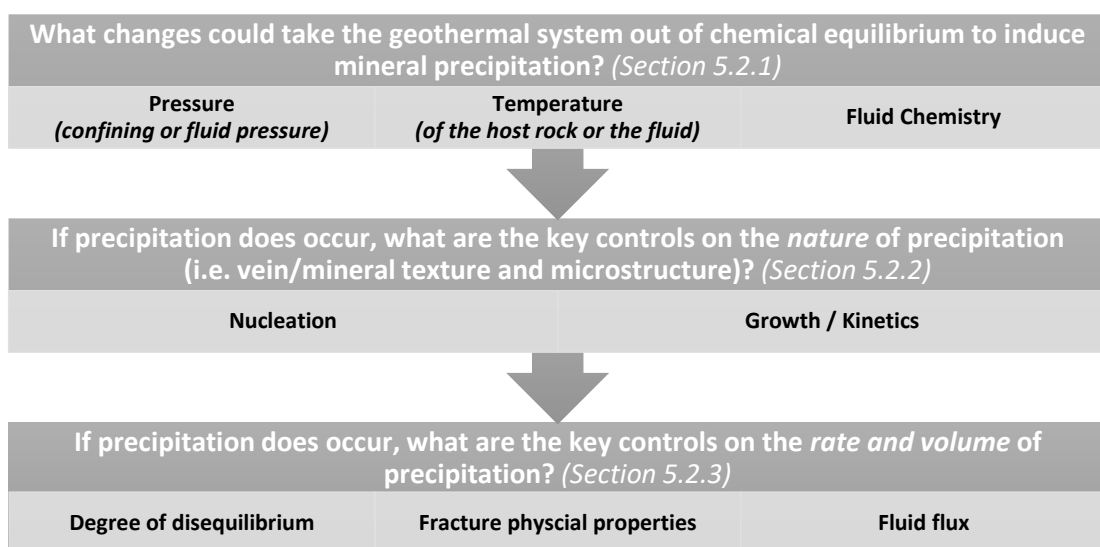


Figure 5.1: A summary of key questions to be addressed within this chapter and through planned experimental work.

In the absence of long-term in-situ monitoring via geothermal wells, an experimental approach can be adopted to obtain relevant data in order to help understand the questions outlined above. Some previous efforts to experimentally address issues similar to those introduced above are discussed in *Section 5.2.4*, however each have their limitations in the range of conditions they are able to replicate. Here, a new apparatus has been designed and built in the University of Liverpool's Rock Deformation Laboratory, aimed to address some of the fundamental questions outlined in *Figure 5.1*. The apparatus can reproduce a wide range of pressure/temperature conditions at depth in the Earth's crust whilst simultaneously allowing the flux of a mineral-doped fluid to be controlled within an experimentally fractured rock core. *Section 5.3* gives a detailed overview of the design, build and calibration of the experimental apparatus, followed by a summary of possible experimental setups and parameters (*Section 5.4*). *Section 5.5* discusses some initial thoughts on to what degree these new experimental methods could address the fundamental questions, outlining some limitations and potential future directions of research, before work is summarised (in the framework of *Figure 5.1*) in *Section 5.6*.

5.2 Potential Controls on the Nature and Volume of Precipitation

5.2.1 Controls on Deviation from Chemical Equilibrium

A good knowledge of the conditions that take a geothermal system out of equilibrium and induce mineral precipitation as veins is essential to the planned experimental work discussed in *Section 5.3.4*. A key factor in governing likely precipitation volumes and rates is how external drivers of disequilibrium affect the concentrations of dissolved minerals within a fluid. The concentration, or solubility, of a mineral phase within a fluid is defined as the maximum amount of solute (mineral) that can dissolve in a known quantity of solvent (fluid) as given physio-chemical conditions. Solutions may be said to be saturated when a solution contains a completely dissolved soluble mineral phase, whereas supersaturated conditions are reached where the mineral phase begins to precipitate. The solubility of a solution may also be described using a Saturation Index (SI), which is calculated by comparing chemical activities of dissolved mineral ions (IAP) with their solubility product (K_{sp}) according to Equation 5.1 (Aquion, 2015):

$$SI = \log_{10} (IAP / K_{sp}) \quad (Eq. 5.1)$$

Negative SI values indicate the potential for mineral dissolution; positive SI values indicate the potential for mineral precipitation; and values of zero indicate that the fluid and mineral are in chemical equilibrium. Minerals theoretically require a $SI > 1$ in order to precipitate, however much higher levels of supersaturation are often needed at certain conditions due to differences in precipitation rates between minerals.

Since silica and calcite scaling in geothermal wells is prevalent (Ármansson et al., 2012) and their solubilities at a range of environmental conditions have been relatively well-studied (e.g.

Ellis, 1959, 1963; Fournier and Rowe, 1966; Crerar and Anderson, 1971; Fournier and Potter, 1982; Fournier, 1989; Rimstidt, 1997; Doubra et al., 2017), these minerals have been chosen for initial experimental analyses detailed in *Section 5.3.4*. For the purposes of the literature review and experimental overview presented within this chapter, only conditions that correspond to a single, liquid water phase are considered (i.e. temperatures of 0-373 °C and effective pressures not falling below 22 MPa (at 373 °C, or below 6.12×10^{-4} MPa at 0 °C)), according to the phase diagram for water (*Figure 5.2*). Changes in conditions that may induce two-phase systems or supercritical fluids, their potential resultant impacts on precipitation mechanisms and relevance to geothermal exploration are briefly discussed later in *Section 5.5.1*.

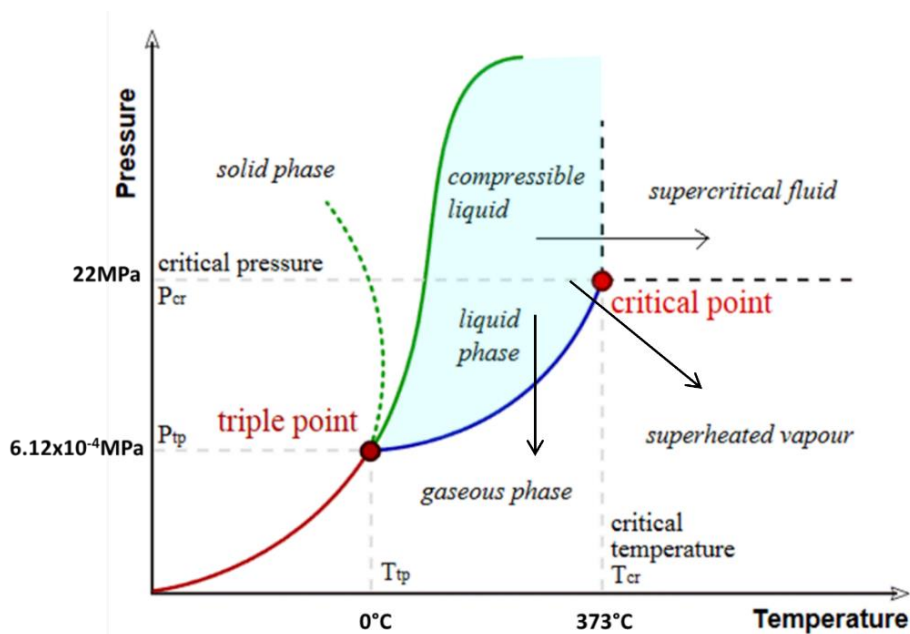


Figure 5.2: Phase diagram for water highlighting the temperature and pressure conditions explored in this study (modified from LibreTexts, 2021). For the proposed experiments described in *Section 5.4* only liquid phases are considered, however future research could also explore crossing phase boundaries.

A summary of published data on silica (SiO_2) and calcite (CaCO_3) solubilities and their dependence on various external drivers (i.e. fluid temperature, pressure and chemistry) is shown in *Figure 5.3*, with *Figure 5.4* further highlighting the combined effect of varying confining pressure and temperature. Whilst silica solubility is mainly dependent on temperature and SiO_2 crystallographic type (i.e. quartz, chalcedony, cristabolite, opal or amorphous silica) (Crerar and Anderson, 1971; Fournier, 1989; Rimstidt, 1997; *Figure 5.3a*), calcite solubility is dependent on a range of factors including confining pressure (Doubra et al., 2017; *Figure 5.3b*), partial pressure of CO_2 (Ellis, 1959; *Figure 5.3c*) and fluid salinity (Ellis, 1963; *Figure 5.3d*).

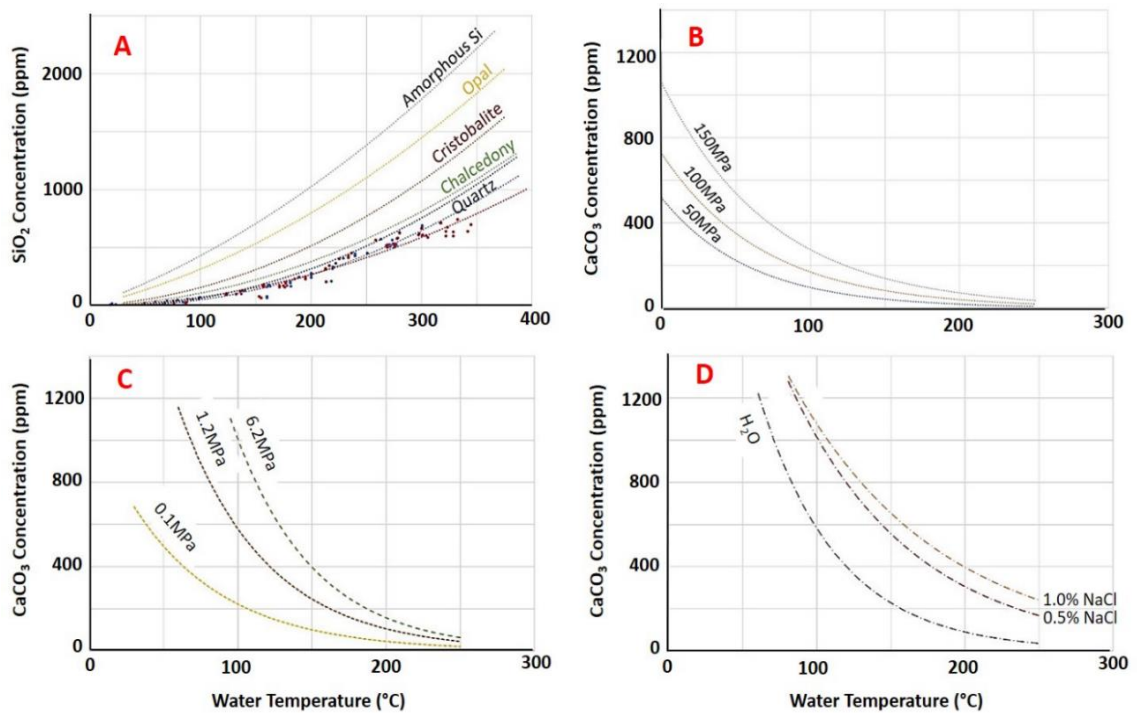


Figure 5.3: Concentration (ppm) v water temperature (°C) plots for a) SiO_2 crystallinity (Fournier, 1989) with point data from (Rimstidt, 1997) (blue) and (Crerar and Anderson, 1971)); b) calcite, at various confining pressures (Doubra et al., 2017); c) calcite, with various partial pressures of CO_2 (Ellis, 1959); and d) calcite, with various water salinities (Ellis, 1963).

Dissolution of silica (SiO_2) in water occurs through the formation of orthosilicic acid, H_4SiO_4 . At low pressures (e.g. <20 MPa), SiO_2 concentrations in geothermal waters at any temperature up to the critical point of water (373 °C) are relatively low (<1750 mg/kg), reaching maximum solubility at ~320 °C at the vapour pressure of the solution, at which point there is a marked change in the specific volume of water (Figure 5.3a) (Fournier and Potter, 1982; Tsuchiya and Hirano, 2007). Further, concentrations at these pressures are governed and further limited by the solubility of the quartz crystal polymorph (i.e. ~300–700 mg/kg (Fournier and Rowe, 1966)). At low temperatures (<200 °C), silica solubility is invariably low, even if pressures are high (e.g. ~1000 ppm at 60 MPa; Figure 5.3a). At room temperature, silica solubility is extremely low, varying between 6 mg/l (microcrystalline silica) and 120 mg/l (amorphous silica) (Rykart, 1995). At higher temperatures, however, silica – particularly amorphous silica - is easily dissolved by percolating fluids: its prograde solubility means that, at 60 MPa, concentrations can increase to >3750 ppm at 373 °C (Fournier and Potter, 1982; Fournier, 1989; Figure 5.3a). Variations due to pressure are much more pronounced at higher temperatures.

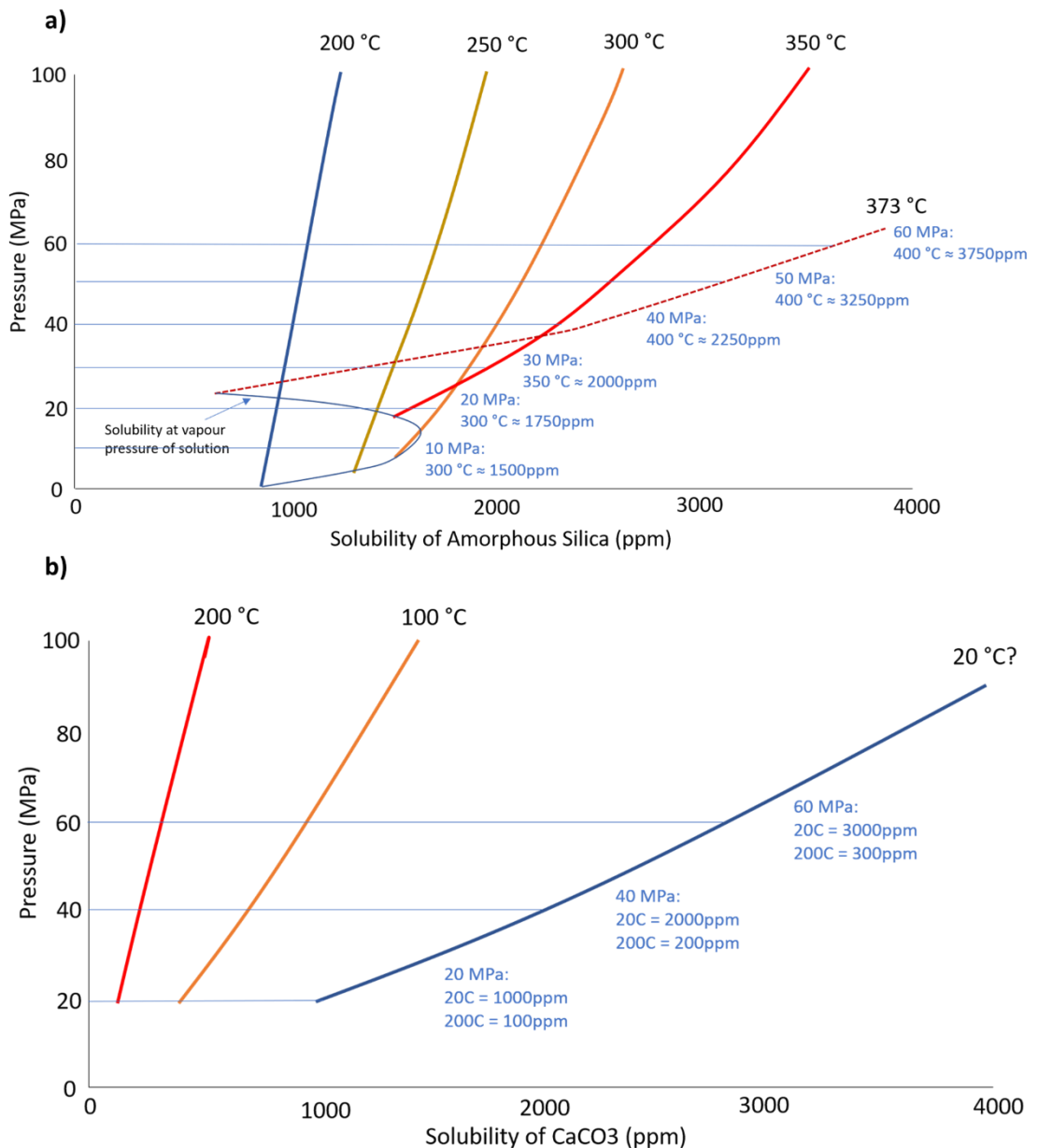


Figure 5.4: Confining Pressure v Dissolved Mineral Concentration (Solubility) with changes in temperature for a) Amorphous Silica and b) Calcite (based on data in Figure 5.3).

For fluids up to ~300 °C, any process that decreases the fluid temperature will supersaturate the fluid with respect to silica, making it more likely to precipitate. Any process that decreases the fluid pressure will also supersaturate the fluid with respect to silica, with the degree of disequilibrium (i.e. difference between maximum and minimum concentrations) greater at higher temperatures. For higher temperature fluids (e.g. 300-373 °C) and low pressures (<~35 MPa), however, silica concentrations conversely decrease upon a drop in temperature or fluid pressure (Figure 5.4a). As a result, a window is created where silica is least likely to be precipitated, making it possible to extract energy from a geothermal fluid without precipitating dissolved silica (Brown, 2013). Conditions beyond the vapour pressure of the solution are not considered here but produce much more complex behaviour that requires further investigation.

Once initiated, silica precipitation can be rapid, particularly from fluids with high degrees of supersaturation with respect to amorphous silica (Steeffel and Van Cappellen, 1990; Lasaga, 1997; Arnórsson and Gudmundsson, 2003). Surface deposits of silica sinter are common in geothermal areas, typically forming when fluids cool to below 100 °C in solutions that have equilibrated at higher pressures and temperatures and rapidly ascended (Fournier and Rowe, 1966; Rimstidt and Barnes, 1980; Tsuchiya and Hirano, 2007; Okamoto and Tsuchiya, 2009). Whilst silica scaling is common in high-temperature geothermal systems, precipitation may also be influenced significantly by fluid chemistry; for example, precipitation of Mg-silicate is common in low-temperature systems where cold groundwater mixes with hot geothermal fluids (Kristmansdóttir, 1989).

Calcite is typically found in geothermal systems with temperatures of ~140–300 °C and where fluids have high concentrations of dissolved CO₂ (Simmons and Christenson, 1994). The behaviour of calcite is controlled primarily by equilibrium in the reaction of solid calcium carbonate (CaCO₃) + carbonic acid (H₂CO₃) = Ca²⁺ + 2HCO₃⁻. Calcite has a retrograde solubility with respect to temperature, partial pressure of CO₂ and salinity (*Figure 5.3b-d; Figure 5.4b*) – i.e. calcite is less soluble in hotter, more CO₂-rich and higher salinity fluids. At low pressures (i.e. <20 MPa), a decrease in temperature from 200 °C to 20 °C increases CaCO₃ concentration from <100 ppm to ~1000 ppm, whilst at higher pressures (i.e. 60 MPa) concentrations increase from ~30 ppm to ~3000 ppm (Doubra et al., 2017; *Figure 5.4b*). An increase in fluid pressure, however, increases the solubility of gases in liquids causing the production of more carbonic acid and dissolution of calcite. Likewise, any process that increases the amount of CO₂ promotes the production of more carbonic acid, causing the calcite to dissolve. Hence, injection of water or CO₂ into a fractured reservoir containing calcite would likely cause a disequilibrium of pore fluid pressure or fluid chemistry and promote CaCO₃ dissolution.

Any process that increases the temperature, decreases the salinity, decreases the confining pressure or reduces the amount of CO₂ in the system will supersaturate the fluid with respect to calcite, making it more likely to precipitate. Whilst calcite is more soluble at lower temperatures, there is plentiful evidence of calcite at the Earth's surface, suggesting that while it may be soluble precipitation is still possible over long time periods. Varying temperature profiles along fluid flow pathways in geothermal systems, particularly at operating sites using coupled production and injection wells, create 'cold' zones where highly reactive calcite can be dissolved and 'hot' zones where it can be precipitated. Precipitation of hydrothermal calcite is largely governed by boiling, dilution, and condensation (Simmons and Christenson, 1994). Low-temperature zones in Iceland, for example, have been found to be supersaturated with calcite where fluids temperatures are >100 °C, however scaling occurs only during boiling (fluid flashing) due to resultant pH increases (Kristmannsdóttir, 1989).

Whilst the above analysis of solubilities at a range of static conditions is a useful starting point in determining whether precipitation will occur as a result of chemical disequilibrium, natural

systems are rarely static and therefore a framework is required whereby disequilibrium-driven precipitation during advective flow can be better understood. Advective mass transport is an important process occurring within the crust that is responsible for significant long-distance mass transfer and precipitation in both geothermal areas and ore deposits (e.g. Cox et al., 2001). The use of dimensionless numbers forms a useful way to combine the physiochemical processes controlling dissolution and deformation regimes in advective fluid flow (Lasaga, 1997; Brosse et al., 2005; Elkhoury et al., 2013). The relative rate of reaction (i.e. mineral precipitation, or dissolution) to fluid flow (i.e. advection) can be represented by the Damkohler number (D_a) (Bekri et al., 1997; Detwiler and Rajaram, 2007; Elkhoury et al., 2013 – Equation 5.2), defined as the product of the reaction rate coefficient (k) and fracture length (L), divided by the product of the mean velocity of the fluid flowing through the fracture (V) and the mean fracture aperture (b):

$$D_a = \frac{kL}{V\langle b \rangle} \quad (\text{Eq. 5.2})$$

Large D_a values indicate that precipitation is able to keep up with fluid supply rates and equilibrium can be assumed along the entire fracture. D_a also describes the relative importance of diffusion versus reaction kinetics, the latter of which become dominant above a critical value of ~ 3 (Martin and Lowell, 2000). A modified form of the Damkohler number, D_a^* (Equation 5.3), representing the relative importance of reaction rates and advective/diffusion timescales, has been used as a parameter to quantify the effect of fracture length (L) and fluid velocity (V) on evolving fracture permeability under transport-limited conditions or fast reaction kinetics (Elkhoury et al., 2013), which would be particularly relevant for low-pH reaction kinetics that are transport-controlled (e.g. Sjöberg and Rickard, 1984). Reaction rate is defined as b/k , whilst the advective timescale (T_a) is defined as L/V , and the diffusion timescale (T_d) is defined as $(b)^2/D_m$, all of which combine to give Equation 5.3:

$$D_a^* = \left[\frac{ShD_m}{2b^2} \right] \frac{L}{V} = \frac{Sh}{2} \frac{\tau_a}{\tau_d} \quad (\text{Eq. 5.3})$$

Dissolution rates may also be approximated using an effective transport limited rate coefficient (k_{eff}), equal to $(ShD_m)/(2b)$, where Sh is the dimensionless Sherwood number (~ 7.56) (Elkhoury et al., 2013). Rates of dissolution are controlled by diffusion and mass transport processes when $T_a \ll T_d$.

5.2.2 Controls on Mineral and Vein Textures

Several models exist for vein formation by advective fluid flow processes that are as yet largely unsupported by quantitative data (Etheridge et al., 1984; Lee et al., 1996; Sibson et al., 1975; Sibson, 1981, 1990) (Figure 5.5). In the seismic pumping model (Sibson et al., 1975) fluid migrates down a potential gradient into a dilation site opened by accumulating differential

stress or increasing fluid pressure, before dilation site collapse expels the fluids. In the fault valve (suction pumping) model (Sibson, 1981; 1990), dilation rate is greater than fluid flux, developing a temporary underpressure in the void and driving fluid into the dilation site. In both scenarios, mineral precipitation may occur as a result of decreasing fluid pressure (as discussed in Section 5.2.1). In the fluid pressure excursion (matrix-to-crack pumping) model (Etheridge et al. 1984), vein opening takes place in regions of local fluid overpressure, and resulting potential gradients promote mineral precipitation. Cyclic hydraulic fracturing may also occur, due to sealing during rapid fluid flow along a pressure gradient followed by extensional failure once the minimum effective stress exceeds the tensile strength (Hilgers and Urai 2002a). Veins may also grow from a static fluid via diffusion and solution transfer creep, as material dissolved in sites of high normal stress diffuses through the pore fluid and precipitates at a dilation site (Fisher and Brantley, 1992; Hilgers and Urai 2002a).

Experimental work discussed in Section 5.3 in part has an ultimate aim to further constrain these models - in particular in terms of how precipitation from fluids is influenced by fluid pressure gradient, temperature, flow rates and crack dimensions - as well as explore the impact of formation mechanisms on vein textures. Whilst limited progress in this regard has been achieved in this study, it is useful to explore the principles of the nature of precipitation as a result of fluid flow in order to guide future research (for example using the experimental apparatus outlined in Section 5.3 to further understand the implications of natural microstructures depicted in Chapter 3).

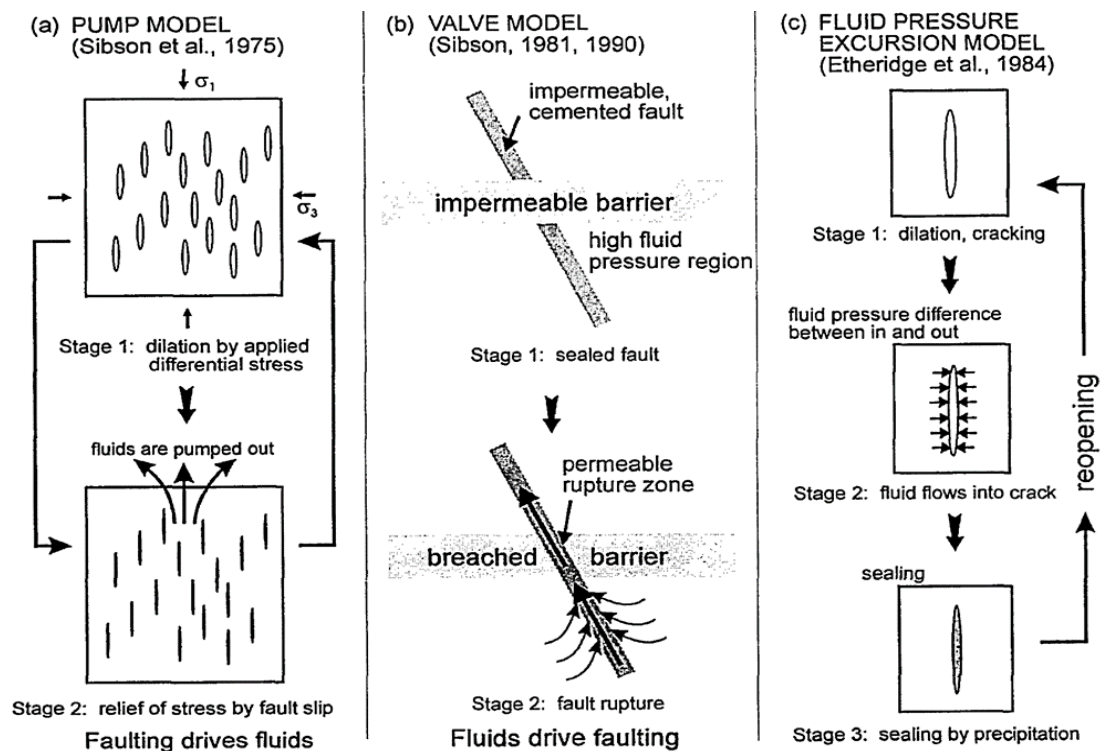


Figure 5.5: Conceptual models for vein formation (after Lee et al., 1996). a) Pump model (Sibson et al., 1975). b) Valve model (Sibson, 1981; 1990). c) Fluid pressure excursion model (Etheridge et al., 1984).

Fractures can experience loss of permeability through two main processes: healing (involving local transport of minerals through diffusion (e.g. Fisher and Brantley, 1992; Hickman and Evans, 1995)), and sealing (where dissolved material is transported some distance via pore fluids) (Smith and Evans, 1984). There are four principal mechanisms involved in vein formation, which almost always combine into less simplified mechanisms making it difficult to assess conditions of vein formation based on textures (Bons, 2000; Smith and Evans, 1984; Okamoto et al., 2010). Each successive mechanism has increasing transport rates and decreasing fluid-rock interaction, and most likely a higher D_a : (1) diffusion of dissolved matter through stagnant pore fluid; (2) flow of fluid with dissolved matter through pores; (3) flow of fluid with dissolved matter through fractures and (4) flow by mobile hydrofractures. Diffusion through a fluid in advecting fluid regimes can occur over long distances (i.e. systems with a high D_a) and is generally more effective than non-advecting fluids, which diffuse relatively slowly over distances of \sim cm (i.e. systems with a low D_a) (Bons, 2000). It has been suggested that fibrous, elongate blocky, blocky and crack-seal textures develop in advective flow regimes (Barker et al., 2006) (*Figure 5.6*). Thermally activated healing processes generally occur near crack tips, where precipitate forms a non-uniform surface creating chemical potential gradients that then cause diffusive material transport and a net reduction of interfacial energy (Smith and Evans, 1984; Barker et al., 2006). In this chapter, however, vein formation by fracture sealing is the main focus. Sealing can occur as a single precipitation event (e.g. a rapid fluid pressure decrease), or as multiple crack-seal events caused by fluid pressure or strain oscillations (Ramsay, 1980).

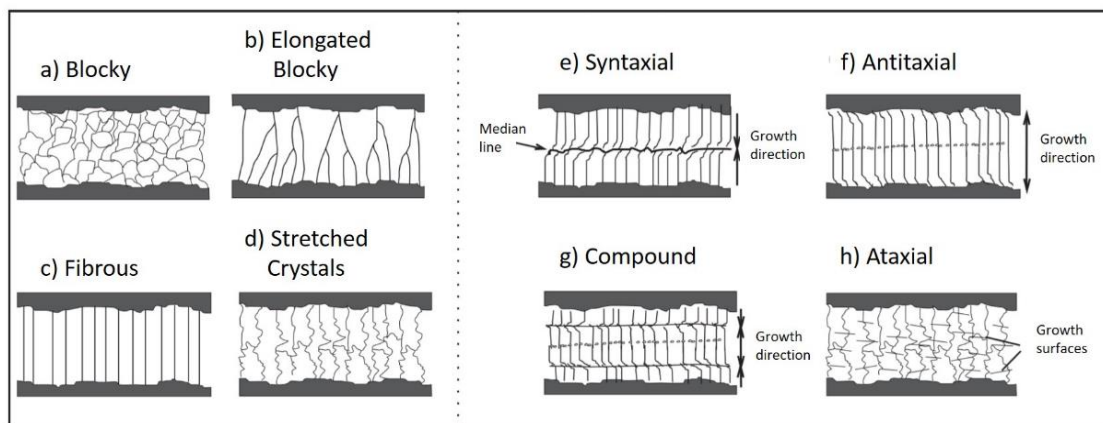


Figure 5.6: Schematic classification of vein textures, modified from Olivares et al. (2010).

The initiation and growth of veins occurs via processes that supersaturate the pore fluid with respect to a particular mineral (Wiltshko and Morse, 2001). Different mechanisms of precipitation can produce distinct vein textures, suggesting that these can be used as indicators of the physiochemical processes involved in their formation (Okamoto et al. 2010). Vein textures (*Figure 5.6*) are largely a function of growth competition, i.e. crystal nucleation and growth/kinetics, which themselves are dictated by environmental conditions as described in *Section 5.2.1*. Alongside this, an understanding of the rate of vein opening, opening vector and wall geometry (i.e. width and roughness of the fracture), as well as growth habits of vein

forming minerals (i.e. crystallographic preferred orientation, force of crystallisation and the effects of dislocation densities of seed crystals is also useful (Bons, 2000; Blenkinsop, 2002; Hilgers and Urai, 2002a,b; Bons et al., 2012).

Mineral nucleation (i.e. when two molecules in a supersaturated solution come together) and crystal growth on the fracture wall can only occur if the threshold supersaturation is exceeded. The driving force behind the nucleation process – and ultimately its rate – is determined by the degree of supersaturation (Brown, 2013). Once nucleation occurs, crystal growth becomes dominant as a result of any external changes that may affect the level of supersaturation (i.e. *Section 5.2.1*). Fracture aperture has also been shown to have some control as wider fractures minimise fluid kinetic rates (Tranter et al., 2020), resulting in a lower D_a . Crystals continue to grow until a new equilibrium is reached and may be locally affected by growth competition (e.g. causing a reduction of the number of actively growing grains and a coarsening of the microstructure away from the fracture wall (Hilgers et al., 2004)).

Vein textures may show either homogeneous nucleation and fluid overgrowth, producing blocky veins (*Figure 5.6a*); epitaxial growth on crystal surfaces forming the fracture walls producing fibrous, elongated blocky, and stretched crystal veins (*Figure 5.6b-d*); or heterogeneous nucleation crystal surfaces to produce syntaxial, antitaxial, compound or ataxial veins with pseudo-fibrous texture (*Figure 5.6e-h*) (Bons, 2000; Oliver and Bons, 2001; Okamoto et al., 2010; Olivares et al., 2010; Bons et al., 2012). Blocky veins are generally considered to form from highly supersaturated fluids, perhaps reflecting crustal conditions where flow rates are high relative to the precipitation rate or where seismicity induces a large pressure drop (e.g. Rimstidt and Barnes, 1980; Fournier, 1985; Bons, 2001; Okamoto and Tsuchiya, 2009). Epitaxial veins are considered to form from lower saturation levels and have been cited as being the result of both diffusion-related processes (e.g., Fisher and Brantley, 1992; Wiltschko and Morse, 2001; Okamoto et al., 2008) as well as advective processes (e.g. Barker et al., 2006). It has also been suggested that euhedral growth veins may remain open over several seismic-interseismic cycles, as fluid pressures remain high enough to prop open the fracture and precipitation rates are slow, whereas continuous crack-seal veins seal during each interseismic period due to faster precipitation or fracture collapse (Oliver and Bons, 2001). Since sufficient evidence is arguably lacking for many of these interpretations, this study (and subsequent research that may come as a result) aims to aid the interpretation of what thermodynamic and chemical conditions - and at what rates - these textures are most likely to form.

5.2.3 Controls on the Rate and Volume of Precipitation

As introduced in *Section 5.1* and *Section 5.2.1*, the growth rate of hydrothermal minerals depends upon a range of factors including the degree of disequilibrium (i.e. difference and rate of change of temperature and pressure) (Arnórsson, 2000; Brown, 2013); fluid flux (Lee et al., 1999; Okamoto and Tsuchia, 2009; Elkhoury et al., 2013) and fracture dimensions (i.e. length

and aperture - Brantley et al., 1990; Elkhoury et al., 2013). The nucleation seed size and orientation, presence of crystal defects and concentration of impurities in the fluid are also important factors to consider in natural hydrothermal systems (Byrappa and Yoshimura, 2001), with Brown (2013) suggesting that mineral colloids require time to form and nucleate and Rimstidt and Barnes (1980) suggesting that the rate of precipitation is linearly related to chemical affinity.

In terms of fracture dimensions, microcracks have a higher D_a , allowing pervasive fluid penetration but healing quickly, whereas larger fractures decrease D_a , channelling more fluid and healing slowly (Brantley et al., 1990; Elkhoury et al., 2013). Fluid flux and resulting precipitation can be affected in multiple ways by the physical properties of the fracture through which it flows. As is the case with permeability and fluid flux (*Chapter 1* - Equations 1.3 and 1.4), precipitation in planar fractures is largely governed by the fracture hydraulic aperture (a_h) as well as the Area/Volume (A/V) and Area/Mass of Fluid (A/M) ratios (Rimstidt and Barnes, 1980), such that:

$$A/V = 2 / a_h, \quad (\text{Eq. 5.4})$$

and

$$A/M = 2V / 1000a_h. \quad (\text{Eq. 5.5})$$

Natural fractures are unlikely to be perfectly planar and will ultimately contain some asperities, and A/V ratios will increase with surface roughness on fracture walls. On the other hand, certain minerals may not act as growth surfaces for silica or calcite, decreasing the expected A/V ratio (Rimstidt and Barnes, 1980). Fracture roughness is also likely to induce some heterogeneity in fluid flow, and as a result minerals may be more likely to precipitate wherever geometry increases flow tortuosity – this may occur both in rough fractures and, in geothermal production areas, within bends in pipes and valves (Brown and Dunstall, 2000). Alongside the dissolution of asperities reducing the fracture aperture, Morrow et al. (2001) partly attributed an order of magnitude permeability reduction in their high-temperature flux experiments through fractured granite to an increase in flow path tortuosity as minerals began to precipitate, however did not speculate as to whether this caused an increase in further rates of precipitation. Whilst it may be supposed that dissolution and precipitation processes could cause further precipitation through increased tortuosity and decreased aperture that will ultimately completely seal a fracture, Morrow et al. (2001) suggest (based on the work of Smith and Evans (1984), Brantley et al. (1990), Fisher and Brantley (1992) and Fisher (1996)), that other factors - such as fracture collapse owing to a drop in fluid pressure or an increase in the relative importance of diffusional processes - ultimately cause fractures to fully seal.

There is evidence to suggest that precipitation rates generally decrease along the length of a fracture during advective flow. As well as likely being a result of increased fracture lengths

decreasing fluid flux (Chapter 1 – Equation 1.3), rate decrease may also be due to a progressive decrease in dissolved mineral concentrations (Lee et al., 1996; Lee and Morse, 1999; Hilgers and Urai, 2002a,b). Such a process is likely to occur in all open natural systems, and ultimately causes an evolution towards self-sealing veins. The length over which this occurs, however, is likely to differ dramatically depending on pressure/temperature conditions, and there may not be a distinction between advective and diffusive flow-related textures over lengths less than tens of metres (Hilgers et al., 2004). Lee et al. (1996) showed using experimentally verified models that flow velocities required to produce a uniform precipitation rate across a fracture increase in proportion to the fracture length at high degrees of supersaturation (> 3), with high flow velocities ($> 10^{-3} \text{ mm}^3\text{s}^{-1}$) required at all but the lowest degrees of supersaturation (< 3).

Regarding the degree of disequilibrium, precipitation will not necessarily occur instantaneously as soon as levels of supersaturation are reached. The minimum fluid volume required for sealing may be estimated by dividing the product of the mineral density and fracture porosity reduction by the concentration of silica in the fluid (Dobson et al., 2003). There is however little understanding of the precipitation kinetics, which can differ under varied subsurface conditions, to give a quantitative estimation of the time and fluid volume required for vein formation (Lee and Morse, 1999). The majority of rate laws describing hydrothermal fluid-mineral reactions indicate that precipitation rates strongly correlate with saturation levels, exceeding the dissolution rate (which does not depend on saturation state) only when the mineral is supersaturated (Lasaga, 1981). Depending on the degree of disequilibrium, fracture sealing during re-equilibration may occur quickly (e.g. over hours to months - Laubach, 1997; Tranter et al., 2020) or slowly (e.g. over tens to millions of years – Lee and Morse, 1999) (*Figure 5.7a*; Rimstidt and Barnes, 1980; Bird et al., 1986; Martin and Lowell, 2000; Okamoto et al., 2010). As an example, Tenthorey et al. (2003) and Morrow et al. (2001) showed (through models and experiments respectively) that a significant permeability reduction may occur in a quartz-water system at temperatures of $\sim 230\text{-}300 \text{ }^\circ\text{C}$ over a few years to a few decades. This timescale is much less than the typical recurrence interval for large earthquakes (which is considered to be in the order of ~ 1000 years - Nicol et al., 2005). Lee et al. (1996) and Lee and Morse (1999) estimated that with a fluid in steady-state flow, with fluid:calcite ratios of $\sim 10^5$ to 10^6 and high levels of supersaturation ($SI > 8$), may only require $\sim 1,200$ litres of fluid to flow over ~ 68 years produce a small, thin vein (~ 2 mm thick, ~ 15 mm wide and ~ 100 mm long). As saturation levels decrease, however (e.g. to $SI < 2$), required fluid volumes and timescales may increase by orders of magnitude (e.g. $\sim 15,000$ litres over $\sim 1,000\text{-}10,000$ years) (*Figure 5.7b*), with timescales potentially increasing to millions of years for veins on a metre-scale (Fisher and Brantley, 1992). At the lowest degrees of supersaturation, extremely high volumes of fluid are expected to be required to seal fractures (i.e. fluid/rock ratios of $\gg 1000$ - Lee et al., 1996; Bons et al., 2000).

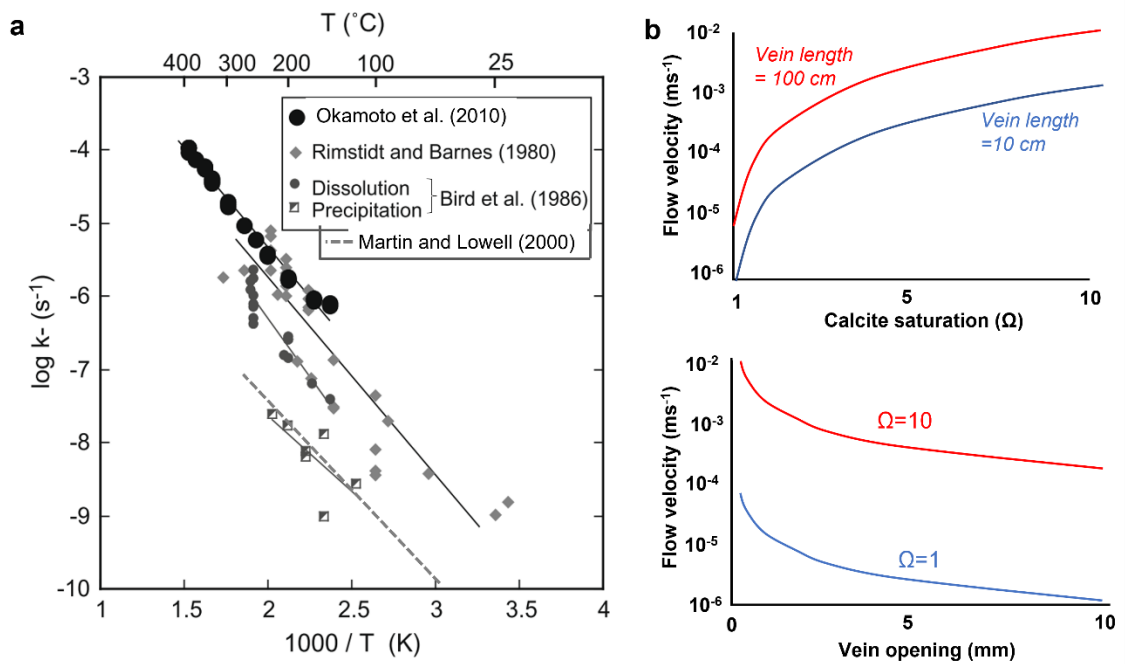


Figure 5.7: a) Quartz precipitation rate constants (s^{-1}) with temperature as estimated by Rimstidt and Barnes (1980); Bird et al. (1986); Martin and Lowell (2000) and Okamoto et al. (2010). b) Calcite saturation and flow velocities required to produce a 10% change in precipitation rate along the length of a 2 mm wide fracture over different lengths; and vein apertures and flow velocities required to produce a 10% change in precipitation rate along the length of a 100 mm long fracture from solutions at different calcite supersaturation levels (after Lee et al., 1996).

As well as factors affecting the degree of disequilibrium, the flux of these high volumes of fluid (i.e. flow rate) has been shown to significantly affect precipitation rates. Fluid flux can be estimated from total vein mass and fluid solute concentrations (Bons, 2001), however the latter are difficult to accurately determine. Furthermore, since vein formation occurs even in stagnant fluids through diffusion (e.g. Fisher and Brantley, 1992), even if fluid flux is known it may not be possible to calculate fluid flow rates and sealing timescales (Okamoto and Tsuchia, 2009). In general, siliceous fracture healing by diffusive flux, or sealing by minerals derived from external fluid, will be greater with depth due to increases in fluid pressure (Fisher and Brantley, 1992). The effect of flow rate on precipitation is mineral-dependent: whilst some minerals precipitate more effectively from static fluids with a low D_a , others (including amorphous silica and calcite) precipitate even where fluid flux and D_a are high (Brown, 2013). Higher rates of silica precipitation have been experimentally observed to coincide with areas of low fluid velocity (i.e. high D_a), with crystal morphology also affected (e.g. producing more elongated crystals in areas of well-directed flow) (Garibaldi, 1980). Mineral dissolution-precipitation reactions are considered to proceed in five generalized steps according to kinetic theory (Bethke, 2007): (1) diffusion of reactants from the fluid to the mineral surface; (2) reactant adsorption onto reactive sites; (3) chemical reaction (breaking and creation of bonds); (4) desorption of reaction products; and (5) diffusion from the mineral surface to the fluid. The reaction is said to be transport-controlled if rates depend on steps 1 and/or 5, and surface-controlled if step 3 limits

precipitation. Much may depend on reaction kinetics for the mineral in question: for example, whilst calcite may precipitate rather quickly, quartz may not precipitate quickly enough to create problems in geothermal production, despite geothermal fluids almost without exception being supersaturated with respect to silica (Arnórsson, 2000; Brown and Dunstall, 2000). Precipitation may be promoted by the decompression of fluid between the reservoir and wellhead, and in the case of calcite also by pH increase (i.e. solubility decrease) due to casing corrosion or removal of CO₂ from the aqueous fluid (Wanner et al., 2017). Predicting the threshold supersaturation is crucial to identifying precipitation rates and the affected fracture length (Tranter et al., 2020).

Precipitation rate calculations for any mineral should account for both nucleation and growth processes. The homogeneous nucleation rate of silica minerals in aqueous fluids (I) is expressed by Equation 5.4 (Steeffel and Van Cappellen, 1990; Lasaga, 1997):

$$I = \frac{2D}{d^5} \exp\left(\frac{-16\pi v \gamma^3}{R^3 T^3 \ln \Omega}\right), \quad (\text{Eq. 5.4})$$

where D is the aqueous diffusion coefficient (e.g. 10⁻⁴ mm²s⁻¹ for silica), d the molecular diameter, R the gas constant, T temperature, Ω degree of supersaturation, v molar volume and γ interfacial energy between the mineral and fluid. For silica, for example, γ decreases with increasing temperature, pressure and Si concentration, and at room temperature is ~46 mJm⁻² for amorphous silica and ~350 mJm⁻² for quartz (Martin and Lowell, 2000).

The rate of dissolution/precipitation (R) of a silica polymorph *i* following nucleation is generally defined by the Equation 5.5 (Martin and Lowell, 2000):

$$R_{\text{SiO}_2,i} = A_{s,i} k_- (Q - K_{i,\text{eq}}), \quad (\text{Eq. 5.5})$$

where A_s is the surface area of the mineral, k₋ is the precipitation rate constant, Q is the activity product and K_{eq} is the equilibrium constant. Positive and negative R values indicate precipitation and dissolution respectively. The precipitation rate of quartz based on experiments performed at <300 °C (Rimstidt and Barnes, 1980) has been defined as in Equation 5.6:

$$k_- = -(M/A_{s,\text{Qtz}}) \ln[(1 - \Omega)/(1 - \Omega^0)]/t, \quad (\text{Eq. 5.6})$$

where M is the mass of fluid and t is the residence time. The reaction rate is therefore proportional to the interfacial area between solid and aqueous phases and inversely proportional to the total mass of fluid. Longer equilibration times are required where time constants are higher. Martin and Lowell (2000) showed that precipitation is a function of initial permeability (which in a geothermal reservoir is expected to be in the order of 10⁻¹⁰ to 10⁻¹⁴ - Lamur et al., 2017), alongside heat transfer coefficient and kinetics. Fast-flowing fluids supersaturated with silica may precipitate relatively little, whereas hotter, lower flux fluids may

precipitate large amounts through conductive cooling at depth (Fournier and Rowe, 1966; Martin and Lowell, 2000). Overall, decreased permeability, crack width and flow rate can together reduce the time taken to precipitate quartz from decades to weeks (*Figure 5.7*).

5.2.4 *Experimental Approaches – A Brief Review*

Whilst many modelling studies considering pressures and temperatures relevant to geothermal systems have been undertaken (Ellis, 1959, 1963; Crerar and Anderson, 1971; Giggenbach, 1981; Fournier, 1989; Brantley et al., 1990; Fisher and Brantley, 1992; Martin and Lowell, 2000; Ghassemi and Kumar, 2007; Griffiths et al., 2016; Ngo et al., 2016; Doubra et al., 2017; Wanner et al., 2017), particularly for quartz, fewer studies have adopted an experimental approach. Of those that have, most are based on dissolution processes alone, largely because the rate obeys the same first-order equation as that of precipitation rate (Lasaga, 1997). None appear to consider the combined effect of pressure, temperature and fluid flow rates in a similar manner to that described in *Section 5.3* that can potentially address the issues of the nature, rate and volume of precipitation simultaneously. Here, some previous laboratory-based efforts to understand sealing mechanisms, rates and achievable volumes are introduced to give context to new high-pressure, high-temperature deformation apparatus designed to carry out experiments in this study. All are discussed further in *Section 5.5*.

Previous experimental studies have investigated silica precipitation rates from a static pore fluid on flat silica surfaces at temperatures <300 °C (Rimstidt and Barnes, 1980; Bird et al., 1986). Few studies consider more natural textures of fractured rock, likely due to the low silica reaction rates experienced under these experimental temperatures (Okamoto et al., 2010). Smith and Evans (1984) investigated the effect of pore fluid, time and temperature on fracture healing, suggesting that at >200 °C microcracks in quartz have geologically short lifetimes. Fractures heal as silica is locally transported by diffusion along the fracture surface, however no change is observed in experiments run without pore fluid, even at temperatures as high as 600 °C.

Several experiments have also been performed whereby a fluid, with controlled flux and saturation levels, has been flowed through simulated fractures to help understand the kinetics of vein formation by advective flow. Investigating calcite, Lee et al. (1996) suggest that flow must be quite rapid ($\sim 10^{-5}$ to 10^{-3} ms⁻¹), or the fluid must be only slightly supersaturated with respect to calcite, to achieve uniform deposition within a vein, proposing also that very large volumes of fluid are required. Lee and Morse (1999) showed that the amount and rate of precipitation for a given vein dimension increases with solution saturation state and decreasing flow velocity. Hilgers and Urai, 2002b illustrated how vein crystal morphology and microstructures of an analogue material (alum) evolves according to complex growth competition, and is dependent on the initial crystallographic orientation and topography of seed crystals. Using the same analogue precipitate, Hilgers et al. (2004) used an advective flow cell to show that fluid flow rate and supersaturation affect vein microstructure such that growth rate is affected by the degree of supersaturation as well as growth competition between

crystals. Hilgers and Tenthorey (2004) and Okamoto et al. (2010) have investigated fracture sealing by quartz in similar flux experiments at higher temperatures (400–800 °C) and 30–40 MPa confining pressure, with the latter showing that ~4 g of amorphous silica can be precipitated in one week from fluids with initial silica concentrations of ~300 ppm (SI≈1.7).

All of the above flux experiments have been shown to lead to a decrease in mineral growth rate away from the fluid inlet as a result of temperature decrease, lower dissolved mineral concentration due to precipitation, and less growth competition. Okamoto et al. (2010) were also able to show that silica polymorphs precipitated in sequence (i.e. nucleation of amorphous silica, followed by opal, chalcedony and then quartz) as saturation levels decreased with precipitation. A high fluid flow velocity and a low supersaturation (i.e. low Damkohler number) increase the potential to seal a vein homogeneously (Hilgers and Urai, 2002a), although it must be noted that low supersaturation levels require unreasonably high fluid volumes to fill natural veins over geological timescales (Lee et al., 1996).

Brown and Dunstall (2000), showed using a water tunnel at room temperatures that precipitation rate and style is dependent on both the hydrodynamic conditions (e.g. flow rates and turbulence, partly dependent on the shape of the void) and particle size of the dissolved mineral, with higher rates of precipitation where flux is low and particle sizes are large. Morrow et al. (2001) found that the permeability of fractured granite decreased by an order of magnitude over several weeks when fluid flow was cycled under a 2 MPa pressure differential, with fracture surfaces showing also increased evidence of dissolution and mineral growth with temperature and time. Fractured granites displayed higher rates of permeability decrease than intact granites at a given temperature, and below 250 °C little change was observed. Experimental studies of mineral growth rates from fluids in fractures have been shown to be orders of magnitude faster than those in porous media (Godinho and Withers, 2018), with dissolution-precipitation rates often fast enough (even at low temperatures) to produce significant permeability changes over timescales of years to decades (e.g. Morrow et al., 2001). Reactive crystal surfaces within less permeable regions grow at a slower rate than that expected from bulk fluid composition, as saturation indices are lower than along main flow paths.

Related experimental studies on fracture mineralisation have also been performed on quartz gouge (Karner et al., 1997) and barite (Griffiths et al., 2016). Using shear experiments at varying velocities (cf. *Chapter 4*), Karner et al. (1997) showed enhanced lithification rates in quartz gouge at elevated temperatures, where friction coefficients increased with both temperature and healing time. Using a combined experimental and kinetic modelling approach, Griffiths et al. (2016) showed that the rate of barite precipitation within open fractures increases dramatically from timescales of months to days as the temperature of the geothermal brine decreases, highlighting the risk of mineral precipitation at geothermal sites, where fluid temperature fluctuates due to circulation through the reservoir rock and fluid mixing around the injection well.

5.3 Design Specifications and Calibration of a High-Temperature, High-Pressure Triaxial Deformation Apparatus

5.3.1 Introduction

A new apparatus capable of reproducing conditions at depth in the Earth's crust has been designed and built in the University of Liverpool's Rock Deformation Laboratory, whereby an internal furnace can heat a fractured rock core up to ~ 750 °C with minimal temperature gradient across the sample, whilst confining pressures can be controlled up to ~ 250 MPa. Fluids with a range of chemistries can be introduced to the sample via an input at either end of the core, and fluid pressures can be carefully held, increased or decreased at a set rate.

The new apparatus design is built upon extensive previous work in developing the wider triaxial deformation apparatus for use in permeability-measuring experiments, first described by Mitchell and Faulkner (2008) and Faulkner and Armitage (2013) amongst others. The triaxial apparatus (*Figure 5.8a*, and described in more detail in *Appendix B (Section B3)*) can perform experiments under confining pressures of up to 250 MPa and pore pressures of up to 200 MPa (both servo-controlled with a resolution better than 0.1 MPa and a measurement resolution better than 0.02 MPa – *Figure 5.8b*). Core samples can also be subjected to a 300 kN axial load, which is generated by a servo-controlled electromechanical actuator, monitored using an internal force gauge (with a resolution better than 0.05 kN) and controlled using displacement or force feedback (Faulkner and Armitage, 2013).

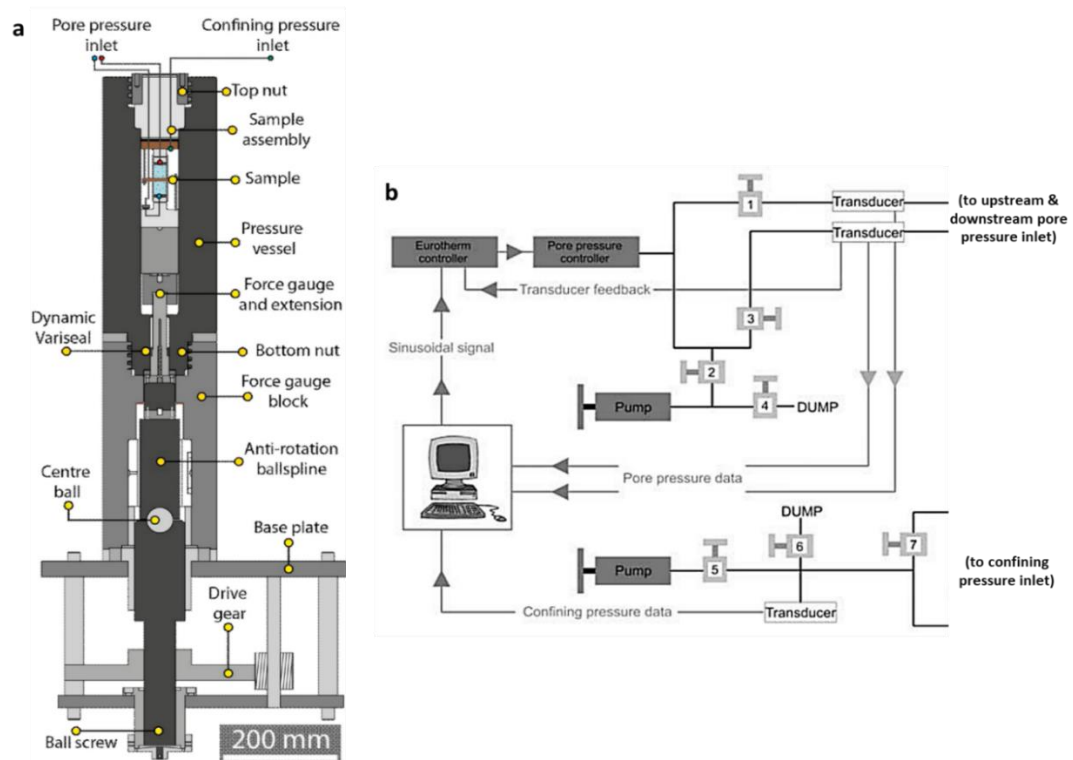


Figure 5.8: a) Schematic drawing of the Faulkner triaxial apparatus within which the new sample assembly is designed to sit (after Allen et al., 2020). b) An illustration of how confining and pore pressures are introduced, controlled and measured (after Mitchell and Faulkner, 2008).

The new sample assembly as described in this chapter is based upon original designs made by Daniel Faulkner, Dan Tatham and Gary Goughlan. Original technical drawings of assembly components are presented in *Appendix C*. Wherever modifications or additions have been made to these, the details and justification will be explained in the text.

Proposed experimental techniques for which the assembly is designed to be used (*Section 5.4*) are in part based on experiments in Armitage et al. (2013), whereby CO₂-saturated water was flowed through a porous sample of a known permeability at a set rate in order to measure the impact of fluid chemistry on permeability at depth. Using an experimental setup as detailed in *Figure 5.9*, a fluid flux of 0.15 cm³hr⁻¹ through a sample with a permeability of 1.5 x 10⁻²⁰ m² at an effective pressure of 25 MPa resulted in an 8-fold increase in permeability, which the authors attributed to dissolution of the host rock by the CO₂-saturated fluid. Experiments proposed here aim to use similar techniques to investigate how mineral-saturated fluids may promote precipitation, on the grounds that Armitage et al. (2013) have shown that supersaturated fluids can be generated and used in triaxial experiments.

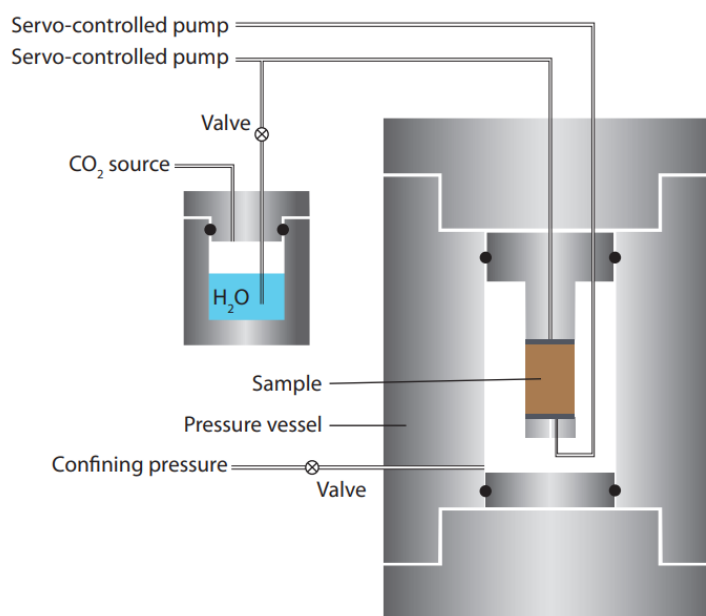


Figure 5.9: Experimental setup used in Armitage et al. (2013) to investigate the impact of fluid chemistry (supersaturated fluids) on rock permeability.

This section describes the fundamental background to the design of the sample assembly containing the new furnace, as well as detailed methodology used in making it, as well as the process used to calibrate temperature. An overview of the design is given in *Section 5.3.2.*, with greater detail regarding particular design specifications, material properties and key considerations documented in *Section 5.3.3*. Finally, an overview of the principal experimental setups that can be used to address the key issues outlined in *Section 5.2* are discussed in *Section 5.3.4*. An instructional guide to setup and use, as well as supplementary information regarding the design, is also provided in *Appendix C (Section C5)*.

5.3.2 Overview of Design

The sample assembly (*Figure 5.10* and *Figure 5.11*) comprises an internal furnace (a hollow alumina ceramic tube wound with kanthal wire (*Section 5.3.3.1*)), insulated with alumina wool and housed in a stainless-steel canister that is capped at both ends by macor plates (*Section 5.3.3.2*). One of the upper plates houses the connections for the furnace wiring and power inputs that allow a current to flow and produce heat (*Section 5.3.3.3*). Two axial pistons, with internal bores to allow pressurised pore fluid access to the upstream and downstream ends of the sample, insert into the inner bore of the furnace, to which the sample is affixed using a copper jacket (*Section 5.3.3.4*); the lower piston is fixed and the upper able to move axially to allow for deformation during experiments. The assembly is designed to fit within a pressure vessel (*Figure 5.11*), where argon gas provides the confining pressure. To prevent the vessel reaching excessive temperatures and provide a barrier in case of any vessel failure (*Section 5.3.3.5*), a series of cooling rings – comprising a hollow tract around which cold water can continuously circulate – have been added to the outside of the vessel, all of which is housed in a steel-framed rig (*Section 5.3.3.5*).

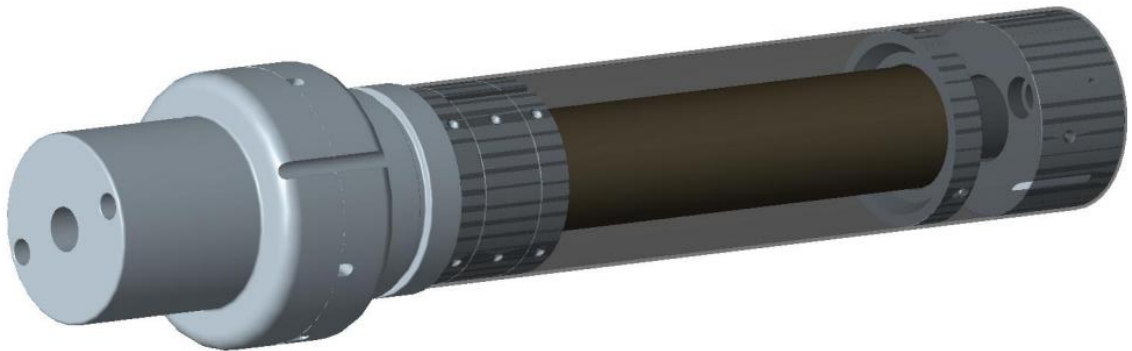


Figure 5.10: Graphical representation of the constructed assembly. The external aluminium canister has been made transparent to allow the internal furnace, MACOR® plates and Inconel baseplate to be visible. Image produced by Gary Coughlan.

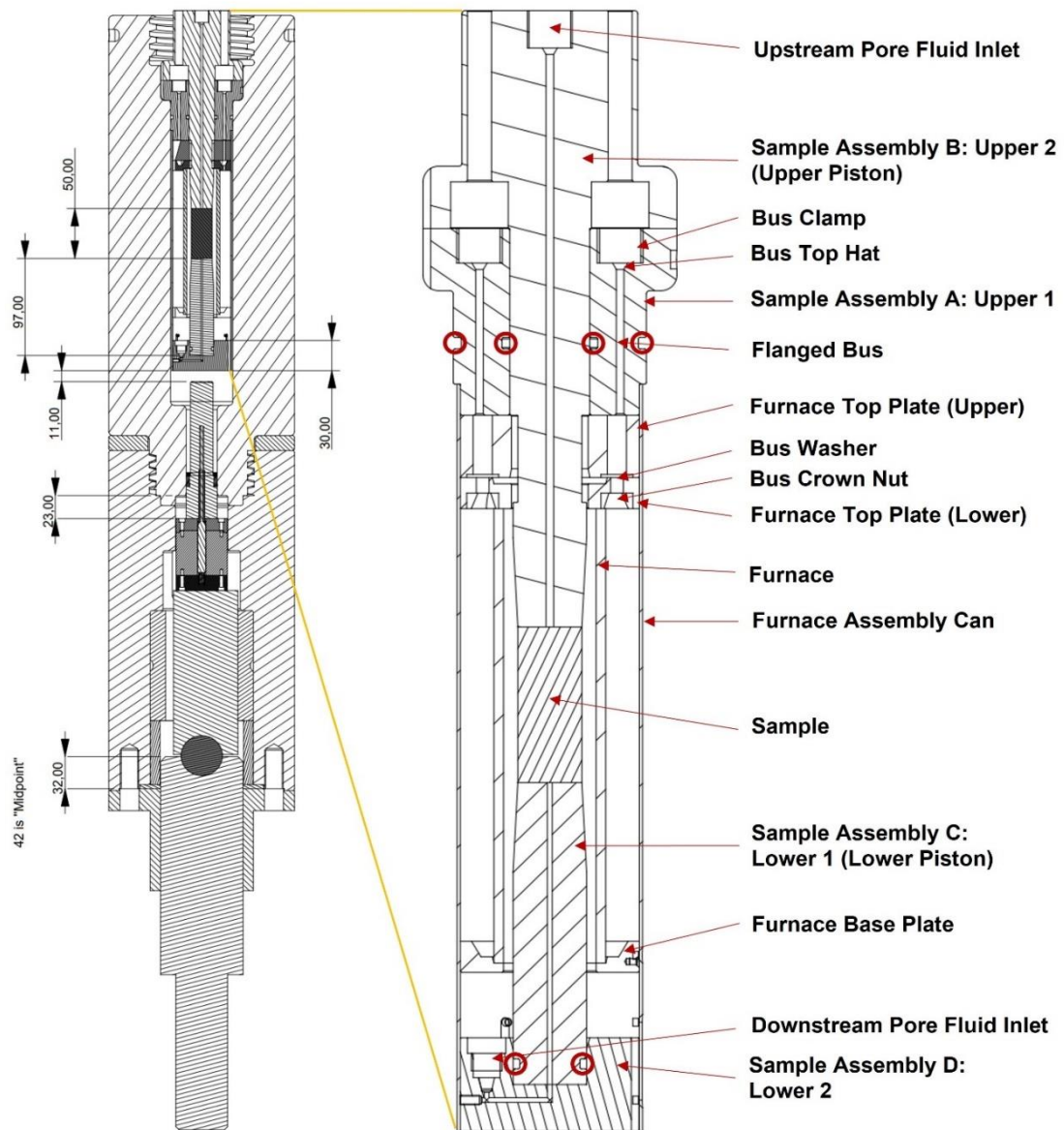


Figure 5.11: Technical drawing of the sample assembly within the ‘HY2’ pressure vessel, with dimensions in mm providing an indication of scale. Blown up section details key parts of the assembly. Red circles indicate key sealing areas. Originally drawn by Dan Tatham; modified by the author plus Gary Coughlan and Daniel Faulkner.

5.3.3 Design Specifics

5.3.3.1 Furnace

The furnace windings are made by winding coils of kanthal wire around an alumina tube and fixing it in place with ceramobond, the properties of which are detailed in *Appendix C– Table C2.1*. High temperature, machinable alumina was used for the main tube, which has an outer diameter of 35 mm and an inner diameter of 28.5 mm. Its high temperature resistance (maximum temperature 1800 °C) and limited thermal expansion ($0.8 \times 10^{-6} \text{ K}^{-1}$) make it a suitable choice for its purpose, while low thermal coefficients ($\sim 0.92\text{-}0.95 \text{ WmK}^{-1}$) allow suitable transfer of heat from the outer windings inwards to the sample. The tube was cut to the required length of 145 mm using a Rexion diamond saw at the University of Manchester (*Figure 5.12*).

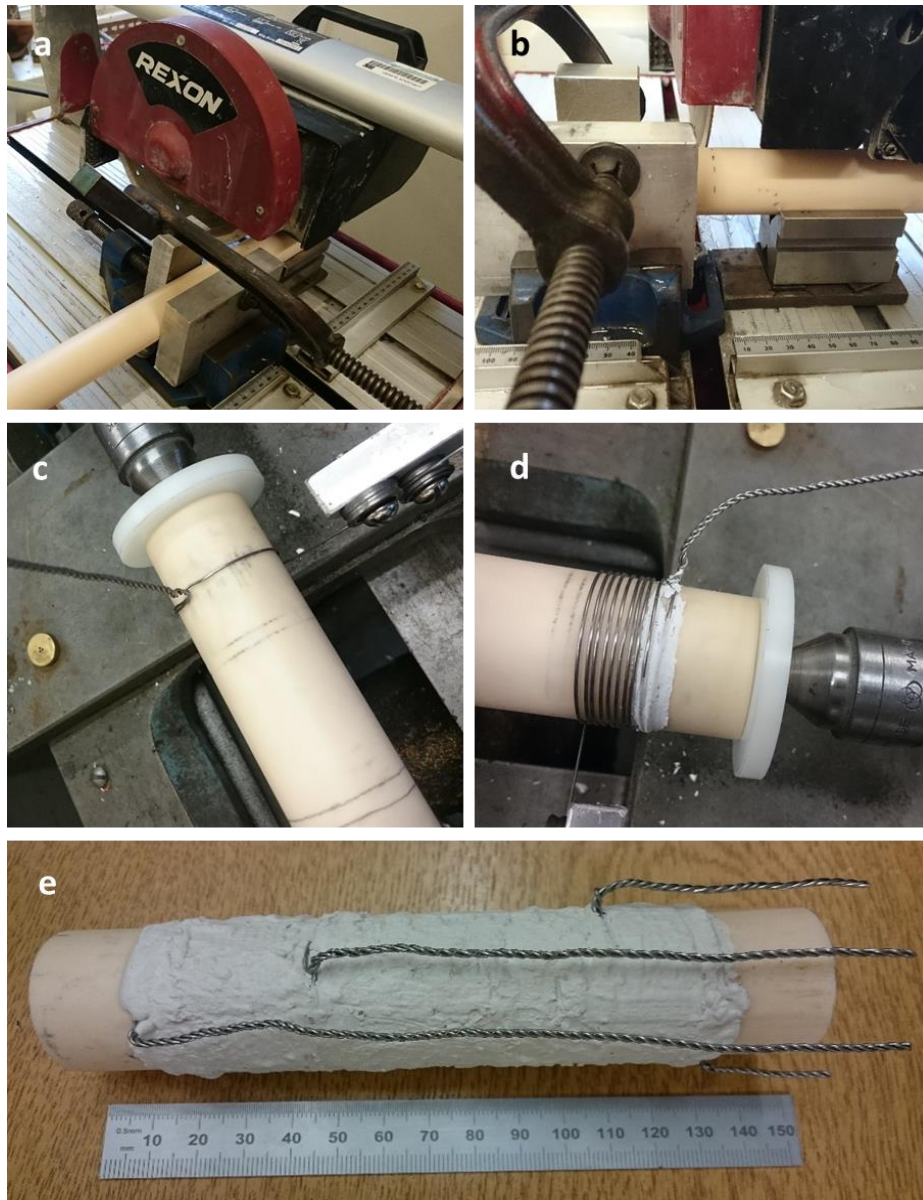


Figure 5.12: Photographs showing furnace preparation at several stages: a) and b) show how the alumina tube was cut using a diamond saw; c) and d) show how kanthal wire was coiled around the alumina tube and held in place with ceramobond, and e) shows the finished furnace with three wire coils, the measurements of which are outlined in Figure 5.14.

Kanthal - an FeCr alloy - was chosen over molybdenum wire (which has been used in other internal furnaces such as within the Paterson rig at the University of Manchester) due largely to its lower linear coefficient of thermal expansion (α) ($14 \times 10^{-6} \text{ } ^\circ\text{C}^{-1}$), meaning that its resistance remains relatively constant during changes in temperature (Figure 5.13). Molybdenum, by contrast, has a much higher coefficient of $4.53 \times 10^{-3} \text{ } ^\circ\text{C}^{-1}$. Its high yield strength means that its cross-sectional area remains consistent during the coiling process, where tensile loads may be experienced (Sandvik, 2012). Its high resistivity means that the wire has a larger cross section than if alternatives such as molybdenum were used; whilst this means that a shorter length of wire can be applied to the same area, it also likely increases the durability of the wire (Sandvik,

2012), allowing more heating-cooling cycles. One disadvantage of using this material is that it may have a high starting resistance compared to molybdenum, hence may require high voltages to provide sufficient current at lower temperatures. For an internal furnace within a gas rig, this may result in flashovers and insulation problems, amongst other issues that are discussed in *Section 5.3.3.5*.

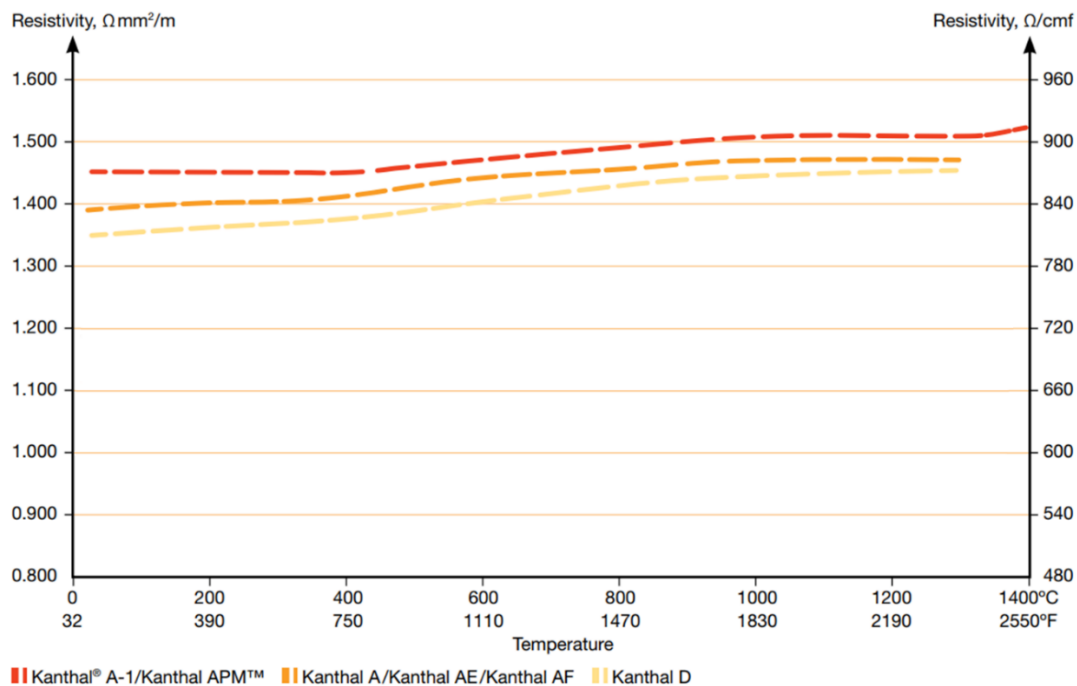


Figure 5.13: A plot illustrating kanthal wire resistivity, indicating that there is minimal change with temperature due to its low alpha coefficient (after Sandvik, 2012).

Three sections of kanthal coil were made (*Figure 5.14*); this allowed for voltage to be independently controlled using variable resistors in order to provide an even heat distribution across the cored sample. The amount of current that is drawn is controlled by the resistance of the winding (since other properties remain the same (*Appendix C Table C2.1*) this is a function of its length) and determines the power. The central coil forms around half the total length of furnace winding (*Figure 5.14*); its higher resistance therefore produces more heat in this area for the same voltage. The bottom and top windings comprise incrementally less length of wire (*Figure 5.12*); since heat will have a tendency to rise through the internal furnace, this arrangement provides a moderate amount of heat to the base of the sample and less still to the top. The outer windings of each coil are tightly twisted with an additional loop of kanthal (*Figure 5.14*): As well as securing the coil in place, this ensures that the electrical feed to the winding has three times the cross-sectional area and therefore one third of the resistance, meaning that this feed to the furnace coils will not get as hot as the rest of the winding.

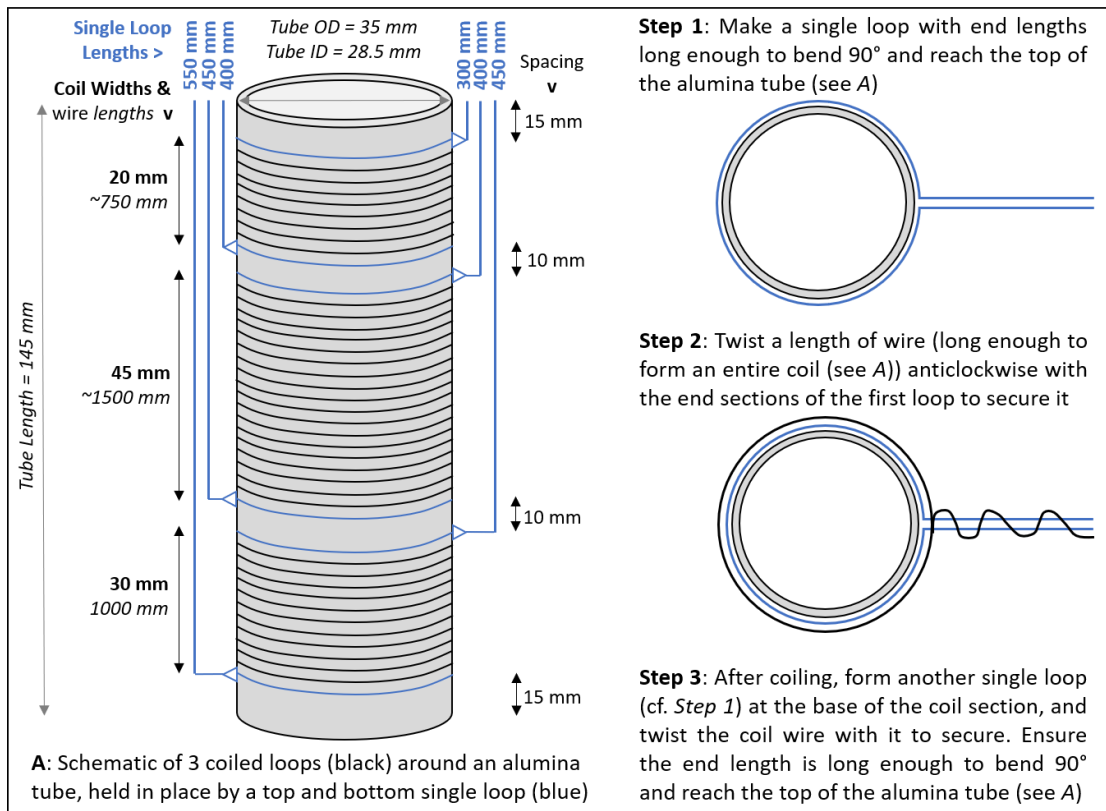


Figure 5.14: Schematic illustration of the furnace and windings, indicating the length of each coil, the spacing between coils, and steps taken during the winding process.

Describing the furnace winding process in more detail, an end loop of 300 mm kanthal wire was positioned around the alumina tube in a tight clove hitch knot, one sixth of the total length from the top. Kanthal wire on the reel was fed through these two protruding wires and twisted together using a brass plug. This twisted wire forms the power input to the top furnace winding. Using a specially designed pulley jig to keep the wire in tension, kanthal wire on the reel was coiled tightly around the alumina tube, ensuring the spacing between each coil was even throughout (at ~1 mm), and that at no point one area of the coil touched another. Alumina cement (Ceramobond; Appendix C Table C2.1) was applied periodically to ensure no movement of the wire took place during tight winding, however the initial clove hitch knot was tight enough so that this was unlikely. Mixed with water at a ratio of 100:14, the cement paste was applied with a paintbrush so as to just cover the diameter of the wire. To speed up the drying time, which at room temperature is ~1 hour, a heat gun was used over cemented areas for ~1 minute, at a distance of ~30 cm to prevent bubbling and cracking of the cement. Once the appropriate length was coiled (Figure 5.14), a lower end loop of 350 mm kanthal wire was positioned around the alumina tube in a tight clove hitch knot, and together with the kanthal wire on the reel, protruding wires were twisted together using a brass plug. A tight, stable coil results if kanthal wire on the reel has been wound in the correct direction. Alumina cement was applied to the entire coil and dried with a heat gun. Finally, protruding ends of twisted wire were cut to length so that, when folded parallel to the alumina tube and pointed towards the

top, ~10 mm of wire extended beyond the top of the tube. These extensions form the input and output power connection to the furnace winding. The above steps were then repeated for the middle and lower coils, using progressively longer end loops towards the bottom of the furnace. Once fully prepared, the furnace was thoroughly dried and stored in a vacuum oven at 80 °C.

5.3.3.2 Sample Assembly

The sample assembly (Figure 5.15) comprises the internal furnace, capped at both ends by MACOR® plates which keep the furnace in place and hold in a layer of tightly packed alumina wool insulation. This setup is contained within a stainless-steel canister, into which the top and bottom Inconel pistons are inserted: one fixed, the other able to move axially. This section describes key elements of the design, the construction process and reasons for materials used.

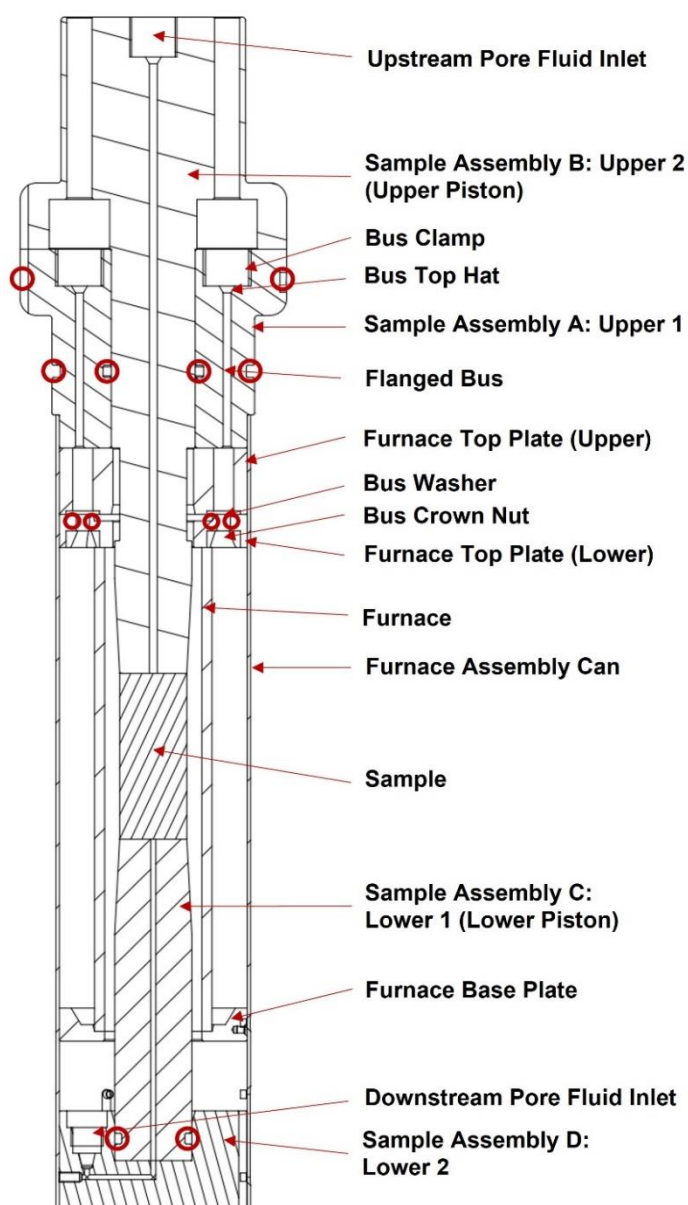


Figure 5.15: Technical drawing of the sample assembly, reproduced from Figure 5.11. Drawn to scale, where total length of the assembly is 360 mm. Red circles indicate key sealing areas. Originally drawn by Dan Tatham; modified by the author plus Gary Coughlan and Daniel Faulkner.

Table 5.1 describes each assembly component in turn, highlighting their purpose, key design features and rationale behind chosen materials (which are described in greater detail in *Appendix C– Table C2.2*). The principal material used within the assembly (Parts A-D – *Figure 5.15*) is Inconel – a nickel-chromium alloy. Inconel is a high-strength material that is capable of withstanding high surface pressures as well as being corrosion-resistant (Special Metals Corporation, 2007). This makes it suitable for being subjected to high confining pressures as well as high axial loads during compressional experiments. Since a gas confining medium at high pressures could exploit even minor imperfections, ensuring the surface remains free of corrosion pitting is crucial in maintaining safe practise (see *Section 5.3.3.5*).

The furnace assembly can and the flanged bus, as well as most screws, comprise stainless-steel. This material was chosen due largely to its malleability and machinability for thin parts (1-4 mm diameter for the can and flanged bus respectively) and, once again, the low risk of corrosion. Neither of these parts are load bearing and therefore do not require the high strength of materials such as Inconel.

The plates that hold the furnace in place within the can, and provide an upper and lower containment for the alumina wool insulation, are made from MACOR®. MACOR® is the trade name of a mica glass ceramic developed by Corning (Corning, 2012), with a composition of ~46 % SiO₂, 17 % MgO, 16 % Al₂O₃, 10% K₂O, 7 % B₂O₃ and 4 % F. The material allows for the machining of complex design shapes, such as required here for the recesses and bores for the banana jacks, the side groove for the pore fluid pipework and the recessed diameters for holding the furnace tube (see technical drawings in *Appendix C*); MACOR® offers tight tolerances capabilities (up to +/- 0.013 mm for dimensions, < 0.5 µm for finished surface and up to 0.013 µm for polished surface). Furthermore, MACOR® remains mechanically stable (i.e. does not creep or deform) at high temperatures (~800-1000 °C), and its coefficient of thermal expansion matches most metals and sealing glasses (Corning, 2012).

PEEK (Polyetheretherketone) was used for washers and nuts on the bus connections that transfer electrical current – and as a result heat - from power cables to the furnace coils. PEEK is a semicrystalline thermoplastic with excellent mechanical and electrical resistance properties retained to relatively high temperatures (The Plastic Shop, 2011; DM Dielectric Manufacturing, 2019). It is therefore well suited to its application in electrically insulating the conducting parts of the bus connections that transfer the current.

Parts of the aforementioned bus connections (i.e. the top clamp) are made from brass. Brass is a copper-zinc alloy that is malleable, corrosion-resistant and thermally and electrically conductive. It is used in this application as it has sufficient electrical conductivity properties so as to allow current to pass through it without significant resistance, therefore causing very little heat generation in this area and ensuring that as much current as possible is transferred directly to the furnace windings.

Insulation around the furnace, in place to ensure as much heat as possible remains directed internally towards the sample and not outwards into the gas-pressurised vessel, is tightly packed alumina wool. The wool comprises fibres with a diameter of 2-4 μm , with a composition of $\text{Al}_2\text{O}_3 + \text{SiO}_2$. The wool's low thermal conductivity, low bulk density and low heat capacity make it an excellent insulator for this purpose, whilst its mouldability and compressibility means that it can be shaped around the furnace windings and pore fluid pipework relatively easily without causing damage, and tightly packed to ensure maximum efficiency. It can also be heated and cooled quickly with little effect on its lifespan (Insulationet, 2019).

Seals, indicated by red circles in *Figure 5.15*, are critical in ensuring that a) there is no leakage of confining pressure to the atmosphere, and b) there is no communication between the confining pressure medium and pore pressure medium. These seals are rings made from viton, and sit within tapered recessed tracks within the Inconel sample assembly parts. Viton is a fluoroelastomer best suited for use in high-temperature and extremely corrosive environments, retaining its elasticity for ~ 48 hours at ~ 316 $^\circ\text{C}$ or for $\sim 3,000$ hours at ~ 232 $^\circ\text{C}$ (Viton, 2017). Section 3.4 explores how even as higher temperatures are reached adjacent to the sample, the areas around the viton seals are not raised significantly above room temperature, yet for safety reasons it is important to leave room for error. Together these properties ensure that the viton rings provide an excellent seal under all expected conditions (at higher temperatures within an argon confining medium).

Table 5.1: Descriptions of fundamental parts of the sample assembly as shown in Figure 5.15, in terms of their material composition and purpose of design.

Part Name	Description: Principal Material and Purpose of Design
Sample Assembly A: Upper 1	Inconel: Houses the bus connections for power input to the furnace coils. Designed to semi-permanently fix to the assembly can and remain in place within the vessel, meaning that electrical feeds do not need to be connected and disconnected for each experiment. A viton ring seal provides a barrier between confining and atmospheric pressure zones.
Sample Assembly B: Upper 2 (Upper Piston)	Inconel: Comprises the upper piston, through which is a bore for upstream pore fluid inlet. Can be removed separately from part 'A' to allow the removal of the sample (affixed to the upper piston via a copper jacket and sealing ring) whilst keeping part 'A' in place within the pressure vessel.
Sample Assembly C: Lower 1 (Lower Piston)	Inconel: Contains a central bore for downstream pore fluid input. Designed to be easily removable with sample assembly 'B' when a sample is affixed via a copper jacket and sealing ring. A viton ring seal at the base of the piston provides a barrier between pore and confining pressure zones.

Table 5.1 (cont.)

Part Name	Description: Principal Material and Purpose of Design
Sample Assembly D: Lower 2	Inconel: An internal bore provides an inlet for downstream pore fluid, which is input via a coiled 1/16" high pressure pipe and high pressure nut. This piece transfers axial force from the axial driver / spacer within the pressure vessel to the lower piston and sample, and is designed to allow the release of the lower piston whilst remaining in place within the vessel.
Furnace Assembly Can	Stainless-Steel: Houses the furnace and surrounding alumina wool insulation. Provides connection points for MACOR® top and base plates, as well as Sample Assembly 'A', via 3mm grub screws.
Furnace Top Plate (Upper)	MACOR®: Houses the bus connections providing power to the furnace windings. The MACOR® insulates this electrical current from the rest of the assembly.
Furnace Top Plate (Lower)	MACOR®: Provides an upper centralising lock to the furnace tube whilst also holding in the alumina wool insulation.
Furnace Base Plate	MACOR®: Provides a lower centralising lock to the furnace tube whilst also holding in the alumina wool insulation.
Flanged Bus	Stainless steel: 6 shafts transition fit into the 2 mm central bore within Sample Assembly part A. Widest section forms a sealing surface for a viton O-ring ensuring that confining pressure is held below the bus connection area. The 2 mm diameter shaft houses all other Bus parts.
Bus Clamp	Brass: Interference fits onto the end of the 6 flanged bus parts ensuring good contact to transfer electrical current. On the side is threaded to allow an M2 threaded brass bar forming the ends of furnace power cables (Figure 5.23) to be securely affixed.
Bus Crown Nut	Peek: Forms a lower insulating surface for bus connections, which fit within an 8 mm diameter recess within the Sample Assembly part A. Contains a central bore through which the flanged bus fits.
Bus Top Hat	Peek: Forms an upper insulating surface for bus connections, which fit within an 8 mm diameter recess within the Sample Assembly part A. Contains a central bore through which the flanged bus fits.
Bus Washer	Peek: Forms an insulating surface for bus connections, which fit within an 8 mm diameter recess within the Sample Assembly part A. Contains a central bore through which the flanged bus fits.
Banana Clip	Brass: One end threads onto an M2 threaded end of the flanged bus parts, whilst the other inserts into the banana jack that is housed within the Upper Furnace Top Plate. Forms part of the connection between the electrically conducting bus parts and the furnace wiring.

Table 5.1 (cont.)

Part Name	Description: Principal Material and Purpose of Design
Banana Jack	Brass: Inserts into the 10 mm bore within the Upper Furnace Top Plate, into which the banana clip at the end of the composite bus connection is inserted. Forms a connection between the electrically conducting bus parts and the furnace wiring, which is secured into the jack via an M3 grub screw.
Sealing Rings	Stainless Steel: When forcibly affixed using an Arbor press, the sealing ring provides a crucial seal of the copper jacket that houses the sample onto the upper and lower pistons by pinching the malleable copper.

The following paragraphs describe the process of constructing the sample assembly from scratch, for which it is advised that the technical drawings of individual components within *Appendix C*, as well as *Figure 5.15*, are referred to for greater understanding. To construct the assembly, the furnace is first affixed to the upper and lower MACOR[®] plates via grub screws. The protruding triple-twisted wires that form each end of each coil are then attached to banana jacks, which fit inside the recesses within the MACOR[®] top plate. The banana jacks insert into the upper MACOR[®] plate to form a composite piece (*Figure 5.16a,b*). The plates and furnace can then be screwed into the stainless-steel canister using M3 grub screws, which are filed down to ensure there is no protrusion from the external part of the can that could scratch the inside of the pressure vessel as it is inserted. Prior to packing the can with alumina wool insulation, the downstream pore fluid pipework is fed through the notch in the MACOR[®] plates, ensuring that it is kept away from the furnace windings to prevent accidental current flow to the pipework. Insulation is packed as tightly as possible into the can around the outer edge of the furnace by removing the lower baseplate (*Figure 5.16c*), before the lower MACOR[®] plate is screwed back in place.

Sample Assembly A (Upper 1) is prepared for insertion into the top of the canister and upper MACOR[®] plates (i.e. the banana jacks) by placing a viton top seal onto the external recessed track and assembling the Bus Connections and securing them in place within the relevant bores. Viton ring seals are first inserted into the recessed diameter within the bores in Sample Assembly A to ensure that confining pressure does not escape upwards past this point. The Bus Connection comprises the flanged bus, onto which the peek crown nut is affixed to the lower sealing end before threading on a banana clip, and the peek bus washer, top hat and brass bus clamp are affixed to the other end. Together, these parts ensure efficient flow of current from the input cables via the brass clamp and flanged bus, through the banana clips into the banana jack and the kanthal wire coils on the furnace. The composite Sample Assembly A (Upper 1) and Bus Connection part is then screwed into place, at the same time feeding through the pore fluid pipe (*Figure 5.16d*).



Figure 5.16: a) The completed furnace, with kanthal wire coils fixed using ceramobond to the alumina tube, attached to the two upper MACOR® plates via banana jacks; b) Detailed view of the banana jacks that sit within the two upper MACOR® plates; c) View from the bottom of the assembly of the furnace within the stainless-steel can, surrounded by tightly packed alumina wool insulation (note the pore fluid pipe is held firmly in place against the canister to the left of the photo to prevent interaction with the furnace); d) Side view of the assembly: the furnace and MACOR® plates have been fixed to the external canister using grub screws, as has the top Inconel piece. The top piston has been inserted through the top of the assembly down through the bore of the furnace tube. The lower base plate (not fixed in place in this photo) is connected to the pore fluid pipe.

The lower end of the pore fluid pipe is hard soldered to a ¼" high-pressure connection, before being coiled to allow axial movement once it is attached to Sample Assembly D (Lower 2). Sample Assembly C (Lower 1) (i.e. the lower piston), which also contains a lower viton seal, slots into the recess within this part. Sample Assembly D connects via the slots in the can using 6 mm long M3 screws, thereby accommodating up to ~13 mm of axial movement. The upper end of the pore fluid pipe, which protrudes at least ~300 mm from the top of the sample assembly to allow connection within the rig, is also hard soldered to a ¼" high-pressure connection. At this stage, the whole of the assembly with the exception of Sample Assembly B (Upper 2) can be fed into the pressure vessel, where it sits on top of a 'spacer' that ensures minimal free space within the pressure vessel to minimise the volume of gas required to provide confining pressure. In terms of orientation, the assembly should align with the bores in the pressure vessel (above the top seal around Sample Assembly A) designed to accommodate the electrical feeds (*Section 5.3.3.5*). *Figure 5.16d* also shows the Sample Assembly B as part of the whole assembly; once in the pressure vessel this feeds down into the central bore of the Sample Assembly A and further into the inner bore of the furnace, ensuring that the pore fluid and confining pressure pipework feeds through the smaller bores either side of the central one, and is designed to be inserted into the rest of the assembly with a configured sample affixed (see *Section 5.3.3.3*). A modified design for a collar to sit within the recessed diameter area of Sample Assembly B (Upper piston) is also shown in *Figure 5.17*, which aims to reduce the amount of gas convection occurring in the upper part of the sample assembly that may occur at higher temperatures.

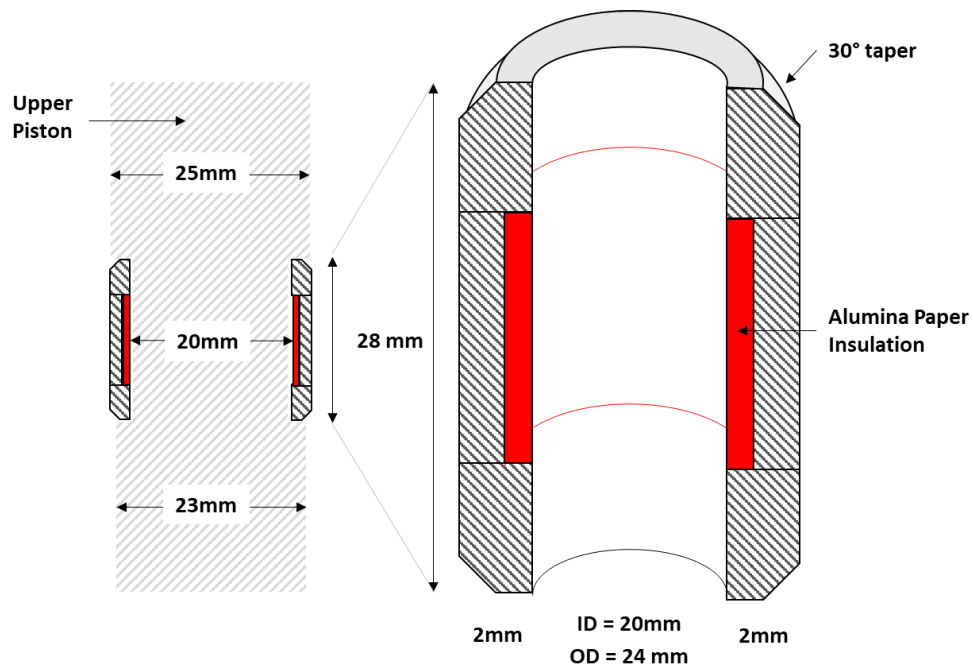


Figure 5.17: Schematic illustration of the new design of a collar to fit the recessed area of the upper piston in Sample Assembly B in order to limit gas convection around the piston (Upper 2).

5.3.3.3 Sample Configuration

The sample assembly has been designed to accommodate a core sample with a diameter of 20 mm and a length of 50 mm (plus a 2 mm disc at each end). Different sample lengths could be used in future applications through modifications of the spacer at the base of the vessel. A calibration sample was made for testing purposes with a diameter of 20 mm and length of 54 mm. The material chosen for this core was MACOR® (see *Appendix C– Table C2.1*), largely due to its suitable thermal properties: its thermal conductivity ($1.46 \text{ Wm}^{-1}\text{C}$) is similar to that of rock samples likely to be used after calibration, and volume change during heating ($9.3\text{-}12.6 \times 10^{-6} \text{ }^\circ\text{C}^{-1}$) is insignificant. It is also a machinable ceramic, which allowed a central 2 mm diameter bore to be drilled through the core's centre (along its axial length; *Figure 5.18*), for the purpose of allowing the passage of thermocouples to measure the temperature profile across the sample during calibration (*Section 5.3.3.4*).

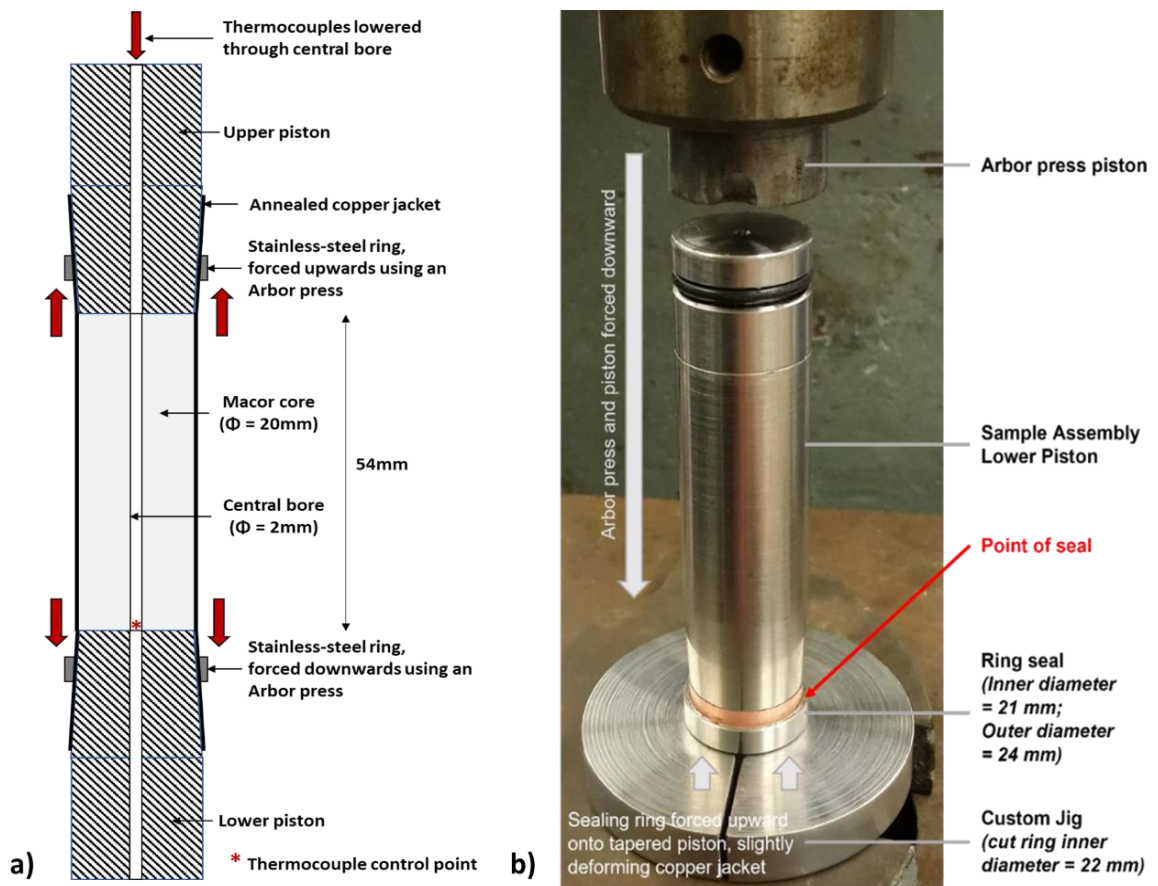


Figure 5.18: Schematic illustration of the sample configuration for calibration, showing a) hollow MACOR® core within an annealed copper jacket, affixed firmly to the upper and lower pistons of the sample assembly using stainless-steel sealing rings. b) Photograph showing the ring jig used to firmly push the rings over the copper jacket onto the tapered piston.

In terms of sample configuration within the assembly, the core must first be placed within a copper jacket, the ends of which are then firmly pushed onto the tapered ends of the upper and lower pistons of the assembly using an Arbor press and a custom jig, comprising a hollow steel ring cut into two with a central bore of ~ 22 mm (i.e. greater than the core sample plus copper jacket, but less than the outer diameter of the sealing ring (Figure 5.18). Care must be taken to ensure that the copper jacket is not punctured during this process. The use of slightly tapered stainless-steel rings increases the sealing capabilities – this is a particularly important consideration when using argon gas as a confining medium, since even the smallest gap between the jacket and piston could cause a leak and pressure drop.

The resulting composite piece comprising the top piston, jacketed sample and lower piston can then be inserted into the assembly within the vessel (Figure 5.19), ensuring that the lower piston passes the lowermost O-ring seal before sealing the assembly in the vessel with the top nut.

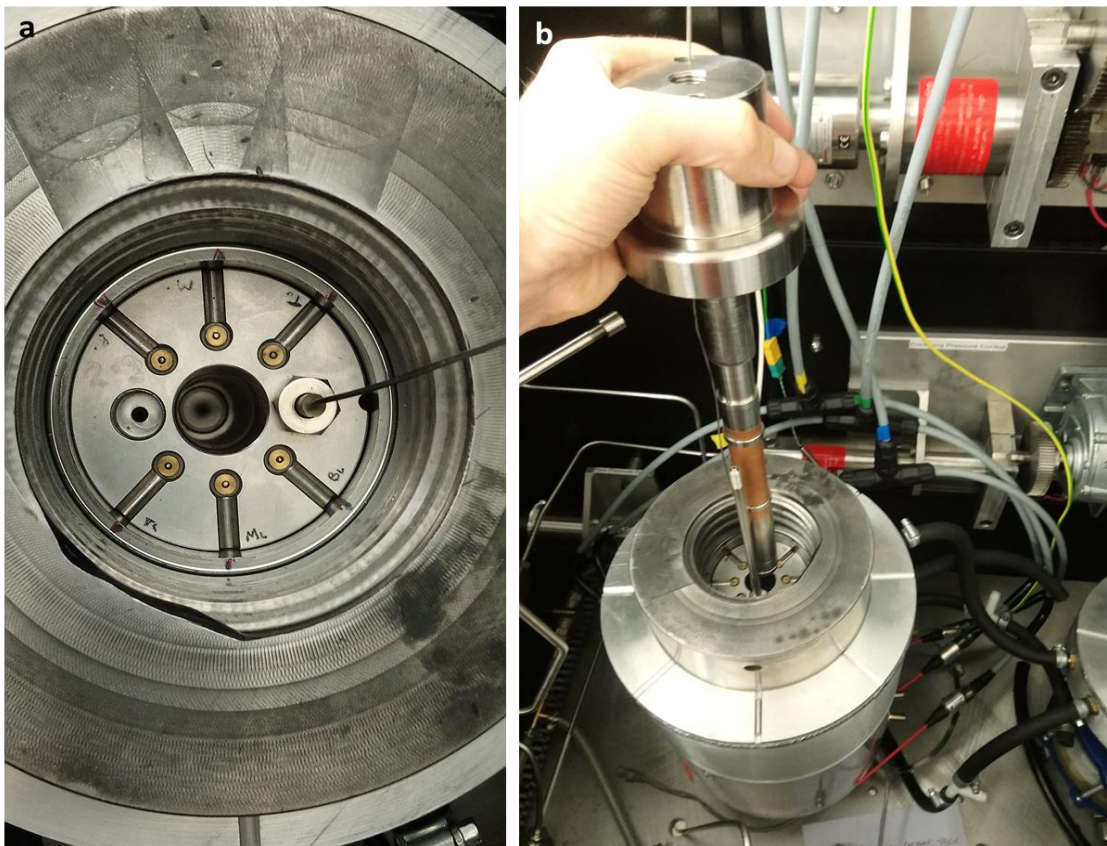


Figure 5.19: a) Top-view photograph showing the constructed assembly (without Sample Assembly B in place) within the pressure vessel. The tracks on the upper side of Sample Assembly A, through which insulated rods forming the ends of power cables are later fed (See Section 3.3.4), and the brass Top Bus Clamps are clearly visible around the central bore. Downstream pore fluid input is on the right, whilst confining pressure pipework feeds through the bore on the left. b) Photograph showing how Sample Assembly B, with jacketed sample and Sample Assembly C attached as in Figure 5.18, is inserted into the central bore, which is then held in place within the pressure vessel by the top nut.

5.3.3.4 Temperature Control

The internal furnace within the sample assembly is connected to a voltage control unit via a split cable, coupled to a brass rod that is threaded into the crown nut of the sample assembly (Figure 5.15 in Section 5.3.3.2) (Figure 5.20). The control unit, which as described was designed for use with a set of Chromalox knuckle band heaters by John Hakes, comprises a 240 V mains input, relayed to three variable resistors, solid state relays (SSRs) and power regulators, which control the voltage supplied to each of the three coils of kanthal winding (Figure 5.21). It also incorporates safety and monitoring features: thermal cut-out switches and controllers for monitoring internal temperatures via thermocouples. This section describes the setup of the control unit and connecting parts and rationale behind some of the specific intrinsic components. It must however be noted that due to various issues experienced during testing and calibration (Section 5.3.4) – as will be discussed - the required setup has not yet been finalised.

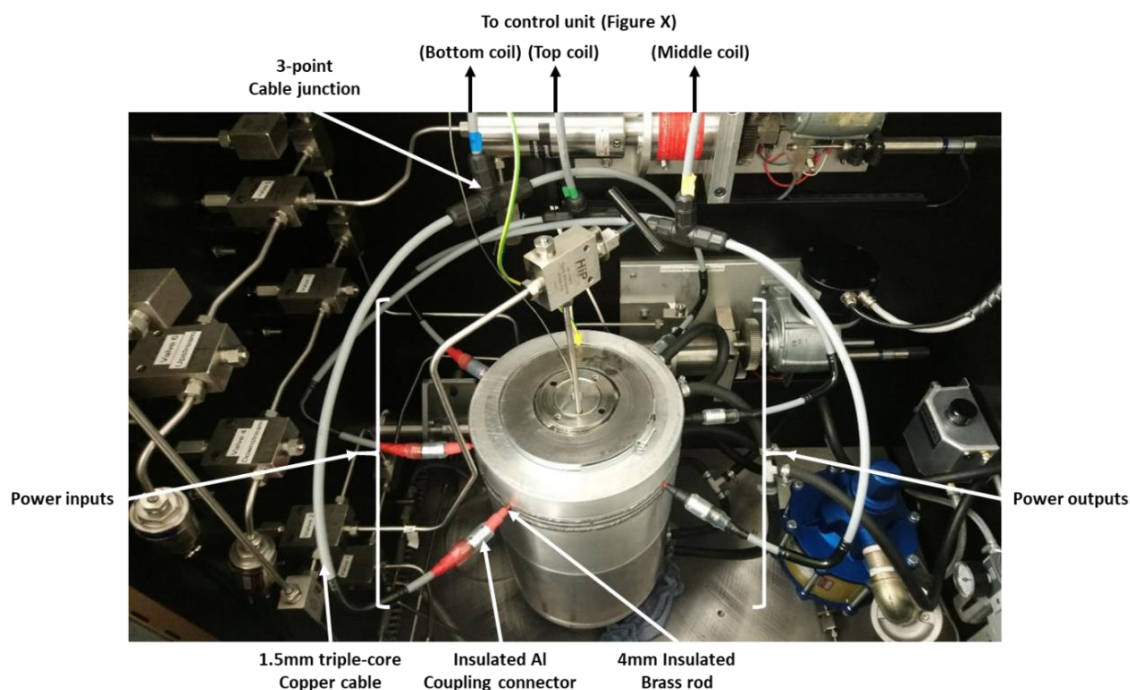


Figure 5.20: Photograph of the pressure vessel and surrounding high-pressure pipework showing the electrical feeds connected up.

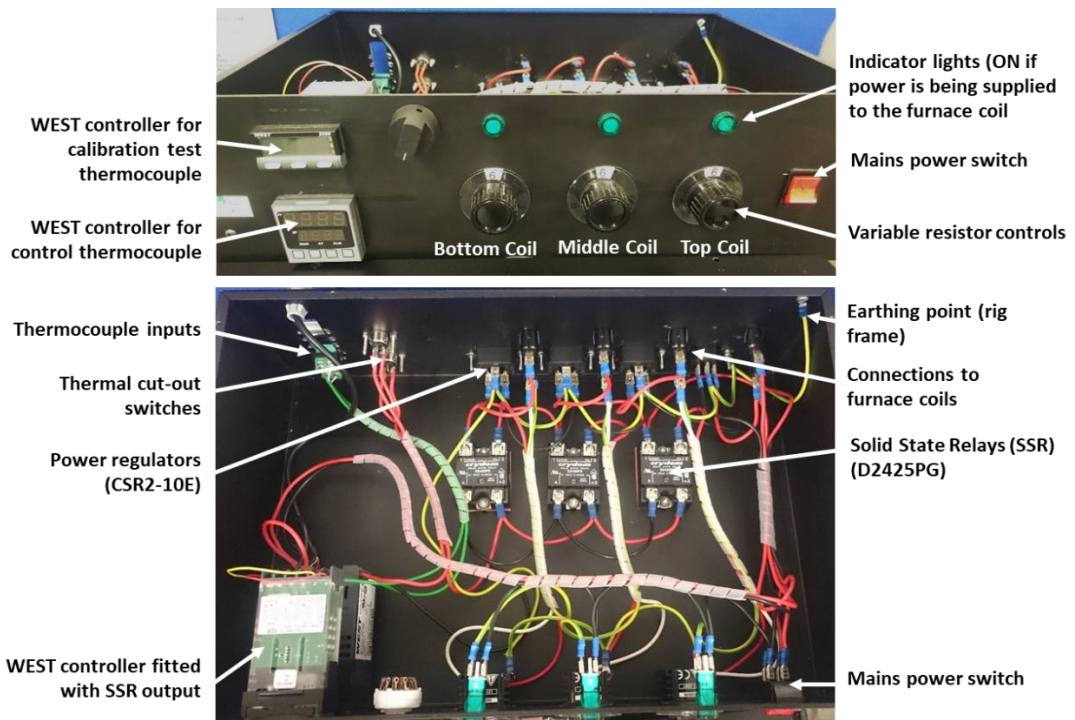


Figure 5.21: Photographs of the temperature control box (top = front panel view; bottom = internal view).

As described in *Section 5.3.3.3*, six crown nuts within the sample assembly form the connection points for electrical inputs and outputs for the three furnace coils. Each connection point is designated according to *Figure 5.22*, such that the live input for a particular coil is directly opposite the neutral output (black). A 16 A-rated, 1.5 mm triple-core copper cable (electrically shielded to prevent current from interfering with transducer readings, with a rating more than sufficient to provide enough power to each furnace coil) forms the main connection between the furnace and the control unit. A Schurler 1038 SW APSA forms the connection with the control unit, and the cable is split into live and neutral feeds via triple junction block connectors (*Figure 3.9*). Each cable is connected to the crown nuts via an insulated aluminium coupling connector and 3mm diameter brass rod, threaded into the crown nuts as depicted in *Figure 5.23*. A threaded connection allows for simple disconnection whenever the assembly is removed from the vessel. The brass rod and aluminium coupling connector have sufficient electrical conductivity properties so as to allow current to pass through to the rod and furnace windings without significant resistance. All elements are individually electrically insulated using a ~1 mm thick layer of heat shrink, with an outer layer of ~3 mm thick heat shrink surrounding the composite piece.

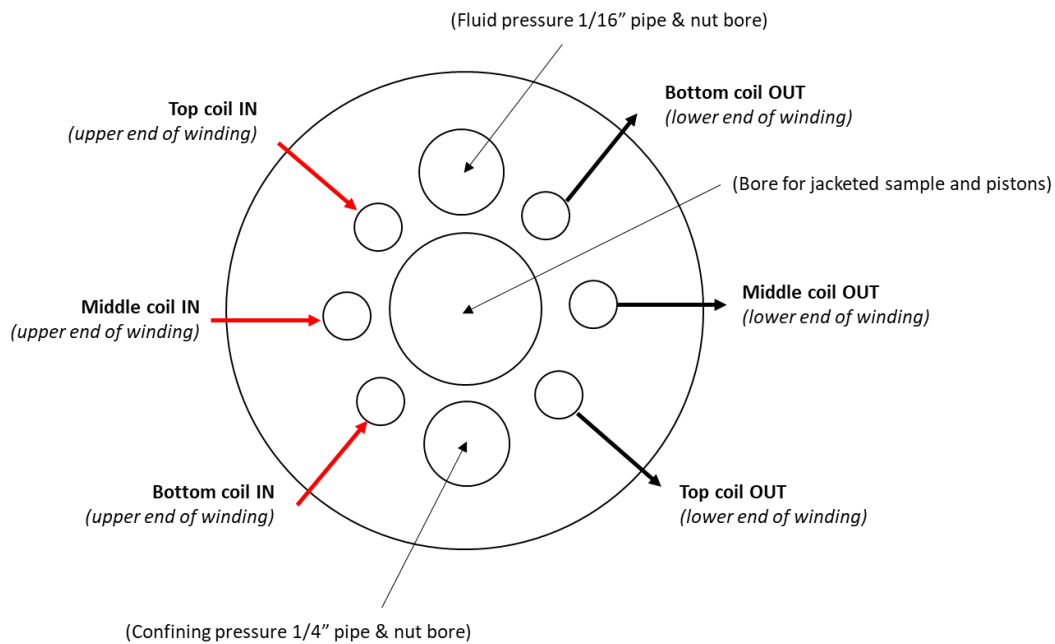


Figure 5.22: Schematic diagram showing a top view of Sample Assembly A, illustrating how connections are made between the temperature control box and the sample assembly.

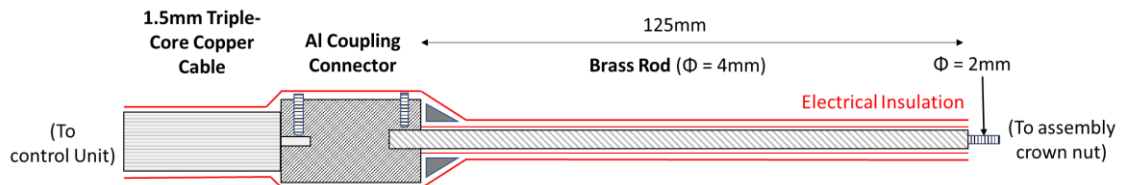


Figure 5.23: A sketch illustrating the connecting end of the furnace power cables that thread into the brass Top Bus Clamps within Sample Assembly A.

Each component of the control unit described below forms a circuit as depicted in *Figure 5.24*. Two WEST controllers (model P6100; *Figure 5.25*) are panel indicators that allow the control, measurement and display of process information, such as temperature. Each have a single thermocouple input and single configurable Solid-State Relay (SSR) output. The SSRs switch AC load from the WEST controller from off to on when the control current reaches a particular value. This AC load is transferred via the power regulators and a set of 5 A fuses to the furnace. 3 SSRs receive voltage from the power input, but only communicate this to the furnace windings when voltage is on the other side (i.e. from the WEST controller and power regulators).

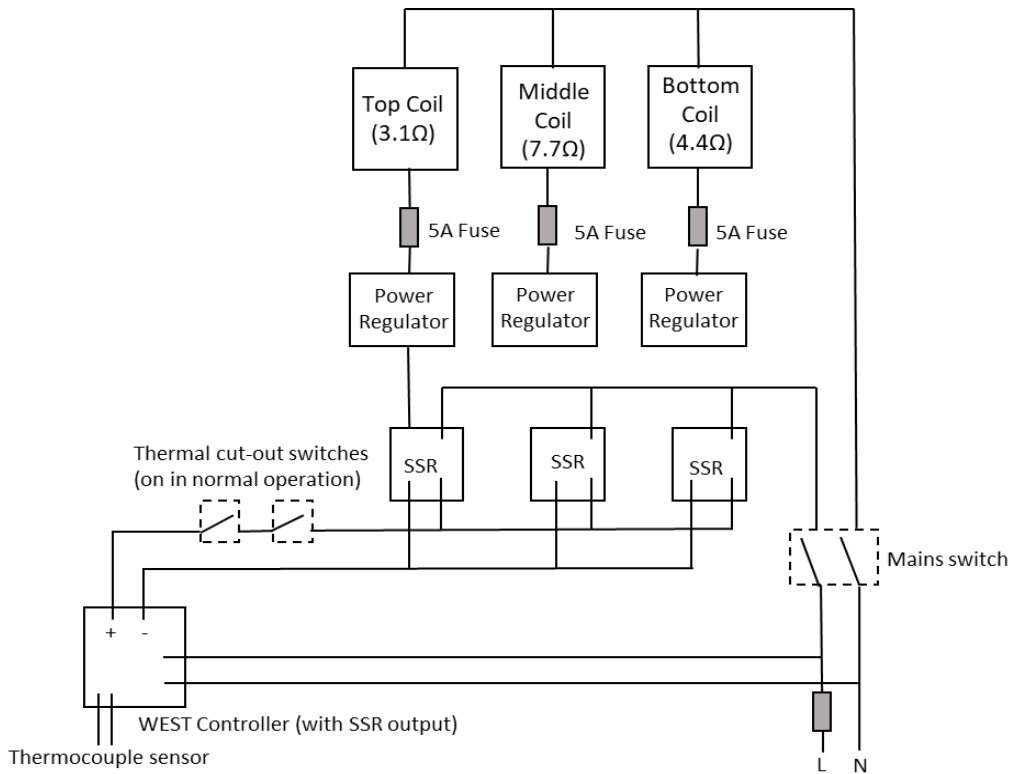


Figure 5.24: Electrical circuit diagram of the temperature control unit.



Figure 5.25: The P6100 WEST Controller (image from RS Components, 2020).

Upon testing and temperature calibration of the furnace (Section 3.4) a problem was encountered in that all 5 A fuses were blown upon the furnace temperature exceeding $\sim 100\text{ }^{\circ}\text{C}$. To help understand why this occurred and what modifications could be made to the control unit, some calculations are presented in *Appendix C (Section C3)* that form the basis of a redesign of the temperature control unit. Based on these calculations, it was decided that an isolating transformer could be added in order to step the mains voltage down from 240 V to $\sim 60\text{ V}$. As part of this change, it also proved necessary to replace the existing power controllers, which operate at 240 V and were rated to 10 A, with thyristor power controllers that can operate at 60 V and up to 15 A. At the time of writing the modifications to the temperature control unit are still in progress and the new design requires testing and further calibration. As

a result, *Sections 5.3.4* onwards are only able to discuss results produced up until this issue occurred. An outline of the new front panel for the control unit (*Figure 5.26*) shows how in future the current supply to each furnace winding will be carefully monitored to ensure similar issues are not repeated.

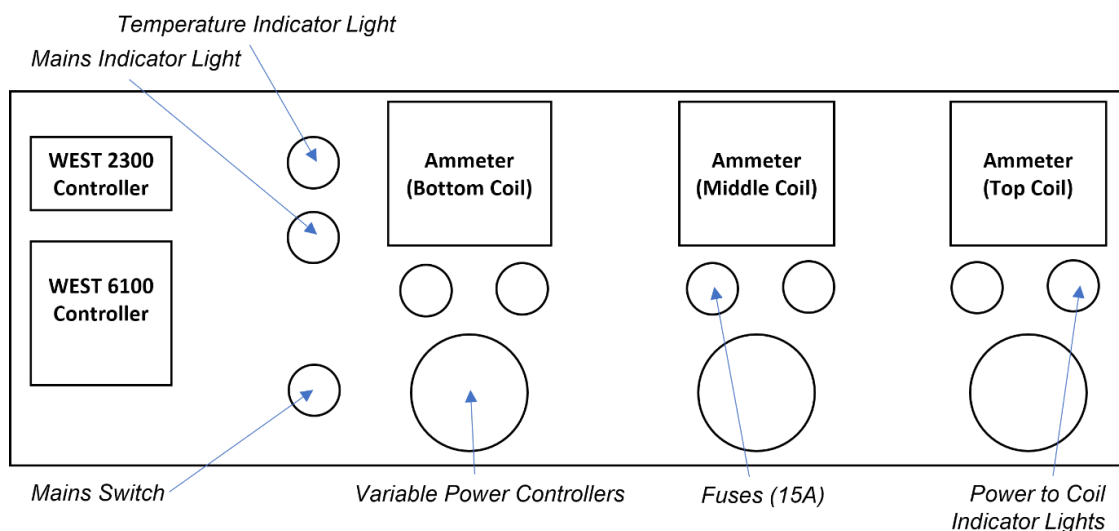


Figure 5.26: Diagram depicting the design of a new front panel for the temperature control unit, where the current flowing through each furnace coil can be easily monitored.

5.3.3.5 Cooling and Vessel Safety

It is important to keep the vessel cool during heating of the samples to very high temperatures. The vessel is made from a hot-worked tool steel (H13) that undergoes a significant reduction in its yield strength above 500 °C. Consequently, the vessel is cooled externally using aluminium ring jackets, hollowed with tracks to allow circulation of water to absorb and dissipate emitted heat. A cooling baseplate also thermally isolates the vessel from the temperature-sensitive force gauge below. For cooling efficiency, two separate aluminium cooling jackets were made, with the upper jacket also divided to allow entry of electrical inputs into the internal furnace (*Figure 5.27* and *Figure 5.28*). Water is fed into hollow tracks within the aluminium jackets from a mains valve via a 10 mm internal diameter hose, which is connected to the top of the upper jacket with a hometail to BSP brass fitting. Internal tracks within the baseplate are also connected to the same water input and output feeds as the outer jackets. The design allows constant flow of room temperature water around the entire outer part of the vessel; water is removed at the base of the bottom jacket after being circulated from top to bottom, since the hottest part of the vessel is likely to be between the centre and top. The heat absorption properties of water are such that most of the heat emitted from the vessel should be removed quickly and efficiently when maximum power is applied to the furnace.

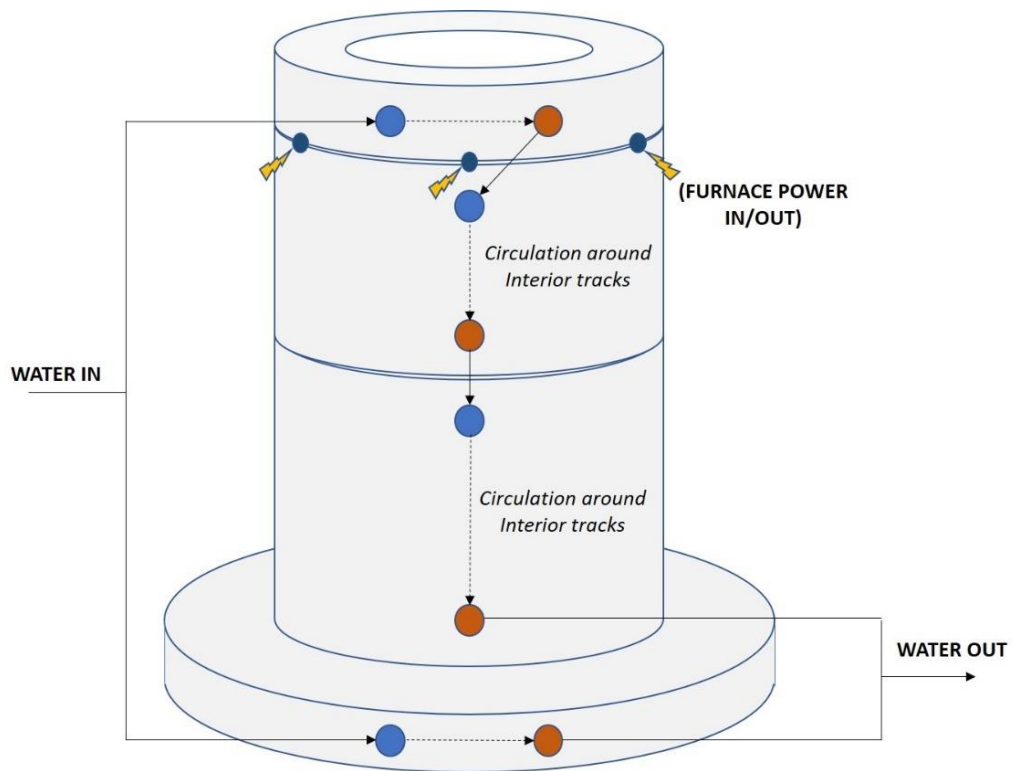


Figure 5.27: Schematic illustration of the cooling jackets and baseplate, showing mains water inputs and outputs either side of interior tracks.

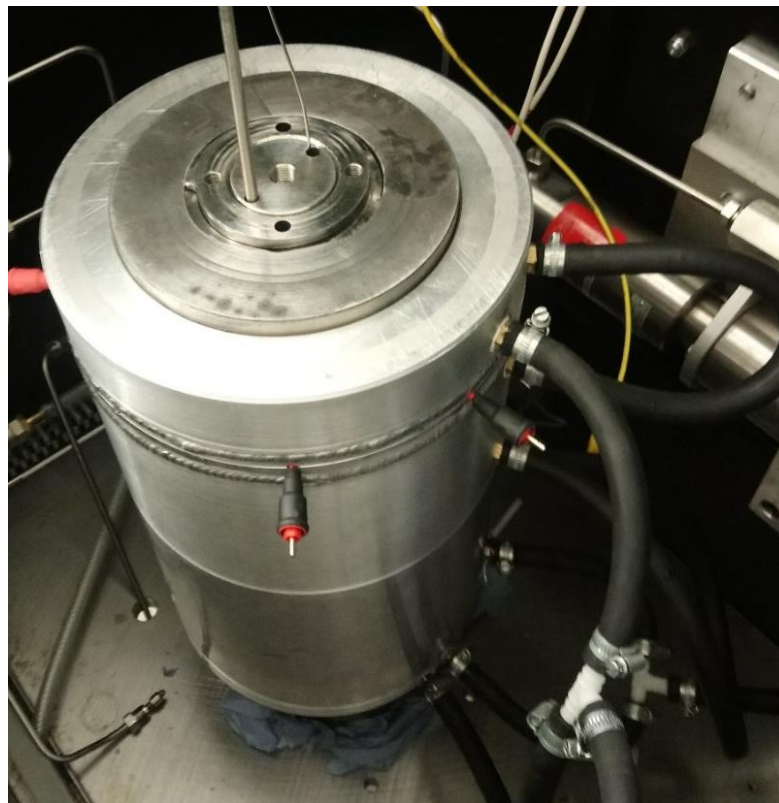


Figure 5.28: Photograph showing the cooling jackets around the pressure vessel and connected to the water mains as depicted in Figure 5.27.

Cooling jackets also factor into safety considerations, since they are the first barrier in case of any vessel failure. This is particularly important when using a gas confining medium such as argon, as is to be used here. Argon has several advantages as a confining medium over common low temperature confining mediums such as silicon oil, the principal one being that it is inert. At high temperatures, silicon oil would likely break down, whilst any confining medium containing oxygen would result in oxidation of parts of the assembly and pressure vessel. However, more importantly, gas confining media also have a much higher compressibility than silicon oil, hence vessel failure would be exploited by pressured gas with a much greater stored energy than with oil.

The compressibility of a gas is defined as the relative change in volume owing to a change in pressure, and can be represented by the Equation 5.7:

$$\beta = -\frac{1}{V} \frac{\partial V}{\partial p}, \quad (\text{Eq. 5.7})$$

where V = volume and P = pressure.

The compressibility factor of argon at 250 MPa and 50 °C is ~160 %, compared to ~13 to ~16 % for silicone oil (for high rates and low rates of pressure and temperature drop respectively) (Maslan and Littman, 1953; Shin Etsu Chemical Co., 2020). Hence the volume increase for argon is likely to be around ten times that of silicone oil under these conditions. Given the high compressibility of argon gas, the build-up of overpressure is not a primary safety concern. Whilst it is possible for overpressure to occur from one of the pressure generators used in priming the compression system, the gas booster is only capable of producing a maximum of 120 MPa, whilst the Novaswiss pump has a small volume of 5 cc and hence would raise the pressure very little. However, safety measures have regardless been put in place to prevent excessive confining pressure build-up, as well as to contain any potential explosive activity. A mechanical pressure limit of 200 MPa is set on the air-driven pump, which delivers the confining medium from the reservoir to the vessel. A software pressure limit limiting the user to 250 MPa is set on the control programme. A rupture disc is fitted to an elbow on the confining pressure control pump. The disc is pressure rated to ~300 MPa; should these pressures be reached confining medium will preferentially escape through this area. Each individual component of the vessel (e.g. the pressure vessel chamber and top nut as well as any high pressure pipework and connections – *Figure 5.8*) has been rated to ~400 MPa. Each component was thoroughly checked for any damage (e.g. scratches where stress could concentrate) prior to use. As well as pressure limiters, the vessel has also been fitted with several thermal cut-out switches (limiting the outside of the vessel to temperatures of 50 °C); these aim to prevent adiabatic pressure rises should any issues arise with controlling power to the furnace.

Should any failure in containing confining medium occur during a high pressure – high temperature experiment, damage limitation must be carefully considered. To contain potential explosive activity, aluminium cooling jackets will provide a relatively soft buffer to any failure perpendicular to the vessel sides. A ~50 mm sheet of wood between two 6mm steel plates above the vessel is in place to absorb the kinetic energy of the vessel's top nut, should it fail and be forced upwards. The vessel is housed inside a safety barrier of 6 mm steel plate, sufficient to block any missiles generated as a result of an explosion (which would have already lost energy via the barriers noted in the points above). Ear defenders are to be worn at all times when the vessel is at high pressures, as rapid expulsion and expansion of gas is likely to be accompanied by a loud noise.

5.3.4 Testing and Calibration

The testing stage comprised two stages: pressure testing, to check that the assembly could hold confining pressure; and temperature testing, to check that the voltage control unit delivered power to the furnace as expected. With the sample in place within the assembly, confining pressure was applied incrementally via a gas booster, and LabView monitoring software was used to test the stability of pressure with time. Confining pressure was held for several days at 5 MPa, 10 MPa, 30 MPa and 60 MPa to ensure sealing was successful in each case (*Appendix C – Table C2.3*); numerous failed attempts at sealing were resolved each time by systematically checking three possible leak points: adjusting the sealing rings holding the copper jacket to the tapered pistons (see *Figure 5.16*); tightening the nut attaching the downstream pore fluid inlet pipe to the Sample Assembly D (Lower 2) (see *Figure 5.15*) and tightening the nut attaching the confining pressure pipe to Sample Assembly B (Upper 2) (see *Figure 5.15*).

With regards to testing the connection between the control unit and furnace windings, when the assembly was held under small confining pressure within the vessel (~5 MPa), a multimeter was used to check for any possible electrical shorting routes via the pressure vessel or rig frame, prior to switching on the unit with variable resistor dials switched to near-zero. It was initially important to induce a small temperature increase at low pressure to reduce the risk of overpressure due to adiabatic pressure rise. According to the Ideal Gas Law, any change in the temperature of the argon confining medium will result in a change in pressure that can be calculated using Equation 5.8; a combination of Gay-Lussac's Law, Boyle's Law and Charles' Law:

$$PV = nRT, \quad (\text{Eq. 5.8})$$

where P = confining pressure, V = vessel volume, n = number of moles of gas, R = the ideal gas constant (a product of the Boltzmann constant and the Avogadro constant equating to 8.3 Jkg⁻¹mol⁻¹), and T = temperature.

For calibration of the furnace, temperatures were raised to the desired level (initially 35 °C) at 5 MPa confining pressure, before allowing the pressure to rise adiabatically as predicted by

Equation 5.8. The argon gas booster was then used to further raise confining pressure. The adiabatic rise in confining pressure, if calculated as greater than the target pressure for a given temperature, can be mitigated by manually releasing pressure in small increments via a valve.

Temperature calibrations aimed to work out the relative power required by each furnace winding to achieve the flattest possible temperature profile across the sample. In order to measure this, two thermocouples of different lengths were inserted through the central bore of the upper piston (i.e. the upstream pore fluid inlet). One thermocouple acted as a control, secured so that the sensor measured temperature at the base of the upper piston and top of the sample (Figure 5.29). Another 'variable' thermocouple extended downwards through the sample and to the base of the bore of the lower piston. This thermocouple was designed to be manoeuvred axially through the interior of the assembly to monitor its temperature profile. Since accessing the vessel within its shielding frame would be a safety concern, the variable thermocouple was designed to be manoeuvred via a simple pulley system, with the sensor's position within the assembly determined via a scale viewed through a webcam (Figure 5.30). Several areas of the assembly besides the sample length were key to monitor in terms of temperature (Figure 5.29). Upper and lower seals are made from viton (Section 5.3.3.3), hence this area needed to be monitored to ensure that temperatures do not exceed the material working limit of ~120 °C. Elements of the connections to the furnace are made from peek (Section 5.3.3.3), hence this area could not exceed the material working limit of ~260 °C.

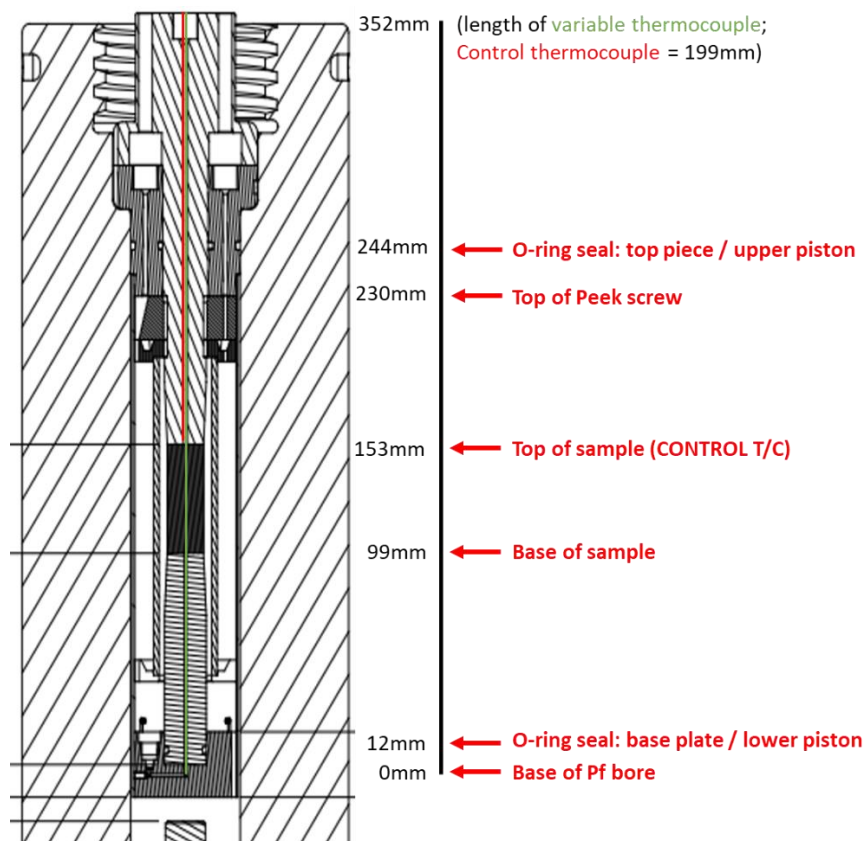


Figure 5.29: Schematic diagram highlighting the key areas to measure temperature with a variable thermocouple, as well as the position of a control thermocouple.

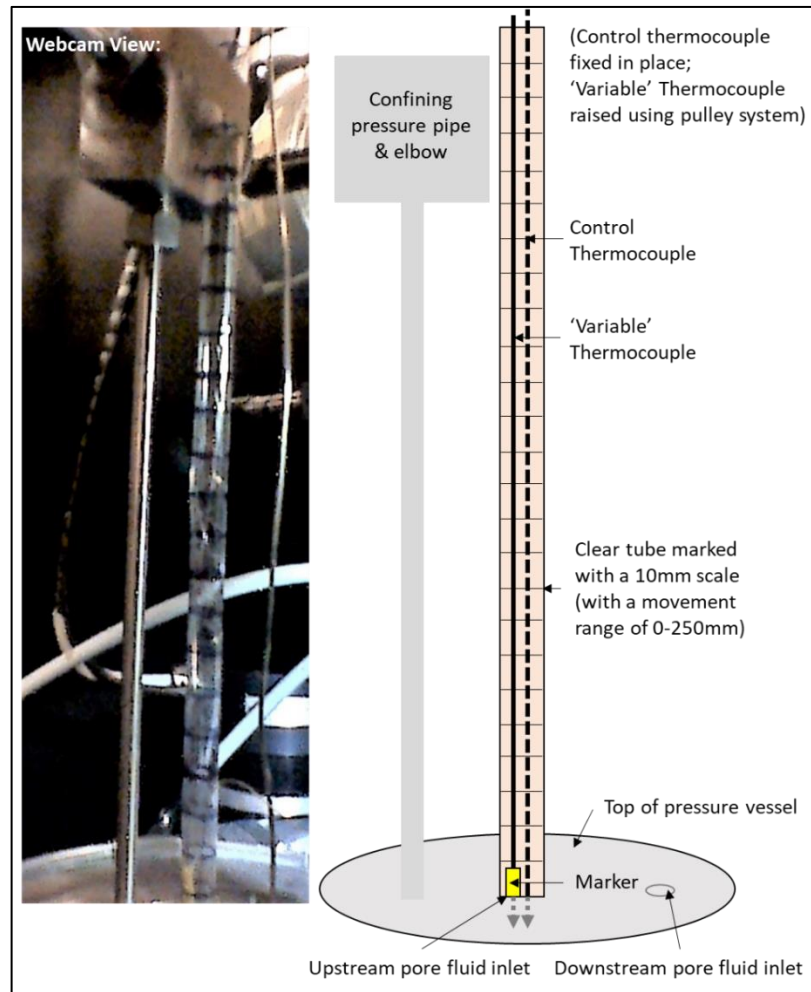


Figure 5.30: A webcam image and schematic representation of the scale used to measure the relative position of the variable and control thermocouples within the sample assembly.

Initially, minimal power was applied to each of the three furnace coils so target temperatures of $<50\text{ }^{\circ}\text{C}$ were measured at the control thermocouple. A temperature ramp of $0.1\text{ }^{\circ}\text{C}\text{s}^{-1}$ was applied via the LabView logging software as an attempt to ensure the target temperature was not significantly overshoot. However, some temperature overshoot ($\sim 8\text{ }^{\circ}\text{C}$) and oscillation ($\pm 4\text{ }^{\circ}\text{C}$) did occur. These problems were largely resolved by adjusting certain parameters on the WEST controller (Section 5.3.3.5). Reducing the power output to 5 % had the effect of creating a shallower ramp of temperature increase upon switching on the power to the furnace. Further improvements to the heating curve were made by adjusting the PID settings; whilst default values are set to $P=10.00$, $I=5.00$ and $D=1.15$, best performance at $<50\text{ }^{\circ}\text{C}$ was achieved with values set to $P=1.00$, $I=0.006$ and $D=1.15$. For a target temperature of $50\text{ }^{\circ}\text{C}$, these settings resulted in just $0.7\text{ }^{\circ}\text{C}$ of overshoot and subsequent minor oscillations of $\pm\sim 0.1\text{ }^{\circ}\text{C}$.

Calibrations performed at $35\text{ }^{\circ}\text{C}$, $44\text{ }^{\circ}\text{C}$ and $52\text{ }^{\circ}\text{C}$ (Figure 5.31; Appendix C– Section C4) show a relatively steady temperature gradient across the sample in all cases, with a $3.7\text{ }^{\circ}\text{C}$ difference in temperature between the top and bottom of the sample at $52\text{ }^{\circ}\text{C}$. In each calibration test, temperatures at the base of the sample are always less than those at the top, suggesting that

in future calibrations slightly more power should be provided to the lower furnace coil relative to the upper two. It is important that the temperature profile across the sample should be as steady as possible in order to prevent unwanted changes in temperature-dependent solubility in different areas of the sample, as has been noted in previous experimental work (Lee and Morse, 1999; Hilgers and Urai, 2002b; Hilgers et al., 2004; Hilgers and Tenthorey, 2004; Okamoto et al., 2010; Lee et al., 2016). A steep temperature gradient drop-off between the sample area and the assembly components either side of the sample is also important to a) prevent significant precipitation within components and adjacent valves and pipework, and b) to ensure the effectiveness of viton o-ring seals and peek components is not compromised by high temperatures. At the point of writing, issues relating to the operation of the furnace power control unit had not been fully resolved, hence calibration has not yet been achieved beyond 52 °C. It is envisaged that the ongoing solutions discussed in *Section 5.3.3.5* will allow calibration to be performed successfully at higher temperatures using the same methods described here.

Future calibrations must consider how an increase in both confining pressure and temperature may affect the temperature profile. Hence, it is suggested that a range of conditions as outlined in Table 5.2 is explored prior to any experimental work. A key safety consideration here is that the use of the upstream pore fluid pressure inlet to accommodate the thermocouples leaves a potential barrier open to argon confining medium escaping; should the sample’s copper jacket fail, high pressure gas would be rapidly drawn towards atmospheric pressure and not buffered by the high-pressure connecting nut that would usually seal this area. It is therefore imperative that all safety precautions, in particular not breaching the rig’s shields and wearing ear defenders, be followed during the calibration stage.

Table 5.2: Suggested calibrations to perform prior to any experimental work (those in green have been done; * indicates failure of the temperature control unit during calibration and ultimately halting of planned work).

Confining Pressure (MPa)	Temperature (°C)
5	30
5	40
5	50
5	100*
30	100
30	200
30	300
30	400
60	100
60	200
60	300
60	400

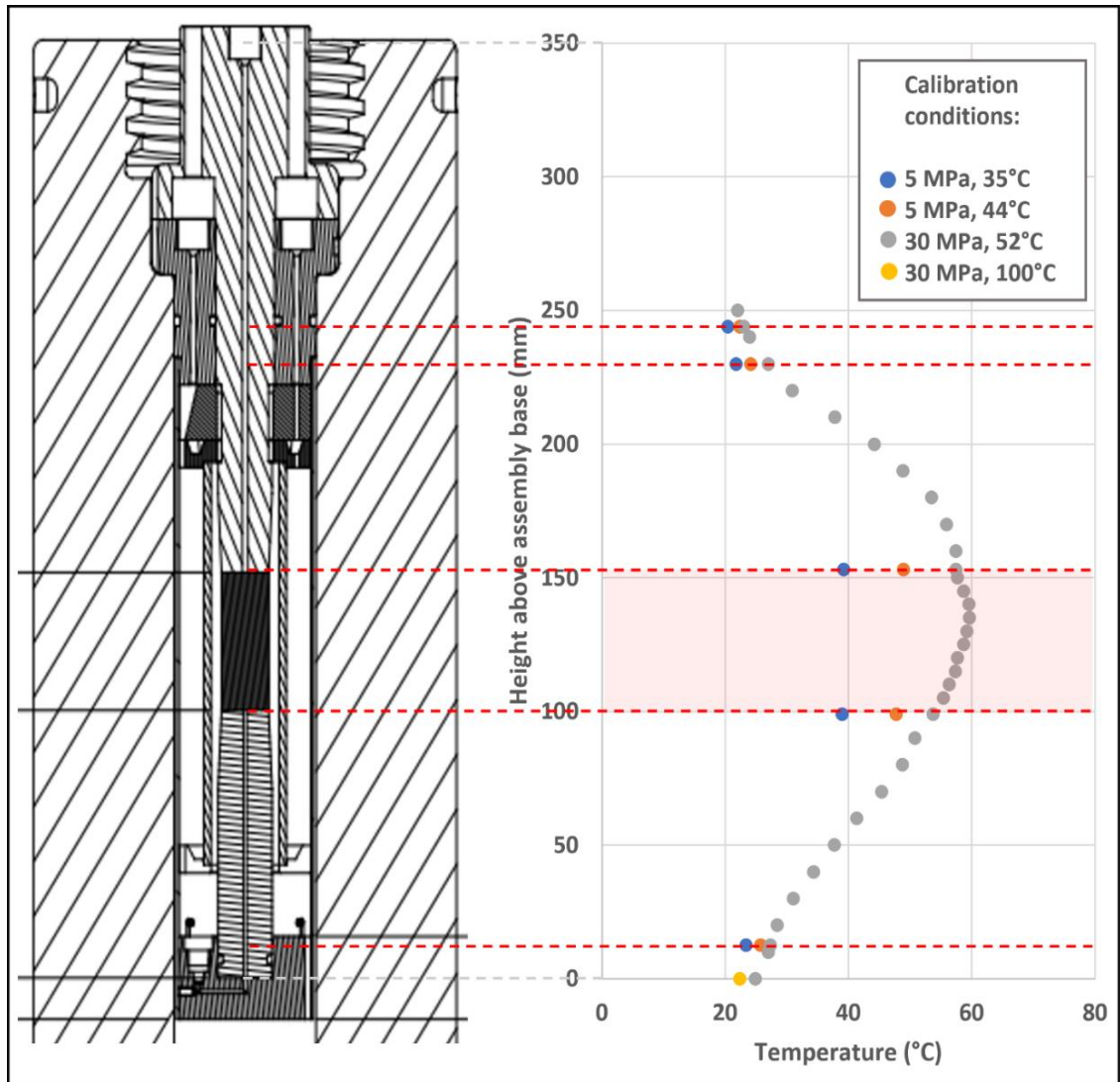


Figure 5.31: A temperature profile recorded by the variable calibration thermocouple, for control thermocouple temperatures of 35 °C (blue) and 44 °C (orange) (at a confining pressure of 5 MPa), and 52 °C (grey) (at a confining pressure of 30 MPa). See Appendix C (Section C4) for data. Measurements at 30 MPa confining pressure were also attempted at a control thermocouple temperature of 100 °C (yellow), however after a single reading failure of the temperature control unit occurred before further measurements could be taken. Dashed red lines indicate key measurement horizons as defined in Figure 5.29, with the shaded region depicting the sample area where the temperature profile should be as flat as possible.

5.4 Experiments to Investigate the Nature, Rate and Volume of Precipitate

5.4.1 Overview

Two main experimental techniques are being considered initially to answer the questions outlined in *Figure 5.1*, namely ‘static’ and ‘dynamic’ experiments that aim to simulate precipitation via diffusional and advective processes respectively. Both setups, outlined below, will use a sample configuration schematically shown in *Figure 5.32*, within the apparatus shown in *Figure 5.15*. Whilst the core samples and mineral aggregates have been prepared, no experimental work has been done to date due to ongoing problem-solving regarding the furnace power control unit (*Section 5.3.3.5*). This section therefore describes the types and ranges of experiments that should be considered in future work initially, however it should be noted that some modifications may be required if early experiments prove unsuccessful.

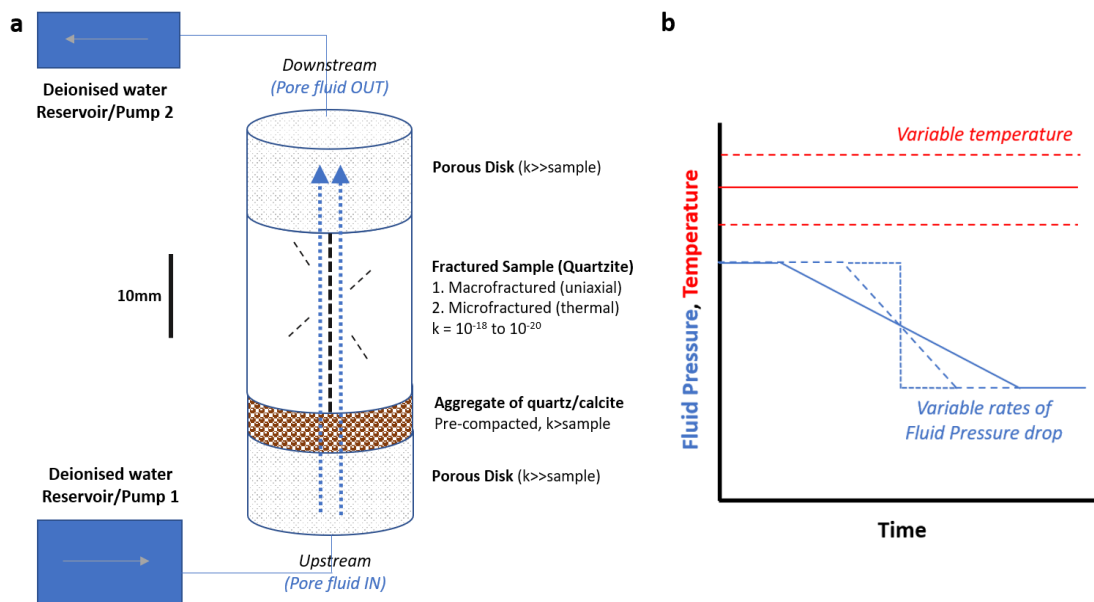


Figure 5.32: Schematic summary diagram of a) the experimental sample setup and b) the range of experimental conditions (varying temperature, fluid pressure and rate of change) as described in the text.

Experimental cores have been prepared using a combination of North Stack Quartzite and Beria Sandstone together with a mineral aggregate/gouge (*Figure 5.32*). The setup is similar to sample configuration type ‘(e)’ in Morrow et al. (2001), where a fractured sample was sandwiched between two layers of coarse crushed gouge. Quartzite was selected for the main core (i.e. the one to be fractured) due to its low intrinsic porosity and permeability, uniform composition and high mechanical strength (e.g. 215-290 MPa - Johnson and Degraff, 1988) (Siddiqui and Evans, 2015). A low intrinsic porosity and permeability allows fluid flow to be controlled as much as possible by the induced macro- or microfractures rather than the host rock’s pore network. A uniform composition of the fracture walls means that there are less chemical impacts on where nucleation may occur – in the case of attempting to precipitate

amorphous silica within induced fractures, a nucleation site comprising quartz is most desirable. A high mechanical strength ensures that, once a fracture has been created, pore fluid pressures are unlikely to increase permeability by further fracturing during experiments.

Quartzite was sampled from a disused quarry near North Stack, Anglesey (*Figure 5.33*). Although some regions of hydrothermal alteration were evident (as can be seen in the photograph in *Figure 5.33* with areas of yellow staining), relatively unaltered cores of quartzite were able to be taken from sampled blocks. Resultant cores have a diameter of 20 mm and were cut and squared to a length of 30 mm. Whilst the assembly has been designed for a core length of 50 mm (plus two 2 mm porous discs either side), 20 mm space was left for the addition of two 8 mm rock discs and 4 mm of mineral aggregate (as detailed in *Figure 5.32*).



Figure 5.33: Aerial maps (Google Maps, 2020) and author's photograph showing the sampling location of quartzite used for experimental cores. The sample location was located at a disused quarry near North Stack on Holy Island / Ynys Cybi (Anglesey / Ynys Môn, North Wales).

The rock type selected for the 8 mm long, 20 mm diameter porous disc at each end of the sample was Berea Sandstone. This was chosen on the basis of its well-documented properties (e.g. Jackson, 1985; Schon, 2015), including relatively high porosity and permeability (12.1-24.1 % and 0.2-1.05 D respectively). The presence of this disc has two main functions: it ensures that pore fluid is suitably dispersed across the sample to allow it to uniformly flow through the fracture, whilst also accommodating any precipitation that may occur outside of the fracture at the ends of the quartzite core – this mitigates against potential permanent damage to high-pressure pipework in the sample assembly and pressure vessel rig.

5.4.2 Creating a Range of Experimental Variables

An outline of the order of preparation and measurements for the proposed experimental work is given in Table 5.3. It is suggested that initial experiments are performed at constant confining pressures in order to only investigate the variables of physical fracture properties, temperature, fluid pressure and rate of pressure change. In future experiments these parameters can also be changed to assess the impact variables such as confining pressure (i.e. depth) may have on precipitation mechanisms.

Table 5.3: An outline of the order of preparation and measurements for the proposed experimental work.

Order	Summary
1	Create macro- or microfractures in the cored quartzite sample and measure the resultant porosity and permeability at room temperature (and if possible, the temperature of the experiment)
2	Insert the sample configuration into the assembly and stabilise the vessel and assembly at the desired confining pressure, pore fluid pressure and temperature conditions
3	Equilibrate: allow sufficient time for the supersaturated fluid to fill all available space within the sample
4 (a)	For 'temperature drop' experiments, switch off the furnace to reduce temperature to room temperature.
4 (b)	For 'static' (diffusion) pore fluid pressure drop experiments, fully release the upstream pore fluid pressure valve to transfer fluid into a pore fluid separator via short, low volume pipework
4 (c)	For 'dynamic' (advective) pore fluid pressure drop experiments, induce a fluid flux through the sample by increasing pore fluid pressure at the downstream end of the sample, whilst controlling pressure at the upstream end at a desired rate
4	Measure the new permeability, remove the sample, and analyse its microstructure

5.4.2.1 Physical Fracture Properties

Planned experiments involve first fracturing the sample to create either a single macrofracture or a series of microfractures. The aim is to create a series of core samples with a range of known fracture apertures, permeabilities and complexities, which will help to understand concepts introduced in *Section 5.2*, such as whether an expected increase in Damkohler number (D_a) in microfractures with respect to macrofractures increases healing rates as expected (Brantley et al., 1990; Elkhoury et al., 2013). The creation of a single microfracture can be achieved by sawing a small notch into each axial surface of the sample, before subjecting the sample to an unconfined Uniaxial Compressional Stress (UCS). Upon failure, the resultant fracture is most likely to propagate between these two artificial crack tips to create a throughgoing Mode I fracture (e.g. Xu et al., 2020). A network of microfractures can be achieved by using the same first step to create axial notches, before heating the sample to a maximum of 573 °C under low confining pressures. These conditions are likely to induce thermal cracking that increases permeability by up to a factor of 4, whilst avoiding crossing to α - β quartz transition (Siddiqui and Evans, 2015). Cooling the heated sample, for example by putting into contact with cold water, will likely induce a secondary set of thermal cracks and create higher permeabilities, particularly where cooling rates are high (e.g. Browning et al., 2016).

In both methods, each component of the sample configuration should be weighed after oven drying prior to running the experiment to allow the mass of precipitate within the porous disc and fractured quartzite to be determined. In order to assess the impact of fracture properties on the nature and rate of precipitation, the porosity and permeability of the core sample should also be measured prior to the experiment, ideally both at room temperature and the planned temperature conditions of the experiment (*Table 5.3* and *Table 5.4*). In order to estimate D_a , it is also important to measure the total fracture length and its aperture prior to further experimentation.

Porosity can be measured using Quantochrome Multipycnometer, whereby a reference cell of known volume is filled with helium gas and pressurised to 17 psi. By opening a valve, this gas is then transferred to a sample cell containing a cored sample, both of known volume. The volume occupied by the gas within the sample can be calculated using Equation 5.9:

$$V_{\text{sample}} = V_{\text{cell}} - V_{\text{ref}} [(P_1 / P_2) - 1], \quad (\text{Eq. 5.9})$$

where V_{cell} is the volume of the sample cell, V_{ref} is the volume of the reference cell, P_1 is the pressure to which the reference cell was pressurised (~17 psi), and P_2 is the pressure to which the sample cell stabilised upon opening the valve connecting this cell to the reference cell.

Permeability (k) can be determined using the pulse-transient method (Brace et al., 1968), whereby a pulse of fluid pressure is introduced to one end of the sample, and the transient decay in fluid pressure over time where fluid flows towards the other end of the sample is recorded. Permeability values can be calculated using Equation 5.10:

$$k = \lambda / (1/ V_{\text{Upstream}} + 1/ V_{\text{Downstream}}) * (\eta \beta L) / A, \quad (\text{Eq. 5.10})$$

where V_{Upstream} and $V_{\text{Downstream}}$ are reservoir volumes either side of the sample; η is fluid viscosity in Pa.s at a known confining pressure; β is fluid compressibility in Pa^{-1} at a known confining pressure and at 20 °C; L is the sample length in m, and A is the sample cross-sectional area in m^2 . λ is calculated by taking a subset of pressure decay data displaying a logarithmic decay and calculating the gradient when plotted against time. Pressure decay (P_{decay}) is determined using Equation 5.11:

$$P_{\text{decay}} = \ln(P_{\text{Upstream}} - P_{\text{calceq}}), \quad (\text{Eq. 5.11})$$

where P_{Upstream} is the fluid pressure in the decaying upstream end of the sample, and P_{calceq} is the calculated equilibrium fluid pressure, as in Equation 5.12:

$$P_{\text{calceq}} = (P_{\text{Upstream}} * V_{\text{Upstream}} + P_{\text{Downstream}} * V_{\text{Downstream}}) / V_{\text{restotal}}, \quad (\text{Eq. 5.12})$$

where P_{Upstream} and $P_{\text{Downstream}}$ are fluid pressures on each end of the sample, V_{Upstream} and $V_{\text{Downstream}}$ are reservoir volumes either side of the sample, and V_{restotal} is the total fluid reservoir volume.

5.4.2.2 Stabilisation and Equilibration

Once the sample is within the sample assembly and pressure and temperature have stabilised at the desired conditions (e.g. see *Section 5.3.4*), the fractured core sample is ready to be supersaturated with a mineral-doped pore fluid. As outlined in *Figure 5.32a*, this may be best achieved by flowing deionised water through a porous disc (to disperse the flow) and a mineral aggregate at the upstream end of the sample. Since the reservoir from which the pore fluid is pumped is limited in volume, large volumes allowing flux over long time periods can be accommodated by alternating the direction of the flow through a layer of mineral aggregate at either side of the fractured sample (cf. Morrow et al., 2001). As described in Moore et al. (1994) and Morrow et al. (2001), a gouge layer can act as a buffer that provides a suitable surface area with which water can interact as well as serving as an additional reservoir for the small volumes used during flux experiments, minimising the effect of dissolved species migration from the heated sample to low-temperature sites within the adjacent assembly. This method has been chosen over, for example, simply filling the pore fluid reservoir with a supersaturated fluid, in order to reduce the contact area between the fluid and high-pressure pipework and hence the risk of mineral precipitation.

In a similar approach, Okamoto et al. (2010) rapidly attained desired near-equilibrium amorphous silica concentrations within a fluid by flowing distilled water through 30 g of 1–2 mm diameter grains of amorphous silica and cristobalite. In this study, it is proposed that a cylindrical area with a radius of 20 mm and thickness of 4 mm (giving a volume of 1.26 cm³) is used for the mineral aggregate (*Figure 5.32*). Since silica gel has a density of ~2200 kgm⁻³, this would give a mass of amorphous silica equating to ~2.77 g. Whilst this mass is >10 times lower than that used by Okamoto et al. (2010), these authors were aiming to precipitate within an experimental apparatus that is 18 times the length, using much higher fluid volumes to precipitate material on larger surface areas (~14.3 cm³, ~23 times greater than the estimated precipitation surface area of ~0.6 cm³ to be used in this study, assuming a perfectly smooth, planar fracture). Hence, it is assumed that any amount of material of a similar grain size with a mass greater than ~1.3-1.7 g will suitably attain saturated conditions. In terms of the time-dependency of attaining equilibrium between the mineral and the fluid, Okamoto et al. (2010) show that Si solubility displays little systematic change with increasing residence times up to ~3.5 hours, indicating that solutions reach near-equilibrium concentrations rapidly. Planned experiments utilise high temperatures and saturation levels compared to many previous experiments (*Section 5.2.4*), thereby ensuring a large amount of precipitate over a reasonable duration.

5.4.2.3 Experimental Procedure

Once pore fluid pressure is equilibrated and sufficient time has been allowed for the fluid to percolate through the mineral aggregate, porous disc and fractured core (and become supersaturated with respect to the mineral in question), 'static' diffusional precipitation experiments can be performed by dropping fluid pressure instantaneously (*Figure 5.32b*) upon opening the downstream valve, allowing fluids to migrate out of the sample and into a second pore fluid reservoir. 'Dynamic' advective precipitation experiments can also be performed by using a servo-controlled system to induce a more controlled flow through the sample, thereby varying the rate at which fluid pressure is dropped. By changing the equilibration temperature, the rate at which fluid pressure is dropped, or the absolute difference in fluid pressure, the degree of disequilibrium and therefore mechanisms by which minerals will precipitate from solution is hypothesized to change (see *Section 5.2*). High degrees of supersaturation relative to previous experiments (e.g. Rimstidt and Barnes, 1980; Bird et al., 1986), on account of being able to reach high pressures and temperatures simultaneously, ensures the largest amount of precipitate over laboratory timescales (e.g. Okamoto et al., 2010).

A range of experimental pressure and temperature parameters (*Table 5.4*) were carefully chosen so that they were applicable to crustal depths relevant to geothermal exploration (i.e. ~2-3 km), whilst ensuring that the amount of precipitation expected at these conditions would be measurable. Based on data outlined in *Section 5.2*, the expected change in solubility, dissolved mass and dissolved volume were calculated for amorphous silica for each of the planned experimental conditions (*Table 5.5*). A visual overview of these experiments is given in *Figure 5.34*, where all arrows indicate a decrease in solubility at a given pressure-temperature condition and hence degree of supersaturation with respect to amorphous silica. The data suggest that at static conditions, even a temperature drop of 380 °C (from 373 °C to 20 °C), which decreases the concentration of amorphous silica in solution by ~3750 ppm, would result in just ~0.14 % of the available space (created by thermal or micro-fracturing) being filled (3.53 mg / 1.33 mm³). Calculations assume that 20 mm diameter, 30 mm length fractured cores would have ~10 % fracture porosity with a volume of ~950 mm³. A maximum pressure drop of 30 MPa (from 60 MPa to ~30 MPa, to avoid vaporising the solution (which would occur at ~22 MPa at temperatures above 373°C (*Figure 5.2*)), is likely to precipitate around half of the material produced by a 380 °C temperature drop, filling just 0.07 % of available pore space (1.62 mg / 0.61 mm³) (*Table 5.5*). Okamoto et al. (2010) found that experiments of this type yielded >80% of the expected precipitate based on fluid solubility modelling. Their overall higher yields (~4 g), despite similar or lower saturation indices for the same fluid chemistry, can be accounted for by the additional consideration of fluid flux and increased time periods, which so far has not been considered in these calculations.

Table 5.4: Range of planned experiments using amorphous silica as a mineral aggregate.

Expt. No.	Soluble Material	Test Specimen	Experiment Description	Temp (°C)	Pc (MPa)	Pf 1 (MPa)	Pf 2 (MPa)	Temp 1 (°C)	Temp 2 (°C)
1	Amorphous Silica	Thermally fractured	Temp Drop (Highest Solubility)	373	70	60	-	373	20
2	Amorphous Silica	Thermally fractured	Large Static Drop (Highest Solubility)	373	70	60	30	-	-
3	Amorphous Silica	Thermally fractured	Small Static Drop Highest Solubility	373	70	60	45	-	-
4	Amorphous Silica	Micro-fractured	Temp Drop (Highest Solubility)	373	70	60	-	373	20
5	Amorphous Silica	Micro-fractured	Large Static Drop (Highest Solubility)	373	70	60	30	-	-
6	Amorphous Silica	Micro-fractured	Small Static Drop (Highest Solubility)	373	70	60	45	-	-
7	Amorphous Silica	Thermally fractured	High-Rate Continuous Flow (Highest Solubility)	373	70	60	30	-	-
8	Amorphous Silica	Thermally fractured	Low-Rate Continuous Flow (Highest Solubility)	373	70	60	30	-	-
9	Amorphous Silica	Micro-fractured	High-Rate Continuous Flow (Highest Solubility)	373	70	60	30	-	-
10	Amorphous Silica	Micro-fractured	Low-Rate Continuous Flow (Highest Solubility)	373	70	60	30	-	-
11	Amorphous Silica	Thermally fractured	Temp Drop (Mid Solubility)	300	70	60	-	300	20
12	Amorphous Silica	Thermally fractured	Large Static Drop (Mid Solubility)	300	70	60	30	-	-
13	Amorphous Silica	Thermally fractured	Temp Drop (Lowest Solubility)	200	70	60	-	200	20
14	Amorphous Silica	Thermally fractured	Large Static Drop (Lowest Solubility)	200	70	60	30	-	-

Table 5.5: Expected results of the above experiments based on theoretical data (*all cores are assumed to have dimensions of 20x30 mm, a volume of 1570 mm³ and have a porosity of 10 %).

Expt. No.	Expected Solubility Change (ppm)	% Solubility Decrease (i.e. Degree of Supersaturation)	Expected dissolved mass (mg)*	Expected dissolved volume (mm ³)*	Max % of space filled
1	3750	99 %	3.53	1.33	0.14%
2	1750	53 %	1.62	0.61	0.07%
3	1000	47 %	2.4	0.6	0.04%
4	3750	99 %	3.53	1.33	0.14%
5	1750	53 %	1.62	0.61	0.07%
6	1000	47 %	0.94	0.36	0.04%
7	1750	53 %	1.62	0.61	0.07%
8	1750	53 %	1.62	0.61	0.07%
9	1750	53 %	1.62	0.61	0.07%
10	1750	53 %	1.62	0.61	0.07%
11	2100	99 %	1.98	0.75	0.08%
12	300	13 %	0.28	0.11	0.01%
13	1000	98 %	0.94	0.36	0.04%
14	100	9 %	0.09	0.04	0.004%

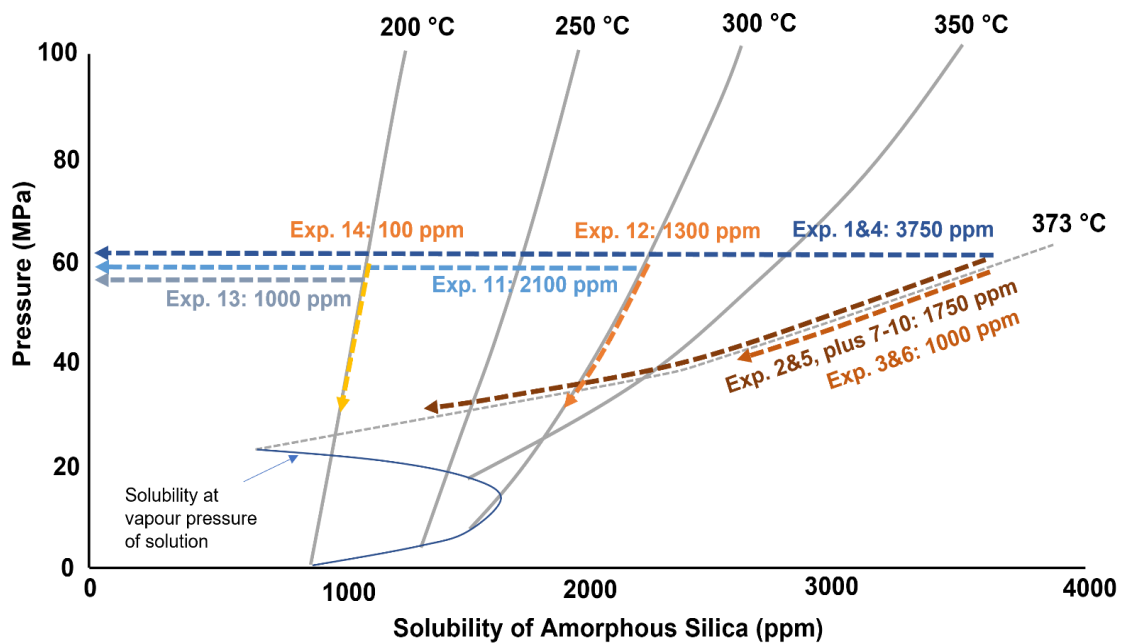


Figure 5.34: A visual overview of the types of experiment to be conducted and expected degrees of disequilibrium of the fluid with respect to amorphous silica for each, as outlined in Table 5.4 and Table 5.5. Blue-grey arrows represent decreases in the concentration of amorphous silica within the fluid upon a decrease in temperature; red-orange arrows indicate a decrease in the concentration of amorphous silica within the fluid upon a decrease in pressure.

The calculations presented in *Table 5.4* and *Table 5.5* have also taken into account the volume of high-pressure pipework that fluids must flow through to reach the sample, and hence the bore surface area on the sample side of the pore fluid valve that may also play host to precipitation. The internal volume of lengths of pipework, valves and parts of the sample assembly (i.e. upstream and downstream pore fluid inlets) is approximately 825 mm³, within which it is estimated that 0.3 – 1.17 mm³ (0.08 – 3.09 mg) of amorphous silica may be able to precipitate at the solubility levels to be explored during experimental work. However, the anticipated steep decrease in temperature gradient either side of the sample (as in *Figure 5.31*) likely means that the fluids would be significantly undersaturated with respect to amorphous silica in these areas (e.g. <200 ppm, inducing an estimated maximum of ~0.06 mm³ of precipitation). Furthermore, a significantly higher D_a value in the pipework with respect to the sample and adjacent porous discs (on account of the increased flow velocity and wider aperture – see Equations 5.2 and 5.3) means that significant precipitation within pipework is unlikely to be an issue.

5.4.2.4 Advective Flow Rates

With regards to flow rates to be induced upon a pressure drop (as illustrated in *Figure 5.32b*), previous work provides a good range of fluxes as a starting point for these experiments. Experimental studies such as those of Hilgers et al. (2004) assume that growth kinetics are purely a function of supersaturation, however this is largely due to the fact that the hydrodynamic effects on growth rates are not well understood. The lower limit of flow velocities typical of crustal fracture systems is $\sim 10^{-8} \text{ ms}^{-1}$ (Carson and Scream, 1998; Oliver and Bons, 2001), ranging to estimates of $\sim 10^{-1} \text{ ms}^{-1}$ (Nakashima, 1993; Oliver and Bons, 2001). In comparable experimental work (see *Section 5.2.4*), Hilgers et al. (2004) used flow rates of $\sim 10^{-5}$ to $\sim 10^{-4} \text{ ms}^{-1}$ (equivalent to 0.05 to 0.5 mLs⁻¹), whilst Okamoto et al. (2010) used flow rates of $\sim 3 \times 10^{-6} \text{ ms}^{-1}$ (0.016 mLs⁻¹). Pressure gradients in the order of $\sim 10^{-2} \text{ MPam}^{-1}$ are considered to be representative of typical conditions within fractured reservoirs (Wilson and Monea, 2004), however other estimates are many orders of magnitude lower (e.g. $\sim 10^{-7} \text{ MPam}^{-1}$ – Hilgers et al., 2004). In similar experiments, Morrow et al. (2001) created a pressure gradient across a fracture of 2 MPa to induce flow, comparable to ‘typical’ values of $\sim 10^{-4}$ to $10^{-2} \text{ MPam}^{-1}$ - Taylor, 1999; Wilson and Monea, 2004). For the experiments proposed here, the pressure gradient that would be required to create the range of flow rates described above (calculated using the cubic law for fluid flow in fractures introduced in *Chapter 1* (Equation 1.3) based on fluid viscosities for temperatures of 100-300 °C and pressures of 30 MPa (Engineering Toolbox, 2004)), is $\sim 1.1 \times 10^{-4}$ to 3.6 MPam⁻¹ (Table 5.6).

Table 5.6: A summary of fluid pressure gradients required to induce flow rates comparable to natural fractured reservoirs and those achieved elsewhere in the literature (see text). Pressure gradients have been calculated using the cubic law for fluid flow in fractures (Equation 1.3 in chapter 1) using the parameters outlined in the table.

Pressure (MPa)	Temperature (°C)	Fluid Viscosity (cP)	Fracture Aperture (mm)	Fracture Length (mm)	Flow Rate (ms ⁻¹)	Pressure Gradient (MPam ⁻¹)
30	300	0.1	1	30	1x10 ⁻⁴	3.6
30	100	0.3	1	30	1x10 ⁻⁴	1.1
30	300	0.1	1	30	1x10 ⁻⁸	3.6x10 ⁻⁴
30	100	0.3	1	30	1x10 ⁻⁸	1.1x10 ⁻⁴

5.4.3 Subsequent Analysis of Experimental Cores

Once experiments have been performed, core samples can be retested for porosity and permeability, before being dried at temperatures slightly above room temperature and weighed to compare to the initial dry mass. The fractured quartzite core can then be thin sectioned perpendicular to the fracture plane at 2-3 intervals across the core length and analysed using a range of microscopy techniques: optical petrology, scanning electron microscopy (SEM), cathodoluminescence (CL), and electron backscatter diffraction (EBSD) (cf. McNamara et al., 2016). In monomineralic experiments (for example, amorphous silica precipitating in fractures within quartzite), CL may prove to be most beneficial, since the trace element contents of any precipitated material are likely to be different to those within the host rock (Pagel et al., 2000; Laubach et al., 2004) allowing clear recognition of experimental sealing. As veins would have formed at known confining pressures, stress/strain orientations, fluid pressures and temperatures, in fractures with well constrained mechanical properties, and since degrees of fluid saturation with respect to quartz and calcite can be reasonably estimated, these microscopy techniques will hopefully aid the interpretation of vein precipitation processes occurring during quartz- and calcite-sealing of micro- and microfractures. Ultimately, the quantification of these processes aims to help improve models of fracture sealing and scaling in fractured geothermal reservoirs in order to improve production efficiency and lifespans of operating geothermal fields.

5.5 Discussion

5.5.1 Relating Chemical Disequilibrium in Simple Systems to More Complex Natural Geothermal Systems

As is the case in this study, laboratory experiments are almost always conducted under closed-system conditions representing a single fluid and mineral phase, where fluids are far from equilibrium with the mineral. In nature, however, reactions are likely to occur over a broad range of saturation states for which laboratory results may not be applicable (Bethke, 2007), with open systems allowing the circulation and inflow of fluids of different conditions and

compositions. Fluids in an open system may therefore never truly reach equilibrium; the degree to which they do will be affected by the reaction time, rate of precipitation of mineral phases present and the rate of fluid recharge (Bethke, 2007). Previous studies of this nature have found that applying laboratory results to natural situations is challenging, with the discrepancy between laboratory dissolution and precipitation rates and rates observed in nature at similar conditions as large as four orders of magnitude (Brantley, 1992; Bethke, 2007). These discrepancies may be attributed to a number of factors, including the difficulty of measuring dissolved mineral concentrations before and after experiments (Crerar et al., 1981; Morrow et al., 2001) and the complexities of fracture walls (e.g. the total surface area of reactive/nucleation surfaces) (Aagaard and Helgeson, 1982). However, the principal reasons are likely to be the use of simplified fluid and rock chemistry in experimental work.

Section 5.4 considered only the potential for precipitation of amorphous silica, based on its suitability for initial experimental work given its large changes in solubility over relatively small changes in pressure and temperature and ease of nucleation at high degrees of supersaturation with respect to other silica polymorphs (e.g. quartz) (Rimstidt and Barnes, 1980; Lasaga, 1997). In natural systems, however (such as the one studied in *Chapter 2* and *Chapter 3*) most quartz-bearing veins do not contain other silica polymorphs (with the exception of some epithermal veins containing chalcedony - Sander and Black, 1988). Since the conditions of many experiments are anticipated to cross the solubility curves of many silica polymorphs (e.g. *Figure 5.3a* and *Figure 5.34*), another useful observation may therefore be to assess whether quartz precipitates directly or by transformation from other silica polymorphs such as amorphous silica, the latter of which has been suggested as the most likely crystallisation pathway in quartz veins (Rimstidt and Barnes, 1980; Okamoto et al., 2010). This may differ depending on whether the system is closed ('static') – in which case quartz is most likely to transition from less stable silica polymorphs by dissolution and reprecipitation – or open ('dynamic'), where the predominant silica phase depends on the silica concentration (Bethke, 1996). In a similar study, Okamoto et al. (2010) observed that as silica solubility decreased in a system equilibrated at 430 °C and 31 MPa, precipitation of amorphous silica dominated at silica concentrations of >280 ppm, cristobalite at 280 –170 ppm, and quartz at < 170 ppm. This sequence is akin to field observations of silica sinter that often form surface manifestations of geothermal systems (e.g. (Ármansson, 2012). The principal benefit of identifying types of silica polymorphs precipitated experimentally would be to estimate the change in sealing rate owing to decreased disequilibrium (Hilgers et al., 2004).

Hydrothermal fluids can be highly variable in the composition of their dissolved solids, dependent in part on their origin (e.g. Fournier, 1977; Giggenbach, 1981, 1984, 1995, 1997). Fluids of meteoric origin, for example, will likely be depleted in most common minerals and salts, whilst those of a magmatic origin may contain a rich assemblage of minerals at saturation point that depends on factors such as the host lithology and tectonic setting. During geothermal production, wherever an initial assessment of fluid chemistry suggests that dissolved mineral

contents are high enough that there is a perceived risk of scaling, chemical antiscalants or acid washes are often pumped into the well prior to any significant fluid extraction, injection or change in temperature conditions (Brown, 2013; Boersma et al., 2018). As a result, chemical inhibitors form bonds with the scaling ions, reducing their supersaturation. This process however introduces large costs to geothermal projects, hence the more that is known about the physiochemical conditions at which minerals will precipitate, the better. The presence of other dissolved solids can significantly affect the fluid properties and hence rate of precipitation (Boden, 2017). The solubility of quartz in pure water, for example, is likely too low to allow significant growth to occur in a short timeframe (*Section 5.2*). However, when effective mineralisers such as NaOH, Na₂CO₃, KOH, and K₂CO₃ are added to the solution, rates of nucleation and growth are increased (Byrappa and Yoshimura, 2001). The morphology of calcite precipitate can be dramatically changed even by the introduction of low levels of Mn, which can impinge calcite crystal growth (Lee et al., 1999). Whichever reaction is studied in the laboratory, it may not be the one that predominates under natural conditions. The use of deionised water in these experiments is such an example: quartz has been shown to dissolve in dilute electrolyte solutions ~30 times faster than in pure water (Dove and Crerar, 1990). Furthermore, more reactive minerals (e.g. clays or zeolites, both common precipitates in geothermal systems) may in fact control the silica concentration, rendering the study of quartz reaction rates meaningless in such a situation. As such, the experiments introduced in this chapter should be used only as an insight for a simplified system, with its main benefit being that several variables can be isolated and controlled in turn, eventually building a more complete understanding of factors controlling the nature and rate of precipitation.

As well as the degree of disequilibrium between the fluid and dissolved mineral, the potential for precipitation and sealing rates also depend on the chemistry and morphology of the surface to which the mineral will nucleate and grow. In geothermal production, for example, this may either be the wall of a fracture or the casing of a well. Few previous studies have experimentally addressed precipitation within 'natural' fractures and host rock, with most using simpler, synthetic apparatus. The use of a natural host rock introduces additional variables including the addition of mineral species to the fluid and heterogeneity in nucleation sites (Brown, 2013; Elkhoury et al., 2013). Morrow et al. (2001), for example, observed that high temperature (up to 400 °C) flux experiments using pure distilled water in fractured granite resulted in the precipitation of smectite, calcite, K-feldspar, albite, quartz, wairakite, K-mica, chlorite and sphalerite, as well as pyroxene, epidote and xonotlite at the highest temperatures. Analyses of fluids after the experiments revealed a complex chemistry with many minerals at near-saturation levels. Okamoto et al. (2010) found that impurities in solution inhibited the precipitation of some silica polymorphs whilst enhancing nucleation of others. Whilst using quartzite with low levels of impurities reduces the potential for additional complexities in fluid chemistry, minor mineral phases may induce some changes that could cause small errors in the quantification of sealing rates.

The literature review and outline of experiments presented within this chapter have not considered the complexities of two-phase or supercritical fluids, which are both common and desirable in geothermal production (Ármansson, 2012). In areas of low fluid recharge, fluid pressure decrease as a result of geothermal fluid extraction may induce boiling (also termed flash vaporisation), separating the fluid into a liquid and vapour phase. Within the supercritical realm, water behaves like both a vapour and a liquid (Boden, 2017; *Figure 5.2*). Successful utilisation of such resources could result in greater fluid enthalpies (e.g. $>3 \text{ MJ kg}^{-1}$) and hence 5-10 times the power output of conventional geothermal systems, as has been estimated from studies of the Krafla geothermal system situated above a shallow ($\sim 2 \text{ km}$) magma intrusion (Scott et al., 2015). One potentially significant consequence of crossing phase boundaries could be that if the fluid was saturated with respect to a mineral prior to boiling, separation of the gaseous phase would render it instantly supersaturated and susceptible to precipitating minerals from solution (Anórsson et al., 2008). At effective pressures of $<100 \text{ MPa}$, silica solubility in water is greatest at the liquid–vapor boundary (or its extension into the supercritical region) (*Figure 5.4*), owing to a distinct change in the specific volume of water (Fournier and Potter, 1982; Tsuchiya and Hirano, 2007). Crossing this boundary could therefore have a significant impact on the volume of precipitation from solution expected. As discussed further in *Section 5.5.2*, it has been suggested that certain vein crystal textures, such as bladed calcite, indicate rapid precipitation from boiling fluids on account of the exsolution of CO_2 (Tulloch, 1982; McNamara et al., 2016). Whilst rapid precipitation may ultimately act to quickly destroy existing structural permeability, such crystallographic forms may also act to prop open fractures and preserve permeability (McNamara et al., 2016). Quantified knowledge of such precipitation mechanisms using the apparatus described here would allow for greater control of where and how much precipitation is allowed to take place in geothermal wells upon boiling, and during production from supercritical fluids (Anórsson et al., 2008).

5.5.2 *Expected Experimental Vein Textures and Their Applicability to Natural Veins*

Many vein and crystal textures in natural veins have been suggested to indicate particular growth rates, however to date lacks significant experimental evidence to support interpretations. Quantifying, and even identifying, the variables involved in natural systems is part of the solution to understanding this problem (e.g. Martin and Lowell, 2000). Whilst most natural veins have usually been subjected to some degree of dynamic recrystallisation and/or annealing rendering them unsuitable for estimates of precipitation rates, some studies exist whereby the textures of relatively undeformed veins have been investigated. Okamoto and Tsuchiya (2009), for example, attributed euhedral quartz crystals with concentric growth zoning, arranged in a blocky texture (*Figure 5.35*), to forming in suspension as downward crystal settling was balanced by high fluid ascent rates of $\sim 10^{-2}$ to 10^{-1} ms^{-1} . Such high ascent rates are considered to account for the high silica concentrations required for nucleation as well as the development of crystal fluid-suspension (Rimstidt and Barnes, 1980).

Textures such as microcrystalline silica and nanospherules observed in the field have also been inferred to have precipitated rapidly from solution (e.g. Herrington and Wilkinson, 1993; Caine et al., 2010; Weatherley and Henley, 2013; Faber et al., 2014) (*Figure 5.35*). These textures have largely been attributed to coseismic boiling, whereby solutions vaporise upon a reduction of fluid pressure and/or temperature and reduce their saturation with respect to silica (as described in *Section 5.5.1*). In many cases, preferred explanations for microcrystalline silica textures also involve elements of fault slip as well as dilation, where faults remobilise pre-existing silica whilst causing large decreases in fluid pressure alongside frictional heating to vaporise the fluid (e.g. Faber et al., 2014). Textural characteristics cited are those where silica forms a porous gel (typically comprising opal polymorphs). However, most textures attributed to near-instantaneous precipitation mechanisms apparently require estimated fluid pressure decreases much greater than those experienced in typical geothermal systems to form (e.g. in the order of ~ 290 MPa – Weatherly and Henley, 2013). Williams et al. (2019) estimate that at the conditions typically experienced in the seismogenic upper crust, negligible amounts of fluid (~ 3 -115 kg per m^3 dilation at 150-350 °C) are able to be boiled as a result of depressurisation, and would only precipitate enough material to fill $\sim 0.005\%$ of available pore space – a lower but comparable value to those estimated in *Section 5.4.2.3*. Bladed calcite textures (*Figure 5.35c*) are another common feature of hydrothermal veins, and have also been suggested to form quickly by precipitation from boiling fluids, via exsolution of CO_2 at lower levels of supersaturation (McNamara et al., 2016). Precipitation rates are again poorly constrained, however some evidence suggests that growth rates are up to 0.1 mm per day (Tulloch, 1982).

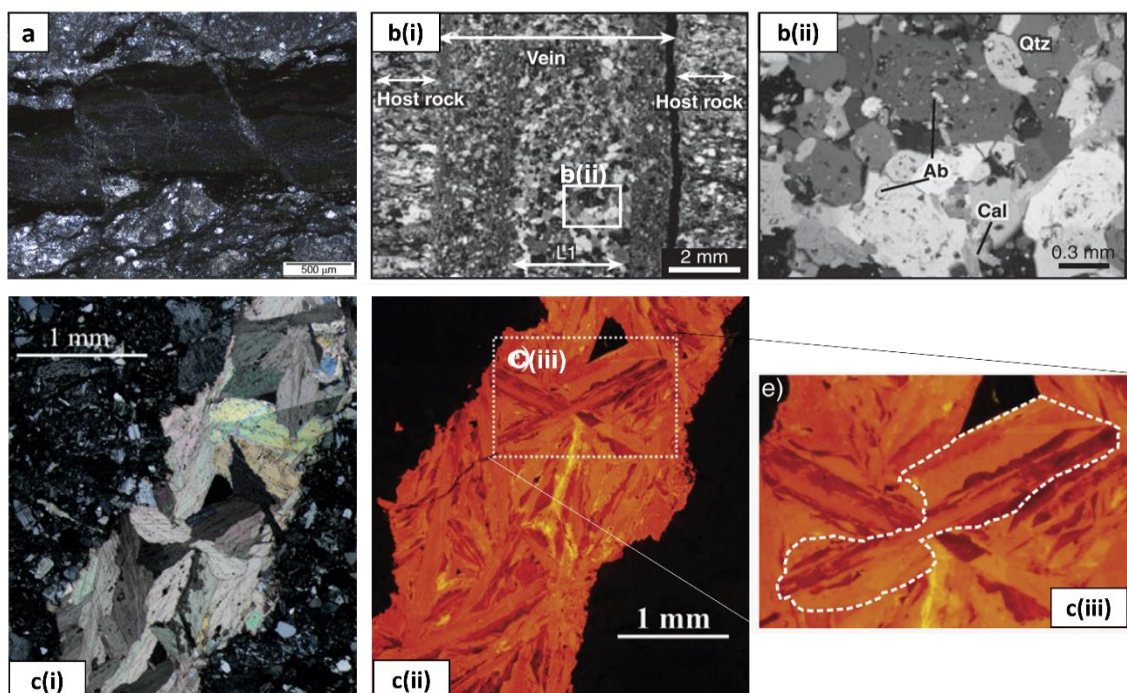


Figure 5.35: Natural vein textures in the literature inferred to have precipitated quickly from supersaturated solutions upon a dramatic change in hydrothermal conditions: a) microcrystalline silica (after Faber et al., 2014); b) Blocky quartz (after Okamoto and Tsuchiya, 2009); c) Bladed calcite (after McNamara et al., 2016). For details, see text.

Few experimental studies have considered the evolution of vein textures in relation to crystal growth rates, with some notable exceptions (e.g. Lee et al., 1996; Hilgers et al., 2004; Okamoto et al., 2010). Of those that do, fewer consider the precipitation textures of minerals such as quartz and calcite on rock surfaces, in part due to their low reaction rates at experimental temperatures (<300 °C) (Okamoto et al., 2010). Volumes of precipitate and growth rates in many experimental studies have been too small to allow analysis of microstructural and textural evolution (e.g. Lee et al., 1996; Lee and Morse, 1999). Whilst some have opted to use analogue minerals with higher reaction rates to achieve more suitable results on a shorter timescale, the alternative approach is to trade temperature for time in laboratory experiments. Rates of reaction in a quartz-water system increase with temperature (Rimstidt and Barnes, 1980); given that the new experimental apparatus described here can achieve temperatures significantly higher than 300 °C, this relationship can be drawn upon by approximating effects of increased reactivity during the time required to reach a given temperature (Karner et al., 1997).

Should this calculated trade-off yield a greater volume of material than predicted in Table 5.5 that can be analysed microscopically, there are a range of textures previously observed in experimental and natural veins and crystals that could aid the interpretation of mineral growth rates at a given set of thermodynamic conditions. Such studies generally indicate that different crystal precipitation mechanisms yield distinct textures, in turn suggesting that vein textures may indeed be used as indicators of palaeo-fluid chemistry within a fracture and hence the thermodynamic conditions of its formation. Experimental work using alum as an analogue has produced vein textures resembling natural syntaxial veins (Hilgers et al., 2004; *Figure 5.36*). These veins show evidence of coarsening crystal sizes away from the fracture wall, interpreted to reflect increased growth competition into the vein centre. At the fluid inlet, growth competition was higher, precipitating coarser crystals at a faster rate as a result of decreasing temperatures and lower dissolved mineral concentrations. Crystal morphologies are apparently dependent on initial crystallographic orientations and topography of seed crystals (i.e. nucleation surfaces) (Hilgers et al., 2002b).

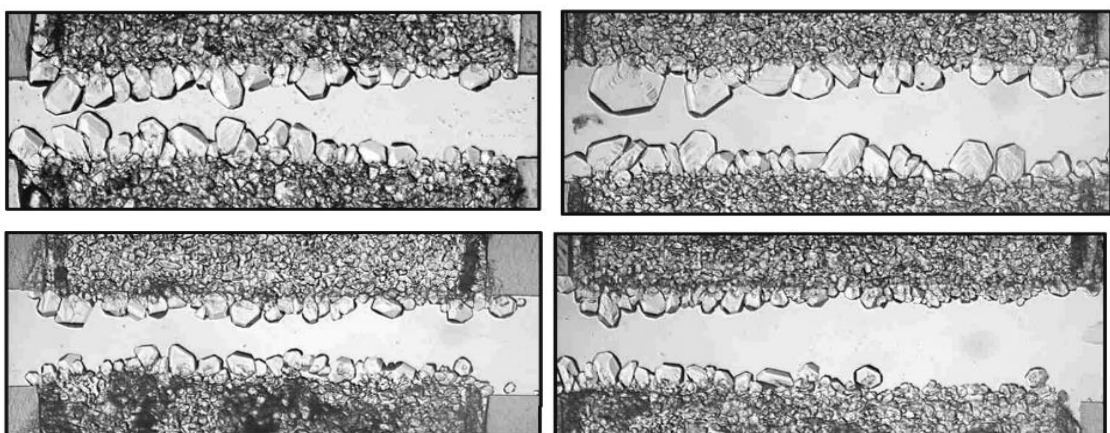


Figure 5.36: Syntaxial alum vein microstructures imaged after 12 hours (supersaturation is low (1.1) in all cases; A = low flow rate, narrow aperture; B = wider aperture and flow rates tripled; C = wide aperture, high flux; D = wide aperture, low flux) (after Hilgers et al., 2004).

Experimental precipitation of silica minerals generally shows evidence of transitional polymorph crystallisation as discussed in *Section 5.5.1*. Okamoto et al. (2010), for example, observed that nucleation of amorphous silica and opal during advective flow at 340 °C and 31 MPa was succeeded by opal overgrowths, with quartz crystals precipitating later as overgrowths of quartz crystals within the fracture wall or nucleating as a fine-grained aggregate on opal (*Figure 5.37*). These experiments were able to precipitate euhedral quartz crystals that grew up to ~300 µm from the fracture wall. Given sufficient time, it is expected that these would have formed blocky vein textures similar to those reported in some epithermal systems as opal is progressively recrystallised and annealed (Fournier, 1985; Bons, 2000; Oliver and Bons, 2001; Hilgers and Urai, 2002a). Where solutions with a low degree of supersaturation with respect to silica (< 1.2) were flowed across the synthetic fracture wall in the study by Okamoto et al. (2010), silica precipitation was restricted to overgrowths on pre-existing quartz surfaces, however at higher degrees of supersaturation precipitation was more widespread.

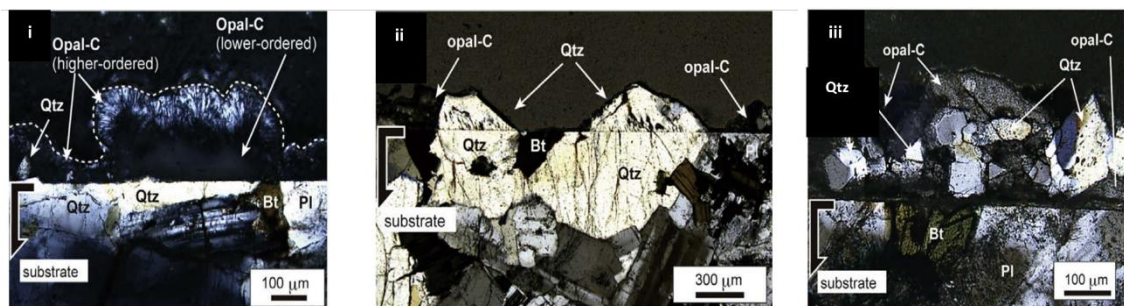


Figure 5.37: Photomicrographs showing the composition and microstructures of SiO₂ precipitate from the experiments of Okamoto et al. (2010). Experiments were performed by flowing a fluid, supersaturated with respect to silica (with initial concentrations of ~330 ppm), along a core of granite at a temperature of ~430 °C and pressure of ~31 MPa. Precipitation of opal occurred where Si concentrations within higher temperature fluids were greater, whilst quartz precipitated in greater abundance from fluids with a lower temperature and Si concentration and more complex chemistry.

The experimental apparatus and methodology presented in this chapter can explore fractures with different morphologies. Any microfractures present within the fracture wall are likely to host small amounts of precipitation (e.g. Hilgers, 2002b) that if not recognised will result in an underrepresentation of fracture sealing amounts and rates. Slight swelling of the wall rock - and hence decreased fracture aperture and permeability – may also occur due to force of crystallisation (Hilgers et al., 2004). Whilst previous work has documented dissolution of the fracture wall occurring alongside precipitation (e.g. Morrow et al., 2001), which could cause widening of the fracture aperture and an underrepresentation of precipitation amounts/rates as well as permeability changes, this must be considered unlikely here given the approach to use highly supersaturated, simple chemical systems, as well as ensuring that conditions are as consistent as possible across the whole sample (e.g. the temperature profile in *Figure 5.31*). Morrow et al. (2001) and Okamoto et al. (2010) recognised that dissolution in experiments preferentially occurred near the fluid inlet to the fracture where fluids were of a slightly lower temperature and therefore able to preferentially dissolve quartz.

5.6 Summary

Few studies have considered the combined effect of pressure, temperature and fluid flow rates that can potentially address the issues of the nature, rate and volume of precipitation simultaneously.

To help understand the processes involved in mineral vein evolution, a new high-pressure, high temperature triaxial deformation apparatus has been designed to simulate a range of upper crustal geothermal gradients whilst under confining pressure. Two types of experiment using variably fractured core samples have been designed to investigate crystal growth mechanisms during fracture sealing by precipitation: 1. 'Static', where diffusive mechanisms are quantified by reducing fluid pressure at varying rates from a stagnant supersaturated fluid, and 2: 'Dynamic', where advective mechanisms are quantified by flowing supersaturated fluids through the sample at different rates. The systematic vein precipitation experiments outlined in this chapter are intended to be used to acquire new evidence on how fluid flow in crustal fractures can influence the nature and rate of fracture sealing, and ultimately also be used to better interpret natural vein textures. By basing elements of the design, experimental configuration and methodology on a solid foundation of theoretical modelling and the successes of previous experimental studies, whilst also aiming to improve results based on their limitations, we can be reasonably confident that this work will provide a sound basis for addressing the fundamental questions outlined in *Section 5.1* in future, as outlined below.

What changes could take the geothermal system out of chemical equilibrium to induce mineral precipitation?

- **Pressure:** Increased pressures would result in increased silica and calcite solubility, hence a larger pressure drop would result in more precipitation from solution. In the new experimental setup, effective pressures can be controlled over a range applicable to geothermal exploration using an argon gas confining medium and distilled water for fluid pressure. Pressure changes that would move fluids into the supercritical realm have not been considered but are a potential consideration for future experiments.
- **Temperature:** For silica, greater temperatures result in increased solubility, hence increase the amount for precipitation from solution upon a change in conditions towards lower temperatures. In calcite, solubility is retrograde, hence precipitation is likely to be more abundant at higher temperatures. In the new experimental setup, well-controlled temperatures of 20 - ~750 °C can be reached using an internal furnace comprising three coils, through which the temperature gradient across a sample can be kept to a minimum to allow for uniform precipitation.
- **Fluid Chemistry:** Whilst geothermal fluids may have complex chemistries, only simplified chemical systems are considered here. Pressure and temperature conditions control the silica polymorphs that precipitate from a silica-saturated solution. Calcite solubility is strongly dependent on the presence and pressure of CO₂, as well as pH and

salinity. In the new experimental setup, distilled water can be flowed through a mineral aggregate at pressure/temperature conditions that will theoretically achieve the highest levels of solubility supersaturation, with time given to equilibrate based on an understanding of mineral kinetics. Since fluid chemistry changes due to dissolution of the fracture wall can strongly influence precipitation mechanisms, quartzite with low impurity levels is to be used as a test sample.

If precipitation does occur, what are the key controls on the nature of precipitation (i.e. vein/mineral texture and microstructure)?

- **Nucleation and Growth/Kinetics:** Vein textures are largely a function of growth competition, i.e. crystal nucleation and growth/kinetics, which themselves are likely largely dictated by processes that control the degree of disequilibrium. In the new experimental setup, the relative importance of both is to be assessed through microstructural analyses (i.e. optical petrography, SEM, EBSD and CL) of experimental vein and crystal textures produced under different conditions and comparing to frameworks established through previous experimental and natural studies. Since no experiments have been conducted to date, little progress has been made in this regard, however such techniques provide significant potential for future study.

If precipitation does occur, what are the key controls on the rate and volume of precipitation?

- **Degree of Disequilibrium:** Relative rates of reaction (i.e. precipitation) to fluid flow (i.e. advection) can be represented by dimensionless numbers, where large values indicate that precipitation is able to keep up with fluid supply rates. In the new experimental setup, this is to be experimentally controlled by independently varying pressure and temperature in order to induce theoretically large changes in mineral solubility.
- **Fracture physical properties:** The length, aperture and asperities that affect flow velocity and tortuosity according to the cubic law for fluid flow in fractures can all affect the nature and rate of precipitation. In the new experimental setup, this is to be varied by inducing synthetic fractures through uniaxial compression (i.e. a single macrofracture with relatively wide aperture) or thermal shock (i.e. many small microfractures with relatively narrow apertures).
- **Fluid Flux:** Estimates of fluid volumes and flux rates required to seal a fracture vary considerably (e.g. from hours to millions of years), and depend on the balance of all factors discussed above. In the new experimental setup, this is to be controlled by adapting the rate at which fluid pressure at the outlet point of the sample assembly is released into a fluid reservoir – this can be achieved at rates that are effectively instantaneous or over periods of several days. To create flow rates comparable to other experimental investigations and natural systems, an initial fluid pressure gradient range of 10^{-4} to 10^{-1} MPa is suggested.

Data emerging from this new experimental setup, when considered alongside natural microstructures and other theoretical and experimental data, may be used to predict the conditions under which precipitation is most likely to increase scaling in wells or reduce reservoir permeability, thereby improving subsurface models of geothermal reservoir production or stimulation. In particular, such understanding has the potential to significantly reduce flow impedance between injection and production wells in geothermal fields, which may produce high pressure and temperature gradients (e.g. Ghassemi, 2012). Knowing where, how and how quickly precipitation is likely to occur at depth would ultimately allow for conditions to be varied with confidence during reservoir operation. In a wider context, knowledge of sealing rates under different conditions aids in quantitative descriptions of the cyclic nature of fault sealing and rupture (e.g. Sibson, 2001). The implications of such experimental work may therefore also be significant in the understanding of earthquake recurrence intervals in different geological settings.

Whilst there remains a considerable body of work to investigate single-phase fluids, as has been outlined within this chapter, it is suggested that future work also considers the effects of crossing water phase boundaries through superheating or extreme depressurisation. Such experimental data would allow for geothermal system models to predict the largest possible amounts of steam extraction during operation (hence maximising energy production (Boden, 2017)), and also provide evidence as to whether coseismic boiling is a viable mechanism for sealing faults within earthquake recurrence intervals (Williams, 2019).

Acknowledgements

Work presented here was fully funded by Natural Environment Research Council (NERC grant ref. no. NE/L002469/1) as part of a PhD conducted via the EAO DTP, whose support is gratefully acknowledged. I am grateful for the support of colleagues in the Rock Deformation Laboratory at the University of Liverpool for invaluable guidance, discussions and support in many aspects of this work; particular thanks is extended to Gary Coughlan for his time and effort. Early advice on the assembly design was given by Dave Lockner at the USGS, amongst others. Advice and assistance in furnace winding and redesign of electrical components came from Julian Mecklenburgh and Ernie Rutter at University of Manchester, and numerous component modifications and adjustments were made by Steve Kewin of CAE Services, Birkenhead.

6 Summary, Implications and Future Work

6.1 Recap of Context and Research Approach

Geothermal systems can vary widely in their structural properties and fluid flow history. In crystalline reservoirs, fluid flow is largely controlled by the permeability of faults and fracture networks, within which high flow rates are required to efficiently transport heat energy (e.g. Rowland and Sibson, 2004; Evans, 2005; Evans et al., 2005; Davatzes and Hickman, 2010; Wallis et al., 2012; Sanchez et al., 2013; Siratovich et al., 2014; Kissling et al., 2015). To understand the evolution of geothermal systems and develop them successfully, the physical properties and spatial distribution of permeable fracture networks within different fault systems must be characterised. This may vary at a range of scales, from interactions between major faults that form a regional structure, to the damage zones of individual faults and microstructural damage surrounding single fractures within it (e.g. Cembrano et al., 2005; Mitchell and Faulkner, 2009; Jensen et al., 2011; Savage and Brodsky, 2011; Nixon et al., 2019).

It is also important to understand the dynamic nature of permeability in terms of the relationship between tectonics and fluid flow, which can be achieved via the study of (for example) clays and epithermal mineral veins precipitated in the fracture network in analogous structural settings (e.g. Sibson, 1996; Bons et al., 2012; Gomila et al., 2016). As well as directly influencing existing structural permeability, hydrothermal fluid flow can create strong discontinuities and cause alteration of the host rock, changing its mechanical response to regional stress and therefore its ability to re-fracture (e.g. Pola et al., 2012, 2014; Heap et al., 2014; Wyering et al., 2014, 2015; Siratovich et al., 2016). Precipitation within fractures can also significantly change their frictional strength and seismic stability, particularly wherever the mineral in question is notoriously frictionally weak (e.g. clays – Byerlee, 1978; Shimamoto and Logan, 1981; Morrow et al., 2000, 2017; Saffer and Marone, 2003; Moore and Lockner, 2004, 2007; Ikari et al., 2007, 2009; Collettini et al., 2009; Tembe et al., 2009; Lockner et al., 2011).

During geothermal production or stimulation by fluid injection, physiochemical properties of fluids are often taken out of equilibrium with the surrounding fractured host rock as a result of changing temperatures, pressures or fluid chemistry (e.g. Fournier and Rowe, 1966; Fournier, 1989; Ármannsson, 2012). As a consequence, mineral precipitation from solution may occur within fracture networks (i.e. fracture sealing to form mineral veins), causing irreversible loss of permeability, efficiency and ultimately production (e.g. Morrow et al., 2001; Griffiths et al., 2016). Fracture sealing has been shown theoretically to be a function of time, temperature and fracture dimensions, and is also dependent on changes in fluid pressure, flow rates and composition, however there is little consistency in experimental work (e.g. Lee et al., 1996; Hilgers and Urai, 2004; Okamoto et al., 2010). Relatively little experimental research has been done to investigate the hydrodynamic effects on fracture sealing, particularly regarding the crystal textures that can help identify precipitation rates and the conditions that control sealing rates and volumes (e.g. Bons et al., 2012; McNamara et al., 2016).

Such processes – and as a result fluid flow properties – vary significantly between the fault core and fault damage zone (e.g. Chester and Logan, 1986; Barton et al., 1995; Caine et al., 1996; Wibberley et al., 2008, Faulkner et al., 2003, 2008, 2010). An understanding of the temporal history of how these fracture networks are created and destroyed (e.g. via sealing by mineral precipitation), as well as the physical properties of the hydrothermally altered host rock and the sealed fractures within, are thus of fundamental importance when considering the long-term development and evolution of a geothermal system and reducing exploration uncertainty. This thesis has demonstrated how a combination of structural geological fieldwork and experimental rock deformation analyses in the laboratory can be used to provide analogue data that can inform models of structural fluid flow within the cores and damage zones of faults, paying specific attention to the processes ongoing in hydrothermal areas.

With regards to field-based analyses, an exhumed transtensional duplex, with evidence of fossil hydrothermal fluid flow in the form of mineral veins, was studied on the basis of its suitability as an analogue for a large proportion of geothermal systems (e.g. Faulds et al., 2011). The studied duplex comprised a coherent crystalline host rock lithology throughout allowing for consistent analysis of structural trends. Duplexes in general represent sites of fault interaction and linkage between overstepping faults, where enhanced structural density and varied geometries create sites that are important for permeability and fluid transport (Sibson, 1987; Peacock and Sanderson, 1991; Leckenby et al., 2005; Berger, 2007; De Paola et al., 2007; Choi et al., 2016; Nixon et al., 2019). Few studies, however, have quantified the damage distribution and intensity within them, or considered how permeability and fluid flow evolves over time. In *Chapters 2 and 3*, structural controls on episodic flow have been characterized using field data to help identify where may have been most prospective in this particular geothermal system in terms of permeability and fluid flux, considering spatial and temporal variability respectively. This has been achieved largely through statistical analyses of mechanical damage and vein mineralogical data collected via 1D linear transects and 2D outcrop surface maps from five structurally different sites across the duplex. Linear transects and subsequent analyses were performed based on some methodological principles outlined by Priest (1993) and Sanderson and Nixon (2015), with systematic data collected on vein orientation, frequency, spacing, thickness (aperture) and composition in the damage zones of second-order faults. Surface mapping was conducted based largely on Healy et al. (2007) and Ostermeijer et al., (2020), using a combination of published geological maps and new vein trace maps of horizontal outcrops. In both cases, some novel analytical approaches have been developed.

A range of analyses on sampled veins and host rock from the studied field area were also performed in the laboratory. The overall purpose of experiments described in *Chapter 3* was to assess the impact of hydrothermal alteration and vein composition/orientation on mechanical strength, as well as the potential for subsequent reactivation to inform on the potential for maintenance of structural permeability in the studied duplex. A systematically sampled subset

of Mode I/II epithermal veins were thin sectioned to investigate their detailed mineralogical composition and texture, with the aim of understanding how fluid flow evolved temporally in different parts of the duplex. Thin sections were analysed using a combination of standard optical petrography, Scanning Electron Microscopy (SEM) and cathodoluminescence (CL), and described based largely on the classifications of Bons (2000) and Bons et al. (2012). Vein and host rock samples collected in the field were also cored for the purpose of rock deformation experiments, namely Unconfined Compressive Strength (UCS) and Brazilian Tensile Strength (BTS) tests. X-Ray Diffraction (XRD) analyses were also performed on altered and non-altered host rocks to quantify the degree of alteration induced by hydrothermal fluid flow.

In addition to fractures sealed by aforementioned epithermal mineralisation, many structurally hosted geothermal systems contain fractures sealed argillic alteration minerals (e.g. many clays) – in particular areas within or adjacent to fault cores. *Chapter 4* therefore described a series of laboratory experiments conducted on clay gouges to assess their impact on the frictional strength and stability of faults and fractures, with a particular focus on the impact of the degree of saturation. Based on a direct shear technique described by Faulkner et al. (2018), together with some key principles outlined by Morrow et al. (2000, 2017) and Moore and Lockner (2004), clay samples were sheared at room temperature under triaxial pressure at a range of measured saturation states controlled by heat and/or the presence of a vacuum. Kaolinite (a 1:1 sheet silicate) and montmorillonite (a 2:1 smectite) were chosen specifically to investigate the effect of dehydration on frictional properties in swelling versus non-swelling clays respectively. Thermogravimetric analysis aimed to quantify the degree of dehydration that had occurred in each sample. Experimental direct shear data were analysed for frictional strength based on Byerlee (1978), and for frictional stability based on Dieterich (1979), Ruina (1983), Marone (1998) and Noda and Shimamoto (2009). Samples from these novel experiments were subsequently analysed using SEM and described using the terminology of Rutter et al. (1986) to assess the evolution of microstructure in progressively dehydrated clay-sealed fractures.

Finally, *Chapter 5* considered how a laboratory-based experimental approach could be used to assess the control of changing fluid pressures, temperatures and chemistries on the nature, rate and volume of fracture sealing by precipitation. With this goal in mind, a new high pressure, high temperature triaxial deformation apparatus has been built to precisely simulate a range of upper crustal geothermal gradients whilst under confining pressure, simultaneously allowing the flux of a fluid containing minerals in solution (e.g. quartz or calcite) to be controlled within an experimentally fractured rock core. The design was based on previous developments of triaxial deformation apparatus for use in permeability-measuring experiments, described by Mitchell and Faulkner (2008) and Faulkner and Armitage (2013) amongst others. Here, the design and calibration of this new assembly has been outlined in detail. A series of experiments has also been proposed based on a comprehensive review of published data regarding the controls on chemical disequilibrium, the nature and rate/volume of precipitation.

6.2 Results and Implications

Research findings presented within the core chapters of this thesis - and their implications for geothermal systems and beyond - are summarised here in the framework of the key research questions identified in *Chapter 1 (Figure 1.14)*.

6.2.1 *How is Fault Damage - and Hence Structural Permeability - Spatially Distributed Across a Fault Zone?*

Measurements of both 1D and 2D vein intensity within the studied fault duplex, as described in *Chapter 2*, suggest that structural damage is heterogenous at multiple scales (i.e. from kilometre- to metre-scale), which is largely in agreement with previous work indicating that duplex systems show self-similarity (e.g. Cembrano et al., 2005; Jensen et al., 2011; Faulkner et al., 2011). Areas within the studied duplex appear to have undergone more brittle deformation than areas outside, with greater fracture connectivity within the duplex also suggesting higher paleo-permeability (cf. Kissling et al. 2015). Vein intensity was also shown to decrease with distance from the cores of major second-order faults, conforming to previous observations that suggest the amount of fault displacement coupled with regional fault density may be the primary causes of intensity variation (e.g. Mitchell and Faulkner, 2009; Savage and Brodsky, 2011). Analysis of mineral fills suggests that fluid flow in general made use of the whole of the open fracture network rather than being confined to a few major conduits. Such investigations have several important implications for geothermal exploration of naturally fractured reservoirs, in that improved knowledge of spatial evolution of structural permeability within an exhumed duplex will aid in the understanding of which areas may be considered suitable targets for drilling geothermal production wells in similar structural settings.

Vein intensity and connectivity has been shown to decrease along strike away from the duplex centre, whilst *Chapter 3* also showed that the majority of fracture sealing by precipitation has also occurred adjacent to the bounding fault closest to the centre of the duplex structure. Connectivity – and hence structural permeability - appears to be in part controlled by the presence of abutting linkage structures, suggesting that fluid flow phases can be tortuous and strongly influenced by pre-existing structures (cf. Cox, 1999). In simplified terms, it can be concluded that the higher the density and connectivity of faulting, the greater the amount of fluid flow has occurred, however there is a degree of complexity to this that *Chapter 3* showed could be attributed to temporal variations in stress and degree of pre-existing hydrothermal alteration. It is suggested that areas of highest structural density and complexity (e.g. high connectivity) are likely to be the best targets for achieving long-term fluid flow as hydrothermal upwelling zones. As well as having significant implications for improving models of contemporary geothermal systems, the improved understanding of fault zone structure gained via such outcrop studies can also aid the interpretation of fault zones at depth as applied to the exploration of hydrocarbon migration in petroleum reservoirs (e.g. Aydin, 2000), suitable siting of deep-waste storage repositories (e.g. Stuckless and Dudley, 2002) and carbon capture and

storage projects (e.g. Dockrill and Shipton, 2010). Post-duplex migration, zones of palaeo-fluid flow in long-lasting epithermal systems are also considered to be suitable areas for the exploration of high-grade ore deposits (e.g. Cox, 1995, 1999; Berger, 2007). The variability of permeability within duplex structures also has important implications for coseismic and post-seismic fluid redistribution, and hence the understanding of seismic rupture nucleation and propagation processes in the upper crust (e.g. Sibson, 1985, 1996, 2000).

6.2.2 How do Early Phases of Fracture Sealing Influence Subsequent Fluid Flow Events, and Therefore the Temporal Evolution of Structural Permeability?

Chapter 3 demonstrated how fracture sealing patterns vary not only according to where within the duplex they precipitated, but also during what stage of the geothermal system's evolution they formed. A timeline of propylitic precipitation was revealed as a mineral assemblage of chlorite, mixed chlorite-epidote, epidote, mixed epidote-quartz, quartz, calcite, and finally palygorskite with salts, demonstrating an evolution in geothermal fluid properties with time that may aid the understanding of hydrothermal fluid evolution in similar tectonic settings. This assemblage likely represents contemporaneous faulting and fluid transport under evolving retrograde low-greenschist facies conditions (~280-350 °C) at depths of ~3 to 6 km (cf. Cembrano et al., 2005; Olivares, 2004; Herrera et al., 2005; Arancibia et al., 2014). The composition and texture of Mode I/II epithermal veins outside of the duplex was in general simpler than those sampled within the duplex, suggesting a more complex history of fluid flow within. Veins within the duplex, for example, displayed a wider range of mineral phases, microcrystalline quartz-epidote phases as well as the blocky and syntaxial textures observed throughout the duplex, a greater amount of post-formation deformation, and more evidence of crack-seal/stretching vein textures (the latter of which implies fracture reactivation – e.g. Ramsay, 1980; Caputo and Hancock, 1999; Wiltschko and Morse, 2001).

Measured vein orientations, combined with a timeline of mineral precipitation, were used to inform on the evolution of the state of stress during fluid flow in this geothermal system (e.g. Healy, 2008). Since geothermal areas can be prone to dynamic stress changes (Grant and Bixley, 2011), these findings have important implications for both naturally fractured reservoirs and elements of production and stimulation by fluid injection within Enhanced Geothermal Systems (EGS). As well as ensuring that permeability is created in the desired orientation, fluid injection/extraction amounts and rates adjusted to the in-situ stress field reduce the risk of wellbore instability and induced seismicity, ultimately improving the economic cost, societal impact and longevity of a geothermal resource (e.g. Moeck et al., 2009; Ghassemi, 2012; Ellsworth, 2013). Sites typically considered favourable for stimulation within EGS reservoirs are those that include pre-existing, critically stressed and optimally oriented fractures (Baria et al., 1999; Sheridan et al., 2003; Megel et al., 2005; Ghassemi, 2012). Within the studied duplex, most vein material was shown to have precipitated in favourably oriented extensional structures perpendicular to the minimum principal stress (σ_3), with narrow aperture fractures

appearing to have more control on fluid flow than wide aperture fractures within this system. Whilst in general fracture permeability decreases with progressive mineral precipitation, crack-seal processes disrupt this trend and conduct fluids over multiple flow events, hence it is useful to recognize where structures favourably oriented to reactivate are likely to be. Reactivated veins in the studied duplex almost always formed sub-parallel to the dominant precipitation orientation, reinforcing the importance of the collection of stress estimates during drilling (e.g. Ghassemi et al., 2012). In the duplex studied here, the preferential structural grain formed by veining does not appear to create new permeability in a different direction to that expected through an assessment of regional stress, however other mineral assemblages are likely to affect this.

6.2.3 *How do Hydrothermal Fluids and Resultant Alteration Mineralogy Affect the Mechanical and Frictional Strength of a Fractured Geothermal Reservoir?*

Due to its control on rock mechanical strength, pre-assessment of the degree of alteration across a fault-hosted geothermal system should form a major consideration when modifying fluid circulation in conventional fractured geothermal systems or targeting areas for stimulation in EGS projects. Host rock alteration also has important implications for the choice of equipment and drilling efficiency (e.g. rate of penetration) (Wyering et al., 2012, 2014). In *Chapter 3*, the mechanical strength of host rock that had been hydrothermally altered within the studied exhumed duplex structure was shown to be greater than that of unaltered host rock. The presence of an epithermal vein within the host rock however, regardless of its orientation, did not significantly affect strength nor influence fracture patterns (cf. Virgo et al., 2013), implying that the degree of alteration (rather than the presence of a vein itself as a planar discontinuity) controls where subsequent creation of structural permeability takes place in the fault damage zone. Choosing operating conditions such as fluid injection and extraction rates in accordance with a good understanding of rock fabric and strength reduces the risk of mechanical failure, and hence negative impacts such as induced seismicity (e.g. Ghassemi, 2012).

This may be particularly true in areas where clay-rich alteration is prevalent within fractures. Shifting the conversation from the fault damage zone to its core, and from typically high-temperature propylitic alteration to typically low-temperature argillic alteration, *Chapter 4* added data to the growing literature that demonstrates the frictional weakness of clay-filled fractures relative to fractures sealed by non-phyllsilicates (e.g. Moore and Lockner, 2004; Ikari et al., 2007; Behnsen and Faulkner, 2012; Morrow et al., 2017). More specifically, experiments showed that as water is removed from clay minerals, frictional strength increases by up to a factor of three, with a greater effect in 2:1 smectites than 1:1 sheet silicates. Analyses of the constitutive frictional parameters that describe fracture stability revealed that the clays displayed velocity-strengthening behaviour under all conditions, however as water is removed the gouges become less frictionally stable. Experimental data coupled with microstructural analyses suggest that the presence of water is key in promoting time- and slip-dependent

frictional changes, constraining operative grain-scale deformation mechanisms to those that are fluid assisted (e.g. sub-critical crack growth, pressure solution or dislocation creep processes (c.f. Kronenberg and Tullis, 1984; Bos et al., 2000; Chester, 1995 and Hickman and Evans, 1995 (amongst others))).

In an applied context, data presented in *Chapter 4* may be particularly applicable to regions of high geothermal gradients and poor fracture connectivity (e.g. EGS reservoirs). As phyllosilicate-rich fractures form and reduce structural permeability (e.g. via mechanical attrition or low-temperature alteration), they may become disconnected from the wider fluid flow network and become partially dry, particularly at depth. Resulting changes in the fracture's frictional strength and stability have the potential to make them more susceptible to unstable, brittle failure and hence recover permeability, once again changing the physical properties. Such considerations are also important to the study of caprocks in carbon capture and storage projects (e.g. De Jong et al., 2014; Vilarrasa and Carrera, 2015). Furthermore, understanding the deformation mechanisms that operate at grain scale ultimately influence fault mechanics at a larger scale. For example, if the effects of fluid-assisted deformation mechanisms in fault zones are not accounted for, crustal strength can be significantly overestimated (Bos and Spiers, 2000). In seismology, the variation of physiochemical properties within fault gouges has hence been cited as a reason for aseismic creep behaviour in major faults (e.g. the San Andreas Fault - Carpenter et al., 2012; Lockner et al., 2011; Chang et al., 2013).

6.2.4 What are the Key Controls on the Nature, Rate and Volume of Precipitation in Structurally Hosted Hydrothermal Systems?

Constraints on the range of physiochemical conditions under which precipitation is most likely to reduce structural permeability in geothermal reservoirs via sealing can significantly improve subsurface models of geothermal production and/or stimulation, and ultimately the productivity, efficiency and longevity of contemporary geothermal systems (e.g. Thien et al., 2015). In *Chapter 5*, a comprehensive literature review summarised and quantified how changes in fluid pressure, temperature and chemistry can take a hydrothermal system out of equilibrium and promote a predictable amount of fracture sealing by precipitation. Data analysis focused on silica and calcite, given that their precipitation is commonly problematic (e.g. within surface equipment and reinjection wells, or at depth, respectively - Ármannsson, 2012). The review found that such disequilibrium promotes a predictable change in fluid solubility with respect to a particular mineral, resulting in dissolution or precipitation of that mineral (e.g. Ellis, 1959, 1963; Fournier and Rowe, 1966; Crerar and Anderson, 1971; Fournier, 1989; Lee et al., 1996; Rimstidt, 1997; Hilgers et al., 2004 and Okamoto et al., 2010). The nature of precipitation is largely a function of function of processes that control the relative dominance of crystal nucleation and growth/kinetics (e.g. Bons, 2000; Oliver and Bons, 2001; Wiltschko and Morse, 2001; Bons et al., 2012). The timescales over which this occurs depend in part on the degree of disequilibrium as well as mineral kinetics (e.g. Lasaga, 1997; Martin and Lowell, 2000;

Elkhoury et al., 2013) and estimates from theory and experiments vary widely from hours to years (Laubach, 1997; Morrow et al., 2001; Tenthorey et al., 2003; Tranter et al., 2020) to millions of years (Lee and Morse, 1999).

With regards to how these factors may practically be addressed within a newly designed and built sample assembly, *Chapter 5* described how a fractured core sample with well-defined physical properties can be produced, and subjected to effective pressures and temperatures over a range suitable to geothermal exploration (e.g. ~30-60 MPa and (initially) up to 373 °C). Argon gas was used as a confining medium and distilled water as a pore fluid, whilst controlled temperatures (with minimal temperature gradient) were produced by powering a furnace surrounding the core sample. Fluid flux can also be controlled by adapting the rate at which fluid pressure at the outlet point of the sample assembly is released into a fluid reservoir. Two types of experiment to investigate the nature, rate and volume of fracture sealing were proposed - 'static' and 'dynamic' - aiming to simulate precipitation via diffusional and advective fluid flow processes respectively. Although the development of this novel laboratory apparatus and sample configuration has to date only reached the calibration phase, it is tentatively suggested (based on this initial study) that even with significant pressure and temperature changes that may occur upon fluid injection or extraction, fractures are likely to seal relatively slowly from potentially huge volumes of fluid at depth, which has positive implications for geothermal production. However, significant further study is required (see *Section 6.3*), particularly concerning calcite-dominated fluids and supercritical fluids, which could have markedly different implications.

As well as directly affecting permeability, the process of fracture sealing may also lead to changes in reservoir mechanics, affecting the system's stability and ability to maintain structural permeability through fracture reactivation. Furthermore, knowing the vein textures that result from such processes would allow for improved use of analogues to help interpret palaeo-seismicity and areas favourable for commercial mineral ore deposits in similar tectonic settings (e.g. Cox et al., 2001). Improved knowledge of the factors that control precipitation mechanisms during fracture sealing has many important implications in the context of the seismic cycle. The cyclic nature of fault sealing and rupture (e.g. Sibson, 1981, 1990, 1992, 2001) suggests that impermeable seals must form within the recurrence time of major earthquakes. By constraining the timescales over which this occurs under different physiochemical conditions, the ability to predict earthquake periodicity in different geological/tectonic settings is improved.

6.3 Suggestions for Future Work

This thesis has explored a range of different topics related to structurally controlled fluid flow in geothermal reservoirs through a combination of field and laboratory techniques. Whilst new research has answered questions posed in *Chapter 1* to a degree, it has also highlighted many elements that require further study to improve knowledge in this field. Some recommendations for future work are outlined in the framework of the four main research questions below.

Research considering the *spatial distribution of fault damage and structural permeability across a fault zone* could be progressed in a number of different ways. In terms of fieldwork, although the dataset collected for this study has been analysed comprehensively, further study would be required to determine whether the selected sites accurately represent the position within the duplex rather than simply highlighting intrinsic variability. Furthermore, since the full methodological approach outlined here has apparently not been presented as a single study elsewhere, it is suggested that this systematic approach to understanding the distribution and history of hydrothermal fluid flow is taken to other structural settings. These may be structural settings significant for geothermal production, such as normal fault terminations (e.g. the horse-tailing ends of major normal faults) or fault intersections (including accommodation zones and displacement transfer zones) (Faulds et al., 2011, 2013; Boden, 2017). To explore another scale dimension, prepared thin sections of field samples could also be studied microstructurally in 2D, in a similar manner to that presented for macro-fractures in *Chapter 2*. Although not presented within this study, some preliminary analyses of X-Ray Fluorescence (XRF) data collected in the field highlight the variation in vein and host rock chemistry within fault damage zones and across the wider regional structure, and in future may be used to provide further understanding regarding the spatial distribution of fluid flow, as well as its impact on hydrothermal alteration and mechanical strength. Preliminary data indicate that hydrothermally altered host rocks are typically enriched in Fe_2O_3 , TiO_2 , MnO , MgO and K_2O – and depleted in Ca – with respect to a ‘fresh’ host rock, possibly reflecting compositional changes such as the breakdown of amphiboles and precipitation of epidote. Preliminary work suggests that alteration chemistry mapping correlates well with observations presented in *Chapters 2 and 3*.

Regarding *how early precipitation phases influence the temporal evolution of structural permeability*, it is first suggested that significant further textural analysis could be performed using a combination of optical petrography, SEM and CL, in greater detail than has been done in *Chapter 3*, but also on a wider range of vein samples. Employing additional techniques such as Electron Back-Scatter Diffraction (EBSD) (cf. McNamara et al., 2016), Energy Dispersive Spectroscopy (EDS) (cf. Goldstein et al., 2003 and Allen, 2017) and fluid inclusion analyses (to investigate crystallographic orientation, chemical evolution and quantitative measurements of fluid pressure/temperature respectively, both between and within vein crystals) would provide more quantitative constraints as to the conditions at which stress evolved and how individual fractures may have sealed. Preparatory work has been performed for all aforementioned techniques, and a study of this nature would partner well with experimental work proposed in *Chapter 5*. Unconfined Compressive Strength (UCS) and Brazilian Tensile Strength (BTS) datasets presented in *Chapter 3* may also be expanded through the testing of a wider range of samples and subsequent microstructural analysis. (e.g. using SEM to more accurately characterise fractured vein microstructures).

As to how the dataset could be improved to assess *how hydrothermal alteration affects the mechanical and frictional strength of fractured reservoirs*, future rock deformation experiments should explore conditions more applicable to those of a typical geothermal reservoir (i.e. high effective pressures and temperatures). This could be achieved through the creation of 'yield curves' for existing hydrothermally altered field samples, whereby the stress at which the onset of inelastic strain occurs (i.e. failure/yield point) is determined experimentally for a range of effective pressures and temperatures within the same sample (cf. Baud et al., 2006; Bedford et al., 2018; Allen et al., 2020). It would also be valuable to assess the impact of pressure and temperature on altered rock permeability (cf. Kushnir et al., 2017). Together these analyses would contribute important findings towards understanding the optimisation of geothermal stimulation by fluid injection (e.g. Ghassemi, 2012), as well as how permeability may evolve during conventional geothermal production (e.g. Gunnarsson, 2011). Further analyses that would benefit from being performed at a wider range of temperatures, are the direct shear experiments in clays presented in *Chapter 4*. The purpose of such experiments would be to investigate the influence of water, temperature and time on the frictional strength, stability and healing rate of clay-filled fractures, in a similar manner to a study of frictional healing in quartz presented by Karner et al. (1997). As well as the addition of temperature to such experiments, the study of a wider range of phyllosilicates would aid the understanding of how crystal structure affects frictional strength and stability, particularly given the large difference between the two clay materials studied here.

Finally, regarding future suggestions for research into *what controls the nature, rate and volume of precipitation in fractured geothermal systems*, *Chapter 5* has presented a range of avenues that can be explored using the newly described and calibrated experimental apparatus. It is suggested that priority is given to performing the recommended suite of systematic experiments detailed here (i.e. fluid flow containing different minerals in solution through a range of fractured rocks with different permeabilities, at a range of applicable temperatures and pressures, varied at different rates). This in itself is a vast body of work, yet it is likely to yield data that will provide important insights into the physiochemical processes that govern sealing rates - and therefore permeability evolution - in hydrothermal systems. Key considerations that must be addressed in ways that have not yet been outlined concern the effects of using more complex fluid chemistries (e.g. Giggenbach, 1981, 1984, 1995, 1997; Arnórsson and Gudmundsson, 2003); comparisons of experimental vein textures to natural vein textures (and in particular how they indicate the relative dominance of crystal nucleation versus growth kinetics, which may be assessed through a range of thin section analyses as discussed above); and the effect of crossing water phase boundaries. The latter point may ultimately become an important focus for future research in this area, since supercritical fluids have higher enthalpies and lower viscosity than water/steam and thus have the potential to significantly increase energy output from geothermal wells (e.g. Fridleifsson et al., 2014; Boden, 2017).

References

- Aagaard, P. and Helgeson, H. C. (1982) 'Thermodynamic and kinetic constraints on reaction rates among minerals and aqueous solutions. I. Theoretical considerations', *American Journal of Science*, 282, pp. 237- 285.
- Aben, F.M., Doan, M.-L., Mitchell, T.M., Toussaint, R., Reuschle, T., Fondriest, M., Gratier, J.-P. and Renard, F. (2016) 'Dynamic fracturing by successive coseismic loadings leads to pulverization in active fault zones', *Journal of Geophysical Research: Solid Earth*, 121, pp. 2338–2360.
- Aharonov, E. and Scholz, C.H. (2018) 'A Physics-Based Rock Friction Constitutive Law: Steady State Friction', *Journal of Geophysical Research: Solid Earth*, 123, pp. 1591–1614.
- Aiyama, K., Mizoguchi, K., Hirano, K. and Takizawa, S. (2019) 'Effects of sample preparation on the microstructural signatures of faulting in clay-bearing fault gouge', *Journal of Structural Geology*, 126, pp.100-108.
- Akayuli, C., Ofosu, B., Nyako, S.O. and Kwabena, O.O. (2013) 'The influence of observed clay content on shear strength and compressibility of residual sandy soils', *International Journal of Engineering Research and Applications*, 3(4), pp. 2538–2542.
- Aksu, I., Bazilevskaya, E. and Karpyn, Z.T. (2015) 'Swelling of clay minerals in unconsolidated porous media and its impact on permeability', *GeoResJ* 7, pp. 1–13.
- Allen, M.J., (2017) *Physicochemical Evolution of an Active Plate Boundary Fault; the Alpine Fault, New Zealand: Insight from the Deep Fault Drilling Project*. PhD Thesis, University of Liverpool. Available at: <https://livrepository.liverpool.ac.uk/3019608/> (Accessed: 15 October 2019).
- Allen, M.J., Faulkner, D.R., Worden, R.H., Rice-Birchall, E., Katirtsidis, N. and Utley, J.E.P. (2020) 'Geomechanical and petrographic assessment of a CO2 storage site: Application to the Acorn CO2 Storage Site, offshore United Kingdom', *International Journal of Greenhouse Gas Control*, 94.
- Anders, M. H., and Wiltschko, D. V. (1994) 'Microfracturing, paleostress and the growth of faults', *Journal of Structural Geology*, 16, pp. 795–815.
- Anderson, E.M. (1951) *The Dynamics of Faulting*, Edinburgh: Oliver & Boyd.
- André, L., Rabemanana, V. and Vuataz, F.D. (2006) 'Influence of water-rock interactions on fracture permeability of the deep reservoir at Soultz-sous-Forêts, France', *Geothermics*, 35 (5–6), pp. 507–531.
- Árnason, K. (2020) 'New Conceptual Model for the Magma-Hydrothermal-Tectonic System of Krafla, NE Iceland', *Geosciences*, 10(34), pp. 1-27
- Arnórsson, S., Axelsson, G. and Sæmundsson, K., 'Geothermal systems in iceland', *Jökull*, 58, pp. 269–302.
- Aquion (2015) *Mineral Solubility and Saturation Index*. Available at: <https://www.aqion.de/site/168> (Accessed 14 June 2018).
- Arancibia, G., Fujita, K., Hoshino, K., Mitchell, T.M., Cembrano, J., Gomila, R., Morata, D., Faulkner, D.R. and Rempe, M. (2014) 'Hydrothermal alteration in an exhumed crustal fault zone: Testing geochemical mobility in the Caleta Coloso Fault, Atacama Fault System, Northern Chile', *Tectonophysics*, 623, pp. 147-168.
- Ármansson, H. (2012) 'Geochemical Aspects of Geothermal Utilization'. In: Sayigh, A. (ed.) *Comprehensive Renewable Energy*, 7, pp. 95–168. Oxford: Elsevier.
- Armitage, P., Faulkner, D.R. and Worden, R.H. (2013) 'Caprock Corrosion', *Nature Geoscience*, 6(2), pp. 79-80.

- Armitage, P.J., Worden, R.H., Faulkner, D.R., Aplin, A.C., Butcher, A.R. and Iliffe, J. (2010) 'Diagenetic and sedimentary controls on porosity in Lower Carboniferous fine-grained lithologies, Krechba field, Algeria: A petrological study of a caprock to a carbon capture site' *Marine and Petroleum Geology*, 27, pp. 1395–1410.
- Arnórsson, S., D'Amore, F., and Gerardo, J. (2000) *Isotopic and chemical techniques in geothermal exploration*. Vienna, International Atomic Energy Agency, 351pp.
- Arnórsson, S., and Gudmundsson, B.T. (2003) 'Geochemical Monitoring of the Response of Geothermal Reservoirs to Production Load – examples from Krafla, Iceland', (Proceedings of the International Geothermal Conference, Reykjavík, 2003), pp. 30–36. Available at: <https://rafhladan.is/bitstream/handle/10802/9392/S07Paper117.pdf?sequence=1>.
- Ashby M.F. and Sammis C.G. (1990) 'The damage mechanics of brittle solids in compression', *Pure Applied Geophysics*, 133(3), pp. 489–521.
- ASTM International (2014) 'D7012-14: Standard Test Methods for Compressive Strength and Elastic Moduli of Intact Rock Core Specimens under Varying States of Stress and Temperatures', *ASTM International Committee D-18 on Soil and Rock*, pp 1-9.
- ASTM International (2016) 'D3967-16: Standard Test Method for Splitting Tensile Strength of Intact Rock Core Specimens', *ASTM International Committee D-18 on Soil and Rock*, pp 1-5.
- Aydin, A. (2000) 'Fractures, faults, and hydrocarbon entrapment, migration and flow', *Marine and Petroleum Geology* 17, pp. 797-814.
- Aydin, A. and Nur, A. (1982) 'Evolution of stepover basins and their scale independence', *Tectonics*, 1, pp. 91–105.
- Aydin, A. and Nur, A. (1985) 'The types and role of step-overs in strike-slip tectonics'. In: Biddle, K. T. & Christie-Blick, N. (Eds) *Strike-Slip Deformation, Basin Formation, and Sedimentation, SEPM Special Publications* 37, pp. 35–44.
- Axelsson, G., Thórhallsson, S. and Björnsson, G. (2006), 'Stimulation of geothermal wells in basaltic rock in Iceland' (ENGINE- Enhanced Geothermal Innovative Network for Europe, Kartause Ittingen, Zürich, 29 June – 1 July, 2006). Available at: https://www.researchgate.net/publication/242234259_Stimulation_of_geothermal_wells_in_basaltic_rock_in_Iceland.
- Bala, P., Samantaray, B.K. and Srivastava, S. (2000) 'Dehydration transformation in Camontmorillonite', *Bulletin of Materials Science*, 23, pp. 61-67.
- Ball, J.L., Stauffer, P.H., Calder, E.S. and Valentine, G.A. (2015) 'The hydrothermal alteration of cooling lava domes', *Bulletin of Volcanology*, 77 (102).
- Baria, R., Baumgärtner, J., Gérard, A., Jung, R. and Garnish, J. (1999) 'European HDR research programme at soultz-sous-Forêts (France) 1987–1996', *Geothermics*, 28, pp. 655–669.
- Barker, S.L.L., Cox, S.F., Eggins, S.M., and Gagan, M.K. (2006) 'Microchemical Evidence for Episodic Growth of Antitaxial Veins During Fracture-Controlled Fluid Flow', *Earth and Planetary Science Letters*, 250, pp. 331–344.
- Barnhoorn, A., Cox, S.F., Robinson, D. and Senden, T.J. (2010) 'Stress- and fluid-driven failure during fracture array growth: Implications for coupled deformation and fluid flow in the crust', *Geology*, 38(9), pp. 779-782.
- Barton, C., Zoback, M.D. and Moos, D. (1995) 'Fluid flow along potentially active faults in crystalline rock', *Geology*, 23(8), pp. 683-686.
- Baud, P., Vajdova, V. and Wong, T. (2006) 'Shear-enhanced compaction and strain localization: inelastic deformation and constitutive modeling of four porous sandstones', *Journal of Geophysical Research, Solid Earth*, 111.
- Bedford, J.D., Faulkner, D.R., Leclère, H. and Wheeler, J. (2018) 'High-resolution mapping of yield curve shape and evolution for porous rock: the effect of inelastic compaction on porous bassanite', *Journal of Geophysical Research, Solid Earth*, 123, pp. 1217–1234.

- Beeler, N.M. and Tullis, T.E. (1995) 'Implications of Coulomb plasticity for the velocity dependence of experimental faults', *Pure and Applied Geophysics*, 144, pp. 251–276.
- Beeler, N.M., Tullis, T.E. and Weeks, J.D. (1994) 'The roles of time and displacement in the evolution effect in rock friction', *Geophysical Research Letters*, 21, pp. 1987–1990.
- Behnsen, J. and Faulkner, D.R. (2012) 'The effect of mineralogy and effective normal stress on frictional strength of sheet silicates', *Journal of Structural Geology*, 42, pp. 49–61.
- Behnsen, J. and Faulkner, D.R. (2013) 'Permeability and frictional strength of cation-exchanged montmorillonite', *Journal of Geophysical Research: Solid Earth*, 118, pp. 2788–2798.
- Békri, S., Thovert, J.-F. and Adler, P.M. (1997) 'Dissolution and deposition in fractures', *Engineering Geology*, 48 (3–4), pp. 283–308.
- Berger, B.R. (2007) 'The 3D fault and vein architecture of strike-slip releasing- and restraining bends: evidence from volcanic-centre-related mineral deposits'. In: Cunningham, W.D. and Mann, P. (Eds), 'Tectonics of Strike-Slip Restraining and Releasing Bends', *Geological Society, London, Special Publications*, 290, pp. 447–471.
- Bertani, R. (2016) 'Geothermal Power Generation in the World 2010-2014 Update Report', *Geothermics*, 60, pp. 31-43.
- Bertram, A. and Kalthoff, J.F. (2003) 'Crack propagation toughness of rock for the range of low to very high crack speeds', *Key Engineering Materials*, 251–252, pp. 423–430.
- Bethke, C.M. (1986) 'Inverse hydrologic analysis of the distribution and origin of Gulf Coast-type geopressed zones', *Journal of Geophysical Research*, 91, pp. 6535–6545.
- Bethke, C.M. (2007) 'Kinetics of dissolution and precipitation'. In: Bethke, C.M. (ed.) *Geochemical and Biogeochemical Reaction Modeling*. Cambridge University Press, pp. 231 – 244.
- Bhattacharya, P., Rubin, A.M. and Beeler, N.M., (2017) 'Does fault strengthening in laboratory rock friction experiments really depend primarily upon time and not slip?', *Journal of Geophysical Research: Solid Earth*, 122, pp. 6389–6430.
- Biegel, R.L., Sammis, C.G. and Dieterich, J.H. (1989) 'The frictional properties of a simulated gouge having a fractal particle distribution', *Journal of Structural Geology*, 11, pp. 827–846.
- Bird G., Boon J. and Stone, T. (1986) 'Silica transport during steam injection into oil sands 1. Dissolution and precipitation kinetics of quartz: new results and review of existing data', *Chemical Geology*, 54, pp. 69–80.
- Blanpied, M., Tullis, T.E. and Weeks, D. (1998) 'Effects of slip, slip rate, and shear heating on the friction of granite', *Journal of Geophysical Research*, 103, pp. 489–511.
- Blenkinsop, T. (2002) *Deformation Microstructures and Mechanisms in Minerals and Rocks*. Dordrecht, Kluwer Academic.
- Boden, D.R. (2017) *Geologic Fundamentals of Geothermal Energy*. CRC Press, 423p.
- Bodvarsson, G. S. (1988) 'Model predictions of Svartsengi reservoir, Iceland' *Water Resources Research*, 24 (10) pp. 1740-1746.
- Boersma, A., Vercauteren, F., Fischer, H. and Pizzocolo, F. (2018) 'Scaling Assessment, Inhibition and Monitoring of Geothermal Wells', (Proceedings of the 43rd Workshop on Geothermal Reservoir Engineering, Stanford, California, February 12-14). Available at: <https://pangea.stanford.edu/ERE/pdf/IGAstandard/SGW/2018/Boersma.pdf>
- Bonnet, E., Bour, O., Odling, N. and Davy, P. (2001) 'Scaling of fracture systems in geological media', *Geophysics*, 39(3), pp. 347-383.
- Bons, P.D. (2000) 'The Formation of Veins and Their (micro-) structures', *Journal of the Virtual Explorer*, 2, pp. 1–47.
- Bons, P.D. (2001) 'The formation of large quartz veins by rapid ascent of fluids in mobile hydrofractures', *Tectonophysics*, 336, pp. 1-17.

- Bons, P.D., Elburg, M.A., and Gomez-Rivas, E. (2012) 'A review of the formation of tectonic veins and their microstructures', *Journal of Structural Geology*, 43, pp. 33–62.
- Boretti, A. (2022) 'Enhanced geothermal systems (EGS) a key component of a renewable energy-only grid', *Arabian Journal of Geosciences*, 15, 72.
- Bos, B., Peach, C.J. and Spiers, C.J. (2000) 'Frictional-viscous flow of simulated fault gouge caused by the combined effects of phyllosilicates and pressure solution', *Tectonophysics*, 327, pp. 173–194.
- Bos, B. and Spiers, C.J. (2000) 'Effect of phyllosilicates on fluid-assisted healing of gouge-bearing faults', *Earth and Planetary Science Letters*, 184, pp. 199–210.
- Bos, B. and Spiers, C.J. (2001) 'Experimental investigation into the microstructural and mechanical evolution of phyllosilicate-bearing fault rock under conditions favouring pressure solution', *Journal of Structural Geology*, 23, pp. 1187–1202.
- Bourouis, S. and Bernard, P. (2007) 'Evidence for coupled seismic and aseismic fault slip during water injection in the geothermal site of Soultz (France), and implications for seismogenic transients', *Geophysical Journal International*, 169(2), pp. 723–732.
- Brace, W.F. (1980) 'Permeability of Crystalline and Argillaceous Rocks', *International Journal of Rock Mechanics and Mining Sciences*, 17, pp. 241–251.
- Brace, W.F., Paulding, B.J.R. and Scholz, C. (1966) 'Dilatancy in the fracture of crystalline rocks', *Journal of Geophysical Research*, 71, pp. 3939–3953.
- Brace, W.F., Walsh, J.B. and Frangos, W.T. (1968) 'Permeability of granite under high pressure', *Journal of Geophysical Research*, 73, pp. 2225–2236.
- Brantley, S.L., Evans, B., Hickman, S.H., and Crerar, D.A. (1990) 'Healing of Microcracks in Quartz: Implications for Fluid Flow', *Geology*, 18(2), pp. 136–139.
- Bromley, C., Brockbank, K., Glynn-Morris, T., Rosenberg, M., Pender, M., O'Sullivan, M., and Currie, S., (2013) 'Geothermal subsidence study at Wairakei-Tauhara, New Zealand' *Proceedings of the Institution of Civil Engineers-Geotechnical Engineering*, 166 (2), pp. 211–223.
- Brosse, E., Magnier, C. and Vincent, B. (2005) 'Modelling fluid–rock interaction induced by the percolation of CO₂-enriched solutions in core samples: the role of reactive surface area', *Oil & Gas Science and Technology – Revue d'IFP Energies Nouvelles*, 60, pp. 287–305.
- Brown, K. (2013) *Mineral scaling in geothermal power production: Technical Report: 2013-39*. Reykjavik, Iceland: United Nations University-Geothermal Training Programme.
- Brown, K.L. and Dunstall, M. (2000) 'Silica scaling under controlled hydrodynamic conditions', (Proceedings of the World Geothermal Congress, Kyushu-Tokyo, Japan, 28 May – 10 June), pp. 3039–3044. Available at: <https://www.geothermal-energy.org/pdf/IGAstandard/WGC/2000/R0249.PDF>.
- Brown, K.M., Kopf, A., Underwood, M.B. and Weinberger, J.L. (2003) 'Compositional and fluid pressure controls on the state of stress on the Nankai subduction thrust: A weak plate boundary', *Earth and Planetary Science Letters*, 214, pp. 589–603.
- Brown, S.R. (1987) 'Fluid flow through rock joints: the effect of surface roughness', *Journal of Geophysical Research: Solid Earth*, 92(B2), pp. 1337–1347.
- Brown, S.R., Stockman, H.W. and Reeves, S. J. (1995) 'Applicability of the Reynolds equation for modeling fluid flow between rough surfaces', *Geophysical Research Letters*, 22 (18), pp. 2537–2540.
- Browning, J. Meredith, P. and Gudmundsson, A. (2016) 'Cooling-dominated cracking in thermally stressed volcanic rocks', *Geophysical Research Letters*, 43(16), pp.8417–8425
- Bucher, K., and Stober, I. (2010) 'Fluids in the Upper Continental Crust', *Geofluids*, 10, pp. 241–253.

- Byerlee, J.D. (1978) 'Friction of rocks', *Pure and Applied Geophysics*, 116, pp. 615–626.
- Byrappa, K. and Yoshimura, M. (2001) 'Hydrothermal Growth of Some Selected Crystals'. In: Byrappa, K. and Yoshimura, M. (ed). *Handbook of Hydrothermal Technology: A Technology for Crystal Growth and Materials Processing*. USA, William Andrew Publishing, LLC.
- Caine, J.S., Evans, J.P. and Forster, C.B. (1996) 'Fault zone architecture and permeability structure', *Geology*, 24, pp. 1025–1028.
- Caine, J.S., Bruhn, R.L., and Forster, C.B. (2010) 'Internal structure, fault rocks, and inferences regarding deformation, fluid flow, and mineralization in the seismogenic Stillwater normal fault, Dixie Valley, Nevada', *Journal of Structural Geology*, 32, pp. 1576–1589.
- Caputo, R. and Hancock, P.L. (1999) 'Crack-jump mechanism and its implications for stress cyclicity during extension fracturing', *Geodynamics*, 27, pp. 45–60.
- Carpenter, B.M., Ikari, M.J. and Marone, C. (2016) 'Laboratory observations of time-dependent frictional strengthening and stress relaxation in natural and synthetic fault gouges', *Journal of Geophysical Research: Solid Earth*, 121, pp. 1183–1201.
- Carpenter, B.M., Saffer, D.M. and Marone, C. (2012) 'Frictional properties and sliding stability of the San Andreas fault from deep drill core', *Geology*, 40(8), pp. 759–762.
- Carson, B., and Sreaton, E.J. (1998) 'Fluid flow in accretionary prisms: Evidence for focused, time-variable discharge', *Reviews of Geophysics*, 36, p. 329–351.
- Cembrano, J., González, G., Arancibia, G., Ahumada, I., Olivares, V., and Herrera, V. (2005) 'Fault Zone Development and Strain Partitioning in an Extensional Strike-Slip Duplex: A Case Study from the Mesozoic Atacama Fault System, Northern Chile', *Tectonophysics*, 400(1–4), pp. 105–125.
- Chang, K.W., Hesse, M.A. and Nicot, J.P., (2013) 'Reduction of lateral pressure propagation due to dissipation into ambient mudrocks during geological carbon dioxide storage', *Water Resource Research*, 49(5), pp. 2573–2588.
- Chester, F.M. (1995) 'A rheologic model for wet crust applied to strike-slip faults' *Journal of Geophysical Research*, 100, pp. 33–44.
- Chester, F.M. and Chester, J.S. (1998) 'Ultracataclasite structure and friction processes of the Punchbowl fault, San Andreas system, California', *Tectonophysics*, 295, pp. 199–221.
- Chester, F.M. and Chester, J.S. (2000) 'Stress and deformation along wavy frictional faults', *Journal of Geophysical Research - Solid Earth*, 105, pp. 23421–23430.
- Chester, F.M., Evans, J.P. and Biegel, R.L. (1993) 'Internal structure and weakening mechanisms of the San Andreas fault', *Journal of Geophysical Research*, 98, pp. 771–786.
- Chester, F.M. and Logan, J.M. (1986) 'Composite planar fabric of gouge from the Punchbowl fault, California', *Journal of Structural Geology*, 9, pp. 621–634.
- Childs, C., Manzocchi, T., Walsh, J.J., Bonson, C.G., Nicol, A. and Schopfer, M.P.J. (2009) 'A geometric model of fault zone and fault rock thickness variations', *Journal of Structural Geology*, 31, pp. 117–127.
- Choi, J.H., Edwards, P., Ko, K. and Kim, Y.S. (2016) 'Definition and classification of fault damage zones: a review and a new methodological approach', *Earth Science Reviews*, 152, pp. 70–87.
- Collettini, C., Niemeijer, A.R., Viti, C. and Marone, C. (2009) 'Fault zone fabric and fault weakness', *Nature*, 462, pp. 907–910.
- Colten-Bradley, V.A. (1987) 'Role of Pressure in Smectite Dehydration - Effects on Geopressure and Smectite-to-illite Transformation' *The American Association of Petroleum Geologists Bulletin*, 71(11), pp. 1414–1427.
- Corning (2012) *MACOR®: Machinable Glass Ceramic For Industrial Applications*. Corning. Available at: <https://www.corning.com/worldwide/en/products/advanced-optics/product->

- materials/specialty-glass-and-glass-ceramics/glass-ceramics/macor.html (Accessed 29 September 2018).
- Cowie, P.A. and Scholz, C.H. (1992) 'Physical explanation for the displacement-length relationship of faults using a post-yield fracture mechanics model', *Journal of Structural Geology*, 14(10), pp. 1133-1148.
- Cox, S.F. (1995) 'Faulting processes at higher fluid pressure: An example of fault valve behavior from Wattle Gully Fault, Victoria, Australia', *Journal of Geophysical Research*, 100, pp. 12841–12859.
- Cox, S.F. (1999) 'Deformational controls on the dynamics of fluid flow in mesothermal gold systems' In: McCaffrey, K.J.W., Lonergan, L.G. and Wilkinson, J.J. (Eds) *Fractures, Fluid Flow and Mineralization*. Geological Society, London, Special Publications 155, 123-140.
- Cox, S.F., (2005) 'Coupling between deformation, fluid pressures and fluid flow in ore-producing hydrothermal environments', *Economic Geology, 100th Anniversary Volume*, pp. 39–75.
- Cox, S.F. (2010) 'The application of failure mode diagrams for exploring the roles of fluid pressure and stress states in controlling styles of fracture-controlled permeability enhancement in faults and shear zones', *Geofluids*, 10, pp. 217–233.
- Cox, S.F., Knackstedt, M.A., and Braun, J. (2001) 'Principles of structural control on permeability and fluid flow in hydrothermal systems', *Reviews in Economic Geology*, 14, p. 1–24.
- Cox, S.J.D. and Scholz, C.H. (1988) 'On the formation and growth of faults: an experimental study', *Journal of Structural Geology*, 10 (4), pp. 413-430.
- Crawford, B.R., Faulkner, D.R. and Rutter, E.H. (2008) 'Strength, porosity, and permeability development during hydrostatic and shear loading of synthetic quartz-clay fault gouge' *Journal of Geophysical Research: Solid Earth*, 113, pp. 1–14.
- Crerar, D.A. and Anderson, G.M. (1971) 'Solubility and Solvation Reactions of Quartz in Dilute Hydrothermal Solutions', *Chemical Geology*, 8(2), pp. 107–122.
- Crerar, D. A., Axtmann, E. V. and Axtmann, R. C. (1981) 'Growth and ripening of silica polymers in aqueous solutions', *Geochimica et Cosmochimica Acta*, 45 (8), pp. 1259-1266.
- Crider, J.G. and Peacock, D.C. (2004) 'Initiation of brittle faults in the upper crust: a review of field observations', *Journal of Structural Geology*, 26, pp. 691–707.
- Crowell, J.C. (1974) 'Origin of late Cenozoic basins of southern California' In: Dickinson, W.R. (Ed) *Tectonics and Sedimentation*. SEPM Special Publications, 22, pp. 190–204.
- Cunningham, W. D. and Mann, P. (2007) 'Tectonics of strike-slip restraining and releasing bends'. In: Cunningham, W.D. and Mann, P. (Eds) 'Tectonics of Strike-Slip Restraining and Releasing Bends', *Geological Society, London, Special Publications*, 290, pp. 1-12.
- Dallmeyer, D., Brown, M., Grocott, J., Taylor, G.K. and Treloar, P. (1996) 'Mesozoic Magmatic and Tectonic Events Within the Andean Plate Boundary Zone, 26°-27° 30', North Chile: Constraints from 40Ar/39Ar Mineral Ages', *Journal of Geology*, 104, pp. 19-40.
- Davatzes, N.C. and Hickman, S. (2010) 'Stress, fracture, and fluid-flow analysis using acoustic and electrical image logs in hot fractured granites of the Coso Geothermal Field, California, U.S.A.' In: Poppelreiter, M., Garcia-Carballido, C., Kraaijveld, M. (Eds.), *Dipmeter and Borehole Image Log Technology: AAPG Memoir 92*, pp. 259–293.
- De Jong, S.M., Spiers, C.J. and Busch, A. (2014) 'Development of swelling strain in smectite clays through exposure to carbon dioxide', *International Journal of Greenhouse Gas Control*, 24, pp. 149–161.
- De Paola, N., Holdsworth, R.E., Collettini, C., McCaffrey, K.J.W. and Barchi, M.R. (2007) 'The structural evolution of dilational stepovers in regional transtensional zones'. In: Cunningham, W.D. and Mann, P. (Eds) 'Tectonics of Strike-Slip Restraining and Releasing Bends', *Geological Society, London, Special Publications*, 290, 433–445.

- Den Hartog, S.A.M. (2013) *Frictional behaviour of megathrust fault gouges under in-situ subduction zone conditions*. PhD Thesis, University of Utrecht. Available at: <https://dspace.library.uu.nl/handle/1874/273873> (Accessed: 12 September 2021).
- Den Hartog, S.A.M., Faulkner, D.R. and Spiers, C.J. (2020) 'Low friction coefficient of phyllosilicate fault gouges quantitatively explained', *Journal of Geophysical Research: Solid Earth*, 125.
- Detwiler, R.L. and Rajaram, H. (2007) 'Predicting dissolution patterns in variable aperture fractures: evaluation of an enhanced depth-averaged computational model', *Water Resources Research*, 43(4), W04403.
- Dewey, J. and Lamb, S.H. (1992) 'Active tectonics of the Andes', *Tectonophysics*, 205, pp. 79–95.
- Dezayes, C., Genter, A., and Valley, B. (2010) 'Overview of the Fracture Network at Different Scales Within the Granite Reservoir of the EGS Soultz Site (Alsace, France)', (Proceedings of the World Geothermal Congress, Bali, Indonesia, 25-29 April, 2010), pp. 25–29. Available at: <https://www.geothermal-energy.org/pdf/IGAstandard/WGC/2010/3116.pdf>.
- Diamond, S. and Kinter, E.B. (1958) 'Surface areas of clay minerals as derived from measurements of glycerol retention', *Clays and Clay Minerals*, 5, pp. 334–347.
- Dieterich, J.H. (1972) 'Time-dependent friction in rocks', *Journal of Geophysical Research*, 77, pp. 3690–3697.
- Dieterich, J.H. (1978) 'Time-dependent friction and the mechanics of stick-slip', *Pure and Applied Geophysics*, 116, pp. 790–806.
- Dieterich, J.H. (1979) 'Modeling of rock friction: 1. Experimental results and constitutive equations', *Journal of Geophysical Research*, 84, pp. 2161–2168.
- Dieterich, J.H. (1981) 'Constitutive Properties of Faults With Simulated Gouge' In: Carter, N., Friedman, M., Logan, J.M. and Stearns, D.W. (Eds.), *Mechanical Behavior of Crustal Rocks: The Handin Volume*. American Geophysical Union, pp. 103–120.
- Dieterich, J.H. and Conrad, G. (1984) 'Effect of Humidity on Time- and Velocity-Dependent Friction in Rocks', *Journal of Geophysical Research*, 89, pp. 4196–4202.
- Dieterich, J.H. and Kilgore, B.D. (1994) 'Direct Observation of Frictional Contacts: New Insights for State-dependent Properties', *Pure and Applied Geophysics*, 143, pp. 283–301.
- Dieterich, J.H. and Kilgore, B.D. (1996) 'Imaging surface contacts: power law contact distributions and contact stresses in quartz, calcite, glass and acrylic plastic', *Tectonophysics*, 256, pp. 219–239.
- DM Dielectric Manufacturing (2019) *PEEK (Polyetheretherketone)*. Available at: <https://dielectricmfg.com/knowledge-base/peek/> (Accessed 14 June 2018).
- Dobson, P.F., Kneafsey, T.J., Hulen, J. and Simmons, A. (2013) 'Porosity, Permeability, and Fluid Flow in the Yellowstone Geothermal System, Wyoming', *Journal of Volcanology and Geothermal Research*, 123, pp. 313–324.
- Dobson, P.F., Kneafsey, T.J., Sonnenthal, E.I., Spycher, N. and Apps, J.A. (2003) 'Experimental and numerical simulation of dissolution and precipitation: implications for fracture sealing at Yucca Mountain, Nevada', *Journal of Contaminant Hydrology*, 62/63, pp. 459–476.
- Donath, F.A. (1961) 'Experimental Study of Shear Failure in Anisotropic Rocks', *Geological Society of America Bulletin*, 72, pp. 985–990.
- Doubra, P., Kamran-Pirzaman, A., Mohammadi, A.H., and Hassanalizadeh, R. (2017) 'Thermodynamic modelling of Scale (Calcite, Barite, Anhydrite and Gypsum) Deposition from Brine', *Journal of Molecular Liquids*, 230, pp. 96–103.
- Dove P.M. and Crerar D.A. (1990) 'Kinetics of quartz dissolution in electrolyte solutions using a hydrothermal mixed flow reactor', *Geochimica et Cosmochimica Acta*, 54, pp. 955–969.

- Eberhardt, E., Stead, D., Stimpson, B. and Read, R.S. (1998) 'Identifying crack initiation and propagation thresholds in brittle rock', *Canadian Geotechnical Journal*, 35, pp. 222–233.
- Elburg, M.A., Bons, P.D., Foden, J., and Passchier, C.W. (2002) 'The origin of fibrous veins: Constraints from geochemistry', in: de Meer, S., Drury, M. R., Bresser, J.H.P. and Pennock, G.M., (eds.) *Deformation mechanisms, rheology and tectonics: Current status and future perspectives*: Geological Society [London] Special Publication 200, pp. 103–118.
- Electronics Tutorials (2020) *Resistors in parallel*. Available at: https://www.electronicstutorials.ws/resistor/res_4.html (Accessed 29 November 2020).
- Elkhouri, J., Ameli, P. and Detwiler, R. (2013) 'Dissolution and deformation in fractured carbonates caused by flow of CO₂-rich brine under reservoir conditions', *International Journal of Greenhouse Gas Control*, 16, pp. 203-215.
- Ellis, A.J. (1959) 'The Solubility of Calcite in Carbon Dioxide Solutions', *American Journal of Science*, 257, pp. 354–365.
- Ellis, A.J. (1963) 'The Solubility of Calcite in Sodium Chloride Solutions At High Temperatures', *American Journal of Science*, 261, pp. 259–267.
- Ellsworth, W.L. (2013) 'Injection induced earthquakes', *Science*, 341, pp. 6142.
- Engelder, T. (1987) 'Joints and shear fractures in rocks'. In: Atkinson, B.K (ed.) *Fracture Mechanics of Rock*. Academic Press, London, pp. 27–69.
- Engineering ToolBox (2004) Steam - Viscosity vs. Pressure. Available at: https://www.engineeringtoolbox.com/steam-viscosity-d_770.html (Accessed 28 April 2018).
- Espinoza, D.N., Kim, S.H. and Santamarina, J.C. (2011) 'CO₂ geological storage – geotechnical implications', *KSCE Journal of Civil Engineering*, 15, pp. 707–719.
- Etheridge, M.A., Wall, V.J., Cox, S.F., and Vernon, R.H. (1984) 'High Fluid Pressures During Regional Metamorphism and Deformation: Implications for Mass Transport and Deformation Mechanisms', *Journal of Geophysical Research*, 89(B6), pp. 4344–4358.
- Euro Inox (2007) *Stainless steel – Tables of physical properties*. Available at: https://www.worldstainless.org/Files/issf/non-image-files/PDF/Euro_Inox/Tables_TechnicalProperties_EN.pdf (Accessed 12 January 2019).
- Evans, K. (2005) 'Permeability creation and damage due to massive fluid injections into granite at 3.5 km at Soultz: 2. Critical stress and fracture strength', *Journal Of Geophysical Research*, 110, B04204.
- Evans, J.P., Forster, C.B. and Goddard, J.V. (1997) 'Permeability of fault-related rocks, and implications for hydraulic structure of fault zones', *Journal of Structural Geology*, 19, pp. 1393–1404.
- Evans, K., Genter, A. and Sausse, J. (2005) 'Permeability creation and damage due to massive fluid injections into granite at 3.5 km at Soultz: 1. Borehole observations', *Journal Of Geophysical Research*, 110, B04203.
- Faber, C., Rowe, C.D., Miller, J.A., Fagereng, Å., and Neethling, J.H. (2014) 'Silica gel in a fault slip surface: Field evidence for palaeo-earthquakes?', *Journal of Structural Geology*, 69, pp. 108–121.
- Farquharson, J., Heap, M.J., Varley, N.R., Baud, P. and Reuschle, T. (2015) 'Permeability and porosity relationships of edifice-forming andesites: a combined field and laboratory study', *Journal of Volcanology and Geothermal Research*, 297, pp. 52–68.
- Faulds, J.E., Hinz, N.H., Coolbaugh, M.F., Cashman, P.H., Kratt, C. and Dering, G. (2011) 'Assessment of Favorable Structural Settings of Geothermal Systems in the Great Basin, Western USA', *Geothermal Resources Council Transactions*, 35, pp. 777–783.

- Faulds, J.E., Hinz, N.H., Dering, G.M., and Siler, D.L. (2013) 'The Hybrid Model - The Most Accommodating Structural Setting for Geothermal Power Generation in Great Basin, Western USA', *Geothermal Resources Council Transactions*, 37, pp. 4–10.
- Faulkner, D.R. and Armitage, P.J. (2013) 'The effect of tectonic environment on permeability development around faults and in the brittle crust', *Earth and Planetary Science Letters*, 375, pp. 71–77.
- Faulkner, D.R., Jackson, C.A.L., Lunn, R.J., Schlische, R.W., Shipton, Z.K., Wibberley, C.A.J., and Withjack, M. O. (2010) 'A review of recent developments concerning the structure, mechanics and fluid flow properties of fault zones', *Journal of Structural Geology*, 32(11), pp. 1557–1575.
- Faulkner, D.R., Lewis, A.C. and Rutter, E.H. (2003) 'On the internal structure and mechanics of large strike-slip faults: field observations from the Carboneras fault, southeastern Spain', *Tectonophysics*, 367, pp. 235-251.
- Faulkner, D.R., Mitchell, T.M., Behnsen, J., Hirose, T. and Shimamoto, T. (2011) 'Stuck in the mud? Earthquake nucleation and propagation through accretionary forearcs', *Geophysical Research Letters*, 38, pp. 1–5.
- Faulkner, D.R., Mitchell, T.M., Healy, D. and Heap, M.J. (2006) 'Slip on 'weak' faults by the rotation of regional stress in the fracture damage zone', *Nature*, 444, pp. 922-925.
- Faulkner, D.R., Mitchell, T.M., Jensen, E., and Cembrano, J. (2011) 'Scaling of fault damage zones with displacement and the implications for fault growth processes', *Journal of Geophysical Research: Solid Earth*, 116(5), pp. 1–11.
- Faulkner, D.R., Mitchell, T.M., Rutter, E.H. and Cembrano, J. (2008) 'On the structure and mechanical properties of large strike-slip faults'. In: Wibberley, C. A. J., Kurz, W., Imber, J., Holdsworth, R. E. and Collettini, C. (Eds) *The Internal Structure of Fault Zones: Implications for Mechanical and Fluid-Flow Properties*, Geological Society, London, Special Publications 299, 139–150.
- Faulkner, D.R., and Rutter, E. H. (2000) 'Comparisons of Water and Argon Permeability in Natural Clay-Bearing Fault Gouge Under High Pressure at 20°C', *Journal of Geophysical Research*, 105(B7), pp. 16415 -16426.
- Faulkner, D.R. and Rutter, E.H. (2001), 'Can the maintenance of overpressured fluids in large strike-slip fault zones explain their apparent weakness?', *Geology*, 29, pp. 503–506.
- Faulkner, D.R., Sanchez-Roa, C., Boulton, C. and den Hartog, S.A.M. (2018), 'Pore-fluid Pressure Development in Compacting Fault Gouge in Theory, Experiments, and Nature', *Journal of Geophysical Research: Solid Earth*, pp. 1–16.
- Fisher, N.I. (1996) *Statistical Analysis of Circular Data*. Cambridge University Press, UK.
- Fisher, D.M., and Brantley, S.L. (1992) 'Models of Quartz Overgrowth and Vein Formation: Deformation and Episodic Fluid Flow in an Ancient Subduction Zone', *Journal of Geophysical Research*, 97, pp. 20043-20061.
- Fournier, R. (1977) 'Chemical geothermometers and mixing models for geothermal systems', *Geothermics*, 5, pp. 41–50.
- Fournier, R.O. (1985) 'The behaviour of silica in hydrothermal solutions' In: Gerger, B.R. and Bethke, P.M. (Eds.), *Geology and Geochemistry of Epithermal Systems, Reviews in Economic Geology*, 2, pp. 45–72.
- Fournier, R.O. (1989) 'Lectures on Geochemical Interpretation of Hydrothermal Waters, UNU' *Geothermal Training Programme*, 10, 73p.
- Fournier, R.O., and Potter, R.W. (1982) 'An Equation Correlating the Solubility of Quartz in Water from 25 to 900°C at Pressures up to 10,000 bars', *Geochimica et Cosmochimica Acta*, 46, pp. 1969–1973.

- Fournier, R.O. and Rowe, J.J. (1966) 'Estimation of Underground Temperatures from the Silica Content of Water from Hot Springs and Wet-Steam Wells', *American Journal of Science*, 264, pp. 685–697.
- Friðleifsson, G.Ó., Elders, W.A. and Albertsson, A. (2014) 'The concept of the Iceland deep drilling project', *Geothermics*, 49, pp. 2-8.
- Frye, K.M. and Marone, C. (2002) 'Effect of humidity on granular friction at room temperature', *Journal of Geophysical Research: Solid Earth*, 107, pp. 2309.
- García-Romero, E. and Suarez, M. (2018) 'A structure-based argument for non-classical crystal growth in natural clay minerals', *Mineralogical Magazine*, 82, pp. 171-180.
- Garibaldi, F. (1980) *The effect of some hydrodynamic parameters on silica deposition*, Diploma Project 80.11, Geothermal Institute, University of Auckland, 44 pp. Available at: <https://www.library.auckland.ac.nz/subject-guides/eng/docs/geothermal.pdf> (Accessed 14 August 2019).
- Gartrell, A., Zhang, Y.H., Lisk, M. and Dewhurst, D. (2004) 'Fault intersections as critical hydrocarbon leakage zones: integrated field study and numerical modelling of an example from the Timor Sea, Australia', *Marine and Petroleum Geology*, 21(9), pp. 1165-1179.
- Gates-Rector, S. and Blanton, T. (2019) 'The Powder Diffraction File: A Quality Materials Characterization Database', *Powder Diffraction*, 34(4), pp. 1-9.
- Genter, A., Evans, K., Cuenot, N., Fritsch, D. and Sanjuan, B. (2010) 'Contribution of the exploration of deep crystalline fractured reservoir of Soultz to the knowledge of enhanced geothermal systems (EGS)', *Comptes Rendus Geoscience*, 342 (7–8), pp. 502-516,
- Ghassemi, A. (2012) 'A Review of Some Rock Mechanics Issues in Geothermal Reservoir Development', *Geotechnical and Geological Engineering*, 30, pp 647–664.
- Ghassemi, A. and Kumar, G. (2007) 'Changes in Fracture Aperture and Fluid Pressure due to Thermal Stress and Silica Dissolution/Precipitation Induced by Heat Extraction from Subsurface Rocks', *Geothermics*, 36(2), pp. 115–140.
- Giese, R.F. (1978) 'Electrostatic Interlayer Forces of Layer Structure Minerals', *Clays and Clay Minerals*, 26, pp. 51–57.
- Giese, R.F. (1979) 'Hydroxyl Orientations in 2:1 Phyllosilicates', *Clays and Clay Minerals*, 27, pp. 213–223.
- Giggenbach, W.F. (1981) 'Geothermal Mineral Equilibria', *Geochimica et Cosmochimica Acta*, 45, pp. 393–410.
- Giggenbach, W.F. (1984) 'Mass transfer in hydrothermal alteration systems - a conceptual approach', *Geochimica et Cosmochimica Acta*, 48 (12), pp. 2693–2711.
- Giggenbach, W.F. (1995) 'Variations in the chemical and isotopic composition of fluids discharged from the Taupo Volcanic Zone, New Zealand', *Journal of Volcanology and Geothermal Research*, 68 (1-3) pp. 89-116.
- Giggenbach, W.F. (1997) 'The origin and evolution of fluids in magmatic-hydrothermal systems'. In: Barnes H.L. (ed.) *Geochemistry of hydrothermal ore deposits*. Wiley, New York, pp. 737–796.
- Gillespie, P. A., Howard, C.B., Walsh, J.J. and Watterson, J. (1993) 'Measurement and Characterization of Spatial Distributions of Fractures', *Tectonophysics*, 226(1-4), pp. 113-141.
- Glowacka, E., González, J., and Fabriol, H. (1999) 'Recent Vertical Deformation in Mexicali Valley and its Relationship with Tectonics, Seismicity, and the Exploitation of the Cerro Prieto Geothermal Field, Mexico', *Pure and Applied Geophysics*, 156(4), pp. 591-614.
- Gobierno de Chile (2003) *Mapa Geológico-Estructural Sector Cerro Coloso-Cerro Mulato, entre las coordenadas geográficas 23°45'00"-24°02'00" S y 70°31'52"-70°30'02" N, Sur y*

- Antofagasta, Chile*. Servicio Nacional de Geología Y Minería: Subdirección Nacional de Geología.
- Mapa Geológico de Chile: Versión Digital
- Godinho, J.R.A. and Withers, P.J. (2018) 'Time-Lapse 3d Imaging of Calcite Precipitation in a Microporous Column', *Geochimica et Cosmochimica Acta*, 222, pp. 156–170.
- Goldstein, J.I., Newbury, D.E., Echlin, P., Joy, D.C., Lyman, C. E., Lifshin, E., Sawyer, L. and Michael, J. R. (2003) *Scanning Electron Microscopy and X-ray Microanalysis*, Springer US, Boston, MA.
- Gomila, R., Arancibia, G., Mitchell, T. M., Cembrano, J. M., and Faulkner, D. R. (2016) 'Palaeopermeability Structure Within Fault Damage Zones: A Snap-Shot from Microfracture Analyses in a Strike-Slip System', *Journal of Structural Geology*, 83, pp. 103–120.
- González, G. and Carrizo, D. (2003) 'Segmentación, cinemática y cronología relativa de la deformación tardía de la Falla Salar del Carmen, Sistema de Fallas de Atacama, (23840'S), norte de Chile', *Revista Geológica de Chile*, 30, pp. 223–244.
- González, G., Cembrano, J., Carrizo, D., Macci, A. and Schneider, H. (2003) 'The link between fore arc tectonics and Pliocene-Quaternary deformation of the Coastal Cordillera, northern Chile', *Journal of South American Earth Sciences*, 16, pp. 321-342.
- González, G., Dunai, T., Carrizo, D., and Allmendinger, R. (2006) 'Young Displacements on the Atacama Fault System, Northern Chile from Field Observations and Cosmogenic ²¹Ne Concentrations', *Tectonics*, 25(3), pp. 1–15.
- Grant, M.A. and Bixley, P.F. (2011) *Geothermal Reservoir Engineering, Second edition*. Academic Press, Burlington, Vermont.
- Grant, M.A., Clearwater, J., Quinão, J., Bixley, P. F. and Le Brun, M. (2013) 'Thermal stimulation of geothermal wells: a review of field data', (Proceedings of the 38th Workshop on Geothermal Reservoir Engineering, Stanford, California, 11-13th February, 2013). Available at: <https://www.proceedings.com/content/018/018451webtoc.pdf>.
- Grasemann, B., Exner, U., and Tschegg, C. (2011) 'Displacement–length scaling of brittle faults in ductile shear', *Journal of Structural Geology*, 33, pp. 1650–1661.
- Griffiths, L., Heap, M.J., Wang, F., Daval, D., Gilg, H.A., Baud, P., Schmittbuhl, J. and Genter, A. (2016) 'Geothermal implications for fracture-filling hydrothermal precipitation', *Geothermics*, 64, pp. 235-245.
- Gudmundsson, A. (2011) *Rock Fractures in Geological Processes*, Cambridge: Cambridge University Press.
- Gudmundsson, A., Berg, S.S., Lyslo, K.B. and Skurtveit, E. (2001) 'Fracture networks and fluid transport in active fault zones', *Journal of Structural Geology*, 23, pp. 343-353.
- Gudmundsson, A., Fjeldskaar, I. and Brenner, S.L. (2002) 'Propagation pathways and fluid transport of hydrofractures in jointed and layered rocks in geothermal fields', *Journal of Volcanology and Geothermal Research*, 116, pp. 257-278.
- Gudmundsson, A., Simmenes, T.H., Larsen, B. and Philipp, S.L. (2010) 'Effects of internal structure and local stresses on fracture propagation, deflection, and arrest in fault zones', *Journal of Structural Geology*, 32, pp. 1643-1655.
- Guéguen, Y. and Palciauskas, V., (1994) *Introduction to the Physics of Rocks*. Princeton University Press.
- Gunnarsson, G. (2011) 'Mastering reinjection in the Hellisheidi field, SW-Iceland: a story of successes and failures', (Proceedings of the Thirty-Sixth Workshop on Geothermal Reservoir Engineering, Stanford, California, 31 January – 2 February, 2011). Available at: <https://pangea.stanford.edu/ERE/pdf/IGAstandard/SGW/2011/gunnarsson1.pdf>.

- Haines, S.H., Kaproth, B., Marone, C., Saffer, D. and Van der Pluijm, B. (2013) 'Shear zones in clay-rich fault gouge: A laboratory study of fabric development and evolution'. *Journal of Structural Geology*, 51, pp. 206–225.
- He, J. and Afolagboye, L.O. (2018) 'Influence of layer orientation and interlayer bonding force on the mechanical behavior of shale under Brazilian test conditions', *Acta Mechanica Sinica*, 34(2), pp. 349-358.
- He, X., Sinan, M., Kwak, H. and Hoteita, H. (2021) 'A corrected cubic law for single-phase laminar flow through rough-walled fractures', *Advances in Water Resources*, 154, 103984.
- Healy, D. (2008) 'Damage patterns, stress rotations and pore fluid pressures in strike-slip fault zones', *Journal of Geophysical Research: Solid Earth*, 113, B12407.
- Healy, D., Jones, R.R. and Holdsworth, R.E. (2006) 'Three-dimensional brittle shear fracturing by tensile crack interaction', *Nature*, 439, pp. 64–67.
- Healy, D., Rizzo, R. E., Cornwell, D. G., Farrell, N. J. C., Watkins, H., and Timms, N. E. (2017) 'FracPaQ: A MATLAB™ Toolbox for the Quantification of Fracture Patterns', *Journal of Structural Geology*, 95, pp. 1-16.
- Heap, M.J. and Kennedy, B.M. (2016) 'Exploring the scale-dependent permeability of fractured andesite', *Earth and Planetary Science Letters*, 447, pp. 139–150.
- Heap, M.J., Baud, P., Kushnir, A., Reuschlé, T., Dauny, F., Farquharson, J., Griffiths, L. and Schmittbuhl, J. (2016) 'The new HPHT triaxial apparatus at IPG Strasbourg (France)', *European Geothermal Congress*, Strasbourg, France, 19-24 Sept 2016.
- Heap, M.J., Lavallée Y., Laumann A., Hess K.-U., Meredith P. G., and Dingwell D. B. (2012) 'How Tough is Tuff in the Event of Fire', *Geology*, 40, pp. 311-314.
- Heap, M.J., Lavallée, Y., Petrakova, L., Baud, P., Reuschlé, T., Varley, N.R. and Dingwell, D.B. (2014) 'Microstructural controls on the physical and mechanical properties of edifice-forming andesites at Volcan de Colima, Mexico', *Journal of Geophysical Research*, pp. 1–39.
- Heap M.J., Mollo, S., Vinciguerra, S., Lavallée, Y., Hess, K.-U., Dingwell, D.B., Baud, P., and Iezzi G. (2013) 'Thermal Weakening of the Carbonate Basement Under Mt. Etna Volcano (Italy): Implications for Volcano Instability', *Journal of Volcanology and Geothermal Research*, 250, pp. 42-60.
- Heap, M.J., Violay, M., Wadsworth, M.B. and Vasseur, J. (2017) 'From rock to magma and back again: The evolution of temperature and deformation mechanism in conduit margin zones', *Earth and Planetary Science Letters*, 463, pp. 92-100.
- Henley, R.W. and Ellis, A.J. (1983) 'Geothermal Systems Ancient and Modern: A Geochemical Review', *Earth-Science Reviews*, 19, pp. 1–50.
- Herrera, V., Cembrano, J., Arancibia, G., Kojima, S., and Prior, D. (2005) 'Synkinematic Fluid Flow and Vein Formation by Depressurization in Magmatic Arcs: A Case Study from Atacama Fault System, Northern Chile', *Society*, pp. 372–375.
- Herrington, R.J. and Wilkinson, J.J. (1993) 'Colloidal gold and silica in mesothermal vein systems: *Geology*, 21, pp. 539–542.
- Hickman, S.H. and Evans, B. (1995) 'Kinetics of pressure solution at halite-silica interfaces and intergranular clay films', *Journal of Geophysical Research*, 100, pp. 13113–13132.
- Hickman, S., Sibson, R., and Bruhn, R. (1995) 'Mechanical involvement of fluids in faulting', *Journal of Geophysical Research*, 100, pp. 12831–12840.
- Hickman, S.H., Younker, L.W., Zoback, M.D. and Cooper, G.A. (1995) 'The San Andreas fault zone drilling project: Scientific objectives and technological objectives', *Journal of Energy Resources Technology*, 117, pp. 263-270.
- Hilgers, C., Dilg-Gruschinski, K., and Urai, J.L. (2004) 'Microstructural Evolution of Syntaxial Veins Formed by Advective Flow', *Geology*, 32(3), pp. 261–264.

- Hilgers, C., Koehn, D., Bons, P.D. and Urai, J.L. (2000) 'Development of crystal morphology during uniaxial growth in a progressively widening vein: II. Numerical simulations of the evolution of antitaxial fibrous veins', *Journal of Structural Geology*, 23, pp. 873–885.
- Hilgers, C., D. Koehn, P. Bons, and J. Urai (2001) 'Development of crystal morphology during uniaxial growth in a progressively widening vein: II. Numerical simulations of the evolution of antitaxial fibrous veins', *Journal of Structural Geology*, 23(6–7), pp. 873–885
- Hilgers, C., and Tentorey, E. (2004) 'Fracture sealing of quartzite under a temperature gradient: Experimental results', *Terra Nova*, 16(4), pp. 173–178.
- Hilgers, C. and Urai, J. L. (2002a) 'Experimental Study of Syntaxial Vein Growth During Lateral Fluid flow in Transmitted Light: First results', *Journal of Structural Geology*, 24(6–7), pp. 1029–1043.
- Hilgers, C. and Urai, J.L. (2002b) 'Microstructural Observations on Natural Syntectonic Fibrous Veins: Implications for the Growth Process', *Tectonophysics*, 352(3–4), pp. 257–274.
- Holdsworth, R.E., van Diggelen, E.W.E., Spiers, C.J., de Bresser, J.H.P., Walker, R.J., Bowen, L. (2011) 'Fault rocks from the SAFOD core samples: Implications for weakening at shallow depths along the San Andreas Fault, California', *Journal of Structural Geology*, 33, pp. 132–144.
- Ikari, M.J., Marone, C. and Saffer, D.M. (2011) 'On the relation between fault strength and frictional stability', *Geology*, 39, pp. 83–86.
- Ikari, M.J., Saffer, D.M. and Marone, C. (2007) 'Effect of hydration state on the frictional properties of montmorillonite-based fault gouge', *Journal of Geophysical Research: Solid Earth*, 112, pp. 1–12.
- Ikari, M.J., Saffer, D.M. and Marone, C. (2009a) 'Frictional and hydrologic properties of clay-rich fault gouge', *Journal of Geophysical Research*, 114, pp. 1–18.
- Ikari, M.J., Saffer, D.M. and Marone, C. (2009b) 'Frictional and hydrologic properties of a major splay fault system, Nankai subduction zone', *Geophysical Research Letters*, 36, pp. 1–5.
- Inoue, M. and Utada, A. (1988) 'Smectite-to-chlorite transformation in thermally metamorphosed volcanoclastic rocks in the Kamikita area, northern Honshu, Japan', *American Mineralogist*, 76, pp. 628–640.
- Insulationet (2019) *High temperature insulation wool*. Available at: <http://insulationet.com/en/materials/high-temperature-wool/> (Accessed on: 12 January 2019).
- Israelachvili, J.N., McGuiggan, P.M. and Homola, A.M. (1988) 'Dynamic Properties of Molecularly Thin Liquid Films', *Science*, 240, pp. 189–191.
- Jackson, D. (1985) 'Petrology, Porosity, and Permeability of Berea Sandstone (Mississippian), Perry Township, Ashland County, Ohio', *AAPG Bulletin*, 69(9), p. 1438.
- Jaeger, J.C., Cook, N.G.W. and Zimmerman, R.W. (2007) *Fundamentals of Rock Mechanics*, London: Blackwell Publishing.
- Jensen, E., Cembrano, J., Faulkner, D., Veloso, E. and Arancibia, G. (2011) 'Development of a self-similar strike-slip duplex system in the Atacama Fault system, Chile', *Journal of Structural Geology*, 33, pp. 1611–1626.
- Johnson, R.B. and DeGraff, J.V. (1988) *Principles of Engineering Geology*, Wiley.
- Karner, S.L., Marone, C., and Evans, B. (1997) 'Laboratory Study of Fault Healing and Lithification in Simulated Fault Gouge Under Hydrothermal Conditions', *Tectonophysics*, 277(1–3), pp. 41–55.
- Karnland, O., Olsson, S. and Nilssen, U. (2016) 'Mineralogy and sealing properties of various bentonites and smectite-rich clay materials', In: Kärnbränslehantering, S. (ed.) *AB Technical Report TR-06-30*, Stockholm, 113p.

- Kattenhorn, S.A. and Marshall, S.T. (2006) 'Fault-induced perturbed stress fields and associated tensile and compressive deformation at fault tips in the ice shell of Europa: implications for fault mechanics', *Journal of Structural Geology*, 28, pp. 2204-2221.
- Kell, G.S. (1975) 'Density, Thermal Expansivity, and Compressibility of Liquid Water from 0° to 150°C: Correlations and Tables for Atmospheric Pressure and Saturation Reviewed and Expressed on 1968 Temperature Scale', *Journal of Chemical and Engineering Data*, 2, pp. 97-105.
- Kissling, W.M., Ellis, S. and McNamara, D. D. (2015) 'Modelling Fluid Flow Through Fractured Rock: Examples Using TVZ Geothermal Reservoirs', (Proceedings of the 37th New Zealand Geothermal Workshop, Taupo, New Zealand, 18-20 November, 2015). Available at: https://www.geothermal-energy.org/pdf/IGASstandard/NZGW/2015/86_Kissling.pdf.
- Kosoglu, L.M., Bickmore, B.R., Filz, G.M. and Madden, A.S. (2010) 'Atomic force microscopy method for measuring smectite coefficients of friction', *Clays and Clay Minerals*, 58, pp. 813-820.
- Kristmannsdóttir, H. (1989) 'Types of scaling occurring by geothermal utilization in Iceland', *Geothermics*, 18, pp. 183-190.
- Kronenberg, A.K. and Tullis, J. (1984) 'Flow strengths of quartz aggregates: Grain size and pressure effects due to hydrolytic weakening', *Journal of Geophysical Research: Solid Earth*, 89, pp. 4281-4297.
- Kushnir, A.R.L., Martel, C., Champallier, R., and Wadsworth, F.B. (2017) 'Permeability Evolution in Variably Glassy Basaltic Andesites Measured Under Magmatic Conditions', *Geophysical Research Letters*, 44 (20), pp. 10262-10271.
- Lamur, A., Kendrick, J.E., Eggertsson, G.H., Wall, R.J., Ashworth, J.D., and Lavallée, Y. (2017) 'The Permeability Of Fractured Rocks in Pressurised Volcanic and Geothermal Systems', *Scientific Reports*, 7(1), 6173.
- Lamur, A., Lavallée, Y., Iddon, F., Hornby, A. J., Kendrick, J. E., von Aulock, F. W., and Wadsworth, F. B. (2018) 'Disclosing the Temperature of Columnar Jointing and Fluid Flow in Lavas', *Nature Communications*, 9, 1432.
- Lasaga, A.C. (1981) 'Rate laws of chemical reactions', in: Lasaga, A.C. and Kirkpatrick, R.J (eds.) *Kinetics of Geochemical Processes*, Mineral Society of America, Washington, D.C. pp 1-68.
- Lasaga, A.C. (1997) *Kinetic theory in the earth sciences*: Princeton, New Jersey: Princeton University Press, 811 p.
- Laubach, S.E. (1997) 'A method to detect natural fracture strike in sandstones', *AAPG Bulletin*, 81, pp. 604-623.
- Laubach, S.E., and Diaz-Tushman, K. (2009) 'Laurentian Palaeostress Trajectories and Ephemeral Fracture Permeability, Cambrian Eriboll Formation sandstones west of the Moine Thrust Zone, NW Scotland', *Journal of the Geological Society*, 166(2), pp. 349-362.
- Laubach, S.E., Eichhubl, P., Hargrove, P., Ellis, M.A. and Hooker, J.N. (2014) 'Fault core and damage zone fracture attributes vary along strike owing to interaction of fracture growth, quartz accumulation, and differing sandstone composition', *Journal of Structural Geology*, 68, pp. 207-226.
- Laubach, S.E., Reed, R.M., Olson, J.E., Lander, R.H. and Bonnell, L.M. (2004) 'Coevolution of crack-seal texture and fracture porosity in sedimentary rocks: cathodoluminescence observations of regional fractures', *Journal of Structural Geology*, 26, pp. 967-982,
- Lawther, S.E.M., Dempster, T.J., Shipton, Z.K. and Boyce, A.J. (2016) 'Effective crustal permeability controls fault evolution: An integrated structural, mineralogical and isotopic study in granitic gneiss, Monte Rosa, northern Italy', *Tectonophysics*, 690 (A), pp. 160-173.

- Lázaro, B.B. (2015) 'Halloysite and Kaolinite: Two clay minerals with geological and technological importance', *La Revista de la Real Academia de Ciencias Zaragoza*, 70, pp. 1-33.
- Leckenby, R.J., Sanderson, D.J. and Lonergan, L. (2005) 'Estimating flow heterogeneity in natural fracture systems', *Journal of Volcanology and Geothermal Research*, 148, pp. 116-129.
- Ledingham, P., Cotton, L. and Law, R. (2019) 'The United Downs Deep Geothermal Power Project', *Proceedings: 44th Workshop on Geothermal Reservoir Engineering, Stanford, California, February 11-13, 2019*.
- Lee, Y. J. and Morse, J. W (1999) 'Calcite precipitation in synthetic veins: implications for the time and fluid volume necessary for vein filling', *Chemical Geology*, 156, pp. 151-170.
- Lee, Y. J., Morse, J. W., and Wiltschko, D. V. (1996) 'An Experimentally Verified Model for Calcite Precipitation in Veins', *Chemical Geology*, 130 (3-4), pp. 203-215.
- Lees, J. M. (2002) 'Three-Dimensional Anatomy of a Geothermal Field, Coso, Southeast-Central California', *Geological Society of America Memoir*, 195, pp. 259-276.
- Legarth, B., Huenges, E. and Zimmermann, G. (2005) 'Hydraulic fracturing in a sedimentary geothermal reservoir: Results and implications', *International Journal of Rock Mechanics and Mining Sciences*, 42 (7-8), pp. 1028-1041.
- LibreTexts (2021) *Phase Diagrams*. Available at: [https://chem.libretexts.org/Bookshelves/Physical_and_Theoretical_Chemistry_Textbook_Maps/Supplemental_Modules_\(Physical_and_Theoretical_Chemistry\)/Physical_Properties_of_Matter/States_of_Matter/Phase_Transitions/Phase_Diagrams](https://chem.libretexts.org/Bookshelves/Physical_and_Theoretical_Chemistry_Textbook_Maps/Supplemental_Modules_(Physical_and_Theoretical_Chemistry)/Physical_Properties_of_Matter/States_of_Matter/Phase_Transitions/Phase_Diagrams) (Accessed on: 20 June 2021).
- Likhachev, E.R. (2003) 'Dependence of water viscosity on temperature and pressure', *Technical Physics*, 48, pp. 514-515.
- Limberger, J., Boxem, T., Pluymaekers, M., Bruhn, D., Manzella, A., and Calcagno, P. (2018) 'Geothermal Energy in Deep Aquifers: A Global Assessment of the Resource Base for Direct Heat Utilization', *Renewable and Sustainable Energy Reviews*, 82, pp. 961-975.
- Lindsay, D., Zentilli, M., and Rojas, J. (1995) 'Evolution of an active ductile to brittle shear system controlling mineralization at the Chuquicamata porphyry copper deposit, Chile' *International Geology Review*, 37, pp. 945-958.
- Linker, M.F. and Dieterich, J.H. (1992) 'Effects of variable normal stress on rock friction: Observations and constitutive equations', *Journal of Geophysical Research*, 97, pp. 4923-4940.
- Lockner, D. A., Byerlee, J.D, Kuksenko, V., Ponomarev, A. and Sidorin, A. (1992) 'Observations of quasistatic fault growth from acoustic emissions, in: Evans, B. and Wong, T.-F. (eds.) *Fault Mechanics and Transport Properties of Rocks: A Festschrift in Honor of W. F. Brace*, Academic Press, London
- Lockner, D.A., Morrow, C.A., Moore, D.E. and Hickman, S.H. (2011) 'Low strength of deep San Andreas fault gouge from SAFOD core', *Nature*, 472, pp. 82-86.
- Lockner, D.A., Naka, H., Tanaka, H., Ito, H. and Ikeda, R. (2000) 'Permeability and strength of core samples from the Nojima fault of the 1995 Kobe earthquake', (Proceedings of the International Workshop on the Nojima Fault Core and Borehole Data Analysis, Tsukuba, Japan, 22-23 November, 1999), pp. 147-152. Available at: https://earthquake.usgs.gov/static/lfs/research/rockphysics/Permeability_strength.pdf.
- Logan, J.M., Dengo, C.A., Higgs, N.G., Wang, Z.Z. (1992) 'Fabrics of Experimental Fault Zones: Their Development and Relationship to Mechanical Behavior', *Fault Mechanics and Transport Properties of Rocks*, pp. 33-67.
- Logan, J.M. and Rauenzahn, K.A. (1987) 'Frictional dependence of gouge mixtures of quartz and montmorillonite on velocity, composition and fabric', *Tectonophysics*, 144, pp. 87-108.

- Long, J.V.P., Agrell, S.O. (1965) 'The cathodoluminescence of minerals in thin section', *Mineralogical Magazine*, 34, pp. 318–326.
- Lowell R. P., Van Cappellen P. and Germanovich L. N. (1993) 'Silica precipitation in fractures and the evolution of permeability in hydrothermal upflow zones', *Science*, 260, pp. 192–194.
- Mackenzie, R.C. (1957) 'Hydration and hydroxylation with special reference to montmorillonite', *Geologiska Föreningen i Stockholm Förhandlingar*, 79, pp. 58–61.
- Mair, K. and Marone, C. (1999) 'Friction of simulated fault gouge for a wide range of velocities and normal stresses', *Journal of Geophysical Research*, 104, pp. 28899–28914.
- Majer, E.L., Baria, R., Stark, M., Oates, S., Bommer, J., Smith, B. and Asanuma, H. (2007) 'Induced seismicity associated with enhanced geothermal systems' *Geothermics*, 36, pp. 185–227
- Majer, E.L. and Peterson, J. E. (2007) 'The impact of injection on seismicity at The Geysers, California Geothermal Field' *International Journal of Rock Mechanics and Mining Sciences*, 44 (8), pp. 1079-1090.
- Manzocchi, T., Heath, A.E., Walsh, J.J. and Childs, C. (2002) 'The representation of two phase fault-rock properties in flow simulation models', *Petroleum Geoscience*, 8, pp. 119-132.
- Marone, C. (1998) 'Laboratory-Derived Friction Laws and Their Application To Seismic Faulting', *Annual Review of Earth and Planetary Sciences*, 26, pp. 643–696.
- Marone, C. and Kilgore, B. (1993) 'Scaling of the critical slip distance for seismic faulting with shear strain in fault zones', *Nature*, 362, pp. 618–621.
- Marone, C. and Scholz, C.H. (1988) 'The Depth of Seismic Faulting and the Upper Transition from Stable to Unstable Slip Regimes', *Geophysical Research Letters*, 15, pp. 621–624.
- Marrett, R. and Laubach, S.E. (1997) 'Diagenetic controls on fracture permeability and sealing', *International Journal of Rock Mechanics and Mining Sciences*, 34 (3-4), pp. 2041-20411.
- Martel, S.J. (1990) 'Formation of compound strike-slip fault zones Mount Abbot quadrangle California', *Journal of Structural Geology*, 12(7), pp. 869-882.
- Martin, J.T. and Lowell, R.P. (2000) 'Precipitation of Quartz During High-Temperature, Fracture-Controlled Hydrothermal Upflow at Ocean Ridges: Equilibrium Versus Linear Kinetics', *Journal of Geophysical Research: Solid Earth*, 105, pp. 869–882.
- Maslan, F. and Littman, T. (1953) 'Compressibility Chart for Hydrogen and Inert Gases', *Industrial and Engineering Chemistry Research*, 45(7), pp. 1566-1568.
- Massiot, C., McNamara, D.D., Nicol, A. and Townend, J. (2015) Fracture width and spacing distributions from borehole televiewer logs and core in the Rotokawa geothermal field, New Zealand, *Proceedings: World Geothermal Congress 2015*.
- Material Properties (2019) *Brass: Density, strength, hardness and melting point*. Available at: <https://material-properties.org/brass-density-strength-hardness-melting-point/> (Accessed on: 10 January 2019).
- Mauldon, M., Dunne, W.M. and Rohrbaugh, M.B. (2001) 'Circular scanlines and circular windows: new tools for characterizing the geometry of fracture traces', *Journal of Structural Geology*, 23(2), pp. 247-258.
- McLean, K. and McNamara, D. D. (2011) 'Fractures Interpreted from Acoustic Formation Imaging Technology: Correlation to Permeability', (Proceedings of the 36th Workshop on Geothermal Reservoir Engineering, Stanford, USA, 31 January – 2 February, 2011), pp. 1-10. Available at: <https://pangea.stanford.edu/ERE/pdf/IGAstandard/SGW/2011/mclean.pdf>.
- McNamara, D.D., Faulkner, D.R. and McCarney, E. (2014) 'Rock Properties of Greywacke Basement Hosting Geothermal Reservoirs, New Zealand: Preliminary Results', (Proceedings of the 39th Workshop on Geothermal Reservoir Engineering, Stanford, USA, 24-26 February, 2014), pp. 1-10. Available at: <https://pangea.stanford.edu/ERE/pdf/IGAstandard/SGW/2014/Mcnamara.pdf>.

- McNamara, D.D., Massiot, C., Lewis, B. and Wallis, I.C. (2015) Heterogeneity of structure and stress in the Rotokawa Geothermal Field, New Zealand, *Journal of Geophysical Research*, 120, pp. 1243–1262.
- McNamara, D.D., Lister, A., and Prior, D.J. (2016) 'Calcite Sealing in a Fractured Geothermal Reservoir: Insights from Combined EBSD and Chemistry Mapping', *Journal of Volcanology and Geothermal Research*, 323, pp. 38–52.
- McNamara, D.D., Milicich, S.D., Massiot, C., Villamor, P., McLean, K., S epulveda, F. and Ries, W.F. (2019) 'Tectonic Controls on Taupo Volcanic Zone Geothermal Expression: Insights From Te Mihi, Wairakei Geothermal Field', *Tectonics*, 38(8), pp. 3011 - 3033.
- Megel, T., Kohl, T. and Rose, P. (2005) 'Reservoir modeling for stimulation planning at the Coso EGS project', *Geothermal Resources Council Transaction*, 29, pp. 173–176.
- Meller, C. and Kohl, T. (2014) 'The significance of hydrothermal alteration zones for the mechanical behavior of a geothermal reservoir', *Geothermal Energy*, 2, pp. 1–21.
- Miller, S.A. (2015) 'Modeling enhanced geothermal systems and the essential nature of large-scale changes in permeability at the onset of slip' *Geofluids*, 15 (1-2), pp. 338-349.
- Mitchell, T.M. and Faulkner, D.R. (2008) 'Experimental measurements of permeability evolution during triaxial compression of initially intact crystalline rocks and implications for fluid flow in fault zones', *Journal of Geophysical Research - Solid Earth*, 113.
- Mitchell, T.M. and Faulkner, D.R. (2009) 'The nature and origin of off-fault damage surrounding strike-slip fault zones with a wide range of displacements: A field study from the Atacama fault system, northern Chile', *Journal of Structural Geology*, 31(8), pp. 802-816.
- Mock, J.E., Tester, J.W. and Wright, P.M. (1997) 'Geothermal energy from the earth: Its potential impact as an environmentally sustainable resource', *Annual Review of Energy and the Environment*, 22, pp. 305-356.
- Moeck, I., Kwiatek, G. and Zimmermann, G. (2009) 'Slip tendency analysis, fault reactivation potential and induced seismicity in a deep geothermal reservoir', *Journal of Structural Geology*, 31 (10), pp. 1174-1182.
- Moore, D.E. and Lockner, D.A. (2004) 'Crystallographic controls on the frictional behavior of dry and water-saturated sheet structure minerals', *Journal of Geophysical Research*, 109, pp. 1–16.
- Moore, D.E. and Lockner, D.A. (2007) 'Friction of the Smectite Clay Montmorillonite: A Review and Interpretation of Data', in: Dixon, T. H., and Moore, J.C. (eds.) *The Seismogenic Zone of Subduction Thrust Faults*. Columbia University Press, pp. 317–345.
- Moore, D.E. and Lockner, D.A. (2011) 'Frictional strengths of talc-serpentine and talc-quartz mixtures', *Journal of Geophysical Research: Solid Earth*, 116, pp. 1–17.
- Moore, D.E., Lockner, D.A. and Byerlee, J.D. (1994) 'Reduction of permeability in granite at elevated temperatures', *Science*, 265, pp. 1558-1561.
- Moore, D.M. and Reynolds Jr., R.C. (1997) *X-Ray Diffraction and the Identification and analysis of Clay Minerals*, 2nd edition, New York, Oxford University Press, 378p.
- Morrow, C.A., Moore, D.E. and Lockner, D.A. (2000) 'The effect of mineral bond strength and adsorbed water on fault gouge frictional strength', *Geophysical Research Letters*, 27, pp. 815–818.
- Morrow, C.A., Moore, D.E., and Lockner, D.A. (2001) 'Permeability Reduction in Granite Under Hydrothermal Conditions', *Journal of Geophysical Research*, 106, pp. 551–560.
- Morrow, C.A., Moore, D.E. and Lockner, D.A. (2017) 'Frictional strength of wet and dry montmorillonite', *Journal of Geophysical Research: Solid Earth*, 122, pp. 3392–3409.
- Morrow, C.A., Radney, B. and Byerlee, J.D. (1992) 'Frictional Strength and the Effective Pressure Law of Montmorillonite and Illite Clays', *International Geophysics*, 51, pp. 69–88.

- Myers, R. and Aydin, A. (2004) 'The evolution of faults formed by shearing across joint zones in sandstones', *Journal of Structural Geology*, 26, pp. 947–966.
- Nakashima, Y. (1993) 'Buoyancy-driven propagation of an isolated fluid-filled crack in rock: Implication for fluid transport in metamorphism', *Contributions to Mineralogy and Petrology*, 114, pp. 289–295.
- Nara, Y., Meredith, P.G., Yoneda, T. and Kaneko, K. (2011) 'Influence of macro-fractures and micro-fractures on permeability and elastic wave velocities in basalt at elevated pressure', *Tectonophysics*, 503, pp. 52–59.
- Ngo, V.V., Lucas, Y., Clément, A., and Fritz, B. (2016) 'Modeling the Impact of Temperature on the Saturation State and Behavior of Minerals in the Soultz-Sous-Forêts Geothermal System', *Geothermics*, 64, pp. 196–208.
- Nicol, A., Walsh, J.J., Manzocchi, T. and Morewood, N. (2005) 'Displacement rates and average earthquake recurrence intervals on normal faults', *Journal of Structural Geology*, 27(3), pp. 541–551.
- Nixon, C., Vaagan, S., Sanderson, D.J. and Gawthorpe, R.L. (2019) 'Spatial distribution of damage and strain within a normal fault relay at Kilve, U.K.', *Journal of Structural Geology*, 118, pp. 194–209.
- Noda, H. and Shimamoto, T. (2005) 'Thermal pressurization and slip-weakening distance of a fault: An example of the Hanaore fault, southwest Japan', *Bulletin of the Seismological Society of America*, 95 (4), pp. 1224–1233.
- Noda, H. and Shimamoto, T. (2009) 'Constitutive properties of clayey fault gouge from the Hanaore fault zone, southwest Japan', *Journal of Geophysical Research: Solid Earth*, 114, pp. 1–29.
- O'Hara, A.P., Jacobi, R.D. and Sheets, H.D. (2017) 'Predicting the width and average fracture frequency of damage zones using a partial least squares statistical analysis: implications for fault zone development', *Journal of Structural Geology*, 98, pp. 38–52.
- Okamoto A., Kikuchi T. and Tsuchiya N. (2008) 'Mineral distribution within polymineralic veins in the Sanbagawa belt, Japan: implications for mass transfer during vein formation', *Contributions to Mineralogy and Petrology*, 156, pp. 323–336.
- Okamoto, A., Saishu, H., Hirano, N. and Tsuchiya, N. (2010) 'Mineralogical and textural variation of silica minerals in hydrothermal flow-through experiments: Implications for quartz vein formation', *Geochimica et Cosmochimica Acta*, 74(13), pp. 3692–3706.
- Okamoto, A. and Tsuchiya, N. (2009) 'Velocity of vertical fluid ascent within vein-forming fractures', *Geology*, 37 (6). pp. 563–566.
- Olivares, V., Cembrano, J. M., Arancibia, G., Reyes, N., Herrera, V., and Faulkner, D. R. (2010) 'Significado Tectónico y Migración de Fluidos Hidrotermales en una Red de Fallas y Vetas de un Duplex de Rumbo: un Ejemplo del Sistema de Falla de Atacama', *Andean Geology*, 37(2), pp. 473–497.
- Oliver, N., and Bons, P. (2001) 'Mechanisms of fluid flow and fluid-rock interaction in fossil metamorphic hydrothermal systems inferred from vein-wall- rock patterns, geometry and microstructure', *Geofluids*, 1, pp. 137–162.
- Ortega, O.J., Marrett, R. and Laubach, S.E. (2006) 'A scale-independent approach to fracture intensity and average fracture spacing', *AAPG Bulletin*, 90, pp. 193–208.
- Ostemeijer, G., Mitchell, T.M., Aben, F.M., Dorsey, M.T., Browning, J., Rockwell, T.K., Fletcher, J.M. and Ostermeijer, F. (2020) 'Damage zone heterogeneity on seismogenic faults in crystalline rock; a field study of the Borrego Fault, Baja California', *Journal of Structural Geology*, 137, 104016.
- Pagel M., Barbin V., Blanc P. and Ohnenstetter D. (2000) *Cathodoluminescence in Geosciences*. Springer, Berlin, Heidelberg.

- Peacock, D.C.P. and Sanderson, D.J. (1991) 'Displacements, segment linkage and relay ramps in normal fault zones', *Journal of Structural Geology*, 13, pp. 721-733.
- Peacock, D.C.P. and Sanderson, D.J. (1995) 'Strike-slip relay ramps', *Journal of Structural Geology*, 17, pp. 1351-1360.
- Pérez-Flores, P., Veloso, E., Cembrano, J., Sánchez-Alfaro, P., Lizama, M., and Arancibia, G. (2017) 'Fracture Networks, Fluid Pathways and Paleostress at the Tolhuaca Geothermal Field', *Journal of Structural Geology*, 96, pp. 134-148.
- Pine, R.J. and Batchelor, A.S. (1984) 'Downward migration of shearing in jointed rock during hydraulic injections', *International Journal of Rock Mechanics and Mining Sciences Geomechanics Abstracts*, 21, pp. 249-263.
- Pluymakers, A., Bakker, R. and Barnhoorn, A. (2020) 'Effect of a heterogeneity on tensile failure : interaction between fractures in a limestone', *EGU General Assembly*.
- Pluymakers, A.M.H. and Spiers, C.J. (2015) 'Compaction creep of simulated anhydrite fault gouge by pressure solution: Theory v. experiments and implications for fault sealing' In: Faulkner, D. R., Mariani, E., Mecklenburgh, J. (eds), *Rock Deformation from Field, Experiments and Theory: A Volume in Honour of Ernie Rutter*. Geological Society, London, Special Publications 409, pp. 107-124.
- Pola, A., Crosta, G., Fusi, N., Barberini, V. and Norini, G. (2012) 'Influence of alteration on physical properties of volcanic rocks', *Tectonophysics*, 566-567, pp. 67-86.
- Pola, A., Crosta, G.B., Fusi, N. and Castellanza, R. (2014) 'General characterization of the mechanical behaviour of different volcanic rocks with respect to alteration', *Engineering Geology*, 169, pp. 1-13.
- Pollard, D.D. and Segall, P. (1987) 'Theoretical displacements and stresses near fractures in rock: with applications to faults, joints, veins, dikes, and solution surfaces'. In: Atkinson, B.K. (Ed.) *Fracture Mechanics of Rock*. London: Academic Press, 277-349.
- Priest, S.D. (1993) *Discontinuity Analysis for Rock Engineering*, Chapman & Hall, London, United Kingdom, pp.473.
- Putnis, A., Prieto, M. and Fernandez-Diaz, L. (1995) 'Fluid supersaturation and crystallization in porous media', *Geological Magazine*, 132, pp. 1-13.
- Ramsay, J.G. (1980) 'The Crack-Seal Mechanism of Rock Deformation', *Nature*, 284, pp. 135-139.
- Ramsay, J.G., and Huber, M.I. (1983) *The techniques of modern structural geology, Volume 1: Strain analysis*: London, Academic Press, 307 p.
- Reinen, L.A., Weeks, J.D. and Tullis, T.E. (1994) 'The frictional behavior of lizardite and antigorite serpentinites: Experiments, constitutive models, and implications for natural faults', *Pure and Applied Geophysics*, 143, pp. 317-358.
- Rempe, M., Mitchell, T., Renner, J., Nippres, S., Ben-Zion, Y., and Rockwell, T. (2013) 'Damage and seismic velocity structure of pulverized rocks near the San Andreas Fault', *Journal of Geophysical Research: Solid Earth*, 118, pp. 2813- 2831.
- Rempe, M., Mitchell, T.M., Renner, J., Smith, S.A.F., Bistacchi, A. and Di Toro, G. (2018) 'The Relationship Between Microfracture Damage and the Physical Properties of Fault-Related Rocks: The Gole Larghe Fault Zone, Italian Southern Alps', *Journal of Geophysical Research: Solid Earth*, 123, pp. 7661-7687.
- Renard, F. and Ortoleva, P. (1997) 'Water films at grain-grain contacts: Debye-Hückel, osmotic model of stress, salinity, and mineralogy dependence', *Geochimica et Cosmochimica Acta*, 61, pp. 1963-1970.
- Rice, J.R., Lapusta, N. and Ranjith, K. (2001) 'Rate and State Dependent Friction and the Stability of Sliding Between Elastically Deformable Solids', *Journal of the Mechanics and Physics of Solids*, 49(9), pp. 1865-1868.

- Rice, J. R., Sammis, C. G and Parsons, R. (2005) 'Off-fault secondary failure induced by a dynamic slip pulse', *Bulletin of the Seismological Society of America*, 95(1), pp. 109–134.
- Rigopoulos, I., Tsikouras, B., Pomonis, P. and Hatzipanagiotou, K. (2010) 'The influence of alteration on the engineering properties of dolerites: the examples from the Pindos and Vourinos ophiolites (northern Greece)', *International Journal of Rock Mechanics and Mining Sciences*, 47, pp. 69–80
- Rimstidt, J.D. (1997) 'Quartz Solubility at Low Temperatures', *Geochimica et Cosmochimica Acta*, 61(13), pp. 2553–2558.
- Rimstidt, J.D., and Barnes, H.L. (1980) 'The Kinetics of Silica-Water Reactions', *Geochimica et Cosmochimica Acta*, 44, pp. 1683–1699.
- Robb, L. (2004) *Introduction to Ore-Forming Processes*, Wiley-Blackwell, 384p.
- Roberts, S., Sanderson, D.J. and Gumiel, P. (1998) 'Fractal analysis of Sn-W mineralization from Central Iberia: Insights into the role of fracture connectivity in the formation of an ore deposit', *Economic Geology*, 93, pp. 360–365.
- Rowland, J.V. and Sibson, R.H. (1998) 'Stress-Controlled Hydrothermal Fluid Flow in Basement Greywacke, Kuaotunu, Coromandel Peninsula, New Zealand', (Proceedings of the 20th New Zealand Geothermal Workshop, Auckland, New Zealand, 11-13 November, 1998), pp. 285-290. Available at: <https://www.geothermal-energy.org/pdf/IGAstandard/NZGW/1998/Rowland.pdf>.
- Royden, L.H. (1993) 'The tectonic expression of slab pull at continental convergent boundaries', *Tectonics*, 12, pp. 303–325.
- RS Components (2020) *West Instruments P6100+ DIN Rail PID Temperature Controller, 48 x 48mm 1 Input, 3 Output Relay, 100 → 240 V ac*. Available at: <https://uk.rs-online.com/web/p/temperature-controllers/1238241/> (Accessed on: 17 October 2020).
- Ruina, A.L. (1983) 'Slip Instability and State Variable Laws', *Journal of Geophysical Research*, 88, pp. 359–370.
- Rutter, E.H. (1983) 'Pressure solution in nature, theory and experiment', *Journal of the Geological Society*, 140, pp. 725–740.
- Rutter, E.H. and Maddock, R.H. (1987) 'On the mechanical properties of synthetic kaolinite / quartz fault gouge', *Terra Nova*, 4, pp. 489–500.
- Rutter, E.H., Maddock, R.H., Hall, S.H. and White, S.H. (1986) 'Comparative microstructures of natural and experimentally produced clay-bearing fault gouges', *Pure and Applied Geophysics*, 124, pp. 3–30.
- Rutter, E.H. and Mainprice, D.H. (1978) 'The effect of water on stress relaxation of faulted and unfaulted sandstone', *Pure and Applied Geophysics*, 116, pp. 634–654.
- Rykart, R. (1995) *Quarz-Monographie - Die Eigenheiten von Bergkristall, Rauchquarz, Amethyst, Chalcedon, Achat, Opal und anderen Varietäten*. Ott, Verlag.
- Saffer, D.M., Frye, K.M., Marone, C. and Mair, K. (2001) 'Laboratory results indicating complex and potentially unstable frictional behavior of smectite clay', *Geophysical Research Letters*, 28, pp. 2297–2300.
- Saffer, D.M. and Marone, C. (2003) 'Comparison of smectite- and illite-rich gouge frictional properties: Application to the updip limit of the seismogenic zone along subduction megathrusts', *Earth and Planetary Science Letters*, 215, pp. 219–235.
- Sahu, A.K. and Roy, A. (2020) 'Clustering and Connectivity of Fractal-Fracture Networks: Are they related?' *22nd EGU General Assembly*, held online 4-8 May, 2020.
- Sakuma, H. and Suehara, S. (2015) 'Interlayer bonding energy of layered minerals: Implication for the relationship with friction coefficient', *Journal of Geophysical Research: Solid Earth*, 120, pp. 2212–2219.

- Sánchez, P.M., Pérez-Flores, P., Arancibia, G., Cembrano, J., and Reich, M. (2013) 'Crustal deformation effects on the chemical evolution of geothermal systems: the intra-arc Liquiñe–Ofqui fault system, Southern Andes', *International Geology Review*, 55, pp. 1384 - 1400.
- Sánchez-Roa, C., Faulkner, D.R., Boulton, C., Jimenez-Milan, J. and Nieto, F. (2017) 'How phyllosilicate mineral structure affects fault strength in Mg-rich fault systems', *Geophysical Research Letters*, 44, pp. 5457–5467.
- Sánchez-Roa, C., Jiménez-Millán, J., Abad, I., Faulkner, D. R., Nieto, F., and García-Tortosa, F. J. (2016) 'Fibrous clay mineral authigenesis induced by fluid-rock interaction in the Galera fault zone (Betic Cordillera, SE Spain) and its influence on fault gouge frictional properties', *Applied Clay Science*, 134, pp. 275–288.
- Sánchez-Roa, C., Vidal, O., Jiménez-Millán, J., Nieto, F. and Faulkner, D. R. (2018) 'Implications of sepiolite dehydration for earthquake nucleation in the Galera Fault Zone: A thermodynamic approach', *Applied Geochemistry*, 89, pp. 219-228.
- Sander, M.V. and Black, J.E. (1988) 'Crystallization and Recrystallization of Growth-Zoned Vein Quartz Crystals from Epithermal Systems: Implications for Fluid Inclusion Studies', *Economic Geology*, 83, pp. 1052-1060.
- Sanderson, D.J. (2016) "Field-based structural studies as analogues to sub-surface reservoirs", In: Bowman, M., Smyth, H.R, Good, T.R., Passey, S.R., Hirst, J.P.P. and Jordan, C.J. (eds.) *The Value of Outcrop Studies in Reducing Subsurface Uncertainty and Risk in Hydrocarbon Exploration and Production*, Geological Society, London, Special Publications.
- Sanderson, D.J., and Nixon, C.W. (2015) 'The Use of Topology in Fracture Network Characterization', *Journal of Structural Geology*, 72, pp. 55-66.
- Sanderson, D.J., Peacock, D.C.P., Nixon, C.W. and Rotevatn, A. (2019) 'Graph theory and the analysis of fracture networks', *Journal of Structural Geology*, 125, pp. 155-165.
- Sanderson, D., Roberts, S., Gumiel, P. and Greenfield, C. (2008) 'Quantitative Analysis of Tin and Tungsten-Bearing Sheeted Vein Systems', *Economic Geology*, 103, pp. 1043-1056.
- Sandvik (2012) *Kanthal – Resistance Heating Alloys for Electric Home Appliances*. Sandvik. Available at: <https://www.kanthal.com/globalassets/kanthal-global/downloads/materials-in-wire-and-strip-form/resistance-heating-wire-and-strip/s-ka026-b-eng-2012-01.pdf> (Accessed on: 19 October 2018).
- Savage, H.M. and Brodsky, E.E. (2011) 'Collateral damage: Evolution with displacement of fracture distribution and secondary fault strands in fault damage zones', *Journal of Geophysical Research: Solid Earth*, 116, 3.
- Scheuber, E., and Andriessen, P. A. M. (1990) 'The Kinematic and Geodynamic Significance of the Atacama Fault Zone, Northern Chile', *Journal of Structural Geology*, 12(2), pp. 243–257.
- Scheuber, E., and González, G. (1999) 'Tectonics of the Jurassic-Early Cretaceous Magmatic Arc of the north Chilean Coastal Cordillera (22°–26° S): A story of Crustal Deformation Along a Convergent Plate Boundary', *Tectonics*, 18(5), pp. 895–910.
- Scheuber, E., Hammerschmidt, K., Friedrichsen, H. (1995) '40 Ar/ 39 Ar and Rb-Sr analyses from ductile shear zones from the Atacama Fault Zone, northern Chile: the age of deformation', *Tectonophysics*, 250 (1-3), pp. 61-87.
- Schleicher, A.M., Hofmann, H. and van der Pluijm, B.A. (2013) 'Constraining clay hydration state and its role in active fault systems', *Geochemistry Geophysics Geosystems*, 14, pp. 1039–1052.
- Schleicher, A.M., van der Pluijm, B.A. and Warr, L.N. (2012) 'Chlorite-smectite clay minerals and fault behavior: new evidence from the San Andreas Fault Observatory at Depth (SAFOD) core', *Lithosphere*, 4, pp. 209–220.
- Scholz, C.H. (1987) 'Wear and gouge formation in brittle faulting', *Geology*, 15, pp. 493–495.

- Scholz, C.H. (1998) 'Earthquakes and friction laws', *Nature*, 391, pp. 37–42.
- Scholz, C.H. (2010) 'A note on the scaling relations for opening mode fractures in rock', *Journal of Structural Geology*, 32(10), pp. 1485–1487.
- Scholz, C.H., Dawers, N.H., Yu, J.-Z., Anders, M.H., Cowie, P.A. (1993) 'Fault growth and fault scaling laws: preliminary results', *Journal of Geophysical Research: Solid Earth*, 98, pp. 21951–21961.
- Schön, J. (2015) Pore Space Properties. In: Schön, J. (2015) *Physical Properties of Rocks, Developments in Petroleum Science* 65, pp. 21-84.
- Schulz, S. E. and Evans, J. P. (2000) 'Mesoscopic structure of the Punchbowl Fault, Southern California and the geologic and geophysical structure of active strike– slip faults', *Journal of Structural Geology*, 22, pp. 913–930.
- Scott, S., Driesner, T., and Weis, P. (2015) 'Geologic controls on supercritical geothermal resources above magmatic intrusions', *Nature Communications*, 6, 7837.
- Sheridan, J., Kovac, K., Rose, P., Barton, C., McCulloch, J., Berad, B., Moore, J., Petty, S. and Spielman, P. (2003) 'In-situ stress, fracture and fluid flow analysis-East flank of the Coso Geothermal Field', (Proceedings of the 28th Workshop on Geothermal Reservoir Engineering, Stanford, California, 27-29 January, 2003). Available at: <https://pangea.stanford.edu/ERE/pdf/IGASstandard/SGW/2003/Sheridan.pdf>.
- Shimamoto, T. and Logan, J.M. (1981) 'Effects of simulated clay gouges on the sliding behavior of Tennessee sandstone', *Tectonophysics*, 75, pp. 243–255.
- Shin Etsu Chemical Co. (2020) *The Unique Properties of Silicones*. Available at: <https://www.shinetsusilicone-global.com/products/type/oil/detail/about/index2.shtml> (Accessed on: 29 October 2020).
- Shipton, Z.K. and Cowie, P.A. (2001) 'Damage zone and slip-surface evolution over μm to km scales in high-porosity Navajo sandstone, Utah', *Journal of Structural Geology*, 23, 12, pp. 1825–1844.
- Sibson, R.H. (1974) 'Frictional constraints on thrust, wrench, and normal faults', *Nature*, 249, pp. 542–544.
- Sibson, R.H. (1981) 'Controls on Low-Stress Hydro-Fracture Dilatancy in Thrust, Wrench and Normal Fault Terrains', *Nature*, 289, pp. 665–667.
- Sibson, R.H. (1985) 'Stopping of earthquake ruptures at dilational fault jogs', *Nature*, 316, pp. 248–251.
- Sibson, R.H. (1987) Earthquake rupturing as a hydrothermal mineralizing agent, *Geology*, 15, 701–704.
- Sibson, R.H. (1990) 'Conditions for Fault-Valve Behavior', *Geological Society of London Special Publication*, 54, pp. 15–28.
- Sibson, R.H. (1994), 'Crustal stress, faulting and fluid flow'. In: Parnell, J. (ed.) *Geofluids: Origin, Migration and Evolution of Fluids in Sedimentary Basins*. Geological Society, London, Special Publications, 78, pp. 69-84.
- Sibson, R.H. (1996) 'Structural Permeability of Fluid-Driven Fault-Fracture Meshes', *Journal of Structural Geology*, 18(8), pp. 1031-1042.
- Sibson, R.H. (2000) 'A Brittle Failure Mode Plot Defining Conditions of High Flux Flow', *Economic Geology*, 95, pp. 41–48.
- Sibson, R. (2001) 'Seismogenic framework for hydrothermal transport and ore deposition', *Reviews in Economic Geology*, 14, pp. 25–50.
- Sibson, R.H., Moore, J. and Rankin, A.H. (1975) 'Seismic pumping – a hydrothermal fluid transport mechanism', *Journal of the Geological Society of London*, 131, pp. 653–659.

- Sibson, R.H., Robert, F. and Poulsen K.H. (1988) 'High-angle reverse faults, fluid-pressure cycling, and mesothermal gold– quartz deposits', *Geology*, 16, pp. 551–555.
- Siddiqui, G. and Evans, B. (2015) 'Permeability and thermal cracking at pressure in Sioux Quartzite'. In: Faulkner, D. R., Mariani, E. and Mecklenburgh, J. (eds) *Rock Deformation from Field, Experiments and Theory: A Volume in Honour of Ernie Rutter*. Geological Society, London, Special Publications, 409, pp. 49–66.
- Simmons, S.F., and Christenson, B. W. (1994) 'Origins of Calcite in a Boiling Geothermal System', *American Journal of Science*, 294, pp. 361–400.
- Simmons, S.F., White, N.C. and John, D. (2005) 'Geological characteristics of epithermal precious and base metal deposits', in: Hedenquist, J.W., Thompson, J.F.H., Goldfarb, R.J. and Richards, J.P. (eds.) *Economic Geology 100th Anniversary Volume 1905-2005*, Society of Economic Geologist Inc., Littleton, Colorado, USA. pp 485-522
- Siratovich, P.A., Heap, M.J., Villeneuve, M.C., Cole, J.W., Kennedy, B.M., Davidson, J. and Reuschlé, T. (2016) 'Mechanical behaviour of the Rotokawa Andesites (New Zealand): Insight into permeability evolution and stress-induced behaviour in an actively utilised geothermal reservoir', *Geothermics*, 64, pp. 163-179.
- Siratovich, P.A., Heap, M.J., Villeneuve, M.C., Cole, J.W. and Reuschlé, T. (2014) 'Physical property relationships of the Rotokawa Andesite, a significant geothermal reservoir rock in the Taupo Volcanic Zone, New Zealand', *Geothermal Energy*, 2(10), pp. 1-31.
- Siratovich, P. A., von Aulock, F. W., Lavallée, Y., Cole, J. W., Kennedy, B. M., and Villeneuve, M. C. (2015) 'Thermoelastic Properties of the Rotokawa Andesite: A Geothermal Reservoir Constraint', *Journal of Volcanology and Geothermal Research*, 301, pp. 1-13.
- Sjöberg, E.L. and Rickard, D.T. (1984) 'Temperature-dependence of calcite dissolution kinetics between 1°C and 62°C at pH 2.7 to 8.4 in aqueous-solutions', *Geochimica et Cosmochimica Acta*, 48(3), pp. 485–493.
- Smith, D.L., and Evans, B. (1984) 'Diffusional Crack Healing in Quartz', *Journal of Geophysical Research*, 89, pp. 4125–4135.
- Sousa, L.M.O., del Rio, L.M.S., Calleja, L., Argandoña, V.G.R. and Rey, A.R. (2005) 'Influence of microfractures and porosity on the physico-mechanical properties and weathering of ornamental granites', *Engineering Geology*, 77, pp. 153–168.
- Special Metals Corporation (2007) *Inconel Alloy 718*. Available at: <https://www.specialmetals.com/documents/technical-bulletins/inconel/inconel-alloy-718.pdf> (Accessed on: 18 December 2018).
- Stanton-Yonge, A., Cembrano, J., Griffith, W.A., Jensen, E. and Mitchell, T.M. (2020), 'Self-similar length-displacement scaling achieved by scale-dependent growth processes: Evidence from the Atacama Fault System', *Journal of Structural Geology*, 133, 103993.
- Steeffel, C. I. and Van Cappellen, P. (1990) 'A new kinetic approach to modeling water–rock interaction, the role of nucleation, precursors, and Ostwald ripening', *Geochimica et Cosmochimica Acta*, 54, pp. 2657–2677
- Stephens, M.A. (1970) 'Use of the Kolmogorov–Smirnov, Cramér–Von Mises and Related Statistics Without Extensive Tables', *Journal of the Royal Statistical Society: Series B (Methodological)*, 32, pp. 115-122.
- Stuckless, J.S. and Dudley, W.W. (2002) 'The geohydrologic setting of Yucca Mountain, Nevada', *Applied Geochemistry*, 17(6), pp. 659-682.
- Summers, R. and Byerlee, J.D. (1977) 'A note on the effect of fault gouge composition on the stability of frictional sliding', *International Journal of Rock Mechanics, Mining Sciences and Geomechanics*, 14, pp. 155–160.

- Takahashi, M., Mizoguchi, K., Masuda, K. (2009) 'Potential of phyllosilicate dehydration and dehydroxylation reactions to trigger earthquakes', *Journal of Geophysical Research*, 114, B02207.
- Taylor, W.L. (1999) 'Fluid flow in discrete joint sets: Field observations and numerical simulations', *Journal of Geophysical Research*, 104, p. 28,983–29,006.
- Taylor, G.K., Grocott, J., Pope, A. and Randall, D.E. (1998) 'Mesozoic fault systems, deformation and fault block rotation in the Andean forearc: a crustal scale strike-slip duplex in the Coastal Cordillera of northern Chile', *Tectonophysics*, 299 (1–3), pp. 93-109.
- Tembe, S., Lockner, D.A. and Wong, T. (2009) 'Constraints on the stress state of the San Andreas Fault with analysis based on core and cuttings from San Andreas Fault Observatory at Depth (SAFOD) drilling phases 1 and 2', *Journal of Geophysical Research*, 114, pp. 1–21.
- Tembe, S., Lockner, D.a. and Wong, T.F. (2010) 'Effect of clay content and mineralogy on frictional sliding behavior of simulated gouges: Binary and ternary mixtures of quartz, illite, and montmorillonite', *Journal of Geophysical Research: Solid Earth*, 115, pp. 1–22.
- Tenthorey, E., Cox, S.F. and Todd, H.F. (2003) 'Evolution of strength recovery and permeability during fluid-rock reaction in experimental fault zones', *Earth and Planetary Science Letters*, 206, pp. 161–72.
- Terzaghi, R. (1965) 'Sources of Error in Joint Surveys', *Geotechnique*, 15, pp. 287-297.
- Tetsuka, H., Katayama, I., Sakuma, H. and Tamura, K. (2018) 'Effects of humidity and interlayer cations on the frictional strength of montmorillonite', *Earth, Planets and Space*, 70, pp. 1–9.
- The Plastic Shop (2011) Ketron 1000 PEEK. Available at: https://www.theplasticshop.co.uk/plastic_technical_data_sheets/peek_1000_technical_data_sheet.pdf (Accessed on: 14 November 2018).
- Thien, B. M. J., Kosakowski, G. and Kulik, D. A. (2015) 'Differential alteration of basaltic lava flows and hyaloclastites in Icelandic hydrothermal systems' *Geothermal Energy*, 3, pp. 32.
- ThoughtCo (2018) *Table of Electrical Resistivity and Conductivity*. Available at: <https://www.thoughtco.com/table-of-electrical-resistivity-conductivity-608499> (Accessed on: 29 October 2019).
- Townend, J. and Zoback, M. D. (2000) 'How faulting keeps the crust strong', *Geology*, 28, pp. 399–402
- Tranter, M., DeLucia, M. and Kühn, M. (2020) Barite scaling in fractures simulated with nucleation and crystal growth kinetics, *EGU General Assembly*.
- Tsuchiya N. and Hirano N. (2007) 'Chemical reaction diversity of geofluids revealed by hydrothermal experiments under sub- and supercritical states', *Island Arc*, 16, pp. 6–15.
- Tulloch, A.J. (1982) 'Mineralogical Observations on Carbonate Scaling in Geothermal Wells at Kawerau and Broadlands', (Proceedings of the 4th New Zealand Geothermal Workshop, Auckland, New Zealand) pp. 131-134. Available at: <http://www.geothermal-energy.org/pdf/IGAstandard/NZGW/1982/Tulloch.pdf>.
- Turichshev, A. and Hadjigeorgiou, J. (2017) 'Quantifying the effects of vein mineralogy, thickness, and orientation on the strength of intact veined rock', *Engineering Geology*, 226, pp. 199-207.
- Underwood, M.B. (2007) 'Clay mineral composition and diagenesis: Effects on the location and behavior of faults in the frontal portions of subduction zones', *Scientific Drilling*, pp. 61–63.
- Vermilye, J. M., and C. H. Scholz (1998) 'The process zone: A microstructural view of fault growth', *Journal of Geophysical Research*, 103(B6), pp. 12,223–12,237.

- Vidal, O. and Dubacq, B. (2009) 'Thermodynamic modelling of clay dehydration, stability and compositional evolution with temperature, pressure and H₂O activity', *Geochimica et Cosmochimica Acta*, 73, pp. 6544-6564.
- Vidal, J., Patrier, P., Genter, A., Beaufort, D., Dezayes, C., Glaas, C., Lerouge, C. and Sanjuan, B. (2018) 'Clay minerals related to the circulation of geothermal fluids in boreholes at Rittershoffen (Alsace, France)', *Journal of Volcanology and Geothermal Research*, 349, pp. 192–204.
- Vilarrasa, V. and Carrera, J. (2015) 'Geologic carbon storage is unlikely to trigger large earthquakes and reactivate faults through which CO₂ could leak', *Proceedings of the National Academy of Sciences*, 112 (19), pp. 5938–5943.
- Virgo, S., Abe, S. and Urai, J.L. (2013) 'Extension fracture propagation in rocks with veins: Insight into the crack-seal process using Discrete Element Method modeling', *Journal of Geophysical Research: Solid Earth*, 118, pp. 5236–5251.
- Virgo, S., Abe, S., & Urai, J. L. (2014) 'The evolution of crack seal vein and fracture networks in an evolving stress field: Insights from discrete element models of fracture sealing' *Journal of Geophysical Research: Solid Earth*, 119, p. 8708–8727.
- Viton (2017) *Viton Fluoroelastomers – Selection Guide*. Available at: <https://www.viton.com/en/-/media/files/viton/viton-selection-guide.pdf> (Accessed on: 12 April 2018).
- Wakabayashi, J., Hengesh, J. V, and Sawyer, T. L. (2004) 'Four-dimensional Transform Fault Processes: Progressive Evolution of Step- Overs and Bends', *Tectonophysics*, 392, pp. 279–301.
- Wallis, I. C., McNamara, D., Rowland, J. V., and Massiot, C. (2012) 'The Nature of Fracture Permeability in the Basement Graywacke at Kawerau Geothermal Field, New Zealand', *37th Workshop on Geothermal Reservoir Engineering*, pp. 1-9.
- Walsh, J.J., Bailey, W.R., Childs, C., Nicol, A. and Bonson, C.G. (2003) 'Formation of segmented normal faults: a 3-D perspective', *Journal of Structural Geology*, 25, pp. 1251–1262.
- Walsh, J.J., Nicol, A. and Childs, C. (2002) 'An alternative model for the growth of faults', *Journal of Structural Geology*, 24, pp. 1669–1675.
- Walsh, J.J., Watterson, J., Heath, A.E. and Childs, C (1998) 'Representation and scaling of faults in fluid flow models', *Petroleum Geoscience*, 4(3), pp. 241-251.
- Wanner, C., Eichinger, F., Jahrfeld, T., and Diamond, L. W. (2017) 'Causes of Abundant Calcite Scaling in Geothermal Wells in the Bavarian Molasse Basin, Southern Germany', *Geothermics*, 70, pp. 324–338.
- Watkins, H., Bond, C. E., Healy, D., and Butler, R. W. H. (2015) 'Appraisal of fracture sampling methods and a new workflow to characterise heterogeneous fracture networks at outcrop', *Journal of Structural Geology*, 72, pp. 67–82.
- Weatherley, D.K. and Henley, R.W. (2013) 'Flash vaporization during earthquakes evidenced by gold deposits', *Nature Geoscience Letters*, 6, pp. 294-298.
- Wennberg, O.P., Azzizadeh, M., Aqrawi, A.A.M., Blanc, E., Brockbank, P., Lyslo, K.B., Pickard, N., Salem, L.D. and Svånå, T. (2007) 'The Khaviz Anticline: An outcrop analogue to giant fractured Asmari Formation reservoirs in SW Iran', *Geological Society Special Publication*, 270, pp. 23–42.
- Wibberley, C. A. J. and Shimamoto, T. (2003) 'Internal structure and permeability of major strike-slip fault zones: the Median Tectonic Line in Mie Prefecture, Southwest Japan', *Journal of Structural Geology*, 25, pp. 59–78.
- Wibberley, C.A.J., Yielding, G. and Di Toro, G. (2008) 'Recent advances in the understanding of fault zone internal structure: a review', In: Wibberley, C.A.J., Kurz, W., Imber, J., Holdsworth,

- R.E. and Collettini, C. (eds.) *The Internal Structure of Fault Zones: Implications for Mechanical and Fluid-Flow Properties*, Geological Society, London, Special Publications.
- Wilcox, R. E., Harding, T.P. and Seely, D. R. (1973) 'Basic wrench tectonics', *American Association of Petroleum Geologists Bulletin*, 57, pp. 74–96.
- Williams, R.T. (2019) 'Coseismic boiling cannot seal faults: Implications for the seismic cycle', *Geology*, 47(5), pp. 461-464.
- Wilson, J. E., Chester, J. S. and Chester, F. M. (2003) 'Microfracture analysis of fault growth and wear processes, Punchbowl Fault, San Andreas system, California', *Journal of Structural Geology*, 25, pp. 1855–1873.
- Wilson, R.W., McCaffrey, K.J.W., Jones, R.R., Clegg, P. and Holdsworth, R.E. (2005) 'Digital Mapping of Lofoten's faults', *Geoscientist*, 15(2), pp. 4–9.
- Wilson, M. and Monea, M. (2004) *IEA GHG Weyburn CO2 monitoring and storage project: summary report 2000–2004*. Regina, Saskatchewan, Canada.
- Wiltshko, D. V. and Morse, J. W. (2001) 'Crystallization Pressure Versus "Crack Seal" as the Mechanism for Banded Veins', *Geology*, 29, pp. 79–82.
- Woodcock, N. H., Dickson, J. A. D., and Tarasewicz, J. P. T. (2007) 'Transient Permeability and Reseal Hardening in Fault Zones: Evidence from Dilation Breccia Textures', *Geological Society of London Special Publications*, 270(1), pp. 43–53.
- Woodcock, N.H. and Fisher, M. (1986) 'Strike-slip duplexes', *Journal of Structural Geology*, 8, pp. 725–735.
- Wyering, L., Villeneuve, M. and Wallis, I. (2012) 'The Effects of Hydrothermal Alteration on Mechanical Rock Properties of the Andesite Breccia and Tahorakuri Formation from the Ngatamariki Geothermal Field, New Zealand and Empirical Relations between Rock Strength and Physical Properties.' (Proceedings of the New Zealand Geothermal Workshop, Auckland, New Zealand, 19-21 November 2012). Available at: <https://www.geothermal-energy.org/pdf/IGAstandard/NZGW/2012/46654final00118.pdf>.
- Wyering, L.D., Villeneuve, M.C., Wallis, I.C., Siratovich, P.A., Kennedy, B.M., Gravley, D.M. and Cant, J.L. (2014) 'Mechanical and physical properties of hydrothermally altered rocks, Taupo Volcanic Zone, New Zealand', *Journal of Volcanology and Geothermal Research*, 288, pp. 76–93.
- Wyering, L.D., Villeneuve, M.C., Wallis, I.C., Siratovich, P.A., Kennedy, B.M. and Gravley, D.M. (2015) 'The development and application of the alteration strength index equation', *Engineering Geology*, 199, pp. 48-61.
- Xu, Y., Yao, W., Zhao, G. and Xi, K. (2020) 'Evaluation of the short core in compression (SCC) method for measuring mode II fracture toughness of rocks', *Engineering Fracture Mechanics*, 224, 106747.
- Zeeb, C., Gomez-Rivas, E., Bons, P. D., and Blum, P. (2013) 'Evaluation of Sampling methods for fracture network characterization using Outcrops', *American Association of Petroleum Geologists*, B., 97, pp. 1545–1566.
- Zimmermann, G., Blocher, G., Reinicke, A. and Brandt, W. (2011) 'Rock specific hydraulic fracturing and matrix acidizing to enhance a geothermal system - Concepts and field results' *Tectonophysics*, 503 (1-2), pp. 146-154.
- Zimmermann, G., Tischner, T., Legarth, B. and Huenges, E. (2009) 'Pressure-dependent production efficiency of an enhanced geothermal system (eds): stimulation results and implications for hydraulic fracture treatments', *Pure and Applied Geophysics*, 166 (5–7), pp. 1089–1106.
- Zimmerman, R.W. and Bodvarsson, G.S. (1996) 'Hydraulic conductivity of rock fractures', *Transport in Porous Media*, 23, pp. 1–30.

- Zimmerman, R.W. and Yeo, I.-W. (2000) 'Fluid flow in rock fractures: From the Navier-Stokes equations to the cubic law. In: Faybishenko, B., Witherspoon, P.A. and Benson, S.M (eds.) *Dynamics of Fluids in Fractured Rock, volume 122*. USA, American Geophysical Union.
- Zoback, M. D. (2010) *Reservoir Geomechanics*, Cambridge University Press, NY, USA, Cambridge University Press.
- Zoback, M.D. and Gorelick, S.M. (2012) 'Earthquake triggering and large-scale geologic storage of carbon dioxide', *Proceedings of the National Academy of Sciences*, 109 (26), pp. 10164–10168.
- Zoback, M. D., Kohli, A., Das, I. and McClure, M. (2012) 'The importance of slow slip on faults during hydraulic fracturing stimulation of shale gas reservoirs'. *SPE Americas Unconventional Resources Conference*, Pittsburgh, PA, 5–7 June.

Appendices

A : Fieldwork Methodology and Data

A1: An Overview of Field Sites and 1D Transects Used in Chapter 2 and Chapter 3



Figure A1.1: Stick plots for each 1D transect, grouped by site (1= Outside of the Duplex, 2 = Northern Splay, 3 = Fault Jog, 4 = Distributed Splay Fault, 5 = Central Duplex). Each line represents a single recorded vein. Grey areas represent limited exposure at the outcrop. All transects are to scale and SW to NE, except where marked by * where transects run SE to NW. Red lines indicate their position with respect to a known third-order fault (3°).

Table A1.1: Descriptions of field sites (data measurement & sampling locations) across the study area.

Site	Description
1 (a+b)	'Outside of the Duplex': Site 1a is a coastal outcrop of the relatively undeformed side of the Bolfin Fault, ~280 m West of the fault core. An 8.5 m structural transect (PE-W-1) was taken on a horizontal outcrop immediately to the East of a potential second order fault defined by sinistral displacement in the order of ~30 cm. Site 1b is in a similar structural setting but ~11 km SSW, ~280 m West of the Bolfin Fault at Site 3 (see below). Here, a 9.5 m transect (FB-S-1) was taken at a sub-vertical outcrop, immediately to the East of a potential but poorly exposed second-order fault. 5 veins were sampled and later thin-sectioned.
2	'Northern Margin': An ~E-W trending arroyo cutting a second-order fault of the Bolfin defined by a partially eroded fault core on the margin of a dyke, ~180 m east of the main fault on the northern margin of the mapped extensional duplex footwall. Structural transects (SQ-S-1,2,3) were taken at sub-vertical outcrops either side of this fault, totaling ~30m. At this site, a ~2.5 m structural transect (SQ-B-1) was also taken in the damage zone of the main Bolfin Fault, immediately adjacent to the core. 7 veins were sampled and later thin-sectioned.
3	'Dilatational Jog': a steep ~NE-SW trending arroyo with good sub-horizontal and sub-vertical exposures. The site, adjacent to a bend in the Bolfin Fault ~8 km SSE of Site 2, is a dilatational jog with complex regional structure. Three structural transects were taken here: A 4 m transect (FB-T-1) was taken parallel to a probable 3 rd order fault with evidence of normal throw and adjacent to a mapped 2 nd order fault within this jog definable by its fault core, at a distance of ~200 m East of the main fault. Nearby, ~290 m and ~370 m East of the Bolfin Fault respectively, another 8 m transect (FB-N-1) and a 5 m transect (FB-C-1) were taken, both adjacent to mapped 2 nd order faults defined by the presence of a fault core, and the latter also parallel to a probable 3 rd order fault. 9 veins were sampled and later thin-sectioned.
4	'Distributed Fault': a distributed second order splay of the Bolfin Fault outcropping in a wide NNE-SSW trending arroyo ~200 m East of the main fault and ~2 km SSE of Site 3. The site is also described in Jensen et al. (2011). The fault as a whole strikes NNW, is ~2 km long and has total distributed fault thickness of ~17 m (Jensen et al., 2011). Three structural transects were also taken at this site: A 6.4 m structural transect (PAR-T-1) and a ~10.5 m transect (PAR-D-1) were taken across the arroyo, both on well exposed horizontal outcrops adjacent to faults at least 10 m long and ~10mm thick, with horizontal displacement estimated at a few metres. ~800 m further East, another 9 m transect (PAR-C-1) was taken perpendicular to a less distributed second-order splay fault, mapped and defined by the presence of a fault core, with sub-vertical outcrop. 7 veins were sampled and later thin-sectioned.
5	'Central Duplex': comprises ~E-W oroyos with both sub-vertical and sub-horizontal outcrops. The site is situated ~3000 m East of the main Bolfin Fault, and ~1950 m West of the Jorgillo Fault that forms the Eastern margin of the duplex, and is also described in Arancibia et al. (2014). Three structural transects were taken here, one 8.5 m long and perpendicular to a mapped planar ~NE-SW second-order fault (CCD-N-1); a 6 m long, also parallel to a third order ~NNE-SSW fault (CCD-T-1). and a ~3 m structural transect (CCD-S-1) taken at a sub-horizontal outcrop ~ 15 m West of a NNW-SSE second-order fault defined by sinistral displacement along a fault core following the margin of a dyke. 5 veins were sampled and later thin-sectioned.

A2: Figures Relevant to Chapter 2

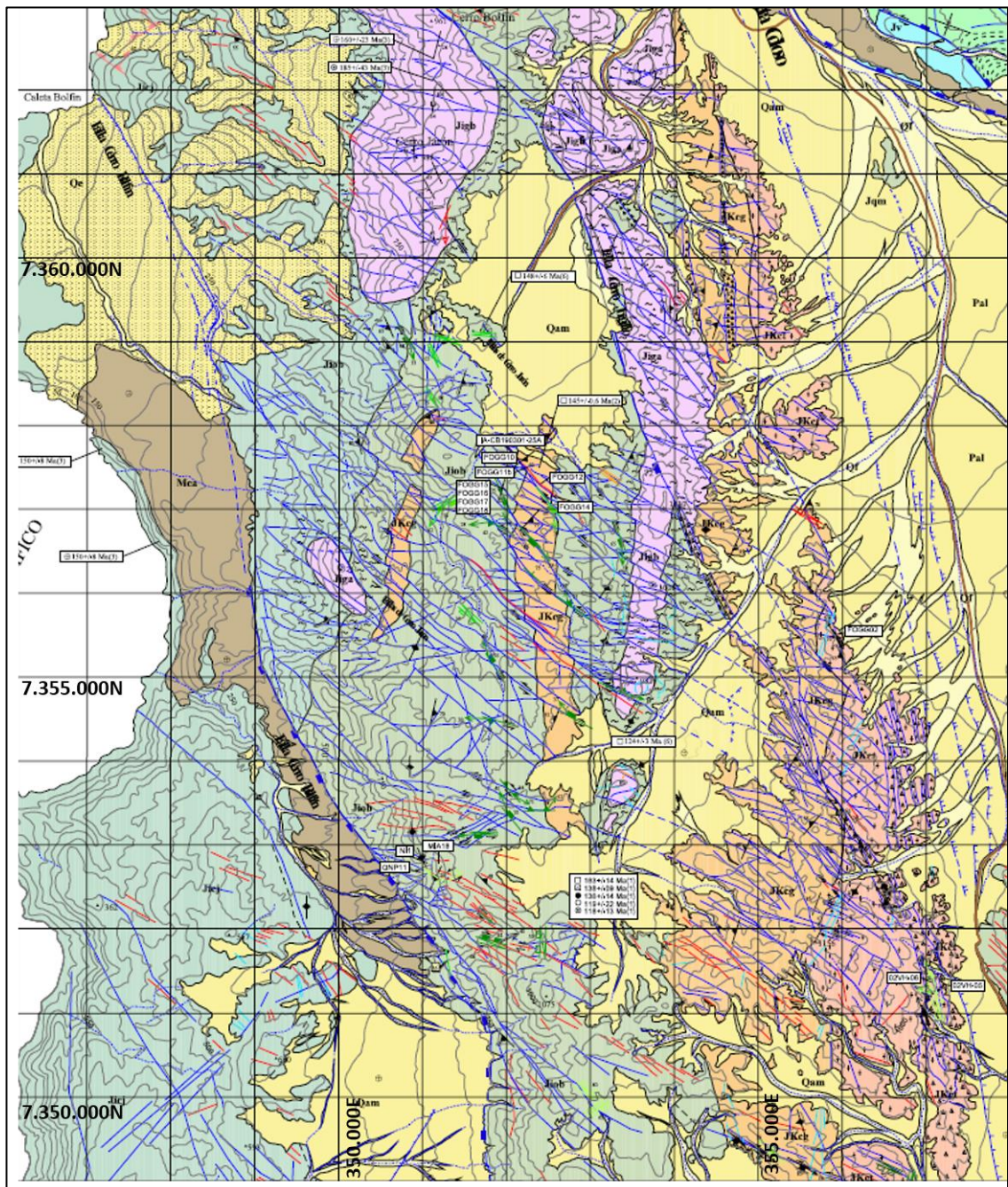


Figure A2.1: Relevant section of the regional geological map (Gobierno de Chile, 2003) used for trace mapping structures in the production of Figure 2.5. Mapped faults are displayed as blue lines; for further details, refer to the original reference.



Figure A2.2: 2D orthomosaic image of a studied outcrop at Site 1a. Veins identifiable within this image were traced in CorelDraw and analysed using FracPaQ to produce Figure 2.8(i) and associated data. The yellow tape running from ~SW-NE marks the position of a studied 1D transect.

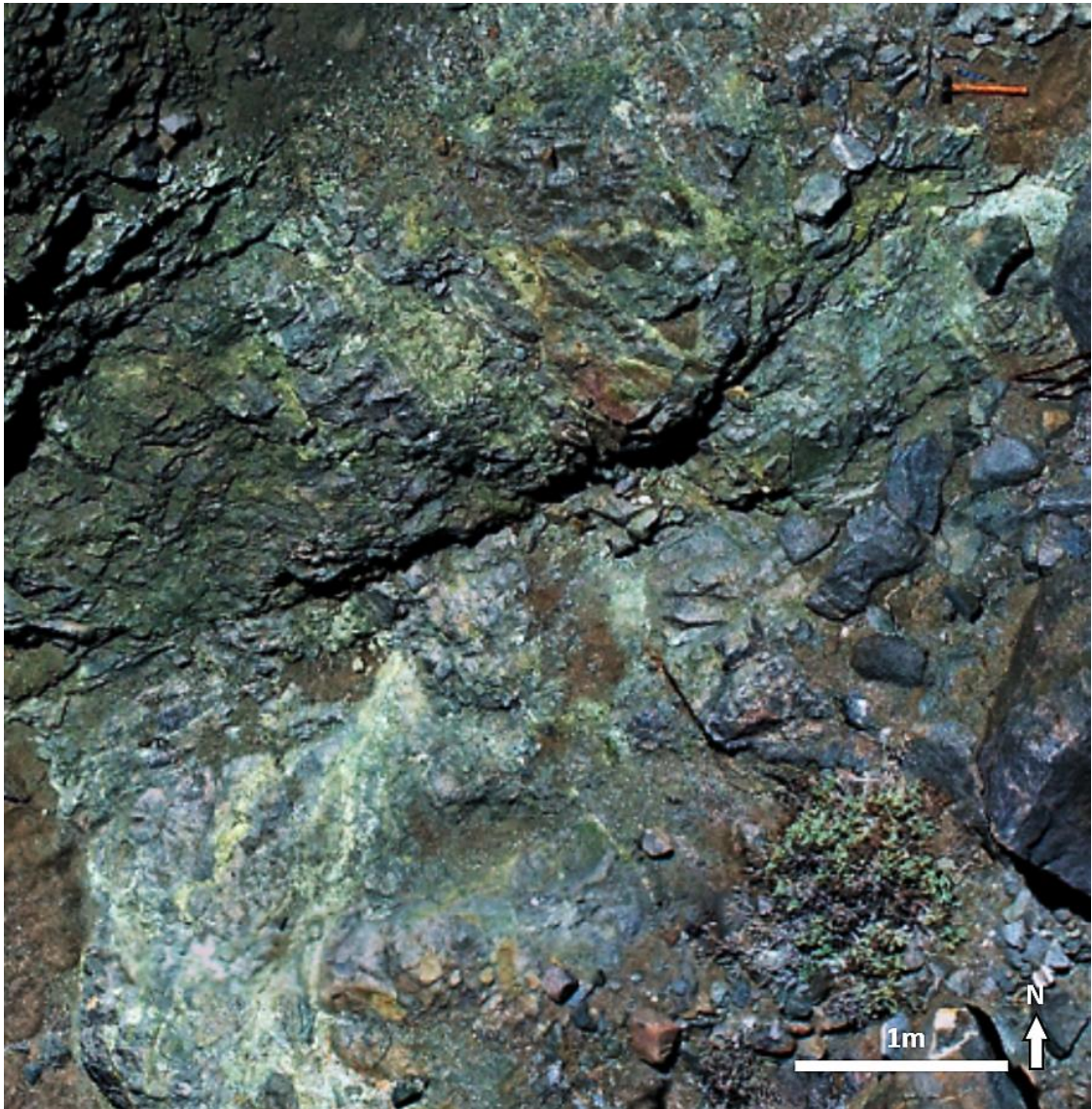


Figure A2.3: 2D orthomosaic image of a studied outcrop at Site 3. Veins identifiable within this image were traced in CorelDraw and analysed using FracPaQ to produce Figure 2.8(ii) and associated data.

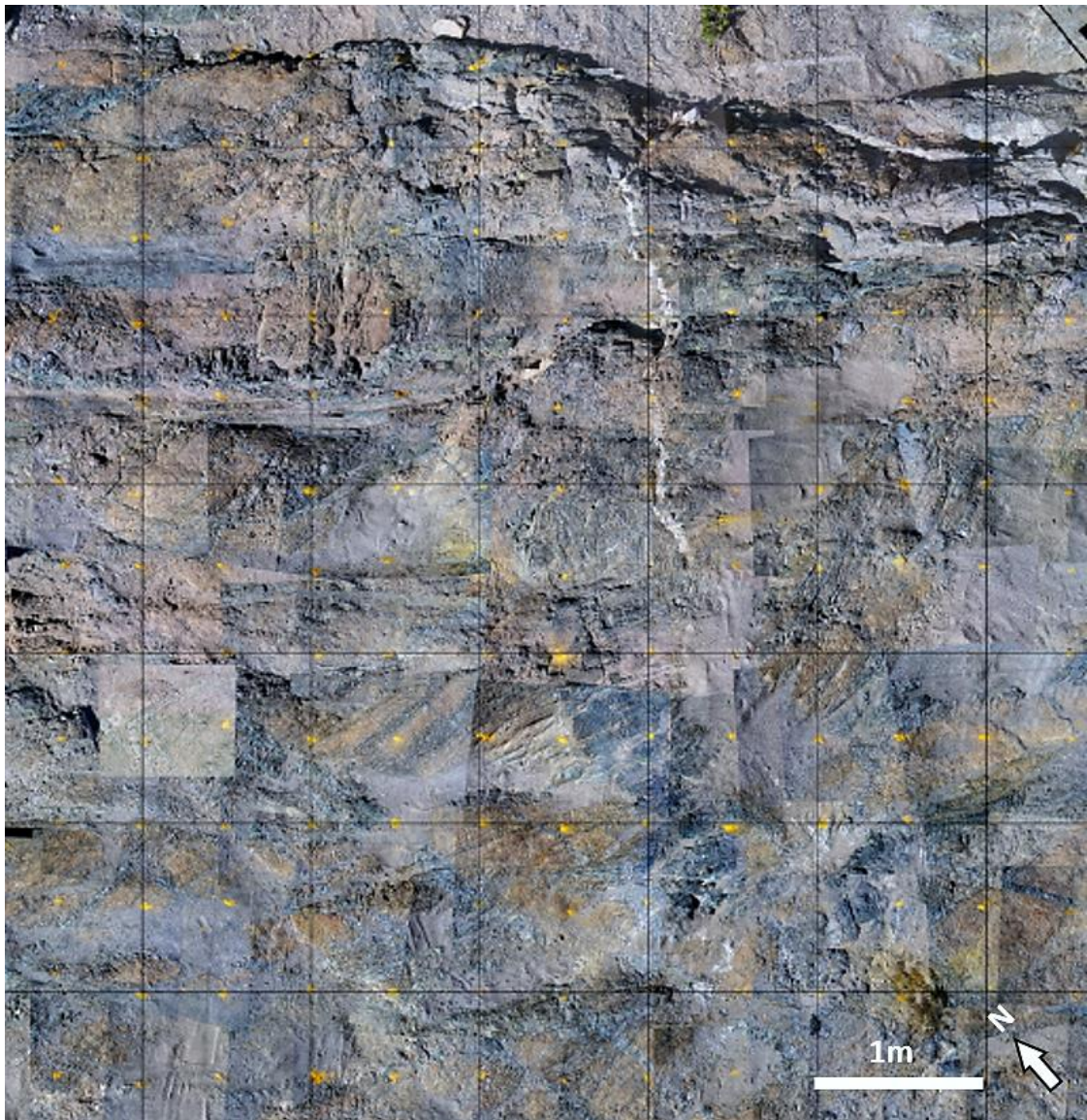
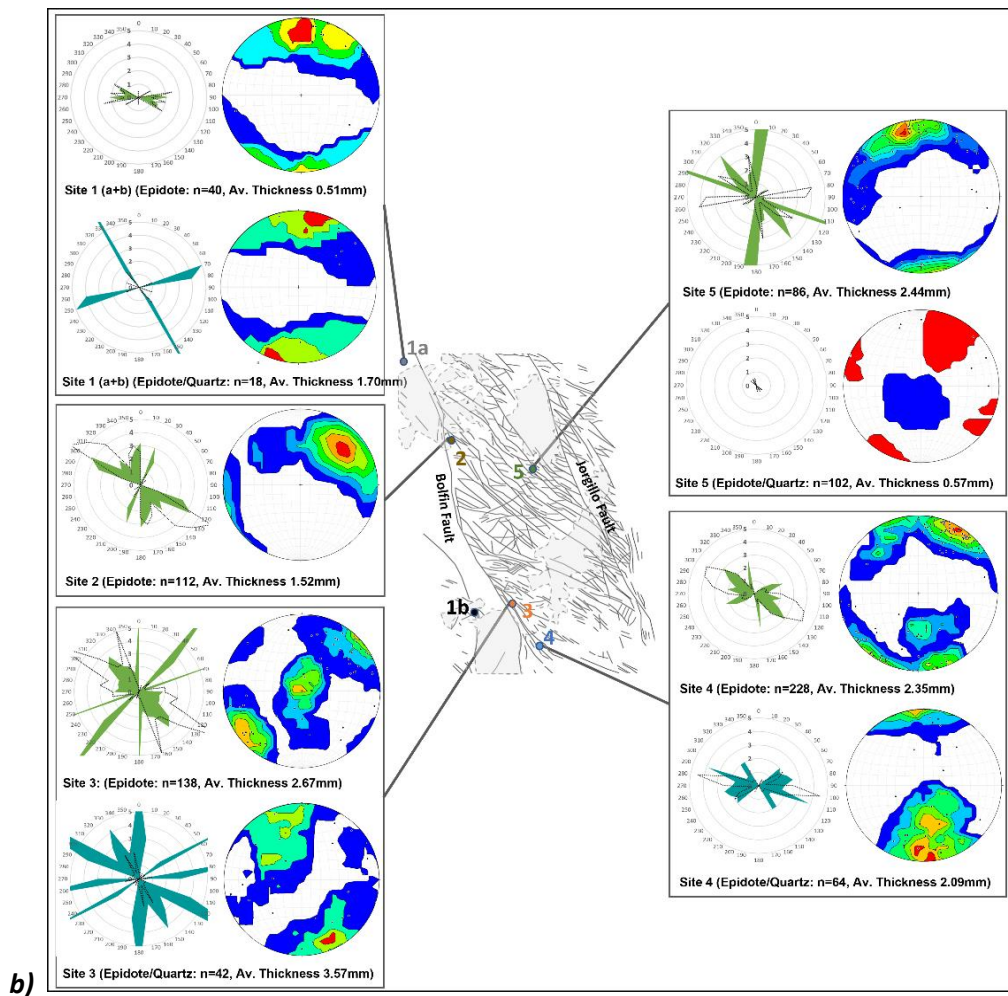
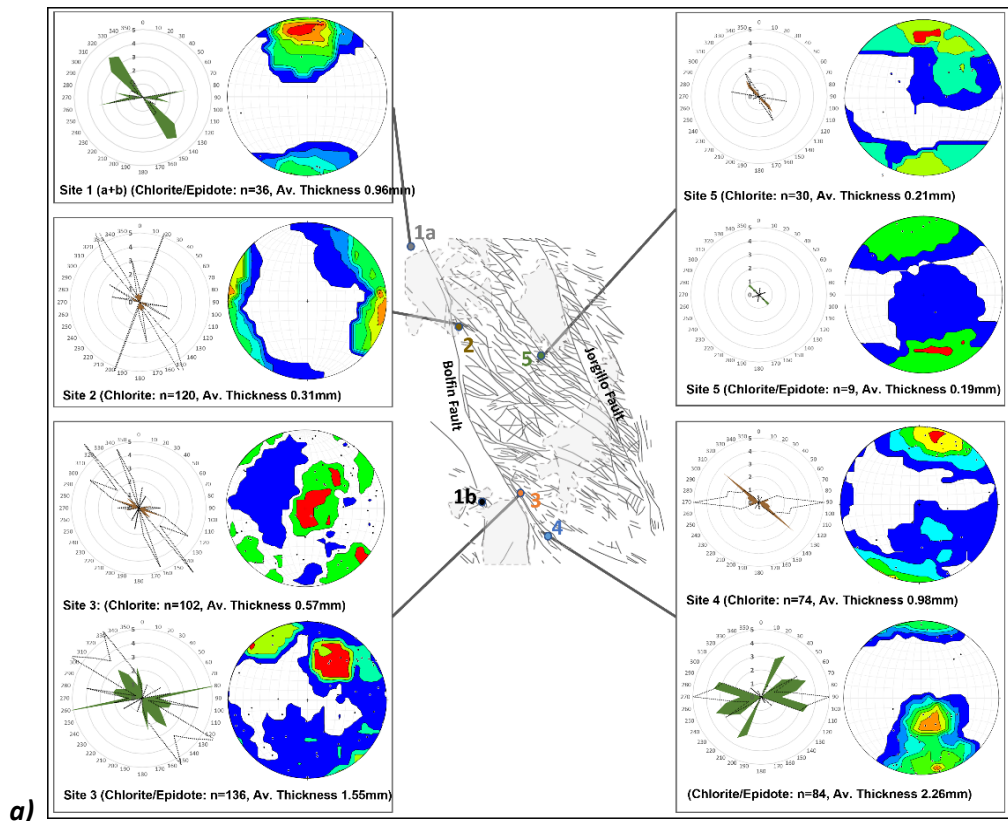


Figure A2.4: 2D orthomosaic image of a studied outcrop at Site 3 (modified from Jensen et al., 2011). Veins identifiable within this image were traced in CorelDraw and analysed using FracPaQ to produce Figure 2.8(iii) and associated data.

A3: Summary Tables and Figures Relevant to Chapter 3



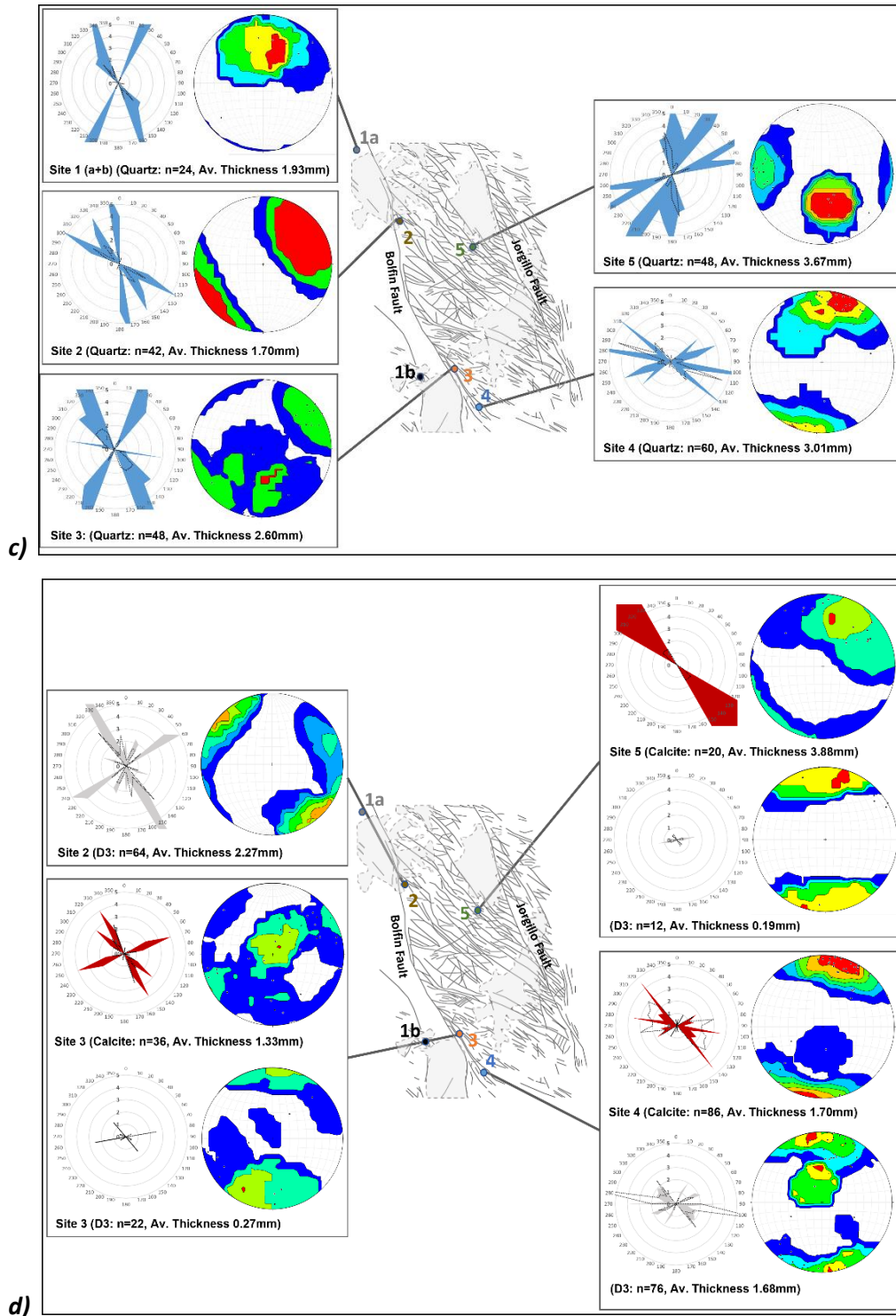


Figure A3.1: Rose plots and Kamb contour stereonets illustrating the relationship between average vein thickness and frequency as well as the variation in local stress for a) Chlorite-dominated vein sets, b) epidote-dominated vein sets, c) quartz-dominated vein sets and d) calcite- and 'D3'-dominated vein sets. Filled colour rose plots display average vein thicknesses per 10° orientation bin for all measured veins of the stated composition. Black lined rose plots display the total number of veins of the stated composition per 10° orientation bin (scale x2). Also shown are Kamb contour plots for all veins of the stated composition.

Table A3.1: Dominant (binned) orientations for vein frequency and average thickness as shown in rose plots in Figure 3.4 and Figure 3.5.

Site	Dominant orientations for total amount of vein precipitate (binned; minor sets in brackets) (Figure 3.4)	Dominant orientations for highest vein frequencies (binned; minor sets in brackets) (Figures 3.4 and 3.5)	Dominant orientations for largest average vein thicknesses (binned; minor sets in brackets) (Figure 3.5)
1	080-260	080-260	020-200
	110-290	110-290	(070-240)
	160-340	130-310	(110-290) 160-340
2	120-300	120-300	120-300
	150-330	150-330	(150-330)
	170-350		170-350
3	(070-240)	(090-270)	000-180
	120-300	120-300	040-220
	140-320	140-320	070-240
	160-340	160-340	(160-340)
4	(060-240)	090-270	020-200
	100-280	100-280	060-240
	110-290	110-290	110-290
	120-300	120-300	
5	(030-210)	080-260	000-180
	(060-240)	130-310	030-210
	130-310	170-350	(060-240)
	(170-350)		110-290 140-320

Table A3.2: Orientation statistics (Fisher analyses) for Kamb contoured stereonet in Figure 3.4 and Figure A3.1. Visual analyses of contoured trends/plunges were read from stereonet by mapping highest density areas (i.e. where Kamb contour standard deviations >10) and listing in order of significance (1-4).

Site	Phase	N	Fisher Analysis				Visual Analysis			
			Trend	Plunge	Kappa	No. of Phases	Trend/Plunge 1	Trend/Plunge 2	Trend/Plunge 3	Trend/Plunge 4
1	ALL	117	53.0	49.2	1.6	2	174/01	021/14	-	-
1	Chl-Ep	39	358.7	29.4	7.7	1				
1	Epidote	26	25.3	22.6	3.3	1				
1	Ep-Qz	12	91.2	26.9	2.0	2				
1	Quartz	26	6.4	47.9	6.4	2				
2	ALL	203	57.0	32.0	2.1	2	290/02	055/12	-	-
2	Chlorite	78	62.3	14.6	2.5	2				
2	Epidote	76	44.9	35.9	4.1	2				
2	Quartz	12	59.2	18.9	2.0	1				
2	D3	65	78.7	46.1	1.5	2				
3	ALL	434	59.2	81.2	1.9	4	028/53	226/14	338/12	048/79
3	Chlorite	107	107.3	71.3	2.1	3				
3	Chl-Ep	118	33.6	61.7	2.0	3				

Table A3.2 (cont.)

Site	Phase	N	Fisher Analysis				Visual Analysis			
			Trend	Plunge	Kappa	Visual No. of Phases	Trend/Plunge 1	Trend/Plunge 2	Trend/Plunge 3	Trend/Plunge 4
3	Epidote	132	287.9	82	2.0	3				
3	Ep-Qz	54	357.8	73	1.9	3				
3	Quartz	28	121.5	60.6	2.2	3				
3	Calcite	67	246.8	85.1	2.2	3				
3	D3	24	190.1	39.3	2.7	3				
3	All Chl-bearing	225	60.8	70.4	2.0	-				
3	All Ep-bearing	304	10.9	76.4	1.9	-				
4	ALL	528	72.5	82.5	1.7	3	156/02	012/08	160/64	-
4	Chlorite	57	23.6	50.5	1.8	3				
4	Chl-Ep	125	160.6	46.4	3.2	2				
4	Epidote	203	49	82.5	1.5	3				
4	Ep-Qz	82	162.2	71.2	1.9	2				
4	Quartz	45	7.2	44.1	2.2	2				
4	Calcite	57	10.9	32.9	1.9	2				
4	D3	80	354	66.5	1.9	2				
4	All Chl-bearing	182	147.4	59.3	2.1	-				
4	All Ep-bearing	410	154.1	67.4	1.8	-				
5	ALL	251	345.2	44.3	2.0	4	349/06	158/62	053/13	269/20
5	Chlorite	33	12.3	25.7	3.6	3				
5	Chl-Ep	19	350.1	42.1	2.5	2				
5	Epidote	107	337.6	25.2	2.6	2				
5	Ep-Qz	7	33.6	21.5	3.6	3				
5	Quartz	59	206.5	62.7	2.9	2				
5	Calcite	19	20.2	30.2	4.4	2				
5	D3	24	0	9.3	2.3	1				
5	All Chl-bearing	52	5.9	31.5	3.0	-				
5	All Ep-bearing	133	342.5	28.1	2.5	-				

Table A3.3: Orientation statistics (Von Mises Distributions) for Kamb contoured stereonets presented in Figure 3.4.

Site	Principal Orientation Bin (°)	Max Value (%)	Mean Vector (°)	Standard Deviation (°)	Circular Variance	Kappa
1	171-180	34.2	2.8	8.1	0.489	1.2
2	111-120	14.3	55.6	13.4	0.814	0.37
3	031-040	10.6	28.2	9	0.782	0.43
4	151-160	21.1	354.3	3.2	0.485	1.19
5	161-170	17.9	345.6	0.68	0.634	0.77

Table A3.4: Summary data table for average vein thickness (mm) and total vein precipitate (mm) in 10° orientation bins, by site, presented as rose plots in Figure 3.4 and Figure 3.5.

Site	Strike Bin (°)	Vein Count	Average Thickness (mm)	Total Precipitate (mm)	Standard Deviation
1	0	1	0.50	0.5	0.000
1	10	0	0.00	0	0.000
1	20	1	7.00	7	0.000
1	30	1	7.00	7	0.000
1	40	0	0.00	0	0.000
1	50	0	0.00	0	0.000
1	60	2	1.25	2.5	0.750
1	70	2	5.00	10	2.000
1	80	15	1.63	24.45	2.630
1	90	5	1.70	8.5	2.670
1	100	7	1.57	10.99	3.000
1	110	8	3.30	26.4	3.050
1	120	8	1.50	12	0.880
1	130	4	1.63	6.52	1.140
1	140	11	3.18	34.98	1.810
1	150	5	5.30	26.5	3.400
1	160	5	5.30	26.5	5.480
1	170	3	0.50	1.5	0.000
2	0	8	2.88	23.04	3.010
2	10	2	0.50	1	0.000
2	20	19	1.11	21.09	2.060
2	30	5	2.00	10	1.640
2	40	0	0.00	0	0.000
2	50	4	3.25	13	1.920
2	60	1	5.00	5	0.000
2	70	0	0.00	0	0.000
2	80	0	0.00	0	0.000
2	90	0	0.00	0	0.000
2	100	4	0.50	2	0.000
2	110	4	5.50	22	3.640
2	120	18	4.80	86.4	5.650
2	130	12	1.71	20.52	1.550
2	140	18	2.94	52.92	2.030
2	150	21	2.93	61.53	5.540
2	160	10	2.35	23.5	1.830
2	170	9	6.11	54.99	7.670
3	0	3	4.66	13.98	2.620
3	10	4	3.38	13.52	3.380
3	20	4	2.50	10	2.600
3	30	6	2.50	15	2.430
3	40	2	6.50	13	2.500
3	50	3	3.66	10.98	1.700
3	60	5	3.50	17.5	2.760
3	70	2	6.00	12	2.000

Table A3.4 (cont.)

Site	Strike Bin (°)	Vein Count	Average Thickness (mm)	Total Precipitate (mm)	Standard Deviation
3	80	15	3.44	51.6	4.150
3	90	10	1.45	14.5	1.100
3	100	18	2.11	37.98	1.530
3	110	12	1.96	23.52	1.600
3	120	37	1.67	61.79	2.080
3	130	22	2.97	65.34	2.390
3	140	28	2.63	73.64	2.640
3	150	22	3.82	84.04	3.350
3	160	26	2.79	72.54	3.440
3	170	11	1.96	21.56	6.380
4	0	1	0.50	0.5	0.000
4	10	1	0.50	0.5	0.000
4	20	1	4.00	4	0.000
4	30	6	2.17	13	1.841
4	40	0	0.00	0	0.000
4	50	5	1.70	8.5	0.872
4	60	16	2.47	39.5	1.916
4	70	11	3.62	39.8	3.342
4	80	16	2.10	33.6	1.517
4	90	37	1.59	58.8	1.683
4	100	43	2.62	112.6	2.845
4	110	40	2.44	97.7	2.638
4	120	29	2.27	65.9	1.991
4	130	26	3.35	87.2	4.723
4	140	15	3.29	49.4	3.730
4	150	3	1.47	4.4	1.159
4	160	4	1.25	5	0.559
4	170	4	1.73	6.9	1.399
5	0	6	5.83	34.98	3.580
5	10	3	4.83	14.49	3.930
5	20	2	3.00	6	1.000
5	30	2	11.75	23.5	10.250
5	40	1	5.00	5	0.000
5	50	2	0.75	1.5	0.250
5	60	3	6.63	19.89	8.750
5	70	6	1.93	11.58	2.130
5	80	10	1.37	13.7	2.370
5	90	9	0.77	6.93	0.660
5	100	5	0.26	1.3	0.210
5	110	1	12.00	12	0.000
5	120	8	5.18	41.44	10.160
5	130	8	9.98	79.84	15.150
5	140	8	4.96	39.68	6.670
5	150	9	3.81	34.29	4.810
5	160	6	2.70	16.2	1.950
5	170	15	2.28	34.2	2.140

Table A3.5: Vein thickness distribution data relevant to histograms within Figure 3.5.

Site	Vein Thickness (mm)						Total Veins
	<1mm	1-2mm	2-3mm	3-4mm	4-5mm	>5mm	
1	25	16	13	7	7	10	78
	32%	21%	17%	9%	9%	13%	
2	54	15	25	8	7	28	137
	39%	11%	18%	6%	5%	20%	
3	55	48	25	18	13	34	193
	28%	25%	13%	9%	7%	18%	
4	67	74	41	25	21	32	260
	26%	28%	16%	10%	8%	12%	
5	38	21	9	7	8	21	104
	37%	20%	9%	7%	8%	20%	

A4: Methodology of Correction of Orientation Bias in 1D Transect Data

Veins parallel or sub-parallel to the strike orientation of 1D transect lines have a lower probability of being intersected and measured than those that are perpendicular or sub-perpendicular, hence field data likely contain an underestimation of sub-parallel orientations and are biased towards those that are more perpendicular to the transect line. A statistical weighting has therefore been applied to each measured vein orientation depending on its acute angle relative to the transect line (δ). The correction factor w first proposed by Terzaghi (1965) was calculated as in Equation A3.1:

$$w = \frac{1}{\cos\delta} \quad (\text{Eq. A3.1})$$

Since w can reach very high values when the vein is almost parallel to the transect, a maximum allowable value was put in place on the recommendation of Priest (1993), corresponding to $\delta = 84.3^\circ$ and $w = 10$.

Data was processed using an Excel template written by David McNamara and Cecile Massiot along with a Linux 'awk' script in Cygwin.

B : Laboratory Methodology and Data

B1: Supplementary Methodology Relevant to Chapter 3

Scanning Electron Microscopy (SEM): As well as standard optical petrography, thin sections of vein and altered host rock samples collected in the field were analysed using a Hitachi TM3000 tabletop SEM. The SEM uses a tungsten filament, and was used for Back Scatter Electron (BSE) imaging operating at an accelerating voltage of 20 kV, 60 – 80 μ A beam current and a spot size of 5 nm. Thin sections were coated with ~10 nm of carbon prior to analysis to prevent charging effects.

Cathodoluminescence (CL): Optical cold-cathode cathodoluminescence was also used for analyses of vein and altered host rock samples collected in the field. An evacuated CL-stage with cathode gun was fitted to an optical microscope, and the thin section was bombarded with a high-energy electron beam to induce luminescence within minerals. An Olympus BX41 microscope with a CITL Mk5-2 cold stage and Nikon C-HGFI camera were used here, with analyses conducted at beam conditions of 9-14 Kv and 470-520 μ A in a vacuum of 0.06-0.08 mbar. Luminescence reflects the emission of photons of a characteristic wavelength, and is influenced by defects in a material's crystal lattice as well as subtle compositional variations that are not visible using standard optical microscopy or SEM-based techniques (Pagel et al., 2000). In quartz and calcite, trace elements involved in creating luminescence are in small concentrations of a few parts per million.

X-Ray Diffraction: XRD samples were prepared using a mill crusher and agate ball crusher to produce a size fraction of <125 μ m. Samples of fraction were then crushed in distilled water to produce a powder <10 μ m using an agate McCrone micronizing mill, and dried at 60 °C. Dried samples were then crushed into a light, loose powder in an agate pestle and mortar, and back-loaded into cavity holders. A Copper X-ray tube was used, with Ni filter to select for Cu k- α radiation. Scans covered the 2 θ range of 4-70°2 θ , with additional scans made after sample saturation with ethylene glycol at 60 °C by the vapour pressure method. Quantification of data was performed using the Relative Intensity Ratio (RIR) method, with reference patterns from Gates-Rector and Blanton (2019).

Brazilian Tensile Strength experiments: Indirect tensile strength tests were conducted on 2 rock discs cored through relatively unaltered host rock, 2 through hydrothermally altered host rock, and 16 through altered host rock containing chlorite (8 samples) and epidote (8 samples) veins at a range of orientations (0°, 30°, 60° and 90° with respect to σ_1). For each experiment, a uniaxial press and a Brazilian test jig were used, set up as in *Figure 3.7a*. Diametric compressive stresses were applied at a constant loading rate to two curved steel bearing platens (D2 steel, hardened to HRC 60) using a fixed plate and hydraulic piston. A chrome ball prevented asymmetric loading once in contact with the fixed plate to two opposing curved surfaces of 20

mm diameter rock discs. Discs were cut and squared to a length of ~11 mm (i.e. diameter to length ratios of ~0.55), in accordance with the D3967-16 laboratory standard (ASTM International, 2016). A uniform tensile stress was generated on the central vertical plane of the sample producing Mode I tensile fractures. Applied loads were measured using a load cell (Tedea-Huntleigh 220) through a National Instruments USB-6210 analogue to digital convertor and logged at 3 Hz using a LabVIEW programme written by the University of Liverpool's Rock Deformation Laboratory. The load cell measurement resolution was ± 20 N. The splitting tensile strength was calculated using the Equation B1.1:

$$\sigma_T = 1.272 P / \pi L D, \quad (\text{Eq. B1.1})$$

where σ_T is the splitting tensile strength (STS) in MPa; P is the maximum force applied to the load cell in N; L is the length of the sample in mm; and D is the diameter of the sample in mm (ASTM International, 2016).

Unconfined Compressive Strength (UCS) experiments: UCS tests (as shown in Figure 3.8c) were conducted on 2 cored samples of hydrothermally altered host rock and 2 cored samples of relatively unaltered host rock, as well as cores of altered host rock containing chlorite- and epidote-filled Mode I veins (2 samples each). Core samples were cut to 20 mm in diameter and ~50 mm long, ensuring a length:diameter ratio that minimises any effect of stress shadows that may result from elastic mismatch of the sample and loading platens, in accordance with the D7012-14 laboratory standard (ASTM International, 2014). Samples were deformed in a uniaxial deformation apparatus driven by a servo-controlled actuator at a rate of $1 \mu\text{ms}^{-1}$ until failure occurred. The uniaxial press was mounted with a load cell to monitor load rate and amplitude. All data were logged at 2 Hz using a LabVIEW programme written by the University of Liverpool's Rock Deformation Laboratory.

B2: Summary Data Tables for Analyses Relevant to Chapter 3

Table B2.1: Summary of Brazilian Tensile Strength (BTS) tests (relevant to Figure 3.7) on discs of unaltered and altered host rock, as well as discs from two separate cores through a chlorite (Chl) vein and an epidote (Ep) vein. Discs were oriented so vein orientation varied between 0° (parallel to the compressional axis) and 90° (perpendicular to the compressional axis).

Vein Composition	Vein Thickness (mm)	Vein Orientation ($^\circ$)	Disc Thickness (mm)	Peak Load (kN)	Tensile Strength (MPa)	Notes
(Unaltered Host Rock) (A)	N/A	N/A	11.8	4.55	7.81	-
(Unaltered Host Rock) (B)	N/A	N/A	11.8	4.46	7.66	-
(Altered Host Rock) (A)	N/A	N/A	10.85	4.64	8.66	-
(Altered Host Rock) (B)	N/A	N/A	10.5	4.22	8.14	-

Table B2.1 (cont.)

Vein Composition	Vein Thickness (mm)	Vein Orientation (°)	Disc Thickness (mm)	Peak Load (kN)	Tensile Strength (MPa)	Notes
Chl (A)	0.5	0	12.0	4.23	7.14	0.5mm off-centre
Chl (A)	0.5	30	11.8	4.45	7.64	0.5mm off-centre
Chl (A)	0.5	60	11.5	3.9	6.87	2mm off-centre
Chl (A)	0.5	90	11.7	5.17	8.95	2mm off-centre
Chl (B)	0.6	0	11.3	5.32	9.54	1.5mm off-centre
Chl (B)	0.4	30	10.2	4.68	9.29	1.5mm off-centre
Chl (B)	0.5	60	11.7	5.52	9.56	1.5mm off-centre
Chl (B)	0.4	90	11.7	5.17	8.95	2mm off-centre
Ep (A)	0.9	0	12.2	5.4	8.97	Central
Ep (A)	1.2	30	11.2	4.13	7.47	2mm off-centre
Ep (A)	1.0	60	11.0	2.8	5.16	2mm off-centre
Ep (A)	0.8	90	10.8	3.96	7.43	2mm off-centre
Ep (B)	1.2	0	11.4	4.58	8.14	Central
Ep (B)	1.1	30	11.3	6.04	10.83	2.5mm off-centre
Ep (B)	1.2	60	11.5	5.78	10.18	2mm off-centre
Ep (B)	1.0	90	11.2	4.04	7.31	1mm off-centre

Table B2.2: Summary of X-Ray Diffraction (XRD) analyses relevant to Figure 3.8.

%	Quartz	Albite	Anorthite	K-feldspar	Amphibole	Calcite	Dolomite	Ankerite	Siderite	Fe-Chlorite	Muscovite/illite	Biotite (approx.)	Kaolinite	Pyrite	Hematite	Total
Unaltered	13	-	44	10	20	-	-	-	-	2	-	10	-	-	-	99
Altered	18	40	-	15	9	-	-	-	-	14	4	-	-	-	-	100

Table B2.3: Summary of Uniaxial Compressive Strength (UCS) tests relevant to Figure 3.8.

Vein	Vein Thickness (mm)	Vein Orientation (°)	Core Length (mm)	Peak Load (kN)	Compressional Strength (MPa)
Relatively Unaltered Host Rock A	0	0	515	32.52	135.21
Relatively Unaltered Host Rock B	0	0	522	34.51	143.48
Mode I Chlorite Vein	0.7	0	509	36.47	151.63
Mode I Epidote Vein	0.9	0	505	41.52	172.63
Relatively Altered Host Rock A	0	0	526	41.95	174.41
Relatively Altered Host Rock B	0	0	491	44.38	184.52

B3: Supplementary methodology relevant to Chapter 4

An overview of the Faulkner triaxial experimental apparatus:

Detailed in **Figure B3.1**, and described in Mitchell and Faulkner (2008), Faulkner and Armitage (2013) and Allen (2017), the apparatus was used for experiments in *Chapter 4*, and is also the starting point for new apparatus designs outlined in *Chapter 5*. The apparatus is capable of triaxial deformation under confining pressures up to 250 MPa, applied using silicon oil confining medium with a viscosity of 20 cSt. Differential stresses can also be applied to a 20 mm diameter core sample (or a direct shear jig as illustrated in *Figure 4.3a*) with a servo-controlled axial loading system. Pore fluid pressure can be induced at either end of a core sample. Upstream fluid pressures are servo-controlled, whilst the downstream is connected to a low-volume fluid reservoir. This system has the capability of measuring permeability to a lower limit of $\sim 10^{-22} \text{ m}^2$ and resolving sample volume changes of less than 0.1 mm^3 ,

Axial force and confining/fluid pressure data are monitored using a force gauge and Honeywell transducers with a resolution of 7000 Pa. Signals are boosted via an amplifier through a National Instruments CompactRio (NI9024) data logging module and to a 4-channel, 16-Bit analogue input module (NI 9215). Signals are then checked against working set points for pressure systems using a servo-loop, and calibration corrections are controlled by user-entered PID parameters (Proportional gain, Integral gain, and Derivative gain). Finally, the signal is again amplified to a higher voltage and current to drive actuators and motors that operate the confining pressure, fluid pressure and axial load systems. Calibrations are performed regularly using high resolution pressure gauges and reference load cells. All data can be viewed and recorded (as raw voltage data and calculated pressures/forces) via LabView software written by Daniel Faulkner (Rock Deformation Laboratory, University of Liverpool).

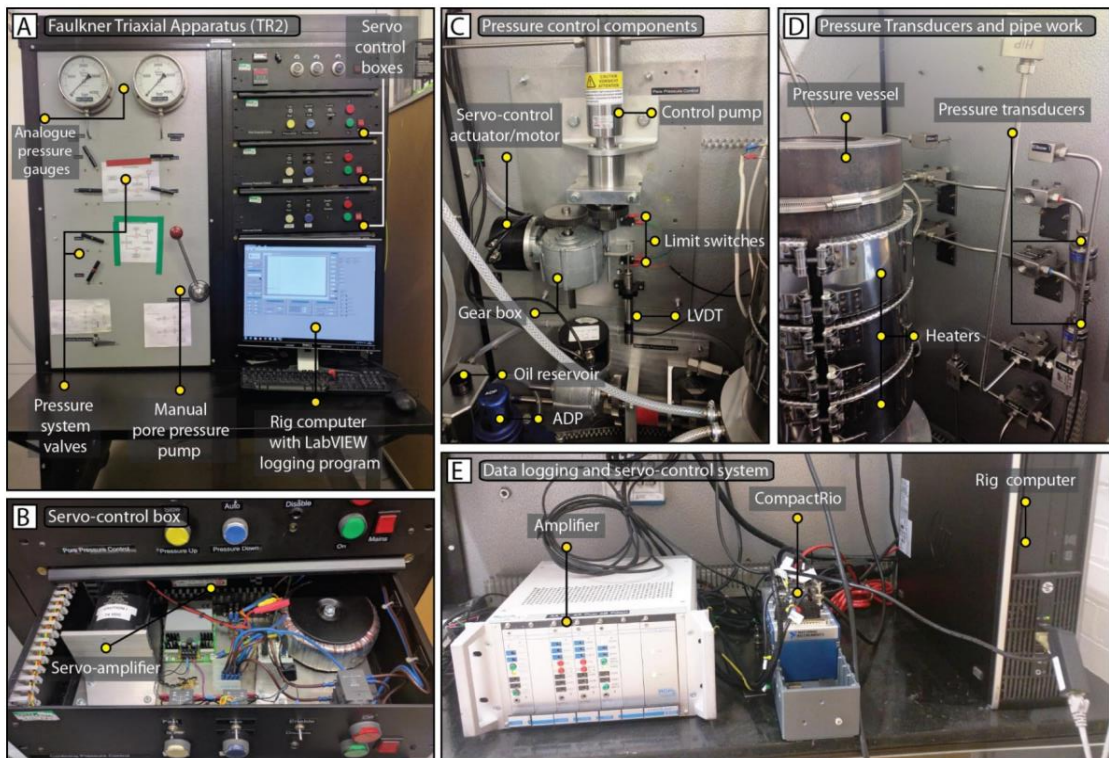
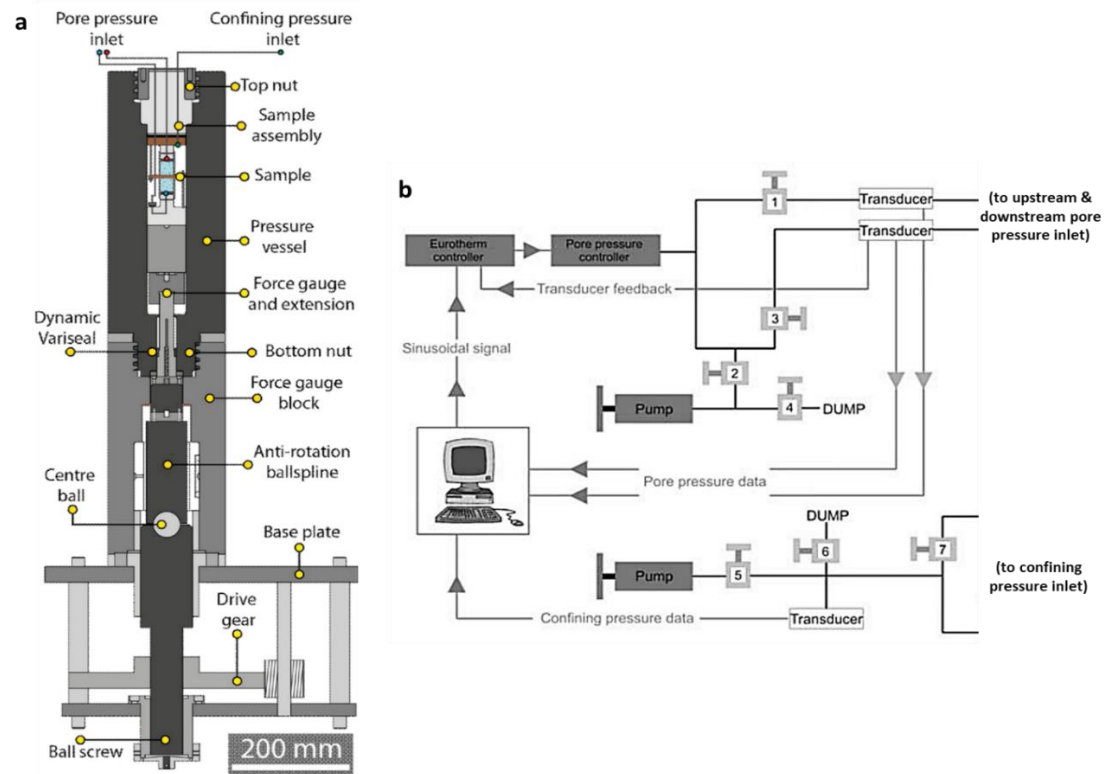


Figure B3.1: a) Schematic drawing of the Faulkner triaxial apparatus (after Allen et al., 2020). b) An illustration of how confining and pore pressures are introduced, controlled and measured (after Mitchell and Faulkner, 2008). c) Images of [A] the control panel and shielding of the apparatus; [B] The servo-control box; [C] The pressure control components (where LVDT = Linear variable differential transformer and ADP = Air Differential Pressure Switches); [D] the pressure transducers and pipework monitoring and containing the pore and confining fluid pressure systems; and [E] the data logging and signal processing equipment for the servo-control system (after Allen, 2017).

A note on comparisons of frictional strength data between laboratories:

The reliability of friction data presented in *Chapter 4* depends in part on the performance capabilities and calibrations of the equipment described above. Hence, a series of tests were conducted whereby the same gouge materials were tested in different laboratories, principally comparing data to that of the United States Geological Survey (USGS) (for which we thank Diane Moore). Yield and steady-state frictional strength data were compared for 6 gouge materials under saturated conditions at effective pressures of 100 MPa and slip rates of 1-3 μms^{-1} . University of Liverpool data were acquired using a direct shear setup (cf. *Chapter 4*), whilst USGS used a sawcut setup (cf. Lockner et al., 2011). Gouge materials tested were westerly granite, material from the SAFOD core, angular quartz, talc, a 50-50 quartz-montmorillonite mixture, kaolinite and margarite.

The frictional strength of measured gouges was in general shown to be comparable between the two laboratories, with friction coefficients (μ) measured at yield point and established steady-state sliding usually within ~ 0.06 . Kaolinite and margarite, however, proved to be exceptions, with differences of 0.21-0.26 in kaolinite and 0.11-0.18 in margarite that are greater at steady-state conditions (**Figure B3.1; Table B3.1**). In both cases, materials were shown to be significantly frictionally weaker in the University of Liverpool's deformation apparatus.

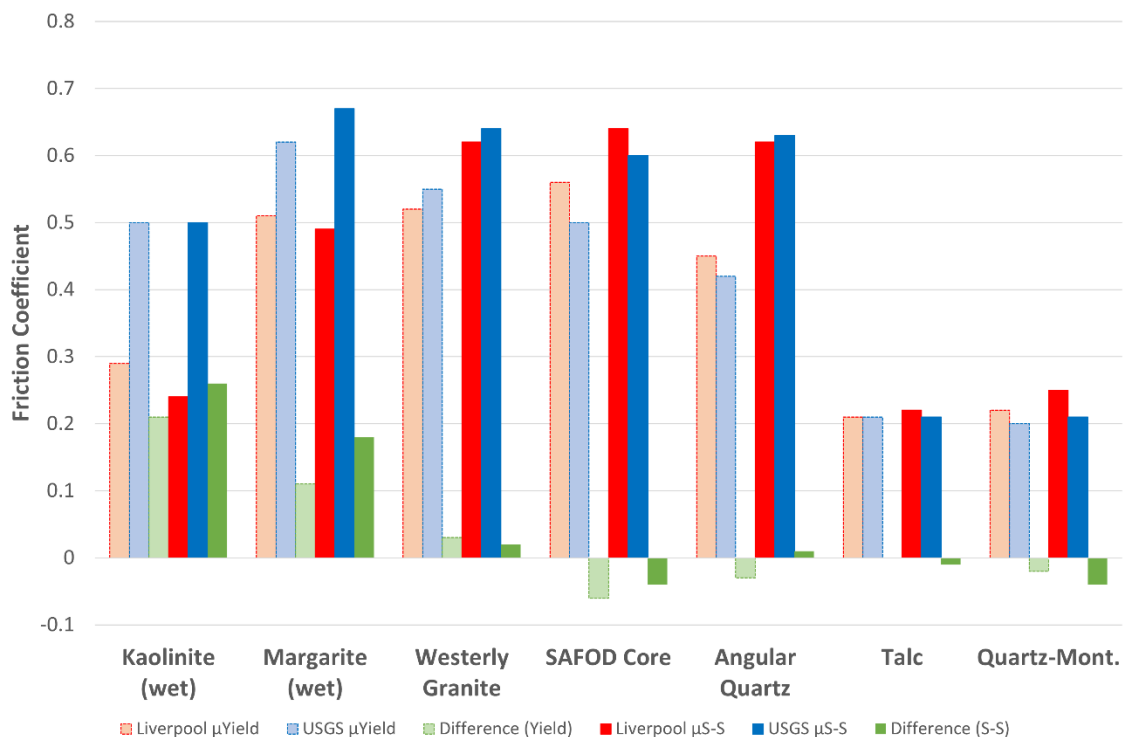


Figure B3.1: Comparisons of yield and steady-state (S-S) frictional strength data from the University of Liverpool and USGS, both achieved via frictional shear of identical materials at similar sliding velocities under saturated conditions.

Table B3.1: Comparison of yield and steady-state (S-S) friction coefficient (μ) data for different gouge materials as measured at the University of Liverpool and USGS. (* indicates strain hardening is still occurring at the point taken as measurement).

Material	μ_y (Liverpool)	μ_{ss} (Liverpool)	μ_{yield} (USGS)	μ_{ss} (USGS)
Westerly Granite	0.52	0.64	0.55	*0.64
SAFOD Core	0.56	0.64	0.50	*0.60
Angular Quartz	0.45	0.62	0.42	*0.63
Talc	0.21	0.22	0.21	*0.21
Quartz-Mont.	0.22	0.25	0.28	*0.26
Margarite (wet)	0.51	0.49	0.62	*0.67
Margarite (dry)	0.45	0.6	0.65	*0.81
Kaolinite (wet)	0.29	0.24	-	0.50
Kaolinite (dry)	0.35	0.44	-	0.82

Data were also analysed to test the difference between dry gouges, for which a notable difference has been observed in previous work (e.g. Morrow et al. (2000); Moore and Lockner (2004); Behnken et al. (2013); this study). Using identical methodology to that used by the USGS, kaolinite and margarite were also tested at dry conditions. The gouge sample and shear assembly were dried in a vacuum oven at 120 °C for 20 hours, pore pressure capillary tubes were evacuated, and the sample was pressurised in the vessel within 20 minutes. Dry samples were sheared under 100 MPa confining pressure at 0.5 μms^{-1} to 4 mm displacement, before 10 MPa pore fluid was introduced and confining pressures were raised to 110 MPa to maintain the same effective pressure. Fluid pressures were left to equilibrate for ~ 3 hours before shearing to 8 mm total displacement. Data show that for both studied materials, there is a large difference between both wet and dry friction coefficients, with greater discrepancy in the latter.

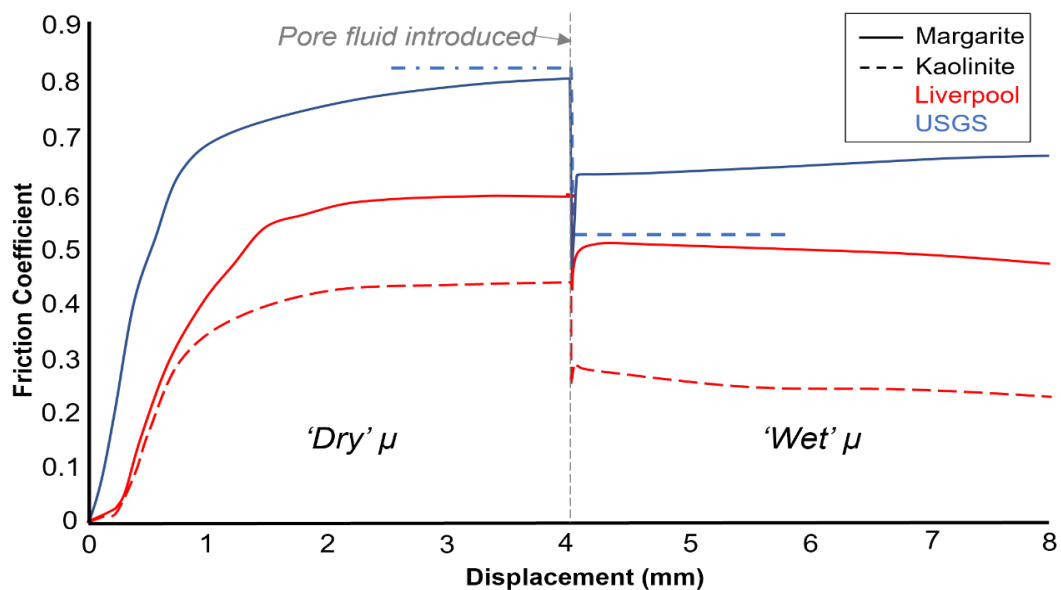


Figure B3.2: Comparison of friction coefficient (μ) data for kaolinite and margarite as measured at the University of Liverpool and USGS, highlighting μ differences in both 'dry' and 'wet' gouge samples.

Finally, frictional strength data were compared for direct shear and sawcut setups. **Figure B3.3** indicates that sawcut data measured at the University of Liverpool produces estimates of friction coefficient that are significantly higher than both sawcut measurements at the USGS and a direct shear setup for the same material, at the same conditions, and in the same triaxial pressure vessel. This appears to particularly be the case in stronger Westerly Granite, which even after 4 mm is still strain hardening.

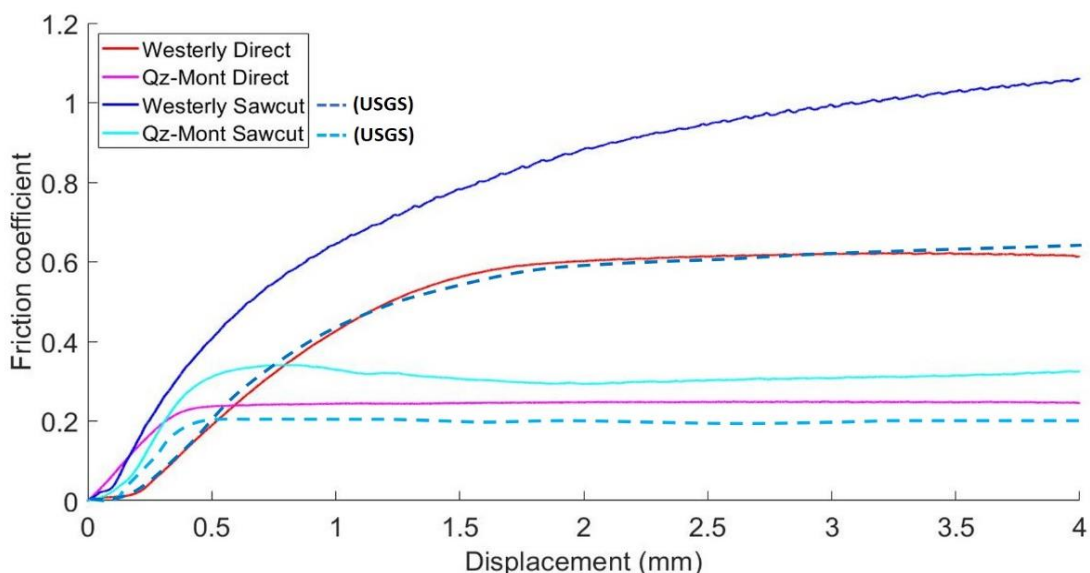


Figure B3.3: Comparison of friction coefficient (μ) data for Westerly Granite and a 50-50 Quartz-montmorillonite mix as measured by direct shear (red/pink) and sawcut (light/dark blue) setups at the University of Liverpool, and by sawcut setups at the USGS (dashed light/dark blue).

Whilst it is too early to draw meaningful conclusions from this preliminary dataset, data presented here indicate that significant discrepancies in frictional strength measurements may occur between laboratories. Evidence suggests that discrepancies may primarily occur due to the type of material studied (although it is not yet clear why this may be the case), or due to the principles of the experimental setup (e.g. direct shear vs. sawcut). Discrepancies appear to be greater in dried samples than in wet samples. Although the point at which friction coefficient data is measured may make some difference (e.g. yield point vs. steady state conditions), this does not appear to be the main contributing factor (however it should still be ensured that measurement points are consistent between laboratories). Further understanding may be gained by considering how sawcut experiments may lead to increased strength relative to direct shear experiments, and how the crystallographic structure or evolving microstructural properties of particular materials may contribute to such differences in frictional strength.

B4: Summary data tables for analyses relevant to Chapter 4

Table B4.1: Rate and state friction data for kaolinite-rich china clay and Mg-montmorillonite. VS = Velocity Step. Refer to Table 4.1 for experiment and sample type. Machine stiffness was estimated as 10 GPa. Data rows left blank were not included due to significant error in the modelling process.

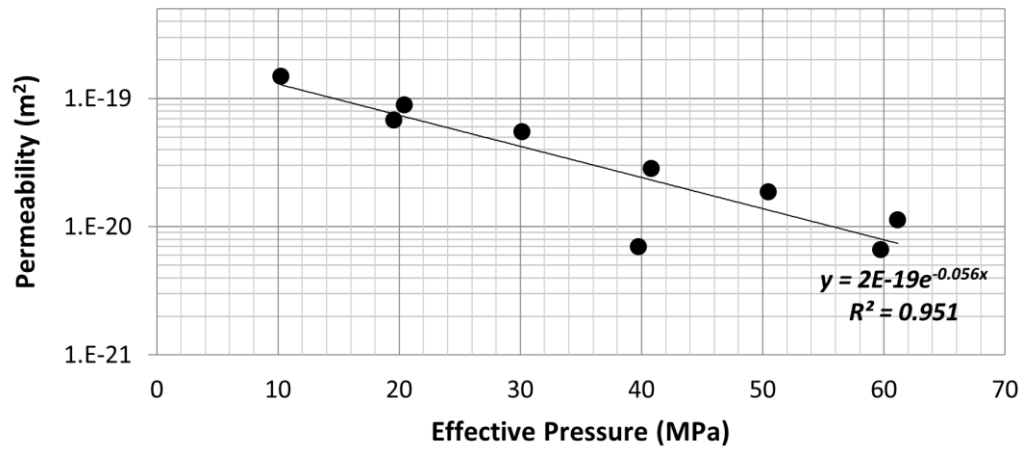
Sample ID	VS	a	a error	b	b error	d _c	d _c error	a-b	a-b error
KLSAT01	1	6.70E-03	5.04E-04	2.65E-03	4.84E-04	1.79E-05	4.18E-06	4.06E-03	9.88E-04
KLSAT01	2	5.05E-03	1.96E-04	1.04E-03	1.77E-04	5.39E-05	2.12E-06	4.00E-03	3.72E-04
KLSAT01	3	5.36E-03	3.12E-04	2.76E-04	2.94E-04	2.90E-05	3.76E-06	5.08E-03	6.06E-04
KLSAT02	1	5.98E-03	3.48E-04	1.18E-03	3.37E-04	2.67E-05	6.64E-06	4.80E-03	6.85E-04
KLSAT02	2	5.09E-03	2.39E-04	4.32E-04	2.28E-04	3.67E-05	2.65E-06	4.66E-03	4.66E-04
KLSAT02	3								
KLSAT03	1	5.49E-03	2.03E-04	1.08E-03	1.94E-04	2.64E-05	6.33E-06	4.41E-03	3.97E-04
KLSAT03	2	5.97E-03	2.76E-04	1.17E-03	2.70E-04	2.09E-05	5.74E-06	4.80E-03	5.46E-04
KLSAT03	3	6.27E-03	2.73E-04	5.54E-04	2.64E-04	1.81E-05	4.32E-06	5.71E-03	5.38E-04
KLRD01	1	4.10E-03	2.43E-04	6.91E-04	2.33E-04	3.22E-05	4.23E-06	3.41E-03	4.76E-04
KLRD01	2	4.45E-03	2.38E-04	7.06E-04	2.24E-04	3.43E-05	3.76E-06	3.74E-03	4.62E-04
KLRD01	3	3.90E-03	4.89E-04	2.31E-04	4.64E-04	1.51E-05	3.45E-06	3.67E-03	9.53E-04
KLRD02	1	2.19E-03	1.76E-04	8.54E-04	1.68E-04	2.14E-05	5.77E-06	1.34E-03	3.45E-04
KLRD02	2	2.59E-03	2.20E-04	3.97E-04	2.15E-04	1.23E-05	2.31E-06	2.19E-03	4.35E-04
KLRD02	3								
KLVD01	1	1.76E-03	1.40E-04	2.19E-04	1.35E-04	2.49E-05	9.03E-06	1.54E-03	2.75E-04
KLVD01	2	2.23E-03	6.08E-05	6.40E-05	1.76E-05	1.87E-05	5.51E-06	2.16E-03	7.84E-05
KLVD01	3								
KLVD02	1	1.71E-03	1.33E-04	6.26E-04	1.28E-04	2.35E-05	6.71E-06	1.09E-03	2.61E-04
KLVD02	2	2.08E-03	1.79E-04	-4.77E-04	-1.71E-04	1.96E-05	4.41E-06	2.55E-03	7.19E-06
KLVD02	3								
KLODX01	1	4.47E-03	4.64E-04	1.21E-03	4.61E-04	3.57E-06	1.49E-06	1.09E-03	2.61E-04
KLODX01	2	3.79E-03	7.12E-05	1.04E-03	6.64E-05	3.86E-06	4.52E-07	2.75E-03	1.38E-04
KLODX01	3	3.59E-03	7.13E-05	-1.20E-04	-6.73E-06	4.38E-06	3.96E-07	3.71E-03	6.46E-05
KLODX02	1	1.48E-03	5.58E-05	-3.59E-04	-8.07E-05	1.04E-05	5.21E-06	1.84E-03	-2.49E-05
KLODX02	2								
KLODX02	3								
KLODV01	1	2.30E-03	6.79E-04	1.04E-03	2.75E-04	2.83E-06	2.77E-08	1.26E-03	9.54E-04
KLODV01	2	1.84E-03	1.75E-04	6.13E-04	1.71E-04	9.05E-06	3.97E-06	1.22E-03	3.46E-04
KLODV01	3	2.13E-03	2.32E-04	7.26E-04	2.29E-04	1.03E-05	4.26E-06	1.41E-03	4.60E-04
KLODV02	1								
KLODV02	2	6.44E-03	3.76E-04	7.22E-03	2.53E-04	8.98E-06	1.83E-06	2.85E-03	6.29E-04
KLODV02	3								
KLVH01	1								
KLVH01	2	8.47E-03	4.55E-04	7.22E-03	2.74E-04	8.06E-06	1.57E-06	1.24E-03	7.29E-04
KLVH01	3	5.41E-03	9.33E-04	2.36E-03	9.31E-04	2.86E-06	1.27E-06	3.06E-03	1.86E-03
KLVH02	1	3.77E-03	3.12E-04	2.56E-03	3.06E-04	6.56E-06	1.10E-06	1.22E-03	6.18E-04

Table B4.1 (cont.)

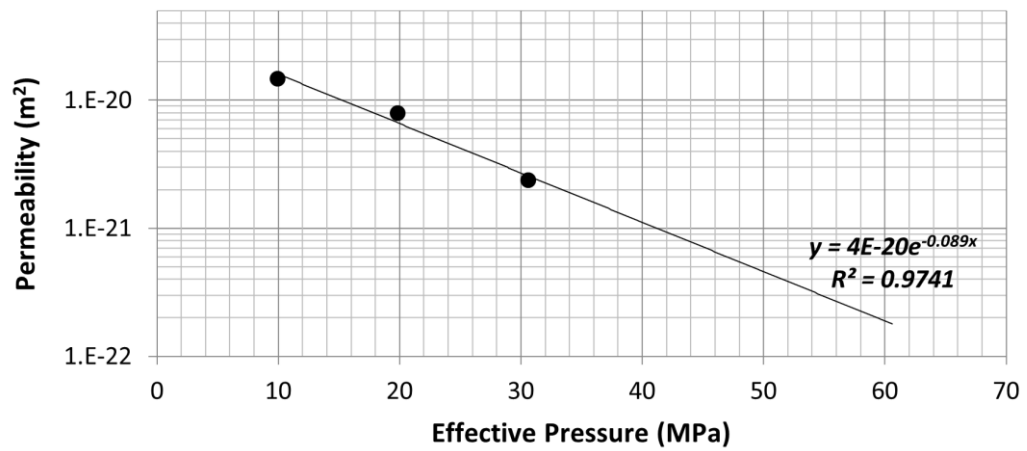
Sample ID	VS	a	a error	b	b error	d _c	d _c error	a-b	a-b error
KLVH02	2								
KLVH02	3	6.82E-03	8.28E-04	4.34E-03	4.77E-04	2.58E-06	9.21E-07	2.48E-03	1.30E-03
MMSAT01	1	3.20E-03	9.88E-05	-4.04E-04	-9.60E-05	2.71E-05	7.55E-06	3.60E-03	2.79E-06
MMSAT01	2	3.45E-03	6.24E-05	-1.02E-03	-5.79E-05	7.92E-05	6.86E-06	4.47E-03	4.58E-06
MMSAT01	3	2.78E-03	6.07E-05	-6.10E-04	-5.68E-05	6.21E-05	9.04E-06	3.39E-03	3.90E-06
MMRH01	1	6.22E-03	9.76E-05	-5.61E-04	-9.13E-05	5.52E-05	1.28E-05	6.78E-03	6.31E-06
MMRH01	2	7.27E-03	7.07E-05	5.87E-04	6.62E-05	9.51E-05	2.16E-05	6.68E-03	1.37E-04
MMRH01	3	6.76E-03	1.02E-04	1.49E-03	9.51E-05	5.95E-05	5.69E-06	5.26E-03	3.90E-06
MMVD01	1								
MMVD01	2	7.51E-03	6.21E-05	-4.15E-04	-7.39E-05	1.10E-04	4.17E-05	7.93E-03	-1.19E-05
MMVD01	3	7.31E-03	1.39E-04	1.05E-03	1.30E-04	6.90E-05	1.92E-05	6.25E-03	2.69E-04
MMODX01	1	6.31E-03	6.51E-04	1.44E-03	8.44E-04	7.33E-06	5.49E-06	4.86E-03	1.11E-03
MMODX01	2	5.90E-03	6.02E-04	2.16E-03	5.90E-04	4.37E-06	1.39E-06	3.74E-03	1.19E-03
MMODX01	3								
MMODV01	1	8.52E-03	3.51E-05	5.35E-03	1.14E-03	1.25E-06	9.13E-07	3.17E-03	1.17E-03
MMODV01	2	7.49E-03	3.42E-04	2.65E-03	6.66E-04	2.76E-06	1.47E-06	4.84E-03	1.01E-03
MMODV01	3								
MMVH01	1								
MMVH01	2	6.17E-03	5.99E-04	3.61E-03	5.71E-04	7.75E-06	1.87E-06	2.57E-03	1.17E-03
MMVH01	3	8.19E-03	6.76E-04	3.73E-03	4.62E-04	6.34E-06	1.55E-06	4.46E-03	1.14E-03

Table B4.2: Permeability values as measured by the pulse transient method for varying effective pressures in kaolinite and montmorillonite gouges used in Chapter 4.

Gouge Material	Effective Pressure (MPa)	Permeability (m ²)
Kaolinite	10.27	1.48E-19
Kaolinite	19.56	6.76E-20
Kaolinite	20.43	8.89E-20
Kaolinite	30.16	5.50E-20
Kaolinite	39.76	6.94E-21
Kaolinite	40.82	2.82E-20
Kaolinite	50.49	1.86E-20
Kaolinite	59.74	6.62E-21
Kaolinite	61.12	1.12E-20
Montmorillonite	9.94	1.47E-20
Montmorillonite	19.87	7.87E-21
Montmorillonite	30.63	2.36E-21



a)



b)

Figure B4.1: Evolution of permeability with effective pressure for a) kaolinite and b) montmorillonite samples used in Chapter 4, as measured by the pulse transient method.

C : Supplementary Information for the New High-Pressure, High-Temperature Deformation Apparatus

C1: Technical Drawings of Sample Assembly Components Described in Chapter 5.

Table C1.1: List of detailed technical drawings of components within the sample assembly presented within this appendix.

Figure Number	Component	Principal Material
Figure C1.1	Sample Assembly A: Upper 1	Inconel
Figure C1.2	Sample Assembly B: Upper 2 (Upper Piston)	Inconel
Figure C1.3	Sample Assembly C: Lower 1 (Lower Piston)	Inconel
Figure C1.4	Sample Assembly D: Lower 2	Inconel
Figure C1.5	Furnace Assembly Can	Aluminium
Figure C1.6	Furnace Top Plate (Upper)	MACOR®
Figure C1.7	Furnace Top Plate (Lower)	MACOR®
Figure C1.8	Furnace Base Plate	MACOR®
Figure C1.9	Flanged Bus	Peek
Figure C1.10	Bus Crown Nut	Peek
Figure C1.11	Bus Top Hat	Peek
Figure C1.12	Bus Clamp	Brass
Figure C1.13	Bus Washer	Peek
Figure C1.14	Banana Jack	Brass
Figure C1.15	Sealing Ring	Viton

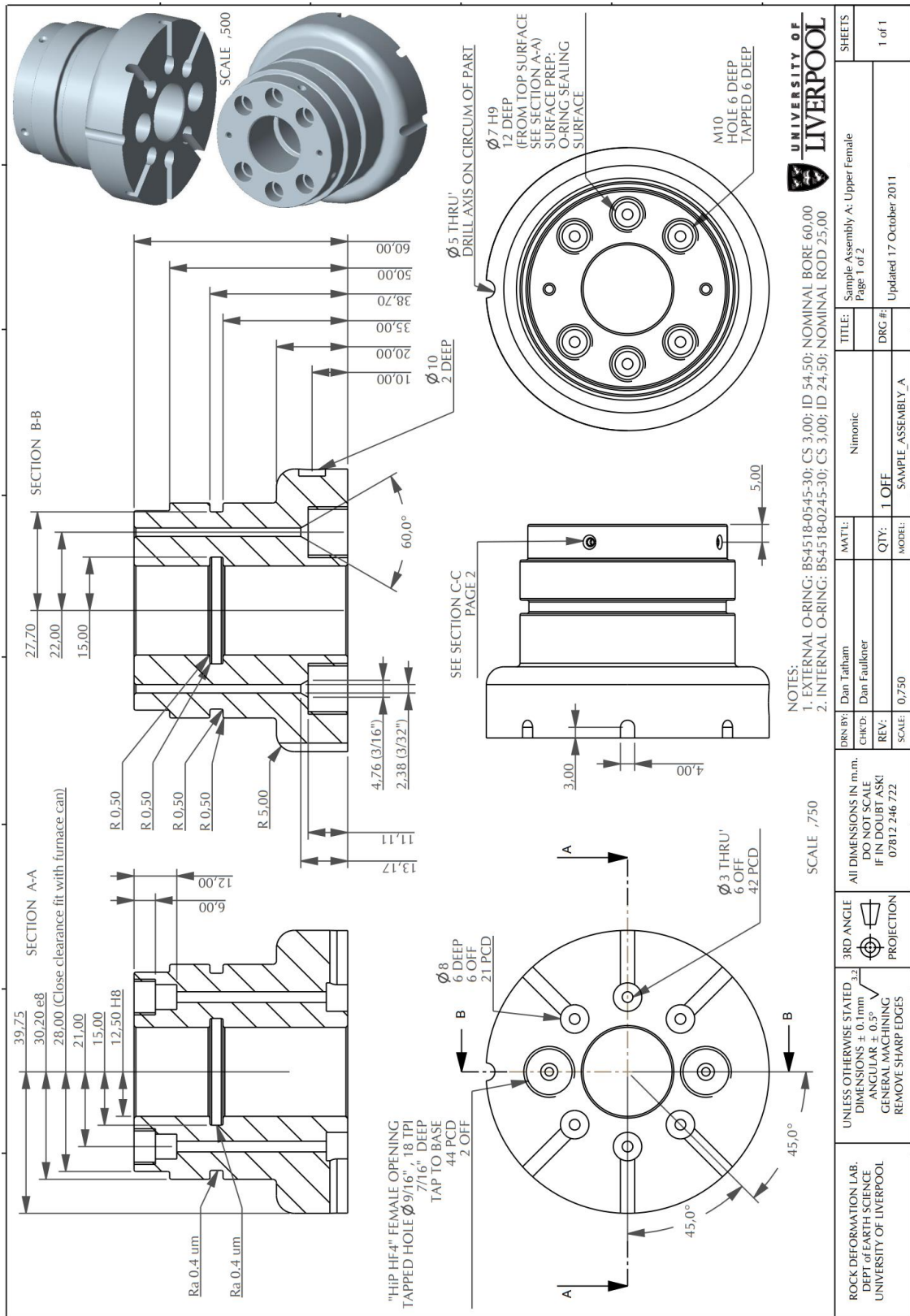


Figure C1.1b: Technical Drawing - Sample Assembly A: Upper 1 (Page 1 of 2).

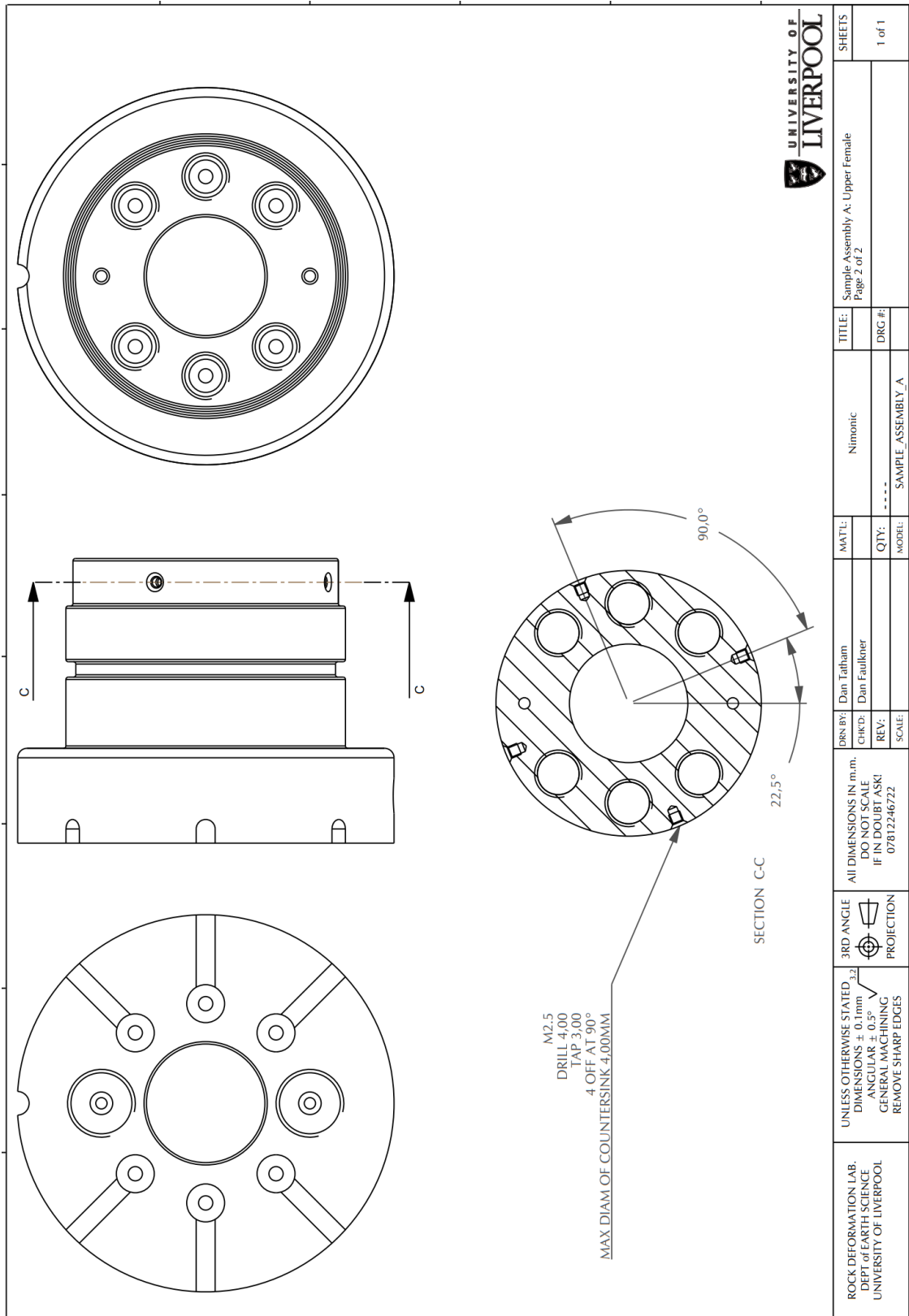


Figure C1.1a: Technical Drawing - Sample Assembly A: Upper 1 (Page 2 of 2).

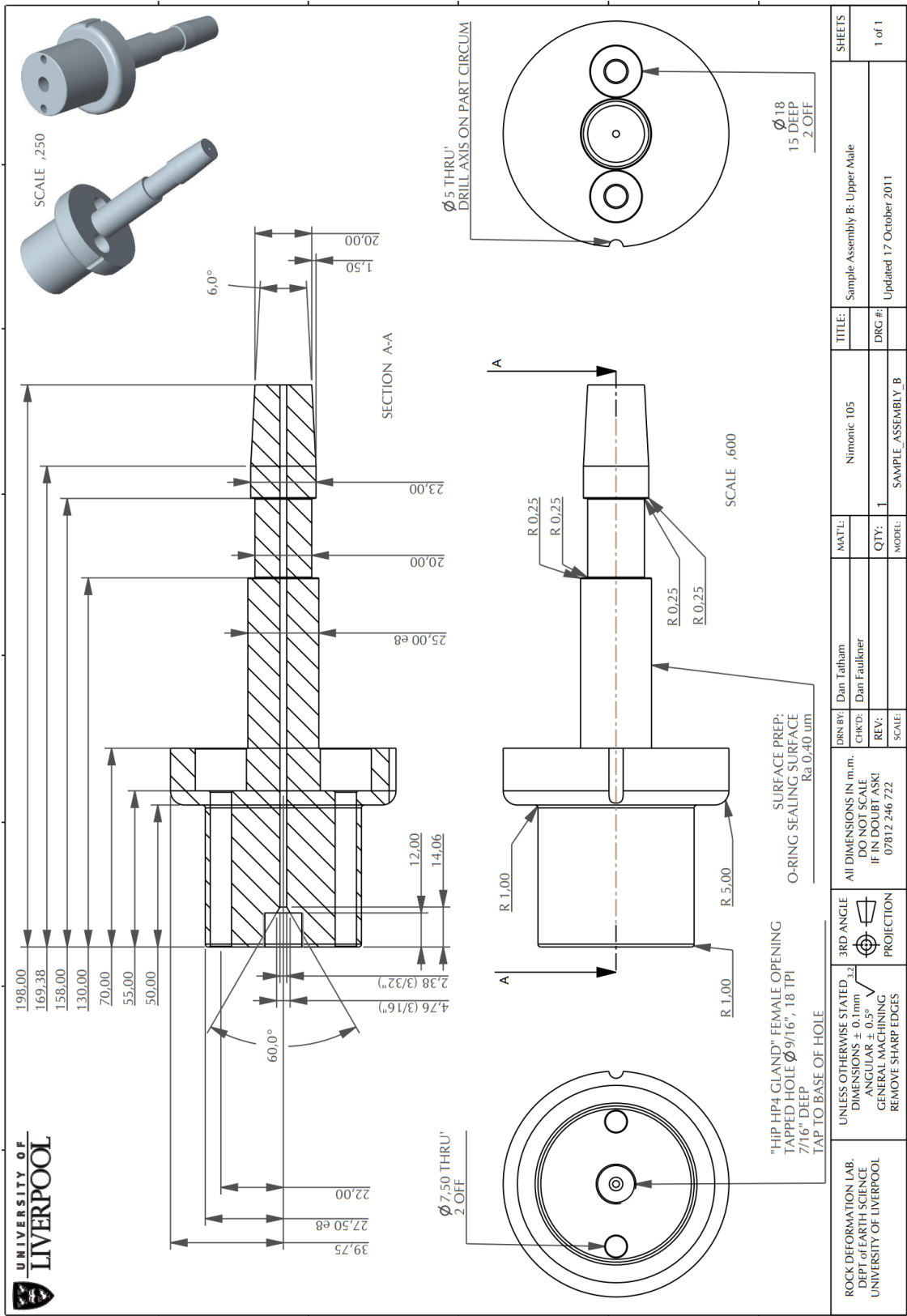


Figure C1.2: Technical Drawing - Sample Assembly B: Upper 2.

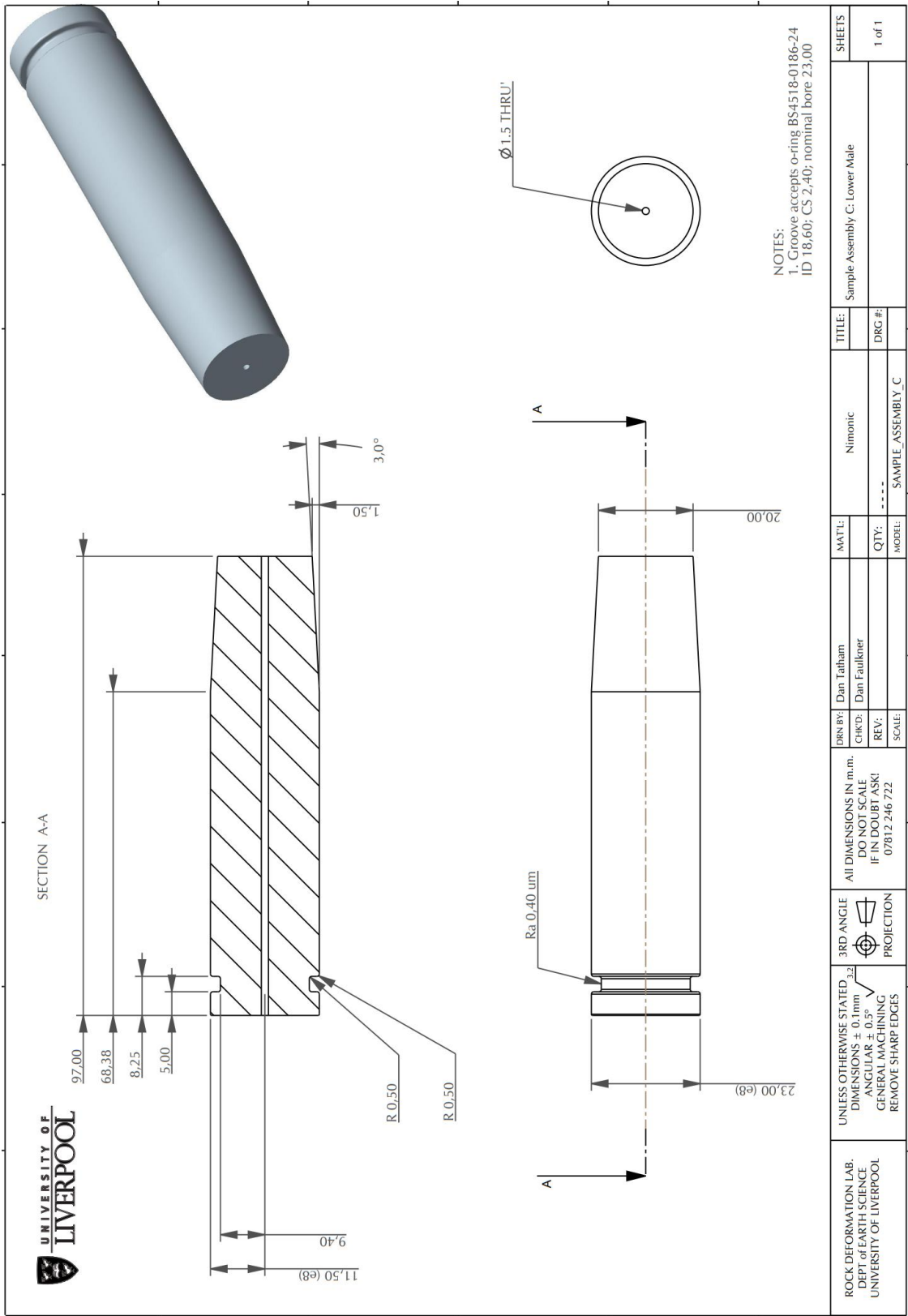


Figure C1.3: Technical Drawing - Sample Assembly C: Lower 1.

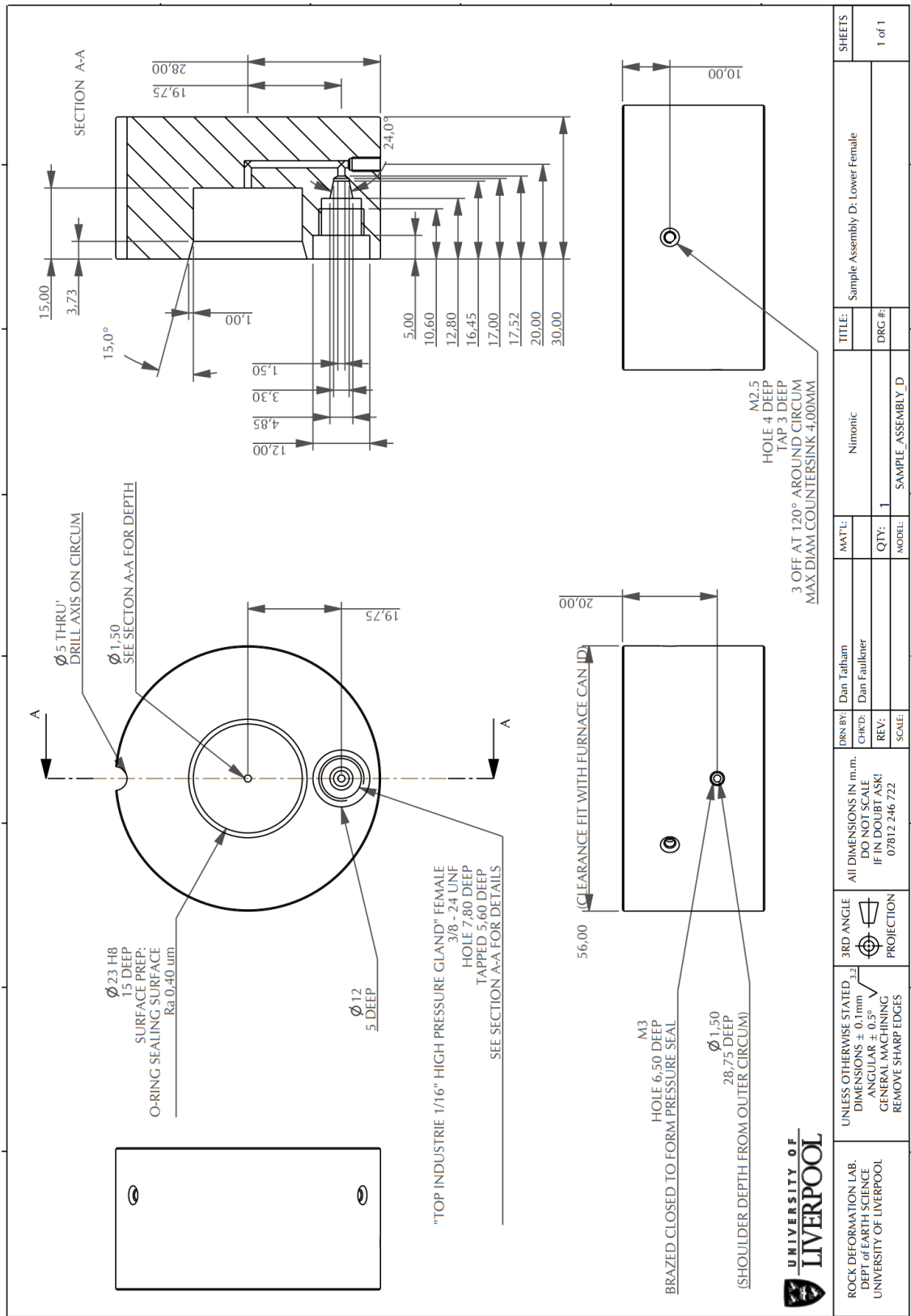


Figure C1.4: Technical Drawing - Sample Assembly D: Lower 2.

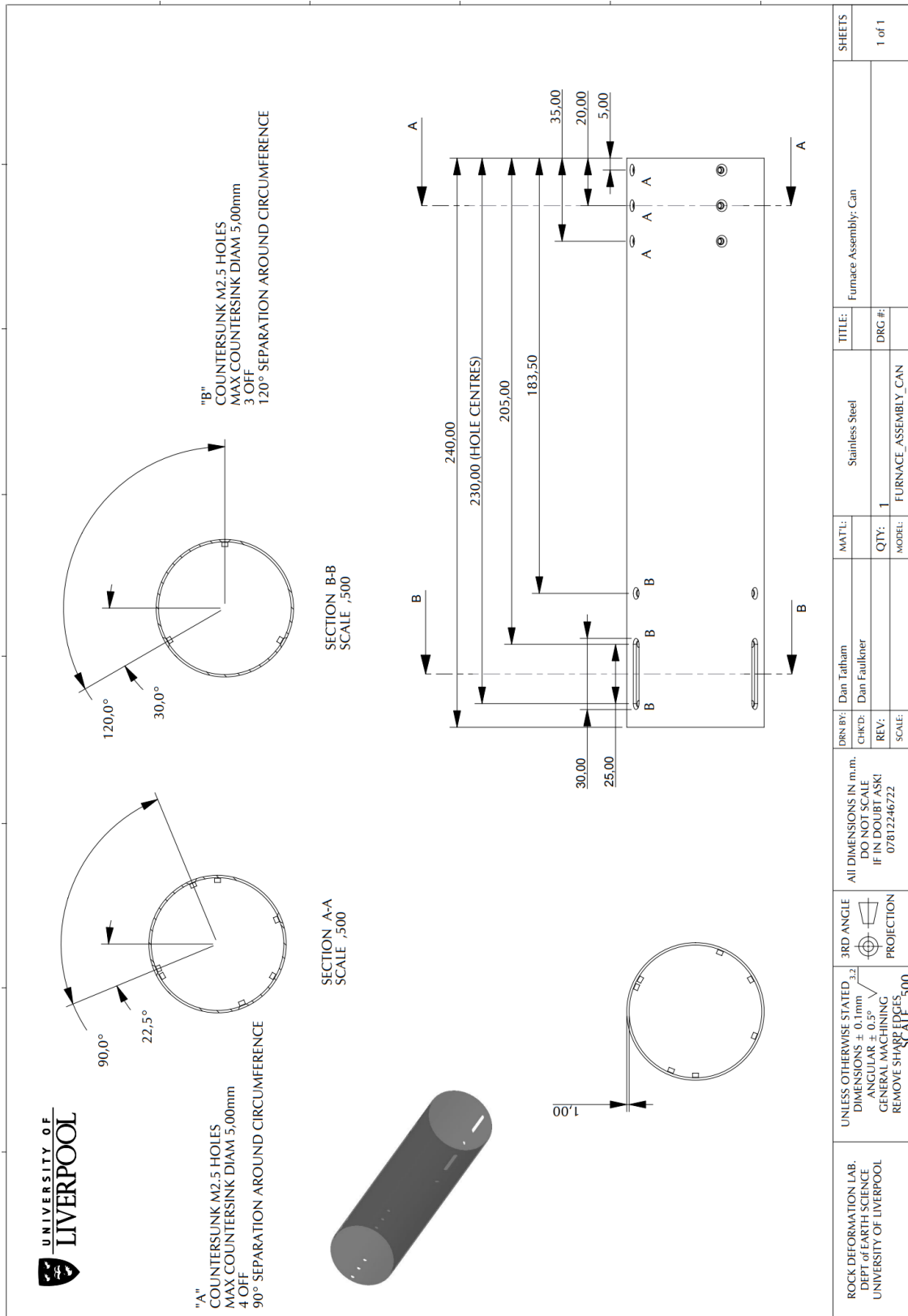


Figure C1.5: Technical Drawing - Furnace Assembly Can.

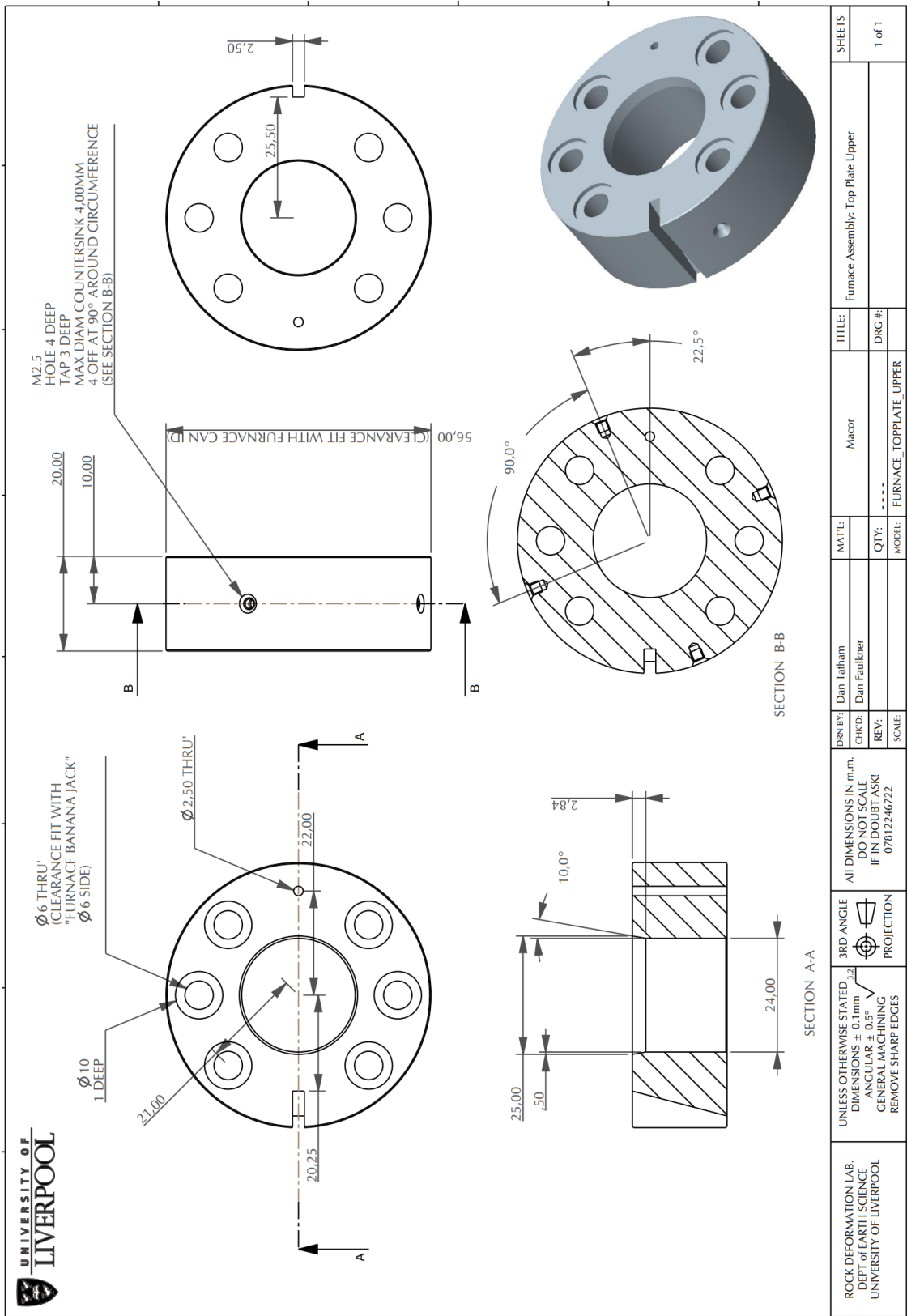


Figure C1.6: Technical Drawing - Furnace Top Plate (Upper).

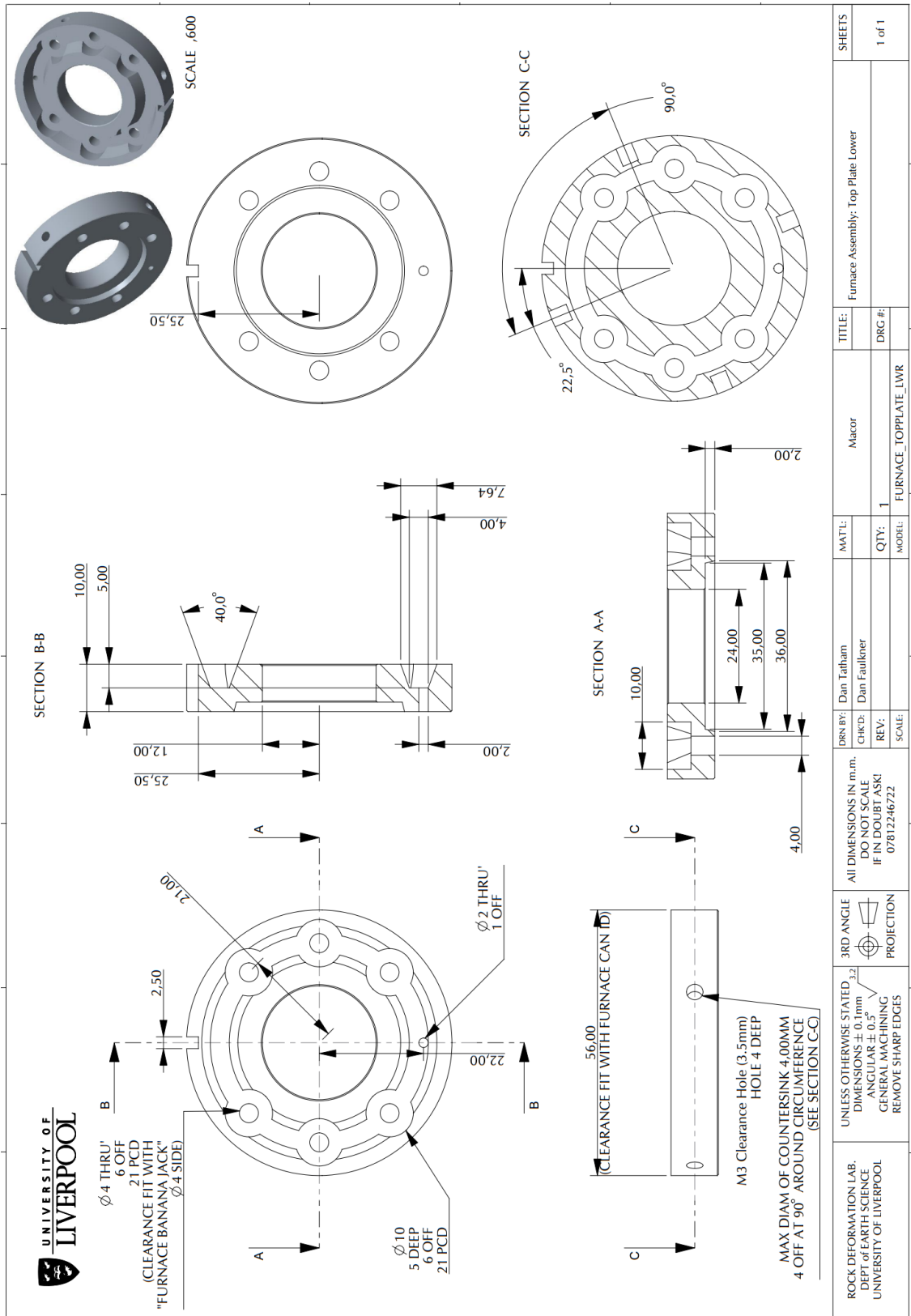


Figure C1.7: Technical Drawing - Furnace Top Plate (Lower).

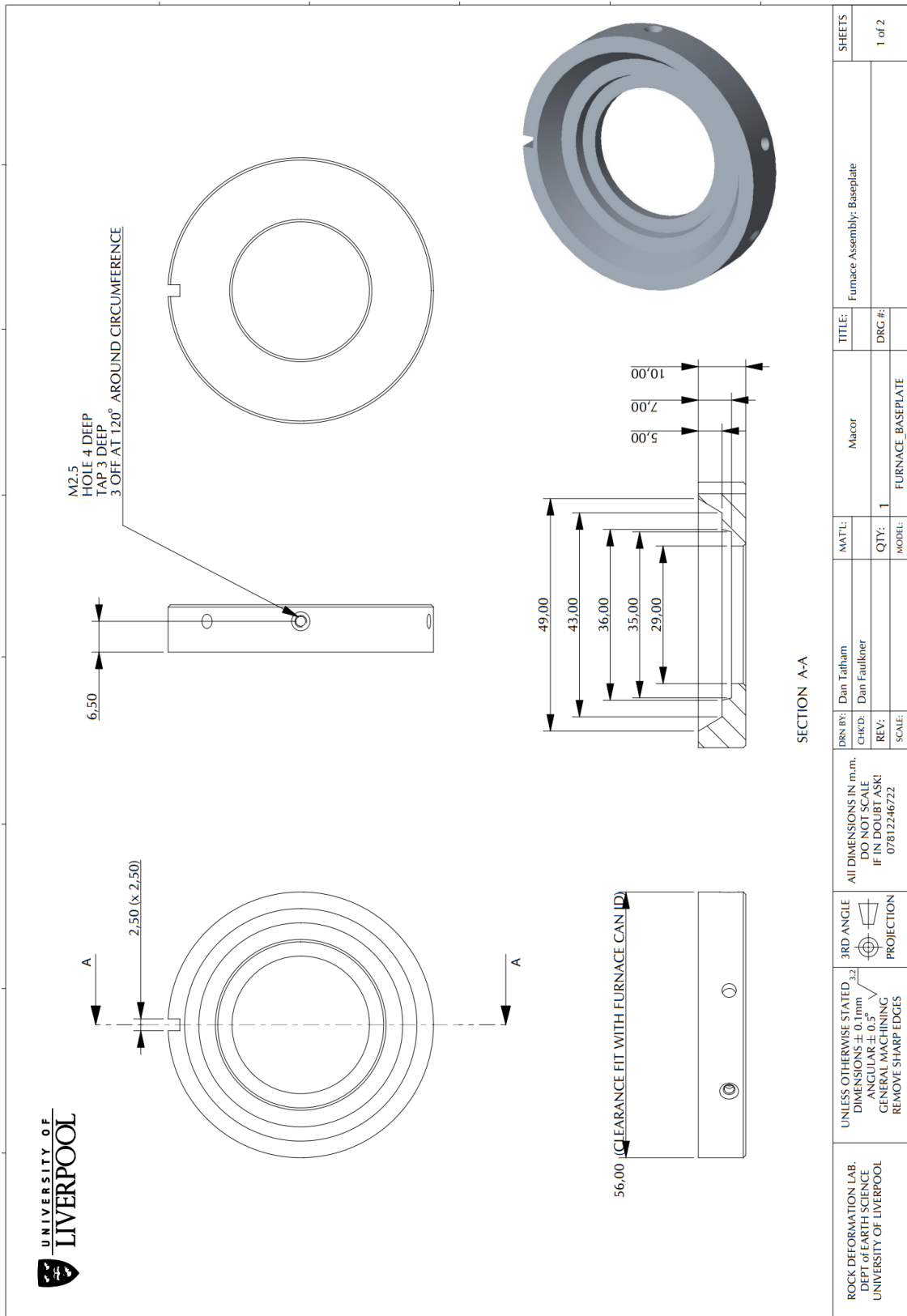


Figure C1.8a: Technical Drawing – Furnace Base Plate (Page 1 of 2).

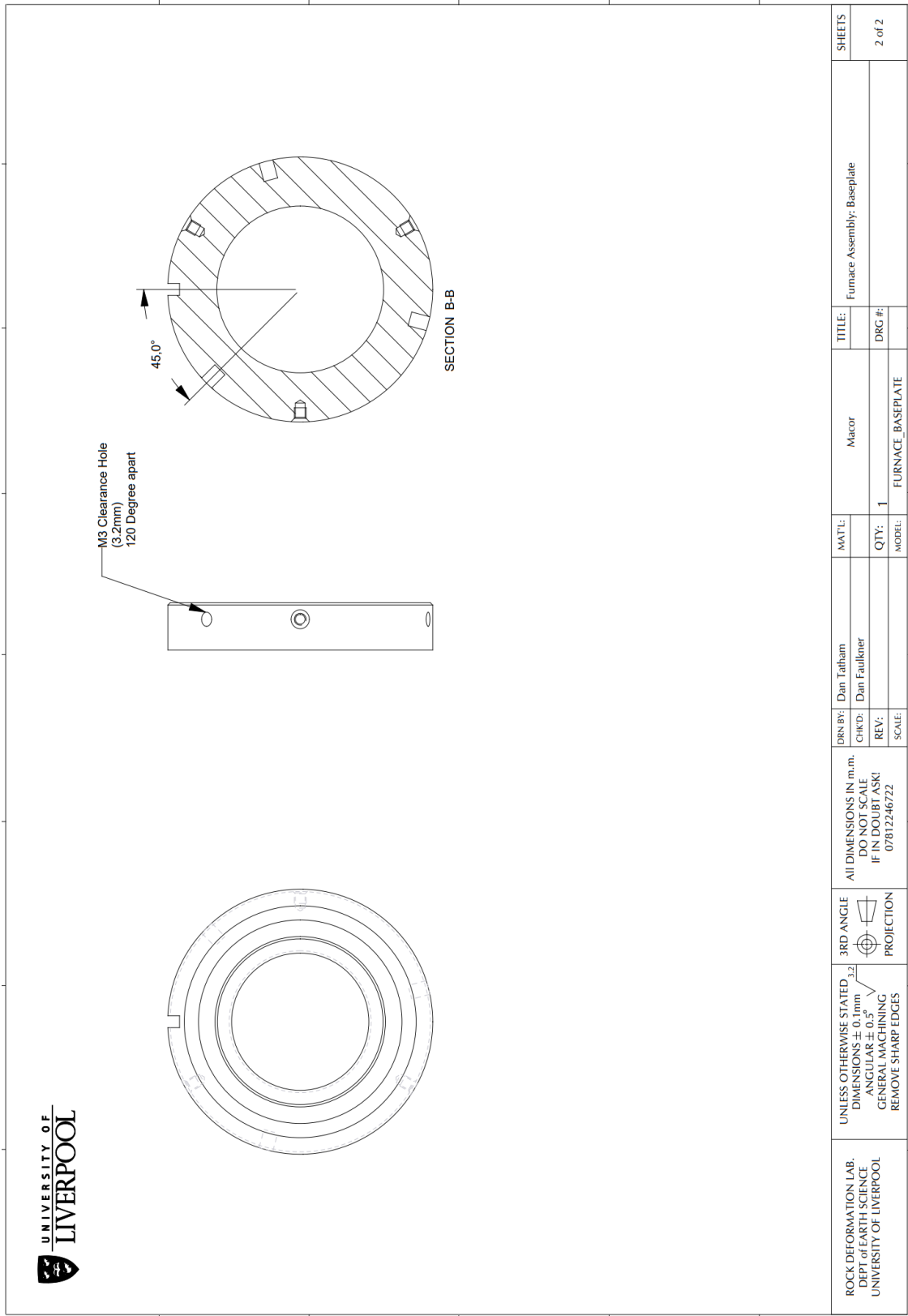


Figure C1.8b: Technical Drawing – Furnace Base Plate (Page 2 of 2).

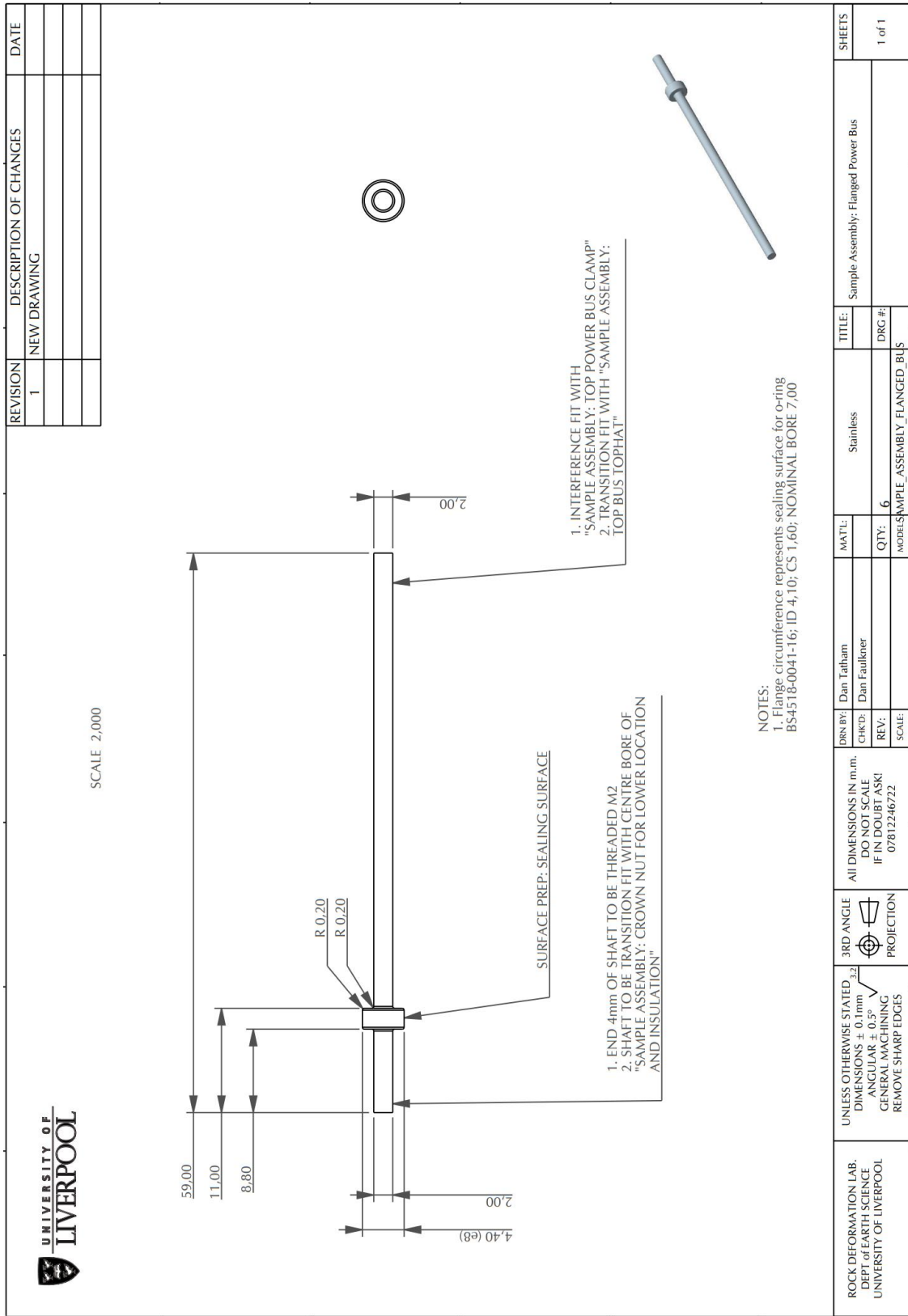


Figure C1.9: Technical Drawing – Flanged Bus.

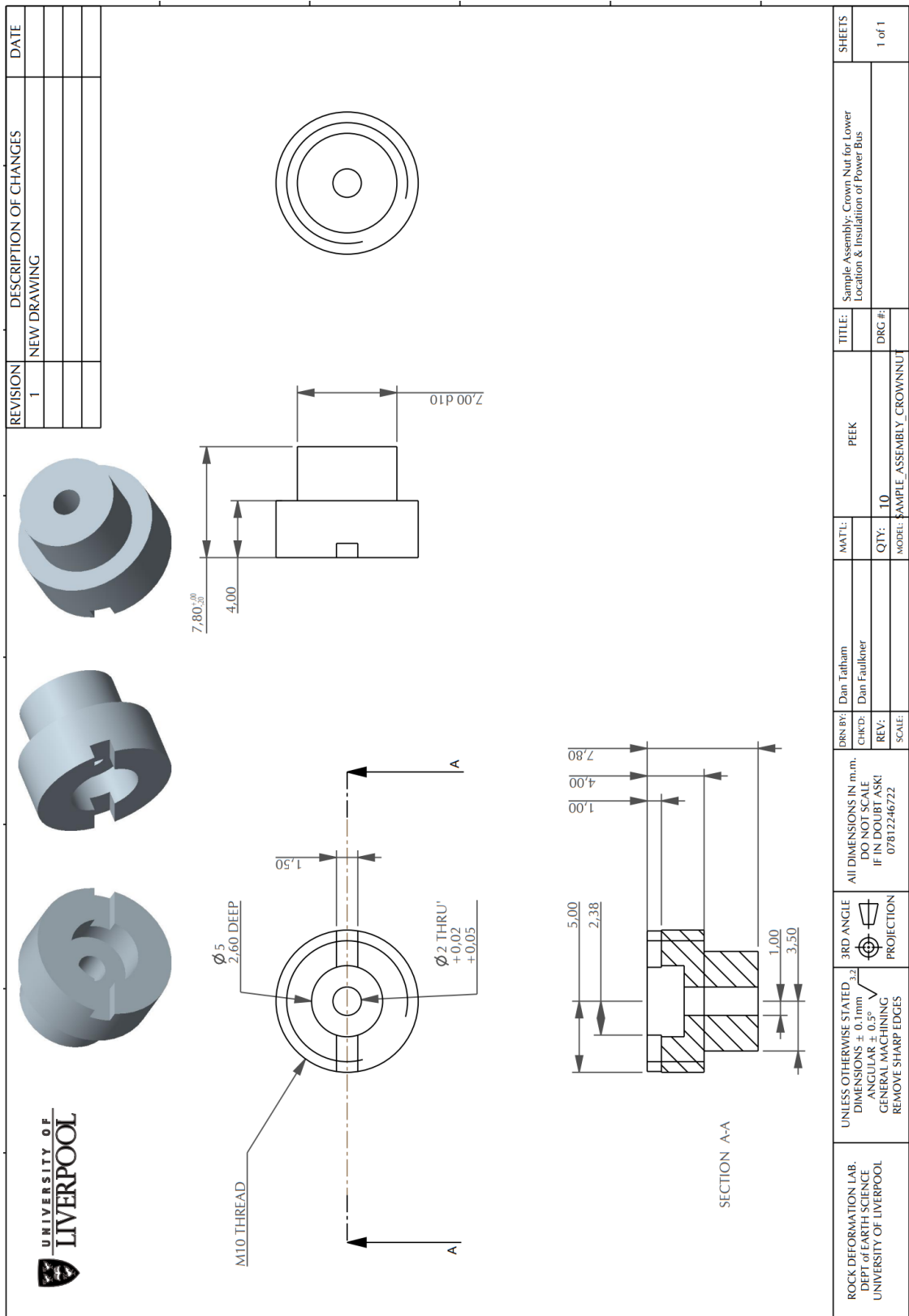


Figure C1.10: Technical Drawing – Crown Nut.

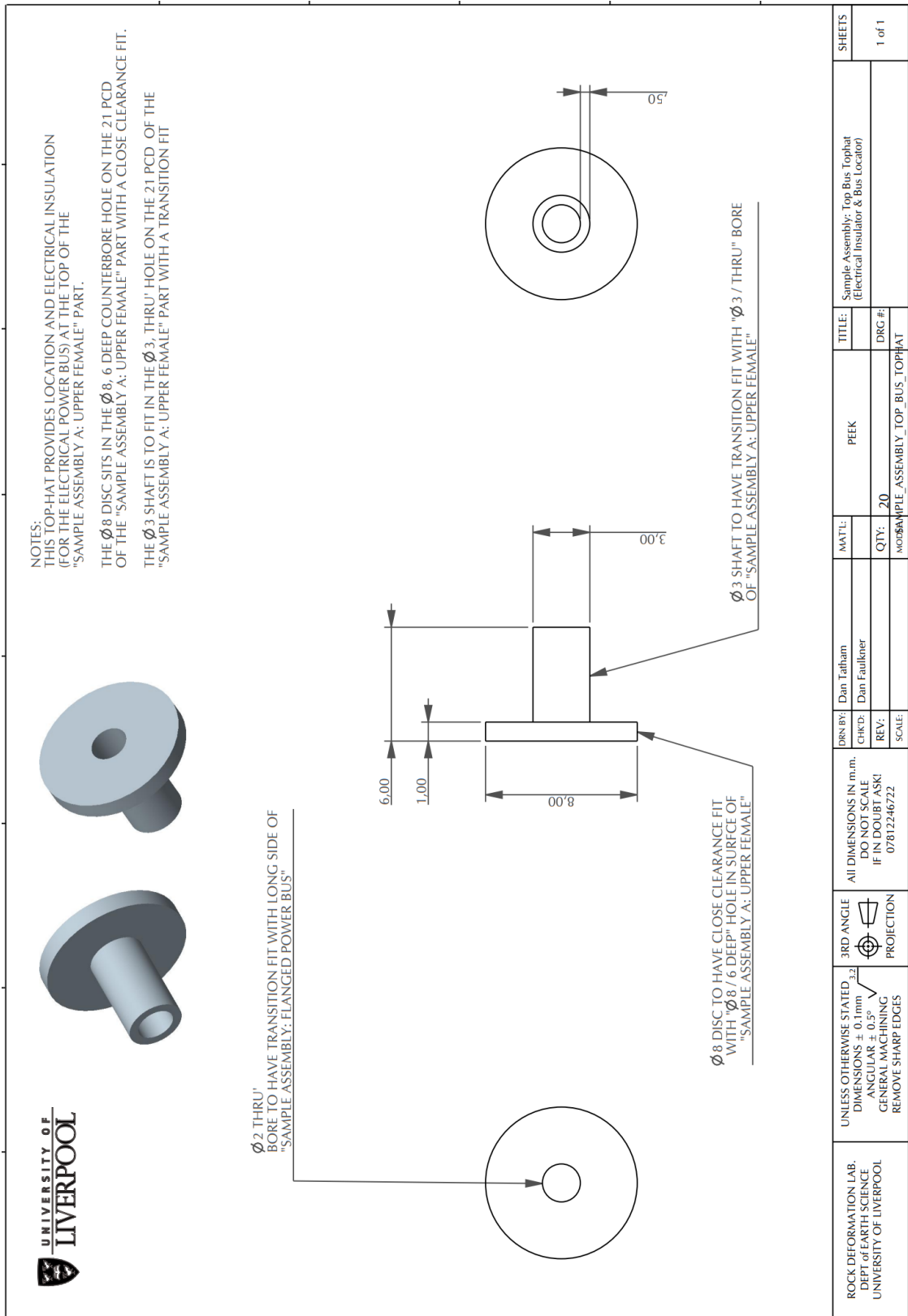


Figure C1.11: Technical Drawing – Bus Top Hat.

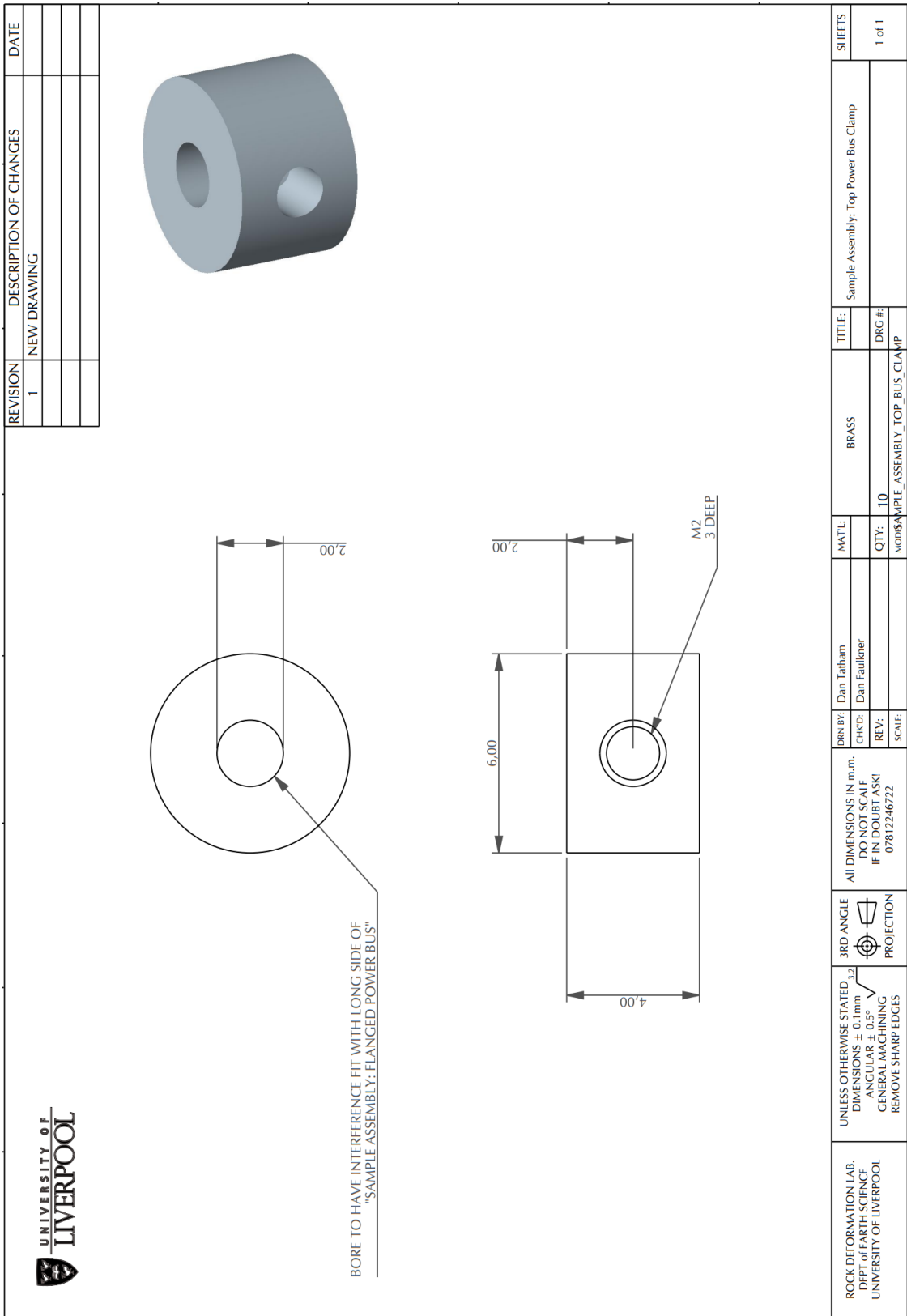


Figure C1.12: Technical Drawing – Bus Clamp.

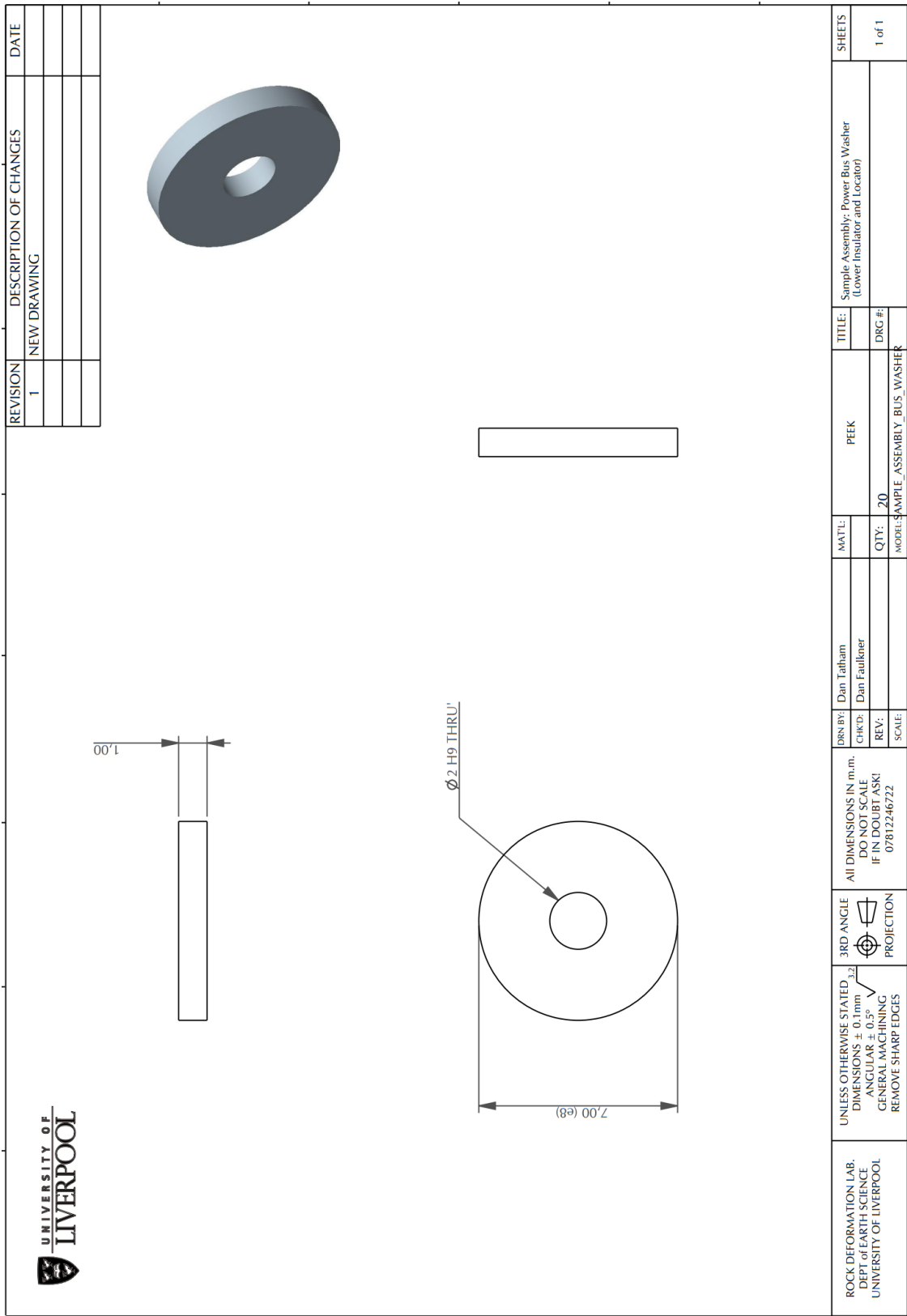


Figure C1.13: Technical Drawing – Bus Washer.

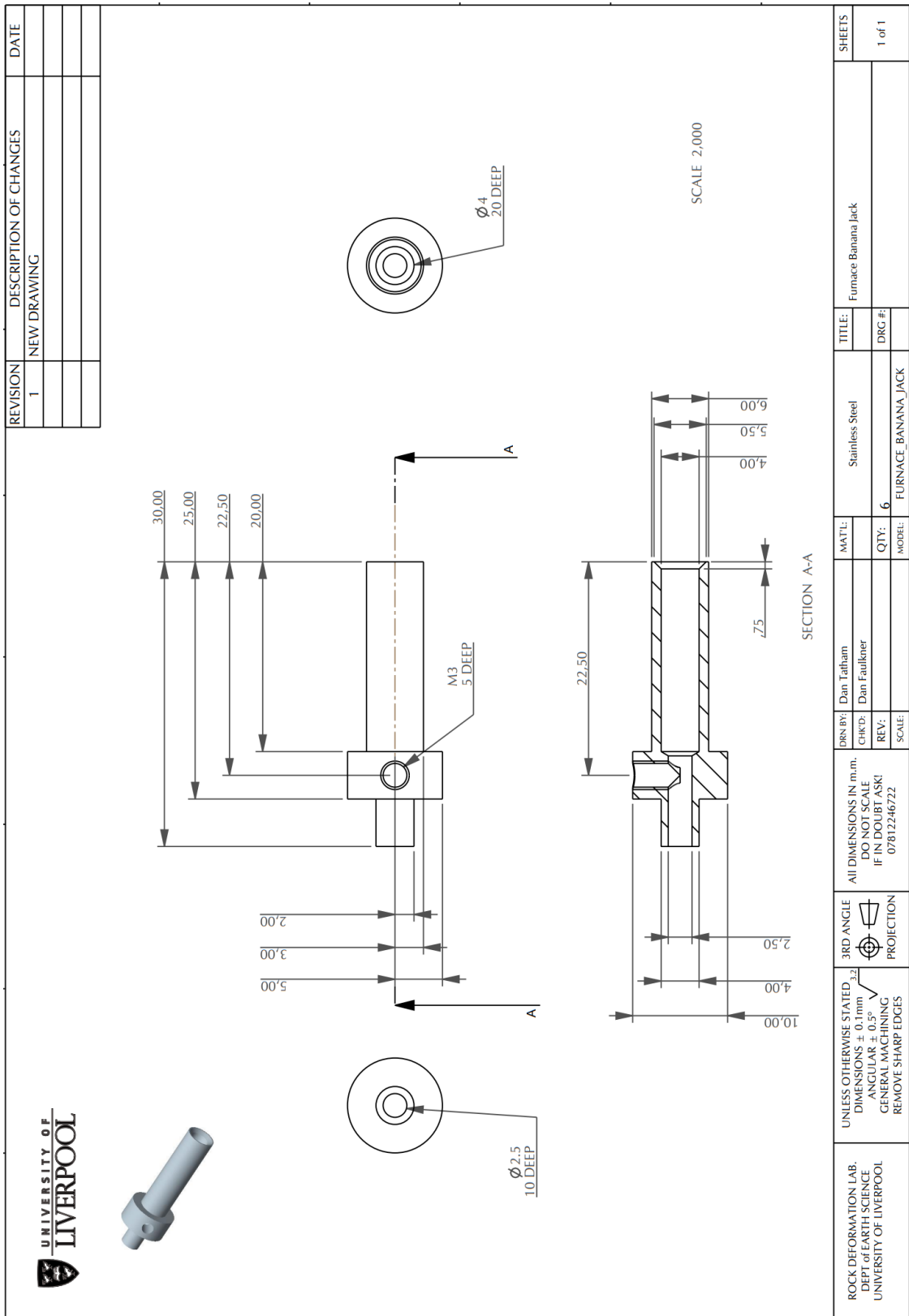


Figure C1.14: Technical Drawing – Banana Jack.

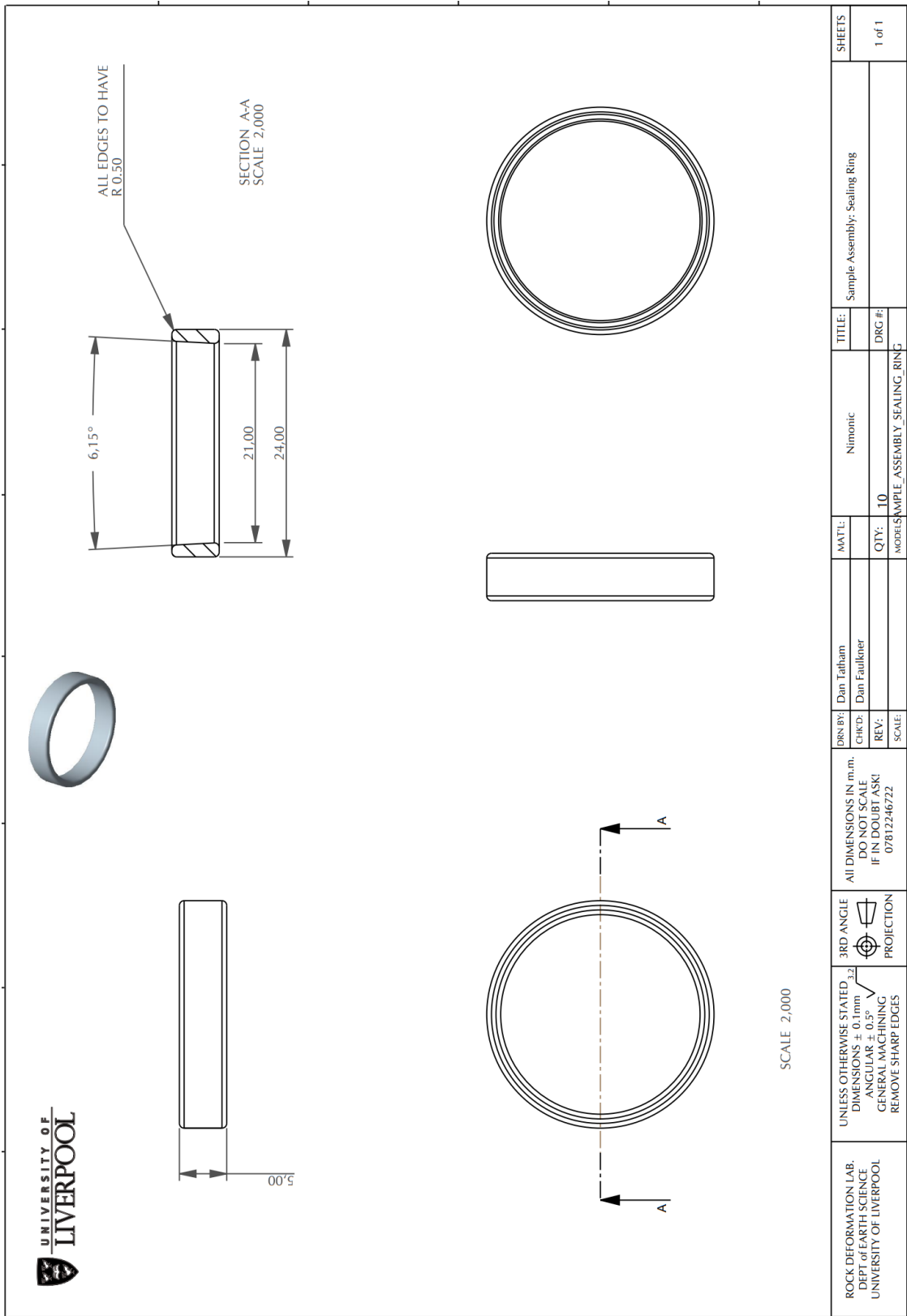


Figure C1.15: Technical Drawing – Sealing Ring.

C2: Data Tables Relevant to Chapter 5

Table C2.1: Design specifics for the furnace, including component dimensions and material properties.

Furnace tube	Alumina
Alumina properties:	Machinable, 92 % alumina; Bulk density = 1550 kgm ⁻² ; Cold crushing strength = 10 kgm ⁻² ; Thermal conductivity = 0.95W/mK at 200C and 0.90W/mK at 1000 °C; Maximum temperature = 1800 °C; Reversible thermal expansion at 80-1000°C = 0.80x10 ⁻⁶ K ⁻¹ (CSC/B-A-180)
Furnace tube dimensions:	Length 145 mm; Outer Diameter 35 mm; Inner Diameter 28.5mm
Furnace coil windings	Kanthal wire
Kanthal wire properties:	FeCr Alloy (Fe72.8 Cr22 Al5 Y0.1 Zr0.1); Density = 7.1 kgm ⁻² ; Maximum temperature = 1400 °C; Diameter = 0.85 mm; Thermal Conductivity = 10.8 W/mK; Tensile Strength = 680 Nmm ⁻² ; Resistivity = 2.502 Ωm ⁻¹ (2.12 Ωmm ² m ⁻¹); Temperature factor of resistivity at 800°C = 1.03; Coefficient of linear thermal expansion, α (20-750°C) = 14x10 ⁻⁶ K ⁻¹
Kanthal wire lengths:	Top Winding = 300 mm coiled + 400 mm end-loop; Middle Winding = 400 mm coiled + 450 mm end-loop; Bottom Winding = 450 mm coiled + 550 mm end-loop; Total length = 2550 mm
Cement	Ceramobond
Ceramobond Properties:	Cerastil V-336 powder, <50 μm particle size; Maximum temperature = 1500 °C; Compressive strength = 35N mm ⁻² ; Water absorption = 2%, Shrinkage = 0.2 %; Coefficient of Thermal Expansion = 9.4ppm K ⁻¹ ; Thermal conductivity = 1.4W m ⁻¹ K; Dielectric Strength = 2.5kV mm ⁻¹ ; Powder:Water mixing ratio = 100:14

Table C2.2: Notable properties of materials used within the assembly. All data sourced are listed within the table, with the exception of electrical conductivity and resistance values that were obtained from ThoughtCo (2018).

Material	Properties
<p>INCONEL (Sample Assembly Parts A-D) (Special Metals Corporation, 2007)</p>	<p>INCONEL® alloy 718 (UNS N07718/W.Nr. 2.4668) is a high-strength, corrosion-resistant nickel-chromium material. Is used in this application as the main material for the sample assembly due to its high strength and resistance to corrosion.</p> <p>Density = 20.81 gcm⁻³ Young's Modulus at 21 °C = 29.0 GPa Young's Modulus at 200 °C = 27.6 GPa Young's Modulus at 425 °C = 25.8 GPa Maximum temperature = 1260 °C Specific Heat Capacity at 21 °C = 0.104 KJkg⁻¹°C Thermal coefficient of expansion at 200 °C = 13.55 x10⁻⁶ °C⁻¹ Thermal coefficient of expansion at 425 °C = 14.35 x10⁻⁶ °C⁻¹ Thermal Conductivity at 21 °C = 133.1 Wm⁻¹°C Thermal Conductivity at 200 °C = 169.5 Wm⁻¹°C Thermal Conductivity at 425 °C = 212.7 Wm⁻¹°C Thermal Conductivity at 20 °C = 9 Wm⁻¹°C Electrical Resistivity at 21 °C = 7.53 Ωmm⁻²m⁻¹ Electrical Resistivity at 200 °C = 7.72 Ωmm⁻²m⁻¹ Electrical Resistivity at 425 °C = 7.84 Ωmm⁻²m⁻¹</p>
<p>STAINLESS-STEEL (Furnace Can and Flanged Bus) (Euro Inox, 2007)</p>	<p>A ferrous alloy containing a minimum of ~11% chromium to prevent corrosion. Used in this application due to its malleability and machinability for thin (1-4 mm diameter) parts and low risk of corrosion.</p> <p>Density = 7.9 gcm⁻³ Young's Modulus at 20 °C = 200 GPa Maximum temperature = 800 °C Specific Heat Capacity at 20 °C = 0.5 KJkg⁻¹°C Thermal coefficient of expansion at 200 °C = 16.5 x10⁻⁶ °C⁻¹ Thermal coefficient of expansion at 25-600 °C = 17.5x10⁻⁶ °C⁻¹ Thermal Conductivity at 20 °C = 15 Wm⁻¹°C Thermal Diffusivity at 25 °C = 7.3 x10⁻⁷ ms⁻² Electrical Resistivity at 20 °C = 0.73 Ωmm⁻²m⁻¹</p>
<p>MACOR® (Internal ceramic plates) (Corning, 2012)</p>	<p>MACOR® is the trade name of a mica glass ceramic developed by Corning. Its composition is ~46 % SiO₂, 17 % MgO, 16 % Al₂O₃, 10% K₂O, 7 % B₂O₃ and 4 % F. Is used in this application as top and base plates for the furnace due to its high machinability and low thermal conductivity.</p> <p>Density = 2.52 gcm⁻³ Young's Modulus at 25 °C = 66.9 GPa Maximum temperature = 800 °C Specific Heat Capacity at 25 °C = 0.79 KJkg⁻¹°C Thermal coefficient of expansion at 25-300 °C = 9.3 x10⁻⁶ °C⁻¹ Thermal coefficient of expansion at 25-600 °C = 12.6 x10⁻⁶ °C⁻¹ Thermal Conductivity at 25 °C = 1.46 Wm⁻¹°C Thermal Diffusivity at 25 °C = 7.3 x10⁻⁷ ms⁻²</p>

Table C2.2 (cont.)

Material	Properties
<p>PEEK (Polyetheretherketone) (Washers, crown nuts and top hats on Bus connections)</p> <p>(The Plastic Shop, 2011; DM Dielectric Manufacturing, 2019)</p>	<p>Polyetheretherketone – a semicrystalline thermoplastic with excellent mechanical and electrical resistance properties retained to relatively high temperatures. It is used in this application to electrically insulate the conducting parts of the bus connections that transfer current via power cables to the furnace windings.</p> <p>Density = 1.23 gcm⁻³ Young's Modulus at 25 °C = 3.76 GPa Maximum temperature = 340 °C Thermal conductivity at 23 °C = 0.25 Wm⁻¹°C Specific Heat Capacity at 25 °C = 1.34 KJkg⁻¹°C Thermal coefficient of expansion (no specified temperature) = 5 to 6 x10⁻⁵ °C⁻¹ Electrical Resistivity at 20 °C = >10⁸ Ωmm⁻²m⁻¹</p>
<p>BRASS (Bus Clamp)</p> <p>(Material Properties, 2019)</p>	<p>A copper-zinc alloy that is malleable, corrosion-resistant and thermally and electrically conductive. Used in this application as it has sufficient electrical conductivity properties so as to allow current to pass through it without significant resistance.</p> <p>Density = 8.53 gcm⁻³ Young's Modulus at ~20 °C = 110 GPa Maximum temperature = 677 °C Thermal conductivity at 20 °C = 120 Wm⁻¹°C Specific Heat Capacity at 20 °C = 0.38 KJkg⁻¹°C Electrical Conductivity at 20 °C = ~60 Wm⁻¹°C Electrical Resistivity at 20 °C = ~0.06 Ωmm⁻²m⁻¹</p>
<p>ALUMINA WOOL (Insulation)</p> <p>(Insulationet, 2019)</p>	<p>Fibres with a diameter of 2-4 microns, with a composition of Al₂O₃ + SiO₂. Used in this application due to its low thermal conductivity, low bulk density and low heat capacity. Its mouldability and compressibility means that it can be shaped around the furnace windings relatively easily, and tightly packed to ensure maximum efficiency It can also be heated and cooled quickly with little effect on its lifespan.</p> <p>Maximum temperature = 650 °C Thermal conductivity at 200 C = ~0.08 Wm⁻¹°C Thermal conductivity at 400 C = ~0.11 Wm⁻¹°C</p>
<p>VITON (Seals)</p> <p>(Viton, 2017)</p>	<p>Viton is a fluoroelastomer best suited for use in high-temperature and extremely corrosive environments, retaining its elasticity for ~48 hours at ~316 °C or for ~3,000 hours at ~232 °C. Used in this application to ensure excellent sealing capabilities at higher temperatures and in the presence of argon confining medium.</p>

Table C2.3: Pressure testing log, checking the sealing points on the new sample assembly. A test is deemed to pass if <5 % confining pressure is lost over 24 hours.

Pressure Test	Date	Pass/Fail	Notes
12 MPa	11/02/2020	Pass*	*<0.1 MPa decrease in pressure over ~8 hours (extrapolated to ~2.5 % per day). Tested without lower piston in place as this was being modified. Hence, the sample configuration was not checked as part of this test. Upstream and downstream pore fluid inputs were 'blanked'. <i>Future testing delayed due to UK government Covid-19 lockdown measures.</i>
5 MPa	29/09/2020	Fail	Leak point either the jacketed sample or confining pressure connection. New jig made to more firmly press stainless-steel rings around the copper jacket to the tapered pistons.
5 MPa	02/10/2020	Fail*	*Pressure dropped to ~3.2 MPa over 7 days (average 5% per day).
5 MPa	09/10/2020	Fail	Upstream end audibly leaking gas; analysis indicated that the copper jacket has been punctured during setup.
5 MPa	09/10/2020	Pass*	*Pressure dropped to ~4.7 MPa over 2 days (average 3 % per day).
10 MPa	11/10/2020	Pass*	*Pressure dropped to ~9.6 MPa over 4 days (average 1 % per day). At this point it was deemed suitable to begin temperature testing.
30 MPa	23/10/2020	Pass*	Due to the small capacity of the gas compressor, pressure increases were made in jumps of ~5 MPa. Between these stages, a pressure decrease of ~0.5 MPa was observed over ~9 minutes. Manual pressure increase was stopped at 24 MPa, at which point temperature increases (to 99°C) were introduced to raise pressures to 30MPa. *Pressure decreased to 27.5 MPa over 7 days (average 1 % per day). <i>Future testing put on hold due to power unit failure – See Section 3.3.5.</i>

C3: Problem Solving - Issues Regarding the Temperature Control Unit

Upon testing and temperature calibration of the furnace (*section 5.3.4*) a problem was encountered in that all fuses were blown once the target temperature had reached ~100 °C. To help understand why this occurred and what modifications could be made to the control unit, the resistance of each furnace winding was measured using a multimeter (**Table C3.1**). Since the furnace windings act as resistors in parallel, each with a resistance of R_1 , R_2 and R_3 respectively (**Figure C3.1**), the total resistance (R_T) can be calculated using Equation C3.1 (Electronics Tutorials, 2020):

$$\frac{1}{R_T} = \frac{1}{R_1} + \frac{1}{R_2} + \frac{1}{R_3} \quad (\text{Eq. C3.1})$$

Hence the total resistance $R_T = ((1/3.1) + (1/7.7) + (1/4.4)) = 1/0.68 = 1.47 \Omega$.

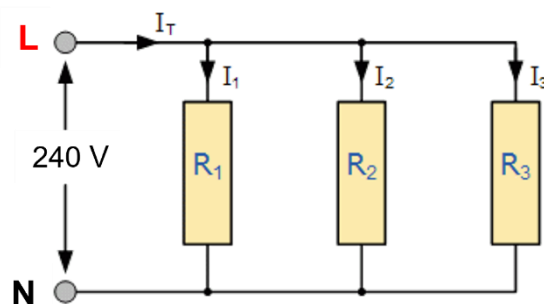


Figure C3.1: The furnace windings act as resistors in parallel (modified from Electronics Tutorials, 2020).

Table C3.1: Total lengths and measured resistances of each furnace coil winding.

Coil	Upper	Middle	Lower
Length of Wire (mm)	750	1500	1000
Measured Resistance (Ω)	3.1	7.7	4.4

The voltage being supplied to the furnace was at the time limited via the WEST controller (*Figure 5.25*) to 5% of the mains voltage (240 V) (i.e. 12 V). Using $I = V/R$, the current being supplied to the furnace windings at the point of failure can be calculated as $I = 12 / 1.47 = 8.16$ A. Using $P = I^2R$, the power at failure can be calculated as $P = (8.16^2) \times 1.47 = 97.96$ W.

Assuming a thermal resistance value of $10.8 \text{ }^\circ\text{C/W}^{-1}$ for kanthal (**Table C2.1**), the maximum temperature that can be achieved with existing components is ~130 °C (**Table C3.2**). To reach a temperature of 400 °C (as anticipated with planned experiments – see *section 5.4*), 320 W of power output is required (**Table C3.2**). Using $P=IV$, it can be calculated that this power output would induce currents of ~6.5 – 10.5 A and requires a potential difference of ~31 – 50 V (**Table C3.3**).

Table C3.2: Power outputs required to achieve different temperatures based on a thermal resistance value for kanthal of 0.8 °C/W¹.

Temperature (°C)	Power (W)
100	80
200	160
300	240
400	320
500	400
600	480
700	560
800	640
900	720
1000	800

Table C3.3: Calculations for current and voltage at room temperature (20 °C) based on the calculated resistances of each furnace winding in Table C3.1.

Power (W)	Resistance (Ω)			Current (A)			Voltage (V)		
	Top	Middle	Bottom	Top	Middle	Bottom	Top	Middle	Bottom
100	3.1	7.7	4.4	5.7	3.6	4.8	17.6	27.7	21.0
200	3.1	7.7	4.4	8.0	5.1	6.7	24.9	39.2	29.7
300	3.1	7.7	4.4	9.8	6.2	8.3	30.5	48.1	36.3
400	3.1	7.7	4.4	11.4	7.2	9.5	35.2	55.5	42.0
500	3.1	7.7	4.4	12.7	8.1	10.7	39.4	62.0	46.9
600	3.1	7.7	4.4	13.9	8.8	11.7	43.1	68.0	51.4
700	3.1	7.7	4.4	15.0	9.5	12.6	46.6	73.4	55.5
800	3.1	7.7	4.4	16.1	10.2	13.5	49.8	78.5	59.3
900	3.1	7.7	4.4	17.0	10.8	14.3	52.8	83.2	62.9
1000	3.1	7.7	4.4	18.0	11.4	15.1	55.7	87.7	66.3

On the basis of these calculations, the addition of an isolating transformer would step the mains voltage down from 240 V to ~60 V, whilst replacing the existing power controllers (which are rated to 10 A operate at 240 V) with thyristor power controllers that can operate at 60 V and up to 15 A is deemed a suitable modification (**Table C3.4**). At the time of writing the modifications to the temperature control unit are still in progress.

Table C3.4: Calculations for current and power at 750 °C assuming mains voltage is stepped down to 60 V.

Voltage	Resistance (Ohms)			Current (A)			Power (W)		
	Top	Middle	Bottom	Top	Middle	Bottom	Top	Middle	Bottom
60	3.33	8.26	4.72	18.0	7.3	12.7	1081.1	435.8	762.7

C4: Calibration Data

Table C4.1: Pressure, temperature and power data from calibration of the furnace.

Run	Confining Pressure (MPa)	Control t/c Temp. (°C)	Height from Base (mm)	Variable t/c Temp. (°C)	Power (Top)	Power (Middle)	Power (Bottom)	P/I/D Settings	Power (%)
1	5	35	12.5	23.4	1	1	1	9/30/5.3	100
1	5	35	99	39	1	1	1	9/30/5.3	100
1	5	35	153	39.2	1	1	1	9/30/5.3	100
1	5	35	230	21.8	1	1	1	9/30/5.3	100
1	5	35	244	20.4	1	1	1	9/30/5.3	100
2	5	44	12.5	25.7	1	1	1	9/30/5.3	100
2	5	44	99	47.7	1	1	1	9/30/5.3	100
2	5	44	153	48.9	1	1	1	9/30/5.3	100
2	5	44	230	24.1	1	1	1	9/30/5.3	100
2	5	44	244	22.4	1	1	1	9/30/5.3	100
3	5	52	0	24.9	2	2	2	1/0.01/1.15	5
3	5	52	10	27	2	2	2	1/0.01/1.15	5
3	5	52	12.5	27.3	2	2	2	1/0.01/1.15	5
3	5	52	20	28.4	2	2	2	1/0.01/1.15	5
3	5	52	30	31	2	2	2	1/0.01/1.15	5
3	5	52	40	34.3	2	2	2	1/0.01/1.15	5
3	5	52	50	37.7	2	2	2	1/0.01/1.15	5
3	5	52	60	41.3	2	2	2	1/0.01/1.15	5
3	5	52	70	45.4	2	2	2	1/0.01/1.15	5
3	5	52	80	48.7	2	2	2	1/0.01/1.15	5
3	5	52	90	50.8	2	2	2	1/0.01/1.15	5
3	5	52	99	53.7	2	2	2	1/0.01/1.15	5
3	5	52	105	55.4	2	2	2	1/0.01/1.15	5
3	5	52	110	56.3	2	2	2	1/0.01/1.15	5
3	5	52	115	57.3	2	2	2	1/0.01/1.15	5
3	5	52	120	57.7	2	2	2	1/0.01/1.15	5
3	5	52	125	58.7	2	2	2	1/0.01/1.15	5
3	5	52	130	59.2	2	2	2	1/0.01/1.15	5
3	5	52	135	59.6	2	2	2	1/0.01/1.15	5
3	5	52	140	59.5	2	2	2	1/0.01/1.15	5
3	5	52	145	58.7	2	2	2	1/0.01/1.15	5
3	5	52	150	57.7	2	2	2	1/0.01/1.15	5
3	5	52	153	57.4	2	2	2	1/0.01/1.15	5
3	5	52	160	57.4	2	2	2	1/0.01/1.15	5
3	5	52	170	55.9	2	2	2	1/0.01/1.15	5
3	5	52	180	53.5	2	2	2	1/0.01/1.15	5
3	5	52	190	48.8	2	2	2	1/0.01/1.15	5
3	5	52	200	44.2	2	2	2	1/0.01/1.15	5
3	5	52	210	37.8	2	2	2	1/0.01/1.15	5
3	5	52	220	30.9	2	2	2	1/0.01/1.15	5
3	5	52	230	27	2	2	2	1/0.01/1.15	5

Table C4.1 (cont.)

Run	Confining Pressure (MPa)	Control t/c Temp. (°C)	Height from Base (mm)	Variable t/c Temp. (°C)	Power (Top)	Power (Middle)	Power (Bottom)	P/I/D Settings	Power (%)
3	5	52	240	24	2	2	2	1/0.01/1.15	5
3	5	52	244	23	2	2	2	1/0.01/1.15	5
3	5	52	250	22	2	2	2	1/0.01/1.15	5
4	30	100	0	22.4	2	2	2	1/0.01/1.5	5
4	30	100	10	-	2	2	2	1/0.01/1.5	5

C5: Laboratory Guidelines for Use of the New HP-HT Assembly on the HY2 Rig

Step-by-step guidelines aimed at future users of the new assembly have been incorporated into a practical guide for a) inserting a sample into the assembly and b) constructing it in the most efficient manner to allow for safe use for the intended purpose.

Part A: *IF* the assembly is currently in the vessel, being kept in an argon atmosphere at low confining pressures, skip to Part B. Part A states how to ensure the bottom part of the assembly is correctly in place assuming it is being kept in the oven at <80 °C.

- Laying the bottom section of the assembly on a stand, ensure that all grub screws are fully in place, the bottom piece is held in place securely within the grooves, and the brass electrical connections are all present and facing outwards.
- Check O-rings for damage and surface for dirt, oil or scratches – clean thoroughly with acetone if necessary, and *report any damage – if in doubt do not proceed to use the assembly.*
- Checking that the correct (labelled) confining pressure inlet pipe is securely in place, hold the assembly piece upright and align so that the circular indent at the top side of the assembly is at the front of the vessel.
- Carefully lower the assembly piece into the vessel, holding the confining pressure pipe and lining up the electrical receivers with the holes in the side of the vessel **[Figure C2.1]**. Some force may be required to ensure it is fully inserted.
- At this point, the lower part of the assembly can be secured in place in the vessel by lifting the top two cooling jackets and inserting the 50mm-long steel rod through the hole in the front of the vessel (this hole is the lowest of 7 in the vessel) **[Figure C2.2]**. Replace the cooling jackets ensuring all holes line up and the water feeds are to the right of the vessel.
- Insert the 6 insulated electrical connections to the furnace through the holes into the vessel, screwing them into the brass connectors in the assembly. The three (red) input feeds should be to the left of the vessel, and the three (black) output feeds should be to the right of the vessel **[see Figure C2.2]**.

Part B: These guidelines assume that the whole assembly is currently kept at low confining pressures in an argon atmosphere within the vessel. They explain how to safely and correctly remove the top piece of the assembly, insert a sample, and replace it ready for an experiment.

1) Removing the top assembly piece from the vessel:

- Remove all confining pressure from the vessel by firstly stopping any automated control via the LabView software, and secondly by *slowly* letting gas escape by gently loosening the nut connecting the confining pressure inlet pipe to the elbow above the vessel. You should hear a steady, quiet hiss.
- Fully disconnect the confining pressure inlet pipe and remove the elbow and nut from the top of the straight pipe in the assembly.
- Remove the top nut from the vessel.
- *Carefully* lift out the top piece of the assembly, ensuring that it is lifted out steadily and vertically so that the top assembly piece, sample and lower piston come out together. Note that the total length to be removed is equal to the height of the vessel.
- Should the sample and/or lower piston not lift out with the top piece of the assembly, use a suitable tool (e.g. long pliers with insulating tape on the metal prongs) to grasp the dropped piece from the vessel, and *carefully* (i.e. without scraping the sides) lift them out of the vessel.

2) Installing a sample and inserting the top assembly piece into the vessel:

- Place a 50mm long, 20mm diameter core sample into an annealed copper jacket with a 2mm porous disk on either side.
- Using the Arbor press and custom jig, press a ring over the jacket to close it onto the lower piston **[Figure C2.3]**.
- Using the same method, press to close the other side of the jacketed sample onto the top piece of the assembly. Ensure that the resulting single piece is straight by using a ruler.
- Check all O-rings are in good condition – if not, replace them.
- In the rig, check all electric feedthroughs are earthed properly by systematically using a multimeter.
- Feed the pore pressure pipe through one of the holes in the top part of the assembly.
- *Carefully* lower the top assembly piece + sample + lower piston into the vessel containing the lower part of the assembly, and press firmly down, ensuring that the nuts for the pore fluid and confining pressure inlets smoothly insert into the receiving holes **[Figure C2.1b]**.
- Screw the vessel top nut in place fully; add a high-pressure nut to the ends of both the pore fluid pipe and the confining pressure pipe before connecting them tightly.

- Connect the top, middle and lower furnace coil control cables to the input and output insulated rods in the side of the vessel, following **Figure C2.2**, and tighten the grub screw. *Double check that connections have been made correctly and securely.*
- Insulate the grub screw using insulation tape.
- Check that all cooling jackets are in place, with hose connections tight and not leaking.
- Proceed to ‘running an experiment’ guidelines.

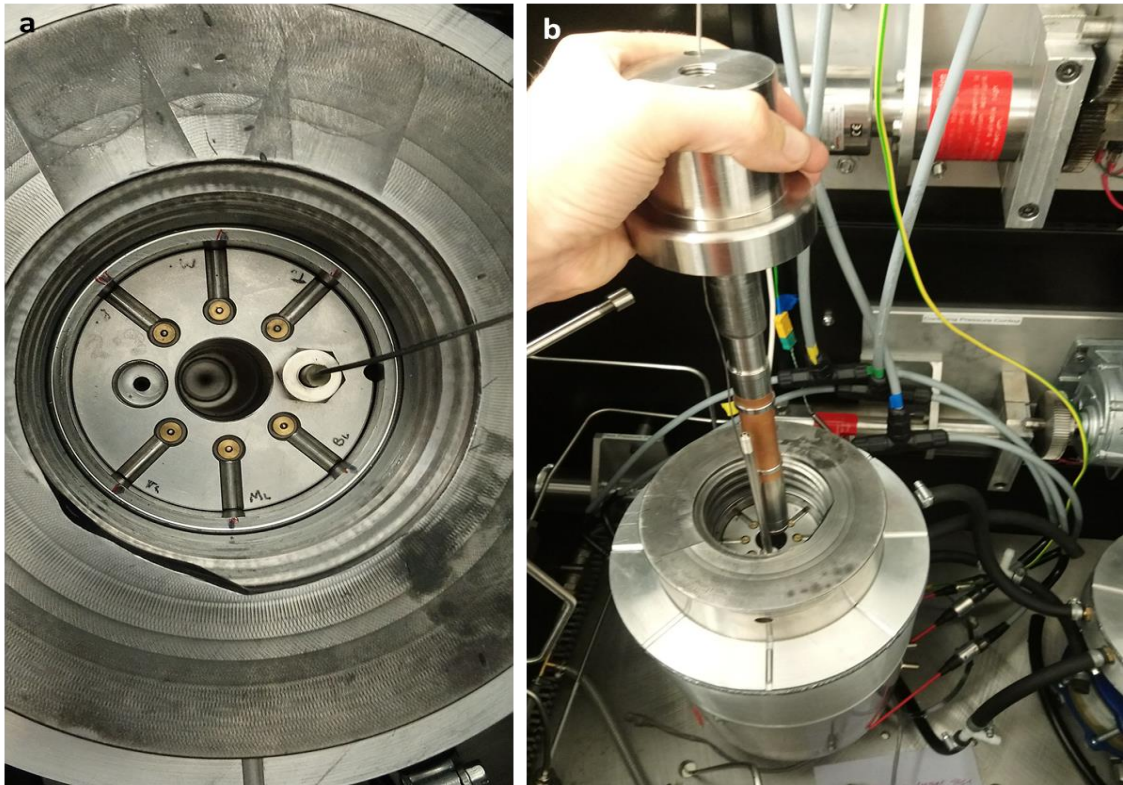


Figure C2.1: *a) Top-view photograph showing the constructed assembly (without Sample Assembly B in place) within the pressure vessel. The tracks on the upper side of Sample Assembly A, through which insulated rods forming the ends of power cables are later fed, and the brass Top Bus Clamps are clearly visible around the central bore. Downstream pore fluid input is on the right, whilst confining pressure pipework feeds through the bore on the left. b) Photograph showing how Sample Assembly B, with jacketed sample and Sample Assembly C attached as in Figure C2.3, is inserted into the central bore, which is then held in place within the pressure vessel by the top nut.*

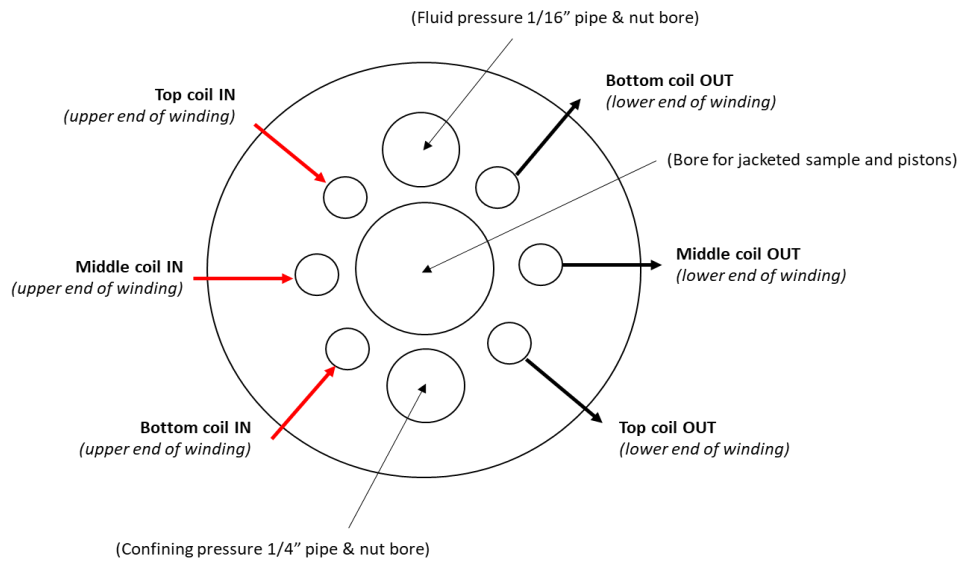


Figure C2.2: Schematic diagram showing a top view of Sample Assembly A, illustrating how connections are made between the temperature control box and the sample assembly.

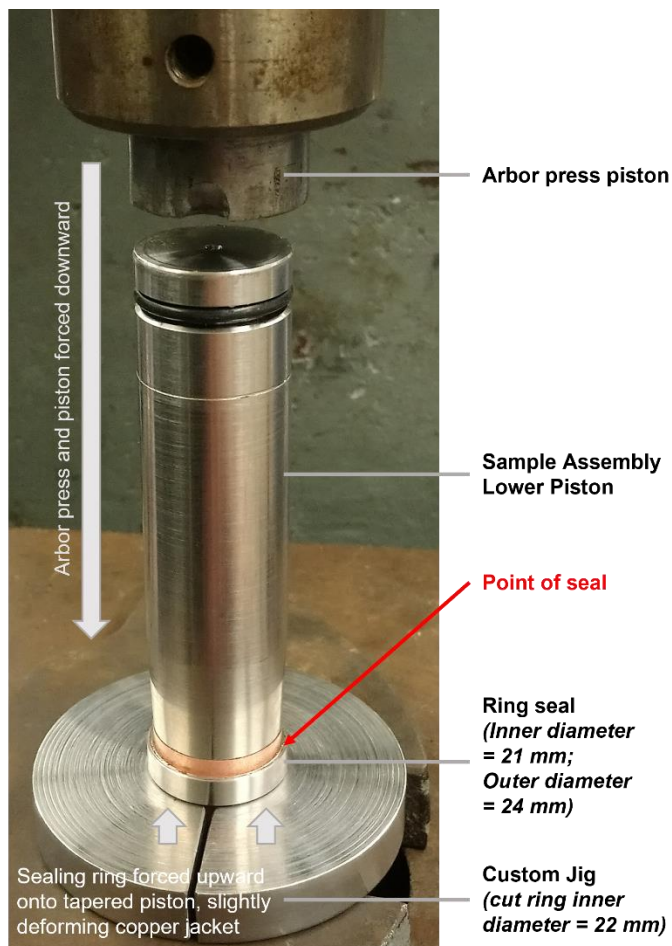


Figure C2.3: Photograph showing the Arbor press and custom ring jig methodology to correctly affix the sealing ring over the sample-bearing copper jacket and onto the tapered piston, ensuring a good seal.

Digital Appendices

The following datasets are also provided as a digital appendix in .xlsx format:

- Beynon_Chapter_2&3_Main_Dataset
(1D field transect data and experimental laboratory data used within Chapters 2 and 3, and associated subsequent analyses)
- Beynon_Chapter_2_FracPaQ_Data
(Vein trace map data and exported map data from FracPaQ, relevant to Chapter 2)
- Beynon_Chapter_3_Orientations_Bias_Corrected
(Bias-corrected orientation data for each 1D field transect, relevant to Chapter 3)
- Beynon_Chapter_4_Main_Dataset
(Experimental data and subsequent analyses relevant to Chapter 4)